Structure and Dynamics by Experiment and Theory: Concerted Applications of Gas Electron Diffraction and Computational Chemistry

Conor Douglas Rankine

Doctor of Philosophy

University of York

Chemistry

June 2019

To everyone in the C/A/057 Phys. Chem. Office:

"*Well …whatever* [your plan] *was, I'm sure it was better than my plan to get out of all this by pretending to be mad. I mean, who would have noticed another madman 'round here?*"

Edmund Blackadder.

"Goodbyeee". Blackadder Goes Forth. BBC. 2 Nov. 1989.

Abstract

To plan and prepare the strongest research proposals for time-resolved gas electron diffraction (TRGED) experiments, the author has launched and overseen the development of two new research programmes in the Wann Electron Diffraction Group.

A time-averaged gas electron diffraction (GED) programme has seen the technique re-established in the UK following the relocation, recommission, and modernisation of a 1960s gas electron diffractometer. Two case studies – a) 4-(dimethylamino)benzonitrile, and b) tin^{II} bis(trifluoroacetate), $ditin^{II}$ μ-oxy-bis-μ-trifluoroacetate, and tin^{IV} tetrakis(trifluoroacetate) – highlight the range of chemical samples that are accessible to study using the upgraded gas electron diffractometer. A computational chemistry programme has seen trajectory surface-hopping dynamics (TSHD) introduced to the Wann Electron Diffraction Group, delivering a paradigm shift in the ability of the research group to plan and interpret TRGED experiments. Parallel Python code has been developed to simulate TRGED data and benchmarked with up to 64 CPU cores as part of this programme. High performance is achieved in the strong and weak parallel scaling regimes.

The interplay between the two programmes is illustrated in three case studies: the photolysis of 1,2-diiodotetrafluoroethane, the photofission of the disulfide bond in 1,2-dithiane, and the photoisomerisation of *E*-cinnamonitrile.

The photolysis of 1,2-diiodotetrafluoroethane is found to take place on the triplet excited-state manifold, and statistical analysis has revealed that secondary dissociation of $I^{\bullet}$ from the primary photolysis product is more likely following primary photolysis of the antiperiplanar (as opposed to the synperiplanar) isomer of 1,2-diiodotetrafluoroethane. A transient bridged intermediate has been characterised for the first time at the intersection of the D_1 and D_0 states; the intermediate may appear in less than 100 fs post-photolysis.

The photofission of the disulfide bond in 1,2-dithiane is found to trigger a classically-intuitive "*Molecular Clackers*" mechanism that couples the S_1 and S_0 states, challenging contemporary understanding of the origin of the photostability of 1,2-dithiane. The "*Molecular Clackers*" mechanism drives periodic collisions between the termini of a transient thiyl biradical that can result in $S_0 \leftarrow S_1$ internal conversion and the permanent recoupling of the termini, repairing the broken disulfide bond on the picosecond timescale.

The photoisomerisation of *E*-cinnamonitrile is revealed to be wavelength-dependent, and several key $S_0 \leftarrow S_1$ internal conversion pathways have been characterised for the first time.

Contents

List of Figures

List of Tables

Acknowledgements

This thesis goes out to…

…Derek Wann, for welcoming me into his research group (over five years ago!), for always having confidence in me, and for encouraging me to have that same confidence in myself. The best academic supervisors give their students the freedom and gentle guidance that they need to launch their own independent academic careers and succeed or fail on their own terms. Derek understands this. He is one of the best.

…João Pedro Nunes, for all the late nights spent troubleshooting our gas electron diffractometer, and every beer we broke out in celebration or commiseration! He is a peerless experimentalist; every hack I know in gas electron diffraction, I learnt from Pedro.

…Fiona Whiting, for all the boardgames we played, and all the gossip! She kept Pedro and me sane; we would have burnt out fast without Fiona.

…everyone else in the C/A/057 Phys. Chem. Office, for the *bon homie* and the delicious cake. A special shout-out to Tomas Lock Feixas, Michi Burrow, Natalie Wong, Jacob Berenbeim, and Fraser Hill-Casey who, in particular, have made these last few years incomparably great by bringing top-shelf banter to our aisle.

…Matthew Robinson, Stuart Young, and Paul Lane, for making me feel at home in the C/A/057 Phys. Chem. Office from day one of my undergraduate summer studentship. I stayed around for the next five years thanks – in no small part! – to their encouragement.

…Andrew Smith at the York Advanced Research Computing Cluster (YARCC), for the bash/scheduler tricks that kept my code running fast and smooth for the last three years.

…Stuart Murray and Mark Roper, Chris Rhodes and Tim Ayers, and Abi Mortimer, at the Department of Chemistry Mechanical, Electrical, and Glassware Workshops, respectively; recommissioning a vintage gas electron diffractometer takes a talented team of artisans!

…the Engineering and Physical Sciences Research Council (EPSRC), who funded the first three years of this research programme (EP/1651146), and…

…my parents, Carol and Doogi Rankine, who bankrolled the subsequent write-up!

…Sarah Vaughan – my partner in all things – for critiquing (and unreservedly judging!) my mathematical equations, and for her love and support. I know Sarah will be proud of me; that alone is enough to make this whole experience worthwhile.

Authorship Declaration

I (the author) declare that this thesis is a presentation of original work, and that I am the only author of its contents. This thesis has not previously been presented for an award at this – or, indeed, any other – university. All sources are acknowledged duly by reference.

Chapter 4 draws heavily from peer-reviewed, published work by the author ("*The Structure of 4-(Dimethylamino)benzonitrile Using Gas Electron Diffraction: A New Lease of Life for the Only Gas Electron Diffractometer in the UK*"; C. D. Rankine, J. P. F. Nunes, T. W. B. Lock Feixas, S. Young, and D. A. Wann, *J. Phys. Chem. A.*, 2018, **122**, 5656 – 5665) and from the contribution of the author to collaborative work that is at the pre-print stage ("*Supramolecular Organization and Evaporation of Polymeric Tin Trifluoroacetates*"; G. Bačić, C. D. Rankine, J. Masuda, D. A. Wann, and S. T. Barry, 2019, chemrXiv.7586459).

Chapter 6 draws heavily from peer-reviewed, published work by the author ("*A Theoretical Investigation of Internal Conversion in 1,2-Dithane Using Non-Adiabatic Multiconfigurational Molecular Dynamics*"; C. D. Rankine, J. P. F. Nunes, M. S. Robinson, P. D. Lane, and D. A. Wann, *Phys. Chem. Chem. Phys*., 2016, **18**, 27170 – 27174).

The author also claims authorship of an additional piece of peer-reviewed, published work ("*The Structure of Tris(chloromethyl)amine in the Gas Phase Using Quantum Chemical Calculations and Gas Electron Diffraction, and as a Solid and Melt Using Raman Spectroscopy*"; C. D. Rankine, S. J. Atkinson, M. R. Waterland, S. L. Masters, and D. A. Wann, *Struct. Chem.*, 2018, 29, 803 – 818) that is not featured in this thesis, but is declared here, nonetheless, to be a product of the research programmes detailed herein.

Conor Rankine

1 Motivation: Time-Resolved Gas Electron Diffraction

1.1 Photochemistry, and "Photographing in the Dark"

Photochemistry is – in lay terms – the study of chemical and physical processes involving light. It is best abstracted as the study of the temporal evolution of electronic and nuclear wavepackets following their perturbation by the absorption or emission of radiation. The absorption of radiation in the visible/ultraviolet (UV) region of the electromagnetic spectrum (*ca.* 200 – 700 nm) is usually sufficient to promote transiently a molecule into a (valence) electronically-excited state. The electronic and nuclear wavepackets then respond to the perturbation, leading either to non-radiative deactivation of the electronically-excited state, or to the emission of radiation after a delay. The entire photochemical process may be over in a few tens or hundreds of femtoseconds – less than one billionth of a second.

The "*Age of Femtochemistry*",[1] beginning with the commercialisation of the femtosecond laser, has seen researchers equipped with powerful time-resolved spectroscopies for studying photochemical processes. Experiments on the same timescale that chemical bonds break and form would have been impossible to imagine only one generation ago and yet, today, the reader could buy an off-the-shelf, table-top time-resolved spectrometer and use it to carry out such experiments in their own laboratory; moreover, they could do it in a "*plug-and-play*" manner. The time-resolved spectrometer is responsible for the contemporary distinction between chemical kinetics and dynamics; kineticists are concerned with the reactants, products, and transition states of a chemical reaction (species that can be trapped/stabilised and subsequently measured), whereas dynamicists – empowered by the time-resolved spectrometer – have been able to investigate the processes that take place between these points. Almost all experimental evidence of electronic and nuclear wavepacket dynamics comes from time-resolved spectroscopy, but the information provided by such experiments on the nuclear wavepacket is second-hand. Nuclear wavepacket dynamics can only be inferred by monitoring the temporal evolution of some other observable, *e.g.* the intensity/wavelength of absorption/emission, the production of photofragments, the response of nuclear spins to an applied magnetic field, *etc.*, and then by using intuition (often coupled with computational chemistry) to interpret the data.

One would ideally like to track directly the temporal evolution of the nuclear wavepacket, and then complement such studies with information on the electronic wavepacket derived

from time-resolved spectroscopies and/or computational chemistry – the latter providing information on both wavepackets simultaneously. But what exactly are the requirements for this, besides the obvious – substituting spectroscopy for diffraction?

The reader is likely already familiar with the principles of "*stop-motion*" photography, which uses cameras with fast mechanical shutters to record photographs of objects in motion. If the mechanical shutter can actuate faster than the object that is being photographed, the object will appear stationary, *i.e.* without motion blurring.[2] The object is said to be temporally resolved as opposed to temporally averaged. The shutter should actuate faster than some characteristic time, τ, for an object of dimension d and speed s; an approximate relationship between τ, d, and s is defined in Eq. 1.1.[2]

$$\tau \approx \frac{d}{s} \qquad \textbf{Eq. 1.1}$$

The reader is invited first to consider a golf ball punching through a melon (Fig. 1.1). A golf ball has a diameter of *ca.* 4 cm ($d \approx 0.04$ m), and a professional golfer could drive the ball at *ca.* 180 mph ($s \approx 80$ m s^{-1}). Here, $\tau \approx 5\times10^{-4}$ s, and so the frames in Fig. 1.1 could have been photographed using a camera with a fast mechanical shutter (although this would have to be a high-quality camera; the fastest mechanical shutters today actuate on an approximately comparable timescale).

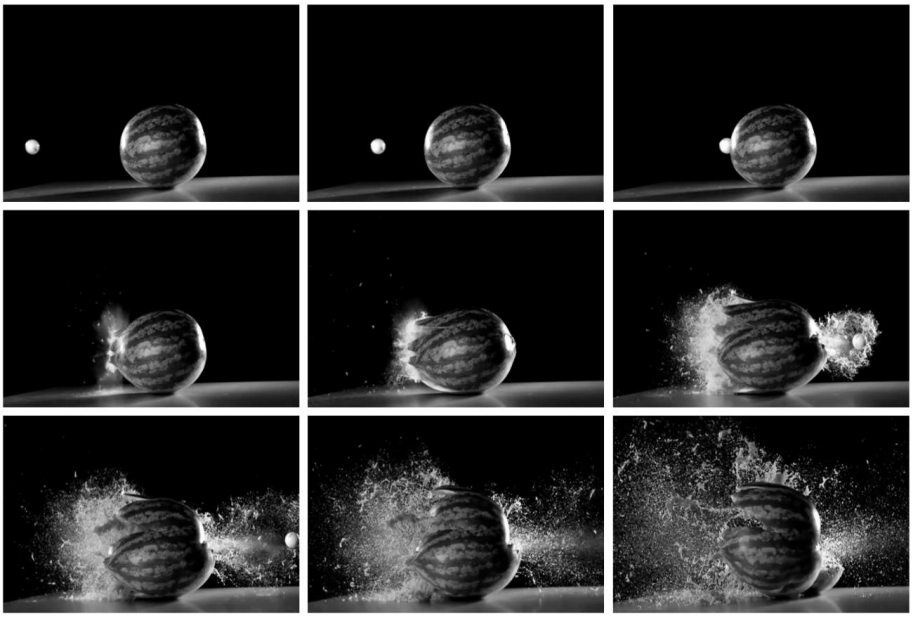

Figure 1.1. Individual frames from a slow-motion video of a golf ball punching through a melon – the frames are presented as an illustration of how objects in motion can be "*frozen*" by "*stop-motion*" or "*stroboscopic*" photography. Screen-captured from Ref. 3.

In this case, however, the golf ball was not driven by a professional golfer. It was fired from a gun, probably at *ca.* 1000 mph ($s \approx 450$ m s^{-1}). Under these conditions, $\tau \approx 1\times10^{-6}$ s; there are no mechanical shutters capable of actuating this fast. To photograph objects in motion at this speed, "*stroboscopic*" photography is used. The camera shutter is left open, and the photograph is taken in the dark. The object in motion is only illuminated for a moment by a sub-μs flash, or "*strobe*", of white light. The principle of "*stroboscopic*" photography underpins all ultrafast time-resolved diffraction/imaging techniques; Sciaini writes that "*…femtosecond… X-ray and electron diffraction techniques are all based on* [this]*: photographing in the darkness.*"[2]

An atom is *ca.* 0.1 – 0.5 nm in diameter ($d \approx 1\times10^{-10}$ m), and the lowest-frequency vibrational modes in a molecule are usually *ca.* 10 – 100 cm^{-1}. A 0.1 nm displacement along one of these vibrational modes ($s \approx 1000$ m s^{-1}) gives $\tau \approx 100$ fs. Sciaini and Miller note that a similar result is obtained from a kinetic treatment;[2,4] the (unimolecular) Arrhenius prefactor (*ca.* 1×10^{13} s^{-1}) – invoked in the context of barrier-crossing kinetics – corresponds to a sampling time of *ca.* 100 fs. The grand challenge in time-resolved diffraction is exactly this: to study the transient structures of barrier-crossing and surface-hopping photochemical processes.[5] The requirement, then, is this: one has to be able to generate ultrashort (*e.g.* fs, certainly sub-ps) "*strobe*" pulses of an appropriate wavelength (*ca.* 10 nm or less) with sufficient coherence to resolve spatiotemporally the structural dynamics of a molecule in motion.[2,4–6] Furthermore, the source that one uses to generate these "*strobe*" pulses has to provide sufficient flux/be brilliant enough to a) permit (condensed-phase) diffraction experiments as close as possible to the single-shot limit, and b) permit (gas-phase) diffraction experiments where the sample density may be low.[2,4–6] This is a tall order!

The choices distil down to time-resolved X-ray diffraction (TRXRD) and time-resolved electron diffraction (TRED).[2,4–6] Both TRXRD and TRED can be applied in the condensed and gas phase. This thesis is concerned exclusively with how one plans and proposes experiments in gas-phase TRED, although the author acknowledges landmark achievements in condensed-phase TRED in Section 1.3; indeed, any history of electron diffraction (ED) would be otherwise incomplete. The author distinguishes thusly: the acronyms TRGED and TRGXRD are introduced for gas-phase diffraction experiments, and the acronyms TRED and TDXRD are reserved for their condensed-phase counterparts. Similarly, the acronyms GED and GXRD are introduced for the time-averaged gas-phase counterparts, while ED and XRD are reserved for the time-averaged condensed-phase experiments.

1.2 Time-Resolved Electron Diffraction

1.2.1 What Is Time-Resolved Gas Electron Diffraction?

A (table-top, or miniaturised) TRGED experiment[2,4–6] is illustrated schematically in Fig. 1.2. One branch of a femtosecond laser – the pump pulse, **A** – is used to populate one or more electronically-excited states in an ensemble of gas-phase molecules, **B**, delivered into the experimental chamber *via* a nozzle, **C**. Another branch of the femtosecond laser – the probe pulse, **D** – is used to illuminate a thin-film photocathode, **E**, generating packets of photoelectrons, **F**, *via* the photoelectric effect. The photoelectron packets are accelerated to high velocity by an anode plate, **G**. Coulombic forces cause the photoelectron packets to broaden longitudinally (*i.e.* in time) and laterally (*i.e.* in space) as they propagate[2,4–6] towards the point of diffraction, **H**. The Coulombic forces – not the temporal profile of the femtosecond laser – dictate the temporal resolution.[2,4–6] One can reduce the number of electrons per packet (trading off against a lower signal-to-noise ratio and longer data acquisition times), accelerate the photoelectron packets to relativistic velocities (requiring beamtime at a national accelerator facility), or reduce the propagation distance,[2,4–6] but it is usual, in any case, to find electron optics between **G** and **H** for reshaping the profile of, or recompressing, the photoelectron packets.

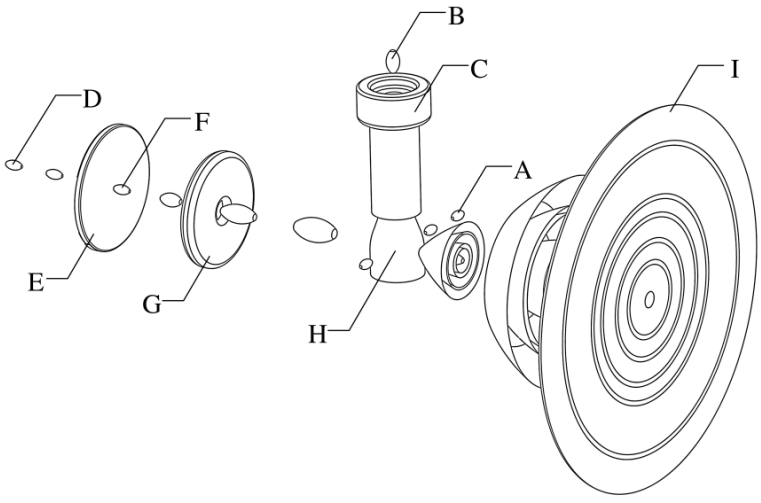

Figure 1.2. Schematic of the contemporary TRGED experiment. The optical pump pulse (**A**), gas-phase sample (**B**), sample delivery nozzle (**C**), optical probe pulse (**D**), thin-film gold photocathode (**E**), photoelectron probe pulse (**F**), anode (**G**), point of diffraction (**H**), and detector plane (**I**) are indicated.

The photoelectrons interact with the gas-phase molecules according to scattering equations (Section 2.1) at **H** and are recorded at the detector plane, **I**. The pump pulse clocks the experiment; the time of arrival of the photoelectron pulse relative to the pump pulse is controlled by adjusting the difference in optical path length between the pump and probe branches. TRGED data are acquired as a function of photoelectron pulse delay.

TRGED developed from GED (Section 1.3). A GED experiment is illustrated schematically in Fig. 1.3 for comparison. GED is one of the two central research programmes associated with this project (Section 1.4); consequently, Chapter 2 is given over to a thorough description of the underlying theory and the contemporary experiment. Here, only the key differences are highlighted to familiarise the reader with the technique: the electron beam is continuous (*e.g.* it is produced *via* continuous thermionic emission from a filament) and there are no lasers; time-averaged data are acquired for the electronic ground state.

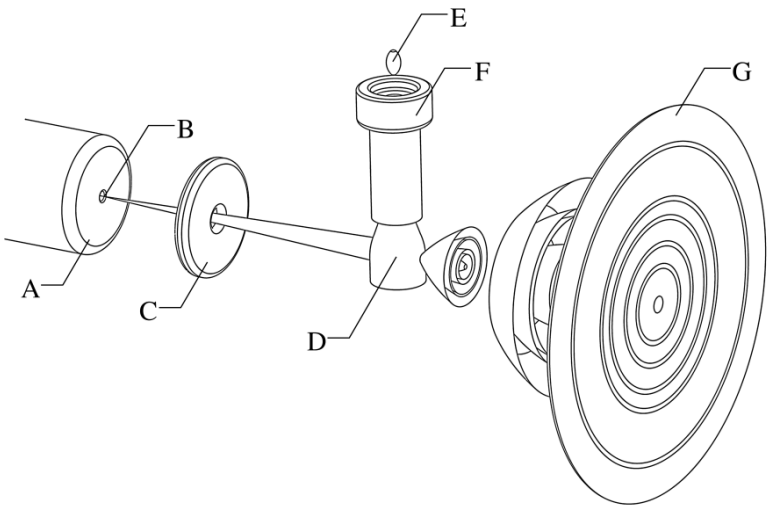

Figure 1.3. Schematic of the contemporary GED experiment. The continuous electron beam source (**A**), continuous electron beam (**B**), anode (**C**), point of diffraction (**D**), gas-phase sample (**E**), sample delivery nozzle (**F**), and detector plane (**G**) are indicated.

1.2.2 Why This?

In principle, one does not have to use photoelectron packets as the probe pulse (Section 1.2) in time-resolved diffraction experiments. However, as Kirrander *et al.* acknowledge in their theoretical comparison of TRGED and TRGXRD, "*…the bet on electron diffraction was clever, because it echoed a similar development in the early days of* [time-averaged] *gas-phase diffraction, where electrons came to supersede X-rays.*"[7] It is no coincidence that the

two Nobel laureates Pauling and Zewail – the fathers of chemical structure and structural dynamics, respectively – began their careers in electron diffraction.

TRGED has three key advantages over TRGXRD and other time-resolved diffraction experiments. Firstly, photoelectron optics/accelerating structures and photoelectron packet generation are better understood and easier, respectively[2,4–6] – this is an important consideration for researchers engaged in the development of table-top/miniaturised implementations. Secondly, photoelectrons interact with both the electronic charge and the nuclei in a molecule (*cf.* X-rays, which interact only with the former, and neutrons, which interact only with the latter); the amount of information that one can obtain *via* TRGED – particularly on photochemical processes – is greater.[2,4–7] Thirdly, photoelectrons have a scattering cross section that is several orders of magnitude (10^4 – 10^6) larger than that of an X-ray of the same energy, and consequently interact more strongly with matter.[2,4–7] A consequence of the latter point is that one does not require such high fluency and such long exposure times in TRGED, compared with TRGXRD, to record data with a comparable signal-to-noise ratio.[2,4–6] Sources of femtosecond X-rays with sufficient brilliance for TRGXRD, *e.g.* synchrotrons and X-ray free-electron lasers (XFEL), are found exclusively at national accelerator facilities and, even though XFEL sources have improved on the brilliance of synchrotron sources by many orders of magnitude in recent years, the same effective brilliance (adjusted for the scattering cross section of the electron) has been obtained in table-top time-resolved gas electron diffractometers.[2]

Beyond TRGED, the high-fluency, brilliant photoelectron sources available today are sufficient, in many cases, for data to be acquired at, or close to, the single-shot limit. This is of paramount importance in TRED, where a maximum exposure time is imposed necessarily by the tolerance of the sample to damage, either from repeated photoexcitation by the pump pulse, or by the probe pulse itself.[2,4–6,8] Not only are photoelectrons less likely to scatter inelastically than X-rays, they deposit less energy to the sample when they do.[8] The energy that photoelectron packets deposit is also more or less independent of the photoelectron beam energy; for X-rays, however, this is not the case.[8] At higher X-ray beam energies, Compton and Auger processes may be activated.[8]

The reader might consider whether time-resolved scattering experiments using packets of other massive particles, *e.g.* neutrons or protons, are possible. While Miller *et al.* have recognised the potential of "...*new* [TRED] *machines* [with] *the ability to use alternative or multiple particle sources… for example, high-energy protons as a probe* [to] *open up a*

completely new window on structural dynamics",[5] and neutron diffraction is a well-established technique, there are very few facilities available for such time-resolved scattering experiments worldwide, and the best temporal resolution (in neutron diffraction) has so far been limited to a few tens or hundreds of milliseconds.[9]

1.2.3 Why Now?

The following should encourage the reader: the popularity (Fig. 1.4) and temporal resolution (Fig. 1.5) of TRGED are on upward and downward trajectories, respectively.

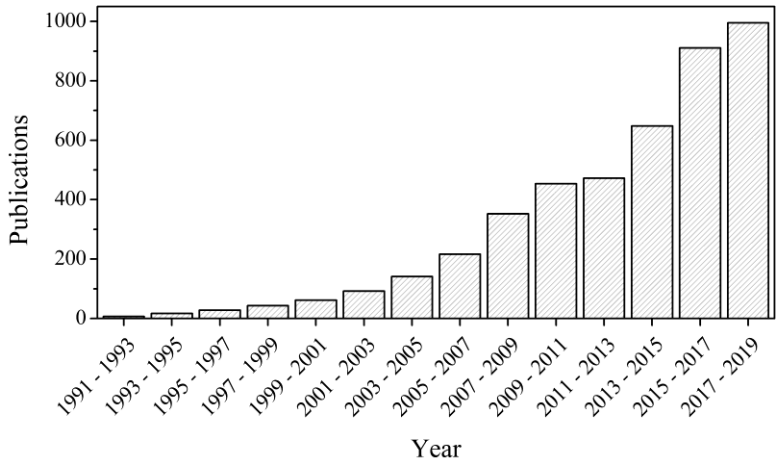

Figure 1.4. Number of publications containing the term "*time-resolved electron diffraction*" or "*ultrafast electron diffraction*" by date, obtained *via* a search on Google Scholar.

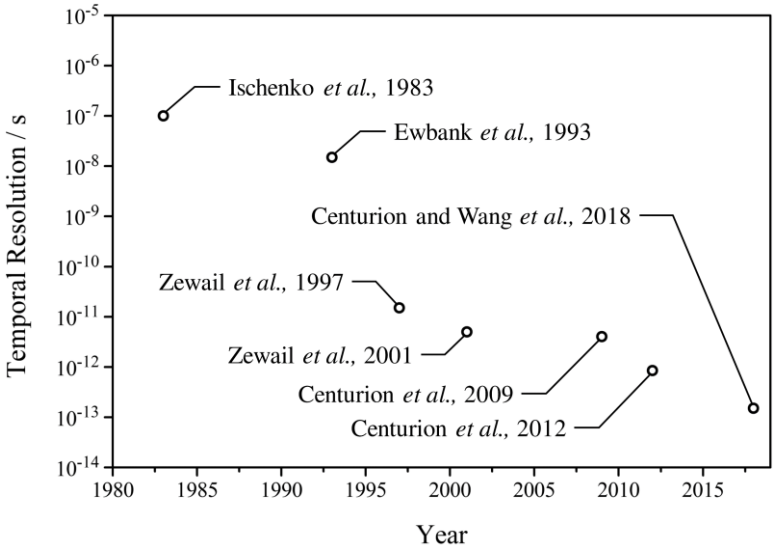

Figure 1.5. Temporal resolution reported in landmark TRGED experiments (Section 1.3) by date. Scatter points are derived from Refs. 10–16.

Landmark TRGED studies that couple experiment and theory have been carried out at the SLAC National Accelerator Laboratory (Stanford, US) by Centurion, Wang, and Martínez during the last twelve months.[16–18] The authors report a record sub-200-fs temporal resolution (*ca.* 150 fs; 1×10^4 photoelectrons/packet), with the coveted 100-fs temporal resolution being well within reach.[16–18] Indeed, their work demonstrates that TRGED experiments that were not possible when the author started compiling this thesis are possible today. The success of Centurion, Wang, and Martínez in "*…resolving the atomic motion on femtosecond timescales for the photochemistry of polyatomic organic molecules that contain exclusively light elements with small scattering cross-sections* …[represents] *a milestone that enables* [TRGED] *for general investigations of ultrafast gas-phase organic photochemistry.*"[18] Their proven ability to acquire TRGED data that allows for "*…a reliable* [and direct] *transformation into real space …without any input from theory or simulation …allows* [one] *to compare …data directly with ab initio simulations of the reaction dynamics*[;] *…as the theory and experiment are completely independent of each other, …comparison provides a compelling test of both.*"[18]

Moreover, the accessibility of TRGED is set to increase. An emerging TRGED programme at Daresbury Laboratory (Daresbury, UK) promises to bring the technique to the UK. New programmes of research at the SLAC National Accelerator Laboratory and Deutsches Elekronen-Synchrotron (DESY; Hamburg, Germany) are expanding the applicability of the technique. China has committed to invest in both the expansion of the existing TRGED programme at the Tsinghua Thomson X-ray Facility (TTX; Beijing, China) and the launch of a new TRGED programme at the Synergetic Extreme Condition User Facility (SECUF; Beijing, China).

The author expects researchers to soon dispense with the tagline "*Towards Time-Resolved Electron Diffraction*"; indeed, the author can only conclude that the "*Era of Atomically-Resolved Dynamics*"[4] has already arrived. To understand how this has happened, and to familiarise themselves with landmark experiments in TRGED/GED, the reader is invited to take a tour through the history of the ED technique (Section 1.3).

1.3 Electron Diffraction 1924 – 2019

The use of an electron beam for diffraction experiments followed from de Broglie's formulation of the relationship between the momentum and wavelength of a particle in 1923 (Section 2.1) – the earliest recognition of the universal duality of particles and waves.[19]

Davisson and Germer (Fig. 1.6a) inadvertently proved the de Broglie hypothesis in 1927 while attempting to study the surface of a crystal of nickel.[20,21] Their experiment (Fig. 1.6b) involved directing an electron beam at a crystal and monitoring how the number of backscattered electrons varied as a function of the angle made by the detector and the surface of the crystal.[20] Instead, Davisson and Germer recorded electron diffraction[21] that was consistent with the laws of Bragg and Bragg.[22] Both were awarded the Nobel Prize in 1937 for their work, as Bragg and Bragg had been in 1915.

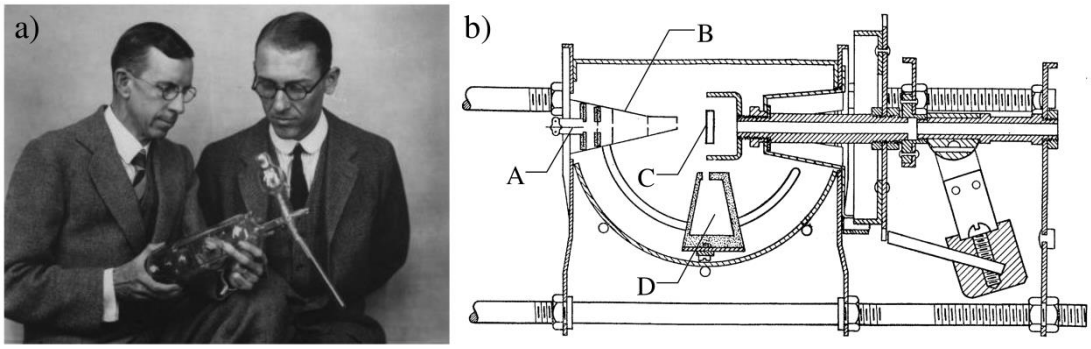

Figure 1.6. a) Davisson (left) and Germer (right), photographed with their "*ship in a bottle*" – the first ever electron diffractometer. Reproduced from the American Institute of Physics Emilio Segrè Visual Archives with the permission of Nokia Corporation and AT&T Archives (copyright Bell Laboratories/Alcatel-Lucent USA Inc.). b) Schematic of the electron diffractometer seen in a). The electron gun, comprising the electron source (**A**), anode, and electron optics (**B**), solid-state sample (**C**; a crystal of nickel), and electron detector (**D**) are indicated. Adapted from Ref. 21.

Mark and Wierl reported the first GED patterns in 1930 (Figs. 1.7b and 1.7c), obtained by exposing carbon tetrachloride (CCl_4) and germanium tetrachloride ($GeCl_4$) to an electron beam for a fraction of a second.[23,24]

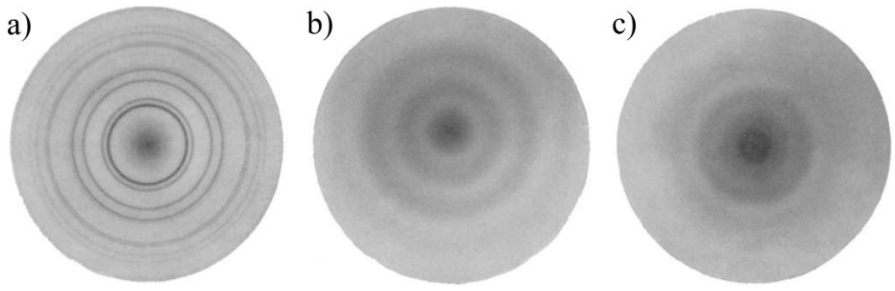

Figure 1.7. ED patterns recorded by Mark and Wierl in 1929; a) ED pattern of polycrystalline silver, and b) GED patterns of CCl_4 and c) $GeCl_4$. Adapted from Ref. 24.

However, as XRD had beaten electron diffraction in the condensed phase, so were Mark and Wierl beaten by Debye, Bewilogua, and Ehrhardt to the first gas-phase experiments; the researchers had recorded gas-phase XRD patterns for carbon tetrachloride earlier that year.[25] Debye had been discussing gas-phase XRD with Scherrer as early as 1916, and Ehrenfest and Lorentz had also given the technique some consideration around the same time.[26] Debye even recounts that Mark had been present at one of his lectures, where the suggestion had been made that he (Debye) should consider using electrons rather than X-rays in his gas diffraction experiments.[26]. Debye apparently did not pursue this.

Gas-phase XRD was in use until the mid-1930s; it was used to determine the structures of several di/triatomics [molecular chlorine (Cl_2) and oxygen (O_2), carbon dioxide (CO_2), and carbon disulfide (CS_2), among others] and, later, assorted halogenated hydrocarbons and benzene. GED developed much more quickly, however. GED data could be acquired in seconds (as opposed to the hours), making it the technique of choice for gas-phase structural studies. Subsequent developments between 1930 – 1950 in electron detection[27,28] and data pre/post-processing,[29–33] followed by the development of computers and punched-card procedures for reliable and reproducible data analysis in the early 1950s,[34] saw GED supersede gas-phase XRD. By the mid-1950s, Brockway and Bartell – pioneers of the technique who had studied under Pauling – were confident enough to laud GED as the "*…best generally applicable tool for determining* [gas-phase structures of] *free molecules for over twenty years*".[35]

The late 1950s – 1970s were the Halcyon days of GED. The popularity of the technique had grown so greatly that commercial gas electron diffractometers were now commonplace. The European-made Eldigraph KD-G2 (Balzers Ltd., Lichtenstein) – based on a much-replicated 1966 design by Zeil, Haase, and Wegmann[36] – and Soviet-made EMR-100 (Sumy Electron Microscope Plant, Ukraine/USSR) dominated the market. A number of contemporary gas electron diffractometers – of which there are only about half a dozen left in the world – are modified from these commercial models. The research groups of Mitzel (Bielefeld University, Germany) and Samdal (Oslo University, Norway) own modified Eldigraph KD-G2 diffractometers,[37,38] and the research group of Girichev (Ivanovo State University, Russia) own a modified EMR-100.[39,40] Many other gas electron diffractometers were built in-house during this period; some are reported by Brockway and Bartell,[35] Bastiansen,[41] and Bonham and Fink,[42] among others. The University of York gas electron diffractometer (Chapter 4) is one such diffractometer. Photographs of some other diffractometers dating back to this period are reproduced in Fig. 1.8.

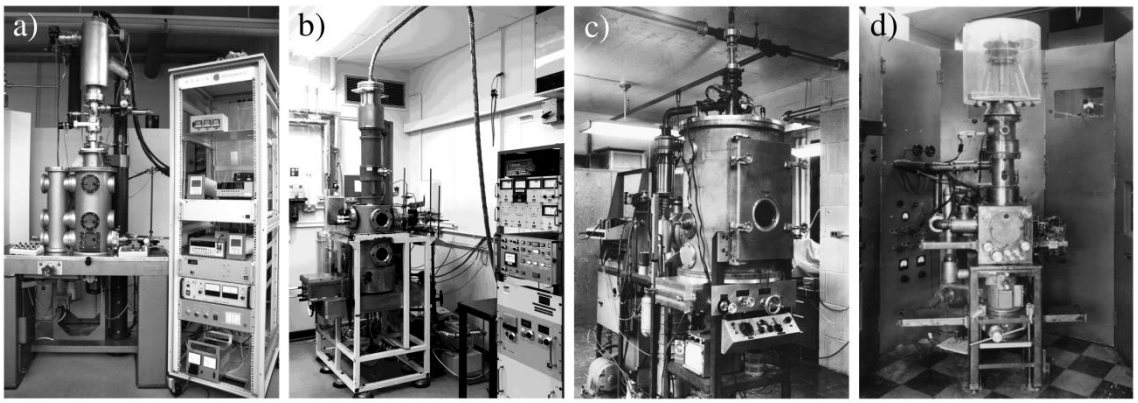

Figure 1.8. "*Same but Different*". Photographs of gas electron diffractometers: a) an Eldigraph KD-G2 housed at Bielefeld University (Germany),[37,38] and gas electron diffractometers built in-house b) at the University of Reading (UK) [now at the University of York[43] (Chapter 4)], c) at Oregon State University (US),[44] and d) at the Naval Research Laboratory in Washington DC (US).[45] Reproduced from Refs. 38 and 44–46.

In the early 1980s, the interest of the structural chemistry community started to shift from equilibrium structures to structural dynamics. Ischenko *et al.* led the renaissance of GED in this decade, publishing the first TRGED experiment in 1983.[10] Ischenko *et al.* reported a "*stroboscopic*" gas electron diffractometer in which plate deflectors were used to streak a continuous electron beam into electron bunches.[10] The technique was not particularly effective, but nonetheless allowed Ischenko *et al.* to study structural dynamics with sub-microsecond temporal resolution;[10] a landmark achievement in GED. The photodissociation of trifluoroiodomethane (CF_3I) was studied in this work, the intention of which was not to study the structural dynamics in a time-resolved manner, but to make transient intermediates, *e.g.* free radicals, accessible to study *via* GED.[10] Rood and Milledge subsequently used their own "*stroboscopic*" gas electron diffractometer for this purpose the following year.[46] Their study targeted free radicals generated by the flash pyrolysis of chlorine dioxide (ClO_2) and 2,3-butanedione ($C_4H_6O_2$).[46]

The mid-1980s saw the contemporary TRGED experiment start to take shape. In 1984, Williamson and Mourou reported on their successes with nanosecond electron diffraction, having presented the first time-resolved electron diffractometer to use a pulsed laser-driven photocathode two years earlier.[47] This would later become the standard for almost all table-top time-resolved electron diffractometers. Williamson and Mourou subsequently used their instrument in TRED experiments to study the melting of aluminium.[48] While Williamson and Mourou focussed on improving the electron source, Ewbank *et al.* focussed

on improving the electron detector.[49–51] The work of Ewbank *et al.*[49–51] was the first significant step away from the recording of GED data on photographic film/imaging plates and towards electronic acquisition, initially *via* photodiode arrays, and later *via* the microchannel plate/scintillating phosphor screen/camera combination used in contemporary table-top time-resolved electron diffractometers. In 1993, Ewbank *et al.* achieved a temporal resolution of *ca.* 15 ns (1×10^{11} photoelectrons/packet).[11]

Throughout the 1990s, the latest developments were incorporated by Zewail *et al.* into each generation of time-resolved electron diffractometer built by his research group. Zewail *et al.* published prolifically on TRED/TRGED and time-resolved spectroscopy; he reported four "*ultrafast electron diffractometers*", designated UED-1, UED-2, UED-3, and UED-4, over the next decade and developed much of the theory that underpins TRED/TRGED.[1] Coupling the pulsed laser-driven photocathode of Williamson and Mourou[47,48] with the femtosecond laser, Zewail was able to achieve *ca.* 15 ps temporal resolution (1×10^{4} photoelectrons/packet) in TRGED by the late 1990s;[12] he had improved this to *ca.* 5 ps (2.5×10^{4} photoelectrons/packet) by the turn of the century.[13] The contemporary understanding of many of the prototypical photochemical processes used in proof-of-principle experiments today is based on the studies of Zewail *et al.* – in particular, his studies on the photolysis of trifluoroiodomethane and 1,2-diiodotetrafluoroethane ($C_2F_4I_2$; this being his flagship experiment; Chapter 5),[52–58] and the photochemical ring-opening of 1,3-cyclohexadiene (C_6H_8).[59] Zewail *et al.* had sufficient temporal resolution to record "*before-and-after*" GED patterns in these experiments, but not to observe directly structural dynamics.[53,54,57–59] The photolysis of 1,2-diiodotetrafluoroethane, for example, had been determined to be a stepwise process with two time constants in earlier experiments by Zewail *et al.*; one being *ca.* 200 fs, and the other being *ca.* 30 ps.[60] Zewail *et al.* were able to acquire data of a sufficiently high quality for the transient free radicals – the products of the first step – such that it could be extracted and refined (*i.e.* subjected to a quantitative GED analysis; Chapter 2).[53,54,57–59] "*Before-and-after*" GED patterns for 1,2-diiodotetrafluoroethane and 1,3-cyclohexadiene are reproduced in Fig. 1.9.

Coulombic forces still limited the temporal resolution of TRED/TRGED into the early 2000s. Miller and Siwick *et al.*[61,62] carried out theoretical work in this period to better understand the propagation dynamics of femtosecond photoelectron packets. Today, Miller and Siwick are recognised equally for their contributions to diffractometer design and development,[63] and their landmark experimental work in TRED.[64–67]

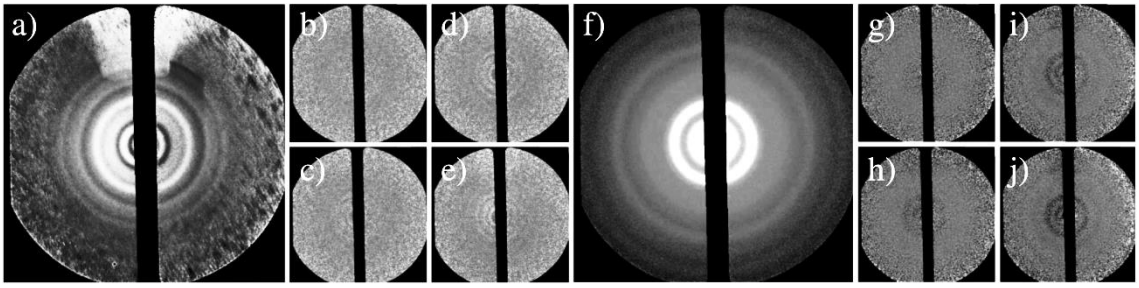

Figure 1.9. a) GED pattern recorded for 1,2-diiodotetrafluoroethane, and "*difference*" GED patterns b) −45 ps, c) 0 ps, d) +80 ps, and e) +405 ps relative to time zero; f) GED pattern recorded for 1,3-cyclohexadiene, and "*difference*" GED patterns g) −50 ps, h) 0 ps, i) +75 ps, and j) 400 ps relative to time zero. Adapted from Ref. 13.

In 2003, Miller and Siwick *et al.* carried out what can probably be considered to be the most important experiment in TRED for a generation.[64] Their theoretical work[61,62] guided the construction of the first sub-picosecond time-resolved electron diffractometer, capable of delivering *ca.* 600 fs photoelectron pulses (6×10^3 photoelectrons/packet) on target.[64] Miller and Siwick *et al.* used their time-resolved electron diffractometer to record the melting of aluminium (Fig. 1.10), as Williamson and Mourou[48] had done twenty years previously, but this time with sufficient spatiotemporal resolution to observe an intermediate superheated phase of aluminium forming before complete collapse of the lattice.[64]

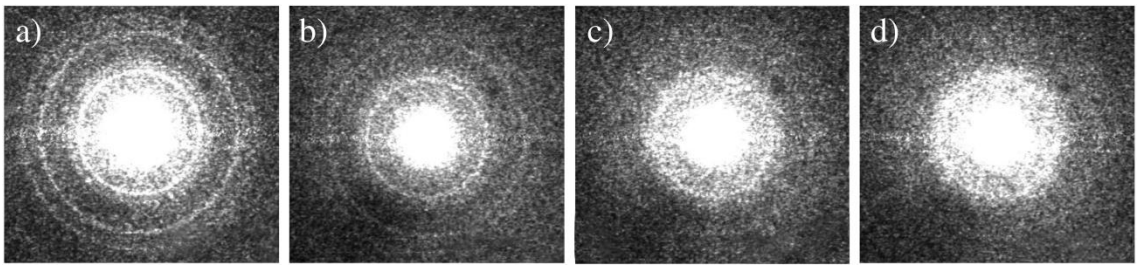

Figure 1.10. ED patterns recorded during the melting of aluminium at a) +0.5 ps, b) +1.5 ps, c) +2.5 ps, and d) +3.5 ps relative to time zero. Adapted from Ref. 64.

Siwick led his own research group into the next decade and continues to carry out pioneering experiments in TRED to this day. Siwick *et al.* pushed the envelope of TRED beyond the melting of metallic thin-films in 2014, reporting – in work of comparable significance to the aforementioned experiment – the observation of a photoinduced metal-like phase of the semiconductor vanadium dioxide (VO_2)[66] and of electron-phonon coupling in graphite.[65] Siwick *et al.* have since revisited vanadium dioxide using TRED

coupled with terahertz spectroscopy[67] – an emergent technique in condensed-phase physics – cementing Siwick at the leading edge of the discipline.

Miller and Siwick continued to lead efforts to overcome Coulombic forces and attain the best possible temporal resolution. As a consequence of their work, which led eventually to a technical demonstration of sub-100-fs temporal resolution in TRED,[68] Miller and Sciaini were able to record the melting of bismuth *via* TRED with sub-350-fs photoelectron packets (1×10^4 photoelectrons/pulse) in 2009.[69] This process is among the fastest structural dynamics to have been recorded using the technique.

The same temporal resolution would not be reached in TRGED for a decade. Miniaturised time-resolved electron diffractometers with both short propagation distances and high accelerating potentials did not perform well in TRGED.[6] It proved difficult to maintain high vacuum at the photoelectron gun when the sample delivery nozzle was as close to the electron gun aperture as condensed-phase samples had been mounted (*ca.* 20 – 30 mm) in high-temporal-resolution TRED experiments.[6] Nonetheless, Centurion[15,70] and Wann[71–74] reported miniaturised time-resolved electron diffractometers designed for TRGED in the early-to-mid-2010s. The diffractometer reported by Wann *et al.*[71,73,74] was capable of delivering *ca.* 1 ps photoelectron pulses (1×10^4 photoelectrons/packet) on target,[72] with the distance between the photoelectron gun and the point of diffraction being 130 mm.[71,73,74] Centurion *et al.* traded off against signal-to-noise to improve their temporal resolution;[15] their diffractometer was capable of delivering *ca.* 500 fs photoelectron pulses (2×10^3 photoelectrons/packet) on target, with the distance between the photoelectron gun and the point of diffraction being 100 mm.[15] This is the shortest propagation distance to be used successfully in TRGED.[6] Their latest diffractometer – reported in 2017 – uses longitudinal recompression of the photoelectron packets to deliver sub-400-fs photoelectron pulses (up to 5×10^5 photoelectrons/packet) on target.[70] Pushing the temporal resolution further in kilovolt electron diffraction is a great challenge.

Since the mid-2000s, TRED/TRGED initiatives at national accelerator facilities have pursued megavolt electron diffraction as an alternative.[68,75–83] The high-fluency, brilliant photoelectron sources available at national accelerator facilities have since allowed researchers to reach the single-shot limit in TRED. Musumeci and Li contributed considerably to this through their work[76–81] with the TRED initiatives at the SLAC National Accelerator Laboratory and the Tsinghua Thomson X-ray Facility, culminating in their independent use of megavolt TRED at the single-shot limit to record the melting of

gold.[77,79] The single-shot limit was subsequently reached at Daresbury Laboratory (Daresbury, UK) in 2015 by Wann and researchers based at the facility.[83] In these experiments, ED data were acquired for polycrystalline platinum in routine fashion (*i.e.* through repeated sampling with 1000 shots; Fig. 1.11a) and at the single-shot limit (Fig. 1.11b), but time-resolved experiments were not carried out.[83]

The photoelectron sources now available at national accelerator facilities have also delivered a paradigm shift in the capabilities of TRGED, allowing researchers to perform ambitious TRGED experiments with sub-200-fs temporal resolution for the first time.

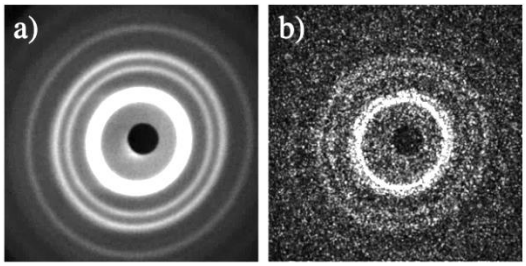

Figure 1.11. ED patterns of polycrystalline platinum: a) a sum of 1000 shots, and b) at the single-shot limit. Data were recorded at Daresbury Laboratory. Adapted from Ref. 83.

Landmark TRGED studies led by Centurion and Wang at the SLAC National Accelerator Laboratory have demonstrated the use of megavolt TRGED in resolving spatiotemporally the rotational and vibrational dynamics of molecular nitrogen (N_2) and iodine (I_2), respectively.[84,85] Subsequent studies by Centurion, Wang, and Martínez have seen some of the classic TRGED/time-resolved spectroscopic experiments of Zewail *et al.*[52–59] revisited with temporal resolution that has since been improved by an order of magnitude.[16–18] Centurion, Wang, and Martínez revisited the photolysis of trifluoroiodomethane with *ca.* 150 fs temporal resolution (1×10^4 photoelectrons/packet) in 2018,[16] distinguishing clearly between the structural dynamics initiated by single- and double-photon absorption to valence and Rydberg electronically-excited states, respectively.[16] The success of this particular TRGED study is lauded by Centurion, Wang, and Martínez as evidence that TRGED is now "*...generally applicable to a wide range of systems in the gas phase, ...*[opening] *the door for studying many important problems in fundamental photochemistry.*"[16] Centurion, Wang, and Martínez subsequently revisited the photolysis of 1,2-diiodotetrafluoroethane (the author made contributions to this study; Chapter 5)[17] and the photochemical ring-opening of 1,3-cyclohexadiene,[18] reporting their results in 2019. The latter had been revisited earlier using TRXRD by Minitti, Weber, and Kirrander.[86]

Centurion, Wang, and Martínez point out that the data range is considerably greater in their TRGED study;[18] so much so, in fact, that it allowed the authors to carry out a reliable transformation of the data from reciprocal space into real space (Chapter 2) without the direct inclusion of theoretical data.[18]

The reader should note, however, that not all contemporary work has focussed on attaining ultimate temporal resolution. Centurion has focussed independently on gas-phase molecular alignment experiments[14,15,87–89] to obtain higher-dimensional data *via* GED/TRGED (GED data is one-dimensional; Chapter 2). With the additional information that is available in these experiments, Centurion *et al.* have demonstrated that one can directly obtain structural solutions for simple molecules without subjecting the data to a full GED analysis (Chapter 2).[14,15,87–89] This technique is not only practical for di/triatomics (with which Centurion has recently demonstrated it;[88,89] Fig. 1.12), but can be applied equally effectively to many of the prototypical favourites; Centurion has also demonstrated the technique with 1,2-diiodotetrafluoroethane[14] and trifluoroiodomethane.[15]

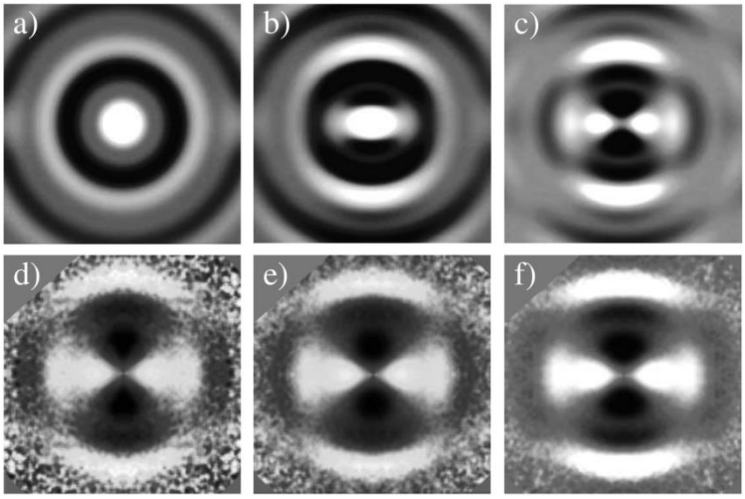

Figure 1.12. Theoretical GED patterns of a) unaligned and b) aligned carbon disulfide (CS_2), and c) the "*difference*" GED pattern of a) and b). Experimental "*difference*" GED patterns recorded for different laser fluencies; d) 0.16, e) 0.48, and f) 0.79 J cm^{-2}. Adapted from Ref. 88.

1.4 Next-Generation Time-Resolved Electron Diffraction Experiments

Kirrander writes, considering all but the most contemporary of the aforementioned developments, that researchers have arrived at a "*…rather promising situation where* [they] *have two powerful ultrafast diffraction techniques, one based on electrons and one based*

on X-rays, both capable of complementing ultrafast spectroscopy [and] *…state-of-the-art …molecular dynamics simulations.*"[7] What, then, are researchers to do with this technique? It is the opinion of the author that one has to begin to push the envelope of TRGED beyond the contemporary studies on di/triatomics[84,85] and revisitations of the early works of Zewail *et al.*[16–18] The paradigm shift in TRGED that has been anticipated by many (including the author; Section 1.2) and delivered during the course of this project (in particular, by Centurion, Wang, and Martínez;[16–18] Section 1.3) has established TRGED as a technique that is comfortably capable of addressing genuine research questions. In addition, by eschewing the direct inclusion of theoretical information in the latest TRGED data analysis protocols, one is likely to be able to obtain unbiased data with which to evaluate the performance of theory. Consequently, the next generation of TRGED experiments have the potential to set up a positive feedback loop that accelerates developments in experiment and theory, and to network experimentalists and theoreticians to take on some of the grand challenges in *in vitro* and *in silico* photochemistry.

To plan and to prepare the strongest research proposals for the next generation of TRGED experiments, the author has coupled experiment and theory to study structure and dynamics. The author has launched and overseen the development of two new research programmes in the Wann Electron Diffraction Group: a GED programme (theory: Chapter 2; implementation: Chapter 4), and a computational chemistry/trajectory surface-hopping dynamics (TSHD) programme (theory: Chapter 3; implementation: Chapter 5). These research programmes provide the necessary information (Fig. 1.13) to a) secure beamtime allocations at national accelerator facilities, b) ensure that allocated beamtime is used as productively as possible, and c) guide the interpretation of experimental data to translate effectively the results of high-cost, high-risk beamline experiments into scientific impact.

The research programmes of the Wann Electron Diffraction Group (comprising the two launched here by the author, and a picosecond TRGED programme;[73,74] the reader should note that the former two are equally capable of supporting the latter) are connected by a unifying strategy: the "*Roadmap to a Molecular Movie*"[74] (Fig 1.14). The strategy was developed by the author and João Pedro Nunes (Ph.D. student; University of York) to consolidate disparate research programmes between 2015 and 2017; it was codified formally by João Pedro Nunes in 2018.[74] Although the "*Roadmap to a Molecular Movie*" highlights the interplay between the research programmes, each is valuable in isolation; indeed, each manuscript published by the author (including those in preparation and pre-print) falls squarely within the remit of a single research programme.

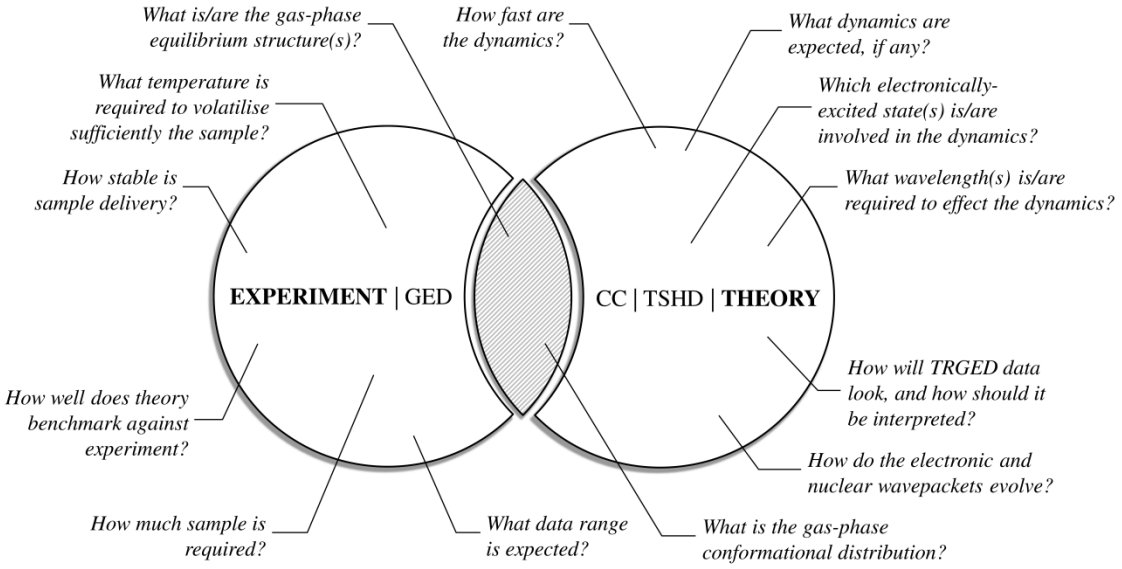

Figure 1.13. Questions that can be answered by one or both of the new research programmes established in the Wann Electron Diffraction Group.

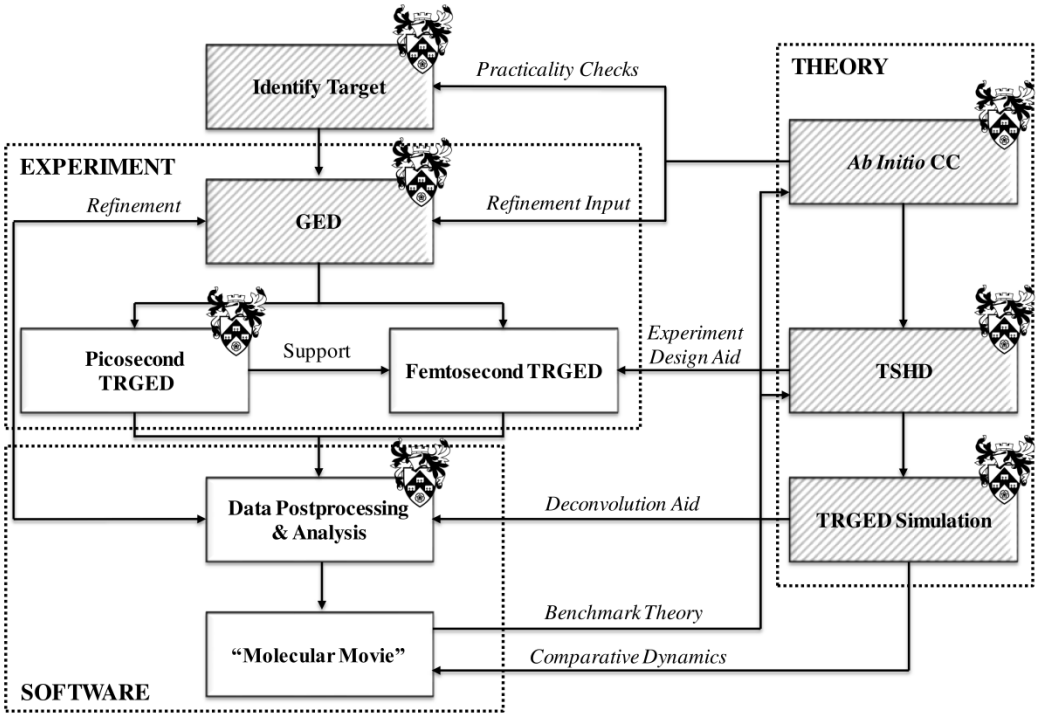

Figure 1.14. "*Roadmap to a Molecular Movie*" strategy, developed by the author and João Pedro Nunes; codified by João Pedro Nunes in Ref. 74. University of York insignia denote parts of the roadmap that can be completed in the Wann Electron Diffraction Group at the University of York. Shading denotes parts of the roadmap that have been either established for the first time or further developed by the author during the course of this project; shading denotes implicitly the scope of this thesis. Adapted from Ref. 74.

1.5 Structure of the Thesis

The reader is encouraged to read this thesis with the "*Roadmap to a Molecular Movie*" strategy (Fig. 1.14) and the complementarity of the research programmes launched by the author (Fig. 1.13) in mind at all times. If a TRGED experiment is a "*Molecular Movie*", then this thesis could be titled "*The Molecular Movie: Behind the Scenes*" – an appropriate title, as it is not overtly concerned with TRGED, but with the work that goes into planning and proposing TRGED experiments. It details the new methods that are now available at the University of York through the launch and development of the GED and TSHD research programmes, and presents examples of how they can be used, both in isolation and concertedly, to study structure and dynamics by experiment and theory.

The theory that underpins GED and TSHD is introduced to the reader in Chapters 2 (*Theory I: Time-Averaged Gas Electron Diffraction*) and 3 (*Theory II: Ab Initio Computational Chemistry and Trajectory Surface-Hopping Dynamics*), respectively.

For each of the research programmes launched by the author, a chapter is given over to an account of the new methods that are now available at the University of York (Fig. 1.14) – key outcomes of the research programmes. These accounts are accompanied by case studies that demonstrate how these methods can be used practicably to provide the information (Fig. 1.13) that one needs to plan and propose TRGED experiments (Section 1.4).

A description of the University of York gas electron diffractometer is given, for the first time, in Chapter 4 (*New Methods and Applications I: A New Lease of Life for the Only Gas Electron Diffractometer in the UK*). The author presents structural solutions for a) 4-(dimethylamino)benzonitrile and b) tin^{II} bis(trifluoroacetate), $ditin^{II}$ μ-oxy-bis-μ-trifluoroacetate, and tin^{IV} tetrakis(trifluoroacetate) in case studies that demonstrate the efficacy and wide-ranging capabilities of the University of York gas electron diffractometer.

A description of a parallel Python code (*py*naMICs) for simulating TRGED is given in Chapter 5 (*New Methods and Applications II: Parallel Code for Simulating Time-Resolved Gas Electron Diffraction*). The author presents benchmarking data that demonstrates that *py*naMICs delivers scalable, high-speed performance, and a case study on the photolysis of 1,2-diiodotetrafluoroethane. The case study demonstrates not only how the *py*naMICs code can be used in practice, but also the kind of *ab initio* computational chemistry that the author has introduced independently to the Wann Electron Diffraction Group.

The new methods introduced in Chapters 4 and 5 are used concertedly in Chapters 6 (*Photofission of the Disulfide Bond in 1,2-Dithiane*) and 7 (*Photoisomerisation of E-Cinnamonitrile*), where two prototypical photochemical processes – photofission and photoisomerisation – are studied in 1,2-dithiane and *E*-cinnamonitrile, respectively. The author couples the experimental (GED) and theoretical (*ab initio* computational chemistry and TSHD) techniques that he has introduced to the Wann Electron Diffraction Group to study structure and dynamics in great detail. The author has successfully secured beamtime for both of the proposed TRGED experiments with the work presented in these Chapters – a testament to the success of the "*Roadmap to a Molecular Movie*" strategy.

The current position of the Wann Electron Diffraction Group is evaluated in Chapter 8 (*The Present and the Future*); here, the author makes recommendations for consolidating and leveraging the advantage that the research group has developed through the new research programmes and their unification under the "*Roadmap to a Molecular Movie*" strategy. The author points to a promising new direction in TRGED that will demand even more from the new research programmes.

2 Theory I: Time-Averaged Gas Electron Diffraction

This Chapter introduces the reader to some useful concepts that underpin time-averaged GED. It comprises an introduction to the electron scattering equations that describe GED (Section 2.1), the interpretation (Section 2.2) and refinement (Section 2.3) of GED data, and the contemporary gas electron diffractometer (Section 2.4). An overview of the challenges and limitations of GED is additionally presented (Section 2.5).

The author considers the books by Hargittai and Hargittai,[90] and Bonham and Fink[91] to contain the most comprehensive descriptions of GED theory available to the specialist, but recommends the more generally-accessible, contemporary overview given by Rankin.[92] If the reader is interested, instead, in lighter reading, the author recommends Hedberg's retrospective,[44] which gives a unique historical/personal insight into GED.

2.1 Gas Electron Diffraction

The universal duality of particles and waves, hypothesised by de Broglie[19] in 1923, was inadvertently proven by early experiments in electron diffraction (Chapter 1). The de Broglie equation, defining the relationship between the wavelength, λ, and the momentum, p, of a massive particle, is given in Eq. 2.1, where h is the Planck constant.

$$\lambda = \frac{h}{p} \qquad \textbf{Eq. 2.1}$$

Eq. 2.1 is applicable to electrons. An electron has a p-dependent wavelength, and is consequently able to diffract and to interfere with other diffracted electrons in a manner that is conceptually analogous to the diffraction and interference of light in Young's 1801 interferometric experiments. As the interference pattern produced by the light in the interferometric experiment gives information on the size and separation of the slits, so does the interference pattern produced by electrons in a GED experiment give information on the charge of the nuclei and the internuclear distances in a molecule. It is by interaction with the charge gradient of the nuclei that the electrons are diffracted.

If an electron is to diffract strongly on interaction with the nuclei in a molecule, λ has to be of an approximately comparable order of magnitude. This necessitates that the electron, having a rest mass, m_e, and elementary charge, e, be accelerated to some high velocity, v, by an external potential, U, as in Eq. 2.2.[90]

$$v = \sqrt{\frac{2eU}{m_e}} \qquad \textbf{Eq. 2.2}$$

Practicably, U is of the order of 40 – 100 kV in a typical GED experiment. At such high accelerating potentials, v reaches a significant fraction of the speed of light, c, and p can no longer be found as the product of m_e and v. Consequently, λ cannot be found from Eq. 2.1, and must instead be found from relativistic mechanics, as in Eq. 2.3.[90]

$$\lambda = \frac{h}{\sqrt{2m_e eU\left(1 + \frac{eU}{2m_e c^2}\right)}} \qquad \textbf{Eq. 2.3}$$

Application of Eq. 2.1 instead of Eq. 2.3 results in an error of several percent in λ that propagates forward, ultimately affecting measurements of internuclear distances made *via* GED.[90]

It is possible to eliminate λ from the electron scattering equations by introducing the concept of an electron scattering vector, $\boldsymbol{s}$. The introduction of $\boldsymbol{s}$ not only simplifies the electron scattering equations aesthetically, but makes comparable GED data acquired from different gas electron diffractometers (in which U, and, by extension, v and λ, may vary). $\boldsymbol{s}$ is defined as the difference in momentum of the incoming and outgoing wave vectors, $\boldsymbol{k_0}$ and $\boldsymbol{k}$, respectively. This is illustrated in Fig. 2.1.

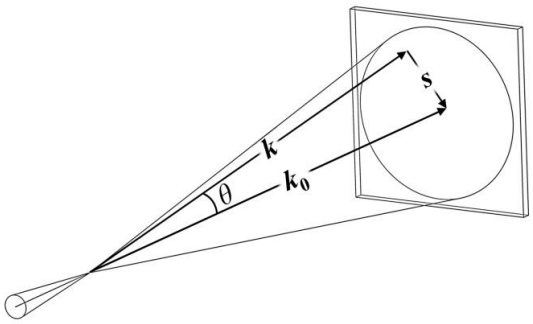

Figure 2.1. Illustration of the electron scattering vector, $\boldsymbol{s}$, defined as the difference in momentum of the incoming and outgoing wave vectors, $\boldsymbol{k_0}$ and $\boldsymbol{k}$, respectively. θ is the polar scattering angle.

To good approximation, electrons that have been accelerated to high velocity scatter elastically (*i.e.* without change in their velocity) in a GED experiment. Consequently, the wave vector magnitudes, $|\boldsymbol{k_0}|$ and $|\boldsymbol{k}|$, are equal in value, and are usually denoted k. The relationship between k and λ is given in Eq. 2.4.[90]

$$|\boldsymbol{k_0}| = |\boldsymbol{k}| = k = \frac{2\pi}{\lambda} \qquad \textbf{Eq. 2.4}$$

The electron scattering vector magnitude, $|\boldsymbol{s}|$, is usually denoted s, and can be calculated *via* trigonometric identities if the polar scattering angle, θ, between $\boldsymbol{k_0}$ and $\boldsymbol{k}$ is known. The relationship between λ and θ is given in Eq. 2.5.[90]

$$|\boldsymbol{s}| = s = \frac{4\pi}{\lambda}\sin\left(\frac{\theta}{2}\right) \qquad \textbf{Eq. 2.5}$$

To acquire data over an adequate s range, scattering is recorded with the electron detector positioned at two (or more) different distances from the point of diffraction in a typical GED experiment. This allows high-θ and low-θ data to be acquired at the shorter and longer distances, respectively. This is illustrated in Fig. 2.2.

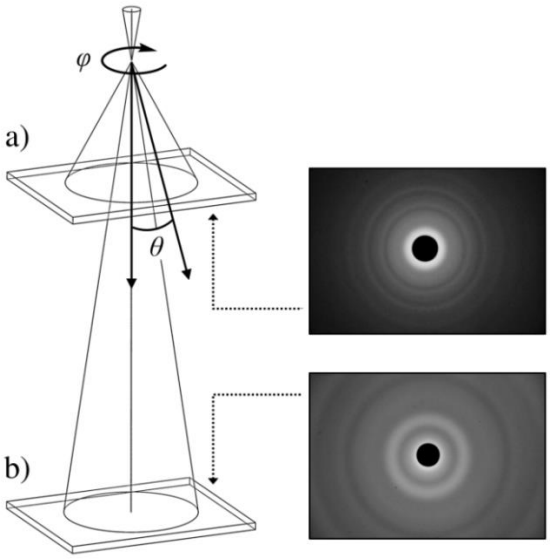

Figure 2.2. GED data acquisition with a) a short and b) a long distance between the point of diffraction and the plane of the electron detector. θ is the polar scattering angle; φ is the azimuthal scattering angle. In a), high-θ scattering is acquired; in b), low-θ scattering is acquired. GED patterns for benzene, acquired during calibration[74] of the University of York gas electron diffractometer[43] (Chapter 4), are presented for illustrative purposes.

The characteristic appearance of GED patterns as diffuse, concentric rings is a consequence of scattering being averaged over the azimuthal scattering angle, φ, by the random orientation of molecules in the gas phase. GED data are consequently one-dimensional. In electron crystallography, however, data are three-dimensional; the diffraction patterns consist of bright spots, reflecting the long-range orientational order of single crystals.[93]

Extracting refinable GED data from the GED pattern – digitised as a two-dimensional intensity matrix – necessitates a reduction in dimensionality; this is achieved by algorithmically locating the centre of the GED pattern and then azimuthally averaging the intensity as a function of s to give a one-dimensional dataset. A new performance-driven programme for GED data extraction, XSTRACT,[74] has recently been developed in the Wann Electron Diffraction Group.

After the subtraction of background scattering and detector readout noise, the scattering intensity, I, can be expressed as a function of s, as in Eq. 2.6.[90]

$$I(s) = \frac{K^2}{R^2} I_0(s) \cdot \sum_i^N \sum_j^N |F_i(s)||F_j(s)| \cdot \int_0^\infty P_{ij}(r) \frac{\sin(sr_{ij})}{sr_{ij}} dr \qquad \textbf{Eq. 2.6}$$

I_0 is the incident electron beam intensity, R is the distance between the electron detector and the point of diffraction, and K substitutes for the collection of constants given in Eq. 2.7.[90]

$$K = \frac{8\pi^2 m_e e^2}{h^2} \qquad \textbf{Eq. 2.7}$$

The summation of the scattering amplitude functions, $F_i(s)$ and $F_j(s)$, in Eq. 2.6 takes place over all N unique pairs of nuclei, i and j, separated by some internuclear distance, r_{ij}. The scattering amplitude function, $F(s)$, for a given atomic nucleus, i, is defined by the nuclear charge, Z_i, and the scattering amplitude, f_i, as is Eq. 2.8.[90]

$$F_i(s) = \frac{Z_i - f_i}{s^2} \qquad \textbf{Eq. 2.8}$$

$P(r)$ is a probability distribution that describes the probability, $P_{ij}(r)\,dr$, of r_{ij} taking some value in the interval r to $(r + dr)$. The inclusion of $P(r)$ in Eq. 2.6 reflects the fact that r_{ij} is not constant on the timescale of the GED experiment – which may be seconds to minutes – as sub-ps molecular vibrations sample a range of possible values of r_{ij} probabilistically. Correcting for molecular vibrations is explored in greater depth in Section 2.5.2.

$I(s)$ contains contributions from two principal types of scattering; atomic scattering, denoted $I_{\text{At.}}(s)$, originating from a single nucleus ($i = j$), and molecular scattering, denoted $I_{\text{Mol.}}(s)$, originating from a pair of nuclei ($i \neq j$). $I(s)$ can consequently be expressed as in Eq. 2.9.

$$I(s) = I_{\text{At.}}(s) + I_{\text{Mol.}}(s) \qquad \textbf{Eq. 2.9}$$

Considering Eq. 2.6 with respect to the conditions $i = j$ and $i \neq j$, it is possible to derive expressions for $I_{\text{At.}}(s)$ and $I_{\text{Mol.}}(s)$, given in Eqs. 2.10 and 2.11, respectively.[90]

$$I_{\text{At.}}(s) = \frac{K^2}{R^2} I_0(s) \cdot \sum_i^N |F_i(s)|^2 \qquad \textbf{Eq. 2.10}$$

$$I_{\text{Mol.}}(s) = \frac{K^2}{R^2} I_0(s) \cdot \sum_i^N \sum_{j\,(j \neq i)}^N |F_i(s)||F_j(s)| \cdot \int_0^\infty P_{ij}(r) \frac{\sin(sr_{ij})}{sr_{ij}} \, dr \qquad \textbf{Eq. 2.11}$$

$I_{\text{At.}}(s)$ and $I_{\text{Mol.}}(s)$ are best understood by considering the diffraction of light under Fraunhofer conditions through a single and double slit, respectively (Fig. 2.3). The latter, through production of an interference pattern, contains information on the size and the separation of the slits; in GED data, $I_{\text{Mol.}}(s)$ consequently contains valuable structural information. The former contains no such information.

Fortunately, there are no quantities in Eq. 2.10 that cannot be computed if the molecular formula of the molecule under study is known. $I_{\text{At.}}(s)$ can be computed trivially, and subtracted from $I(s)$ to leave $I_{\text{Mol.}}(s)$.

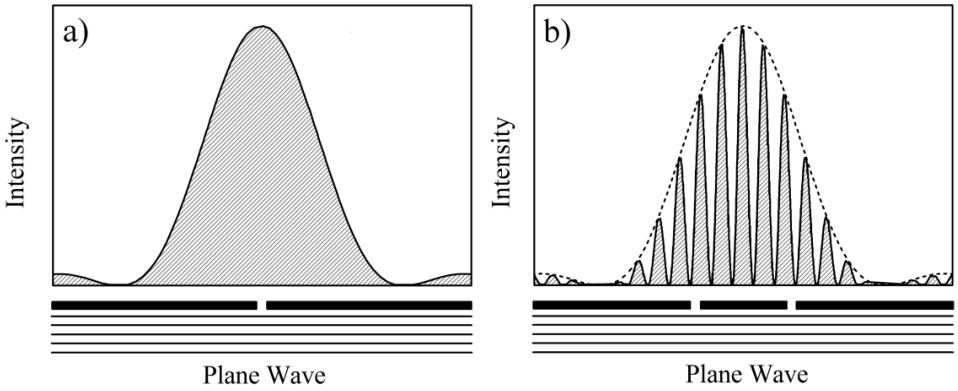

Figure 2.3. Diffraction of a plane wave under Fraunhofer conditions from a) a single slit and b) a double slit. The dotted line in b) represents the intensity envelope of a). The effects of interference appear as high- and low-intensity bands within the limits of this envelope.

2.2 Molecular Intensity and Radial Distribution Curves

The plot of $I_{\text{Mol.}}(s)$ is referred to as a "*molecular intensity curve*" (MIC; Fig. 2.4). Transformation of the MIC from reciprocal space into real space gives a "*radial distribution curve*"[29] (RDC; Fig. 2.5), and is achievable, in principle, *via* application of the Fourier-like function, given in Eq. 2.12, thereby generating the radial distribution function, $D(r)$.[90]

$$D(r) = \int_0^\infty s I_{\text{Mol.}}(s) \sin(sr) \, ds \qquad \textbf{Eq. 2.12}$$

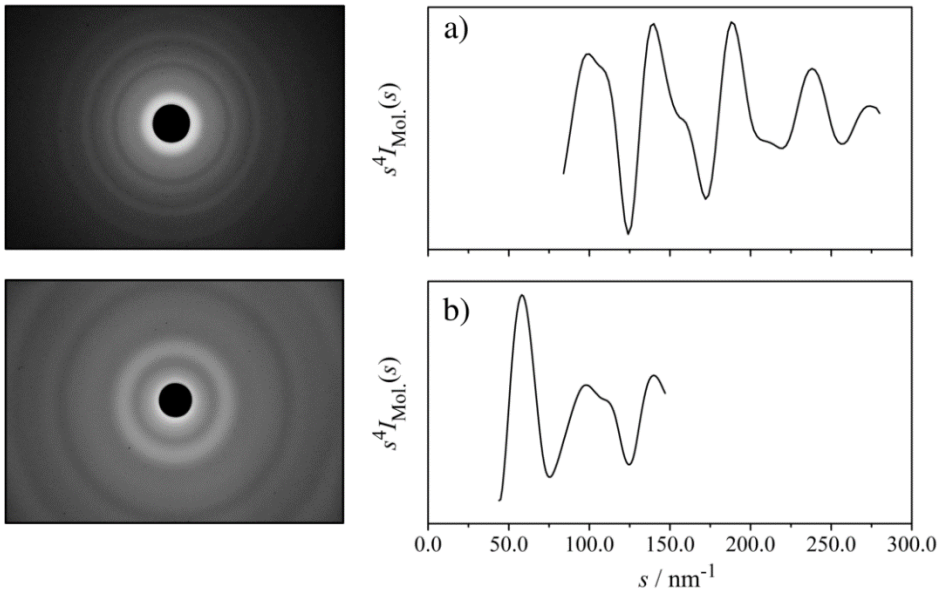

Figure 2.4. MICs for benzene, acquired with a) a short and b) a long distance between the point of diffraction and the plane of the electron detector. When combined, a) and b) give a more complete GED dataset spanning 44.0 – 280.0 nm^{-1}. Data were acquired during calibration[74] of the University of York gas electron diffractometer[43] (Chapter 4).

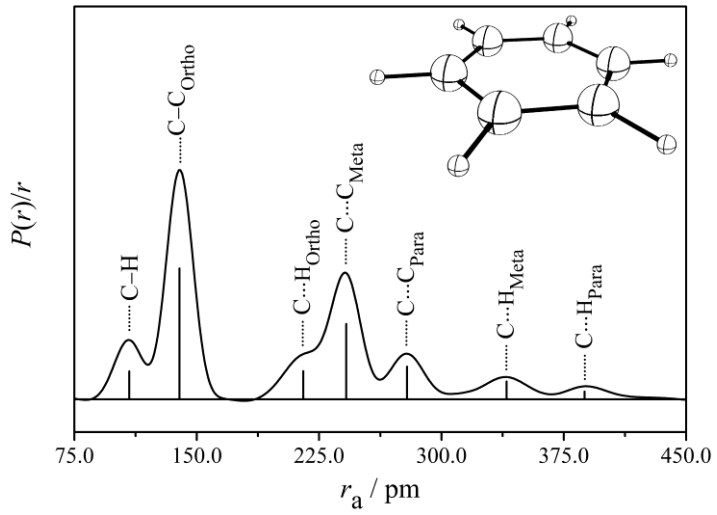

Figure 2.5. RDC for benzene, obtained on transformation of the MICs for benzene (Fig. 2.4) from reciprocal space into real space. Data were acquired during calibration[74] of the University of York gas electron diffractometer[43] (Chapter 4).

In practice, however, $I_{Mol.}(s)$ can only be recorded over some limited range, $s_{min} \leq s \leq s_{max}$, where $s_{min} \leq 0$. Consequently, $I_{Mol.}(s)$ is multiplied by an exponential function pre-transformation, and $D(r)$ is practicably generated as $D'(r)$ in Eq. 2.13.[90] α takes some very small value such that Eq. 2.14 is satisfied.[90]

$$D'(r) = \int_0^\infty sI_{\text{Mol.}}(s)\, e^{(-\alpha s^2)} \sin(sr)\, ds \qquad \textbf{Eq. 2.13}$$

$$\lim_{\alpha \to 0} D'(r) = D(r) \qquad \textbf{Eq. 2.14}$$

A peak exists in the RDC for every unique pair of nuclei; the maxima of these peaks occur at r_{ij} and each peak is broadened by molecular vibrations according to $P_{ij}(r)\, dr$. The areas, a, of the peaks are proportional to Z_i and Z_j, and inversely proportional to r_{ij}, as in Eq. 2.15.[90]

$$a \propto \frac{Z_i Z_j}{r_{ij}} \qquad \textbf{Eq. 2.15}$$

Two important consequences of Eq. 2.15 are a) that the positions of hydrogen nuclei are almost always poorly determined *via* GED, and b) that peaks from pairs of nuclei at similar internuclear distances generally overlap in the RDC, making their identification more challenging.

The RDC was introduced by Pauling and Brockway[29] in 1934 as an intuitive way of visualising the internuclear distances in a molecule and had a transformative effect on the analysis of GED data. Before the introduction of the RDC, theoretical MICs had to be manually drawn up for every sensible molecular structure and compared to the experimentally-acquired MICs. The latter were estimated by eye, and using a ruler, from the ring diameters and intensities of the GED patterns. These steps were highly subjective and could not provide quantitatively-accurate structural information.[29,33] Nonetheless, the visual interpretation of GED patterns remained common practice for close to two decades after the introduction of the RDC, the potential of which took time to be realised.[33] The transformation of Eq. 2.13 was challenging for early computers, early GED data were of poor quality, and automated punched-card procedures for extracting the data from GED patterns in a reproducible manner were not developed until 1945.[34]

2.3 Refinement

Refinement provides quantitatively-accurate structural information *via* least-squares fitting of a parameterised molecular model to experimentally-acquired GED data. The earliest punched-card procedures for least-squares refinement date back to the late 1940s;[34] today, it can be carried out much more easily in the ED@ED,[94] KCED,[95] and UNEX[96] software suites, used at the University of Canterbury (New Zealand), Ivanovo and Moscow State Universities (Russia), and Bielefeld University (Germany), respectively.

Each parameterised molecular model is bespoke and must be programmed judiciously to define the molecule under study within the constraints of its symmetry point group, and using as few parameters as possible to minimise redundancy, over-definition, and correlation. The parameters typically comprise internuclear distances, angles, and dihedral angles, although additional parameters such as conformer/molecular fraction may also be programmed into the parameterised molecular model.

The parameters and amplitudes of vibration (determined theoretically for all pairs of nuclei in the first instance, and consequently affecting $P_{ij}(r)$; see Section 2.5.2) may be sequentially refined to obtain the best fit to the experimentally-acquired GED data. The quality of the refinement can be assessed quantitatively by the "*goodness-of-fit*" *R* factors, R_G and R_D, and qualitatively by visual inspection of the RDC. R_G and R_D quantify the quality of the fit with and without respect to the correlation of the parameters, respectively; it is generally acknowledged that the *R* factors should be below 0.10 for a refinement to be considered of publishable quality.[97]

Only GED data for the simplest and most-highly-symmetric molecules can be refined directly to publishable quality without additional input. The results from theoretical calculations and/or experimental data from complementary techniques are incorporated into every contemporary least-squares refinement. Supplementing GED data in this manner has had a transformative effect on the scope of the technique, extending the applicability of GED to encompass significantly larger and less-symmetric molecules.

The earliest attempts to do this were *via* the Molecular-Orbital-Constrained Electron Diffraction (MOCED)[98] approach, in which some parameters were not refined but, instead, fixed to theoretically-determined values. Uncertainties from MOCED refinements were generally heavily underestimated, as parameters that were fixed were not associated with uncertainties; the problem was acute for refinable parameters that were correlated with fixed parameters. The MOCED[98] approach was superseded by the Structural Analysis Restrained by *Ab Initio* Calculations for Electron Diffraction (SARACEN)[99–101] approach, in which parameters are subject to flexible restraint that is centered on a theoretically-determined value and has some approximate uncertainty associated with it, estimated from a scaling range of theoretical calculations. It is even possible to incorporate theory much more directly into the least-squares refinement *via* the Dynamic Interaction of Theory and Experiment (DYNAMITE)[102] approach; using DYNAMITE, parameters can be optimised by molecular mechanics in real-time during the least-squares refinement procedure.

2.4 Gas Electron Diffractometers

There is no typical gas electron diffractometer; of the less than half a dozen operational time-averaged gas electron diffractometers around the world, all have been built bespoke, or modified from 1960s commercial diffractometers by generations of researchers.[37–41,43] Nonetheless, all require a high-vacuum chamber, an electron source (Section 2.4.1) and electron optics, a mechanism for sample delivery (Section 2.4.2), and an electron detector (Section 2.4.3), so all are similar in this respect. Some of the options are reviewed here.

2.4.1 Electron Source

A beam of electrons suitable for time-averaged GED can be produced *via* thermionic emission from a hot tungsten filament cathode mounted in the classic "*triode*" geometry (Fig. 2.6).[91]

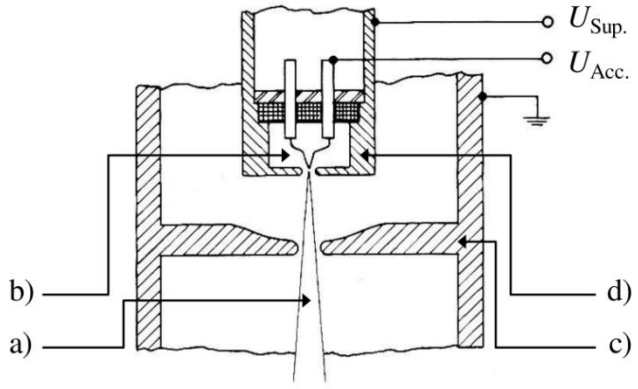

Figure 2.6. Generation of a) an electron beam from a "*triode*" electron gun that comprises b) a tungsten filament cathode, c) anode plate, and d) Wehnelt cylinder. Accelerating and supressing voltages, $U_{Acc.}$ and $U_{Sup.}$, respectively, are indicated. Adapted from Ref. 91.

An accelerating voltage, $U_{Acc.}$, is applied between the cathode and anode to produce an electric field that extends through the aperture of the Wehnelt cylinder and strips electrons from the tip of the hot tungsten filament. A variable voltage, $U_{Sup.}$, is applied to the Wehnelt cylinder, such that $U_{Sup.} < U_{Acc.}$; the application of $U_{Sup.}$ suppresses emission from the electron gun, creating a space-charge cloud in front of the hot tungsten filament and limiting the extent of the cloud at the sides. By varying $U_{Sup.}$, the intensity of the electron beam can be controlled.[91] Classic "*triode*" electron guns can produce high-quality electron beams when correctly optimised, but have two disadvantages: a) the electron beam may leave the

electron gun with a high angle of divergence[91] and b) the geometry (which defines the shape of the electric field around the cathode and, consequently, dictates the electron beam characteristics) is essentially fixed; it can only be modified in between experiments by disassembling and reconstructing the electron gun.

Other common electron gun designs used in GED instruments, like the telefocus electron gun of Steigerwald,[103] allow for the "*triode*" geometry to be adjusted in real time to enable telescopic focussing and on-the-fly adjustment, but can be challenging to optimise.

2.4.2 Sample Input

Sample is typically admitted into a high-vacuum chamber as a molecular beam from an effusive nozzle. The effusive nozzle is mounted perpendicular to, and with the tip of the nozzle positioned <1 mm away from, the axis of propagation of the electron beam. Two requirements are fulfilled in this case: a) that the intersection between the molecular and electron beams is point-like,[91] minimising extraneous background and multiple scattering events, and b) that the temperature of the sample is known, to a good approximation.[91] The effusive nozzle causes little-to-no collisional cooling, and consequently the temperature of the molecular beam can be assumed to be the same as the temperature of the tip of the nozzle,[91] which may be easily measured *via* a thermocouple.

Contemporary GED instruments use heated effusive nozzles to make accessible to study molecules with low vapour pressures and rates of vapourisation under ambient conditions (Section 2.5.1).[37–40,43,104] A typical heated effusive nozzle can be used at temperatures up to *ca.* 600 – 700 K,[37,38,43] but heated effusive nozzles for very-high-temperature GED (VHT-GED) have been developed that can reach temperatures of *ca.* 1100 K.[104,105] Beyond molecules with low volatility, VHT-GED has made thermal decomposition and pyrolysis products accessible to study *via* the technique.[105]

2.4.3 Electron Detection

Recording a GED pattern necessitates an electron detector with high dynamic range, as $I_{\text{Mol.}}(s)$ drops off steeply in intensity to the fourth power with θ (Section 2.2).[90] A differential filter must be located upstream of the electron detector to flatten the GED pattern by shielding the inner portion of the electron detector from low-θ scattering to a greater extent than the outer portion of the electron detector is shielded from high-θ scattering. The earliest differential filters of this kind – first used by Debye and termed

rotating sectors (Fig. 2.7) – were mechanical; rotating sectors are still found in most GED instruments today. The rotating sector is spun about its axis at >100 rpm during data acquisition to optically flatten the GED pattern. It is typically machined – with high precision – as either an r^3 or an r^4 function, where r is the distance from the centre of the rotating sector.[90]

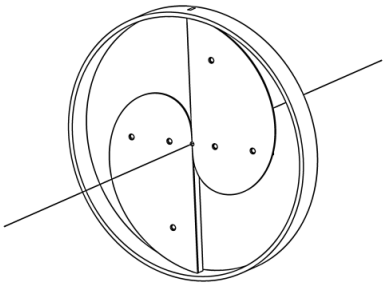

Figure 2.7. Diagram of a rotating sector – the earliest mechanical differential filter. The rotating sector is spun about its axis at >100 rpm during data acquisition. Adapted from technical drawings by João Pedro Nunes.[106]

GED data are generally acquired *via* exposures of photographic film or electron-sensitive image plates. These electron detectors have good dynamic range when coupled with a rotating sector and high sensitivity (being suitable for use with electron beam currents as low as 0.1 μA);[91] they are therefore a well-rounded choice, but only some small number of them (typically <10) can be installed in a GED instrument at any one time. After exposure, the vacuum of the instrument needs to be broken and the photographic film/image plates removed. The photographic film subsequently needs to be developed *via* darkroom techniques, as in traditional photography; the image plates subsequently need to be digitised.[91] A single GED experiment can consequently take an entire day, and there is no guarantee that, when the photographic film is developed, or the image plates are digitised, any GED patterns will have been successfully recorded, or that those that have been will be of useable quality.

Contemporary GED instruments[107] are typically equipped with charge-coupled device (CCD) cameras and scintillating phosphor screens onto which GED patterns are projected. An apodising optical filter usually replaces the rotating sector in these electron detectors.[107] Practicably, there is no limit to the number of exposures that can be acquired, the vacuum of the instrument need not be broken to inspect the results, and no time need be spent developing or digitising the GED pattern. Whether the GED pattern is of useable

quality can be tested by on-the-fly extraction. Throughput can be increased by orders of magnitude with these electron detectors, but retrofitting 1960s GED instruments with the CCD/scintillating phosphor screen combination presents a considerable challenge in many cases, and making these GED instruments reliant on digital technology arguably makes them less robust.

2.5 Challenges and Limitations in Gas Electron Diffraction

2.5.1 Volatilisation

The scope of GED is limited most greatly by sample volatility. A suitably high vapour pressure and rate of vapourisation is required for GED data to be acquired practicably; both must be attainable at temperatures below that at which the molecule thermally decomposes. The minimum requisite vapour pressure, P, in Pa can be approximated from the empirically-derived relationship given in Eq. 2.16,[90] reflecting the increased scattering power of heavier nuclei, although the absolute pressure need not be known at all.[90]

$$P \approx 4\times10^{6}\left(\sum_{i}^{N} Z_i^2\right)^{-1} \qquad \textbf{Eq. 2.16}$$

Most gas electron diffractometers – including the University of York gas electron diffractometer[43] (Chapter 4) – are fitted with high-temperature heated nozzles (Section 2.4.2) to make accessible to study molecules with low vapour pressures and rates of vapourisation under ambient conditions.

There are practical considerations, however: a) the conformational distribution of the molecule under study may significantly broaden with temperature, and b) it becomes more challenging to handle molecular vibrations at high temperature (Section 2.5.2); these are typically the greatest source of uncertainty in GED measurements, even under ambient conditions.

2.5.2 Correcting for Molecular Vibrations

Each individual electron that diffracts in accordance with the electron scattering equations (Section 2.1) probes the instantaneous positions of the nuclei in a molecule, and many millions of diffracted electrons contribute to the formation of the GED pattern. As the positions of nuclei are not constant on the timescale of the GED experiment – which may be seconds to minutes – the GED pattern is averaged over all molecular vibrations.

Averaged internuclear distances, r_a, are of little value as they cannot be compared directly to the equilibrium internuclear distances, r_e, that the chemist is generally interested in. r_a is underestimated with respect to r_e by the "*shrinkage*" effect, which the reader can understand by considering the difference between r_a and r_e for a linear triatomic molecule (Fig 2.8).

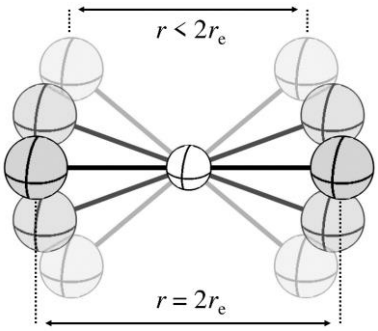

Figure 2.8. Vibration of a simple linear triatomic molecule. The internuclear distance, r, between the two terminal nuclei is shorter, on average, than the equilibrium internuclear distance, r_e, on account of the vibrational motion.

On account of vibrational motion, the molecule is bent for a greater amount of time than it is linear; the GED pattern will consequently contain a greater contribution from the bent (vibrationally-averaged), rather than linear (equilibrium), geometry. If uncorrected for, least-squares refinement of the GED data for this linear triatomic molecule would – incorrectly – achieve a better fit to a bent geometry. The relationship between r_a and r_e – with the correction between them being denoted K – is given in Eq. 2.17.[97]

$$r_e - r_a = K = \frac{u^2}{r_a} - k - \delta a - \delta r \qquad \textbf{Eq. 2.17}$$

u is root-mean-square (RMS) amplitude of motion, k is the "*shrinkage*" (or perpendicular distance) correction, and δa and δr are corrections for anharmonicity and centrifugal distortion from rotational motion, respectively. δa and δr can be neglected for simplicity; the latter is negligibly small and the former is not greatly important, the caveat being that this assumption only holds well if the nuclei do not move far from their equilibrium positions. Eq. 2.17 can consequently be simplified to Eq. 2.18.[97]

$$r_e - r_a \approx \frac{u^2}{r_a} - k \qquad \textbf{Eq. 2.18}$$

Under the harmonic approximation, u and k can both be obtained from theoretically-calculated force constants and classical mechanics; this functionality is available in both the

SHRINK[108,109] and VIBMODULE[110] software packages. Structures solved in this way are termed r_{h1}-type; the majority of structures solved *via* GED are of this type.

This simplification of Eq. 2.17 to Eq. 2.18 does not hold so well for molecules with low-frequency, large-amplitude vibrational modes, or for VHT-GED.[97] In these cases, δa should be included, either by referring to tabulated values, or by direct computation. Structures solved in this way are termed r_{a3t}-type and r_{a3}-type, respectively. In particularly challenging cases,[111–114] K should be determined *via* molecular dynamics as a single-step correction[115] that implicitly accounts for all the terms in Eq. 2.17. Structures solved in this way are termed $r_{e,MD}$-type.

3 Theory II: *Ab Initio* Computational Chemistry and Trajectory Surface-Hopping Dynamics

This Chapter introduces the reader to some useful concepts that underpin *ab initio* computational chemistry and TSHD. It comprises an introduction to the time-dependent and time-independent forms of the Schrödinger equation (Section 3.1), the Born-Oppenheimer approximation (Section 3.2) and its breakdown (Section 3.3), single- and multireference wavefunctions (Section 3.4), and the TSHD algorithm (Section 3.5).

Attempting to cover satisfactorily all of this material would be a Herculean task. This Chapter aims, instead, at equipping the reader to appreciate the content of this thesis and cataloguing (from Section 3.3 onwards) new knowledge that the author has brought to the Wann Electron Diffraction Group over the course of this project. To explore advanced topics in multireference computational chemistry, the breakdown of the Born-Oppenheimer approximation, and TSHD, the comprehensive articles of Lischka *et al.*,[116] Crespo-Otero and Barbatti,[117] and Worth and Cederbaum[118] are highly recommended by the author.

3.1 Schrödinger Equation

The Schrödinger equation is at the heart of quantum mechanics. The time-dependent form of the Schrödinger equation, describing the wavefunction, $\Psi(\boldsymbol{r}, t)$, (with a dependency on spatial coordinates, $\boldsymbol{r}$, and time, t) for a quantum mechanical system, is given in Eq. 3.1, where $\hbar$ is the reduced Planck constant. Eq. 3.1 is a first order differential equation in t, such that $\Psi(\boldsymbol{r}, t_0)$ determines $\Psi(\boldsymbol{r}, t)$ for all t, and a linear equation for Ψ, such that if Ψ_i and Ψ_j are both valid solutions, then so are linear combinations of Ψ_i and Ψ_j.

$$\hat{H}\Psi(\boldsymbol{r}, t) = i\hbar \frac{\partial \Psi(\boldsymbol{r}, t)}{\partial t} \qquad \textbf{Eq. 3.1}$$

The Hamiltonian operator, $\hat{H}$, is given in Eq. 3.2, where m is the mass of a particle in the system under the effect of a potential, $V(\boldsymbol{r}, t)$ that, similarly, has a dependency on spatial coordinates and time. $\hat{H}$ has both kinetic, $\hat{T}$, and potential, $\hat{V}$, components.

$$\hat{H} = \hat{T} + \hat{V} = -\frac{\hbar^2}{2m}\frac{\partial^2}{\partial \boldsymbol{r}^2} + V(\boldsymbol{r}, t) \qquad \textbf{Eq. 3.2}$$

Defining an energy operator, $\hat{E}$, as in Eq. 3.3 allows Eq. 3.1 to be rewritten as Eq. 3.4.

$$\hat{E} = i\hbar\frac{\partial}{\partial t} \qquad \textbf{Eq. 3.3}$$

$$\hat{H}\Psi(\boldsymbol{r}, t) = \hat{E}\Psi(\boldsymbol{r}, t) \qquad \textbf{Eq. 3.4}$$

To obtain the time-independent form of the Schrödinger equation, $\Psi(\boldsymbol{r}, t)$ is separated into its spatial, $\psi(\boldsymbol{r})$, and temporal, $e^{-iEt/\hbar}$, components, as in Eq. 3.5, where E is energy.

$$\Psi(\boldsymbol{r}, t) = \psi(\boldsymbol{r})\psi(t) = \psi(\boldsymbol{r})e^{-iEt/\hbar} \qquad \textbf{Eq. 3.5}$$

The formulation of Eq. 3.5 ensures that the probability density, ρ, is made independent of time, as in Eq. 3.6, and allows the time-independent form of the Schrödinger equation to be obtained *via* substitution of the expression for $\Psi(\boldsymbol{r}, t)$ obtained in Eq. 3.5 into Eq. 3.1, as in Eq. 3.7.

$$\rho = \Psi(\boldsymbol{r}, t)\Psi^*(\boldsymbol{r}, t) = \psi(\boldsymbol{r})\psi^*(\boldsymbol{r}) \qquad \textbf{Eq. 3.6}$$

$$\hat{H}\Psi(\boldsymbol{r}) = E\Psi(\boldsymbol{r}) \qquad \textbf{Eq. 3.7}$$

The time-dependent (Eq. 3.1) and time-independent (Eq. 3.7) forms of the Schrödinger equation quickly become insoluble for many-body molecular systems (*i.e.* systems comprising many electrons and nuclei). The Hamiltonian operator (Eq. 3.2) for a molecular system comprises both electronic and nuclear components, as in Eq. 3.8, where $\hat{T}_\mathrm{e}$ and $\hat{T}_\mathrm{N}$ are the kinetic energy operators for the electrons and nuclei, respectively, and $\hat{V}_\mathrm{ee}$, $\hat{V}_\mathrm{NN}$, and $\hat{V}_\mathrm{eN}$ are potential energy operators describing electron-electron, nuclear-nuclear, and electron-nuclear interactions, respectively.

$$\hat{H} = \hat{T}_\mathrm{e} + \hat{T}_\mathrm{N} + \hat{V}_\mathrm{ee} + \hat{V}_\mathrm{NN} + \hat{V}_\mathrm{eN} \qquad \textbf{Eq. 3.8}$$

The expanded form of Eq. 3.8 is given in Eq. 3.9, where $\boldsymbol{R}$ and $\boldsymbol{r}$ are the spatial coordinates of the nuclei and the electrons, respectively, Z and e represent the nuclear and elementary charge, respectively, and ε_0 is the vacuum permittivity. Indices for electrons are given in lower case; indices for nuclei are given in upper case.

$$\hat{H} = \sum_i -\frac{\hbar^2}{2m_i}\frac{\partial^2}{\partial^2 \boldsymbol{r}_i} + \sum_I -\frac{\hbar^2}{2m_I}\frac{\partial^2}{\partial^2 \boldsymbol{R}_I} + \sum_i\sum_{j>i}\frac{e^2}{4\pi\varepsilon_0|\boldsymbol{r}_i - \boldsymbol{r}_j|} + \sum_I\sum_{J>I}\frac{Z_I Z_J e^2}{4\pi\varepsilon_0|\boldsymbol{R}_I - \boldsymbol{R}_J|} - \sum_i\sum_I\frac{Z_I e^2}{4\pi\varepsilon_0|\boldsymbol{r}_i - \boldsymbol{R}_I|} \qquad \textbf{Eq. 3.9}$$

This problem is overcome *via* invocation of the Born-Oppenheimer approximation.

3.2 Born-Oppenheimer Approximation

The Born-Oppenheimer approximation is predicated on the assumption that the electronic and nuclear components of a wavefunction, $\Psi(\boldsymbol{r}, \boldsymbol{R})$, are separable to good approximation; since nuclei are more massive and move slower than electrons, the electrons can be considered to move in a fixed potential effected by stationary nuclei. Under the Born-Oppenheimer approximation, the Schrödinger equation is solved for a fixed nuclear configuration, $\boldsymbol{R}_\mathrm{f}$. $\Psi(\boldsymbol{r}, \boldsymbol{R})$ is partitioned into an electronic, $\Psi(\boldsymbol{r}, \boldsymbol{R}_\mathrm{f})$, and nuclear, $\chi(\boldsymbol{R})$, component, as in Eq. 3.10. The latter component is dependent only on $\boldsymbol{R}$; the former is dependent on $\boldsymbol{r}$ and $\boldsymbol{R}$, but the dependence on $\boldsymbol{R}$ is only parametric.

$$\Psi(\boldsymbol{r}, \boldsymbol{R}) = \Psi(\boldsymbol{r}, \boldsymbol{R}_\mathrm{f})\chi(\boldsymbol{R}) \qquad \textbf{Eq. 3.10}$$

The Hamiltonian operator (Eq. 3.8 and 3.9) is consequently simplified under the Born-Oppenheimer approximation; one can omit $\hat{T}_\mathrm{N}$ from Eq. 3.8, and $\hat{V}_\mathrm{NN}$ becomes constant. An electronic Hamiltonian operator, $\hat{H}_\mathrm{e}$, is given in Eq. 3.11 – the expanded form should be apparent to the reader (*cf.* Eq. 3.9).

$$\hat{H}_\mathrm{e} = \hat{T}_\mathrm{e} + \hat{V}_\mathrm{ee} + \hat{V}_\mathrm{NN} + \hat{V}_\mathrm{eN} \qquad \textbf{Eq. 3.11}$$

$\hat{H}_\mathrm{e}$ can be used in the "*clamped nuclei*" electronic Schrödinger equation, given in Eq. 3.12, to obtain an electronic energy, E_e; on reintroduction of $\hat{T}_\mathrm{N}$, one arrives at the nuclear Schrödinger equation, given in Eq. 3.13.

$$\hat{H}_\mathrm{e}\Psi(\boldsymbol{r}, \boldsymbol{R}_\mathrm{f}) = E_\mathrm{e}\Psi(\boldsymbol{r}, \boldsymbol{R}_\mathrm{f}) \qquad \textbf{Eq. 3.12}$$

$$(\hat{T}_\mathrm{N} + E_\mathrm{e})\chi(\boldsymbol{R}) = E\chi(\boldsymbol{R}) \qquad \textbf{Eq. 3.13}$$

As the Schrödinger equation is at the heart of quantum mechanics, so is the Born-Oppenheimer approximation at the heart of contemporary computational chemistry, and it holds satisfactorily in most cases. However, if one is interested in photochemical processes, then one should expect to have to go beyond the Born-Oppenheimer approximation as a matter of course.[118] Where the potential energy surfaces of electronic states are close in energy, the coupling between electronic and nuclear dynamics (termed "*vibronic*" or "*non-adiabatic*" coupling) can become large and, here, the assumptions on which the Born-Oppenheimer approximation is predicated begin to break down.[118] Levine and Martínez write that "*…breakdown of the* [Born-Oppenheimer approximation] *is the rule in photochemical processes…*",[119] and Barbatti writes that *"…the occurrence of non-*

adiabatic effects is not only common …but is also the basis for key biochemical phenomena such as light detection and the photostability of the genetic code."[120]

3.3 Breakdown of the Born-Oppenheimer Approximation

The breakdown of the Born-Oppenheimer approximation at the point of intersection between two potential energy surfaces gives rise to curious topological features with singular non-adiabatic coupling.[118,121] The topology of the potential energy surfaces around the point of intersection is that of a "*diabolo*", or double-cone;[118,121] the feature is termed a "*conical intersection*", or "*photochemical funnel*". The conical intersection funnels wavepackets from higher-lying electronic states into lower-lying electronic states (or *vice versa*, if the conical intersection has the right topology). Non-radiative internal conversion (IC) – one of the ways in which an electronically-excited state can be deactivated – is promoted in the vicinity of a conical intersection.

The conical intersection was not fully appreciated when first described by Neumann and Wigner[122] in the late 1920s and, subsequently, by Teller[123] in the 1930s, but today, the conical intersection is invoked in almost all contemporary descriptions of non-radiative photochemistry.[118,121] This paradigm shift was delivered by commercialisation of the femtosecond laser, allowing experimentalists to measure for the first time lifetimes of electronically-excited states that were too short to be consistent with models that did not invoke the conical intersection, and parallel developments in computational chemistry that providing theoreticians with efficient algorithms and systematic approaches for locating minimum-energy conical intersections (MECI).[118,121]

The reader might begin by considering a two-state, near-degenerate quantum system. The electronic Hamiltonian matrix, $\hat{\boldsymbol{H}}_{\mathrm{e}}$, for a two-state system is given in Eq. 3.14.

$$\hat{\boldsymbol{H}}_{\mathrm{e}} = \begin{pmatrix} H_{ii} & H_{ij} \\ H_{ji} & H_{jj} \end{pmatrix} \qquad \textbf{Eq. 3.14}$$

The matrix elements of $\hat{\boldsymbol{H}}_{\mathrm{e}}$ in Eq. 3.14 take the form given in Eq. 3.15.

$$H_{\mathrm{ij}} = \left\langle \Psi_i \middle| \hat{H}_{\mathrm{e}} \middle| \Psi_j \right\rangle \qquad \textbf{Eq. 3.15}$$

Diagonalisation of $\hat{\boldsymbol{H}}_{\mathrm{e}}$ – in this case – is trivial and yields the eigenvalues, E_{e}, given in Eq. 3.16, where ΔH_{+} and ΔH_{-} are as given in Eq. 3.17 and 3.18, respectively.

$$E_{\mathrm{e}} = \Delta H_{+} \pm \sqrt{\Delta H_{-}^2 + H_{ij}^2} \qquad \textbf{Eq. 3.16}$$

$$\Delta H_{+} = \frac{1}{2}(H_{ii} + H_{jj}) \qquad \textbf{Eq. 3.17}$$

$$\Delta H_{-} = \frac{1}{2}(H_{ii} - H_{jj}) \qquad \textbf{Eq. 3.18}$$

The reader will recognise immediately that there are two conditions that have to be fulfilled for the two eigenvalues to be degenerate and, consequently, for the potential energy surfaces to intersect; these conditions are given in Eq. 3.19 and 3.20.

$$H_{ii} = H_{jj} \qquad \textbf{Eq. 3.19}$$

$$H_{ij} = 0 \qquad \textbf{Eq. 3.20}$$

As two degrees of freedom are necessary to fulfil the two conditions, the dimensionality of a conical intersection is $N - 2$, where N is the number of internal coordinates in the molecule. The two internal coordinates that lift the degeneracy of the potential energy surfaces to the first order are typically illustrated in the "*g/h*" or "*branching*" plane of the conical intersection. By expanding the matrix elements of $\hat{\boldsymbol{H}}_{e}$ as a first-order Taylor series around the conical intersection, as in Eq. 3.21, one obtains the equations given in Eq. 3.22 and 3.23 and, consequently, the conditions given in Eq. 3.24 and 3.25. $\nabla\Delta H_{-}$ is the $\boldsymbol{g}$ vector; ∇H_{ij} is the $\boldsymbol{h}$ vector.

$$H(\boldsymbol{R}) = H(\boldsymbol{R}_0) + \nabla H(\boldsymbol{R}_0) \cdot \Delta\boldsymbol{R} \qquad \textbf{Eq. 3.21}$$

$$\Delta H_{-}(\boldsymbol{R}) = 0 + \nabla\Delta H_{-}(\boldsymbol{R}_0) \cdot \Delta\boldsymbol{R} \qquad \textbf{Eq. 3.22}$$

$$H_{ij}(\boldsymbol{R}) = 0 + \nabla H_{ij}(\boldsymbol{R}_0) \cdot \Delta\boldsymbol{R} \qquad \textbf{Eq. 3.23}$$

$$\nabla\Delta H_{-}(\boldsymbol{R}_0) \cdot \Delta\boldsymbol{R} = 0 \qquad \textbf{Eq. 3.24}$$

$$\nabla H_{ij}(\boldsymbol{R}_0) \cdot \Delta\boldsymbol{R} = 0 \qquad \textbf{Eq. 3.25}$$

Examples of different conical intersection topologies (all examples of MECI that have been optimised *ab initio* over the course of this project) are given in Fig. 3.1.

While conical intersection topology is often invoked to describe intuitively the rate of IC (with glancing conical intersections being less efficient at directing/driving dynamics towards IC than peaked, strongly-funnelling conical intersections), contemporary work by Hynes and Malhado[124] suggests that conical intersection topology has no effect on the strength of interstate coupling and, therefore, on the probability of IC.

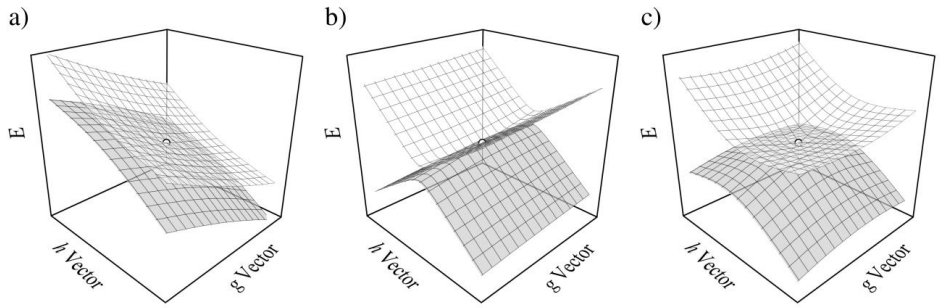

Figure 3.1. Examples of different (S_1/S_0) MECI topologies located during the course of this project: a) 1,2-dithiane ($MECI_{Sølling}$; Chapter 6, Section 6.3.2), b) 1,2-dithiin (Chapter 8, Section 8.3), and c) *E*-cinnamonitrile (*tp*$MECI_{E,\alpha}$; Chapter 7, Section 7.3.2). The darker and lighter wireframes represent the S_0 and S_1 potential energy surfaces, respectively.

3.4 Single- and Multireference Wavefunctions

An arbitrary *N*-electron determinant, Φ, suitable for describing an *N*-electron system can be constructed from *N* single-electron wavefunctions. To define a single-electron wavefunction requires three spatial variables and a spin variable. An expression for Φ is given in Eq. 3.26, where ψ and $\overline{\psi}$ are spatial orbitals paired with α and β spin functions, respectively.[125] The spatial orbitals are typically expanded in a finite basis of Gaussian-type functions – referred to as the basis set, {φ} – as in Eq. 3.27.[125]

$$\Phi = \left|\psi_i\overline{\psi}_i\psi_j\overline{\psi}_j\ldots\psi_N\overline{\psi}_N\right\rangle \qquad \textbf{Eq. 3.26}$$

$$\psi_i = \sum_j c_{ji}\varphi_j \qquad \textbf{Eq. 3.27}$$

Of all wavefunction *ansätze*, configuration interaction (CI) is conceptually the simplest.[125] CI expansion of Ψ in a basis of *N*-electron determinants, {Φ}, allows for exact computation of the energies of the electronic ground state and all electronically-excited states in principle, if {Φ} is complete.[125] A CI wavefunction *ansatz* is given in Eq. 3.28.[125]

$$|\Psi\rangle = \sum_i c_i\,|\Phi_i\rangle \qquad \textbf{Eq. 3.28}$$

Full CI (FCI) expands enormously with *N* and the number of spatial orbitals, *n*; it is insoluble for all but the simplest of molecules. An alternative is to expand Ψ in a basis that comprises a single reference (SR) determinant, Φ_0, and determinants that differ from Φ_0 by being singly-excited (S; Φ_a^i), doubly-excited (D; Φ_{ab}^{ij}), triply-excited (T; Φ_{abc}^{ijk}) *etc.*, up to and including *N*-tuply excited determinants, as in Eq. 3.29.[125]

$$|\Psi\rangle = c_0|\Phi_0\rangle + \sum_{\substack{a \\ i}} c_a^i|\Phi_a^i\rangle + \sum_{\substack{a<b \\ i<j}} c_{ab}^{ij}|\Phi_{ab}^{ij}\rangle + \sum_{\substack{a<b<c \\ i<j<k}} c_{abc}^{ijk}|\Phi_{abc}^{ijk}\rangle + \ldots \qquad \textbf{Eq. 3.29}$$

One arrives at the CIS, CISD, *etc.* approaches, depending on where the CI expansion is truncated.[125] However, this approach is only valid if the system can be adequately described by a single reference determinant, *i.e.* if c_0 dominates in the CI expansion of Eq. 3.29.[125] If one is interested in photochemical processes (among other applications), one is likely to encounter cases where a single reference determinant does not suffice, *i.e.* at the S_1/S_0 crossing seam, and in bond photofission processes.[116] Here, one of the following multireference (MR) approaches (used throughout this thesis) is necessitated. One arrives at the complete-active-space self-consistent field (CASSCF)[126] approach *via* FCI within a limited subspace of orbitals – the active space. Construction of the active space has been described as an art; it is not always trivial.[127] The CI and orbital expansion coefficients in Eq. 3.27 and Eq. 3.28 are optimised simultaneously in the CASSCF approach. The CASSCF approach can be improved *via* perturbation theory; one arrives at the complete-active-space perturbation theory to the second order (CASPT2)[128–131] approach in this way. An alternative is to take a set of reference determinants in place of Φ_0 in the truncated CI expansion of Eq. 3.29, chosen judiciously to span the important configurations of Ψ and to resolve quasi-degeneracies in the reference space of orbitals. One arrives at the multireference CI (MRCI) approaches in this way, *e.g.* MRCIS, MRCISD, *etc.*, depending on where the CI expansion is truncated.[116] A MRCI expression for Ψ is given in Eq. 3.30.[116] Each of the reference determinants is excited independently, such that Φ_i collects all the possible excited configurations within the reference space, Φ_S^a collects single excitations out of the reference space, and Φ_D^{ab} collects double excitations out of the reference space, *etc.*[116]

$$|\Psi\rangle = \sum_i c_i|\Phi_i\rangle + \sum_{S,\,a} c_S^a|\Phi_S^a\rangle + \sum_{D,\,a,\,b} c_D^{ab}|\Phi_D^{ab}\rangle + \ldots \qquad \textbf{Eq. 3.30}$$

The orbital and CI expansion coefficients in Eq. 3.26 and Eq. 3.28 are optimised separately. CI and CASSCF can be computationally expensive and resource-hungry, but massively-parallel algorithms[132–135] have made possible CI expansions containing one trillion determinants[135] – this holds the current record for the largest conventional expansion ever carried out.[135] For the average user, CASSCF active spaces larger than fourteen electrons in fourteen orbitals (*ca.* three million configurations) are not particularly practicable.

3.5 Trajectory Surface-Hopping Dynamics

TSHD is one of the most successful flavours of semi-classical, or "*non-adiabatic mixed quantum-classical*" (NA-MQC), MD approaches for dynamics at the crossing seam between electronic states.[117,120] The approach has been reviewed most accessibly by Barbatti,[120] and most comprehensively by Crespo-Otero and Barbatti[117] in a contemporary article; both are recommended in the strongest possible terms to the interested reader.

TSHD is predicated on the supposition that the temporal evolution of a wavepacket – accounting, in particular, for non-adiabatic effects like bifurcation of the wavepacket at the crossing seam – can be approximated by a sufficiently large ensemble, or "*swarm*", of semi-classical trajectories that are able to swap, or "*hop*", probabilistically between different potential energy surfaces.[117,120] This is illustrated in Fig. 3.2. The a) conceptual simplicity, b) on-the-fly implementation, c) full treatment of all nuclear degrees of freedom, d) high potential for trivial parallelisation, and e) straightforward interfacing with contemporary electronic structure techniques (requiring only that they are capable of delivering cost-effectively energies, energy gradients, and non-adiabatic couplings) give TSHD an edge over full quantum-mechanical wavepacket dynamics.

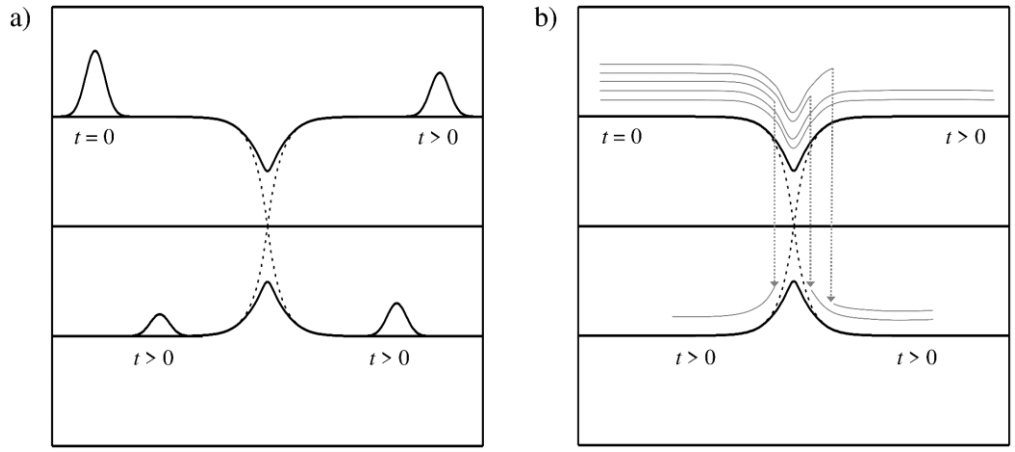

Figure 3.2. Illustrations of a) wavepacket dynamics and b) TSHD at the crossing seam. At $t = 0$, the wavepacket has not visited the crossing seam; by $t > 0$, the wavepacket has bifurcated and left the crossing seam. The bifurcation of the wavepacket at the crossing seam can be approximated by a sufficiently large ensemble, or "*swarm*", of semi-classical trajectories. Adapted from Ref. 120; credit to Mario Barbatti.

A flowchart outlining the TSHD algorithm is presented in Fig. 3.3. The algorithm comprises the following steps: generation of suitable initial conditions (Section 3.5.1), on-

the-fly computation of energies, energy gradients, and non-adiabatic couplings for propagation of the electrons and nuclei (Section 3.5.2) *via* quantum-mechanical and classical-mechanical equations of motion (EOM), correction of the artificial electronic coherency (Section 3.5.3), and evaluation of surface-hopping probabilities (Section 3.5.4).

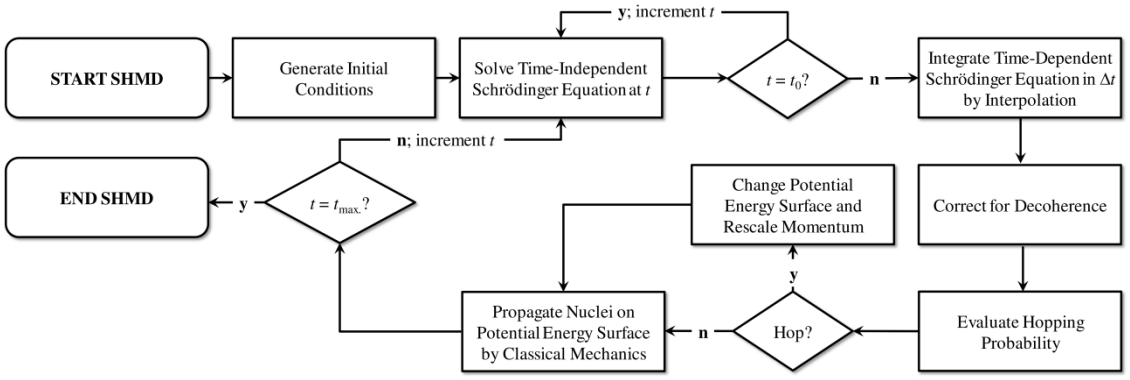

Figure 3.3. Flowchart outlining the workflow for TSHD.

3.5.1 Initial Conditions

A ground-state nuclear ensemble, $\eta(\boldsymbol{R}, \boldsymbol{P})$, with nuclear coordinates, $\boldsymbol{R}$, and momenta, $\boldsymbol{P}$, has to be constructed pre-transformation into the electronic state of interest.[117,120] There are two commonly-employed ways to construct $\eta(\boldsymbol{R}, \boldsymbol{P})$. The first is to propagate independent MD trajectories (or a single, long-timescale MD trajectory) on the ground-state potential energy surface and construct $\eta(\boldsymbol{R}, \boldsymbol{P})$ by sampling randomly points from the MD trajectories. The second is to sample from a model nuclear phase-space probability distribution. A popular option is the Wigner distribution for a quantum harmonic oscillator. The latter is often a better choice; work by Barbatti and Sen[136] has demonstrated that where MD trajectories are thermalised at ambient temperature (*i.e.* 298 K) – as is standard practice – the resultant nuclear phase-space distribution is too narrow.

3.5.2 Propagation

The electrons are propagated according to the time-dependent Schrödinger equation (Section 3.1; Eq. 3.1) where Ψ is expanded in a basis of electronic states, $\{\varphi\}$. An expression for Ψ (with parametric dependence on $\boldsymbol{R}$, which is fixed and consequently denoted $\boldsymbol{R}_\mathrm{f}$; Section 3.2) is given in Eq. 3.31.[120]

$$\Psi(\boldsymbol{r}, \boldsymbol{R}_\mathrm{f}, t) = \sum_i c_i(t)\varphi_i(\boldsymbol{r}, \boldsymbol{R}_\mathrm{f}) \qquad \textbf{Eq. 3.31}$$

A set of differential equations, given in Eq. 3.32,[120] is obtained when Eq. 3.31 is substituted in Eq. 3.1. Coupling between pairs of electronic states is accounted for by the nonadiabatic coupling vector, $\boldsymbol{F}_{ij}$. The form of $\boldsymbol{F}_{ij}$ is as given in Eq. 3.33.[120] In Eq. 3.32, H_{ij} is a matrix element of $\hat{\boldsymbol{H}}_{\mathrm{e}}$, as in Eq. 3.15, and $\boldsymbol{v}$ is a nuclear velocity vector.

$$i\hbar\frac{\partial c_i}{\partial t} + \sum_j -c_j(H_{\mathrm{ij}} + i\hbar\boldsymbol{F}_{\mathrm{ij}} \cdot \boldsymbol{v}) = 0 \qquad \textbf{Eq. 3.32}$$

$$\boldsymbol{F}_{\mathrm{ij}} = \langle\varphi_i|\nabla_{\boldsymbol{R}}|\varphi_j\rangle \qquad \textbf{Eq. 3.33}$$

The nuclei are propagated on a Born-Oppenheimer potential energy surface *via* classical mechanics using a Newtonian EOM. The equation for propagating a nucleus is given in Eq. 3.34,[120] where m is the mass of the nucleus, and the force acting on the nucleus is proportional to the gradient of the potential energy surface, ∇H_{ii}.

$$\frac{d^2\boldsymbol{R}}{dt^2} + \frac{\nabla H_{ii}}{m} = 0 \qquad \textbf{Eq. 3.34}$$

Since nuclei are more massive and move slower than electrons (Section 3.2), the integration of the EOM for the electrons and nuclei does not have to be carried out with the same integration time step, dt – indeed, computational cost can be limited by integrating judiciously the quantum-mechanical and classical-mechanical EOM with different dt.[117,120] The latter are typically integrated with $0.25 \leq dt \leq 1$ fs (with Δt dictated by both the fastest nuclear vibrations, and how strictly it is necessary to ensure that momentum is well-conserved); the former are typically integrated with $0.005 \leq dt \leq 0.02$ fs.[117,120] Fortunately, it is not necessary to solve the time-dependent Schrödinger equation (the bottleneck in the TSHD algorithm) this frequently; if it were, TSHD would prove intractable. The time-dependent Schrödinger equation is instead solved only once at each classical-mechanical time step; the necessary quantities are interpolated between each classical-mechanical time steps (pre-integration of the quantum-mechanical EOM; Fig. 3.3).[117,120]

3.5.3 Decoherence Correction

TSHD trajectories are artificially coherent if uncorrected; electronic wavepacket correlation, termed "*overcoherence*", results because the nuclear wavepacket in each TSHD trajectory is constrained to be propagated on a single potential energy surface, with amplitude $c_i(t)$. The amplitudes, $c_j(t)$ ($j \neq i$), of the remaining "*ghost states*" are consequently constrained to be propagated along the same nuclear trajectory, even though

these amplitudes could potentially dissipate in different directions on their respective potential energy surfaces if unconstrained.[117,120] The off-diagonal elements, $\rho_{ij}(t) = c_i(t)c_j(t)^*$, of the probability density matrix, $\rho(t)$, do not vanish and, as a consequence, internal consistency is not usually achieved because the average adiabatic populations – the diagonal elements, $\rho_{ii}(t) = c_i(t)c_i(t)^*$, of $\rho(t)$ – diverge from the fractional populations of the electronic states, $N_i(t)/N_{\text{Traj.}}$, such that the equality in Eq. 3.35 is not met.[117,120]

$$\frac{1}{N_{\text{Traj.}}}\sum_{N}^{N_{\text{Traj.}}}\rho_{ii} = \frac{N_i(t)}{N_{\text{Traj.}}} \qquad \textbf{Eq. 3.35}$$

Several recipes for decoherence correction exist,[117,120] but the *decay-of-mixing* approach of Truhlar *et al.*[137–139] is a particularly popular choice, as it is highly effective. c_j and c_i are corrected at each time step (post-integration of the time-dependent Schrödinger equation; Fig. 3.3) according to Eq. 3.36 and 3.37, respectively.[117,120]

$$c'_j = c'_j e^{-dt/\tau_{ij}},\ \forall\ i \neq j \qquad \textbf{Eq. 3.36}$$

$$c'_i = \frac{c_i}{|c_i|}\sqrt{1 - \sum_{j \neq i}|c'_j|} \qquad \textbf{Eq. 3.37}$$

The phenomenological decoherence time, τ_{ij}, is given in Eq. 3.38.[117,120] Here, T_{N} is the nuclear kinetic energy, and ε is the decoherence parameter. ε can be set to any appropriate value, but is usually allowed to default to 0.1 a.u.

$$\tau_{ij} = \frac{\hbar}{|H_{jj} - H_{ii}|}\left(1 + \frac{\varepsilon}{T_{\text{N}}}\right) \qquad \textbf{Eq. 3.38}$$

3.5.4 Surface-Hopping

Several recipes for probabilistic surface-hopping exist.[117,120] Among these, the fewest-switches surface-hopping (FSSH) algorithm of Tully[140,141] has probably been the most influential on the development of TSHD, and can be credited with popularising the approach in the late 1990s; FSSH has since seen more or less universal adoption.[117,120]

FSSH minimises the number of trajectories that are required to swap (or "*switch*") between the Born-Oppenheimer potential energy surfaces in *dt* to maintain the average adiabatic populations of the electronic states. The key result of the FSSH derivation by Tully[140,141] is given in Eq. 3.39, which describes how the probability density matrix element, $\rho_{ii}(t)$, for some active state changes as a function of time.

$$\rho_{ii}(t) = \frac{2}{\hbar}\sum_{j} Im\left(H_{ij}\cdot\rho_{ji}(t)\right) - 2Re\left(i\hbar\boldsymbol{F}_{ij}\cdot\boldsymbol{v}\cdot\rho_{ji}(t)\right) \qquad \textbf{Eq. 3.39}$$

It is then straightforward to derive an expression for the flux of population out of the active state to all other states over *dt*; this expression is given in Eq. 3.40.

$$\frac{\rho_{ii}(t+dt) - \rho_{ii}(t)}{\rho_{ii}(t)} \approx \frac{2}{\rho_{ii}(t)\hbar}\sum_{j} Im\left(H_{ij}\cdot\rho_{ji}(t)\right) - 2Re\left(i\hbar\boldsymbol{F}_{ij}\cdot\boldsymbol{v}\cdot\rho_{ji}(t)\right)dt \qquad \textbf{Eq. 3.40}$$

It follows, then, that the probability of swapping from the potential energy surface for the active state to some other potential energy surface can be written as in Eq. 3.41.

$$P_{j\leftarrow i}^{\mathrm{FSSH}}(t) \approx \frac{2}{\rho_{ii}(t)\hbar}\left\{Im\left(H_{ij}\cdot\rho_{ji}(t)\right) - 2Re\left(i\hbar\boldsymbol{F}_{ij}\cdot\boldsymbol{v}\cdot\rho_{ji}(t)\right)\right\}dt \qquad \textbf{Eq. 3.41}$$

The instantaneous probability is evaluated at every classical-mechanical time step. The trajectory will swap potential energy surface if a) a uniformly-sampled random number, $rt \in [0, 1]$, is smaller than the probability of surface hopping, and b) energy can be conserved.[117,120] In order to satisfy the latter requirement, $\boldsymbol{v}$ can be rescaled. If $\boldsymbol{F}_{ij}$ has been explicitly computed, rescaling should be carried out in the direction of $\boldsymbol{F}_{ij}$ – otherwise, rescaling can be carried out in the direction of $\boldsymbol{v}$.[117,120] If $\boldsymbol{v}$ cannot be rescaled such that the requirement for conservation of energy is satisfied (*e.g.* if the requisite reduction in a component of $\boldsymbol{v}$ is greater than the magnitude of that component), then the trajectory does not swap potential energy surface and the event is recorded as a "*rejected*", or "*frustrated*", hop.[117,120] Tully[140] recommended that the direction of $\boldsymbol{v}$ should be reversed along $\boldsymbol{F}_{ij}$ following a "*frustrated*", hop.

3.5.5 Practical Considerations in Trajectory Surface-Hopping Dynamics

Balancing computational cost against accuracy and return on expenditure is paramount. Barbatti writes, bluntly, that "...[the reader] *must ask* [themselves]*: is it really worth doing dynamics?*".[142] The computational cost of TSHD is proportional to the time, t_{C}, taken to compute the energies, energy gradients, and non-adiabatic couplings (the bottleneck of the TSHD algorithm; t_{C} is molecule-, electronic-structure-approach- and resource/hardware-dependent), the total time, $t_{\mathrm{Tot.}}$, and time step, *dt*, required to simulate the photochemical process of interest, and the number of trajectories, $N_{\mathrm{Traj.}}$, that need to be propagated to

obtain statistically-converged results.[142] A back-of-the-envelope expression for the computational cost of TSHD (t_{TSHD}, usually expressed in CPU·h) is given in Eq. 3.42.[142]

$$t_{\mathrm{TSHD}} \propto N_{\mathrm{Traj.}} \cdot t_{\mathrm{C}} \cdot \frac{t_{\mathrm{Tot.}}}{dt} \qquad \textbf{Eq. 3.42}$$

The reader is invited to consider the computational cost of routine TSHD, *e.g.* TSHD of 1,2-dithiane (Chapter 6; Section 6.3.3). Here, where $t_{\mathrm{C}} \approx 0.2$ CPU·h, $t_{\mathrm{Tot.}} = 1$ ps, $dt = 0.5$ fs, and $N_{\mathrm{Traj.}} = 100$, an allocation of *ca.* 40,000 CPU·h is required (equivalent to a wallclock time of *ca.* four and a half years) if TSHD is carried out in serial – this assumes (optimistically) that any I/O overheads are negligible. TSHD might be made tractable by trivial parallelisation over 100 CPU cores ($N_{\mathrm{Traj.}}$ CPU$^{-1} = 1$); in the former case, all the TSHD trajectories could be recorded within a wallclock time of *ca.* two weeks, but one may not have 100 CPU cores available to commit exclusively to TSHD for two weeks. The computational cost could be reduced further by parallelising the computation of the energies, energy gradients, and non-adiabatic couplings – Martínez *et al.*[143–148] have made great progress in this particular direction *via* GPU acceleration – but a) many MR approaches (Section 3.4) are not efficiently parallelised in existing electronic structure packages, b) even more computational resources are required than in the preceding example, c) additional parallel overheads are introduced in t_{C}, and d) the reduction in CPU·h with increasing core count is not often linear. On the national ARCHER (Cray XC30) HPC, the cost of 40,000 CPU·h for this example would be *ca.* £8,000.[149]

Motivation to minimise the computational cost of TSHD is strong. $t_{\mathrm{Tot.}}$ and dt cannot be reduced and increased, respectively, to minimise the computational cost as these parameters are necessarily dictated by the photochemical process of interest. The former is already limited to a few hundred fs to a few ps, in any case, by the computational cost.[117,120] $N_{\mathrm{Traj.}}$ and t_{C} are usually reduced instead (in the latter case, this is achieved by downgrading the level of electronic structure approach), impacting the quality and accuracy of TSHD.[117,120] On cursory examination of the literature (including this thesis), the reader will note that the following is true of the overwhelming majority of TSHD simulations.

Firstly, $N_{\mathrm{Traj.}}$ is reduced routinely below the recommended value for statistical convergence ($N_{\mathrm{Traj.}} = 400$). A multiple-ensemble approach – where many unique ensembles in nuclear phase-space are generated (Section 3.5.1), and many trajectories are propagated from each initial starting structure to respect the stochasticity of the TSHD algorithm (Section 3.5.4) – is generally forgone in favour of a single ensemble in nuclear phase-space, or a double

ensemble in nuclear phase-space and a basis of electronic states, with a single trajectory being propagated from each member of the ensemble.[117,120]

Secondly, t_C is reduced routinely by working in the small (double-ζ) basis limit,[117,120] and with lower-level electronic structure approaches,[117,120] *e.g.* CASSCF (sometimes with truncated active spaces), or time-dependent density functional theory (TDDFT; Tapavicza *et al.*[150] and Tavernelli[151] review comprehensively TSHD interfaced with TDDFT). Crespo-Otero and Barbatti[117] illustrate how significant the consequences of downgrading the level of electronic structure approach can be. The authors collate a number of contemporary TSHD studies to demonstrate that TSHD of the canonical nucleobases (9-H)adenine[152,153] and thymine[154] delivers different results for the lifetimes of the electronically-excited states depending on whether *ab initio* or TDDFT approaches are employed, and that (CASSCF) TSHD of 2-aminopyrimidine[155] is sensitive to the construction of the active space. Indeed, one does not necessarily need to downgrade the level of electronic structure approach to obtain incorrect results; even the highest-level electronic structure approaches are not without fault and, for a great number of photochemical processes, are not able to describe the whole phase-space explored in the process in a balanced fashion.

What, then, does this mean? The author strongly agrees with Crespo-Otero and Barbatti, in that this "*…does not mean that there is nothing to do… but to expect better and faster electronic structure methods to be developed. On the contrary, …a careful selection of methods, with a cross-comparison between methodologies from different families,… and with respect to the limits of each approximation, will effectively allow one to set up dynamics for most of the systems of interest.*".[117]

In this spirit, the lower-level electronic structure approaches that have been interfaced with TSHD in this thesis have all been validated against higher-level electronic structure approaches and (where possible) experiment. Benchmarking has been performed using *ab initio* calculations at key geometries and along electronically-excited-state pathways connecting these geometries as a matter of course. The latest data analysis protocols in TRGED are increasingly eschewing the direct inclusion of theoretical information (*cf.* GED), and are likely to soon provide unbiased data with which to evaluate the performance of electronic structure approaches that have been interfaced with TSHD.

4 New Methods & Applications I: A New Lease of Life for the Only Gas Electron Diffractometer in the UK

The University of York gas electron diffractometer was formerly housed at the University of Reading and was initially commissioned in the 1960s. From the early 1980s and through into the new millennium, Rice and Page oversaw operation of the diffractometer, published prolifically[156–165] on the gas-phase equilibrium structures of organometallic, organic, and main-group molecules, and carried out collaborative work with leading gas electron diffractionists such as Rankin,[160,161] Hedberg,[156–158] and Hagen.[156–158]

The diffractometer was acquired by the Wann Electron Diffraction Group and relocated to the University of York in 2015 where it was reassembled and repaired, subjected to comprehensive modernisation of the mechanical and electronic components, calibrated,[74] and retrofitted with an air-heated effusive nozzle assembly to considerably extend the range of chemical samples accessible to study *via* GED.[43] The University of York gas electron diffractometer is currently the only one of its kind in the UK and one of only a handful of operational time-averaged gas electron diffractometers worldwide.[37–41] The gas-phase structural determination service that the Wann Electron Diffraction Group has been able to offer post-recommission has consequently proved popular with researchers worldwide. The author has acquired GED data for 23 chemical samples over the duration of this project, amounting to over 240 hours of electron beam uptime.

This Chapter comprises a description of the University of York gas electron diffractometer and two case studies drawn from published work that illustrate the efficacy of the diffractometer for obtaining well-resolved structures of isolated molecules in the gas phase. The case studies have been selected a) to highlight the breadth of chemical samples that are accessible to study *via* GED using the University of York gas electron diffractometer and b) to draw on collaborative work.

In the first case study, the gas-phase equilibrium structure of 4-(dimethylamino)benzonitrile (DMABN) is presented.[43] The low vapour pressure of DMABN at 298 K (<80 mbar) pushes the limits of the air-heated effusive nozzle assembly. In the second case study, the gas-phase equilibrium structures of tin^{II} bis(trifluoroacetate), $ditin^{II}$ μ-oxy-bis-μ-trifluoroacetate, and tin^{IV} tetrakis(trifluoroacetate) are presented.[166] These examples have been selected to showcase the results of a collaboration between the Wann Electron Diffraction Group and researchers at Carleton University (Ottawa, Canada).

4.1 University of York Gas Electron Diffractometer

The University of York gas electron diffractometer, schematically illustrated and photographed in Fig. 4.1, comprises a column module, chamber module, and detector module.

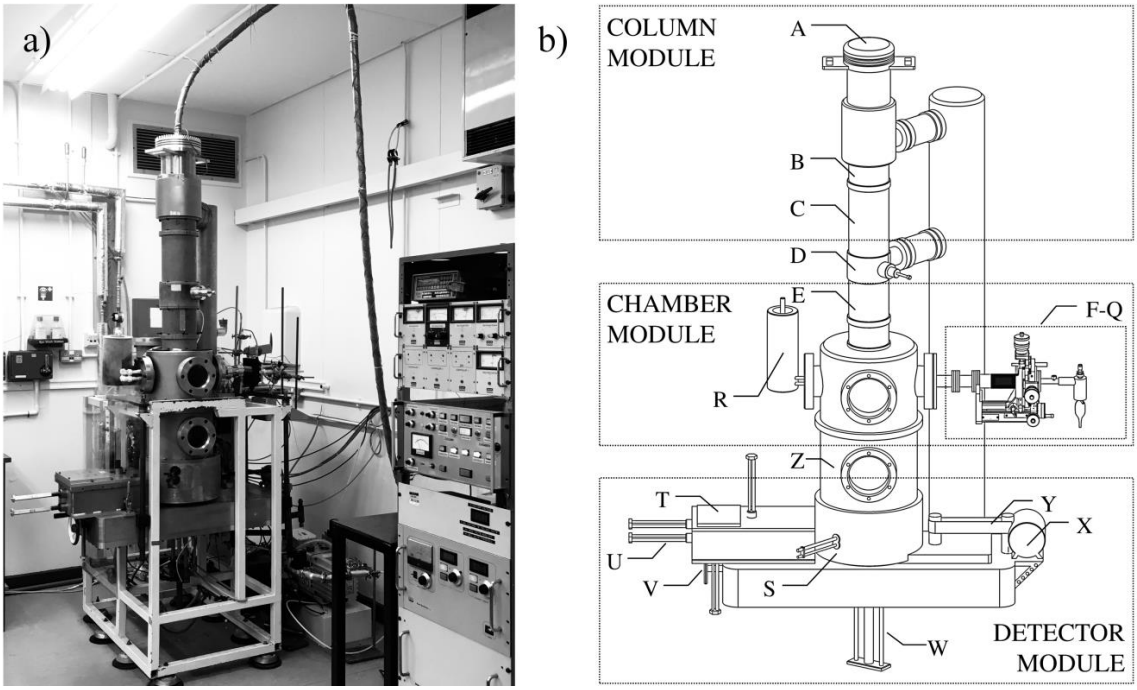

Figure 4.1. University of York gas electron diffractometer, a) photographed and b) schematically illustrated. The electron source (**A**), solenoid deflectors (**B**), electron flight tube (**C**), electron beam shutter (**D**), solenoid lens (**E**), air-heated effusive nozzle assembly (**F** – **Q**), liquid nitrogen trap (**R**), retractable scintillator screen (**S**), image plate magazine (**T**), image plate manipulators (**U**) and conveyor turn-handle (**V**), pneumatic actuator (**W**), rotating sector drive motor (**X**) and belt (**Y**), and removable spacer module (**Z**) are indicated. Components associated with the vacuum system described in Section 4.1.1 are omitted for clarity. Components **A** – **Z** are described in Sections 4.1.2 – 5. Components **F** – **Q** are schematically illustrated in Fig. 4.4. Adapted from Fig. 1 and Fig. 2 of Ref. 43.

The features of the University of York gas electron diffractometer are reviewed in Sections 4.1.1 to 4.1.5; the labels of Fig. 4.1 are referred to throughout.

4.1.1 Vacuum System

The delimitation of the column module and the chamber module allows for differential pumping of the diffractometer, provided that the electron beam shutter is in the closed position. The column module and the chamber module can be reduced to pressures in the range of 10^{-5} to 10^{-6} mbar, respectively, by the action of two independent oil diffusion pumps (Edwards E06 and E04, respectively) that are backed by a single rotatory pump (Edwards ED200) – these elements comprise the main vacuum manifold. A second rotatory pump (Edwards E2M30) bypasses the main vacuum manifold and is connected directly to the detector module. If the chamber module and detector module are vented to atmospheric pressure after data acquisition so that the image plate magazine (see Section 1.1.5) can be retrieved from the latter module, action of this rotary pump can reduce both modules to a pressures in the range of 10^{-3} to 10^{-4} mbar, sufficient for the oil diffusion pump to take over again once the rotatory pump has been isolated by manual closure of a quarter-turn isolation valve (Edwards IBV40MKS). Pumping in the main vacuum manifold is regulated by remotely-operated pneumatic butterfly valves (Edwards QSB5P and QSB3P) positioned directly above the oil diffusion pumps and solenoid valves (Edwards PLV25P).

4.1.2 Electron Source

The electron source (**A**) is mounted at the top of the column module and comprises a hairpin tungsten filament (Agar A050), Wehnelt cap, and anode plate arranged in the classic "triode" geometry (see Section 2.4.1). These components are photographed in Fig. 4.2.

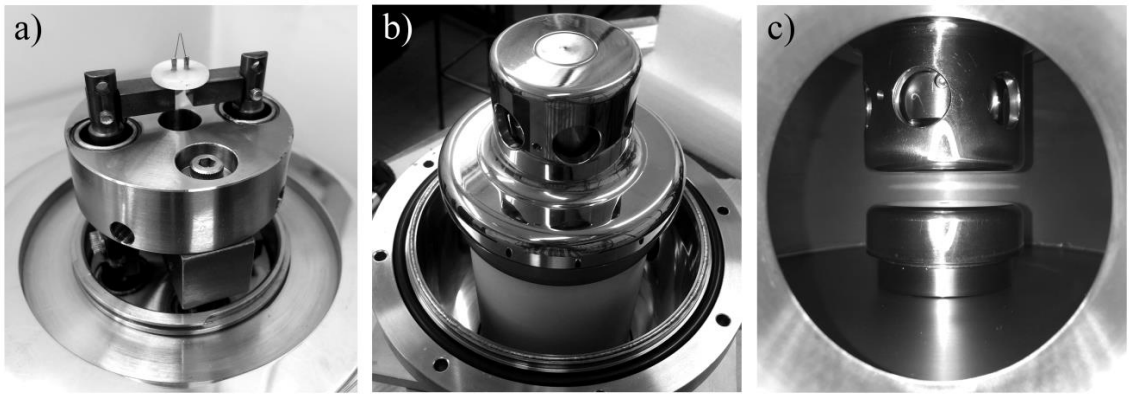

Figure 4.2. Photographs of the hairpin tungsten filament *ex situ* with the Wehnelt cap a) removed and b) installed, and c) *in situ*, spaced from the anode plate, with the components comprising the classic "triode" geometry. Fig. 4.2a is reproduced from Fig. 3 of Ref. 43.

A high-voltage power supply (Start Spellman; model unknown) is used to apply a variable accelerating potential (up to 50.0 kV), generating a continuous electron beam with a specific electron wavelength and a controllable electron emission current.

4.1.3 Electron Optics

A set of solenoid deflectors (**B**) steer the electron beam along the axis of the column module *via* a flight tube (**C**) and collimating aperture positioned inside the electron beam shutter (**D**). A solenoid lens (**E**) controls the transverse profile and the position of the focal plane of the electron beam. These components are photographed in Fig. 4.3.

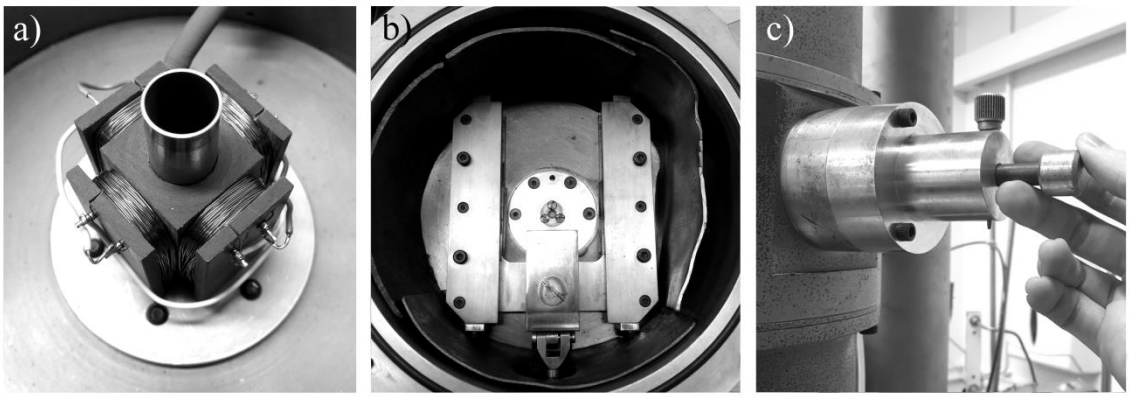

Figure 4.3. Photographs of a) the solenoid deflectors (**B**) and flight tube (**C**), b) the electron beam shutter (**D**) and collimating aperture inside the column module, and c) the electron beam shutter outside the column module. Fig. 4.3a is reproduced from Fig. 3 of Ref. 43.

4.1.4 Sample Input

A retrofitted air-heated effusive nozzle assembly (originally designed[107] and machined for a diffractometer formerly housed at the University of Edinburgh) is schematically illustrated in Fig. 4.4 and photographed in Fig. 4.5. The assembly allows samples with low volatility at room temperature to be input into the chamber module at the point of diffraction.

The air-heated effusive nozzle is coupled to a triple-axis translator (**F**) that can be used to position the nozzle tip *ca.* 250–500 μm from the axis of propagation of the electron beam. The nozzle shaft (**G**) and sample vial (**H**) can be heated independently up to a maximum of 220 °C by a continuous flow of compressed air (50 psi) that is branched into two channels, heated in-line, then delivered and exhausted by independent air inlets (**I**, **J**) and outlets (**K**, **L**), respectively.

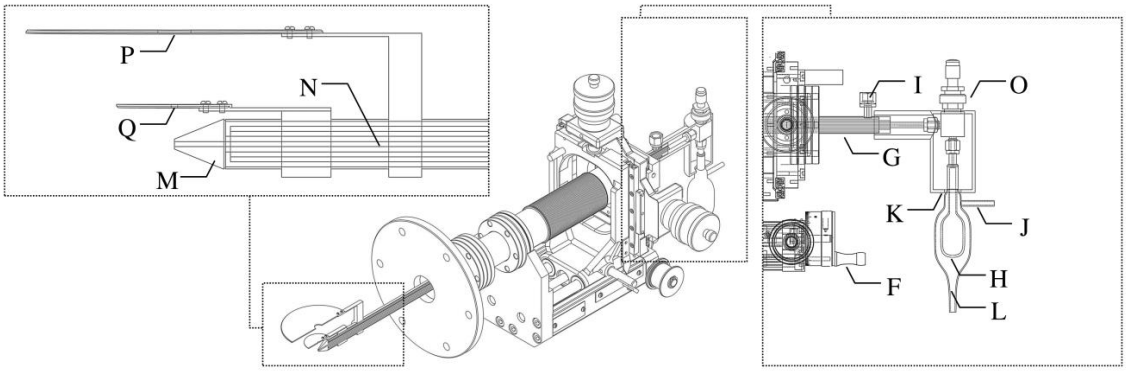

Figure 4.4. Schematic illustration of the air-heated effusive nozzle assembly; the illustration is cut away and expansions of the nozzle tip and sample vial sections are presented. The triple-axis translator (**F**), nozzle shaft (**G**), sample vial (**H**), air inlets (**I**, **J**) and outlets (**K**, **L**), nozzle tip (**M**), delivery tube (**N**), metering valve (**O**), 15 mm aperture (**P**), and 1 mm aperture (**Q**) are indicated. Adapted from Fig. 4 of Ref. 43.

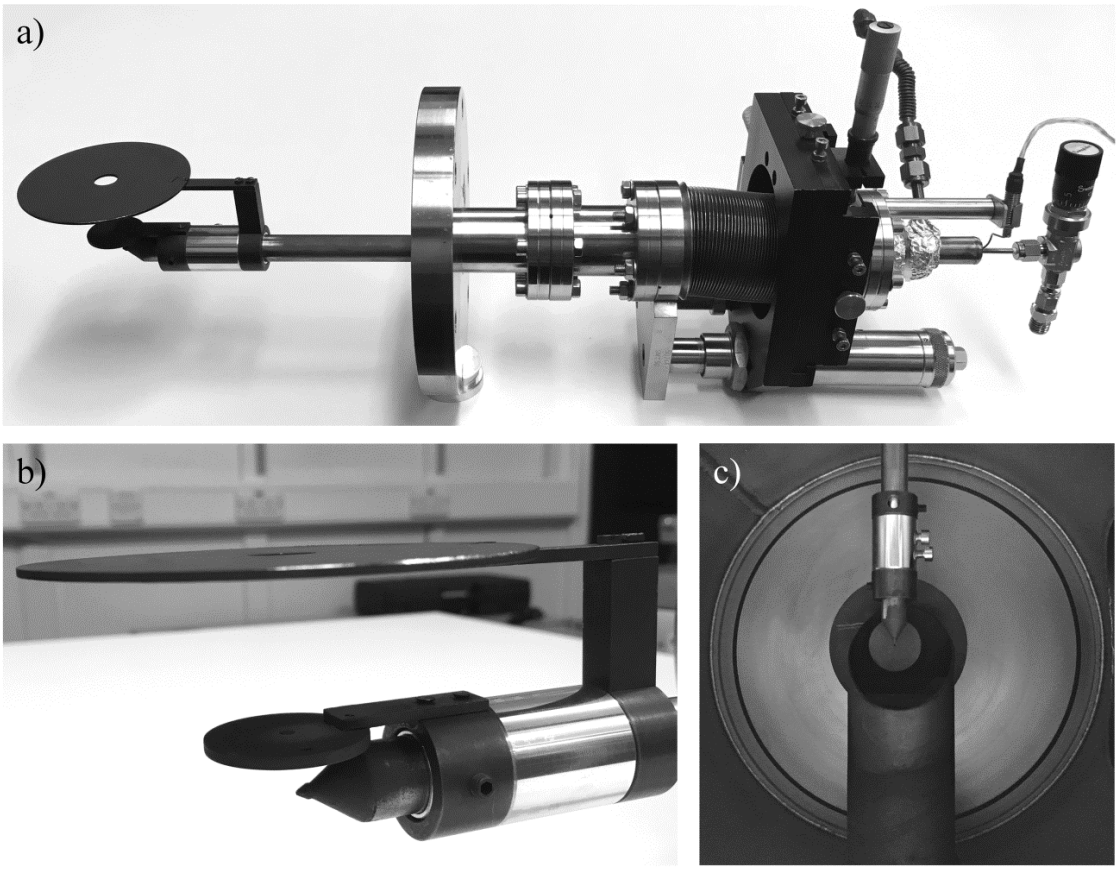

Figure 4.5. Photographs of a) the air-heated effusive nozzle assembly mounted onto the triple-axis translator (**F**) *ex situ*, b) the nozzle tip (**M**), 15 mm aperture (**P**), and 1 mm aperture (**Q**) *ex situ*, and c) the the nozzle tip (**F**), 15 mm aperture (**M**), and 1 mm aperture (**Q**) *in situ*, positioned opposite the liquid nitrogen trap (**R**) inside the chamber module.

Two independent proportional-integral-derivative (PID) controllers can be used to regulate the power supplied to the in-line heating elements, providing temperature stability of ±1 °C. A positive temperature gradient is often established between the sample vial and the nozzle tip (**M**) to prevent gaseous sample from condensing inside the delivery tube (**N**) and blocking flow into the chamber module.

The sample vial and the delivery tube are delimited by a metering valve (**O**, Swagelok SS-2MA-MH), allowing for fine control and reproducibility of sample input.

Two apertures are mounted onto the nozzle shaft and centered with respect to the axis of propagation of the electron beam; the apertures ensure that optimum electron beam quality is obtained at the point of diffraction. The first aperture (**P**) measures 15 mm in diameter and is fixed a few centimetres above the point of diffraction; the purpose of this aperture is to preclude stray electrons travelling at high angles from reaching the detector module. The second aperture (**Q**) measures 1 mm in diameter and is fixed a few millimetres above the point of diffraction; the purpose of this aperture is to collimate the electron beam.

A liquid nitrogen trap (**R**) mounted opposite the air-heated effusive nozzle assembly condenses the gaseous sample after interaction with the electron beam to preclude secondary scattering events, reduce background noise and lower the pressure in the chamber module.

4.1.5 Electron Detection

A retractable scintillator screen (**S**) coated with zinc sulphide grains that are doped with copper[167] can be used to make a visual assessment of the transverse profile and brightness of the electron beam before data acquisition.

If the operator is satisfied, data are recorded onto reusable image plates (Fuji BAS-IP MS 2025). These image plates comprise polyester films coated with barium fluorobromide grains that are doped with trace amounts of europium. On interaction with scattered electrons, the europium ions entrained in the barium fluorobromide lattice are oxidised from the +II state to the +III state; electron impacts are consequently encoded onto each image plate in the form of a position-dependent oxidation state distribution. This distribution is then digitized by scanning each image plate with visible light using a tabletop image plate scanner (Fuji BAS-1800II), reducing the europium ions from the +III state to the +II state and emitting a photon in the process that is collected by a photomultiplier tube. Each image plate can potentially be reused thousands of times, the only caveats being that they must not

be exposed to intense radiation and must be kept flat, clean, and contaminant-free. The image plate magazine (**T**) can support the loading of up to five image plates, each mounted on an aluminium retaining tray. The loaded retaining trays are manually cycled into and out of (before and after data acquisition, respectively) the detector module *via* the actuation of four manipulators (**U**) that translate the retaining trays inside the image plate magazine and a turn-handle (**V**) that drives a conveyor belt *via* which the retaining trays are translated into position above a pneumatic actuator (**W**). The pneumatic actuator is located on the underside of the detector module and lifts and lowers the loaded retaining trays to and from their data acquisition position underneath the rotating sector. An AC motor (**X**, Parvalux; model unknown) and belt (**Y**) drives the rotating sector at approximately 144 rpm, effectively applying an r^3-type function to the acquired data, where r is the distance the from the centre of the diffraction data (and, by extension, the image plate); the dynamic range of the detector is consequently improved considerably.

An image plate, the image plate magazine, and rotating sector are photographed in Fig. 4.6.

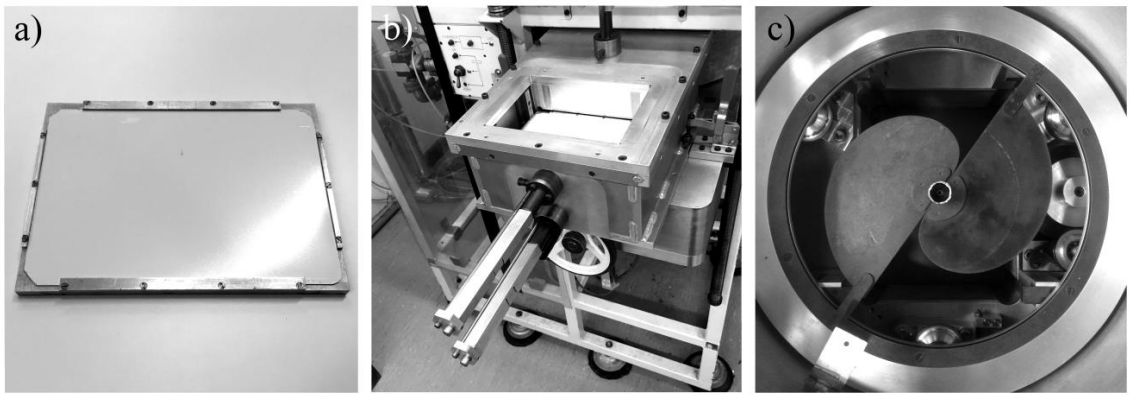

Figure 4.6. Photographs of a) an image plate on a retaining tray *ex situ*, b) a stack of image plates on retaining trays loaded into the image plate magazine (**T**) with manipulators (**U**) and conveyor turn-handle (**V**) visible, and c) the rotating sector with retracted scintillator screen (**S**) visible in the bottom left. Fig. 4.6.a is reproduced from Fig. 3 of Ref. 43.

The detector module is suspended on a long-travel linear translator, allowing for data acquisition at two different nozzle-to-image-plate distances. To acquire data at the longer of the two nozzle-to-image-plate distances, the detector module is lowered on the long-travel linear translator and a spacer module (**Z**) is installed between the detector module and the chamber module. To acquire data at the shorter of the two nozzle-to-image-plate distances, the detector module is raised on the long-travel linear translator; the spacer module is

redundant in this configuration. The ranges of nozzle-to-image-plate distances accessible at each configuration are 485.0 ± 5.0 and 235.0 ± 5.0 mm. Under routine electron gun operating conditions (see Section 4.1.2), and given the dimensions of an image plate, diffraction can be registered over an *s* range of *ca.* 39.5 ± 0.5 to 341.5 ± 6.7 nm^{-1}.

4.2 Gas-Phase Structure of 4-(Dimethylamino)benzonitrile

4.2.1 4-(Dimethyl)aminobenzonitrile

The apparent simplicity of DMABN – illustrated in Fig. 4.7 – is deceptive; there are few molecules in the chemical literature that have fuelled research activity and caused controversy to a comparable extent (see Ref. 43 and references therein).

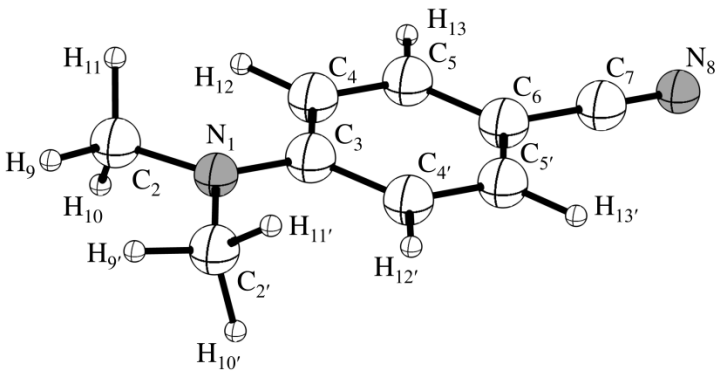

Figure 4.7. Ground-state structure of DMABN. The atomic labelling scheme is outlined and used hereafter.

The photophysical behaviour of DMABN was first reported by Lippert *et al.* in 1961;[168] nearly 60 years later, theoretical methods of the kind employed in this project [CASSCF/CASPT2,[169,170] MR-CISD,[171] ADC(2)[171,172]], and others beyond the scope of it (EOM-CCSD,[173] GPU-accelerated TDDFT[174,175]), are still put to the test on DMABN.

Although the starting point for the application of these theoretical methods is to the gas phase, the gas-phase equilibrium structure of DMABN had not been fully characterised experimentally until publication of Ref. 43; only the partial gas-phase structural solutions of Kajimoto *et al.*[176] and Pratt *et al.*,[177] obtained *via* microwave spectroscopy, had been presented. Heine *et al.*[178] had previously presented structural solutions for DMABN and a number of analogous aminobenzonitriles in the crystalline state, obtained *via* XRD, but, as demonstrated by Mitzel *et al.*,[179–183] structural differences between the crystalline state and

the gas phase are not necessarily always negligible and, where measureable, are often found to be larger than the accuracy of theoretical methods that are accessible today.

4.2.2 Data Acquisition

DMABN was purchased from Sigma-Aldrich (Aldrich-D139505, DMABN, 98%) and used as received. GED data were acquired using the University of York gas electron diffractometer.[43] An accelerating potential of 42.22 kV was applied to produce a continuous electron beam with an electron emission current of 0.66 μA and electron wavelength of *ca.* 5.85 pm. GED data were acquired *via* the exposure of reusable image plates (Fuji BAS-IP MS 2025) at nozzle-to-image-plate distances of 234.5 and 487.0 mm and subsequently digitised using a tabletop image plate scanner (Fuji BAS-1800II) as outlined in Section 4.1.5. Three exposures were recorded at each nozzle-to-image-plate distance. DMABN was delivered to the point of diffraction *via* the air-heated effusive nozzle assembly outlined in Section 4.1.4. The sample of DMABN and the effusive nozzle tip were heated to 371 and 393 K, respectively, during exposures at the longer nozzle-to-image-plate distance and to 395 and 413 K, respectively, during exposures at the shorter nozzle-to-image-plate distance. These experimental conditions are summarised in Table A1.

4.2.3 Density Functional Theory Calculations

All DFT calculations were carried out using the GAUSSIAN09[184] software suite on the University of York Advanced Research Computing Cluster (YARCC). All geometry optimisations were carried out in the C_s symmetry point group. The highest-level geometry optimisations employed the B2PLYP[185] density functional of Grimme *et al.* coupled with a scaling range of basis sets (cc-pV*n*X, $n \in \{D, T, Q\}$)[186] of increasing completeness. All bonded internuclear distances were extrapolated to the complete basis set (CBS) limit *via* the fitting of the bonded internuclear distances determined using the cc-pVDZ, cc-pVTZ, and cc-pVQZ basis sets with a function of the form in Eq. 4.1:

$$r_{ij}(x) = r_{ij,\mathrm{CBS}} + \beta e^{-\alpha x}, x \in \{2, 3, 4\} \qquad \textbf{Eq. 4.1}$$

in which $r_{ij,\mathrm{CBS}}$ represents the internuclear distance r_{ij} at the CBS limit and α and β are fitting parameters. The corresponding results are hereafter denoted B2PLYP/CBS. The choice of the B2PLYP density functional for the highest-level geometry optimisations was motivated by the quantitative agreement that key structural parameters computed at this level showed with the experimentally-determined structural parameters of Kajimoto *et al.*

and Pratt *et al.* (Section 4.2.5) – something that other density functionals notably failed to achieve. Flexible restraints for use in the SARACEN-type[99–101] least-squares refinement procedure were determined by supplementary geometry optimisations employing the B3LYP,[187,188] B3P86,[187,189] B3PW91,[187,190] PBEH1PBE,[191] and HSEH1PBE[192–195] density functionals coupled with a scaling range of basis sets (cc-pV*n*X, $n \in \{D, T, Q\}$)[186] of increasing completeness. The convergence of all geometry optimisations to minima on the ground-state potential energy surface was verified *via* vibrational frequency analysis. Cartesian coordinates of all optimised geometries are tabulated in Tables A2–19.

Theoretical r_{h1}-type amplitudes of vibration (u_{h1}) and curvilinear shrinkage corrections (k_{h1}) were generated from vibrational frequencies computed at the B2PLYP/cc-pVDZ level using the SHRINK[108,109] software package.

4.2.4 Data Reduction and Refinement

The in-house-developed data extraction package XSTRACT[74] was used to reduce digitised diffraction patterns to MICs *via* azimuthal averaging. MICs were refined using the ED@ED v3.0[94] least-squares refinement package with the scattering factors of Ross *et al.*[196]

4.2.4.1 Refinement Protocol

The least-squares refinement procedure employed a parameterised molecular model, programmed in FORTRAN90, describing DMABN within the constraints of the C_s symmetry point group in terms of 16 refinable parameters comprising 9 distances ($p_1 - p_9$), 5 angles ($p_{10} - p_{14}$), and 2 dihedral angles (p_{15} and p_{16}). The contributions to parameters $p_1 - p_{16}$ are tabulated in Table 4.1.

Table 4.1. Summary of contributions to parameters $p_1 - p_{16}$.

Parameter		Contributions
p_1	rCC, rCN[a]	$^2/_{10}\, r_{1,2} + {}^1/_{10}\, r_{1,3} + {}^2/_{10}\, r_{3,4} + {}^2/_{10}\, r_{4,5} + {}^2/_{10}\, r_{5,6} + {}^1/_{10}\, r_{6,7}$
p_2	rCC, rCN[b]	$^1/_2\, r_{3,4} + {}^1/_2\, r_{5,6} - r_{4,5}$
p_3	rCC, rCN[b]	$r_{3,4} - r_{5,6}$
p_4	rCC, rCN[b]	$(^1/_4\, r_{6,7} + {}^1/_4\, r_{1,3} + {}^1/_2\, r_{1,2}) - (^1/_3\, r_{3,4} + {}^1/_3\, r_{4,5} + {}^1/_3\, r_{5,6})$
p_5	rCC, rCN[b]	$^1/_3\, r_{6,7} + {}^2/_3\, r_{1,2} - r_{1,3}$
p_6	rCC, rCN[b]	$r_{1,2} - r_{6,7}$
p_7	$r\mathrm{CN}_{\mathrm{Nitrile}}$	$r_{7,8}$
p_8	$r\mathrm{CH}_{\mathrm{Methyl}}$	$^1/_3\, r_{2,9} + {}^1/_3\, r_{2,10} + {}^1/_3\, r_{2,11}$
p_9	$r\mathrm{CH}_{\mathrm{Benzyl}}$	$^1/_2\, r_{4,12} + {}^1/_2\, r_{5,13}$

Table 4.1. *Cont.*

Parameter		Contributions
p_{10}	aCCC	$a_{4,3,4'}$
p_{11}	aCCC	$a_{5,6,5'}$
p_{12}	aCCH$_{\text{Methyl}}$	$^1/_3\ a_{1,2,9} + {}^1/_3\ a_{1,2,10} + {}^1/_3\ a_{1,2,11}$
p_{13}	aCCH$_{\text{Benzyl}}$	$^1/_2\ a_{3,4,12} + {}^1/_2\ a_{6,5,13}$
p_{14}	aCNC	$a_{2,1,2'}$
p_{15}	ϕCCNC	$\phi_{4,3,1,2}$
p_{16}	ϕCNCH	$\phi_{3,1,2,9}$

[a] Multiplicity-weighted average parameter. [b] Difference parameter.

To prevent the correlation of internuclear distances of a similar length precluding an independent refinement, $p_1 - p_6$ were constructed as mix of multiplicity-weighted-average and refinable difference parameters. It is possible to reconstruct six unique bonded internuclear distances between 2$^{\text{nd}}$-row nuclei in DMABN ($r_{1,2}$, $r_{1,3}$, $r_{3,4}$, $r_{4,5}$, $r_{5,6}$, and $r_{6,7}$) *via* linear combination of p_1 and refinable difference parameters $p_2 - p_6$, as outlined in Table 4.2.

Table 4.2. Reconstruction of unique bonded internuclear distances in DMABN *via* linear combination of parameters $p_1 - p_6$.

Coordinate	Linear Combination of Parameters
$r_{1,2}$	$p_1 + {}^3/_5\ p_4 + {}^1/_4\ p_5 + {}^1/_3\ p_6$
$r_{1,3}$	$p_1 + {}^3/_5\ p_4 - {}^3/_4\ p_5$
$r_{3,4}$	$p_1 - {}^2/_5\ p_4 + {}^1/_3\ p_2 + {}^1/_2\ p_3$
$r_{4,5}$	$p_1 - {}^2/_5\ p_4 - {}^2/_3\ p_2$
$r_{5,6}$	$p_1 - {}^2/_5\ p_4 + {}^1/_3\ p_2 - {}^1/_2\ p_3$
$r_{6,7}$	$p_1 + {}^3/_5\ p_4 + {}^1/_4\ p_5 - {}^2/_3\ p_6$

The least-squares refinement procedure followed the SARACEN[99–101] protocol and gave internuclear distances of the r_{h1} type. All amplitudes of vibration associated with a given peak in the RDC were coupled by a fixed ratio to the amplitude of vibration associated with the nuclei giving rise to the largest scattering effect under that peak; only this amplitude of vibration was refined.

4.2.4.2 Refinement Results

The experimentally-acquired and experimental-minus-theoretical "*difference*" MICs are reproduced in Fig. 4.8; the RDCs are reproduced in Fig. 4.9.

The R_G and R_D for the least-squares refinement of DMABN were 0.055 and 0.036, respectively.

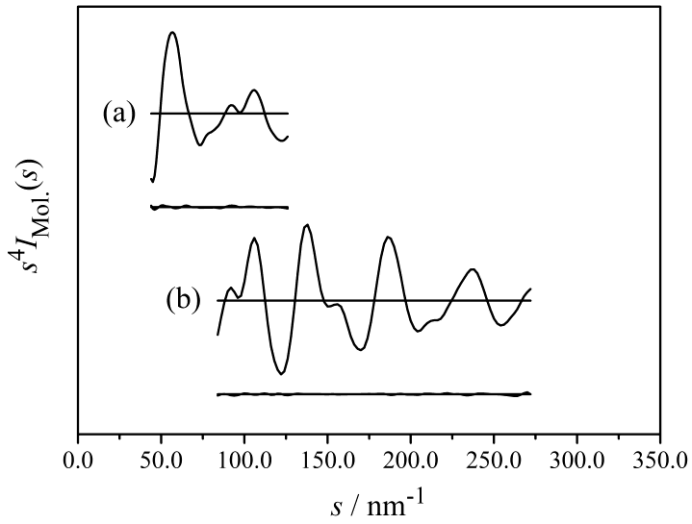

Figure 4.8. MICs and experimental-minus-theoretical "*difference*" MICs obtained after refinement of GED data acquired for DMABN at a) long and b) short nozzle-to-image-plate distances. Reproduced from Fig. 6 of Ref. 43.

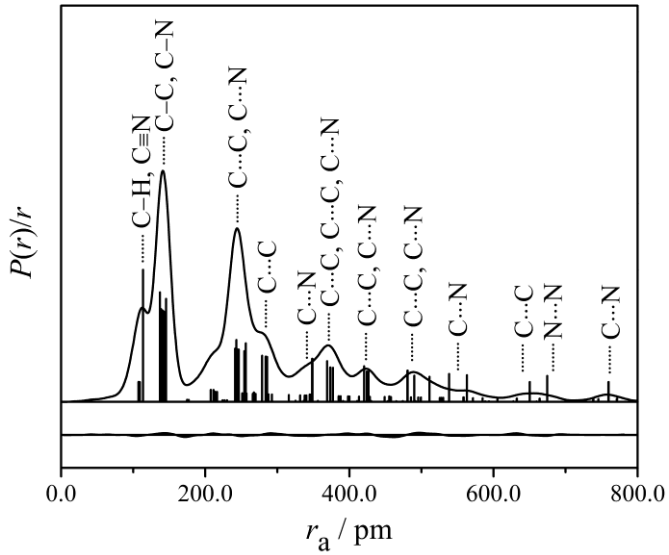

Figure 4.9. RDC and experimental-minus-theoretical "*difference*" RDC obtained after refinement of GED data acquired for DMABN. Reproduced from Fig. 7 of Ref. 43.

The weighting points for off-diagonal weight matrices, scaling factors, and least-squares correlation parameters are found in Table A20; the least-squares correlation matrix is found in Table A21. The refined (r_{h1}-type) and theoretical (r_e-type; B2PLYP/CBS) parameters are tabulated in Table A22. All internuclear distances, refined and theoretical amplitudes of

vibration, r_{h1}-type shrinkage corrections, and SARACEN[99–101] restraints (where applied) are tabulated in Table A23. Cartesian coordinates for the refined r_{h1}-type structure of DMABN are tabulated in Table A24.

The results of the least-squares refinement procedure are presented in a visually-intuitive way in Fig. 4.10; experimentally-determined internuclear distances and angles, alongside their theoretical counterparts computed at the B2PLYP/CBS level, are overlaid onto a schematic illustration of DMABN.

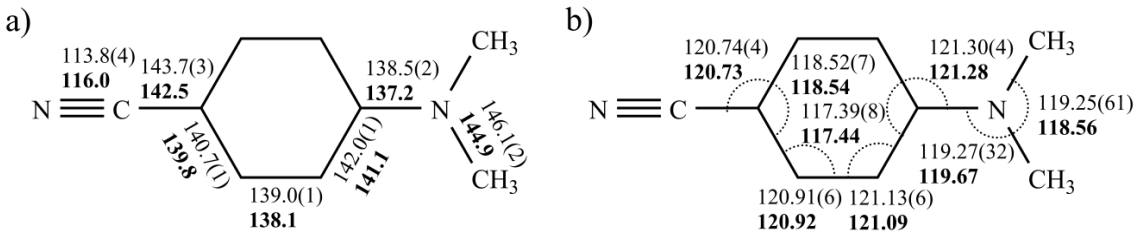

Figure 4.10. Experimental r_{h1}-type (regular typeface) and B2PLYP/CBS (bold typeface) geometric parameters determined for DMABN. All a) internuclear distances are reported in picometers. All b) angles are reported in degrees. Adapted from Fig. 8 of Ref. 43.

4.2.5 Discussion

Refined experimental internuclear distances and angles are tabulated in Table 4.3 alongside their theoretical counterparts computed at the B2PLYP/CBS level and structural data acquired for DMABN in the crystalline state and the gas phase *via* XRD (Heine *et al.*)[178] and microwave spectroscopy (Kajimoto *et al.*),[176] respectively. All internuclear distances and angles between heavy nuclei are well-determined to 0.8(3) pm and 0.1(2)° of their theoretical counterparts, attesting to the best-in-class accuracy characteristic of the B2PLYP density functional for this application. Acceptable agreement is found between the solution obtained here and that obtained *via* XRD; all internuclear distances between heavy nuclei are determined to 1.5(6) pm of their XRD counterparts and their ratios to one another (that may be trivially approximated from valence bond theory) are well-conserved. A minor systematic deviation towards shorter internuclear distances in the XRD solution is apparent; all internuclear distances between heavy nuclei (with the exception of $r_{7,8}$) are shorter by a factor of 0.988(1). A deviation of this magnitude is to be expected where direct comparisons are made between internuclear distances derived from r_{h1}-type equilibrium structures determined *via* GED and thermally-averaged reciprocal lattice positions determined *via* XRD.

Table 4.3. Summary of refined (r_{h1}-type) GED, theoretical (r_e-type; B2PLYP/CBS), XRD (recorded at 253 K), and microwave spectroscopic measurements of internuclear distances[a] and angles[b] in DMABN. Reproduced from Table 1 of Ref. 43.

Coordinate	GED (r_{h1})	r_e	XRD	MWS
$r_{1,2}$	146.1(2)	144.9	144.9(3)[c]	–
$r_{1,3}$	138.5(2)	137.2	136.5(3)	137.9[e]
$r_{3,4}$	142.0(1)	141.1	140.0(4)	–
$r_{4,5}$	139.0(1)	138.1	137.0(4)	–
$r_{5,6}$	140.7(1)	139.8	138.8(4)	–
$r_{6,7}$	143.7(3)	142.5	142.7(5)	145.4[e]
$r_{7,8}$	113.8(3)	116.0	114.5(4)	–
$r_{2,9}$	108.7(4)	108.4	96.0[f]	–
$r_{2,10}$	109.6(4)	109.3	96.0[f]	–
$r_{2,11}$	109.2(4)	108.9	96.0[f]	–
$r_{4,12}$	107.7(4)	107.7	93.0[f]	–
$r_{5,13}$	107.7(4)	107.9	93.0[f]	–
$a_{2,1,2'}$	119.25(61)	118.56	116.4(3)	115.7[e]
$a_{2,1,3}$	119.27(32)	119.67	121.1(3)[d]	–
$a_{1,3,4}$	121.30(4)	121.28	121.0[f]	–
$a_{3,4,5}$	121.13(6)	121.09	121.1[f]	–
$a_{4,3,4'}$	117.39(8)	117.44	117.1[f]	–
$a_{4,5,6}$	120.91(6)	120.92	121.5[f]	–
$a_{5,6,5'}$	118.52(7)	118.54	117.9[f]	–
$a_{5,6,7}$	120.74(4)	120.73	120.3[f]	–
$a_{1,2,9}$	108.92(8)	108.93	109.4[f]	–
$a_{1,2,10}$	112.41(8)	112.42	109.4[f]	–
$a_{1,2,11}$	111.06(8)	111.07	109.4[f]	–
$a_{3,4,12}$	120.42(4)	120.42	119.4[f]	–
$a_{6,5,13}$	119.50(4)	119.50	119.2[f]	–
$\phi_{4,3,1,2}$	7.5[e]	8.49	7.7[f]	–
$\phi_{3,1,2,9}$	181.39[e]	181.39	182.2[f]	–
$\phi_{3,1,2,10}$	121.39[e]	121.39	122.3[f]	–
$\phi_{3,1,2,11}$	61.39[e]	61.39	62.3[f]	

[a] All internuclear distances ($r_{i,j}$) are tabulated in picometers. [b] All angles ($a_{i,j,k}$) and dihedral angles ($\phi_{i,j,k,l}$) are tabulated in degrees. [c] Presented as an average of the XRD measurements of $r_{1,2}$ and $r_{1,2'}$. [d] Presented as an average of the XRD measurements of $a_{2,1,3}$ and $a_{2',1,3}$. [e] Uncertainties unavailable; unrefined. [f] Uncertainties unavailable; measured directly from *.cif* data.

It is not possible to comment on the agreement between the solution obtained here and the partial solution obtained *via* microwave spectroscopy as only three structural parameters ($r_{1,3}$, $r_{6,7}$, and $a_{2,1,2'}$) were determined and reported without accompanying uncertainties.

The interested reader should refer to Ref. 43 for a full discussion on the gas-phase equilibrium structure of DMABN; here, in the interest of brevity, a condensed discussion is presented on the three structural subunits of DMABN – the nitrile, benzyl, and dimethylamino.

4.2.5.1 Nitrile Subunit

The nitrile subunit comprises $r_{6,7}$ and $r_{7,8}$. The former is the longest bonded internuclear distance of the extended π system in the GED [143.7(3) pm] and XRD [142.7(5) pm][178] solutions, effectively decoupling the C≡N bond from the benzyl subunit. The latter is the shortest bonded internuclear distance of the extended π system in the GED [113.8(3) pm] and XRD [114.5(4) pm][178] solutions, and the only example of a bonded internuclear distance determined to be shorter in the GED solution than in the XRD solution. It is of note that the length of $r_{7,8}$ is considerably overestimated at the B2PLYP/CBS level, and that it is affected – more so than any other bonded internuclear distance in DMABN – by the extent of basis set completion, regardless of the density functional employed; $r_{7,8}$ shortens by 1.25(3) pm on transition from cc-pVDZ to CBS-quality results, whereas all other bonded internuclear distances shorten only by 0.84(3) pm over the same transition.

4.2.5.2 Benzyl Subunit

The benzyl subunit comprises $r_{3,4}$, $r_{4,5}$, and $r_{5,6}$. All bonded internuclear distances are well-determined in the GED solution to within 0.9(1) and 2.0(5) pm of their values computed at the B2PLYP/CBS level and in the XRD solution, respectively, and the ratio $r_{3,4}$:$r_{4,5}$:$r_{5,6}$ is well-conserved between theoretical calculations at the B2PLYP/CBS level and the GED and XRD solutions. As is characteristic of para-substituted benzyl subunits containing both an electron-withdrawing (nitrile) and an electron-donating (dimethylamino) substituent, the benzyl subunit is quinoidally distorted such that $r_{4,5}<r_{5,6}<r_{3,4}$.

4.2.5.3 Dimethylamino Subunit

The dimethylamino subunit comprises $r_{1,2}$ and $r_{1,3}$. Here, an inversion angle, ϑ_i, is defined as the angle between the plane of the benzyl subunit and the plane containing N_1, C_2, and $C_{2'}$;

it is dependent on $\phi_{4,3,1,2}$. ϑ_i is found to be non-zero by experiment, both in the crystalline state, as measured by Heine *et al.* [10.8(2)°, 298 K; 11.9(3)°, 253 K][178] *via* XRD, and in the gas phase, as measured by Kajimoto *et al.* (15°)[176] and, subsequently, by Pratt *et al.* (14.6°)[177] *via* microwave spectroscopy. In contrast, common hybrid density functionals (*i.e.* B3LYP, B3P86, *etc.*) compute near-C_{2v}-symmetric structures where ϑ_i is close to zero; the performance of the B2PLYP density functional can be considered best-in-class for this application, therefore, as ϑ_i (14.3°) can be computed in excellent agreement with that determined by both Kajimoto *et al.* and Pratt *et al.* ϑ_i is apparently difficult to compute at equilibrium; this is likely a consequence of the shallow dual-minimum potential profile of $\phi_{4,3,1,2}$, presented in Fig. 4.11a, and the negligible barrier to inversion (<0.1 kJ mol^{-1}) through $\phi_{4,3,1,2}$ = 0.0° (determined at the B2PLYP/CBS level *via* direct optimisation of the C_{2v}-symmetric saddle point). It is also challenging to measure ϑ_i in the gas phase. Refinement of $\phi_{4,3,1,2}$ was precluded by free inversion of the dimethylamino subunit on a timescale significantly shorter than that of measurement *via* GED; similarly, refinement of $\phi_{3,1,2,9}$, $\phi_{3,1,2,10}$, and $\phi_{3,1,2,11}$ was precluded by free rotation of the methyl subunits. *In lieu* of a measurement for $\phi_{4,3,1,2}$ and, by extension, ϑ_i, a number of independent refinements were carried out with $\phi_{4,3,1,2}$ fixed at values between 0.0 and 13.0°, corresponding to values of ϑ_i between 0.0 and *ca.* 21.5°. The quality of the least-squares refinement, quantified by an *R*-factor ratio, $R_G/R_{G,Min.}$, is presented as a function of $\phi_{4,3,1,2}$ in Fig. 4.11b.

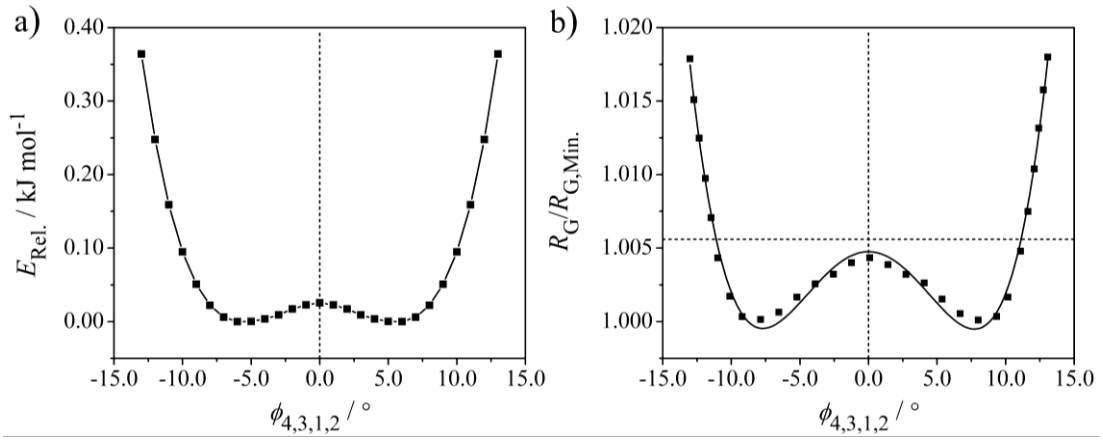

Figure 4.11. Evaluation of the a) potential energy, as computed at the B2PLYP/CBS level, and b) quality of the least-squares refinement of DMABN, quantified by an *R*-factor ratio, $R_G/R_{G,Min.}$, as a function of $\phi_{4,3,1,2}$. The vertical dashed lines in a) and b) represent $\phi_{4,3,1,2}$ = 0.0°. The horizontal dashed line in b) represents the 95% confidence limit, approximately equal to 2σ. The continuous line in b) represents a quartic function that has been fitted to the data points. Adapted from Figs. 9 and 10 of Ref. 43.

The $R_G/R_{G,Min.}$ data points in Fig. 4.11b have been fitted with a quartic function; the minima in this function (*ca.* ±7.5°) correspond to values of $\phi_{4,3,1,2}$. It is not possible to rule out a hypothetical C_{2v}-symmetric structure at the 95% confidence limit, but the value of ϑ_i (*ca.* 12.7°) that gives the best fit to the experimental GED data is a) in qualitative agreement with the observation of Kajimoto *et al.* that ϑ_i is larger in the gas phase than in the crystal,[176] and b) in good quantitative agreement with the revised ϑ_i of Pratt *et al.*[177]

4.3 Gas-Phase Structures of Fluorine-Doped Tin Oxide Precursors

4.3.1 Fluorine-Doped Tin Oxide Precursors

A family of low-cost, green, single-source precursors to fluorine-doped tin oxide (F-doped SnO_2; FTO)[197] have been developed at Carleton University and characterised *via* GED at the University of York as part of a recently-established collaboration between the author and Goran Bačić (Ph.D. student; Carleton University).[166]

Research into FTO – which can be layered onto a suitable substrate *via* chemical vapour deposition (CVD)[198] – is growing in response to the demand for low-cost, transparent, conducting metal oxides in the optoelectronics industry. The latest generation of single-source FTO precursors, like those pioneered at Carleton University,[166] are a promising alternative to fluorine-doping during CVD, which is hazardous and difficult to perform. Routine structural characterisation of this family of precursors, *e.g.* by XRD, has proven difficult as many are polymeric in the solid state.[199] In any case, it should be apparent to the reader that a gas-phase structural solution is more valuable for a FTO precursor, as the precursor will be in the gas phase *in operando*.

Two single-source FTO precursors that have been developed at Carleton University have been characterised for the first time *via* GED over the course of this project: tin^{II} bis(trifluoroacetate) [$Sn(TFA)_2$; Fig. 4.12a] and tin^{IV} tetrakis(trifluoroacetate) [$Sn(TFA)_4$; Fig. 4.13].[166] The latter sublimes (*ca.* 1 Torr at 357 K)[166] as a monomer; the former intermediately forms polymeric hexatin^{II} di-μ_3-oxy-octakis-μ-trifluoroacetate before subsequently subliming (*ca.* 1 Torr at 464 K)[166] as a mixture of $Sn(TFA)_2$ and bis(stannylene) ditin^{II} μ-oxy-bis-μ-trifluoroacetate [$Sn_2O(TFA)_2$; Fig. 4.12b]. Of interest to the reader will be the following: a) individual structural solutions for $Sn(TFA)_2$ and $Sn_2O(TFA)_2$ have been obtained from the mixed vapour in a single GED experiment, and b) the structural solutions for $Sn(TFA)_2$, $Sn_2O(TFA)_2$, and $Sn(TFA)_4$ are all from "*blind*" GED, where no information beyond the stoichiometry was initially known.

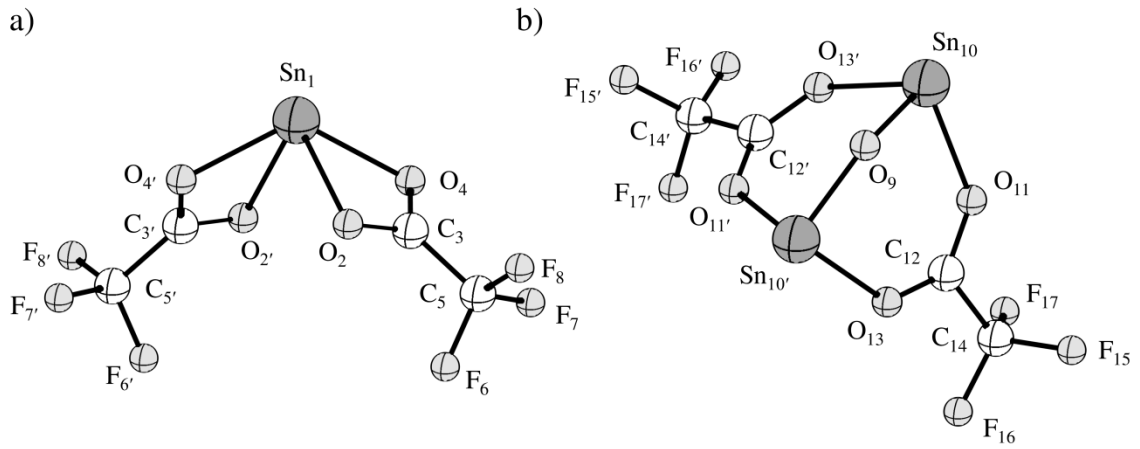

Figure 4.12. Ground-state structures of a) tin^{II} bis(trifluoroacetate) [$Sn(TFA)_2$] and b) bis(stannylene) ditin-μ-oxy-bis-μ-trifluoroacetate [$Sn_2O(TFA)_2$]. The atomic labelling scheme is outlined and used hereafter.

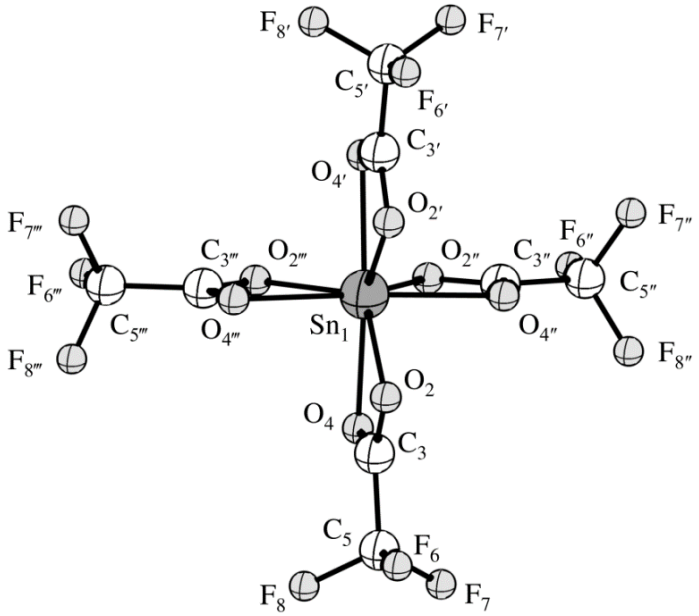

Figure 4.13. Ground-state structure of tin^{IV} tetrakis(trifluoroacetate) [$Sn(TFA)_4$]. The atomic labelling scheme is outlined and used hereafter.

4.3.2 Data Acquisition

$Sn(TFA)_2$ and $Sn(TFA)_4$ were synthesised at Carleton University and delivered to the University of York for characterisation *via* GED. An accelerating potential of 42.22 kV was applied to produce a continuous electron beam with an electron emission current of 0.66 μA and electron wavelength of *ca.* 5.85 pm. GED data were acquired *via* the exposure of reusable image plates (Fuji BAS-IP MS 2025) at nozzle-to-image-plate distances of 234.5

and 477.0 mm for $Sn(TFA)_2$ and 233.5 and 486.0 mm for $Sn(TFA)_4$. The image plates were subsequently digitised using a tabletop image plate scanner (Fuji BAS-1800II) as outlined in Section 4.1.5. Four and three exposures were recorded at the longer and shorter nozzle-to-image-plate distances, respectively, for $Sn(TFA)_2$; five and four exposures were recorded at the longer and shorter nozzle-to-image-plate distances, respectively, for $Sn(TFA)_4$. $Sn(TFA)_2$ and $Sn(TFA)_4$ were delivered to the point of diffraction *via* the air-heated effusive nozzle assembly outlined in Section 4.1.4. To acquire GED data for $Sn(TFA)_2$, the sample and the effusive nozzle tip were heated to 398 and 408 K, respectively, during exposures at both nozzle-to-image-plate distances; for $Sn(TFA)_2$, the sample and the effusive nozzle tip were heated to 463 and 473 K, respectively, during exposures at both nozzle-to-image-plate distances. The experimental conditions used to acquire GED data for $Sn(TFA)_2$ and $Sn(TFA)_4$ are summarised in Tables A25 and A26, respectively.

4.3.3 Density Functional Theory Calculations

All DFT calculations were carried out using the GAUSSIAN09[184] software suite on the University of York Advanced Research Computing Cluster (YARCC). All geometry optimisations of $Sn(TFA)_2$ and $Sn_2O(TFA)_2$ were carried out in the C_2 symmetry point group; all geometry optimisation of $Sn(TFA)_4$ were carried out in the D_{2d} symmetry point group. The highest-level geometry optimisations used the 2nd-order Douglas-Kroll-Hess (DKH) Hamiltonian[200] and employed the SOGGA11-X[201] density functional of Truhlar and Peverati coupled with the double- and triple-ζ DKH relativistic all-electron basis sets[202–204] of Jorge *et al.* Flexible restraints for use in the SARACEN-type[99–101] least-squares refinement procedure were determined by supplementary geometry optimisations employing the M06,[205] M11,[206] and SOGGA11-X[201] density functionals coupled with a scaling range of basis sets (*def*2-*n*VP, $n \in \{S, TZ, QZ\}$)[207] of increasing completeness and the corresponding effective core potentials (ECP) for Sn. Uniquely among the case studies presented in this thesis, the density functionals were selected exclusively from the Minnesota family for their specific parameterisation and balanced treatment of organometallic and main-group molecules. The convergence of all geometry optimisations to minima on the ground-state potential energy surface was verified *via* vibrational frequency analysis. Cartesian coordinates of all optimised geometries are tabulated in Tables A27–59. Theoretical r_{h1}-type amplitudes of vibration (u_{h1}) and curvilinear shrinkage corrections (k_{h1}) were generated from vibrational frequencies computed at the SOGGA11-X/double-ζ-DKH level using the SHRINK[108,109] software package.

4.3.4 Data Reduction and Refinement

The in-house-developed data extraction package XSTRACT[74] was used to reduce digitised diffraction patterns to MICs *via* azimuthal averaging. MICs were refined using the ED@ED v3.0[94] least-squares refinement package with the scattering factors of Ross *et al.*[196]

4.3.4.1 Refinement Protocol

Two independent least-squares refinements were carried out – one to obtain a structural solution for $Sn(TFA)_2$ and $Sn_2O(TFA)_2$, and one to obtain a structural solution for $Sn(TFA)_4$. Each least-squares refinement procedure employed a parameterised molecular model, programmed in FORTRAN90.

The parameterised molecular model describing $Sn(TFA)_2$ and $Sn_2O(TFA)_2$ was constructed within the constraints of the C_2 symmetry point group in terms of 23 refinable parameters comprising 11 distances ($p_1 - p_{11}$), 5 angles ($p_{12} - p_{14}$, p_{19}, and p_{23}), and 7 dihedrals ($p_{15} - p_{18}$, and $p_{20} - p_{22}$). 10 parameters were global ($p_1 - p_4$, and $p_7 - p_{12}$); 13 parameters (p_5, p_6, and $p_{13} - p_{23}$) were specific to one of $Sn(TFA)_2$/$Sn_2O(TFA)_2$. The contributions to $p_1 - p_{23}$ are tabulated in Table 4.4. An additional parameter, $p_{24} \in [0, 1]$, allowed the abundances of $Sn(TFA)_2$ and $Sn_2O(TFA)_2$ to be dynamically adjusted during least-squares refinement. Local symmetry approximations were employed where appropriate.

Table 4.4. Summary of contributions to parameters $p_1 - p_{23}$ used in the parameterised molecular model of $Sn(TFA)_2$ and $Sn_2O(TFA)_2$.

Parameter		Contributions
p_1	rSnO^a	$^2/_5\, r_{9,10} + {}^1/_5\, r_{10,11} + {}^1/_5\, r_{1,2} + {}^1/_5\, r_{1,4}$
p_2	rSnO^b	$(^2/_3\, r_{9,10} + {}^1/_3\, r_{10,11}) - (^1/_2\, r_{1,2} + {}^1/_2\, r_{1,4}\})$
p_3	rSnO^b	$r_{9,10} - r_{10,11}$
p_4	rSnO^b	$r_{1,2} - r_{1,4}$
p_5	rSnC^c	$r_{1,3}$
p_6	rSnC^d	$r_{10,12}$
p_7	rCO^a	$^1/_2\, r_{11,12} + {}^1/_4\, r_{2,3} + {}^1/_4\, r_{3,4}$
p_8	rCO^b	$r_{11,12} - (^1/_2\, r_{2,3} + {}^1/_2\, r_{3,4})$
p_9	rCO^b	$r_{3,4} - r_{2,3}$
p_{10}	rCC^a	$^1/_2\, r_{12,14} + {}^1/_2\, r_{3,5}$
p_{11}	rCF^a	$^1/_6\, (r_{5,6} + r_{5,7} + r_{5,8} + r_{14,15} + r_{14,16} + r_{14,17})$
p_{12}	aCCF^a	$^1/_6\, (a_{3,5,6} + a_{3,5,7} + a_{3,5,8} + a_{12,14,15} + a_{12,14,16} + a_{12,14,17})$
p_{13}	aOCC^c	$a_{2,3,5}$

Table 4.4. *Cont.*

Parameter		Contributions
p_{14}	aCSnC[c]	$a_{3,1,3'}$
p_{15}	ϕOCCF[c]	$\phi_{2,3,5,6}$
p_{16}	ϕOCCF[c]	$\phi_{2,3,5,7}$
p_{17}	ϕOCCF[c]	$\phi_{2,3,5,8}$
p_{18}	ϕX[e]SnCO[c]	$\phi_{X,1,3,2}$
p_{19}	aSnOSn[d]	$a_{10,9,10'}$
p_{20}	ϕOCCF[d]	$\phi_{11,12,14,15}$
p_{21}	ϕOCCF[d]	$\phi_{11,12,14,16}$
p_{22}	ϕOCCF[d]	$\phi_{11,12,14,17}$
p_{23}	aCX[f]C[d]	$a_{12,X,12'}$

[a] Multiplicity-weighted average parameter. [b] Difference parameter. [c] Specific to $Sn(TFA)_2$. [d] Specific to $Sn(TFA)_4$. [e] X lies on the principle symmetry axis of $Sn(TFA)_2$. [f] X lies at the centroid of Sn_{10} and $Sn_{10'}$.

It is possible to reconstruct the ten bonded internuclear distances ($r_{1,2}$, $r_{1,4}$, $r_{2,3}$, $r_{3,4}$, $r_{9,10}$, $r_{9,10'}$, $r_{10,11}$, $r_{10',13}$, $r_{11,12}$, and $r_{12,13}$) that would otherwise be correlated *via* linear combination of $p_1 - p_4$ and $p_7 - p_9$, as outlined in Table 4.5.

Table 4.5. Reconstruction of unique bonded internuclear distances in $Sn(TFA)_2$ and $Sn_2O(TFA)_2$ *via* linear combination of parameters $p_1 - p_4$ and $p_7 - p_9$.

Coordinate	Linear Combination of Parameters
$r_{1,2}$	$p_1 - {}^3/_5\, p_2 + {}^1/_2\, p_4$
$r_{1,4}$	$p_1 - {}^3/_5\, p_2 - {}^1/_2\, p_4$
$r_{2,3}$	$p_7 - {}^1/_2\, p_8 - {}^1/_2\, p_9$
$r_{3,4}$	$p_7 - {}^1/_2\, p_8 + {}^1/_2\, p_9$
$r_{9,10}$	$p_1 + {}^2/_5\, p_2 - {}^2/_3\, p_3$
$r_{9,10'}$	$p_1 + {}^2/_5\, p_2 - {}^2/_3\, p_3$
$r_{10,11}$	$p_1 + {}^2/_5\, p_2 + {}^1/_3\, p_3$
$r_{10',13}$	$p_1 + {}^2/_5\, p_2 + {}^1/_3\, p_3$
$r_{11,12}$	$p_7 + {}^1/_2\, p_8$
$r_{12,13}$	$p_7 + {}^1/_2\, p_8$

The parameterised molecular model describing $Sn(TFA)_4$ was constructed within the constraints of the D_{2d} symmetry point group in terms of 12 refinable parameters comprising 8 distances ($p_1 - p_8$) and 4 angles ($p_9 - p_{12}$). The contributions to $p_1 - p_{12}$ are tabulated in Table 4.6. Local symmetry approximations were employed where appropriate.

Table 4.6. Summary of contributions to parameters p_1 – p_{12} used in the parameterised molecular model of $Sn(TFA)_4$.

Parameter		Contributions
p_1	rSnO[a]	$^1/_2\ r_{1,2} + {}^1/_2\ r_{1,4}$
p_2	rSnO[b]	$r_{1,4} - r_{1,2}$
p_3	rCO[a]	$^1/_2\ r_{2,3} + {}^1/_2\ r_{3,4}$
p_4	rCO[b]	$r_{2,3} - r_{3,4}$
p_5	rSnC	$r_{1,3}$
p_6	rCC	$r_{3,5}$
p_7	rCF[a]	$^1/_3\ r_{5,6} + {}^2/_3\ r_{5,7}$
p_8	rCF[b]	$r_{5,7} - r_{5,6}$
p_9	aOCC	$a_{2,3,5}$
p_{10}	aCCF[a]	$^1/_3\ a_{3,5,6} + {}^2/_3\ a_{3,5,7}$
p_{11}	aCCF[b]	$a_{3,5,6} - a_{3,5,7}$
p_{12}	aOSnO	$a_{2,1,2'}$

[a] Multiplicity-weighted average parameter. [b] Difference parameter.

It is possible to reconstruct the six bonded internuclear distances ($r_{1,2}$, $r_{1,3}$, $r_{3,4}$, $r_{4,5}$, $r_{5,6}$, and $r_{6,7}$) and two angles ($a_{3,5,6}$ and $a_{3,5,7}$) that would otherwise be correlated *via* linear combination of $p_1 - p_8$, p_{10}, and p_{11}, as outlined in Table 4.7.

Table 4.7. Reconstruction of unique bonded internuclear distances in $Sn(TFA)_4$ *via* linear combination of parameters $p_1 - p_8$, p_{10}, and p_{11}.

Coordinate	Linear Combination of Parameters
$r_{1,2}$	$p_1 - {}^1/_2\ p_2$
$r_{1,4}$	$p_1 + {}^1/_2\ p_2$
$r_{2,3}$	$p_3 + {}^1/_2\ p_4$
$r_{3,4}$	$p_3 - {}^1/_2\ p_4$
$r_{5,6}$	$p_7 - {}^2/_3\ p_8$
$r_{5,7}$	$p_7 + {}^1/_3\ p_8$
$a_{3,5,6}$	$p_{10} + {}^2/_3\ p_{11}$
$a_{3,5,7}$	$p_{10} - {}^1/_3\ p_{11}$

The least-squares refinement procedures followed the SARACEN[99–101] protocol and gave internuclear distances of the r_{h1} type. All amplitudes of vibration associated with a given peak in the RDC were coupled by a fixed ratio to the amplitude of vibration associated with the nuclei giving rise to the largest scattering effect under that peak; only this amplitude of vibration was refined.

4.3.4.2 Refinement Results

The experimentally-acquired and experimental-minus-theoretical "*difference*" MICs and RDCs obtained after refinement of GED data acquired for $Sn(TFA)_2$ and $Sn_2O(TFA)_2$ are reproduced in Figs. 4.14 and 4.15, respectively. The experimentally-acquired and experimental-minus-theoretical "*difference*" MICs and RDCs obtained after refinement of GED data acquired for $Sn(TFA)_4$ are reproduced in Figs. 4.16 and 4.17, respectively.

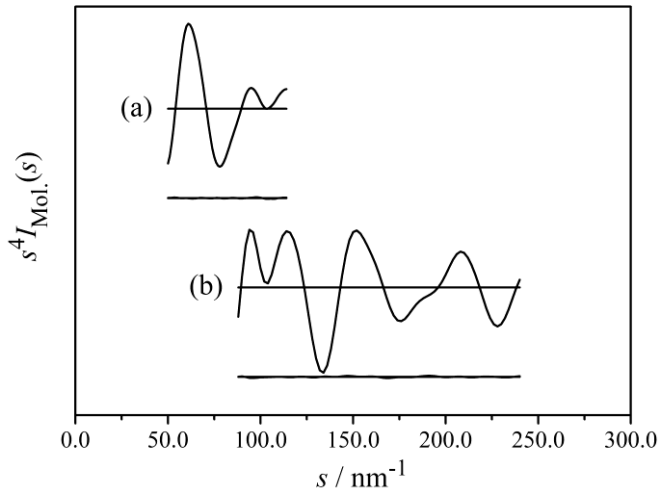

Figure 4.14. MICs and experimental-minus-theoretical "*difference*" MICs obtained after refinement of GED data acquired for $Sn(TFA)_2$ and $Sn_2O(TFA)_2$ at a) long and b) short nozzle-to-image-plate distances.

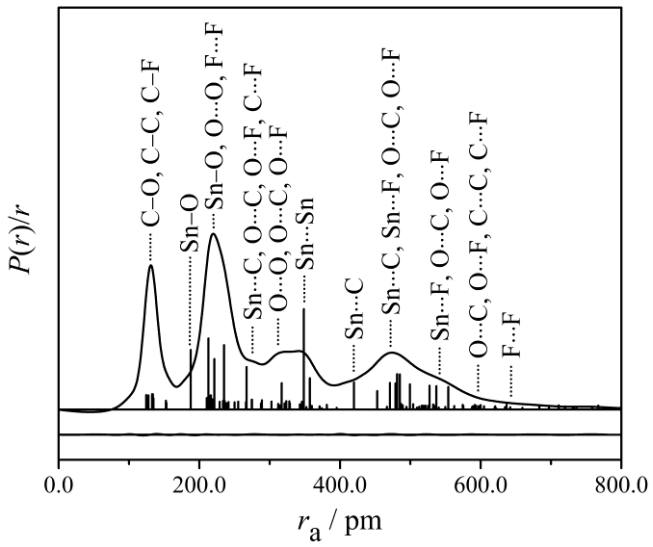

Figure 4.15. RDC and experimental-minus-theoretical "*difference*" RDC obtained after refinement of GED data acquired for $Sn(TFA)_2$ and $Sn_2O(TFA)_2$.

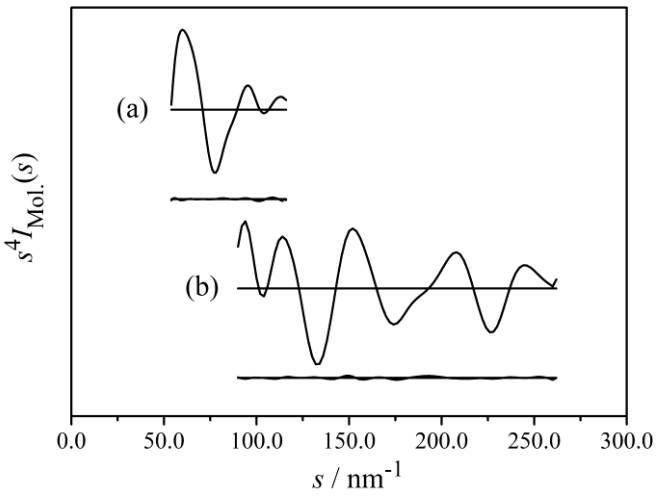

Figure 4.16. MICs and experimental-minus-theoretical "*difference*" MICs obtained after refinement of GED data acquired for $Sn(TFA)_4$ at a) long and b) short nozzle-to-image-plate distances.

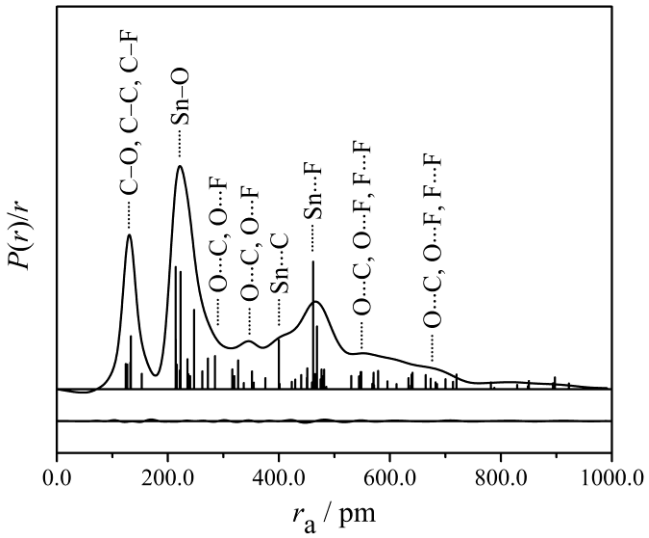

Figure 4.17. RDC and experimental-minus-theoretical "*difference*" RDC obtained after refinement of GED data acquired for $Sn(TFA)_4$.

The R_G and R_D for the least-squares refinement of $Sn(TFA)_2$ and $Sn_2O(TFA)_2$ were 0.042 and 0.029, respectively; for the least-squares refinement of $Sn(TFA)_4$, the R_G and R_D were 0.064 and 0.046, respectively.

The weighting points for off-diagonal weight matrices, scaling factors, and least-squares correlation parameters are found in Tables A60 and A61; the least-squares correlation matrices are found in Tables A62 and A63. The refined (r_{h1}-type) and theoretical (r_e-type; SOGGA11-X/triple-ζ-DKH) parameters are tabulated in Tables A64 and A65. All

internuclear distances, refined and theoretical amplitudes of vibration, r_{h1}-type shrinkage corrections, and SARACEN[99–101] restraints (where applied) are tabulated in Tables A66 and A67. Cartesian coordinates for the refined r_{h1}-type structures of $Sn(TFA)_2$, $Sn_2O(TFA)_2$, and $Sn(TFA)_4$ are tabulated in Tables A68, A69, and A70, respectively.

4.3.5 Discussion

Refined experimental internuclear distances and angles for $Sn(TFA)_2$, $Sn_2O(TFA)_2$, and $Sn(TFA)_4$ are tabulated in Tables 4.8, 4.9, and 4.10, respectively, alongside their SOGGA11-X/triple-ζ-DKH counterparts.

Table 4.8. Summary of refined (r_{h1}-type) GED and theoretical (r_e-type; SOGGA11-X/triple-ζ-DKH) measurements of internuclear distances[a] and angles[b] in $Sn(TFA)_2$.

Coordinate	GED (r_{h1})	r_e
$r_{1,2}$	234.1(14)	236.1
$r_{1,4}$	213.7(14)	214.6
$r_{2,3}$	124.4(3)	123.4
$r_{3,4}$	127.8(3)	126.8
$r_{3,5}$	152.8(7)	154.3
$r_{5,6}$	133.4(2)	132.5
$r_{5,7}$	132.9(2)	132.0
$r_{5,8}$	134.0(2)	133.2
$a_{2,1,4}$	55.8(3)	57.97
$a_{2,1,4'}$	85.1(2)	83.18
$a_{1,2,3}$	95.8(5)	85.34
$a_{1,4,3}$	100.3(8)	94.33
$a_{2,3,4}$	113.3(8)	122.33
$a_{2,3,5}$	120.8(3)	120.76
$a_{4,3,5}$	125.9(9)	116.88
$a_{3,5,6}$	110.8(1)	110.57
$a_{3,5,7}$	111.5(1)	111.24
$a_{3,5,8}$	109.1(1)	109.02
$\phi_{3,2,1,2'}$	-52.6(2)	-52.42
$\phi_{3,2,1,4'}$	-93.9(2)	-94.26
$\phi_{3,4,1,2'}$	139.3(2)	141.35
$\phi_{3,4,1,4'}$	83.7(2)	83.52

[a] All internuclear distances ($r_{i,j}$) are tabulated in picometers. [b] All angles ($a_{i,j,k}$) and dihedral angles ($\phi_{i,j,k,l}$) are tabulated in degrees.

Table 4.9. Summary of refined (r_{h1}-type) GED and theoretical (r_e-type; SOGGA11-X/triple-ζ-DKH) measurements of internuclear distances[a] and angles[b] in $Sn_2O(TFA)_2$.

Coordinate	GED (r_{h1})	r_e
$r_{9,10}$	187.9(10)	192.3
$r_{10,11}$	221.4(9)	222.4
$r_{11,12}$	125.6(3)	124.5
$r_{12,13}$	125.6(3)	124.4
$r_{12,14}$	153.4(7)	155.4
$r_{14,15}$	134.9(1)	133.4
$r_{14,16}$	133.6(1)	132.2
$r_{14,17}$	133.8(1)	132.7
$a_{9,10,11}$	89.0(7)	91.30
$a_{10,9,10'}$	137.4(17)	131.40
$a_{10,11,12}$	130.1(8)	131.19
$a_{11,12,13}$	131.5(12)	129.65
$a_{11,10,13'}$	89.6(2)	86.07
$a_{11,12,14}$	114.2(6)	114.26
$a_{13,12,14}$	116.2(6)	116.09
$a_{12,14,15}$	108.8(1)	109.08
$a_{12,14,16}$	112.0(1)	111.91
$a_{12,14,17}$	110.7(1)	110.61
$\phi_{9,10,11,12}$	15.5(6)	10.00
$\phi_{9,10',13,12}$	-15.5(6)	-13.92
$\phi_{11,10,9,10'}$	44.8(1)	43.64
$\phi_{13,10',9,10}$	-44.8(1)	-42.46

[a] All internuclear distances ($r_{i,j}$) are tabulated in picometers. [b] All angles ($a_{i,j,k}$) and dihedral angles ($\phi_{i,j,k,l}$) are tabulated in degrees.

Table 4.10. Summary of refined (r_{h1}-type) GED and theoretical (r_e-type; SOGGA11-X/triple-ζ-DKH) measurements of internuclear distances[a] and angles[b] in $Sn(TFA)_4$.

Coordinate	GED (r_{h1})	r_e
$r_{1,2}$	214.2(4)	213.7
$r_{1,4}$	222.9(4)	222.8
$r_{2,3}$	126.9(3)	126.4
$r_{3,4}$	124.2(3)	123.8
$r_{3,5}$	154.1(3)	154.3
$r_{5,6}$	132.4(2)	131.8
$r_{5,7}$	133.2(2)	132.6

Table 4.10. *Cont.*

Coordinate	GED (r_{h1})	r_e
$a_{2,1,4}$	60.9(2)	59.69
$a_{1,2,3}$	89.1(3)	91.58
$a_{1,4,3}$	85.9(2)	88.09
$a_{2,3,4}$	124.0(3)	120.64
$a_{2,3,5}$	117.8(5)	118.03
$a_{4,3,5}$	118.2(5)	121.33
$a_{3,5,6}$	112.1(2)	111.07
$a_{3,5,7}$	110.4(2)	109.39
$a_{2,1,2'}$	158.7(3)	158.89
$a_{4,1,4'}$	80.5(3)	81.73

[a] All internuclear distances ($r_{i,j}$) are tabulated in picometers. [b] All angles ($a_{i,j,k}$) are tabulated in degrees.

4.3.5.1 $Sn(TFA)_2$ and $Sn_2O(TFA)_2$

$Sn(TFA)_2$ intermediately forms polymeric hexatin^{II} di-μ_3-oxy-octakis-μ-trifluoroacetate on sublimation (isolated exclusively for the first time and characterised using mass spectrometry, NMR spectroscopy, and XRD by researchers at Carleton University; Ref. 166 is recommended to the interested reader), before subsequently subliming (*ca.* 1 Torr at 464 K)[166] as a 1:1 mixture of $Sn(TFA)_2$ and $Sn_2O(TFA)_2$ (Section 4.3.1). To confirm that this was the composition of the vapour, a number of independent refinements were carried out with p_{24} fixed at values between 0.40 and 0.60, corresponding to $Sn(TFA)_2$:$Sn_2O(TFA)_2$ ratios of between 0.67:1 and 1:0.67.

The quality of the least-squares refinement, quantified by an *R*-factor ratio, $R_G/R_{G,Min.}$, is presented as a function of p_{24} in Fig. 4.18.

The best fit to the experimental GED data is obtained where the $Sn(TFA)_2$:$Sn_2O(TFA)_2$ ratio is 1:0.89 (p_{24} = 0.53), with the 1:1 ratio (p_{24} = 0.50) within the two standard deviations (2σ) of the measurement. Consequently, the reader can be satisfied that both $Sn(TFA)_2$ and $Sn_2O(TFA)_2$ were present in the vapour as a 1:1 mixture at the 95% confidence limit and that sublimation of the polymeric hexatin^{II} di-μ_3-oxy-octakis-μ-trifluoroacetate is essentially stoichiometric. This did not preclude a successful least-squares refinement; on the contrary, the reader will note that the R_G and R_D (0.042 and 0.029, respectively; Section 4.3.4.2) obtained in this least-squares refinement is the lowest reported in this thesis.

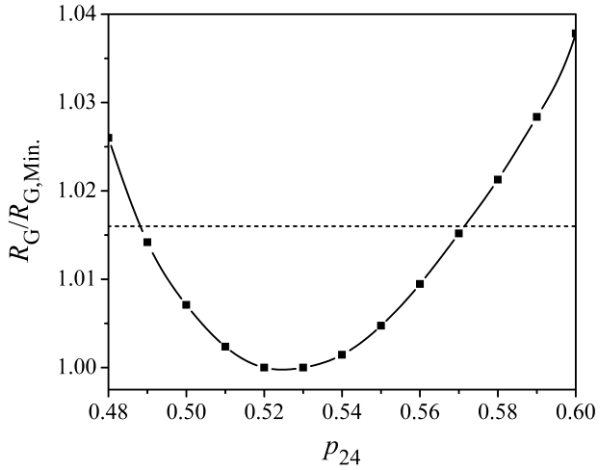

Figure 4.18. Quality of the least-squares refinement of $Sn(TFA)_2$ and $Sn_2O(TFA)_2$, quantified by an *R*-factor ratio, $R_G/R_{G,Min.}$, as a function of p_{24}. The horizontal dashed line represents the 95% confidence limit, approximately equal to 2σ.

The gas-phase equilibrium structure of $Sn(TFA)_2$ is directly comparable to that of $Sn(ac)_2$ as reported by Rankin and Mitzel *et al.*[208] It can be described either as a heavily-distorted trigonal bipyramid in which O_2, $O_{2'}$, and the lone electron pair occupy the equatorial positions and O_4 and $O_{4'}$ occupy the axial positions, or as a rhomboid-based pyramid where O_2, $O_{2'}$, O_4, and $O_{4'}$ form the base of the pyramid, with sides of 303(2) and 211(1) pm, and Sn_1 is at the apex. In the trigonal bipyramid picture, the distortion is effected by the tight bite angle of the two TFA subunits which forces asymmetric chelation, such that $r_{1,2}$ [231.4(14) pm] > $r_{1,4}$ [213.7(14) pm], to relieve steric overcrowding at the tin core.

The gas-phase equilibrium structure of $Sn_2O(TFA)_2$ is unique; to the best of the author's knowledge, Ref. 166 is the first report of such a structure. It can be described as a rectangular-based "*tent*", where O_{11}, $O_{11'}$, O_{13}, and $O_{13'}$ form the base, with sides of 312(2) and 229(1) pm, and Sn_{10}, $Sn_{10'}$, and O_9 are at the apices. The two TFA subunits chelate the Sn_{10}–O_9–$Sn_{10'}$ bridge symmetrically, such that $r_{10,11} \approx r_{10',13}$ [221.4(9) pm].

One cannot compute tin-oxygen chelation distances for $Sn(TFA)_2$ or $Sn_2O(TFA)_2$ to within 2σ of the structural solutions presented here *via* non-relativistic DFT; one has to go beyond this approximation. Relativistic DFT using the Douglas-Kroll Hamiltonian (Section 4.3.3), even with a modest triple-ζ basis set, improves theoretical tin-oxygen chelation distances considerably. The surprising agreement between the experimentally- and theoretically-determined [HF/3-21G(d)][208] structural parameters obtained by Rankin and Mitzel *et al.*[208] for $Sn(ac)_2$ is almost certainly the result of fortuitous cancellation of errors.

4.3.5.2 $Sn(TFA)_4$

The four bidentate TFA subunits adopt a flattened dodecahedral chelation configuration around the tin core of $Sn(TFA)_4$. The TFA subunits chelate asymmetrically, such that $r_{1,2}$ [214.2(4) pm] < $r_{1,4}$ [222.9(4) pm], relieving steric overcrowding at the tin core.

This chelation configuration is comparable to that of tin^{IV} acetate [$Sn(ac)_4$] in the crystalline state,[209] but, in contrast, crystal packing distorts the individual $Sn(ac)_4$ molecules in the unit cell out of ideal D_{2d} symmetry, and steric overcrowding results in a longer average tin-oxygen chelation distance [221.8(47)].[209] Appreciable variability in chelation distance [213.1(23) – 229.6(19)][209] is noted in this structural solution. Comparison can also be drawn with the structure of $lead^{IV}$ acetate [$Pb(ac)_4$] in the crystalline state.[210] Predictably, the larger size of the lead core is reflected in a longer average lead-oxygen chelation distance [227.5(23)][210] and the consequential relief of steric overcrowding results in less variability in chelation distance [222.4(12) – 231.2(13)][210] compared with $Sn(ac)_4$.

4.4 Conclusions

Time-averaged GED has been re-established in the UK after its disappearance a decade ago. The University of York is now the only institution housing an operational gas electron diffractometer in the UK, and one of only three in Europe. The relocation and recommission of the gas electron diffractometer that was formerly housed at the University of Reading has seen the University of York take its place among the group of less than half a dozen other institutions worldwide that are home to active GED laboratories. The structural studies in Sections 4.2 and 4.3 demonstrate the efficacy and wide-ranging capabilities of the University of York gas electron diffractometer, but are only two of many; twelve other structural studies that the author has led are given in Chapter 8.

The ability to acquire gas-phase equilibrium structures in-house *via* GED is powerful when coupled with computational chemistry/TSHD expertise; together, they allow the strongest proposals for TRGED beam time to be prepared (Chapter 1). In Chapters 6 and 7, gas-phase equilibrium structures acquired using the University of York gas electron diffractometer are presented again in this context. To continue to leverage the advantage that the Wann Electron Diffraction Group now has as a consequence of this research programme, the gas electron diffractometer will need to be continually developed in line with the latest standards. The necessary upgrades are discussed in Chapter 8.

5 New Methods & Applications II: Parallel Code for Simulating Time-Resolved Gas Electron Diffraction

Simulating TRGED data *via* TSHD is imperative pre-, mid-, and post-experiment. In the former case, it can be used to optimise experimental conditions ahead-of-time and in the latter case, it can be used to interpret and/or post-process the data, ensuring the best possible translation of the results of high-cost, high-risk beamline experiments into scientific impact (Chapter 1). High-speed simulation is critical, as TRGED experiments may be allocated narrow time windows and this information can often be requested with little notice.

TSHD necessarily results in population of the semiclassical nuclear phase space over time, generating nuclear ensembles, $\eta(\mathbf{R}, \mathbf{P})$ of N points with nuclear coordinates, $\mathbf{R}$, and momenta, $\mathbf{P}$. These distributions in nuclear phase space can be used *via* the nuclear ensemble approach (NEA) to simulate experiment accurately. Crespo-Otero and Barbatti[117] give an excellent overview of this approach with reference to spectroscopic simulation in Section 5 of Ref. 117. The effects of disorder and inhomogeneous broadening can be simulated *via* the NEA in steady-state spectra,[211–213] while the effects of dynamics in electronically-excited states can be accounted for in simulations of time-resolved spectra.[213–218] In the latter case, one might segment TSHD trajectories into time intervals, Δt, and use the nuclear ensembles $\eta_t(\mathbf{R}, \mathbf{P})$ for each interval, $t + \Delta t$, to compute an individual spectrum. One might then arrange the individual spectra into a time-ordered matrix and convolute the result with an instrument response function (IRF) to reflect the finite temporal resolution of the experiment. This is exactly the approach that Polli *et al.*[219] used to simulate time-resolved spectra of the retinal chromophore in a seminal Nature publication.

The NEA is conceptually simple to understand, practicably simple in its implementation, and highly parallelisable in principle. It is well-suited to the simulation of TRGED data as no additional electronic structure calculations are necessary (*cf.* spectral simulation); the MIC and RDC can be built for each time interval according to Eq. 2.10, 2.11, and 2.13 (Section 2.1) knowing only the nuclear coordinates, *i.e.* from $\eta_t(\mathbf{R}, \mathbf{P})$ alone.[7]

5.1 *py*naMICs

A cross-platform, highly-optimised, and parallelisable code, *py*naMICs, has been programmed in Python v2.7 to deliver computationally-efficient, on-the-fly simulation of

TRGED data from TSHD *via* the NEA. *py*naMICs has been designed from the outset with parallelisation, deployability, and the requirements and computational resources of end users in mind. The code is suitable for execution either in serial or in parallel with up to 64 CPUs; in this Chapter, parallel scaling performance has been benchmarked in the strong (Section 5.1.2) and weak (Section 5.1.3) scaling regimes. In the latter case, the benchmarking datasets contain between 16 and 1024 TSHD trajectories of between 500 and 32,000 steps, ranging from routine [*ca.* 100 – 200 trajectories; 2000 – 4000 steps (1 – 2 ps)] to highly-ambitious TSHD.

*py*naMICs improves on its only predecessor, TDSIMMIC,[74] in that it is:

- **Open-source:** Programmed in Python (v2.7) as opposed to the proprietary programming language, MATLAB (R2014a), used in TDSIMMIC.[74]
- **Deployable:** NUMPY, SCIPY and MATPLOTLIB libraries are the only dependencies, and are installed as standard on regional and national HPC.
- **Streamlined:** Reduced redundancy in routines (**SR1**; Section 5.1.1) for reading molecular geometries and electron scattering factors, and for reduction of the former to unique internuclear distances; improved performance relative to TDSIMMIC[74] for longer TSHD trajectories and molecules with a greater number of nuclei, extending the applicability of the code.
- **Parallelised:** Parallelised to a greater extent than TDSIMMIC,[74] in which only routines for computing $I_{\mathrm{Mol.}}(s)$ were parallelised; the transformation of MICs to RDCs (**PR2**; Section 5.1.1) is additionally parallelised in *py*naMICs, and existing parallel routines (**PR1**; Section 5.1.1) have been optimised. Non-parallel routines presently account for less than *ca.* 0.5% of the total (serial) execution time.
- **Interfaced directly to ELSEPA:** Interfaced directly with the FORTRAN77 Elastic Scattering of Electrons and Positrons by Neutral Atoms (ELSEPA) package of Salvat *et al.*[220] for on-the-fly computation of electron scattering factors with electron energies between 10 eV and 1 GeV. Alternatively, these may be read from an inbuilt library of electron scattering factors computed at 3.7 MeV.
- **Customisable:** Provides a number of options for the user to customise the simulation parameters; these options can be passed as arguments to *py*naMICs *via* a command-line interface.
- **Faster:** Up to 60% faster execution than TDSIMMIC[74] for processing routine TSHD on a desktop PC (Section 5.1.5).

5.1.1 Workflow

The workflow for *py*naMICs is outlined diagrammatically in Fig. 5.1.

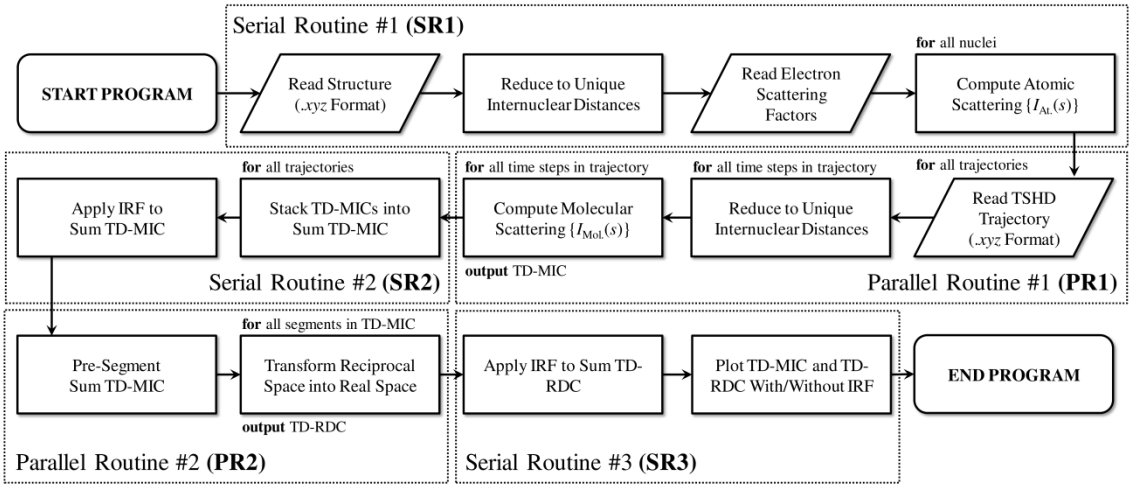

Figure 5.1. Flowchart outlining the workflow for *py*naMICs.

The user provides a minimum of three (if using pre-computed electron scattering factors) or four (if using the direct ELSEPA[220] interface) inputs, passed as arguments to *py*naMICs *via* the command-line interface. These inputs are a) a molecular geometry file (in *.xyz* format), b) the path to a directory containing TSHD trajectory files (in *.xyz* format), and c) either the path to a directory containing ELSEPA[220] output files (if using pre-computed electron scattering factors) or the path to the ELSEPA[220] executable and the electron energy in MeV (if using the direct ELSEPA[220] interface). The user can further pass optional arguments to *py*naMICs *via* the command-line interface to customise the simulation. All arguments that can be passed to *py*naMICs are summarised in Table 5.1.

In **SR1**, the molecular geometry file is read and the unique nuclei and internuclear distances are determined; electron scattering factors are read for the unique nuclei only, and $I_{At.}(s)$ is computed according to Eq. 2.10 (Section 2.1). Performing these tasks only once in this initial serial routine reduces file I/O in *py*naMICs to <0.5% of file I/O in TDSIMMIC[74] for routine TSHD (*e.g.* **BD1**; Section 5.1.2), and eliminates most I/O overheads from **PR1**. The TSHD trajectories are read in **PR1** and distributed over the available CPU cores for processing in parallel. The molecular geometry at each time step is reduced to unique internuclear distances. $I_{Mol.}(s)$ is then computed according to Eq. 2.11 (Section 2.1) for each time step, yielding a time-dependent MIC (TDMIC) matrix for each TSHD trajectory. The TDMICs are subsequently stacked in **SR2**, yielding a sum TDMIC *via* the NEA.

Table 5.1. Summary of positional and optional arguments that can be passed to *py*naMICs *via* the command line. Default values are tabulated where appropriate.

Argument	Optional?	Description	Default
[*geomfile*]	×	Molecular geometry file (*.xyz* format)	–
[*tdir*]	×	Directory containing TSHD trajectories	–
[*edir*]	~	Directory containing ELSEPA output	–
-els [*inp*]	~	Path to the ELSEPA executables	–
-ele [*inp*]	~	Electron energy in MeV	–
-nproc [*inp*]	✓	Number of (parallel) processes to launch	1
-irf [*inp*]	✓	FWHM of the (Gaussian) IRF	120.0 (fs)
-smin [*inp*]	✓	Minimum *s* value, $s_{\text{Min.}}$	0.0 (nm^{-1})
-smax [*inp*]	✓	Maximum *s* value, $s_{\text{Max.}}$	100.0 (nm^{-1})
-sint [*inp*]	✓	Resolution; points between $s_{\text{Min.}}$ and $s_{\text{Max.}}$	200
-tmin [*inp*]	✓	Initial time in TSHD	0.0 (fs)
-tint [*inp*]	✓	Time interval between steps in TSHD	0.5 (fs)
-save	✓	Save TDMIC and TDRDC in *.png* format	–
-h	✓	Display help documentation	–

In **PR2**, the sum TDMIC is and transformed from reciprocal space into real space according to Eq. 2.13 (Section 2.1) with $\alpha = -0.05$ to yield a time-dependent RDC matrix (TDRDC). Presegmentation of the sum TDMIC, with distribution of the segments over the available CPU cores, limits the number of CPU calls and improves performance. The TDMIC and TDRDC are plotted with and without an IRF in **SR3** for the user to assess.

5.1.2 Benchmark Details

All benchmarks reported in Sections 5.1.3 and 5.1.4 were recorded during beta testing of the University of York VIKING HPC cluster on standard compute nodes [2× Intel Xeon 6138 CPUs (20-core; 2.0 GHz), 192 GB RAM] running CentOS. Python v2.7.15 was used with the NUMPY v1.14.5 and SCIPY v1.1.0 libraries. All benchmarks reported in Section 5.1.5 were recorded on a desktop PC [1× AMD FX-8320E CPU (8-core; 3.2 GHz), 16 GB RAM] running Windows 10. Python v2.7.11 was used with the NUMPY v1.11.3 and SCIPY v0.18.1 libraries to benchmark *py*naMICs; MATLAB R2014a was used to benchmark TDSIMMIC.[74] Every benchmarking datapoint presented in Sections 5.1.3 – 5.1.5 is an average of 64 independent measurements. Care was taken to ensure that constant load was kept on each system during benchmarking. Four benchmarking datasets – **BD1**, **BD2**, **BD3**, and **BD4**, constructed as in Table 5.2 – have been used throughout this section.

Table 5.2. Summary of benchmarking datasets used throughout Section 5.1. The total number of nuclei, $N_{\text{At.}}$, (with the number of unique nuclei given in parentheses), trajectories, $N_{\text{Traj.}}$, and time steps, N_{Step}, are tabulated.

	$N_{\text{At.}}$	$N_{\text{Traj.}}$	N_{Step}
BD1	14 (3)	64	2000
BD2	14 (3)	16 CPU^{-1}	2000
BD3	14 (3)	64	500 CPU^{-1}
BD4	14 (3)	2^n, $n \in \{3, ..., 7\}$	2000

5.1.3 Strong Scaling Benchmarks

The strong scaling performance of *py*naMICs – *i.e.* how the execution time for a fixed-size problem (**BD1**) varies with the number of parallel processes – is investigated in this section. The strong scaling performance is indicative of the extent to which code is CPU-bound, and understanding performance in the strong scaling regime is valuable for finding the best balance between simultaneously accelerating execution by increasing the number of CPU cores, N_{CPU}, and consequently decelerating execution by increasing indirectly parallel/communication overheads, idling and wasted CPU cycles. The execution time of *py*naMICs in strong scaling tests is presented as a function of N_{CPU} in Fig. 5.2.

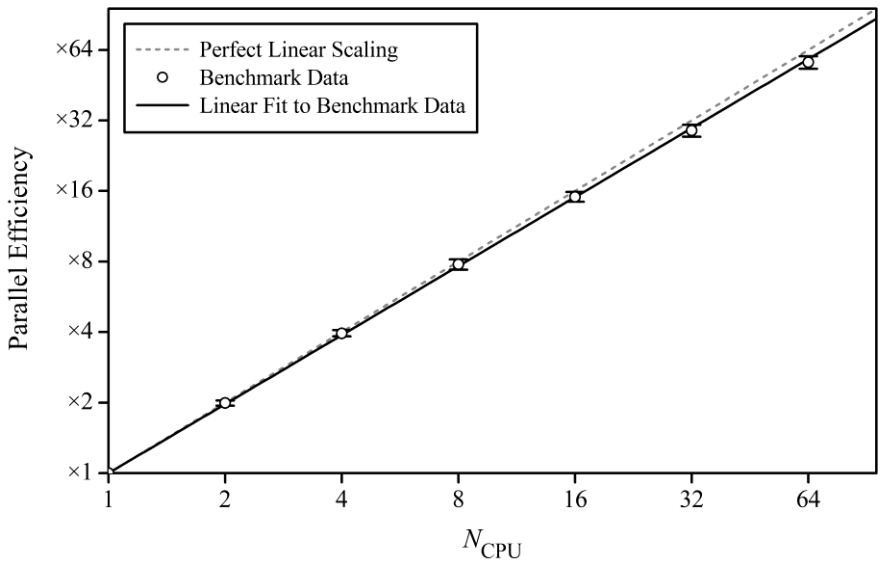

Figure 5.2. Execution time of *py*naMICs in strong scaling tests as a function of the number of CPU cores, N_{CPU}. **BD1** was used for benchmarking. The solid line represents a linear fit to the benchmark data ($R^2 = 0.999$). The dashed line represents perfect linear scaling.

*py*naMICs delivers high performance in the strong scaling regime, with strong scaling efficiencies (as a percentage of perfect linear scaling) that are >97% where N_{CPU} <8 (*i.e.* for routine desktop usage) and that remain over 90% up to N_{CPU} = 64. The current version of *py*naMICs is not likely to be executed with higher N_{CPU}, but performance is projected to remain satisfactory at higher core counts. The reader should note that the best attainable scaling is, predictably, less than perfectly linear – **SR1**, **SR2**, and **SR3** do not benefit from increases in N_{CPU} (Fig. 5.3).

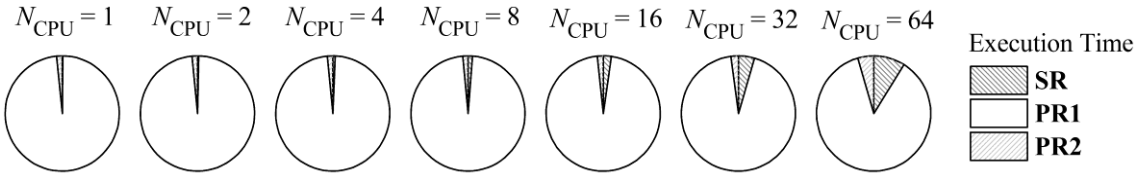

Figure 5.3. Execution times as a fraction of the total execution time for all serial routines (collectively; **SR**), **PR1**, and **PR2** with N_{CPU} = 1, 2, 4, 8, 16, 32, and 64.

Increasing N_{CPU} beyond $N_{Traj.}$ will not result in improved performance in this version of *py*naMICs, but one will typically not have more CPU cores at their disposal than TSHD trajectories to process in any case.

5.1.4 Weak Scaling Benchmarks

The weak scaling performance of *py*naMICs – *i.e.* how the execution time varies with the number of parallel processes for a fixed-size problem per parallel process (**BD2** and **BD3**) – is investigated in this section. The weak scaling performance is indicative of the extent to which the code is memory/resource-bound; in weak scaling tests, each parallel process handles a problem of a fixed size and more parallel processes are invoked to solve a larger problem than would otherwise be possible/efficient in serial. These tests are valuable for understanding how the parallel overheads vary relative to the size of the problem.

There are two possible ways to increase the size of the problem for *py*naMICs; one can either increase $N_{Traj.}$ (**BD2**) or $N_{Step.}$ (**BD3**). The former only affects **PR1**. After the TDMICs are stacked by **SR2**, only one TDMIC needs transforming into a TDRDC by **PR2**; **PR2** is consequently independent of $N_{Traj.}$. The latter affects both **PR1** and **PR2**. Consequently, the execution time of **PR1** in weak scaling tests is presented as a function of N_{CPU} and $N_{Traj.}$ in Fig. 5.4, and the execution times of **PR1** and **PR2** are presented as a function of N_{CPU} and N_{Step} in Fig. 5.5 and 5.6, respectively.

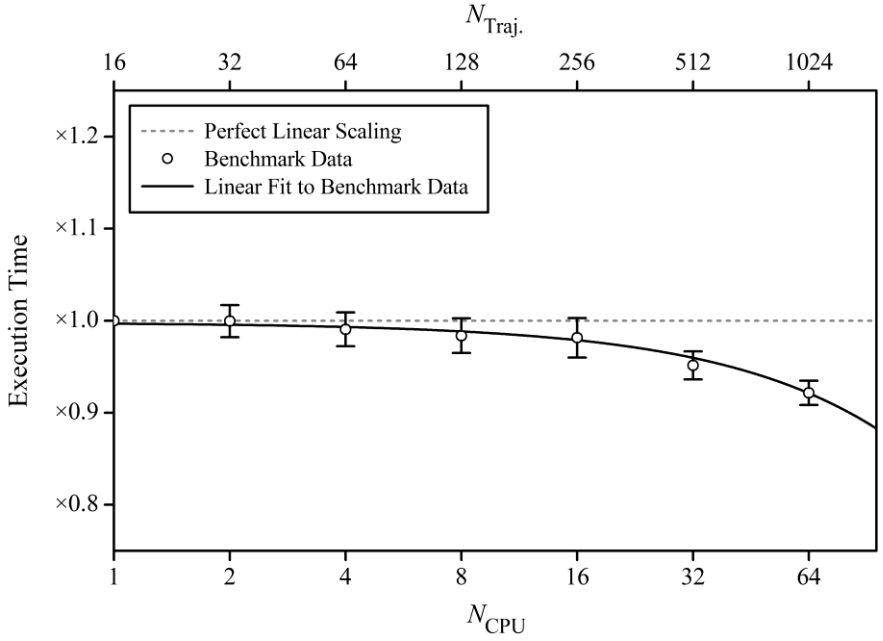

Figure 5.4. Execution time of **PR1** as a function of the number of CPU cores, N_{CPU}, and the number of TSHD trajectories, $N_{\text{Traj.}}$, where $N_{\text{Traj.}}$ = 16 CPU^{-1}. **BD2** was used for benchmarking. The solid line represents a linear fit to the benchmark data (R^2 = 0.977). The dashed line represents perfect linear scaling.

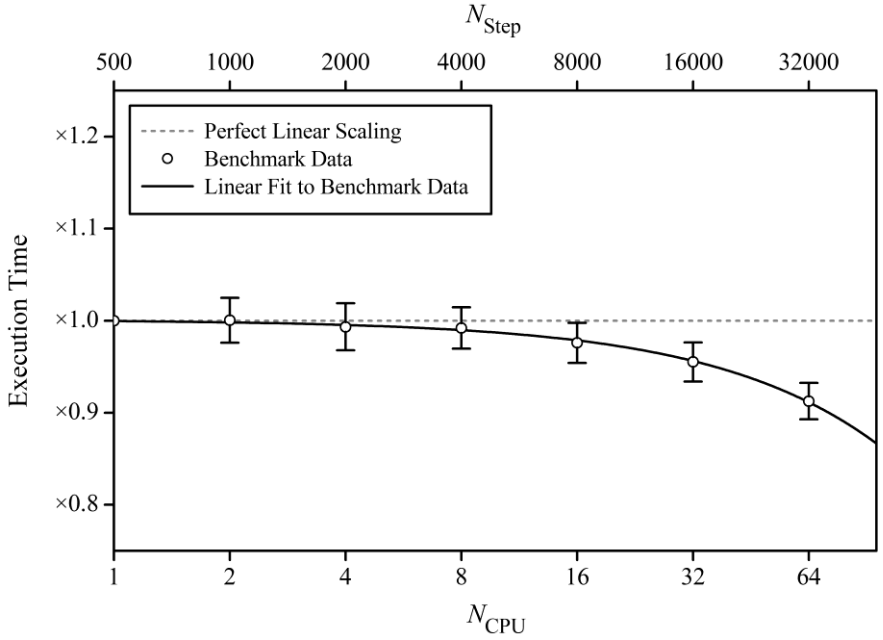

Figure 5.5. Execution time of **PR1** as a function of the number of CPU cores, N_{CPU}, and the number of TSHD steps, N_{Step}, where N_{Step} = 500 CPU^{-1}. **BD3** was used for benchmarking. The solid line represents a linear fit to the benchmark data (R^2 = 0.996). The dashed line represents perfect linear scaling.

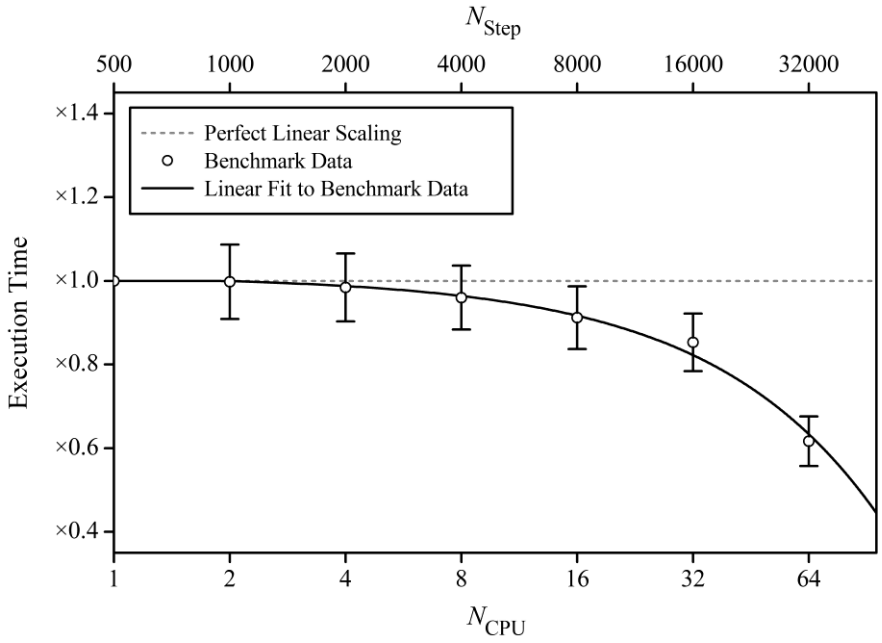

Figure 5.6. Execution time of **PR2** as a function of the number of CPU cores, N_{CPU}, and the number of TSHD steps, N_{Step}, where N_{Step} = 500 CPU^{-1}. **BD3** was used for benchmarking. The solid line represents a linear fit to the benchmark data (R^2 = 0.989). The dashed line represents perfect linear scaling.

PR1 delivers high performance in the weak scaling regime for increases in $N_{Traj.}$ (Fig. 5.4) and N_{Step} (Fig. 5.5), although is ultimately resource-bound at higher core counts where more, and larger, TDMICs need to be stored in the memory, respectively. Nonetheless, even at N_{CPU} = 64 ($N_{Traj.}$ = 1024; N_{Step} = 32,000) one can attain weak scaling efficiencies (as a percentage of perfect linear scaling) that are >90% and, in the regimes that *py*naMICs is likely to be used routinely ($N_{Traj.}$ = *ca.* 100 – 200; N_{Step} = *ca.* 2000 – 4000), weak scaling efficiencies of >97% are attainable. The performance of **PR2** is not as strong in the weak scaling regime (Fig. 5.6), particularly at higher core counts; weak scaling efficiency is reduced to <60% at N_{CPU} = 64 (N_{Step} = 32,000). **PR2** is more strongly resource-bound than **PR1** (good weak scaling performance is typically more difficult to achieve for similar classes of transformation, *e.g.* fast fourier transforms and transposes) but the reader should recognise that the execution time of **PR2** is significantly shorter than that of **PR1** (Fig. 5.3); overheads associated with initialisation of the parallel processes might therefore be expected to contribute significantly to the total execution time of **PR2** and likely account for the weaker performance at higher core counts. Nonetheless, as was found for **PR1**, better weak scaling efficiencies can be attained in the regimes that *py*naMICs is likely to be used routinely (N_{Step} = *ca.* 2000 – 4000); weak scaling efficiencies for **PR2** are >95% here.

Presegmentation of the TDMIC into N_{CPU} segments before **PR1** (Fig. 5.1) considerably improves performance over line-by-line transformation from reciprocal space into real space by limiting the number of CPU calls and consequently reducing the communication overhead. At lower core counts (N_{CPU} <16), execution time can be up to 20% faster with presegmentation, but at higher core counts the performance is still dominated by the overheads associated with initialisation of the parallel processes.

5.1.5 Benchmarking Against TDSIMMIC

With the aim of acquiring representative benchmarks for routine usage in the Wann Electron Diffraction Group, *py*naMICs was tested directly against TDSIMMIC[74] on a desktop PC [1× AMD FX-8320E CPU (8-core; 3.2 GHz), 16 GB RAM] running Windows 10 (Section 5.1.2); this is a comparable environment to that in which the Wann Electron Diffraction Group is most likely to use *py*naMICs for real applications. **BD4** was constructed to be representative of the TSHD datasets recorded over the course of this project (*e.g.* Sections 5.3.3, 6.3.3, and 7.3.4).

The execution times of *py*naMICs and TDSIMMIC[74] are presented as a function of $N_{Traj.}$ in Fig. 5.7.

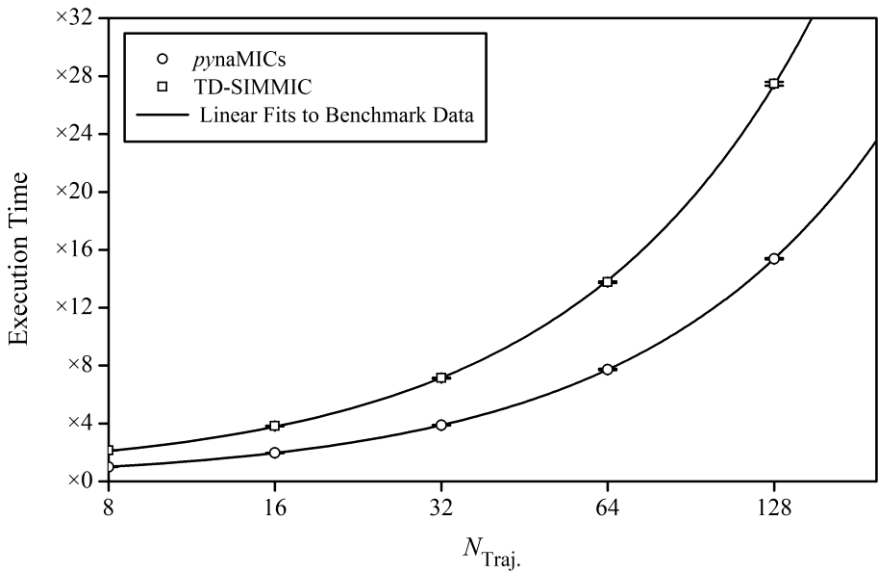

Figure 5.7. Execution time of *py*naMICs and TDSIMMIC[74] as a function of the number of TSHD trajectories, $N_{Traj.}$. **BD4** was used for benchmarking. Computational resources (N_{CPU} = 8, RAM = 16 GB) were fixed. The solid lines represent linear fits to the benchmark data for *py*naMICs (R^2 = 0.999) and TDSIMMIC (R^2 = 0.999).

Where computational resources are limited and (essentially) fixed, *i.e.* the case here, where *py*naMICs is used on a desktop PC rather than a workstation or in a HPC environment, *py*naMICs outperforms TDSIMMIC,[74] delivering better than 50% faster execution for any given $N_{\text{Traj.}}$ and exhibiting improved scaling behaviour. The same result is expected in the high-core-count and high-memory limit.

5.1.6 An Application of *py*naMICs

While it is straightforward to convince the reader of the improved performance of *py*naMICs over TDSIMMIC[74] (Sections 5.13 – 5.15), it is difficult to provide evidence that TDMICs simulated by *py*naMICs or TDSIMMIC[74] reproduce accurately experiment. This is primarily because genuinely "*ultrafast*" (sub-ps) TRGED (*i.e.* TRGED on a comparative temporal scale to routine TSHD simulation) is a relatively new discipline. TDMICs are not yet routinely published with reports of TRGED experiments; standardisation/development of convention has not yet taken place, and it is not clear what direction it will ultimately take if, and when, it does. There are some encouraging signs of standardisation in recent studies emerging from the SLAC National Accelerator Laboratory, however.[16–18]

In lieu of providing a side-by-side comparison of an experimental and theoretical TDMIC, *py*naMICs is instead demonstrated with the photolysis of 1,2-diiodotetrafluoroethane (1,2-DITFE; Sections 5.2 – 5.4) as a case study. Firstly, TSHD (Section 5.3.3) have already been recorded for 1,2-DITFE in support of contemporary TRGED experiments at the SLAC National Accelerator Laboratory[17] as part of a complementary side project, *i.e.* an input for *py*naMICs has been produced unintentionally over the course of this project. Secondly, the photolysis of 1,2-DITFE is known to produce an enduring (ps) and clear signature in TRGED experiments (*cf.* 1,2-dithiane or *E*-cinnamonitrile; Sections 6.4 and 7.4); even in earliest TRGED experiments of Zewail and Ihee,[53,54,57] the photolysis signature was unambiguous, despite the limited spatiotemporal resolution available.

5.2 Photolysis of 1,2-Diiodotetrafluoroethane

Zewail and Ihee *et al.* describe the photolysis of 1,2-DITFE (Fig. 5.8) as the "*…prototypical reaction in ultrafast spectroscopic studies of photoinitiated reactions…*";[57] indeed, one can consider it to have been the flagship time-resolved experiment of Zewail and Ihee, not only in TRGED,[53,54,57] but also in TRXRD[221] and time-resolved spectroscopy.[52] Both authors have also contributed to contemporary theoretical understanding.[55,56,222]

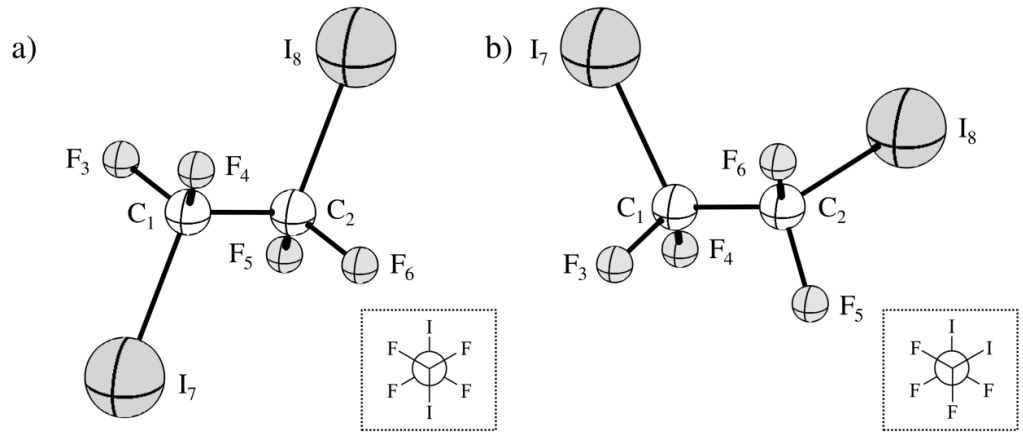

Figure 5.8. Ground-state structures of a) *ap*-1,2-DITFE and b) *sc*-1,2-DITFE. The inserts (bottom-right) depict Newman projections. The atomic labelling scheme is outlined and used throughout Sections 5.2 – 5.4.

There are two stable conformations of 1,2-DITFE; one with an anti-periplanar (*ap*) configuration (*ap*-1,2-DITFE; Fig. 5.8a), and one with a synclinal (*sc*) configuration (*sc*-1,2,-DITFE; Fig. 5.8b). The former is the dominant conformation in the gas phase.[223]

Photolysis of *ap*-1,2-DITFE and *sc*-1,2-DITFE promptly generates the iodotetrafluoroethyl (ITFE) radicals *ap*-ITFE$^{\bullet}$ and *sc*-ITFE$^{\bullet}$, respectively. Secondary dissociation of I$^{\bullet}$ may then lead to generation of tetrafluoroethene (TFE). Whether the ITFE radicals adopt a "*classical*" or "*bridged*" (λ^2-ITFE$^{\bullet}$; Fig. 5.9) structure is still a somewhat controversial topic in the TRGED community. Improvements in spatiotemporal resolution since the early experiments of Zewail and Ihee *et al.*[53,54,57] have encouraged researchers to revisit 1,2-DITFE in contemporary experiments at the SLAC National Accelerator Laboratory.[17]

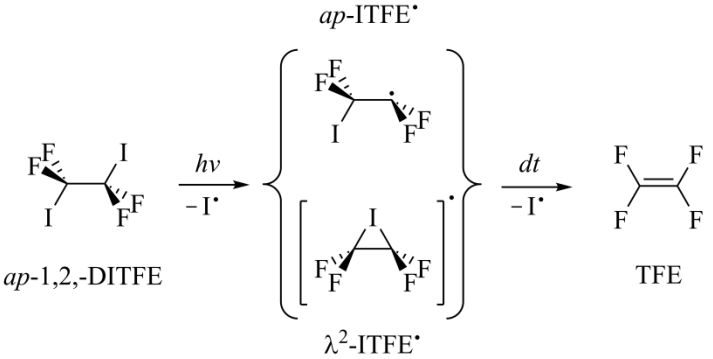

Figure 5.9. Photolysis scheme for *ap*-1,2-DITFE. Photolysis of *ap*-1,2-DITFE generates I$^{\bullet}$ and *ap*-ITFE$^{\bullet}$; the geometry of the latter may be "*classical*" (*ap*-ITFE$^{\bullet}$) or "*bridged*" (λ^2-ITFE$^{\bullet}$). Secondary dissociation after some time interval, *dt*, generates I$^{\bullet}$ and TFE.

5.3 Electronically-Excited States of 1,2-Diiodotetrafluoroethane

5.3.1 *Ab Initio* Calculations

All *ab initio* calculations detailed in this section were carried out on the University of York Advanced Research Computing Cluster; all CASSCF and multistate CASPT2 (MS-CASPT2) calculations were carried out using OPENMOLCAS v8.3.[224]

The CASSCF active space (Fig. 5.10) used for *ap*-1,2-DITFE comprised twelve electrons distributed in eight orbitals – three of A_g symmetry, one of A_u symmetry, one of B_g symmetry, and three of B_u symmetry. Two pairs of $\sigma_{C–I}$ (B_u, A_g) and $\sigma^*_{C–I}$ (B_u, A_g) orbitals, and four n_I (B_u, A_u, B_g, A_g) orbitals were used to construct the active space. In singlet-state calculations, state-averaging was carried out over the five lowest-energy singlet states – two of A_g symmetry, and one of each A_u, B_g, and B_g symmetry. In triplet-state calculations, state-averaging was carried out over the four lowest-energy triplet states – one of each A_g, A_u, B_g, and B_u symmetry. All states were equally weighted. These calculations are denoted SA(5/4)-CASSCF(12,8).

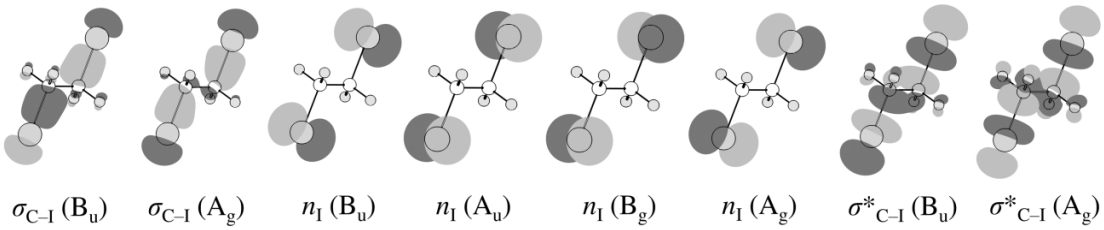

Figure 5.10. SA(5/4)-CASSCF(12,8) active space constructed for *ap*-1,2-DITFE, comprising two pairs of $\sigma_{C–I}$ (B_u, A_g) and $\sigma^*_{C–I}$ (B_u, A_g) orbitals, and four n_I (B_u, A_u, B_g, A_g) orbitals.

MS-CASPT2 calculations for *ap*-1,2-DITFE used the reference space of Fig. 5.10. The five lowest-energy singlet states – two of A_g symmetry, and one of each A_u, B_g, and B_g symmetry – and four lowest-energy triplet states – one of each A_g, A_u, B_g, and B_u symmetry – were included in the multistate treatment for independent singlet-state and triplet-state calculations, respectively. These calculations are denoted MS-CASPT2(12,8).

The CASSCF active space and MS-CASPT2 reference space used for *sc*-1,2-DITFE comprised the same set of orbitals as used for *ap*-1,2-DITFE, but with different symmetries. Two pairs of $\sigma_{C–I}$ (B, A) and $\sigma^*_{C–I}$ (B, A) orbitals, and four n_I (B, A, B, A) orbitals were used to construct the active space. Accordingly, the corresponding state-

averaging/multistate treatments included five singlet states – three of A symmetry and two of B symmetry – and four triplet states – two of each A and B symmetry. Calculations were otherwise carried out exactly as for *ap*-1,2-DITFE.

The CASSCF active space (Fig. 5.11) used for *ap*-ITFE$^{\bullet}$ comprised seven electrons distributed in five orbitals – four of A′ symmetry and two of A″ symmetry. A pair of $\sigma_{C–I}$ (A′) and $\sigma^*_{C–I}$ (A′) orbitals, two n_I (A′, A″) orbitals, and a n_C (A′) orbital were used to construct the active space. State-averaging was carried out over the five lowest-energy doublet states – three of A′ symmetry and two of A″ symmetry – with equal weighting of all states. The CASSCF active space used for *sc*-ITFE$^{\bullet}$ comprised the same set of orbitals as used for *ap*-ITFE$^{\bullet}$ but without symmetry. Calculations were otherwise carried out exactly as for *ap*-ITFE$^{\bullet}$. These calculations are collectively denoted SA5-CASSCF(7,5).

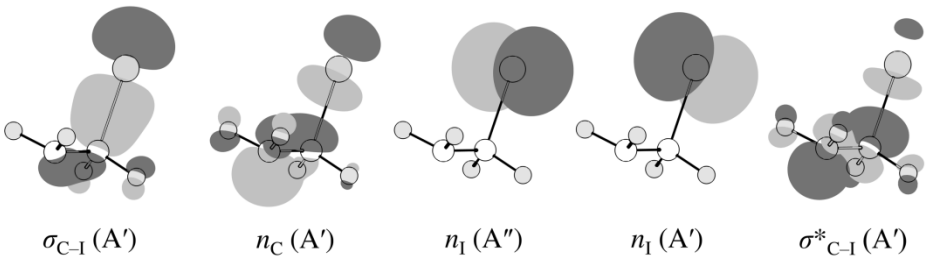

Figure 5.11. SA5-CASSCF(7,5) active space constructed for *ap*-ITFE$^{\bullet}$, comprising a pair of $\sigma_{C–I}$ (A′) and $\sigma^*_{C–I}$ (A′) orbitals, two n_I (A′, A″) orbitals, and a n_C (A′) orbital.

The CASSCF active space (Fig. 5.12) used for λ^2-ITFE$^{\bullet}$ is a variant of that used for *ap*-ITFE$^{\bullet}$ and *sc*-ITFE$^{\bullet}$, constructed in the C_{2v} symmetry point group.

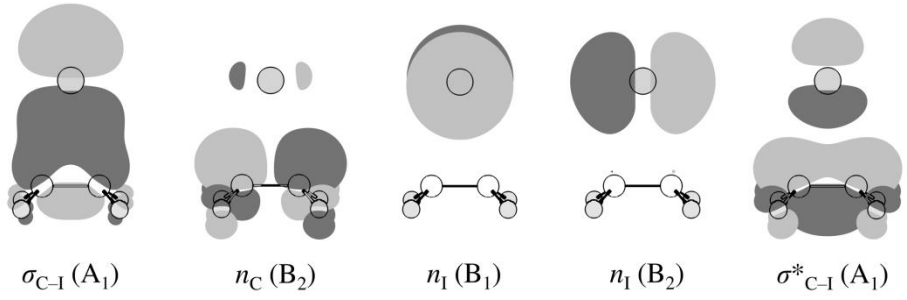

Figure 5.12. SA5-CASSCF(7,5) active space constructed for λ^2-ITFE$^{\bullet}$, comprising a pair of $\sigma_{C–I}$ (A$_1$) and $\sigma^*_{C–I}$ (A$_1$) orbitals, two n_I (B$_1$, B$_2$) orbitals, and a n_C (B$_2$) orbital.

The basis sets and corresponding core potentials of Stoll and Preuss *et al.*[225,226] were used throughout to limit computational cost. The suitability of these basis sets were validated against all-electron calculations using the ANO-RCC basis set of Roos *et al.*[227] that are not discussed here in the interest of brevity.

The proper convergence of all geometry optimisations to minima was verified *via* vibrational frequency inspection.

5.3.2 Potential Energy Surface Geography

The C_{2h}-symmetric and C_2-symmetric S_0 minima, *ap*-1,2-DITFE and *sc*-1,2-DITFE, respectively, have been fully optimised at the SA(5/4)-CASSCF(12,8) and MS-CASPT2(12,8) levels. Cartesian coordinates are tabulated in Tables B1–4. Vertical transition energies and oscillator strengths are tabulated in Table 5.3 for transitions to the manifold of singlet (S_1, S_2, S_3, and S_4) and triplet (T_1, T_2, T_3, and T_4) states that originate from *ap*-1,2-DITFE and *sc*-1,2-DITFE.

Table 5.3. Summary of transition energies, ΔE,[a] and oscillator strengths, f, for *ap*-1,2-DITFE and *sc*-1,2-DITFE as computed at the SA(5/4)-CASSCF(12,8) and MS-CASPT2(12,8) levels.

	SA(5/4)-CASSCF(12,8)				MS-CASPT2(12,8)			
	ap-1,2-DITFE		*sc*-1,2-DITFE		*ap*-1,2-DITFE		*sc*-1,2-DITFE	
Transition	ΔE	f	ΔE	f	ΔE	f	ΔE	f
$T_1 \leftarrow S_0$	3.71	<0.001	3.90	<0.001	3.89	<0.001	4.09	<0.001
$T_2 \leftarrow S_0$	3.72	<0.001	3.91	<0.001	3.89	<0.001	4.10	<0.001
$T_3 \leftarrow S_0$	3.74	<0.001	3.95	<0.001	3.93	<0.001	4.15	<0.001
$T_4 \leftarrow S_0$	3.80	<0.001	3.96	<0.001	4.03	<0.001	4.15	<0.001
$S_1 \leftarrow S_0$	4.20	0.004	4.39	0.003	4.45	0.006	4.65	0.003
$S_2 \leftarrow S_0$	4.22	0.004	4.43	0.001	4.45	0.005	4.69	0.001
$S_3 \leftarrow S_0$	4.24	<0.001	4.48	0.005	4.50	<0.001	4.74	0.006
$S_4 \leftarrow S_0$	4.30	<0.001	4.49	0.002	4.60	<0.001	4.75	0.002

[a] All transition energies are tabulated in eV.

Excellent agreement is found between the values computed at the SA(5/4)-CASSCF(12,8) and MS-CASPT2(12,8) levels (Table 5.1). Vertical transition energies for *ap*-1,2-DITFE and *sc*-1,2-DITFE are only underestimated by *ca.* 0.2 eV at the SA(5/4)-CASSCF(12,8) level and the underestimation is consistent for both *ap*-1,2-DITFE and *sc*-1,2-DITFE, and across the singlet and triplet manifolds. Scaling of energies and gradients computed at the

SA(5/4)-CASSCF(12,8) level by a factor of *ca.* 1.05 could therefore be used for high-quality TSHD (Section 5.3.3). Where specific values are quoted in this section, these have been computed at the SA(5/4)-CASSCF(12,8) level, and the reader may be satisfied with their accuracy.

The manifold of singlet and triplet states are accessed from the S_0 minimum *via* $\sigma^*_{C–I} \leftarrow n_I$ excitation and are all, accordingly, strongly dissociative along the carbon-iodine stretching coordinate. Single-photon absorption at *ca.* 260 – 280 nm should make accessible the manifold of singlet states. The singlet and triplet states couple together along the carbon-iodine stretching coordinate; potential energy surfaces have been constructed along this coordinate *via* linear interpolation in internal coordinates (LIIC). In the interest of brevity, potential energy surfaces are only presented along the symmetric carbon-iodine stretching coordinate, and only for *ap*-1,2-DITFE; there is no discernible difference – in qualitative terms – between the potential energy surfaces that are constructed in this manner for *ap*-1,2-DITFE and *sc*-1,2-DITFE. Independent single-point-energy evaluations have been carried out on 12 interpolated geometries between $r_{1,7} \equiv r_{2,8}$ = 200.0 and 350.0 pm at the SA(5/4)-CASSCF(12,8) and MS-CASPT2(12,8) levels. The potential energy surfaces for the singlet and triplet manifolds are presented in Fig. 5.13a and 5.13b, respectively.

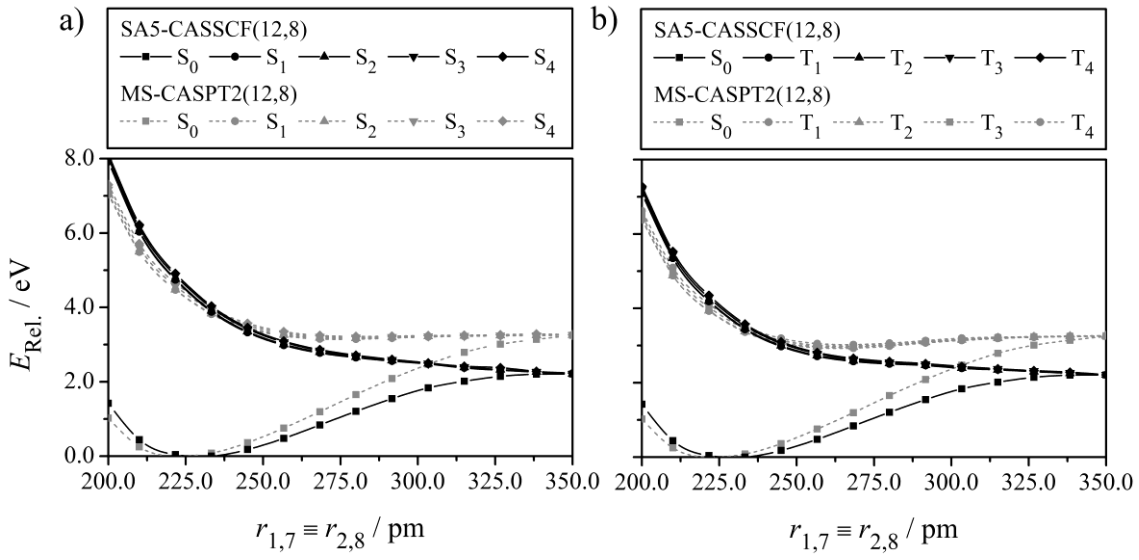

Figure 5.13. a) Singlet- (S_1, S_2, S_3, and S_4) and b) triplet-state (T_1, T_2, T_3, and T_4) potential energy surfaces along the symmetric carbon-iodine stretching coordinate between $r_{1,7} \equiv r_{2,8}$ = 200.0 and 350.0 pm, mapped *via* LIIC and computed at the SA(5/4)-CASSCF(12,8) and MS-CASPT2(12,8) levels. MS-CASPT2(12,8) calculations are carried out at SA(5/4)-CASSCF(12,8) geometries.

The C_s-symmetric and C_1-symmetric D_0 minima, *ap*-ITFE· and *sc*-ITFE·, have been fully optimised at the SA(5)-CASSCF(7,5) level; Cartesian coordinates are tabulated in Tables B5 and B6. The C_{2v}-symmetric "*bridged*" geometry, λ^2-ITFE•, has also been fully optimised at the SA(5)-CASSCF(7,5) level; Cartesian coordinates are tabulated in Table B7. λ^2-ITFE• is located on the crossing seam between the D_1 and D_0 states (Section 5.3.4), a result that does not appear to have been appreciated in earlier theoretical work[55,56,222] where DFT was employed.

5.3.3 Trajectory Surface-Hopping Dynamics

TSHD simulations were recorded at the SA(5/4)-CASSCF(12,8) level (set up as described in Section 5.3.1) using SHARC v1.0[228–230] interfaced with OPENMOLCAS v8.3.[224] All analytical gradients were computed on-the-fly by routines integrated into OPENMOLCAS v8.3;[224] non-adiabatic transition probabilities were accounted for using the augmented fewest-switches algorithm of Hammes-Schiffer and Tully,[140,141] as implemented in SHARC v1.0.[228–230]

Each member of a Wigner-distributed ensemble containing 500 independent S_0-state starting geometries (250 corresponding to each *ap*-1,2-DITFE and *sc*-1,2-DITFE) was transformed into the manifold of singlet states. The brightest 100 starting geometries corresponding to each *ap*-1,2-DITFE and *sc*-1,2-DITFE were selected from the initial conditions for TSHD.

200 independent trajectories were obtained by propagating each geometry for 200 fs. The nuclei were propagated *via* integration of Newton's classical equations in time steps of 0.25 fs using the velocity-Verlet algorithm.[231] The time-dependent Schrödinger equation was integrated in time steps of 0.01 fs using the classical 4^{th}-order Runge-Kutta algorithm. The decoherence parameter, α, was set to 0.1 a.u. Energies and gradients computed at the SA(5/4)-CASSCF(12,8) level were scaled by a factor of 1.05 to match results computed at the MS-CASPT2(12,8) level (Section 5.3.2).

5.3.4 Discussion

A weighted TSHD dataset comprising 100 independent trajectories was constructed from the 200 independent trajectories that were recorded (Section 5.3.3) by combining the brightest *n ap*-1,2-DITFE and (100 – *n*) *sc*-1,2-DITFE trajectories, with *n* being determined from the conformer ratio of *ap*-1,2-DITFE : *sc*-1,2-DITFE. The conformer ratio has been

determined experimentally *via* GED at 293, 393, and 473 K by Hedberg *et al.*;[223] the result of the former experiment (*ap*-1,2-DITFE : *sc*-1,2-DITFE = 1 : 0.24 at 293 K) was used here to construct a dataset of 81 *ap*-1,2-DITFE and 19 *sc*-1,2-DITFE trajectories. This weighted TSHD dataset is used throughout, unless otherwise indicated.

Photodissociation of I$^{\bullet}$ from 1,2-DITFE is prompt along the carbon-iodine stretching coordinate and occurs on the triplet potential energy surface. The populations of the singlet and triplet manifolds as a function of time are presented in Fig. 5.14.

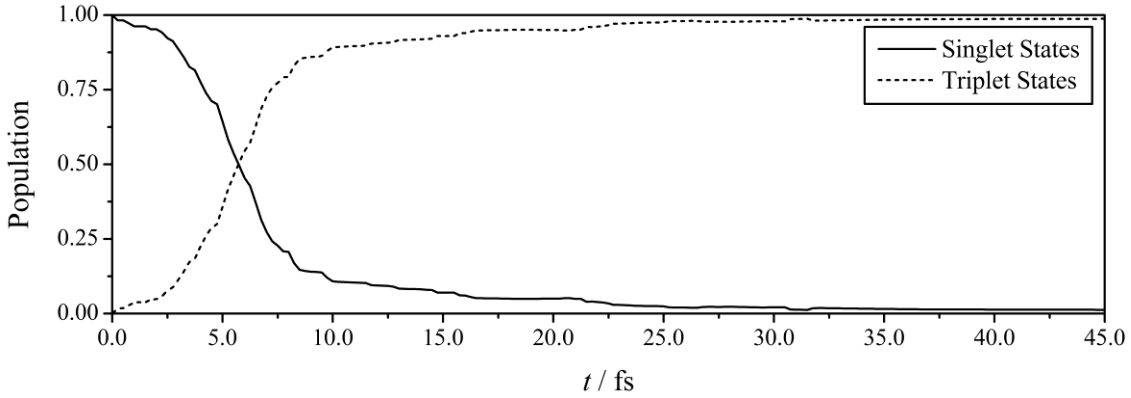

Figure 5.14. Sum populations of the singlet (S_1, S_2, S_3, and S_4) and triplet (T_1, T_2, T_3, and T_4) states as a function of time, *t*.

ISC is ultrafast (sub-10-fs), with the lifetime, τ, of the states in the singlet manifold being 6 ± 2 fs. I$^{\bullet}$ is extruded in the first instance to give ITFE$^{\bullet}$ + I$^{\bullet}$; ITFE$^{\bullet}$ may then subsequently extrude a second I$^{\bullet}$ to give TFE + I$^{\bullet}$, or persist until the end of TSHD. The evolution of $r_{1,7}$ and $r_{2,8}$ as a function of time are presented in Figs. 5.15a and 5.15b, respectively. Photodissociation generally proceeds stepwise, as evidenced by Fig. 5.15c – a result that is consistent with experimental measurements in the gas phase[53,54,57] and in solution.[221]

On analysis of all 200 independent trajectories, the following is revealed: *ap*-ITFE$^{\bullet}$ is considerably more likely to extrude a second I$^{\bullet}$ on the sub-200-fs timescale compared to *sc*-ITFE·. Secondary dissociation is recorded in 67% of *ap*-ITFE$^{\bullet}$ trajectories but in only 5% of *sc*-ITFE$^{\bullet}$ trajectories. Statistical significance testing quantifies what should already be obvious to the reader; the different behaviour of the *ap*-ITFE$^{\bullet}$ and *sc*-ITFE$^{\bullet}$ trajectories is significant beyond the 99.9% confidence level. The reader should note the special significance of this particular result as *sc*-ITFE$^{\bullet}$ is also closer in geometric space to the λ^2-ITFE$^{\bullet}$ than *ap*-ITFE$^{\bullet}$; the former is at a distance of only 784.1 pm Da$^{-½}$ and the latter is at a distance of 1400.5 pm Da$^{-½}$ from λ^2-ITFE$^{\bullet}$.

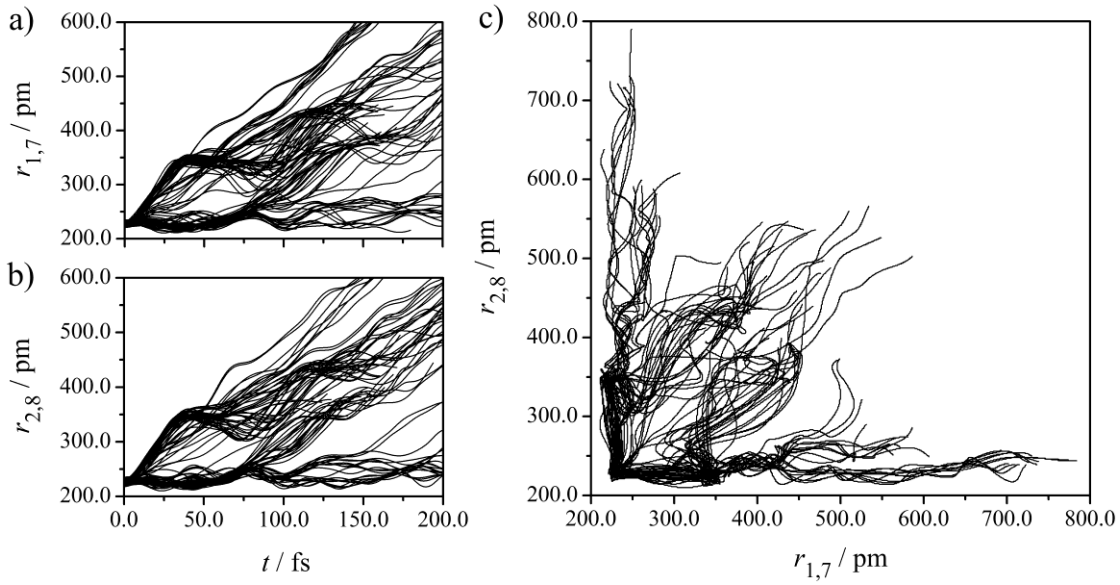

Figure 5.15. Evolution of a) $r_{1,7}$ and b) $r_{2,8}$ as a function of time, t, and c) $r_{1,7}$ plotted against $r_{2,8}$. All 100 trajectories are plotted independently.

The two aforementioned points – these being that *sc*-ITFE$^{\bullet}$ is closer in geometric space to λ^2-ITFE$^{\bullet}$, and is considerably more likely to be formed following photodissociation of *sc*-1,2-DITFE than is *ap*-ITFE$^{\bullet}$ following photodissociation of *ap*-1,2-DITFE – make favourable the transient formation of λ^2-ITFE$^{\bullet}$. As λ^2-ITFE$^{\bullet}$ is found on the crossing seam between the D_1 and D_0 states, the trajectory swarm might not be expected to localise around λ^2-ITFE$^{\bullet}$, but this geometry might be visited transiently, and might also be observed directly as a consequence of improvements in the spatiotemporal resolution of TRGED. The potential energy surfaces for the doublet states between *sc*-ITFE$^{\bullet}$ and λ^2-ITFE$^{\bullet}$ have been constructed *via* LIIC; independent single-point-energy evaluations have been carried out on seven interpolated geometries at the SA5-CASSCF(7,5) and MS-CASPT2(7,5) levels. The potential energy surfaces are presented in Fig. 5.16.

λ^2-ITFE$^{\bullet}$ was not observed in the early TRGED studies of Zewail *et al.*[53,54,57] – the inclusion of λ^2-ITFE$^{\bullet}$ was found to have a detrimental effect on the quality of the least-squares refinement – but whether or not this intermediate exists, even transiently, is still considered an open question in TRGED (Section 5.2). The results communicated in this Chapter, and in contemporary (pre-print) work from the SLAC National Accelerator Laboratory,[17] support fully this question remaining so. If λ^2-ITFE$^{\bullet}$ appears transiently on the sub-ps timescale, then it would not have been observed in the early TRGED study of Zewail *et al.*,[53,54,57] because the temporal resolution (*ca.* 2 – 5 ps) would have been insufficient to detect it.

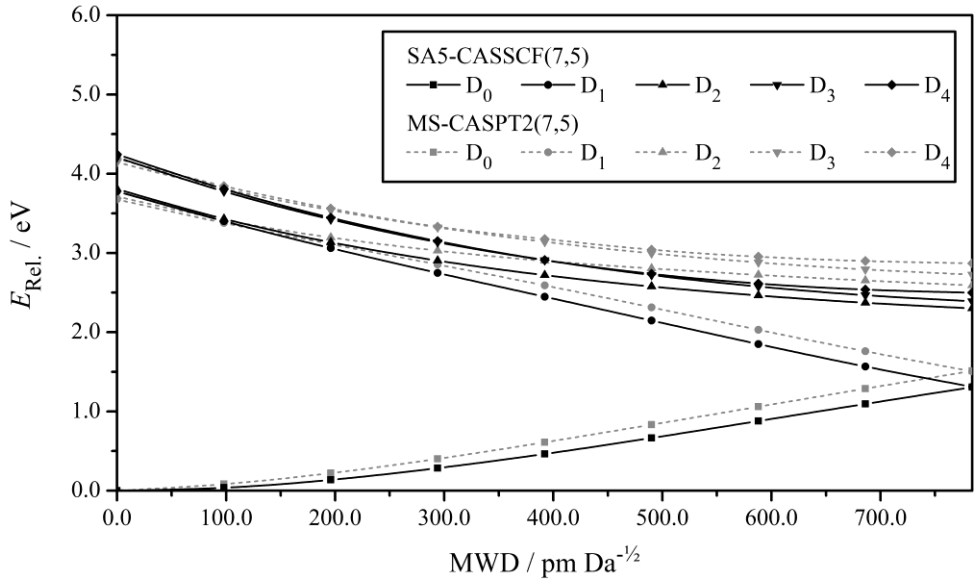

Figure 5.16. Doublet-state (D_0, D_1, D_2, D_3, and D_4) potential energy surfaces between *sc*-ITFE$^{\bullet}$ and λ^2-ITFE$^{\bullet}$, mapped *via* LIIC and computed at the SA5-CASSCF(7,5) and MS-CASPT2(7,5) levels. MS-CASPT2(7,5) calculations are carried out at SA5-CASSCF(7,5) geometries.

5.4 Simulations of Time-Resolved Gas Electron Diffraction

Simulations of the TDMIC and TDRDC for 1,2-DITFE with and without a 120 fs IRF applied, in each case, are reproduced in Figs. 5.17 and 5.18, respectively. The IRF used for these simulations was chosen to be comparable to that of the TRGED instrument at the SLAC National Accelerator Laboratory.

The photolysis signature of 1,2-DITFE appears clearly in both the temporal and spatial coordinates of the TDMIC (Fig. 5.17a). In the former, it manifests as a damping of the molecular scattering intensity as a function of time – a consequence of the reduction in unique internuclear distances and extrusion of I$^{\bullet}$ (the nucleus with the most powerful electron scattering effect) – as 1,2-DITFE photofragments to ITFE$^{\bullet}$ and TFE. In the latter, it manifests as a shifting of the features at *ca.* 25 nm^{-1} (I···I), 45 nm^{-1} (I···F), and 60 – 70 nm^{-1} (C–I) towards the lower end of the *s* range, corresponding to a lengthening of all the associated internuclear distances.

The reduction in the amount of structural information available at later time is also evident on transformation of the TDMIC (Fig. 5.17a) into the TDRDC (Fig. 5.18a), where the damping of feature intensity as a function of time is most apparent in the features at *ca.* 350 – 400 (I···F) and 700 – 750 pm (I···I). The bifurcation of the former feature

contains information on secondary dissociation versus persistence of ITFE•; it is possible to determine the branching ratio from the relative intensities of the features.[74]

Application of the 120 fs IRF to the TDMIC and TDRDC obscures the fine structure in the TDMIC (Fig. 5.17b) but the photolysis signature remains clear in reciprocal and real space (Fig. 5.18b). The photolysis signature might manifest more clearly over a longer timescale (*cf.* the early TRGED experiments of Zewail *et al.*);[53,54,57] here, the FWHM of the IRF is comparable to the timescale of TSHD, but structural dynamics continue beyond it.

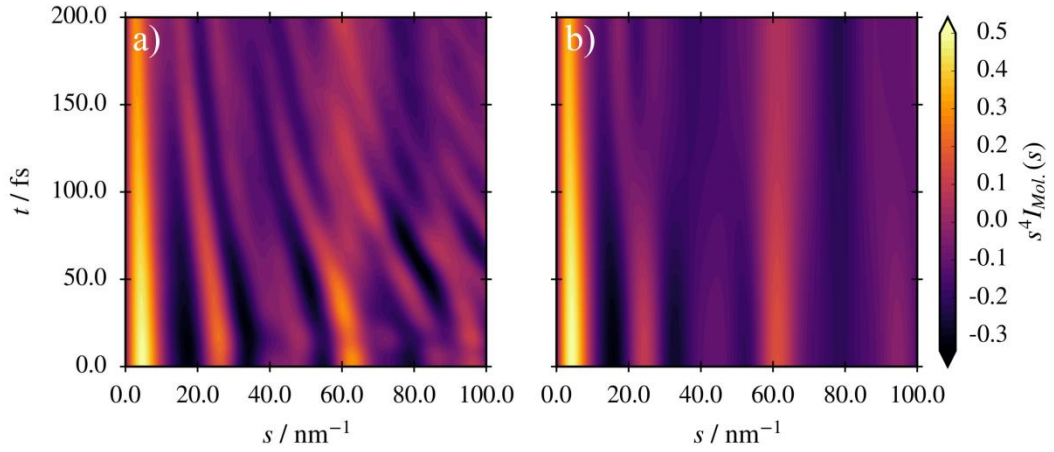

Figure 5.17. Theoretical TDMIC matrices for 1,2-DITFE a) with 0.25 fs temporal resolution and b) convoluted with a 120 fs (FWHM) Gaussian kernel. The conformer-weighted TSHD data (Section 5.3.4) were used to model the TDMICs.

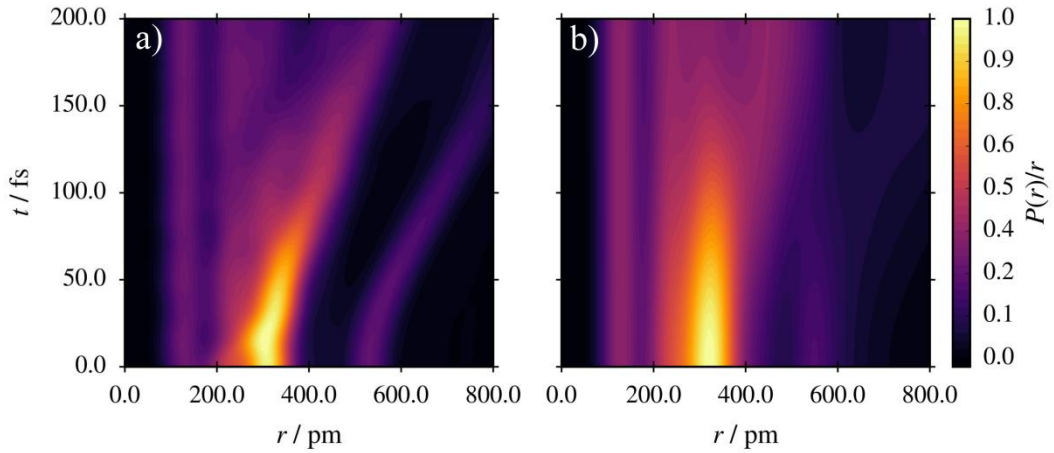

Figure 5.18. Theoretical TDRDC matrices for 1,2-DITFE transformed from a) a theoretical TDMIC matrix with 0.25 fs temporal resolution and b) a theoretical TDMIC matrix convoluted with a 120 fs (FWHM) Gaussian kernel. The conformer-weighted TSHD data (Section 5.3.4) were used to model the TDMICs.

5.5 Conclusions

*py*naMICs – an open-source, cross-platform, highly-optimised, and parallelisable code for simulating TRGED *via* TSHD with the NEA – has been programmed in Python 2.7 and benchmarked both in the weak and strong scaling regimes (Sections 5.1.3 and 5.1.4), and against its predecessor, TDSIMMIC[74] (Section 5.1.5). *py*naMICs demonstrably outperforms TDSIMMIC[74] in benchmarking tests, and further improves on its predecessor *via* incorporation of new features, *e.g.* a direct interface to the electron scattering code, ELSEPA,[220] and command-line interface (Section 5.1) *py*naMICs is suitable for use on contemporary desktop PCs, but the performance of the code in the weak and strong scaling regimes (Sections 5.1.3 and 5.1.4) demonstrates that it is equally suitable for use on desktop workstations, or in a HPC environment. Parallel efficiencies of *ca.* 90% are attainable in the strong scaling regime up to 64 CPU cores. As the accessibility and power of computational resources increases over the next decade, and as the influence of advanced approaches such as GPU acceleration[232] and machine learning[233] is felt in computational chemistry, it is in the HPC environment that *py*naMICs will need increasingly to be used to handle larger molecules, larger TSHD ensembles, and longer TSHD trajectories. *py*naMICs was designed with an acute awareness of this, and improves on TDSIMMIC[74] for these problems. Further development of *py*naMICs is discussed in Chapter 8.

To demonstrate how one might use *py*naMICs, TSHD simulations (Section 5.3.3) recorded at the SA(5/4)-CASSCF(12,8) level have been used to model the photolysis of 1,2-DITFE in support of contemporary TRGED experiments at the SLAC National Accelerator Laboratory. Statistical analysis has revealed that secondary dissociation of $I^{\bullet}$ from the primary photolysis product, $ITFE^{\bullet}$, is considerably more likely from *ap*-$ITFE^{\bullet}$ than from *sc*-$ITFE^{\bullet}$ – a result that has considerable bearing on the dynamics (Section 5.3.4).

Complementary *ab initio* calculations (Section 5.3.2) at the SA(5/4)-CASSCF(12,8) level have revealed that the transient "*bridged*" intermediate, λ^2-$ITFE^{\bullet}$, postulated by Zewail and Ihee lies on, or close to, the crossing seam between the D_1 and D_0 states – a result that has not been appreciated in earlier theoretical studies.[55,56,222] The transient formation of λ^2-$ITFE^{\bullet}$ should not be ruled out on the basis of these results presented in this Chapter. Indeed, disclosures from contemporary TRGED experiments at the SLAC National Accelerator Laboratory[17] support the transient formation of λ^2-$ITFE^{\bullet}$, but even these experiments have insufficient temporal resolution to detect λ^2-$ITFE^{\bullet}$ unambiguously.[17] The work detailed in this Chapter was instrumental in identifying the signature of λ^2-$ITFE^{\bullet}$.[17]

6 Photofission of the Disulfide Bond in 1,2-Dithiane

The disulfide bond is ubiquitous in the natural world. Covalent disulfide bonds between cysteine residues fold the polypeptide skeletons of proteins into their native state – only in these configurations are proteins operational and able to realise their biological function.[234]

In highly-specialised proteins, disulfide bonds can be the key to survival under extreme conditions.[235] Archaea that thrive in hot springs and deep-sea hydrothermal vents – considered to be among the most unforgiving environments found on Earth – share a common set of protein adaptations. An increased number of disulfide bonds is one such adaptation. This adaptation provides protection against thermal denaturing and allows for the retention of biological function at high temperature.[236–239]

It has been speculatively suggested that disulfide bonds are also able to provide photostability to proteins by acting as a sink for harmful UV fluorescence originating from tryptophan residues.[240–242] Strategically-placed disulfide bonds have been found close to tryptophan residues in well-conserved sequences.[243] Photostability was one of the greatest evolutionary selection pressures to influence molecular structure on the early Earth[244,245] due to the heightened UV activity of the young sun[246] and absence of an ozone layer.[247]

That disulfide bonds are the molecular structures of choice in the natural world for these demanding and mission-critical applications should come as a surprise to any reader familiar with aliphatic, acyclic disulfides. The disulfide bonds in aliphatic, acyclic disulfides are neither stable to heat[248,249] nor to light in the mid-UV[250–252] (Fig. 6.1). Although it is typically stronger than the neighbouring sulfur-carbon bonds,[252] photofission of the disulfide bond takes place readily *via* a sub-picosecond photochemical channel on the S_1 potential energy surface in response to illumination by light in the mid-UV.[242,253] Thiyl radicals are evolved with a quantum yield approaching unity.

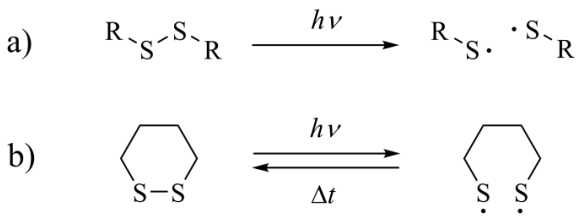

Figure 6.1. Photofission of the disulfide bond in a) a generic aliphatic acyclic disulfide, and b) the aliphatic cyclic disulfide 1,2-dithiane. Adapted from Ref. 254.

In contrast, aliphatic cyclic disulfides appear comparatively photostable with respect to light in the mid-UV[242,255–257] (Fig. 6.1), leading some researchers to conclude that the photostability of the disulfide bond is linked to structure. Understanding the mechanism of the photofission of disulfide bonds underpins a number of real-world challenges, from the design of disulfide-based self-healing materials[258] to determining the final destination of disulfides and thiyl radicals in atmospheric and oceanic sulfur cycles.[259]

6.1 1,2-Dithiane

1,2-dithiane, illustrated in Fig. 6.2, is a simple aliphatic cyclic disulfide. The contemporary picture of the photofission of the disulfide bond in 1,2-dithiane comes from the elegant time-resolved mass spectrometry (TRMS) experiments and theoretical work of Sølling *et al.*,[255,256] published in 2012. This work has been collated with comparative studies on aliphatic acyclic disulfides,[242] and featured in a mini-review article[257] published in 2014. The contemporary picture was contested by the publication of Ref. 254 in 2016, in which a classically-intuitive reinterpretation of the experimental data acquired by Sølling *et al.*[255,256] was put forward ahead of TRGED experiments by Wann *et al*. The TRGED experiments took place at the SLAC National Accelerator Laboratory in 2017.[74]

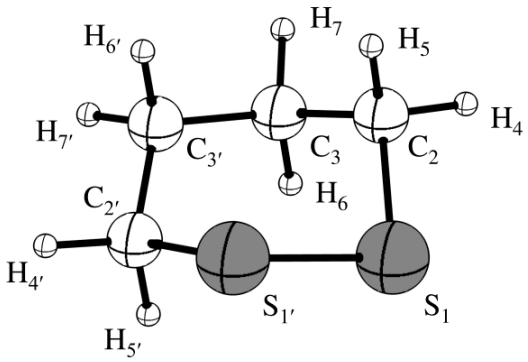

Figure 6.2. Ground-state structure of 1,2-dithiane. The atomic labelling scheme is outlined and used hereafter.

Familiarity with the contemporary picture of Sølling *et al.*[255,256] is a prerequisite, and so it is briefly reviewed here. Homolytic photofission of the disulfide bond in 1,2-dithiane occurs *via* a sub-picosecond, electronically-excited-state channel on the S_1 potential energy surface, generating the transient $^{\bullet}S–(CH_2)_4–S^{\bullet}$ thiyl biradical. The S_1 and S_0 potential energy surfaces couple together along the sulfur-sulfur stretching coordinate – activated on photoexcitation – *via* a MECI; the nuclear wavepacket is funnelled towards this

MECI.[256,260] The mechanism of Sølling *et al.*[256,260] and the mechanism of Ref. 254 diverge here. The dynamics inferred by Sølling *et al.*[256,260] are highly non-ergodic; the nuclear wavepacket becomes localised on the S_1 potential energy surface, and a low-frequency vibrational mode (80.2 cm^{-1})[256,260] shuttles the wavepacket to and from the MECI. $S_0 \leftarrow S_1$ IC outcompetes intramolecular vibrational relaxation (IVR), and the thiyl termini recouple on the S_0 potential energy surface more quickly than the nuclear wavepacket delocalises. The excess energy is thermalised to the environment after IC.[256,257,260] Sølling *et al.*[256,260] captured consistent dynamics in action *via* TRMS. An oscillating ion-current signal was acquired after photoexcitation – a clear marker of molecular motion.

This Chapter comprises a significant extension of the preliminary work published in Ref. 254, including a full structural solution for 1,2-dithiane in the gas phase (Section 6.2), deeper analysis of the TSHD simulations detailed in Ref. 254 (Section 6.3), and simulations of TRGED (Section 6.4), presented to the Scientific Panel at the SLAC National Accelerator Laboratory as proof-of-concept work.

6.2 Structure of 1,2-Dithiane

The following sections detail the synthesis and structural characterisation of 1,2-dithiane *via* GED and XRD, carried out at the University of York in advance of TRGED experiments at the SLAC National Accelerator Laboratory.

6.2.1 Synthesis and Characterisation of 1,2-Dithiane

6.2.1.1 Synthesis

1,2-Dithiane was synthesised in accordance with the procedure outlined by Singh and Whitesides[261] *via* hydrogen-halide-catalysed (HCl, 37 wt% aqueous; 0.7 mL, 8.6 mmol) oxidation[262] of 1,4-butanedithiol (1.0 mL, 21.5 mmol) by dimethylsulfoxide (17.0 mL). The synthetic scheme is outlined in Fig. 6.3.

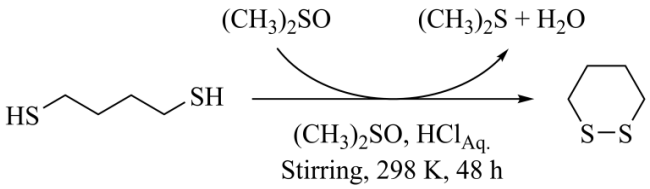

Figure 6.3. Synthetic scheme for the hydrogen-halide-catalysed oxidation[262] of 1,4-butanedithiol to 1,2-dithiane by dimethylsulfoxide.

6.2.1.2 Characterisation

1,2-dithiane was characterised at the University of York *via* ^{1}H NMR [δ 2.83 (s, 4H), δ 1.95 (s, 4H); lit. δ 2.85 (s, 4H), δ 1.97 (s, 4H)], ^{13}C NMR [δ 27.88, δ 33.44], and XRD.

^{1}H and ^{13}C NMR spectra were acquired in deuterated chloroform ($CDCl_3$) using a 500 MHz Bruker AVIIIHD500 NMR spectrometer by the University of York NMR Service. ^{1}H and ^{13}C NMR spectra are reproduced, with peak assignments, in Figs. A1 and A2, respectively. XRD data were acquired using an Oxford Diffraction SuperNova diffractometer by the University of York Crystallographic Service. Acquisition conditions are summarised in Table A71. Cartesian coordinates for the refined XRD structure of 1,2-dithiane are tabulated in Table A72.

The details of the crystallographic unit cell for 1,2-dithiane are summarised in Table 6.1. Projections of the crystallographic unit cell along the *a*, *b*, and *c* axes are illustrated in Fig. 6.4.

Table 6.1. Details of the crystallographic unit cell for 1,2-dithiane, comprising the unit cell descriptor, space group, and dimensions.[a]

Unit Cell Descriptor	Space Group	*a*	*b*	*c*
Orthorhombic[b]	*Pnm*2	531.77(3)	777.66(4)	675.47(4)

[a] All dimensions are tabulated in picometers. [b] $\alpha = \beta = \gamma = 90°$.

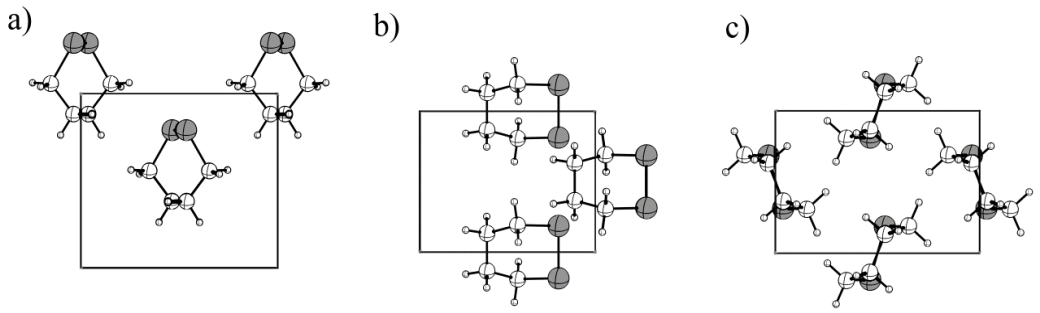

Figure 6.4. Projections along the a) *a*, b) *b*, and c) *c* axes of the crystallographic unit cell for 1,2-dithiane.

6.2.2 Data Acquisition

GED data were acquired using the University of York gas electron diffractometer.[43] An accelerating potential of 42.22 kV was applied to produce a continuous electron beam with an electron emission current of 0.66 μA and electron wavelength of *ca.* 5.85 pm. GED data

were acquired *via* the exposure of reusable image plates (Fuji BAS-IP MS 2025) at nozzle-to-image-plate distances of 244.0 and 489.0 mm and subsequently digitised using a tabletop image plate scanner (Fuji BAS-1800II) as outlined in Section 4.1.5. Four exposures were recorded at each nozzle-to-image-plate distance. 1,2-dithiane was delivered to the point of diffraction *via* the air-heated effusive nozzle assembly outlined in Section 4.1.4. The sample of 1,2-dithiane was not heated so as to preclude thermal polymerisation; the nozzle tip was maintained at 298 K during exposures at both nozzle-to-image-plate distances. These experimental conditions are summarised in Table A73.

6.2.3 Density Functional Theory Calculations

All DFT calculations were carried out using the GAUSSIAN09[184] software suite on the University of York Advanced Research Computing Cluster (YARCC). Geometry optimisations of the chair conformation of 1,2-dithiane were carried out in the C_2 symmetry point group, and used the B3LYP,[187,188] B3P86,[187,189] B3PW91,[187,190] B2PLYP,[185] PBEH1PBE,[191] and HSEH1PBE[192–195] density functionals coupled with a range of basis sets (cc-pV*n*X, $n \in \{D, T, Q\}$)[186] of increasing completeness. Geometry optimisations of the half-chair, twist-boat, and boat conformations of 1,2-dithiane were carried out in the C_1, C_2, and C_s symmetry point groups, respectively, and used the B3LYP density functional coupled with the same range of basis sets. The density functionals were selected to balance effectively computational cost against accuracy, with a bias towards the former. One should not expect a simple organic molecule like 1,2-dithiane to present any particular challenges that might require a more exotic density functional; the best-in-class B2PLYP functional was used here to confirm that this was the case. Consequently, this set was chosen to represent across a spectrum of the most popular low-cost density functionals. All bonded internuclear distances were extrapolated to the CBS limit *via* the fitting of the bonded internuclear distances determined using the cc-pVDZ, cc-pVTZ, and cc-pVQZ basis sets with a function of the form introduced in Section 4.2. The proper convergence of all geometry optimisations to minima or transition states on the ground-state potential energy surface was verified *via* vibrational frequency analysis. Cartesian coordinates of all optimised geometries are tabulated in Tables A74–91.

Theoretical r_{h1}-type amplitudes of vibration (u_{h1}) and curvilinear shrinkage corrections (k_{h1}) were generated from vibrational frequencies computed at the B3LYP/cc-pVDZ level using the SHRINK[108,109] software package.

6.2.4 Data Reduction and Refinement

The in-house data extraction package XSTRACT[74] was used to reduce digitised diffraction patterns to MICs *via* azimuthal averaging. MICs were refined using the ED@ED v3.0[94] least-squares refinement package coupled with the scattering factors of Ross *et al.*[196]

6.2.4.1 Refinement Protocol

The least-squares refinement procedure employed a parameterised molecular model, programmed in FORTRAN90, describing 1,2-dithiane within the constraints of the C_2 symmetry point group in terms of twelve refinable parameters comprising four distances (p_1 – p_4), six angles (p_5 – p_{10}), and two dihedral angles (p_{11} and p_{12}). The contributions to parameters $p_1 – p_{12}$ are tabulated in Table 6.2.

Table 6.2. Summary of contributions to parameters $p_1 – p_{12}$.

Parameter		Contributions
p_1	rSS	$r_{1,1'}$
p_2	rSC	$r_{1,2}$
p_3	rCC	$r_{2,3}$
p_4	rCH	$^1/_4\, r_{2,4} + {}^1/_4\, r_{2,5} + {}^1/_4\, r_{3,6} + {}^1/_4\, r_{3,7}$
p_5	aSSC	$a_{1',1,2}$
p_6	aSCH$_{Eq.}$	$a_{1,2,4}$
p_7	aSCH$_{Ax.}$	$a_{1,2,5}$
p_8	aSCC	$a_{1,2,3}$
p_9	aCCH$_{Eq.}$	$a_{2,3,7}$
p_{10}	aCCH$_{Ax.}$	$a_{2,3,6}$
p_{11}	ϕCSSC	$\phi_{2',1',1,2}$
p_{12}	ϕSSCC	$\phi_{1',1,2,3}$

The least-squares refinement procedure followed the SARACEN[99–101] protocol and gave internuclear distances of the r_{h1} type. All amplitudes of vibration associated with a given peak in the RDC were coupled by a fixed ratio to the amplitude of vibration associated with the nuclei giving rise to the largest scattering effect under that peak; only this amplitude of vibration was refined.

6.2.4.2 Refinement Results

The experimentally-acquired and experimental-minus-theoretical "*difference*" MICs are reproduced in Fig. 6.5; the RDCs are reproduced in Fig. 6.6.

The R_G and R_D for the least-squares refinement procedure were 0.082 and 0.051, respectively.

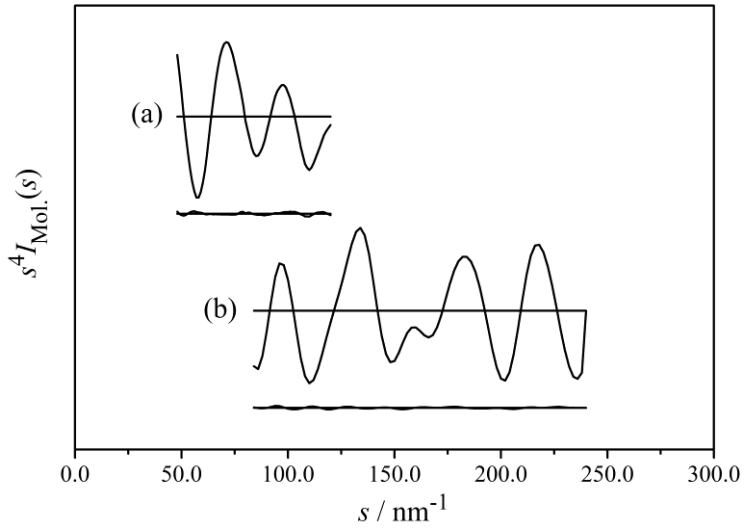

Figure 6.5. MICs and experimental-minus-theoretical "*difference*" MICs obtained after refinement of GED data acquired for 1,2-dithiane at a) long and b) short nozzle-to-image-plate distances.

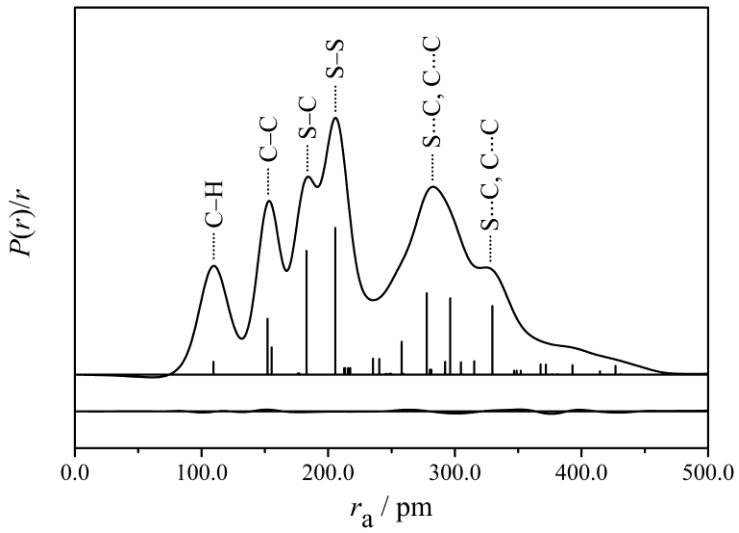

Figure 6.6. RDC and experimental-minus-theoretical "*difference*" RDC obtained after refinement of GED data acquired for 1,2-dithiane.

The weighting points for off-diagonal weight matrices, scaling factors, and least-squares correlation parameters are found in Table A92; the least-squares correlation matrix is found in Table A93. The refined (r_{h1}-type) and theoretical (r_e-type; B3LYP/CBS) parameters p_1 – p_{12} are tabulated in Table A94. All internuclear distances, refined and theoretical amplitudes of vibration, r_{h1}-type shrinkage corrections, and SARACEN[99–101] restraints (where applied) are tabulated in Table A95. Cartesian coordinates for the refined r_{h1}-type structure of 1,2-dithiane are tabulated in Table A96.

In Fig. 6.7; experimentally-determined internuclear distances and angles, alongside their theoretical counterparts computed at the B3LYP/CBS level, are overlaid onto schematic illustrations of 1,2-dithiane.

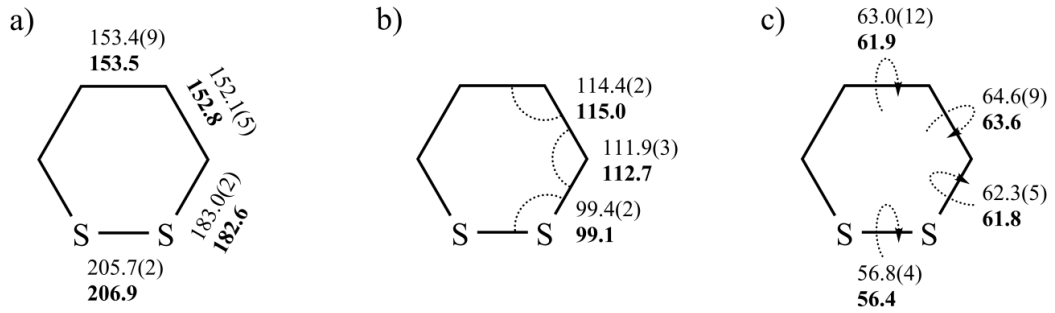

Figure 6.7. Experimental r_{h1}-type (regular typeface) and B3LYP/CBS (bold typeface) geometric parameters determined for 1,2-dithiane. All a) internuclear distances are reported in picometers. All b) angles and c) dihedrals are reported in degrees.

6.2.5 Discussion

Refined experimental internuclear distances and angles are tabulated in Table 6.3 alongside their theoretical counterparts computed at the B3LYP/CBS level and structural data acquired for a single crystal of 1,2-dithiane *via* XRD (Section 6.2.1.2).

All internuclear distances and angles between 2nd-row nuclei are well-determined to 0.8(5) pm and 0.7(6)° of their theoretical counterparts in the GED solution. The XRD and GED solutions are in good agreement with each other – to 0.8(6) pm and 0.7(7)° for internuclear distances and angles, respectively – with the expected systematic deviation towards shorter internuclear distances in the XRD solution being apparent (Section 4.2.5); all internuclear distances between 2nd-row nuclei are shorter by a factor of 0.996(2). Structural parameters computed at the B3LYP/CBS level are in equally good agreement – to 1.0(7) pm and 0.6(4)° for internuclear distances and angles, respectively – with the XRD solution.

The agreement indicates that the ground-state structure of 1,2-dithiane can be computed cheaply and effectively. Experimental GED data are encouragingly straightforward to refine as the three bond types in 1,2-dithiane – S–S ($r_{1,1'}$), S–C ($r_{1,2}$), and C–C ($r_{2,3}$ and $r_{3,3'}$) – are well-separated in the RDC (Fig. 6.6).

Table 6.3. Summary of refined (r_{h1}-type) GED, theoretical (r_e-type; B3LYP/CBS), and XRD (recorded at 110 K) measurements of internuclear distances[a] and angles[b] in 1,2-dithiane.

Coordinate	GED (r_{h1})	r_e	XRD
$r_{1,1'}$	205.7(2)	206.9	205.3(1)
$r_{1,2}$	183.0(2)	182.6	181.9(4)
$r_{2,3}$	152.1(5)	152.8	151.1(6)
$r_{3,3'}$	153.4(9)	153.5	153.1(8)
$r_{2,4}$	109.4(3)	109.1	97.0[c]
$r_{2,5}$	109.4(3)	109.0	97.0[c]
$r_{3,6}$	109.4(3)	109.2	97.0[c]
$r_{3,7}$	109.4(3)	109.3	97.0[c]
$a_{1',1,2}$	99.4(2)	99.1	98.8(1)
$a_{1,2,3}$	111.9(3)	112.7	112.2(3)
$a_{1,2,4}$	104.9(2)	104.8	109.2[c]
$a_{1,2,5}$	108.4(1)	108.4	109.2[c]
$a_{2,3,3'}$	114.4(2)	115.0	114.6(3)
$a_{2,3,6}$	108.8(1)	108.8	108.6[c]
$a_{2,3,7}$	108.2(1)	108.2	108.6[c]
$\phi_{2',1',1,2}$	56.8(4)	56.4	57.4[c]
$\phi_{1',1,2,3}$	62.3(5)	61.8	62.9(3)
$\phi_{1',1,2,4}$	176.0(1)	177.8	176.0[c]
$\phi_{1',1,2,5}$	59.9(1)	62.4	58.3[c]
$\phi_{1,2,3,3'}$	64.6(9)	63.6	64.5(4)
$\phi_{1,2,3,6}$	57.9(1)	59.6	57.2[c]
$\phi_{1,2,3,7}$	174.0(1)	175.1	173.9[c]
$\phi_{2,3,3',2'}$	63.0(12)	61.9	62.0[c]

[a] All internuclear distances ($r_{i,j}$) are tabulated in picometers. [b] All angles ($a_{i,j,k}$) and dihedral angles ($\phi_{i,j,k,l}$) are tabulated in degrees. [c] Uncertainties unavailable; measured directly from *.cif* data.

The ground-state conformational landscape of 1,2-dithiane, presented in Fig. 6.8, is qualitatively the same as that of cyclohexane, in so far as there exist two minimum-energy

conformations – the chair and twist-boat (+19.6 kJ mol^{-1}; B3LYP/CBS) – connected by transition states – the half-chair (or envelope) (+49.9 kJ mol^{-1}; B3LYP/CBS) and the boat (+44.0 kJ mol^{-1}; B3LYP/CBS) – along an interconversion coordinate. Only the chair conformation was accounted for in the least-squares refinement as the steady-state population of the twist-boat was estimated to be less than *ca.* 0.1% at 298 K. Interconversion between the chair and twist-boat conformations has small rate constant, *k*, at 298 K, corresponding to a slow turnover of *ca.* 50,000 molecules s^{-1} (B3LYP/CBS).

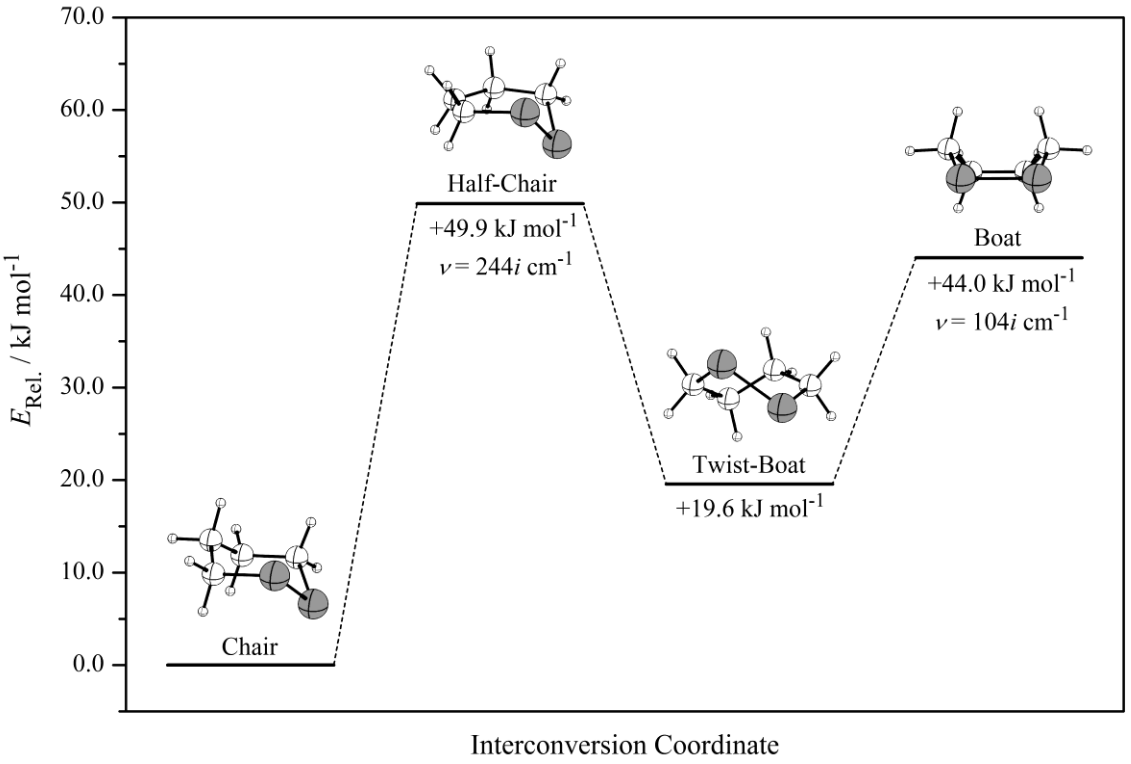

Figure 6.8. Illustration of the chair-to-boat interconversion pathway of 1,2-dithiane. Relative energies, $E_{Rel.}$, are given in units of kJ mol^{-1} with respect to energy of the chair conformation. Frequencies, ν, for the imaginary modes of transition states are given in units of i cm^{-1}. All values are reported as computed at the B3LYP/CBS level.

Following the successful synthesis of 1,2-dithiane, empirical determination of suitable experimental conditions for GED, and refinement of the gas-phase equilibrium structure, it is necessary to consider the nature of, and behaviour of 1,2-dithiane in, the relevant electronically-excited states. Both are explored in-depth in Section 6.3.

6.3 Electronically-Excited States of 1,2-Dithiane

6.3.1 *Ab Initio* Calculations

All *ab initio* calculations detailed in this section were carried out on the University of York Advanced Research Computing Cluster; CASSCF and MR-CISD calculations were carried out using COLUMBUS v7.0[263–265] and MS-CASPT2 calculations were carried out using OPENMOLCAS v8.3.[224]

The CASSCF active space (Fig. 6.9) comprised ten electrons distributed in eight orbitals – four of A symmetry and four of B symmetry. The $\sigma_{S–S}$ (A) and $\sigma^*_{S–S}$ (B) orbitals, two n_S (A, B) orbitals, and two pairs of $\sigma_{S–C}$ (A, B) and $\sigma^*_{S–C}$ (A, B) orbitals were used to construct the active space. State-averaging was carried out over the three lowest-energy singlet states – two of A symmetry and one of B symmetry – with equal weighting of all states. These calculations are denoted SA3-CASSCF(10,8). Tight convergence criteria of $<1\times10^{-10}$ and $<1\times10^{-8}$ a.u. were used for the energy and gradient, respectively.

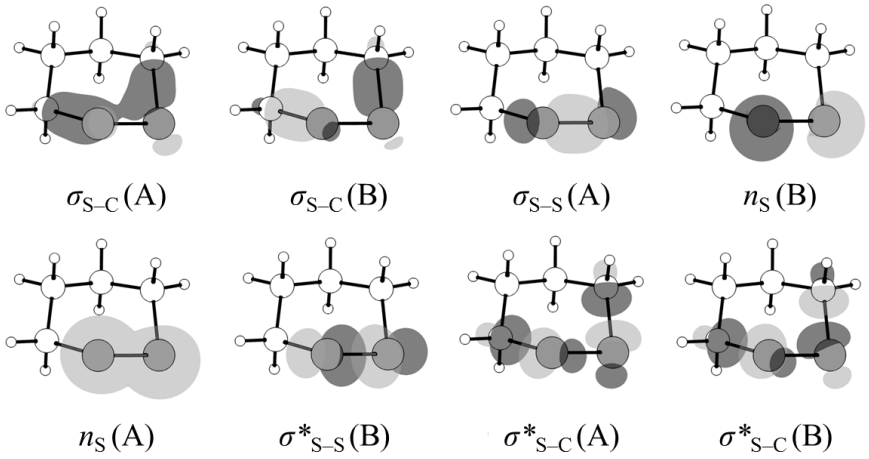

Figure 6.9. SA3-CASSCF(10,8) active space constructed for 1,2-dithiane, comprising the $\sigma_{S–S}$ (A) and $\sigma^*_{S–S}$ (B) orbitals, two n_S (A, B) orbitals, and two pairs of $\sigma_{S–C}$ (A, B) and $\sigma^*_{S–C}$ (A, B) orbitals.

MR-CISD calculations used a truncated reference space comprising six electrons distributed in four orbitals – two of A symmetry and two of B symmetry – equivalent to the active space of Fig. 6.9, but with both pairs of $\sigma_{S–C}$ (A, B) and $\sigma^*_{S–C}$ (A, B) orbitals (the two lowest- and two highest-energy orbitals, respectively) discarded. The six lowest-energy core orbitals were frozen in the MR-CISD treatment. These calculations comprised 17,761,053 configurations, with 10 contained in the reference space. The Meissner correction[266] was

used to correct the MR-CISD calculations for size-extensivity. These calculations are denoted MR-CISD(6,4).

MS-CASPT2 calculations used the reference space of Fig. 6.9. The six lowest-energy core orbitals were frozen in the MS-CASPT2 treatment. The three lowest-energy singlet states – two of A symmetry and one of B symmetry –were included in the multistate treatment. These calculations are denoted MS-CASPT2(10,8).

The *def*2-SV(P)[207] basis set was used throughout.

The proper convergence of all geometry optimisations to minima was verified *via* vibrational frequency inspection.

6.3.2 Potential Energy Surface Geography

The C_2-symmetric S_0 minimum (equivalent to the deckchair conformation characterised *via* GED in Section 6.2) and a C_2-symmetric S_1 van der Waals minimum have been located at the SA3-CASSCF(10,8), MR-CISD(6,4) and MS-CASPT2(10,8) levels. Cartesian coordinates are tabulated in Tables B8–13. Vertical transition energies and oscillator strengths are tabulated in Table 6.4 for transitions to the S_1 and S_2 states that originate from the S_0 minimum. The excellent agreement between the results in Table 6.4 is noteworthy; the absence of dynamical correlation in the cost-effective SA3-CASSCF(10,8) treatment is no obstacle to computing accurately the transition energies and oscillator strengths at equilibrium, or to obtaining the correct ordering of states. Where specific values are quoted in this section, therefore, these have been computed at the SA3-CASSCF(10,8) level, and the reader may be satisfied with their accuracy.

Table 6.4. Summary of vertical transition energies, ΔE,[a] and oscillator strengths, f, for 1,2-dithiane as computed at the SA3-CASSCF(10,8), MR-CISD(6,4) and MS-CASPT2(10,8) levels.

	SA3-CASSCF(10,8)		MR-CISD(6,4)		MS-CASPT2(10,8)	
Transition	ΔE	f	ΔE	f	ΔE	f
$S_1 \leftarrow S_0$	4.47	<0.01	4.44	<0.01	4.52	<0.01
$S_2 \leftarrow S_0$	5.47	<0.01	5.43	<0.01	5.51	<0.01

[a] All transition energies are tabulated in eV.

The S_1 and S_2 states are accessed from the S_0 minimum *via* $\sigma^*_{S–S} \leftarrow n_S$ excitation and are, accordingly, strongly dissociative along the sulfur-sulfur stretching coordinate. Single-

photon absorption at 277 nm should make accessible the S_1 state; practicably, however, the S_1 state is likely to be accessed using readily-available 266 nm light. The S_1 van der Waals minimum ($r_{1,1'}$ = 355.6 pm) is located 2.49 eV below the Franck-Condon point ($r_{1,1'}$ = 214.4 pm) in a shallow potential well at a distance of 577.7 pm $Da^{-½}$. The S_1 Van der Waals minimum is loosely bound and near-degenerate with the lowest-energy, C_{2h}-symmetric conformation of the open-chain disulfide biradical, being only *ca.* 0.1 eV less stable. The S_0, S_1, and S_2 states couple together along the sulfur-sulfur stretching coordinate; at the S_1 van der Waals minimum, the separation of the S_0, S_1, and S_2 states is reduced to <0.2 eV.

A near-C_2-symmetric S_1/S_0 MECI, denoted $MECI_{Sølling}$ in recognition of the earliest reports by Sølling *et al.*,[256,260] exists in the vicinity of the S_1 van der Waals minimum, at a distance of only 161.9 pm $Da^{-½}$. $MECI_{Sølling}$ has been located at the SA3-CASSCF(10,8) level. Cartesian coordinates are tabulated in Table B14.

S_0, S_1, and S_2 potential energy surfaces between the S_0 minimum/Franck-Condon point and $MECI_{Sølling}$ have been constructed *via* linear interpolation in internal coordinates (LIIC), and are presented in Fig. 6.10. Independent single-point-energy evaluations have been carried out on 9 interpolated geometries at the SA3-CASSCF(10,8) and MR-CISD(6,4) levels.

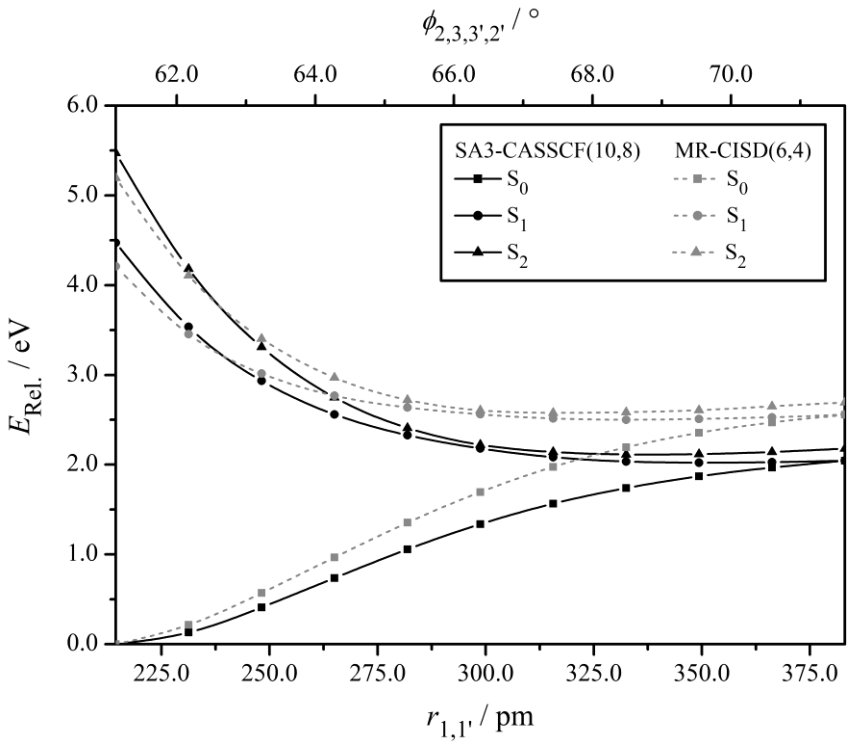

Figure 6.10. S_0, S_1, and S_2 potential energy surfaces between the S_0 minimum and $MECI_{Sølling}$, mapped *via* LIIC and computed at the SA3-CASSCF(10,8) and MR-CISD(6,4) levels. MR-CISD(6,4) calculations are carried out at SA3-CASSCF(10,8) geometries.

Cursory examination of the potential energy surface geography does not support the kind of dynamics inferred by Sølling *et al.*[256,260] The potential energy surface is flat around the S_1 van der Waals minimum and $MECI_{Sølling}$; this part of the potential energy surface is accessed *via* steep descent from the Franck-Condon point and, consequently, localisation of the nuclear wavepacket nearby is unlikely. The loosely-bound S_1 van der Waals minimum cannot be expected to trap the highly-energetic nuclear wavepacket effectively. The same can be concluded with respect to the funneling capacity of $MECI_{Sølling}$, which – on examination of the topology of the feature, presented in Fig. 6.11 – is found to be a glancing, steeply-sloped intersection. Such intersections are not generally able to trap highly-energetic nuclear wavepackets for long enough to efficiently funnel population between electronically-excited states; it would be surprising if it were the case that non-ergodic $S_0 \leftarrow S_1$ internal conversion *via* $MECI_{Sølling}$ was able to out-compete IVR.

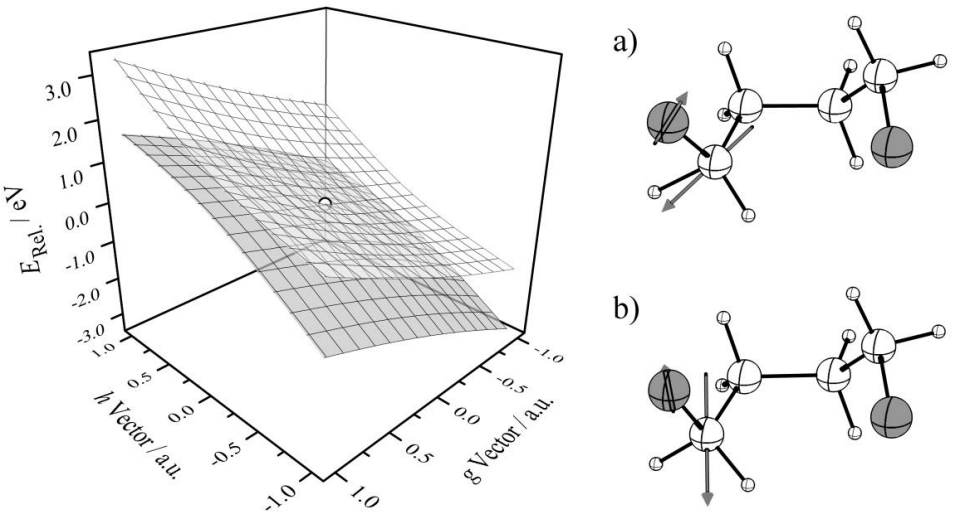

Figure 6.11. Topology of $MECI_{Sølling}$ in the branching space of the a) ***g*** and b) ***h*** vectors. The scatter point represents $MECI_{Sølling}$. The darker and lighter wireframes represent the S_0 and S_1 potential energy surfaces, respectively.

If it is not highly-non-ergodic dynamics – the kind proposed by Sølling *et al.*[256,260] in which the nuclear wavepacket localises around the S_1 van der Waals minimum and $MECI_{Sølling}$ – that promotes recoupling of the thiyl termini by enforced proximity, then a) an

alternative mechanism must be proposed, and b) the mechanism may not be one that can be inferred from a limited, two-dimensional slice of the potential energy surface (Fig. 6.10).

TSHD are requisite to this end. The performance of the cost-effective SA3-CASSCF(10,8) calculations, evaluated by comparison with the MR-CISD(6,4) calculations, is excellent at the Franck-Condon point (Table 6.4) and beyond in the part of the potential energy surface of immediate interest (Figure 6.10). MS-CASPT2(10,8) calculations confirm this assertion for the former case (and, in preliminary work,[254] for the latter case too). The reader may therefore be satisfied with the suitability of the SA3-CASSCF(10,8) treatment for use with TSHD.

The necessary calculations are not simply facilitated by the simpler SA3-CASSCF(10,8) treatment, but made computationally tractable.

6.3.3 Trajectory Surface-Hopping Dynamics

TSHD simulations were recorded at the SA3-CASSCF(10,8) level (set up as described in Section 6.3.1) using NEWTON-X v2.0[267,268] interfaced with COLUMBUS v7.0.[263–265] All analytical gradients[269–271] and non-adiabatic coupling vectors[272,273] were computed on-the-fly by routines integrated into COLUMBUS v7.0;[263–265] non-adiabatic transition probabilities were accounted for using the augmented fewest-switches algorithm of Hammes-Schiffer and Tully,[140,141] as implemented in NEWTON-X.[267,268]

Each member of a Wigner-distributed ensemble containing 100 independent S_0-state starting geometries was transformed into the S_1 state.[274] The S_1 excitation band, having a width of *ca.* 2.0 eV, is indicated by a shaded overlay on top of a UV absorption spectra computed at the SA5-CASSCF(10,8) level (Fig. 6.12a). Two additional electronically-excited states – $\sigma^*_{S–C} \leftarrow n_S$ excitations of B and A symmetry – have been added to the SA3-CASSCF(10,8) treatment to reproduce the characteristic double-peaked feature around *ca.* 6.2 eV (200 nm) that is observed experimentally[74] in the gas phase (Fig 6.12b).

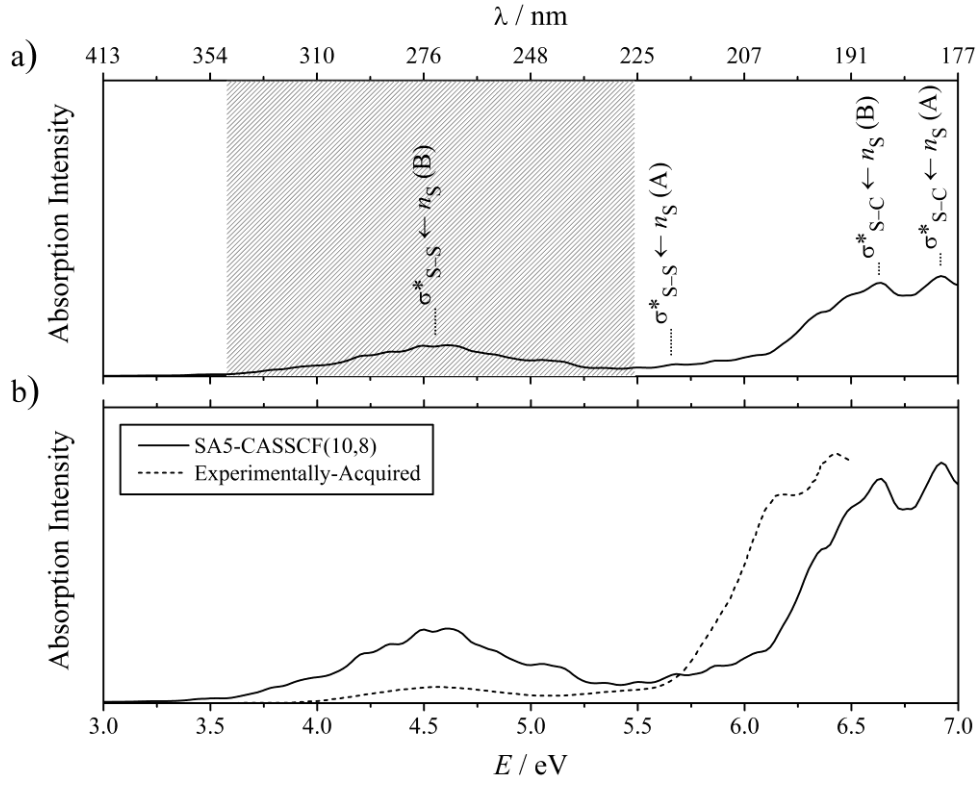

Figure 6.12. UV absorption spectra of 1,2-dithiane a) as computed at the SA5-CASSCF(10,8) level and b) as acquired experimentally[74] in the gas phase. The shaded overlay in a) corresponds to the S_1 excitation band for the Wigner-distributed ensemble.

The $\sigma^*_{S–S} \leftarrow n_S$ excitations of interest are computed in excellent agreement with experiment; the $\sigma^*_{S–C} \leftarrow n_S$ excitations are computed with sufficient qualitative accuracy for illustrative purposes, but are hypsochromatically shifted by *ca.* 1.0 eV.

100 independent S_1-state trajectories were obtained by propagating each geometry through time for 1 ps. The nuclei were propagated *via* integration of Newton's classical equations in time steps of 0.5 fs using the velocity-Verlet algorithm.[231] The time-dependent Schrödinger equation was integrated in time steps of 0.025 fs using the classical 4th-order Runge-Kutta algorithm. The decoherence parameter, α, was set to 0.1 a.u.

6.3.4 Discussion

6.3.4.1 "*Molecular Clackers*"

TSHD revealed a classically-intuitive "*Molecular Clackers*" mechanism[254] (Fig. 6.13), named as such since the mechanism evokes clackers,[275] a popular toy in the 1960s and

1970s. This terminology supersedes the earlier description of the mechanism as a "*Molecular Newton's Cradle*", used in preliminary published work.[254]

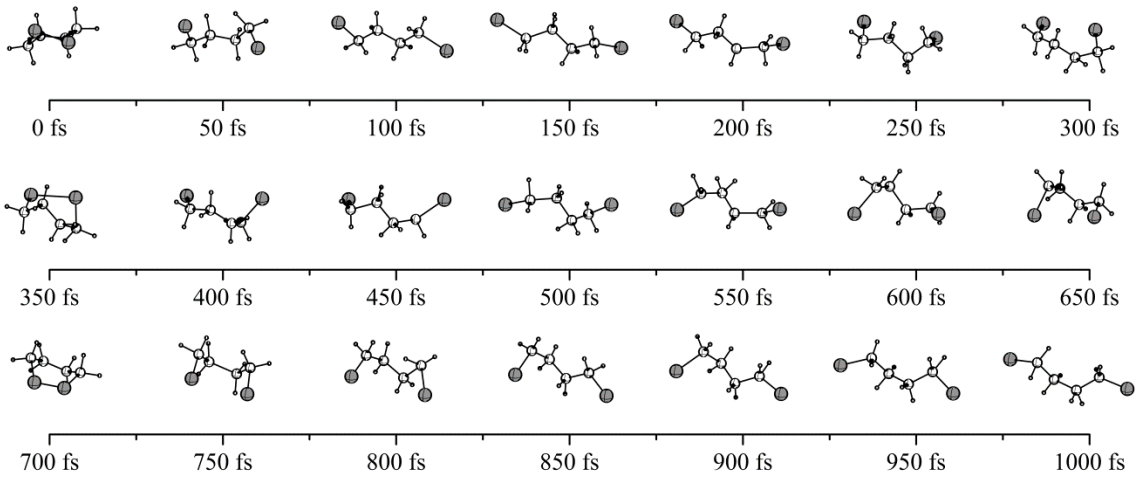

Figure 6.13. Series of time-stamped stop-motion frames from a single TSHD trajectory representative of the "*Molecular Clackers*" mechanism.

It is useful to visualise the "*Molecular Clackers*" mechanism[254] using a two-dimensional phase-space mapped in terms of the two principal degrees of freedom, $r_{1,1'}$, and $\phi_{2,3,3',2'}$ (Fig. 6.14). No evidence is found to support localisation of the nuclear wavepacket to the S_1 van der Waals minimum or $MECI_{Sølling}$.

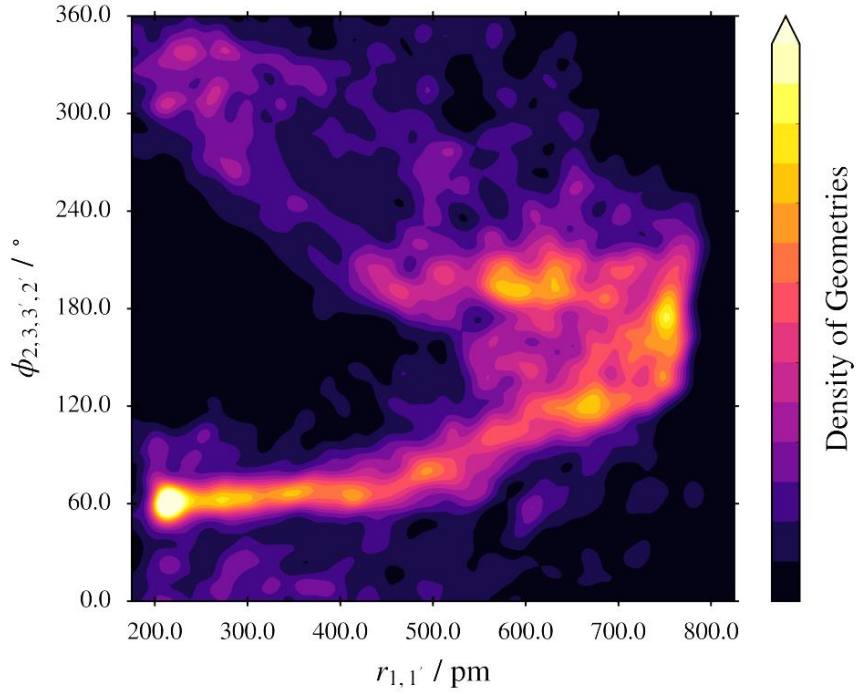

Figure 6.14. Two-dimensional heat-density map of geometric parameters; data are derived from 100 independent TSHD trajectories, each recorded for 1 ps in 0.5 fs time steps.

6.3.4.2 Sub-100-fs Dynamics

Photofission of the S–S ($r_{1,1'}$) bond begins immediately after $\sigma^*_{S-S} \leftarrow n_S$ excitation to the S_1 state. The trajectory swarm makes its closest approach to $MECI_{Sølling}$, coming to within 222.2 ± 44.1 pm $Da^{-½}$, in 42 ± 3 fs post-photoexcitation, then subsequently moves away (Fig 6.15a and 6.15b). This could be consistent with the first "*rocking*" cycle of the dynamics inferred by Sølling *et al.*,[256,260] but this is found not to be the case. After making its closest approach to $MECI_{Sølling}$, the trajectory swarm continues to move away from the Franck-Condon point/S_0 minimum, rather than reversing direction (Fig. 6.15c and 6.15d). At 100 fs, the trajectory swarm has travelled 1812.4 ± 107.2 and 1158.9 ± 112.2 pm $Da^{-½}$ from the Franck-Condon point and $MECI_{Sølling}$, respectively; it has clearly left the part of the potential energy surface around the S_1 van der Waals minimum and $MECI_{Sølling}$.

$S_0 \leftarrow S_1$ IC events begin to be recorded as early, on average, as 68 ± 25 fs; the onset of the events is more or less coincident with the closest approach to $MECI_{Sølling}$. $S_1 \leftrightarrow S_2$ IC events begin to be recorded even earlier – as early, on average, as 37 ± 14 fs – and their onset lies near the crossing of the S_1 and S_2 states ($r_{1,1'}$ = *ca.* 300.0 pm; Fig. 6.10). Beyond $MECI_{Sølling}$ lies a continuum where interstate coupling is high and bidirectional $S_0 \leftrightarrow S_1$ and $S_1 \leftrightarrow S_2$ IC events increase in frequency.[254]

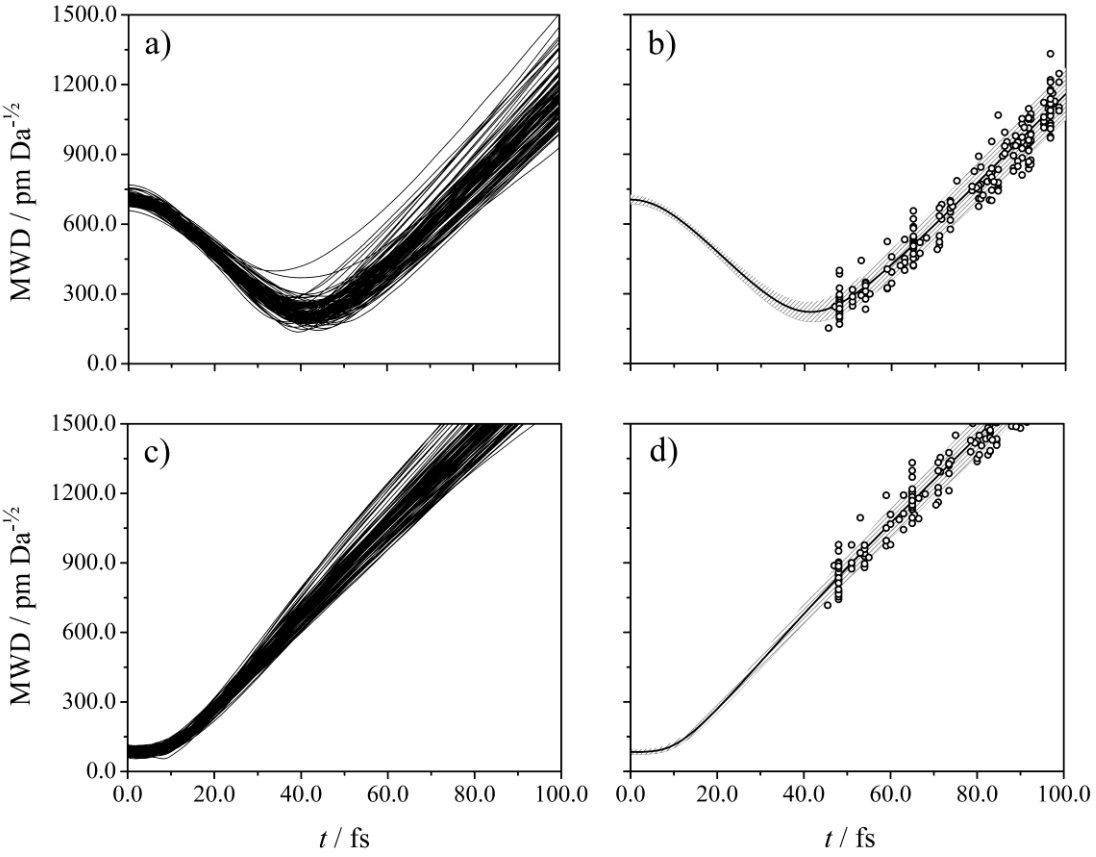

Figure 6.15. Sub-100-fs evolution of the mass-weighted distance from $MECI_{Sølling}$, in a) and b), and the Franck-Condon point/S_0 minimum, in c) and d), as a function of time, *t*. All 100 trajectories are plotted independently in a) and c); an average and standard deviation (indicated by the shaded overlay) are plotted in b) and d). Circular markers indicate where $S_0 \leftarrow S_1$ IC was recorded in b) and d).

6.3.4.3 Sub-ps Dynamics

The trajectory swarm continues to move away from the Franck-Condon point, reaching a peak distance of 2619.0 ± 125.9 pm Da$^{-½}$ in 152 ± 11 fs post-photoexcitation. It then reverses direction and returns to within 617.7 ± 176.1 pm Da$^{-½}$ of the S_0 minimum/Franck-Condon point by 338 ± 23 fs.

This process repeats, giving the evolution of the distance from the S_0 minimum/Franck-Condon point as a function of time (Fig. 6.16) an oscillatory profile. It becomes clear that the photostability of 1,2-dithiane arises not because the nuclear wavepacket is trapped by the S_1 van der Waals minimum or $MECI_{Sølling}$, but because this part of the potential energy surface is revisited periodically.[254] The signature of this process is apparent even when dimensionality is reduced down to the evolution of $r_{1,1'}$ as a function of time (Fig. 6.17).[254]

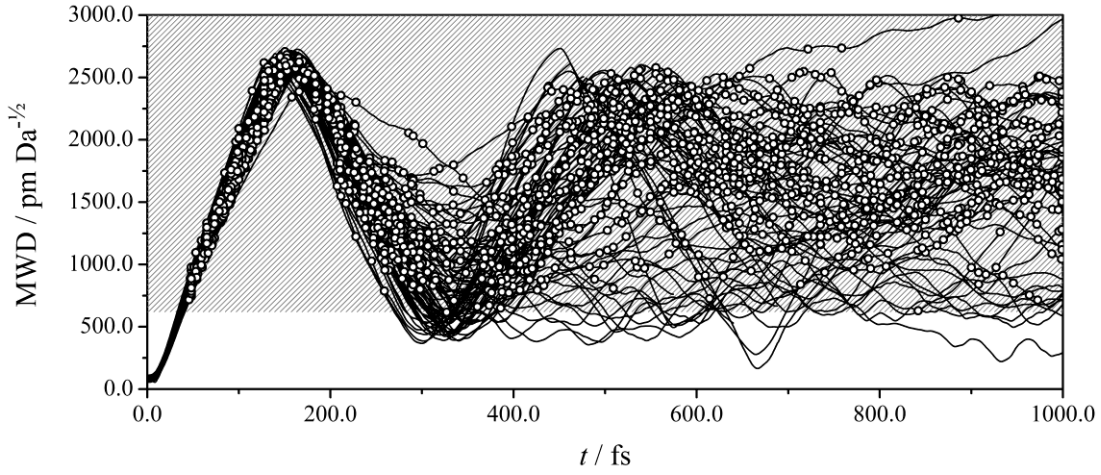

Figure 6.16. Sub-ps evolution of the mass-weighted distance from the Franck-Condon point/S_0 minimum as a function of time, *t*. All 100 trajectories are plotted independently. Circular markers indicate where $S_0 \leftarrow S_1$ IC was recorded. The shaded overlay covers a coupling region where the separation in energy of the S_0, S_1, and S_2 states is <0.2 eV.

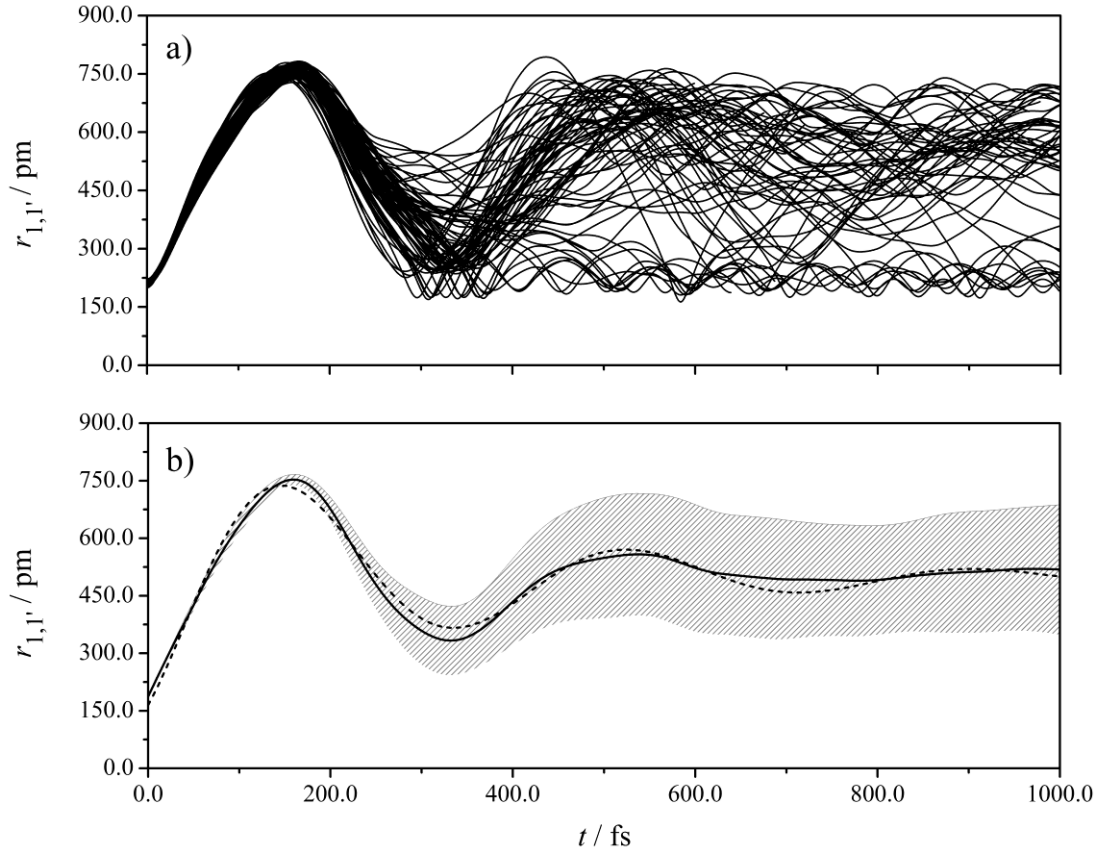

Figure 6.17. Sub-ps evolution of $r_{1,1'}$ as a function of time, *t*. All 100 trajectories are plotted independently in a); an average and standard deviation (indicated by the shaded overlay) are plotted in b). The dotted line is a damped sine function that has been fitted to the data.

Reduction in dimensionality is useful for three reasons. Firstly, and most obviously, it simplifies any discussion of the "*Molecular Clackers*" mechanism.[254] The mechanism can be intuitively understood as one that promotes periodic collisions of the thiyl termini, offering periodically-occurring recoupling opportunities. Evidence of permanent recoupling is observed for a small fraction of trajectories (*ca.* 10%) with each collision event (Fig. 6.17a). Secondly, it enables direct comparison with the experimental measurements of Sølling *et al*.,[256,260] which have been interpreted purely in the context of the sulfur-sulfur internuclear distance, $r_{1,1'}$. Thirdly, as GED measurements are more sensitive to $r_{1,1'}$ than to any other internuclear distance in 1,2-dithiane (Section 6.2.4.2), it is in this context, too, that any TRGED data are best interpreted in the first instance.[74]

In Section 6.3.4.4, the experimental measurements of Sølling *et al*.[256,260] are reviewed in the context of the "*Molecular Clackers*" mechanism.[254] In Section 6.3.4.5, IC and recoupling are discussed, and the photostability of 1,2-dithiane[242,256,257,260] is explained.

6.3.4.4 Experimental Evidence

A damped sine function was fitted to the evolution of the average value of $r_{1,1'}$ as a function of time (Fig. 6.17b) to determine parameters characterising the "*Molecular Clackers*" mechanism.[254] The time to the first peak in $r_{1,1'}$, t_{peak}, the period, t_{period}, decay constant, t_0, and projected lifetime, τ, of the transient disulfide biradical are tabulated in Table 6.5.

In all cases where data are available, these parameters are determined in outstanding agreement with the experimental measurements of Sølling *et al.*[256,260]

Table 6.5. Summary of parameters[a] describing the "*Molecular Clackers*" mechanism[254] as computed *via* TSHD and measured experimentally *via* TRMS.[256,260]

	TSHD	TRMS[257,260]
t_{peak}[b]	152 ± 11	177 ± 17
t_{period}[c]	378 ± 20	411 ± 27
t_0[c]	316 ± 3	–
τ[d]	2646 ± 140	2750 ± 230

[a] All parameters are tabulated in fs. [b] Determined from all 100 trajectories. [c] Determined from the fitting of a damped sine function to the average of all 100 trajectories. [d] Depletion of the population of the (open-chain) disulfide biradical down to 1/*e* of the initial population; projected approximately by assuming that the first collision event is representative of all subsequent collision events.[254]

Deriving the parameters from 100 TSHD trajectories is seen to have improved the agreement with experiment over the earlier derivation of the same parameters from only 50 TSHD trajectories in preliminary work.[254]

The "*Molecular Clackers*" mechanism[254] is moreover compatible with the form of the TRMS ion-current signal acquired by Sølling *et al.*,[256,260] and the origin of the decay components used to fit the data in their work can be accounted for under its framework.

The TRMS ion-current signal evolves out-of-phase with respect to the change in value of $r_{1,1'}$ (Fig. 6.18), which is the expected behaviour. Sølling *et al.* explain that "…*the* [disulfide biradical is] *easier to ionise when the sulfur atoms are close to each other, because… the positive charge on the one sulfur atom can be stabilised by the lone pair on the other… the result is a peak in the signal when the sulfur atoms are in proximity, and a valley when they are apart.*"[260]

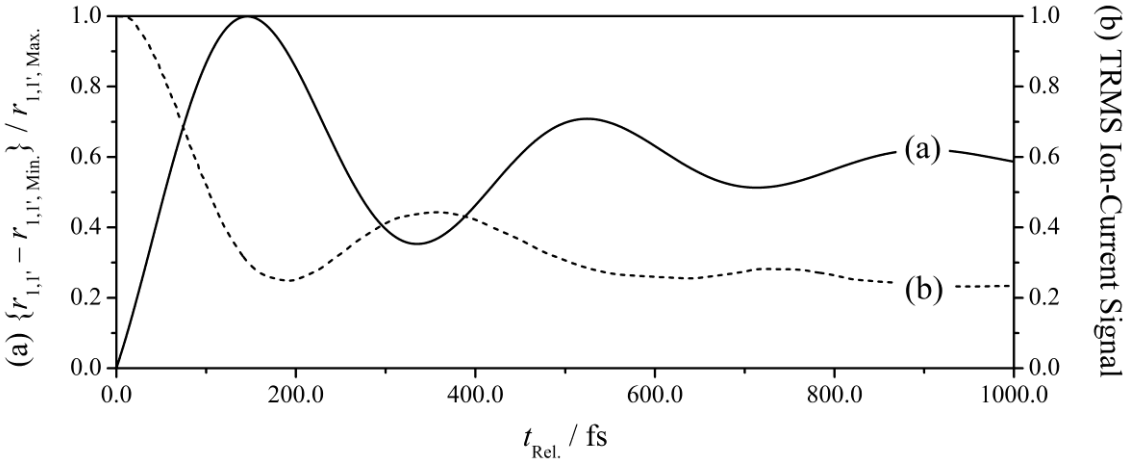

Figure 6.18. Normalised temporal profiles of a) the change in value of $r_{1,1'}$, quantified as $(r_{1,1'} - r_{1,1',\,\mathrm{Min.}})/r_{1,1',\,\mathrm{Max.}}$ and derived from the damped sine fit in Fig. 6.17b, and b) the TRMS ion-current signal acquired experimentally by Sølling *et al.*[256,260] The TRMS ion-current signal has been temporally shifted to account for the rise time.

The damping of the oscillatory component in both the TRMS ion-current signal and the evolution of $r_{1,1'}$ as a function of time is a consequence of the stochastic dephasing of the trajectory swarm (Fig. 6.17a). The overall damping of the TRMS ion-current signal on the ps timescale appears to have been correctly identified by Sølling *et al.*[256,260] as evidence of the permanent recoupling of thiyl termini following $S_0 \leftarrow S_1$ IC. No such damping is observed in the TSHD data (Fig. 6.17b), and neither should it be expected, since a) the timescale of the TSHD simulations is considerably shorter than that of the TRMS

experiment, and b) trajectories displaying permanent recoupling of sulfur termini following $S_0 \leftarrow S_1$ IC may still be included in the statistical analyses here; in the TRMS experiment of Sølling *et al.*,[256,260] the same trajectories would be invisible to the TRMS probe following $S_0 \leftarrow S_1$ IC.

The key differences between the dynamics inferred by Sølling *et al.*[256,260] and those obtained *via* TSHD therefore lie in a) what the peak in $r_{1,1'}$ is taken to represent, and b) the amplitude of the periodic motion responsible for the oscillatory profile.

Sølling *et al.*[256,260] link peaks in $r_{1,1'}$ to $MECI_{Sølling}$; it is therefore inferred that the intersection is visited in 177 ± 17 fs – equivalent to t_{peak} – and $r_{1,1'}$ does not exceed *ca.* 380 pm. A single period of the oscillatory motion covers only *ca.* 320 pm $Da^{-½}$ in 411 ± 27 fs. In contrast, TSHD indicate that $MECI_{Sølling}$ is visited much earlier (Section 6.3.4.2), and that full ring-opening subsequently occurs. $r_{1,1'}$ peaks at *ca.* 680 pm in 152 ± 11 fs. A single period of the oscillatory motion covers *ca.* 2720 pm $Da^{-½}$, an order of magnitude greater than inferred by Sølling *et al.*[256,260]

6.3.4.5 Internal Conversion and Disulfide Recoupling

Between collision events, the trajectory swarm travels through an extensive coupling region (Figure 6.16) where the separation in energy of the S_0, S_1, and S_2 states is <0.2 eV and interstate coupling is high.[254] Spurious $S_0 \leftrightarrow S_1$ and $S_1 \leftrightarrow S_2$ IC events occur; over 8600 are recorded, averaging a rate of 120 ± 40 ps^{-1}.

$S_0 \leftarrow S_1$ IC events are both spatially and temporally well-distributed. They are able to occur far from $MECI_{Sølling}$ (Fig. 6.19a), which appears to be unimportant to post-50-fs IC, but cannot occur close to the S_0 minimum/Franck-Condon point (Fig. 6.19b), where the separation in energy of the S_0 and S_1 states is large. Consequently, the first collision event (occurring 338 ± 23 fs post-photoexcitation, when the trajectory swarm is still largely coherent) is concurrent with a drop in the frequency of $S_0 \leftarrow S_1$ IC events that is apparent even on cursory examination of Fig. 6.19c.

It should be implicitly understood that (permanent) recoupling of the thiyl termini can only occur if the trajectory is on, and thereafter remains on, the S_0 potential energy surface. If $S_0 \leftarrow S_1$ IC is not possible close to the S_0 minimum/Franck-Condon point, then the necessary S_0 population has to be established in advance of collision events. This is achieved by periodic passage through the coupling region, during which time the S_0, S_1, and S_2 states become strongly mixed, and the populations are equilibrated, or "*shaken up*" (Fig.

6.20). A fraction of trajectories will always leave the coupling region on the S_0 potential energy surface, and these trajectories are able to attempt recoupling if, and when, the thiyl termini return into proximity.[254]

Recoupling can be frustrated if a) the thiyl termini do not return into sufficiently close proximity or b) if they collide too forcefully.[254] In the latter case, $r_{1,1'}$ may be compressed significantly below its equilibrium bonded length and the disulfide bond consequently subjected to a strong restoring force that springs it apart. Statistical significance testing on the values of $r_{1,1'}$ associated with successful and unsuccessful recoupling events at *ca.* 375 fs reveals a difference in the mean values of $r_{1,1'}$ for the two populations at the 95% confidence level, with the mean value of $r_{1,1'}$ for successful recoupling events being lower. There evidently exists a "*sweet spot*" for recoupling. Recoupling can also be frustrated by translocalisation of the radical sites from the thiyl termini to other positions on the carbon chain *via* hydrogen abstraction; this process is observed *via* TSHD but is more or less negligible in the gas phase.[254] It is known to be of greater importance in solution.[276]

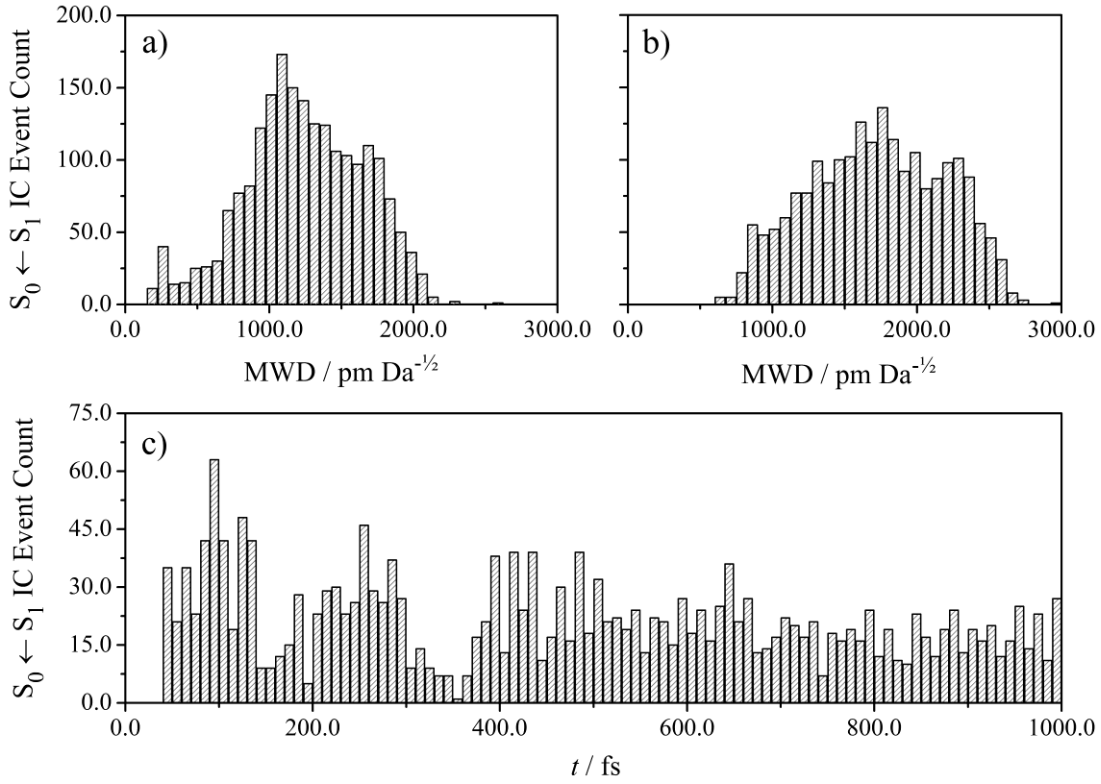

Figure 6.19. Histograms illustrating the distribution of $S_0 \leftarrow S_1$ IC events with respect to the mass-weighted-distance from a) $MECI_{Sølling}$ and b) the S_0 minimum/Franck-Condon point, and c) throughout TSHD simulation as a function of time, *t*.

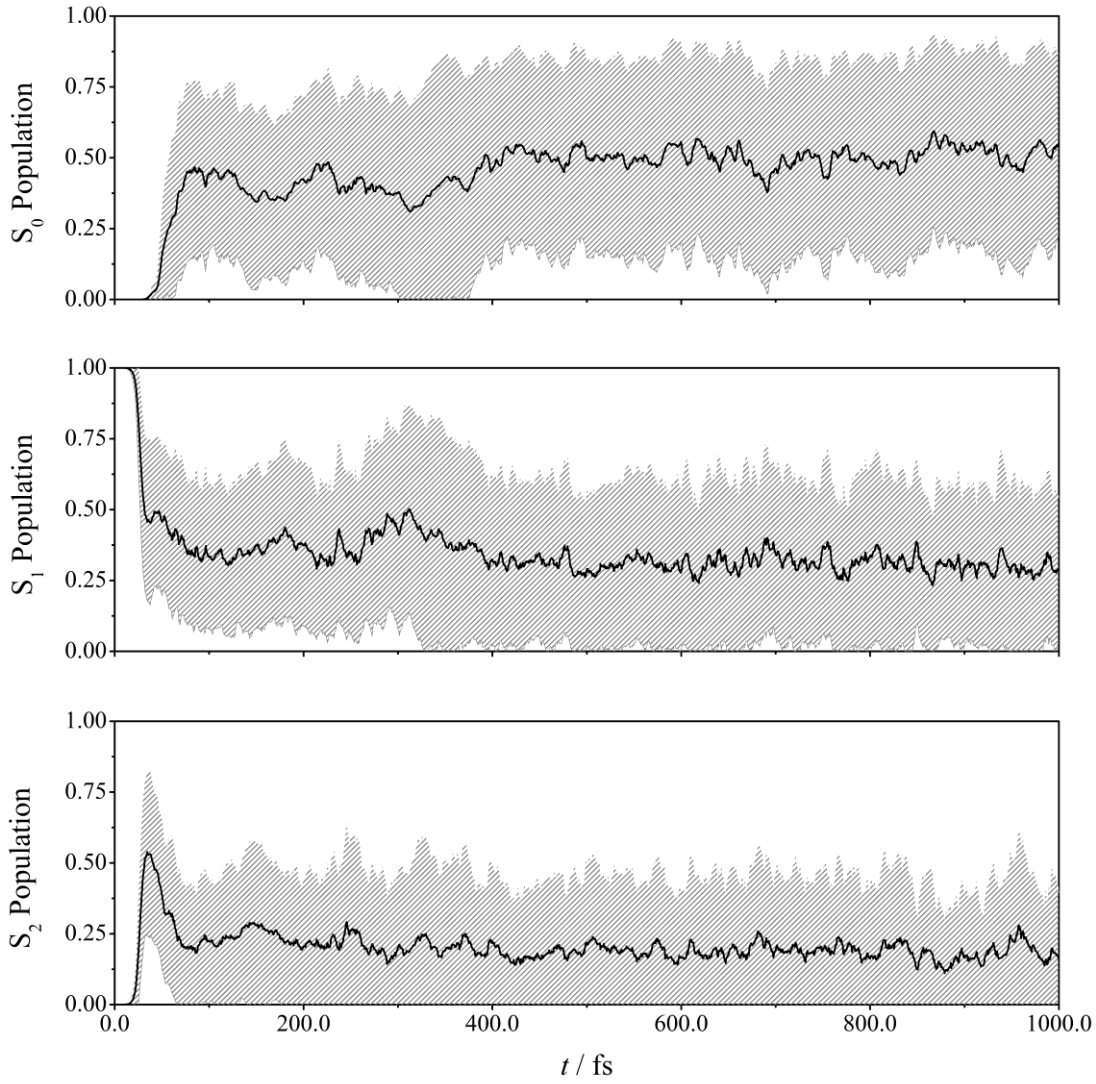

Figure 6.20. Populations of the S_0, S_1 and S_2 states as a function of time, *t*. An average and standard deviation (indicated by the shaded overlay) are plotted.

6.4 Simulations of Time-Resolved Gas Electron Diffraction

TRGED finds an application in discriminating between the dynamics inferred by Sølling *et al.*[256,260] and the "*Molecular Clackers*" mechanism,[254] since a technique that is able to measure directly internuclear distances is necessitated. The reduction of the dimensionality of the dynamics (Section 6.3.4.3) simplifies the research question to a binary one; are sulfur-sulfur internuclear distances greater than *ca.* 600 – 700 pm observed in the TRGED data? The answer to this question allows for a conclusion in favour, or in refutation, of the "*Molecular Clackers*" mechanism[254] to be advanced. Simulations of the TDMIC and TDRDC, with a 120 fs IRF applied, are reproduced in Figs. 6.21 and 6.22, respectively.

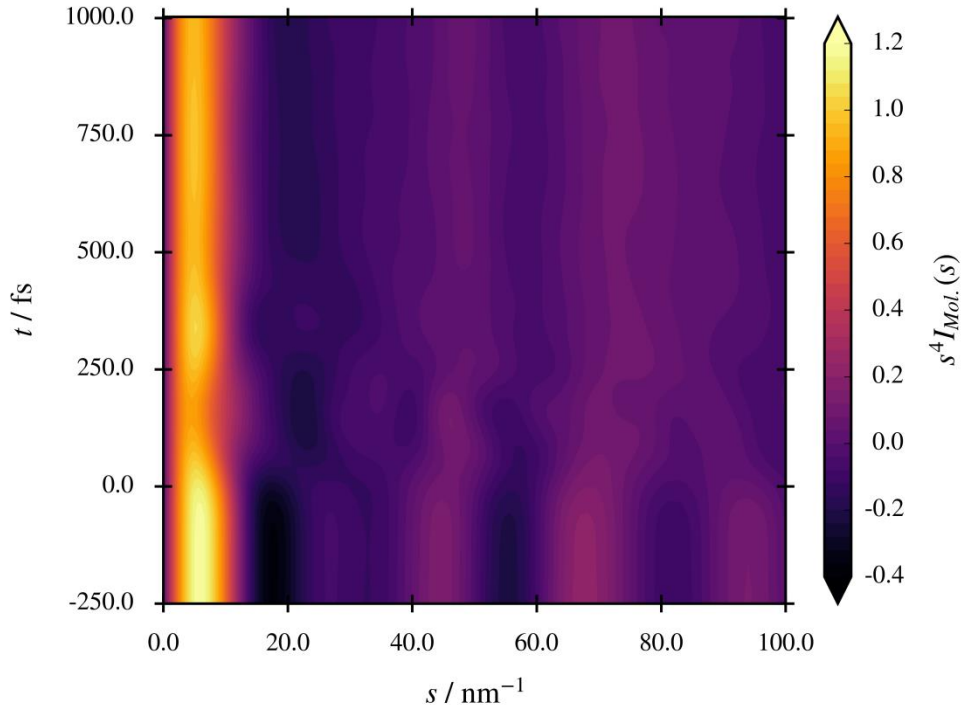

Figure 6.21. Theoretical TDMIC matrix for 1,2-dithiane; convoluted with a 120 fs (FWHM) Gaussian kernel.

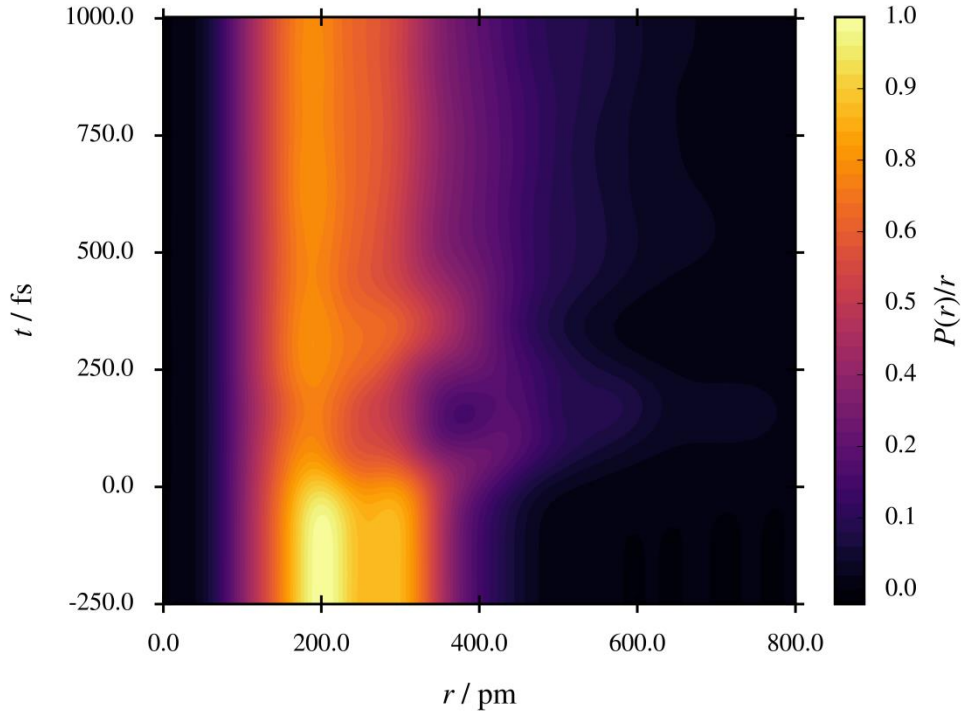

Figure 6.22. Theoretical TDRDC matrix for 1,2-dithiane; transformed from a theoretical TDMIC matrix post-convolution with a 120 fs (FWHM) Gaussian kernel.

Simulations of the TDMIC and TDRDC pre-application of the IRF are reproduced in Figs. B1 and B2, respectively.

To simulate the pre-time-zero signal, 100 additional S_0-state trajectories were computed as detailed for the S_1-state trajectories in Section 6.3.3, but with each geometry propagated through time for 250 fs. To reduce the computational cost, non-adiabatic coupling vectors were not computed and surface-hopping was switched off.

Comparison of the TDMIC and TDRDC pre- and post-application of the IRF makes apparent that fine structure – particularly in the TDMIC – is obscured by the finite temporal resolution of TRGED. That this is the case even with a narrow-FWHM IRF attests to the demanding temporal resolution required to resolve the "*Molecular Clackers*" mechanism[254] *via* TRGED. The table-top TRGED instrument housed at the University of York[71,73,74] does not have the necessary temporal resolution;[72] the IRF used for the simulations – a 120 fs (FWHM) Gaussian kernel – was consequently chosen to be comparable to that of the TRGED instrument at the SLAC National Accelerator Laboratory. The TDMIC and TDRDC were submitted to the Scientific Panel at the SLAC National Accelerator Laboratory ahead of time as proof-of-concept work, and proved instrumental in securing beamtime for João Pedro Nunes to carry out the TRGED experiments on 1,2-dithiane in 2016.[74]

The signature of the "*Molecular Clackers*" mechanism[254] appears most prominently in the TDMIC matrix as a periodic, out-of-phase rise and fall of the features at *ca.* 15 and 25 nm^{-1} and begins immediately at time zero. The default geometry of the electron detector in the TRGED instrument at the SLAC National Accelerator Laboratory cannot detect scattering below *ca.* 25 nm^{-1}, but by having simulated the signature beforehand, João Pedro Nunes was able to adjust the geometry accordingly before data acquisition and make the best use of the allocated beamtime.[74]

The appearance of internuclear distances greater than *ca.* 600 – 700 pm, associated with the open-chain disulfide biradical, is apparent on transformation of TDMIC into the TDRDC, as is the periodic bleaching of the shorter internuclear distances, measuring *ca.* 200 – 300 pm, associated with the S_0 minimum.

6.5 Conclusions

TSHD simulations, recorded at the SA3-CASSCF(10,8)/*def*2-SV(P) level, have challenged contemporary understanding of the photofission of the disulfide bond in 1,2-dithiane by

presenting a classically-intuitive reinterpretation[254] of the experimental measurements of Sølling *et al.*[256,260] The "*Molecular Clackers*" mechanism[254] presents an alternative in which the photostability of 1,2-dithiane arises not because the dynamics are highly non-ergodic, such that the thiyl termini of the transient $^{\bullet}S–(CH_2)_4–S^{\bullet}$ biradical cannot move apart, but because the termini collide periodically. These collision events can, under the right circumstances, result in permanent recoupling of the thiyl termini, repairing broken disulfide bonds in the ensemble on the picosecond timescale.

The work detailed in this Chapter highlights – more so than any other part of this thesis – the power of having a) the ability to acquire gas-phase equilibrium structures *via* GED, and b) complementary TSHD/theoretical expertise together in the same research group. TSHD simulations were used, in the first instance, to frame the research question and provide detailed and independently-publishable mechanistic information. TRGED simulations using the TSHD dataset were used to establish whether TRGED experiments would be worthwhile, what should constitute a successful TRGED experiment in this context, and to secure competitive beamtime at the SLAC National Accelerator Laboratory for the experiments to take place.

João Pedro Nunes lead the first TRGED experiments on 1,2-dithiane at the SLAC National Accelerator Laboratory in 2016.[74] Details of these TRGED experiments, and the analysis of the data, have already been compiled into a Ph.D. thesis.[74] Additional data were collected for 1,2-dithiane during a second experimental season at the SLAC National Accelerator Laboratory in 2018. The data acquired in both experimental seasons are heavily in favour of the "Molecular Clackers" mechanism,[254] with the signature of the mechanism being reproduced in the TDMIC, and internuclear distances greater than 600 pm being evident in the TDRDC.[74] The work is currently in preparation for publication.

Sølling *et al.* have closed the Chapter on 1,2-dithiane by publishing recently new spectroscopic evidence[277] in favour of the "*Molecular Clackers*" mechanism.

This Chapter is a highly-significant contribution, but only scratches the surface of the rich photochemistry of disulfides. Other disulfides have been similarly studied over the duration of this project, and follow-up studies are planned for future work. These studies are discussed in Chapter 8.

7 Photoisomerisation of *E*-Cinnamonitrile

$E \leftrightarrow Z$ photoisomerisation around a π bond in a conjugated molecule is one of the most fundamental photochemical transformations; indeed, it is likely to be the first photochemical transformation that the chemist encounters. As the "*...simplest mechanism for converting light energy into mechanical motion on a molecular scale…*",[119] controllable and reversible $E \leftrightarrow Z$ photoisomerisation of tailor-made conjugated molecules has found applications in technology (*e.g.* optical memory/data storage, optoelectronics, and photo-switching), in synthetic transformations,[278] and in the functionalisation of materials – most recently for *in vivo* photoswitching.[279,280]

The ubiquity, conceptual simplicity, and centrality of $E \leftrightarrow Z$ photoisomerisation to photochemistry has encouraged theoreticians to study the process *in silico*. Martínez *et al.*[281] write, in their contemporary theoretical work, that the "*…apparent… simplicity* [of $E \leftrightarrow Z$ photoisomerisation] *belies* [the] *complex excited state dynamics…*"[281] and, further, that while "*…the excited state dynamics of the smallest unsaturated hydrocarbon,* [ethene], *are now relatively well understood… the smallest polyene, trans-1,3-butadiene, displays a remarkable complexity in its excited state dynamics and continues to be the subject of considerable controversy.*"[281] $E \leftrightarrow Z$ photoisomerisation remains one of the great challenges in theoretical chemistry, even for the simplest of molecules.

Consequently, theoretical studies have concentrated on paradigmatic examples of $E \leftrightarrow Z$ photoisomerisation in model molecules, *e.g.* in ethene,[119,282–286] stilbene,[119,282,287,288] and azobenzene,[289,290] or otherwise on obvious examples from the natural world, *e.g.* the $E \leftrightarrow Z$ photoisomerisation of the retinal protonated Schiff base (RPSB),[119,291–293] the chromophore for a family of rhodopsins central to visual perception. In the latter case, truncated model analogues have had to be used until very recently[294] to make accessible the highest-level theoretical methods.

The contemporary understanding of $E \leftrightarrow Z$ photoisomerisation – this being that it occurs *via* an S_1/S_0 MECI and requires at least two geometric coordinates and electronically-excited states to be described theoretically with qualitative accuracy[119] – has developed largely from these studies alone. Nonetheless, this model is highly generalisable to other examples of $E \leftrightarrow Z$ photoisomerisation; it is summarised most accessibly in the review article of Levine and Martínez,[119] to which the interested reader is directed.

7.1 *E*-Cinnamonitrile

It is apt that this Chapter has opened with a discussion of model systems. Titan, the largest moon of Saturn, is considered a model system for prebiotic Earth,[295] and is an ideal off-world location for the study of organic (photo)chemistry on the planetary scale.[296,297] It is the only such location in the solar system to have the requisite temperature and pressure to permit a hydrological cycle[296,297] and the atmosphere is weakly reducing, nitrogen-heavy, and rich in trace organic molecules[296–298] such as methane, benzene, and nitrile-containing hydrocarbons[299–302] – the building blocks of more complex molecules. Analysis of data logs from fly-by missions, particularly from NASA's CASSINI probe, continues to provide new insight;[299–302] the interested reader is directed towards the comprehensive reviews of Willis *et al.*,[297] and Raulin and Owen.[298]

E-cinnamonitrile, illustrated in Fig. 7.1, may be found in the atmosphere of Titan.[303]

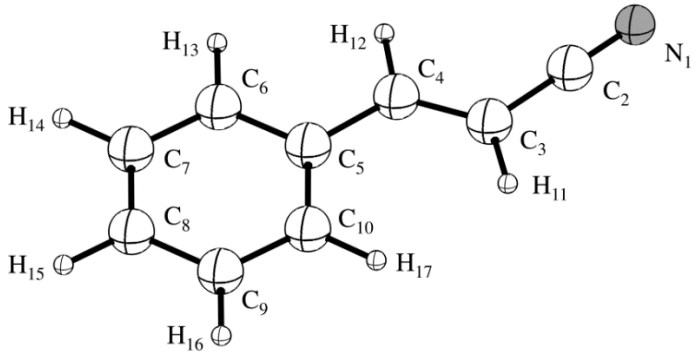

Figure 7.1. Ground-state structure of *E*-cinnamonitrile. The atomic labelling scheme is outlined and used hereafter.

UV light, cosmic rays and high-energy electrons from the magnetosphere of Saturn[296–298,304] are all potential sources of energy for the trace organic molecules in the atmosphere of Titan – this energy can promote fragmentation, photofission, and photochemical transformation to produce reactive intermediates. The end products of the organic photochemistry form dense orange aerosol clouds (*tholins*).[297] Atmospheric models of Titan are still quite incomplete,[304] and are especially lacking in their ability to account for many of the larger constituents of the *tholins*. It is thought that these could be polymeric, polyaromatic, and contain nitrogen, *i.e.* that polyaromatic nitrogen heterocycles (PANH) – the "*building blocks of life*" – could be present on Titan, and that understanding their synthesis here could provide clues to their synthesis on prebiotic Earth. The synthesis of

PANH from smaller organic components at high temperature has been reported recently by Alexander *et al.*,[305] and Zwier *et al.*[303] have investigated PANH formation *via* unimolecular photoisomerisation in contemporary work. Zwier *et al.*[303] speculated that the synthesis of the simplest PANH, quinoline, might occur on Titan *via* cyclisation of its structural isomer, *Z*-cinnamonitrile, with this process preceded by the $Z \leftarrow E$ photoisomerisation of *E*-cinnamonitrile. The (simplified) scheme of Zwier *et al.*[303] is outlined in Fig. 7.2.

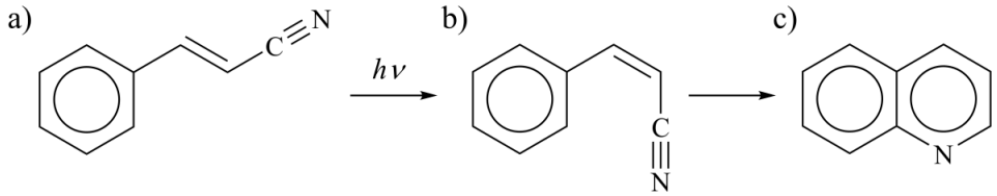

Figure 7.2. Structural isomers of C_9H_7N: a) *E*-cinnamonitrile, b) *Z*-cinnamonitrile, and c) quinoline, the simplest PANH. The transformation scheme is that of Zwier *et al.*[303]

Zwier *et al.*[303] found no evidence for the synthesis of quinoline on the timescale of their experiment (*ca.* 40 μs) following $Z \leftarrow E$ photoisomerisation of *E*-cinnamonitrile. In these experiments, $Z \leftarrow E$ photoisomerisation was promoted *via* photoexcitation to the lowest-lying electronically-excited state, however, in the atmosphere of Titan, where high-energy photons can be absorbed,[296–298,304] new pathways may be unlocked by excitation to higher-lying electronically-excited states.

This Chapter comprises the first study of $E \leftrightarrow Z$ photoisomerisation *via* TSHD coupled with the second-order algebraic diagrammatic construction/Møller-Plesset perturbation theory approach [ADC(2)/MP2]. Some of the limitations of CASSCF for this class of problem (Sections 7.3.2 and 7.3.3) are overcome at a computational cost that is considerably lower than that of MR-CISD or MS-CASPT2. It includes a full GED structural solution for *E*-cinnamonitrile (Section 7.2), an *ab initio* assessment of the suitability of the ADC(2)/MP2 treatment (Sections 7.3.2 and 7.3.3), analysis of the TSHD simulations (Section 7.3.5), and simulations of a TDMIC and TDRDC (Section 7.4).

7.2 Structure of *E*-Cinnamonitrile

The following sections (Sections 7.2.1 – 7.2.4) detail the structural characterisation of *E*-cinnamonitrile using GED. *E*-cinnamonitrile was purchased from Sigma-Aldrich (Aldrich-C81004, *E*-cinnamonitrile, 97%) and used as received.

7.2.1 Data Acquisition

GED data were acquired using the University of York gas electron diffractometer.[43] An accelerating potential of 42.22 kV was applied to produce a continuous electron beam with an electron emission current of 0.66 μA and electron wavelength of *ca.* 5.85 pm. GED data were acquired *via* the exposure of reusable image plates (Fuji BAS-IP MS 2025) at nozzle-to-image-plate distances of 235.5 and 487.0 mm and digitised using a tabletop image plate scanner (Fuji BAS-1800II) as outlined in Section 4.1.5. Two and four exposures were recorded at the shorter and longer nozzle-to-image-plate distances, respectively. *E*-cinnamonitrile was delivered to the point of diffraction *via* the air-heated effusive nozzle assembly outlined in Section 4.1.4. The sample of *E*-cinnamonitrile and the effusive nozzle tip were heated to 443 and 448 K, respectively, during exposures at the longer nozzle-to-image-plate distance and to 448 and 453 K, respectively, at the shorter nozzle-to-image-plate distance. These experimental conditions are summarised in Table A97.

7.2.2 Density Functional Theory Calculations

All DFT calculations were carried out using the GAUSSIAN09[184] software suite on the University of York Advanced Research Computing Cluster (YARCC). Geometry optimisations of *E*-cinnamonitrile were carried out in the C_s symmetry point group and used the B3LYP,[187,188] B3P86,[187,189] B3PW91,[187,190] B2PLYP,[185] PBEH1PBE,[191] and HSEH1PBE[192–195] density functionals coupled with a range of basis sets (cc-pV*n*X, $n \in$ {D, T, Q})[186] of increasing completeness. As in Section 6.2.3; the density functionals were selected to balance effectively computational cost against accuracy. This set was chosen to represent across a spectrum of the most popular low-cost density functionals, with favouring of low computational cost over accuracy justified by higher-level calculations with the best-in-class B2PLYP density functional. All bonded internuclear distances were extrapolated to the CBS limit *via* the fitting of the bonded internuclear distances determined using the cc-pVDZ, cc-pVTZ, and cc-pVQZ basis sets with a function of the form introduced in Section 4.2. The proper convergence of all geometry optimisations to minima on the ground-state potential energy surface was verified *via* vibrational frequency analysis. Cartesian coordinates of all optimised geometries are tabulated in Tables A98–115.

Theoretical r_{h1}-type amplitudes of vibration (u_{h1}) and curvilinear shrinkage corrections (k_{h1}) were generated from vibrational frequencies computed at the B3LYP/cc-pVDZ level using the SHRINK[108,109] software package.

7.2.3 Data Reduction and Refinement

The in-house data extraction package XSTRACT[74] was used to reduce digitised diffraction patterns to MICs *via* azimuthal averaging. MICs were refined using the ED@ED v3.0[94] least-squares refinement package coupled with the scattering factors of Ross *et al.*[196]

7.2.3.1 Refinement Protocol

The least-squares refinement procedure employed a parameterised molecular model, programmed in FORTRAN90, describing *E*-cinnamonitrile within the constraints of the C_s symmetry point group in terms of twenty-one refinable parameters comprising eleven distances ($p_1 - p_{11}$) and ten angles ($p_{12} - p_{21}$). The contributions to parameters $p_1 - p_{21}$ are tabulated in Table 7.1.

Table 7.1. Summary of contributions to parameters $p_1 - p_{21}$.

Parameter		Contributions
p_1	rCN	$r_{1,2}$
p_2	rCC[a]	$^1/_9\ (r_{2,3} + r_{3,4} + r_{4,5} + r_{5,6} + r_{6,7} + r_{7,8} + r_{8,9} + r_{9,10} + r_{10,5})$
p_3	rCC[b]	$[^1/_3\ (r_{2,3} + r_{3,4} + r_{4,5})] - [^1/_6\ (r_{5,6} + r_{6,7} + r_{7,8} + r_{8,9} + r_{9,10} + r_{10,5})]$
p_4	rCC[b]	$[^1/_2\ (r_{2,3} + r_{4,5})] - r_{3,4}$
p_5	rCC[b]	$r_{4,5} - r_{2,3}$
p_6	rCC[b]	$[^1/_4\ (r_{5,6} + r_{7,8} + r_{8,9} + r_{10,5})] - [^1/_2\ (r_{6,7} + r_{9,10})]$
p_7	rCC[b]	$[^1/_2\ (r_{5,6} + r_{10,5})] - [^1/_2\ (r_{7,8} + r_{8,9})]$
p_8	rCC[b]	$r_{6,7} - r_{9,10}$
p_9	rCC[b]	$r_{5,6} - r_{10,5}$
p_{10}	rCC[b]	$r_{7,8} - r_{8,9}$
p_{11}	rCH[a]	$^1/_7\ (r_{3,11} + r_{4,12} + r_{6,13} + r_{7,14} + r_{8,15} + r_{9,16} + r_{10,17})$
p_{12}	aCCC	$a_{2,3,4}$
p_{13}	aCCC	$a_{3,4,5}$
p_{14}	aCCC	$a_{4,5,6}$
p_{15}	aCCC[b]	$[^1/_4\ (a_{5,6,7} + a_{6,7,8} + a_{8,9,10} + a_{9,10,5})] - [^1/_2\ (a_{7,8,9} + a_{10,5,6})]$
p_{16}	aCCC[b]	$a_{7,8,9} - a_{10,5,6}$
p_{17}	aCCC[b]	$[^1/_2\ (a_{5,6,7} + a_{9,10,5})] - [^1/_2\ (a_{6,7,8} + a_{8,9,10})]$
p_{18}	aCCC[b]	$a_{9,10,5} - a_{5,6,7}$
p_{19}	aCCC[b]	$a_{8,9,10} - a_{6,7,8}$
p_{20}	aCCH	$a_{2,3,11}$
p_{21}	aCCH	$a_{3,4,12}$

[a] Multiplicity-weighted average parameter. [b] Difference parameter.

To prevent the correlation of internuclear distances of a similar length and angles of a similar size precluding an independent refinement, $p_2 - p_{10}$ and $p_{15} - p_{19}$ were constructed as a mix of multiplicity-weighted-average and refinable difference parameters. It is possible to reconstruct the nine unique bonded internuclear distances ($r_{2,3}$, $r_{3,4}$, $r_{4,5}$, $r_{5,6}$, $r_{6,7}$, $r_{7,8}$, $r_{8,9}$, $r_{9,10}$, and $r_{10,5}$) and six unique angles ($a_{5,6,7}$, $a_{6,7,8}$, $a_{7,8,9}$, $a_{8,9,10}$, and $a_{9,10,5}$) between the second-row nuclei in *E*-cinnamonitrile *via* linear combinations of parameters $p_2 - p_{10}$ and $p_{15} - p_{19}$, respectively, as outlined in Table 7.2.

Table 7.2. Reconstruction of unique bonded internuclear distances and angles in *E*-cinnamonitrile *via* linear combination of parameters $p_2 - p_{10}$ and $p_{15} - p_{19}$.

Coordinate	Linear Combination of Parameters
$r_{2,3}$	$p_2 + {}^2/_3\, p_3 + {}^1/_3\, p_4 - {}^1/_2\, p_5$
$r_{3,4}$	$p_2 + {}^2/_3\, p_3 - {}^2/_3\, p_4$
$r_{4,5}$	$p_2 + {}^2/_3\, p_3 + {}^1/_3\, p_4 + {}^1/_2\, p_5$
$r_{5,6}$	$p_2 - {}^1/_3\, p_3 + {}^1/_3\, p_6 + {}^1/_2\, p_7 + {}^1/_2\, p_9$
$r_{6,7}$	$p_2 - {}^1/_3\, p_3 - {}^2/_3\, p_6 + {}^1/_2\, p_8$
$r_{7,8}$	$p_2 - {}^1/_3\, p_3 + {}^1/_3\, p_6 - {}^1/_2\, p_7 + {}^1/_2\, p_{10}$
$r_{8,9}$	$p_2 - {}^1/_3\, p_3 + {}^1/_3\, p_6 - {}^1/_2\, p_7 - {}^1/_2\, p_{10}$
$r_{9,10}$	$p_2 - {}^1/_3\, p_3 - {}^2/_3\, p_6 - {}^1/_2\, p_8$
$r_{10,5}$	$p_2 - {}^1/_3\, p_3 + {}^1/_3\, p_6 + {}^1/_2\, p_7 - {}^1/_2\, p_9$
$a_{5,6,7}$	$120.0 + {}^1/_3\, p_{15} + {}^1/_2\, p_{17} - {}^1/_2\, p_{18}$
$a_{6,7,8}$	$120.0 + {}^1/_3\, p_{15} - {}^1/_2\, p_{17} - {}^1/_2\, p_{19}$
$a_{7,8,9}$	$120.0 - {}^2/_3\, p_{15} + {}^1/_2\, p_{16}$
$a_{8,9,10}$	$120.0 + {}^1/_3\, p_{15} - {}^1/_2\, p_{17} + {}^1/_2\, p_{19}$
$a_{9,10,5}$	$120.0 + {}^1/_3\, p_{15} + {}^1/_2\, p_{17} + {}^1/_2\, p_{18}$
$a_{10,5,6}$	$120.0 - {}^2/_3\, p_{15} - {}^1/_2\, p_{16}$

The least-squares refinement procedure followed the SARACEN[99–101] protocol and gave internuclear distances of the r_{h1} type. All amplitudes of vibration associated with a given peak in the RDC were coupled by a fixed ratio to the amplitude of vibration associated with the nuclei giving rise to the largest scattering effect under that peak; only this amplitude of vibration was refined.

7.2.3.2 Refinement Results

The experimentally-acquired and experimental-minus-theoretical "*difference*" MICs are reproduced in Fig. 7.3; the RDCs are reproduced in Fig. 7.4.

The R_G and R_D for the least-squares refinement procedure were 0.083 and 0.046, respectively.

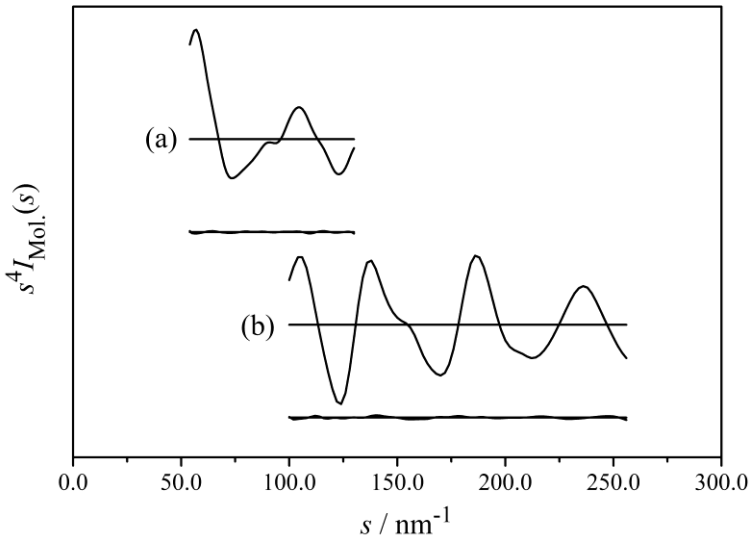

Figure 7.3. MICs and experimental-minus-theoretical "*difference*" MICs obtained after refinement of GED data acquired for *E*-cinnamonitrile at a) long and b) short nozzle-to-image-plate distances.

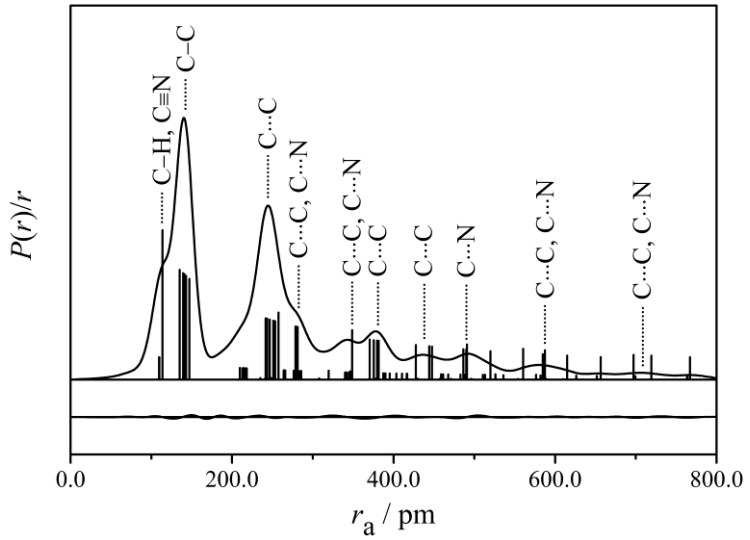

Figure 7.4. RDC and experimental-minus-theoretical "*difference*" RDC obtained after refinement of GED data acquired for *E*-cinnamonitrile.

The weighting points for off-diagonal weight matrices, scaling factors, and least-squares correlation parameters are found in Table A116; the least-squares correlation matrix is found in Table A117. The refined (r_{h1}-type) and theoretical (r_e-type; B3LYP/CBS) parameters p_1 – p_{21} are tabulated in Table A118. All internuclear distances, refined and

theoretical amplitudes of vibration, r_{h1}-type shrinkage corrections, and SARACEN[99–101] restraints (where applied) are tabulated in Table A119. Cartesian coordinates for the refined r_{h1}-type structure of 1,2-dithiane are tabulated in Table A120.

In Fig. 7.5; experimentally-determined internuclear distances and angles, alongside their theoretical counterparts computed at the B3LYP/CBS level, are overlaid onto schematic illustrations of *E*-cinnamonitrile.

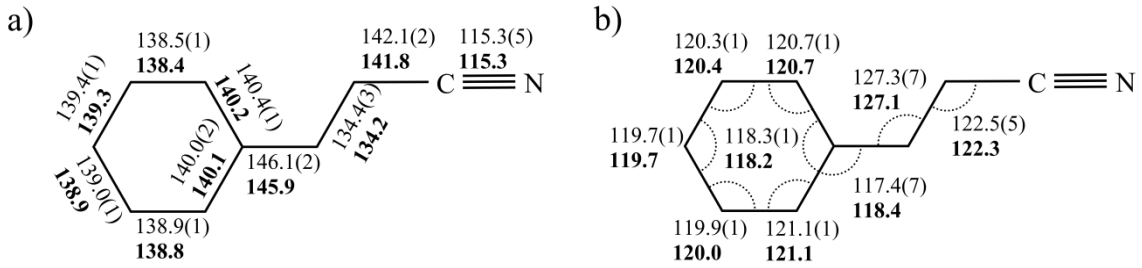

Figure 7.5. Experimental r_{h1}-type (regular typeface) and B3LYP/CBS (bold typeface) geometric parameters determined for *E*-cinnamonitrile. All a) internuclear distances are reported in picometers. All b) angles are reported in degrees.

7.2.4 Discussion

Refined experimental internuclear distances and angles are tabulated in Table 7.3 alongside their theoretical counterparts computed at the B3LYP/CBS level and refined GED[306] and XRD[307] data for styrene, a close analogue of *E*-cinnamonitrile.

All internuclear distances and angles between 2nd-row nuclei are well-determined to 0.8(5) pm and 0.7(6)° of their theoretical counterparts in the GED solution. The GED solution for *E*-cinnamonitrile compares satisfactorily with both the GED[306] and XRD[307] solutions for styrene; all internuclear distances are determined to 0.8(5) and 0.6(5) pm, and all angles to 1.3(12) and 0.5(4)°, of their counterparts in the GED[306] and XRD[307] solutions, respectively. It is difficult to comment on the differences between *E*-cinnamonitrile and styrene when comparing only with the GED[306] solution for the latter; uncertainties on the structural parameters likely to be most affected by nitrile substitution ($r_{3,4}$ and $r_{4,5}$) are very large, and the assumption of equivalence for $r_{5,6}$, $r_{6,7}$, $r_{7,8}$, $r_{8,9}$, $r_{9,10}$, and $r_{10,5}$ means that the GED[306] solution provides no information on the distortion of the benzyl subunit. In the XRD[307] solution for styrene, however, $r_{3,4}$ and $r_{4,5}$ are measured to be shorter by 1.9(5) pm and longer by 1.3(3) pm, respectively, than in *E*-cinnamonitrile, consistent with the effect of nitrile substitution that one can predict trivially *via* valence bond theory.

Table 7.3. Summary of refined (r_{h1}-type) GED and theoretical (r_e-type; B3LYP/CBS measurements of internuclear distances[a] and angles[b] in *E*-cinnamonitrile. Refined (r_{h1}-type) GED[306] and XRD[307] (recorded at 83 K) measurements of internuclear distances[a] and angles[b] in styrene are tabulated for comparison.

Coordinate	GED (r_{h1})	r_e	GED (Styrene)[306]	XRD (Styrene)[307]
$r_{1,2}$	115.3(5)	115.3	N/A	N/A
$r_{2,3}$	142.1(2)	141.8	N/A	N/A
$r_{3,4}$	134.4(3)	134.2	135.5(16)	132.5(2)
$r_{4,5}$	146.1(2)	145.9	147.5(23)	147.4(1)
$r_{5,6}$	140.4(1)	140.2	139.9(3)[c]	140.2(1)
$r_{6,7}$	138.5(1)	138.4	139.9(3)[c]	138.8(1)
$r_{7,8}$	139.4(1)	139.3	139.9(3)[c]	139.2(1)
$r_{8,9}$	139.0(1)	138.9	139.9(3)[c]	138.8(1)
$r_{9,10}$	138.9(1)	138.8	139.9(3)[c]	139.0(1)
$r_{10,5}$	140.0(2)	140.1	139.9(3)[c]	139.5(1)
$r_{3,11}$	108.0(4)	108.1	110.0(7)	96.7[d]
$r_{4,12}$	108.2(4)	108.3	110.0(7)	98.1[d]
$r_{6,13}$	108.0(4)	108.1	110.0(7)	98.9[d]
$r_{7,14}$	108.0(4)	108.1	110.0(7)	99.1[d]
$r_{8,15}$	108.0(4)	108.1	110.0(7)	100.9[d]
$r_{9,16}$	108.0(4)	108.1	110.0(7)	97.4[d]
$r_{10,17}$	108.1(4)	108.2	110.0(7)	98.3[d]
$a_{2,3,4}$	122.5(5)	122.3	N/A	N/A
$a_{3,4,5}$	127.3(7)	127.1	126.9(24)	126.8[d]
$a_{4,5,6}$	124.2(8)	123.4	122.0(24)	122.7[d]
$a_{5,6,7}$	120.68(5)	120.7	120.0[c]	121.1[d]
$a_{6,7,8}$	120.34(5)	120.4	120.0[c]	120.1[d]
$a_{7,8,9}$	119.70(9)	119.7	120.0[c]	119.4[d]
$a_{8,9,10}$	119.94(5)	120.0	120.0[c]	120.5[d]
$a_{9,10,5}$	121.10(9)	121.1	120.0[c]	120.6[d]
$a_{10,5,6}$	118.25(9)	118.2	120.0[c]	118.3[d]
$a_{10,5,4}$	117.4(7)	118.4	N/A	N/A
$a_{2,3,11}$	115.6(3)	115.6	N/A	N/A
$a_{3,4,12}$	117.6(2)	117.6	N/A	N/A

[a] All internuclear distances ($r_{i,j}$) are tabulated in picometers. [b] All angles ($a_{i,j,k}$) are tabulated in degrees. [c] All C–C internuclear distances and C–C–C angles in the benzyl subunit were assumed to be equivalent in the least-squares refinement;[306] a heavy approximation. [d] Uncertainties unavailable; measured directly from *.cif* data.

7.3 Electronically-Excited States of 1,2-Dithiane

7.3.1 *Ab Initio* Calculations

All *ab initio* calculations detailed in this section were carried out on the University of York Advanced Research Computing Cluster; CASSCF and MR-CISD calculations were carried out using COLUMBUS v7.0,[263–265] MS-CASPT2 calculations were carried out using OPENMOLCAS v8.3,[224] and ADC(2)/MP2 calculations were carried out using TURBOMOLE v6.3.1.[308]

The CASSCF active space (Fig. 7.6) comprised twelve electrons distributed in twelve orbitals – ten of A″ symmetry and two of A′ symmetry. The complete π-space (comprising bonding orbitals π_1, π_2, and $\pi_4 - \pi_6$, antibonding orbitals $\pi^*_1 - \pi^*_3$, π^*_5, and π^*_6, and the in-plane C≡N π orbitals, π_3 and π^*_4) was used construct the active space.

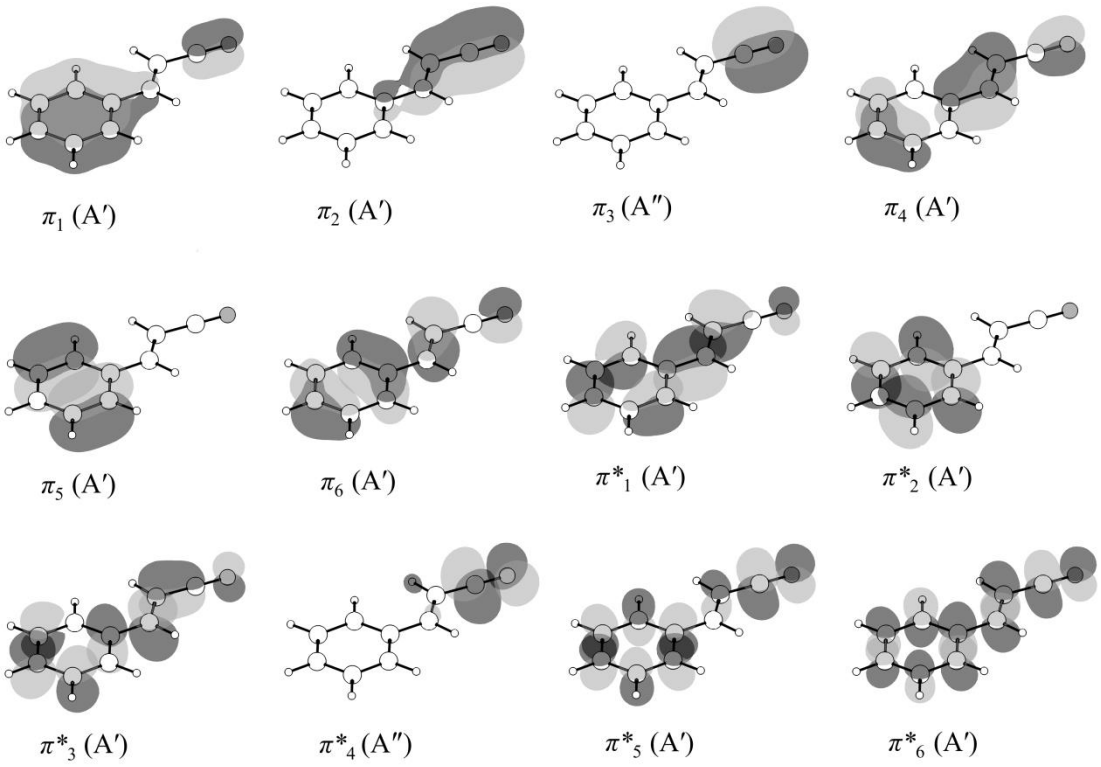

Figure 7.6. SA4-CASSCF(12,12) active space constructed for *E*-cinnamonitrile, comprising bonding orbitals π_1, π_2, and $\pi_4 - \pi_6$, antibonding orbitals $\pi^*_1 - \pi^*_3$, π^*_5, and π^*_6, and the in-plane C≡N π orbitals, π_3 and π^*_4.

State-averaging was carried out over the four lowest-energy singlet states – all of A′ symmetry – with equal weighting of all states. These calculations are denoted SA4-

CASSCF(12,12). Tight convergence criteria of $<1\times10^{-10}$ and $<1\times10^{-8}$ a.u. were used for the energy and gradient, respectively.

MR-CISD calculations used a truncated reference space comprising six electrons distributed in six orbitals – all of A′ symmetry – equivalent to the active space of Fig. 7.6, but with π_1 – π_3 and π^*_4 – π^*_6 (the three lowest- and three highest-energy orbitals, respectively) discarded. The ten lowest-energy core orbitals were frozen in the MR-CISD treatment. These calculations comprised 150,124,191 configurations, with 175 contained in the reference space, and were made tractable by using the massively-parallel implementation of MR-CISD in COLUMBUS v7.0. The Meissner correction[266] was used to correct the MR-CISD calculations for size-extensivity. These calculations are denoted MR-CISD(6,6).

MS-CASPT2 calculations used the reference space of Fig. 7.6. The ten lowest-energy core orbitals were frozen in the MS-CASPT2 treatment. The four lowest-energy singlet states – all of A′ symmetry – were included in the multistate treatment. These calculations are denoted MS-CASPT2(12,12).

ADC(2)/MP2 calculations used the CC2[309–312] module of TURBOMOLE v6.3.1.[308] The ten lowest-energy core orbitals were frozen in the ADC(2)/MP2 treatment. MECI were fully optimised at the ADC(2)/MP2 level using the approach of Martínez *et al.*[313] as implemented in code developed by, and provided courtesy of, Rafał Szabla.[314,315] The code was modified to interface with TURBOMOLE v6.3.1.[308]

The cc-(p)VDZ basis set (a customised version of the cc-pVDZ basis set of Dunning[186] in which polarisation functions are omitted for all hydrogen nuclei) was used throughout.

The proper convergence of all geometry optimisations to minima was verified *via* vibrational frequency inspection.

7.3.2 Potential Energy Surface Geography

The C_s-symmetric, planar S_0 minima of *E*- (equivalent to the structure characterised *via* GED in Section 7.2) and *Z*-cinnamonitrile have been fully optimised at the SA4-CASSCF(12,12), MR-CISD(6,6), and MS-CASPT2(12,12) levels. These minima are denoted *E*-S_0 and *Z*-S_0. Cartesian coordinates are tabulated in Tables B15–20 respectively.

Vertical transition energies and oscillator strengths are tabulated in Table 7.4 for transitions to the S_1, S_2, and S_3 states that originate from *E*-S_0 and *Z*-S_0.

Table 7.4. Summary of vertical transition energies, ΔE,[a] and oscillator strengths, f, for E-S_0 and Z-S_0 as computed at the SA4-CASSCF(12,12), MR-CISD(6,6) and MS-CASPT2(12,12) levels.

	SA4-CASSCF(12,12)		MR-CISD(6,6)		MS-CASPT2(12,12)	
Transition	ΔE	f	ΔE	f	ΔE	f
$S_1 \leftarrow S_0$ (E-S_0)	4.61	<0.01	4.55	0.02	4.59	0.02
$S_1 \leftarrow S_0$ (Z-S_0)	4.60	<0.01	4.54	0.02	4.59	<0.01
$S_2 \leftarrow S_0$ (E-S_0)	6.07	<0.01	5.23	0.82	5.02	0.69
$S_2 \leftarrow S_0$ (Z-S_0)	6.08	<0.01	5.17	0.65	4.96	0.55
$S_3 \leftarrow S_0$ (E-S_0)	6.70	0.88	6.04	<0.01	5.99	<0.01
$S_3 \leftarrow S_0$ (Z-S_0)	6.66	0.71	6.12	0.03	6.03	0.02

[a] All transition energies are tabulated in eV.

SA4-CASSCF(12,12) performs quantitatively well for the $S_1 \leftarrow S_0$ excitations, but does not reproduce the correct energetic ordering of the $S_2 \leftarrow S_0$ and $S_3 \leftarrow S_0$ excitations with respect either to the higher-level MR-CISD(6,6) and MS-CASPT2(12,12) calculations or to spectroscopic measurement. The S_2 and S_3 states are swapped in energetic order at the SA4-CASSCF(12,12) level; this is apparent from inspection of both the oscillator strengths for the corresponding transitions and the characters of the S_2 and S_3 states as calculated at the MR-CISD(6,6) and MS-CASPT2(12,12) levels. The latter are tabulated in Table 7.5.

Where these states are referenced in this section (Section 7.3.2), therefore, the correct energetic ordering (that obtained at the MR-CISD(6,6) and MS-CASPT2(12,12) levels) is assumed, *i.e.* the S_2 is the bright, $\pi^*_1 \leftarrow \pi_6$ state and the S_3 is the mixed $\pi^*_1 \leftarrow \pi_6$ / $\pi^*_3 \leftarrow \pi_6$ / $\pi^*_1 \leftarrow \pi_4$ state.

In this picture, SA4-CASSCF(12,12) therefore also performs quantitatively well for the $S_3 \leftarrow S_0$ excitations with respect to the higher-level MR-CISD(6,6) and MS-CASPT2(12,12) calculations and describes the S_3 state accurately; the incorrect energetic ordering of states is obtained purely because the S_2 state is placed too high in energy (by >1.5 eV) at the SA4-CASSCF(12,12) level. The same result has been reported in calculations of the vertical excitation energies of ethene,[119,283–286] stilbene,[119,282,287,288] and styrene,[316,317] and is a consequence of the ionic character of the S_2-state wavefunction,[283] the description of which has very different correlation requirements to the descriptions of the covalent S_1 and S_3 states. Inclusion of dynamical correlation *via* MR-CISD(6,6) and MS-CASPT2(12,12) calculations is used here to recover successfully the correct energetic ordering of the S_2 and S_3 states.

Table 7.5. Summary of the contributions[a] of excited configurations to the electronically-excited states of *E*-S_0 and *Z*-S_0 as computed at the SA4-CASSCF(12,12), MR-CISD(6,6) and MS-CASPT2(12,12) levels.

	SA4-CASSCF(12,12)		MR-CISD(6,6)		MS-CASPT2(12,12)	
State	Excitation	Weight	Excitation	Weight	Excitation	Weight
S_1 (*E*-S_0)	$\pi^*_2 \leftarrow \pi_6$	0.263	$\pi^*_2 \leftarrow \pi_6$	0.262	$\pi^*_2 \leftarrow \pi_6$	0.241
	$\pi^*_1 \leftarrow \pi_5$	0.356	$\pi^*_1 \leftarrow \pi_5$	0.335	$\pi^*_1 \leftarrow \pi_5$	0.450
S_1 (*Z*-S_0)	$\pi^*_2 \leftarrow \pi_6$	0.253	$\pi^*_2 \leftarrow \pi_6$	0.253	$\pi^*_2 \leftarrow \pi_6$	
	$\pi^*_1 \leftarrow \pi_5$	0.368	$\pi^*_1 \leftarrow \pi_5$	0.355	$\pi^*_1 \leftarrow \pi_5$	
S_2 (*E*-S_0)	$\pi^*_1 \leftarrow \pi_6$[b]	0.283	$\pi^*_1 \leftarrow \pi_6$	0.738	$\pi^*_1 \leftarrow \pi_6$	0.704
	$\pi^*_3 \leftarrow \pi_6$	0.120				
	$\pi^*_1 \leftarrow \pi_4$	0.214				
S_2 (*Z*-S_0)	$\pi^*_1 \leftarrow \pi_6$[b]	0.273	$\pi^*_1 \leftarrow \pi_6$	0.731	$\pi^*_1 \leftarrow \pi_6$	
	$\pi^*_3 \leftarrow \pi_6$	0.126				
	$\pi^*_1 \leftarrow \pi_4$	0.216				
S_3 (*E*-S_0)	$\pi^*_1 \leftarrow \pi_6$	0.762	$\pi^*_1 \leftarrow \pi_6$[b]	0.279	$\pi^*_1 \leftarrow \pi_6$[b]	
			$\pi^*_3 \leftarrow \pi_6$	0.108	$\pi^*_3 \leftarrow \pi_6$	
			$\pi^*_1 \leftarrow \pi_4$	0.212	$\pi^*_1 \leftarrow \pi_4$	
S_3 (*Z*-S_0)	$\pi^*_1 \leftarrow \pi_6$	0.755	$\pi^*_1 \leftarrow \pi_6$[b]	0.266	$\pi^*_1 \leftarrow \pi_6$[b]	0.269
			$\pi^*_3 \leftarrow \pi_6$	0.103	$\pi^*_3 \leftarrow \pi_6$	0.114
			$\pi^*_1 \leftarrow \pi_4$	0.212	$\pi^*_1 \leftarrow \pi_4$	0.309

[a] Only contributions >0.05 have been tabulated. [b] Double excitation.

Adopting additional σ orbitals into the active space to account for π/σ correlation has proved effective in improving the description of the low-lying, electronically-excited ionic state in ethene,[283] but such a treatment is impractical here; the active space cannot be expanded without the calculations that employ it becoming computationally intractable.

It is apparent, then, that one has to go beyond the CASSCF approximation in order to describe the electronically-excited states of *E*- and *Z*-cinnamonitrile with even qualitative accuracy. SA4-CASSCF(12,12) is consequently unsuitable for use with TSHD: a) the overestimation of the energy of $S_2 \leftarrow S_0$ excitations would result in artificially-accelerated dynamics, and b) IC events would be described incorrectly. While uniform scaling of the energies and gradients could be used to address the former problem, a) the latter problem cannot be addressed in this way, b) the scaling factor would have to be considerably larger than what is generally considered appropriate, and c) the other states – described quantitatively well at the SA4-CASSCF(12,12) level – would be adversely impacted. An alternative treatment for use with TSHD is explored in Section 7.3.2.4.

Nonetheless, the SA4-CASSCF(12,12) treatment is still suitable for (comparatively) cheap exploration of the potential energy surface geography; minima on the S_1 potential energy surface can be fully optimised, as can a number of S_1/S_0 MECI. Robb *et al.*[316] concluded to this effect in their early theoretical work on styrene; the absence of dynamical and π/σ correlation in their CASSCF(8,8) treatment was expected to "*…affect the barrier heights… but not the existence (or otherwise) of the minima and intersections characterised…*".[316]

Their accurate prediction of the effect that inclusion of dynamical and π/σ correlation would have on the ordering of states appears to have been ahead-of-its-time, not least because the correct ordering of states had not yet been determined *via* experiment, nor does it appear that higher-level theoretical calculations existed for reference.

Where specific values are quoted in this section (Section 7.3), therefore, these have been computed at the SA4-CASSCF(12,12) level, unless otherwise indicated.

The reader should nonetheless remain mindful of the weaknesses of the SA4-CASSCF(12,12) treatment that have been revealed so far, and those that are revealed in subsequent sections (Sections 7.3.2.2 and 7.3.2.3).

7.3.2.1 Minima

C_s-symmetric, planar minima are located on the S_1 potential energy surface of *E*- and *Z*-cinnamonitrile; both have been fully optimised at the SA4-CASSCF(12,12), MR-CISD(6,6), and MS-CASPT2(12,12) levels. These minima are denoted *E*-S_1 and *Z*-S_1. Cartesian coordinates are tabulated in Tables B21–26 respectively. *E*-S_1 is located 0.25 eV below the corresponding S_1 Franck-Condon point at a distance of 36.3 pm $Da^{-½}$. Similarly, *Z*-S_1 is located 0.24 eV below the corresponding S_1 Franck-Condon point at a distance of 36.1 pm $Da^{-½}$. Accessing either *E*-S_1 or *Z*-S_1 from the corresponding Franck-Condon point requires relatively little structural reorganisation, and both are encountered directly along the natural S_1-state relaxation coordinate.

7.3.2.2 Twisted-Pyramidalised Conical Intersections

Four C_1-symmetric, twisted-pyramidalised S_1/S_0 MECI (*tp*MECI) – of the kind well-known to be involved in photoisomerisation of conjugated organic molecules – have been fully optimised at the SA4-CASSCF(12,12) level. Cartesian coordinates are tabulated in Tables B27–30. The geometries of all four *tp*MECI are characterised by being twisted about $r_{3,4}$ (*i.e.* $\phi_{2,3,4,5} \neq 180.0$, $\phi_{11,3,4,5}$ and $\phi_{12,4,3,2} \neq 0.0$) and pyramidalised at either the α (*i.e.* $a_{2,3,4}$ +

$a_{2,3,11} + a_{4,3,11} \neq 120.0$) or β (*i.e.* $a_{3,4,5} + a_{3,4,12} + a_{5,4,12} \neq 120.0$) position relative to the nitrile substituent.

The pyramidalisation is quantified here by the introduction of a pyramidalisation descriptor, $\theta_{\text{Pyr.}}$, defined as in Eq. 7.1, where *i* is the index of the pyramidalised position and *j*, *k*, and *l* are the indices of the neighbouring positions, as defined in Fig. 7.2.

$$\theta_{\text{Pyr.}} = 1 - \frac{a_{\text{j,i,k}} + a_{\text{j,i,l}} + a_{\text{k,i,l}}}{360.0} \qquad \textbf{Eq. 7.1}$$

There are four unique *tp*MECI – denoted *tp*MECI$_{E,\alpha}$, *tp*MECI$_{E,\beta}$, *tp*MECI$_{Z,\alpha}$, and *tp*MECI$_{Z,\beta}$, and illustrated in Fig. 7.7 – reflecting that pyramidalisation can proceed at either the α or β position, and that it can proceed either above or below the plane perpendicular to the plane of the benzyl subunit. Each *tp*MECI has a stereoisomer, reflecting that twisting about $r_{3,4}$ can proceed in either a clockwise or anticlockwise manner.

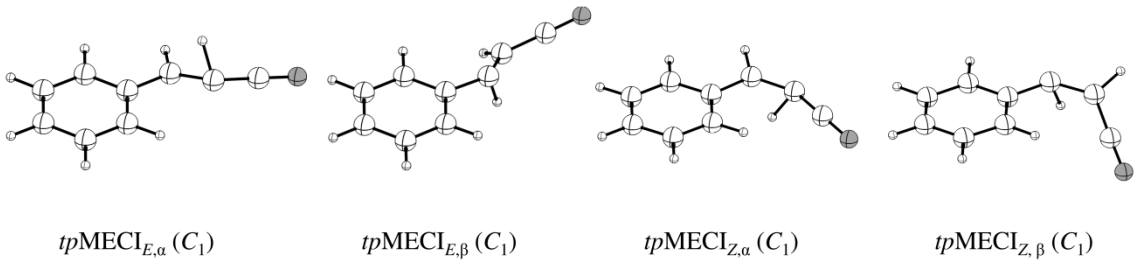

Figure 7.7. Geometries of C_1-symmetric, twisted-pyramidalised S_1/S_0 MECI, *tp*MECI$_{E,\alpha}$, *tp*MECI$_{E,\beta}$, *tp*MECI$_{Z,\alpha}$, and *tp*MECI$_{Z,\beta}$, as computed at the SA4-CASSCF(12,12) level.

Properties of interest for the four unique *tp*MECI are tabulated in Table 7.6.

Table 7.6. Summary of the properties of *tp*MECI as computed at the SA4-CASSCF(12,12) level. Geometric parameters ($\phi_{2,3,4,5}$, $\phi_{11,3,4,5}$, $\phi_{12,4,3,2}$,[a] and $\theta_{\text{Pyr.}}$[b]), relative energies, $E_{\text{Rel.}}$,[c] with respect to *E*-S_1 and *Z*-S_1, and distances[d] from *E*-S_1 and *Z*-S_1 are tabulated.

MECI	$\phi_{2,3,4,5}$	$\phi_{11,3,4,5}$	$\theta_{\text{Pyr.}}$	$E_{\text{Rel.}}$ *E*-S_1	$E_{\text{Rel.}}$ *Z*-S_1	Dist. *E*-S_1	Dist. *Z*-S_1
*tp*MECI$_{E,\alpha}$	159.5	72.3	0.143	1.12	1.05	365.4	1058.5
*tp*MECI$_{E,\beta}$	163.7	73.1	0.144	1.76	1.69	291.8	1290.6
MECI	$\phi_{2,3,4,5}$	$\phi_{12,4,3,2}$	$\theta_{\text{Pyr.}}$	$E_{\text{Rel.}}$ *E*-S_1	$E_{\text{Rel.}}$ *Z*-S_1	Dist. *E*-S_1	Dist. *Z*-S_1
*tp*MECI$_{Z,\alpha}$	23.9	67.2	0.118	1.35	1.28	1007.2	328.6
*tp*MECI$_{Z,\beta}$	26.4	65.5	0.132	1.81	1.73	1104.4	476.9

[a] Tabulated in degrees. [b] Defined in Eq. 7.1. [c] Tabulated in eV. [d] Tabulated in pm $Da^{-½}$.

*tp*MECI$_{Z,\alpha}$ and *tp*MECI$_{Z,\beta}$, being closer to *Z*-S_1 than to *E*-S_1, are not likely to be involved in the photoisomerisation of *E*-cinnamonitrile; they are discussed no further. Of *tp*MECI$_{E,\alpha}$ and *tp*MECI$_{E,\beta}$, the former is a) more stable, and b) well-known to be involved in the photoisomerisation of ethene,[119,282,284–286] stilbene,[119,282,287,288] and styrene;[317–320] it is therefore considered exclusively here. S_0, S_1, S_2, and S_3 potential energy surfaces between *E*-S_1 and *tp*MECI$_{E,\alpha}$ have been constructed *via* LIIC, and are presented in Fig. 7.8. Independent single-point-energy evaluations have been carried out on eight interpolated geometries at the SA4-CASSCF(12,12) and MS-CASPT2(12,12) levels.

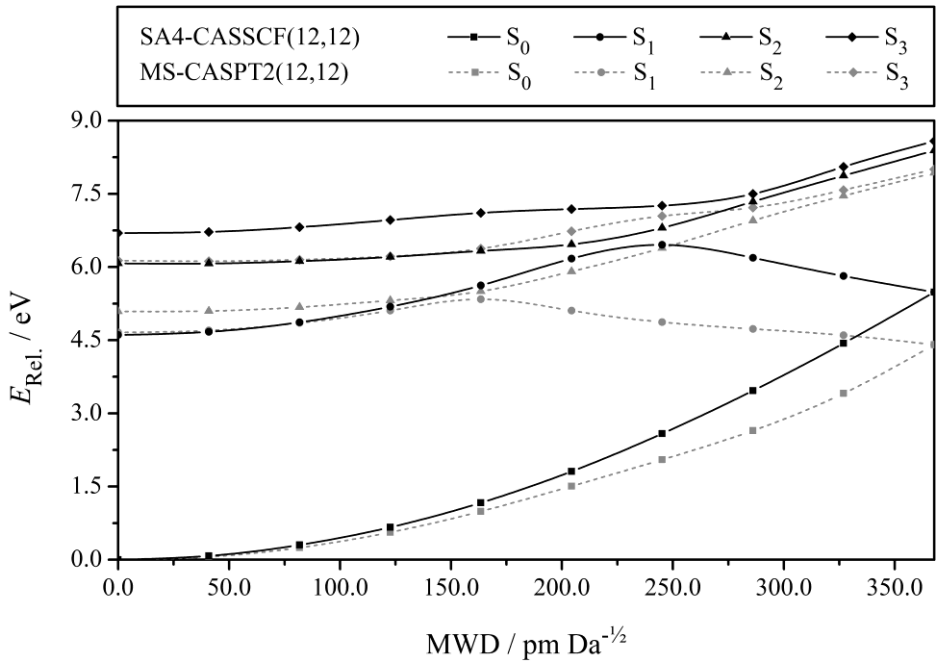

Figure 7.8. S_0, S_1, S_2, and S_3 potential energy surfaces between *E*-S_1 and *tp*MECI$_{E,\alpha}$, mapped *via* LIIC and computed at the SA4-CASSCF(12,12) and MS-CASPT2(12,12) levels. MS-CASPT2(12,12) calculations are carried out at SA4-CASSCF(12,12) geometries. The MS-CASPT2(12,12) energy at *tp*MECI$_{E,\alpha}$ is taken as the average of the S_0- and S_1-state energies to account for their non-degeneracy under this approximation.

A barrier exists to *tp*MECI$_{E,\alpha}$ at both at the SA4-CASSCF(12,12) and MS-CASPT2(12,12) levels, consistent with the observation of fluorescence for *E*-cinnamonitrile post-photoexcitation to the S_1 state.[303] The performance of the SA4-CASSCF(12,12) treatment is unsatisfactory in its description of this barrier; the position of the barrier relative to *E*-S_1 is incorrect [SA4-CASSCF(12,12), *ca.* 250 pm Da$^{-½}$; MS-CASPT2(12,12), *ca.* 160 pm Da$^{-½}$], as is the upper limit to the height of the barrier [SA4-CASSCF(12,12), *ca.* 1.85 eV; MS-CASPT2(12,12), *ca.* 0.70 eV].

At the SA4-CASSCF(12,12) level, where the incorrect ordering of states is obtained (Tables 7.4 and 7.5), the barrier originates from a crossing with the mixed $\pi^*_1 \leftarrow \pi_6$ / $\pi^*_3 \leftarrow \pi_6$ / $\pi^*_1 \leftarrow \pi_4$ state; at the MS-CASPT2(12,12) level, the crossing is, instead, with the $\pi^*_1 \leftarrow \pi_6$ state. Nonetheless, at both the SA4-CASSCF(12,12) and MS-CASPT2(12,12) levels, the following is true: crossing over the barrier induces polarisation that is indicative of the development of ionic character in the S_1-state wavefunction.[119,317]

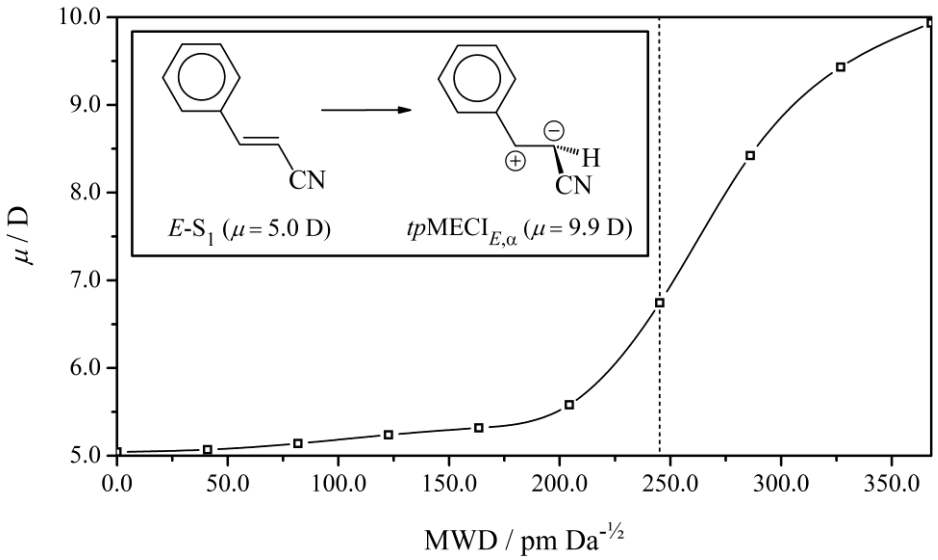

Figure 7.9. Evolution of the S_1-state dipole moment, μ, between *E*-S_1 and *tp*$MECI_{E,\alpha}$, mapped *via* LIIC and computed at the SA4-CASSCF(12,12) level. The dotted line indicates the position of the barrier as computed at the SA4-CASSCF(12,12) level. The insert depicts the structures of *E*-S_1 and *tp*$MECI_{E,\alpha}$.

Indeed, the characters of the S_1, S_2, and S_3 states at *tp*$MECI_{E,\alpha}$, tabulated in Table 7.7, are considerably different to their characters at the Franck-Condon point/*E*-S_0 (Table 7.5).

The character of the S_1 state at *tp*$MECI_{E,\alpha}$ is ionic, and dominated by the $\pi^*_1 \leftarrow \pi_6$ excitation (the other dominant component being the unexcited, closed-shell configuration). As is the case for the vertical excitation energies (Table 7.4), the relative energy of *tp*$MECI_{E,\alpha}$ is overestimated, being placed 0.88 and 1.12 eV above the S_1 Franck-Condon point and *E*-S_1, respectively. At the MS-CASPT2(12,12) level, *tp*$MECI_{E,\alpha}$ is located (at least) 0.13 eV below the S_1 Franck-Condon point and (at most) 0.11 eV above *E*-S_1 (*via* single-point energy evaluation at the SA4-CASSCF(12,12) geometry of *tp*$MECI_{E,\alpha}$), respectively. Were *tp*$MECI_{E,\alpha}$ to be fully optimised at the MS-CASPT2(12,12) level, it is highly likely that it would be located at lower energy than *E*-S_1.

Table 7.7. Summary of the contributions[a] of excited configurations to the electronically-excited states of *tp*MECI, as computed at the SA4-CASSCF(12,12) level.

		*tp*MECI$_{E,\alpha}$	*tp*MECI$_{E,\beta}$	*tp*MECI$_{Z,\alpha}$	*tp*MECI$_{Z,\beta}$
State	Excitation	Weight	Weight	Weight	Weight
S_1	$\pi^*_1 \leftarrow \pi_6$	0.723	0.419	0.623	0.598
S_2	$\pi^*_1 \leftarrow \pi_6$[b]		0.125		0.136
	$\pi^*_2 \leftarrow \pi_6$		0.121		0.094
	$\pi^*_3 \leftarrow \pi_6$	0.296		0.275	
	$\pi^*_1 \leftarrow \pi_4$		0.204		0.251
	$\pi^*_1 \leftarrow \pi_6$ / $\pi^*_1 \leftarrow \pi_5$	0.357		0.332	
S_3	$\pi^*_2 \leftarrow \pi_6$	0.346		0.330	
	$\pi^*_3 \leftarrow \pi_6$		0.115		0.082
	$\pi^*_1 \leftarrow \pi_5$		0.321		0.398
	$\pi^*_1 \leftarrow \pi_6$ / $\pi^*_1 \leftarrow \pi_4$	0.287		0.271	

[a] Only contributions >0.05 have been tabulated. [b] Double excitation.

It may even be the global minimum on the S_1 potential energy surface, as has been speculated by Quenneville and Martínez[282] for the *tp*MECI of stilbene. Attempts to fully optimise a minimum in the vicinity of *tp*MECI$_{E,\alpha}$ are successful at the SA4-CASSCF(12,12) level and resolve to a minimum-energy, twisted-pyramidalised geometry with $\phi_{2,3,4,5}$ = 71.7 and $\theta_{Pyr.}$ = 0.056, located 664.6 pm Da$^{-½}$ from *tp*MECI$_{E,\alpha}$, but are unsuccessful at the MS-CASPT2(12,12) level. In the latter case, convergence criteria are not met, but optimisations resolve towards geometries where $\Delta E(S_1,S_0)$ <0.1 eV; these geometries are likely to be good approximations to *tp*MECI$_{E,\alpha}$ at the MS-CASPT2(12,12) level or, at least, to geometries that lie on the crossing seam. Indeed, the key structural differences (a larger $\phi_{2,3,4,5}$ and $\theta_{Pyr.}$) found between these MS-CASPT2(12,12) geometries and the geometry of *tp*MECI$_{E,\alpha}$ at the SA4-CASSCF(12,12) level are in line with those found between the CASPT2 and CASSCF geometries of the key *tp*MECI in stilbene.[282]

In any case, a large dynamical correlation differential exists both "*horizontally*" along the pathway between *E*-S_1 and *tp*MECI$_{E,\alpha}$ and "*vertically*" between the manifold of electronically-excited states. The different correlation requirements of the ionic and covalent states cannot be met by the SA4-CASSCF(12,12) treatment, which underperforms at all points of interest. The reader should be satisfied, at this point, that the poor performance of the SA4-CASSCF(12,12) treatment for this application is pathological, and it is consequently unsuitable for use with TSHD. An alternative treatment for use with TSHD is explored in Section (7.3.2.4).

A final noteworthy consequence of the character of the S_1 state being dominated by the $\pi^*_1 \leftarrow \pi_6$ excitation and the unexcited, closed-shell configuration at *tp*MECI is that the full SA4-CASSCF(12,12) treatment need not be used to locate *tp*MECI in the first instance. A SA2-CASSCF(2,2) treatment – in which the five highest- and lowest-lying orbitals ($\pi_1 - \pi_5$ and $\pi^*_2 - \pi^*_6$, respectively; Fig. 7.6) are discarded, leaving only π_6 and π^*_1 in the active space, and in which state averaging is carried out over the two lowest-energy singlet states – is sufficient. In fact, a SA4-CASSCF(6,6) treatment is sufficient to compute the pathway between *E*-S_1 and any of the *tp*MECI with qualitative accuracy that the SA4-CASSCF(12,12) treatment cannot improve on. The computational cost is correspondingly reduced from hours/days to minutes. The comprehensive *ab initio* work of Amatatsu[318–320] on styrene in the small-active-space limit is testament to this.

7.3.2.3 Prefulvene-Like Conical Intersections

Four C_1-symmetric, prefulvene-like S_1/S_0 MECI (*pf*MECI) – analogous to the prefulvene form of benzene – have been fully optimised at the SA4-CASSCF(12,12) level. Cartesian coordinates are tabulated in Tables B31–34. The geometries of *pf*MECI are characterised by non-planar/puckered benzyl subunits, and can consequently be labelled uniquely according to Cremer-Pople notation;[321] the four *pf*MECI are denoted *pf*MECI$_E$ **E$_5$**, *pf*MECI$_E$ **E$_7$**, *pf*MECI$_E$ **E$_8$**, and *pf*MECI$_E$ **E$_9$**, and illustrated in Fig. 7.10. *pf*MECI$_E$ **E$_6$** and *pf*MECI$_E$ **E$_{10}$** could not be optimised. No attempts were made to optimise the corresponding *pf*MECI$_Z$ **E$_5$**, *pf*MECI$_Z$ **E$_7$**, *pf*MECI$_Z$ **E$_8$**, and *pf*MECI$_Z$ **E$_9$**, although there is no reason to assume that they do not exist.

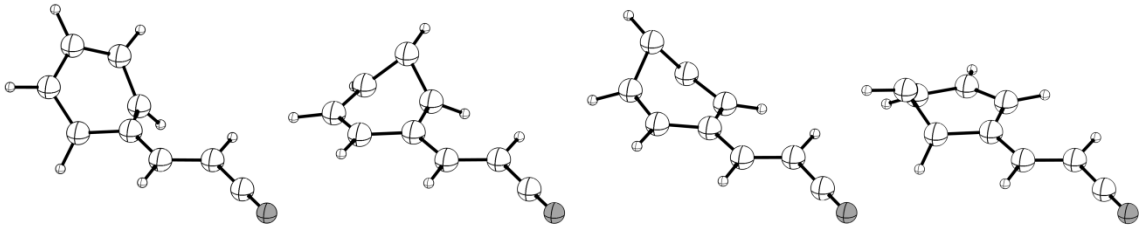

Figure 7.10. Geometries of C_1-symmetric, prefulvene-like S_1/S_0 MECI, *pf*MECI$_E$ **E$_5$**, *pf*MECI$_E$ **E$_7$**, *pf*MECI$_E$ **E$_8$**, and *pf*MECI$_E$ **E$_9$**, as computed at the SA4-CASSCF(12,12) level.

The Cremer-Pople descriptors (Q, θ, and φ)[321] and other properties of interest for the *pf*MECI are tabulated in Table 7.8.

Table 7.8. Summary of the properties of *pf*MECI as computed at the SA4-CASSCF(12,12) level. Cremer-Pople descriptors (Q,[a] θ,[b] and φ[c]),[321] relative energies, $E_{\text{Rel.}}$,[d] with respect to E-S_1, and distances[e] from E-S_1 are tabulated.

MECI	Q	θ	φ	$E_{\text{Rel.}}$ (E-S_1)	Dist. (E-S_1)
*pf*MECI$_E$ **E$_5$**	0.62	60.1	0.2	0.61	490.3
*pf*MECI$_E$ **E$_7$**	0.65	60.8	119.0	0.78	345.8
*pf*MECI$_E$ **E$_8$**	0.66	118.9	359.3	1.03	385.7
*pf*MECI$_E$ **E$_9$**	0.65	61.0	241.6	0.83	336.9

[a] Q is the magnitude of puckering.[321] [b] θ is the azimuthal angle in the spherical polar representation of the Cremer-Pople descriptors,[321] and is tabulated in degrees. [c] φ is the meridional angle in the spherical polar representation of the Cremer-Pople descriptors,[321] and is tabulated in degrees. [d] Tabulated in eV. [e] Tabulated in pm $Da^{-½}$.

S_0, S_1, S_2, and S_3 potential energy surfaces between E-S_1 and all four *pf*MECI have been constructed *via* LIIC, and are presented in Fig. 7.11. Independent single-point-energy evaluations have been carried out on eight interpolated geometries at the SA4-CASSCF(12,12) and MS-CASPT2(12,12) levels.

The S_2 and S_3 states are well-displaced from the S_0 and S_1 states at all four *pf*MECI, and the latter two states, being covalent in character (*cf. tp*MECI; Section 7.3.2.2), are described quantitatively accurately at the SA4-CASSCF(12,12) level with respect to the higher-level MS-CASPT2(12,12) calculations. Barriers exist on the S_1 potential energy surface between E-S_1 and *pf*MECI$_E$ **E$_5$**, *pf*MECI$_E$ **E$_7$**, *pf*MECI$_E$ **E$_8$**, and *pf*MECI$_E$ **E$_9$** of (at most) 1.31, 1.22, 1.28, and 1.19 eV, respectively; the barriers are found at *ca.* 270, 190, 250, and 180 pm $Da^{-½}$ from E-S_1, respectively.

The upper limit to the barrier height as approximated *via* LIIC predictably transpires to be a sizeable overestimation of the actual barrier height. For *pf*MECI$_E$ **E$_5$** and *pf*MECI$_E$ **E$_8$**, the corresponding transition states, *pf*MECI$_{E,\text{TS}}$ **E$_5$** and *pf*MECI$_{E,\text{TS}}$ **E$_8$**, have been fully optimised at the SA4-CASSCF(12,12) level. Cartesian coordinates are tabulated in Tables B35 and B36. *pf*MECI$_{E,\text{TS}}$ **E$_5$** and *pf*MECI$_{E,\text{TS}}$ **E$_8$** are located 31.5 and 66.5 pm $Da^{-½}$ from *pf*MECI$_E$ **E$_5$** and *pf*MECI$_E$ **E$_8$**, respectively, and present barriers of 0.62 and 0.64 eV, respectively, to accessing the corresponding *pf*MECI from E-S_1.

With respect to *tp*MECI$_{E,\alpha}$ and *tp*MECI$_{E,\beta}$ (Section 7.3.2.2), *pf*MECI are not necessarily located any further from E-S_1, but are a) found at higher energy, b) present greater barriers to access, and c) are not located along the natural S_1-state relaxation coordinate.

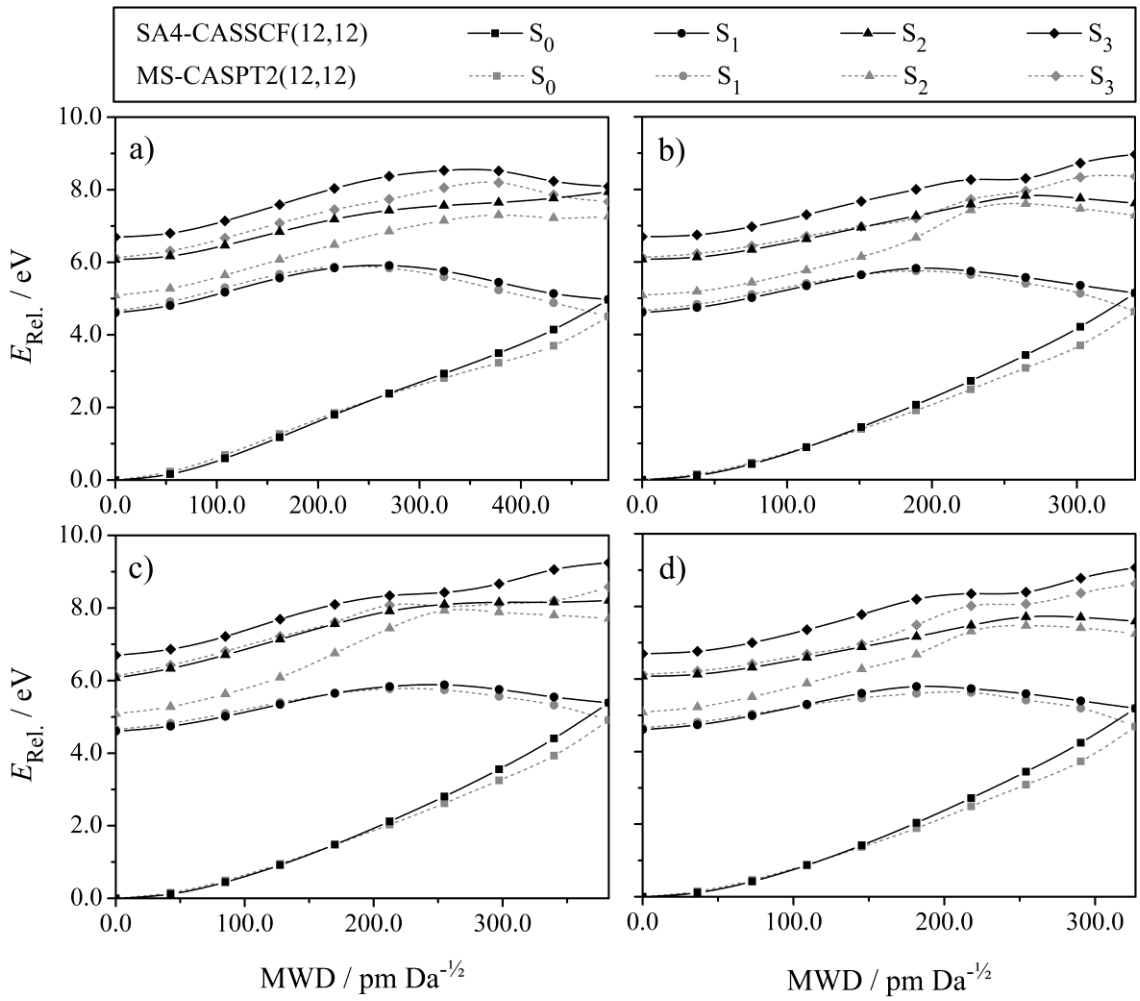

Figure 7.11. S_0, S_1, S_2, and S_3 potential energy surfaces between *E*-S_1 and a) *pf*MECI$_E$ **E$_5$**, b) *pf*MECI$_E$ **E$_7$**, c) *pf*MECI$_E$ **E$_8$**, and d) *pf*MECI$_E$ **E$_9$**, mapped *via* LIIC and computed at the SA4-CASSCF(12,12) and MS-CASPT2(12,12) levels. MS-CASPT2(12,12) calculations are carried out at SA4-CASSCF(12,12) geometries. The MS-CASPT2(12,12) energies at *pf*MECI$_E$ **E$_5$**, *pf*MECI$_E$ **E$_7$**, *pf*MECI$_E$ **E$_8$**, and *pf*MECI$_E$ **E$_9$** are taken as the average of the S_0- and S_1-state energies to account for their non-degeneracy under this approximation.

In the former cases, the reader is reminded that the energies of *tp*MECI$_{E,\alpha}$ and *tp*MECI$_{E,\beta}$, being ionic in character, are considerably overestimated at the SA4-CASSCF(12,12) level, but are described more correctly at the MS-CASPT2(12,12) level (Section 7.3.2.2).

Accordingly, $S_0 \leftarrow S_1$ IC *via pf*MECI is not to be expected post-photoexcitation to the low-lying electronically-excited states considered here. It has been explored nonetheless because $S_0 \leftarrow S_1$ IC *via* a MECI similar to *pf*MECI$_E$ **E$_5$** has been suggested by Robb *et al.* in both their theoretical[316] and experimental[322] work on styrene, and because $S_0 \leftarrow S_1$ IC *via pf*MECI has the potential to be highly efficient if sufficient energy is available that *pf*MECI

are made accessible, *e.g.* if the S_1 state has been accessed indirectly some time after initial photoexcitation to a higher-lying electronically-excited state. This kind of excitation could be promoted in the atmosphere of Titan by high-energy solar photons[296–298,304] (Section 7.1), and open up new parts of the S_0-state potential energy surface.

In contemporary high-level theoretical work on aniline by Fielding *et al.*,[323] it has been suggested that $S_0 \leftarrow S_1$ IC *via pf*MECI could lead to an S_0-state minimum analogous to the Dewar form of benzene.

7.3.3 Assessment of the ADC(2)/MP2 Treatment

The unsuitability of the SA4-CASSCF(12,12) treatment for this application (Section 7.3.2) and the prohibitively-high computational cost of the obvious multireference alternatives, *e.g.* MR-CISD or MS-CASPT2, demands a new approach. The (single-reference) ADC(2)/MP2 treatment, where the S_0 state is computed at the MP2 level and the electronically-excited S_1, S_2 and S_3 states are computed *via* the ADC(2) scheme, gives an acceptable balance of computational cost and accuracy. The ADC(2)/MP2 treatment is evaluated in this section with respect to what has already been learnt about *E*- and *Z*-cinnamonitrile at the SA4-CASSCF(12,12), MR-CISD(6,6), and MS-CASPT2(12,12) levels in the previous section (Section 7.3.2). The strengths and weaknesses of the ADC(2)/MP2 treatment are highlighted. The former are many (Sections 7.3.3.1 – 7.3.3.3) and, by comparison with the SA4-CASSCF(12,12) treatment, the latter are more manageable, although their management comes at the cost of the amount of information one can obtain about the photoisomerisation dynamics – the bifurcation of the nuclear wavepacket at *tp*MECI$_{E,\alpha}$, for example, cannot be reliably recorded, and $S_0 \leftarrow S_1$ IC can only be estimated, as TSHD has to be terminated at the crossing seam (Section 7.3.4).

7.3.3.1 Minima

E-S_0, *E*-S_1, *Z*-S_0, and *Z*-S_1 have been fully optimised at the ADC(2)/MP2 level. Cartesian coordinates are tabulated in Tables B37–40. Vertical transition energies and oscillator strengths are tabulated in Table 7.9 for transitions to the S_1, S_2, and S_3 states that originate from *E*-S_0 and *Z*-S_0.

ADC(2)/MP2 performs qualitatively well for all excitations with respect to the higher-level MR-CISD(6,6) and MS-CASPT2(12,12) calculations (Section 7.3.2), particularly in the case of the $S_2 \leftarrow S_0$ excitation, where quantitative performance is attained.

Table 7.9. Summary of vertical transition energies, ΔE,[a] and oscillator strengths, f, for E-S_0 and Z-S_0 as computed at the ADC(2)/MP2 level.

	ADC(2)/MP2	
Transition	ΔE	f
$S_1 \leftarrow S_0$ (E-S_0)	4.78	0.05
$S_1 \leftarrow S_0$ (Z-S_0)	4.73	0.04
$S_2 \leftarrow S_0$ (E-S_0)	5.01	0.80
$S_2 \leftarrow S_0$ (Z-S_0)	4.95	0.59
$S_3 \leftarrow S_0$ (E-S_0)	6.40	0.33
$S_3 \leftarrow S_0$ (Z-S_0)	6.36	0.27

[a] All transition energies are tabulated in eV.

The reader should note that the correct energetic ordering of the $S_2 \leftarrow S_0$ and $S_3 \leftarrow S_0$ excitations is recovered. As in Section 7.3.2, this is apparent from inspection of both the oscillator strengths for the corresponding transitions and the characters of the S_2 and S_3 states as calculated at the ADC(2)/MP2 level. The latter are tabulated in Table 7.10.

Table 7.10. Summary of the contributions[a] of excited configurations to the electronically-excited states of E-S_0 and Z-S_0 as computed at the ADC(2)/MP2 level.

	ADC(2)/MP2	
State	Excitation	Weight
S_1 (E-S_0)	$\pi^*_2 \leftarrow \pi_6$	0.292
	$\pi^*_1 \leftarrow \pi_5$	0.568
S_1 (Z-S_0)	$\pi^*_2 \leftarrow \pi_6$	0.253
	$\pi^*_1 \leftarrow \pi_5$	0.640
S_2 (E-S_0)	$\pi^*_1 \leftarrow \pi_6$	0.902
S_2 (Z-S_0)	$\pi^*_1 \leftarrow \pi_6$	0.928
S_3 (E-S_0)	$\pi^*_2 \leftarrow \pi_6$	0.563
	$\pi^*_1 \leftarrow \pi_5$	0.343
S_3 (Z-S_0)	$\pi^*_2 \leftarrow \pi_6$	0.578
	$\pi^*_1 \leftarrow \pi_5$	0.297

[a] Only contributions >0.1 have been tabulated.

The $S_1 \leftarrow S_0$ and $S_3 \leftarrow S_0$ excitations are slightly overestimated at the ADC(2)/MP2 level with respect to the higher-level MR-CISD(6,6) and MS-CASPT2(12,12) calculations (Section 7.3.2) on account of their higher degree of double-excitation character. The doubly-excited configuration is missing from the character of the S_3 state at the ADC(2)/MP2 level, resulting in an $S_3 \leftarrow S_0$ excitation at E-S_0 that is overestimated by 0.36

and 0.41 eV with reference to the higher-level MR-CISD(6,6) and MS-CASPT2(12,12) calculations, respectively. The overestimation of the $S_1 \leftarrow S_0$ excitation at *E*-S_0 (by 0.23 and 0.19 eV with reference to the higher-level MR-CISD(6,6) and MS-CASPT2(12,12) calculations, respectively) is less significant, reflecting the smaller contribution of doubly-excited configurations to the character of the S_1 state.

The placement of the S_2 state with respect to the S_1 state is computed accurately with respect to spectroscopic measurements at the ADC(2)/MP2 level; further improvement is anticipated beyond the small-basis limit. Zwier *et al.*[303] have reported "*…absorptions that carry significant oscillator strength in the region from 35500 cm*$^{-1}$ [*ca.* 4.40 eV] *onward, but do not fluoresce…*"[303] in the fluorescence spectrum of *E*-cinnamonitrile, consistent with $S_2 \leftarrow S_0$ excitation (although not labelled accordingly by Zwier *et al.*). Fluorescence is supressed and ultrafast IC takes over *ca.* 1600 cm^{-1} (0.20 eV) above the adiabatic $S_1 \leftarrow S_0$ transition energy.[303] As there are no minima on the S_2 potential energy surface and, consequently, neither an adiabatic $S_2 \leftarrow S_0$ or $S_2 \leftarrow S_1$ transition energy can be computed for direct comparison with spectroscopic measurement, the difference in energy between the S_1 and S_2 states at *E*-S_1 (Table 7.11) has been taken as an approximation to the additional energy above the adiabatic $S_1 \leftarrow S_0$ transition (Table 7.11) required to supress fluorescence. This value – corresponding to a vertical $S_2 \leftarrow S_1$ transition – consequently represents an upper bound to the additional energy required, and gives an upper bound to the $S_2 \leftarrow S_0$ transition energy after addition of the adiabatic $S_1 \leftarrow S_0$ transition. It is computed as 2508 cm^{-1} (0.30 eV; Table 7.11) at the ADC(2)/MP2 level – an improvement with respect to spectroscopic measurement on the same quantity as computed at either the MR-CISD(6,6) (6065 cm^{-1}; 0.45 eV) or MS-CASPT2(12,12) (4460 cm^{-1}; 0.52 eV) levels.

Table 7.11. Summary of adiabatic $S_1 \leftarrow S_0$ transition energies and vertical $S_2 \leftarrow S_1$ transition energies at *E*-S_1 and *Z*-S_1, ΔE,[a] as computed at the ADC(2)/MP2, MR-CISD(6,6) and MS-CASPT2(12,12) levels. Data from Zwier *et al.*[303] are additionally tabulated.

	Spectr.[303]	ADC(2)/MP2	MR-CISD(6,6)	MS-CASPT2(12,12)
Transition	ΔE	ΔE	ΔE	ΔE
E-$S_1 \leftarrow$ *E*-S_0	33,827	36,970 (*4.58*)	34,844 (*4.32*)	35,336 (*4.38*)
Z-$S_1 \leftarrow$ *Z*-S_0	33,707	36,529 (*4.52*)	34,623 (*4.29*)	35,235 (*4.38*)
$S_2 \leftarrow S_1$ (*E*-S_1)	≈ 1600	2508 (*0.31*)	6065 (*0.75*)	4460 (*0.55*)
$S_2 \leftarrow S_1$ (*Z*-S_1)	–	2646 (*0.33*)	5880 (*0.73*)	4186 (*0.52*)

[a] All transition energies are tabulated in cm^{-1}; values in parentheses are tabulated in eV.

7.3.3.2 Twisted-Pyramidalised Conical Intersections

*tp*MECI$_{E,\alpha}$ – identified as the most important *tp*MECI in Section 7.3.2 – has been fully optimised at the ADC(2)/MP2 level as described in Section 7.3.1. Cartesian coordinates are tabulated in Table B41. S_0, S_1, S_2, and S_3 potential energy surfaces between *E*-S_1 and *tp*MECI$_{E,\alpha}$ have been constructed *via* LIIC, and are presented in Fig. 7.12a. Independent single-point-energy evaluations have been carried out on eight interpolated geometries at the ADC(2)/MP2 level. The D_1 diagnostic for the ADC(2)/MP2 treatment has also been evaluated at each point, and its evolution between *E*-S_1 and *tp*MECI$_{E,\alpha}$ is presented in Fig. 7.12b.

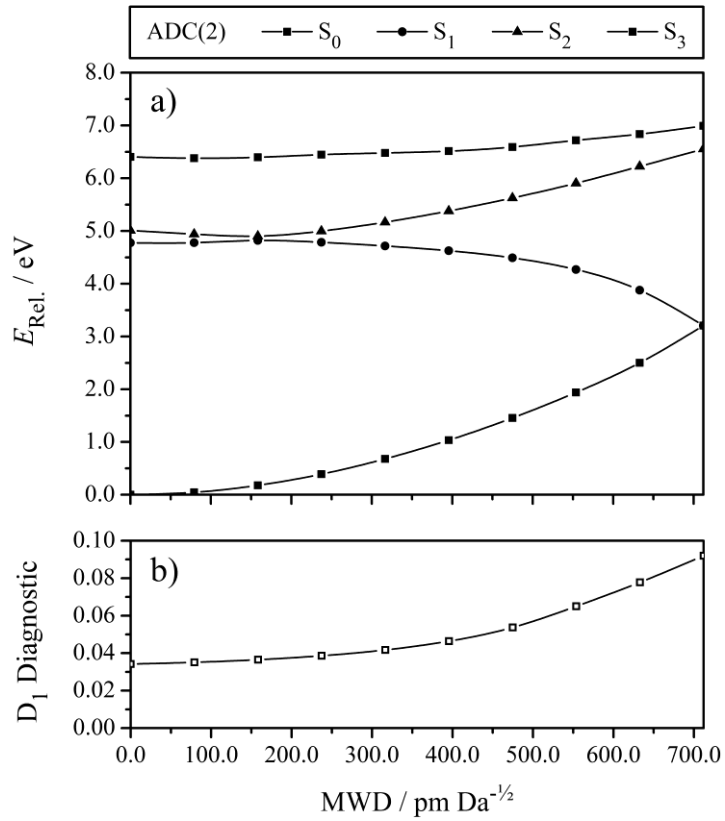

Figure 7.12. a) S_0, S_1, S_2, and S_3 potential energy surfaces and b) the evolution of the D_1 diagnostic between *E*-S_1 and *tp*MECI$_{E,\alpha}$, mapped *via* LIIC and computed at the ADC(2)/MP2 level.

*tp*MECI$_{E,\alpha}$ is characterised by greater twisting about $r_{3,4}$ ($\phi_{2,3,4,5}$ = 113.6°; $\phi_{11,3,4,5}$ = 82.2°) and a smaller pyramidalisation descriptor ($\theta_{Pyr.}$ = 0.022) at the ADC(2)/MP2 level with respect to its counterpart at the SA4-CASSCF(12,12) level, placing *tp*MECI$_{E,\alpha}$ at almost twice the distance (712.1 pm Da$^{-½}$) from *E*-S_1. The geometric differences are in line with

those predicted to be found between *tp*MECI$_{E,\alpha}$ as computed at the SA4-CASSCF(12,12) and MS-CASPT2(12,12) levels (Section 7.3.2.2); the geometry of *tp*MECI$_{E,\alpha}$ at the ADC(2)/MP2 level is a closer approximation to the latter, which is probably also located considerably further from *E*-S_1, than the former.

The barrier between *E*-S_1 and *tp*MECI$_{E,\alpha}$ is suppressed at the ADC(2)/MP2 level with respect to the higher-level MS-CASPT2(12,12) calculations, requiring only 0.24 eV of additional energy above *E*-S_1 to surmount, and is almost submerged relative to the S_1 Franck-Condon point. It is possible that the barrier is over-supressed at the ADC(2)/MP2 level, but a) a barrier of 0.24 eV is in quantitative agreement with the additional *ca.* 0.20 eV necessary to trigger ultrafast IC (spectroscopically measured by Zwier *et al.*;[303] Section 7.3.3.1), and b) low enough to be consistent with the observation of Zwier *et al.*[303] that photoisomerisation is possible even when the adiabatic $S_1 \leftarrow S_0$ transition is pumped and no excess energy is provided, although photoisomerisation (in this case) probably occurs metadynamically.

The evolution of the D_1 diagnostic is exactly as expected. According to the recommendation of Barbatti, Crespo-Otero, and Plasser *et al.*[117,152] (this being that a D_1 diagnostic below *ca.* 0.06 is acceptable, with the caveat being that this is highly system-dependent), the quality of the ADC(2)/MP2 treatment remains acceptable at, and beyond, the barrier. This is important for high-quality TSHD (Section 7.3.5). Köhn and Hättig[311,312] have suggested that, in some cases, D_1 diagnostic values up to 0.15 may still be acceptable, but this recommendation does not merit acknowledgement here; at *tp*MECI$_{E,\alpha}$, the S_0 state is clearly no longer able to be described well with a single reference, and here a D_1 diagnostic of 0.09 is computed.

The ADC(2)/MP2 treatment is promising for use with TSHD (Section 7.3.4). The reader can be satisfied with the quality of TSHD on the S_2 and S_1 potential energy surfaces as these states are well-described by singly-excited configurations, and TSHD on the S_3 potential energy surface might be expected to have – at least – qualitative accuracy.

7.3.3.3 Conical Intersections Between Higher-Lying States

The correct energetic ordering of the $S_2 \leftarrow S_0$ and $S_3 \leftarrow S_0$ excitations at the ADC(2)/MP2 level permitted a search for S_3/S_2 MECI and S_2/S_1 MECI for the first time. Two MECI, denoted *pl*MECI$_{E,2\leftarrow3}$ and *pl*MECI$_{E,1\leftarrow2}$, respectively, have been fully optimised for *E*-cinnamonitrile; no attempts were made to locate the corresponding *pl*MECI$_{Z,2\leftarrow3}$ and

*pl*MECI$_{Z,1\leftarrow2}$ for *Z*-cinnamonitrile but, as for *tp*MECI$_Z$ (Section 7.3.2.3), there is no reason to assume that they do not exist. Cartesian coordinates are tabulated in Tables B42 and B43.

*pl*MECI$_{E,1\leftarrow2}$ is C_s-symmetric and planar; it is found 0.33 eV below the S_2 Franck-Condon point at a distance of 43.7 pm Da$^{-½}$. $S_1 \leftarrow S_2$ IC should be expected to be ultrafast (on the order of femtoseconds), as *pl*MECI$_{E,1\leftarrow2}$ is encountered along the natural S_2-state relaxation coordinate. *pl*MECI$_{E,2\leftarrow3}$, similarly, is C_s-symmetric and planar; it is found 0.46 eV below the S_3 Franck-Condon point at a distance of 46.6 pm Da$^{-½}$. *pl*MECI$_{E,2\leftarrow3}$ is not encountered along the natural S_3-state relaxation coordinate; $S_2 \leftarrow S_3$ IC *via* *pl*MECI$_{E,2\leftarrow3}$ is consequently likely to be slower than $S_1 \leftarrow S_2$ IC *via* *pl*MECI$_{E,1\leftarrow2}$, but should still be ultrafast (on the order of tens or hundreds of femtoseconds) on account of the proximity of the intersection to the S_3 Franck-Condon point.

7.3.4 Trajectory Surface-Hopping Dynamics

TSHD simulations were recorded at the ADC(2)/MP2 level using NEWTON-X v2.0[267,268] interfaced with TURBOMOLE v6.3.1.[308] All analytical gradients were computed on-the-fly by routines integrated into TURBOMOLE v6.3.1;[311,312] non-adiabatic transition probabilities were accounted for using the augmented fewest-switches algorithm of Hammes-Schiffer and Tully,[140,141] as implemented in NEWTON-X.[267,268]

Each member of a Wigner-distributed ensemble containing 100 independent S_0-state starting geometries was transformed into each of the S_1, S_2, and S_3 states.[274] The S_1, S_2, and S_3 excitation bands, each having widths of *ca.* 1.0 eV, are indicated by shaded overlays on top of a UV absorption spectra computed at the ADC(2)/MP2 level (Fig. 7.13).

270 independent trajectories were obtained (100 starting in each of the S_2 and S_3 states, and 70 starting in the S_1 state) by propagating each geometry through time for 750 fs. The nuclei were propagated *via* integration of Newton's classical equations in time steps of 0.5 fs using the velocity-Verlet algorithm.[231] The time-dependent Schrödinger equation was integrated in time steps of 0.025 fs using the classical fourth-order Runge-Kutta algorithm. The decoherence parameter, α, was set to 0.1 a.u. As the ADC(2)/MP2 treatment was not expected to handle correctly crossings between the S_1 and S_0 states and, consequently, give qualitatively-correct dynamics thereafter, a killswitch was implemented to terminate trajectories where $\Delta E(S_1,S_0) < 0.1$ eV according to the recommendation of Barbatti, Crespo-Otero, and Plasser *et al.*[117,152] $S_0 \leftarrow S_1$ IC was assumed to take place when the killswitch was triggered.

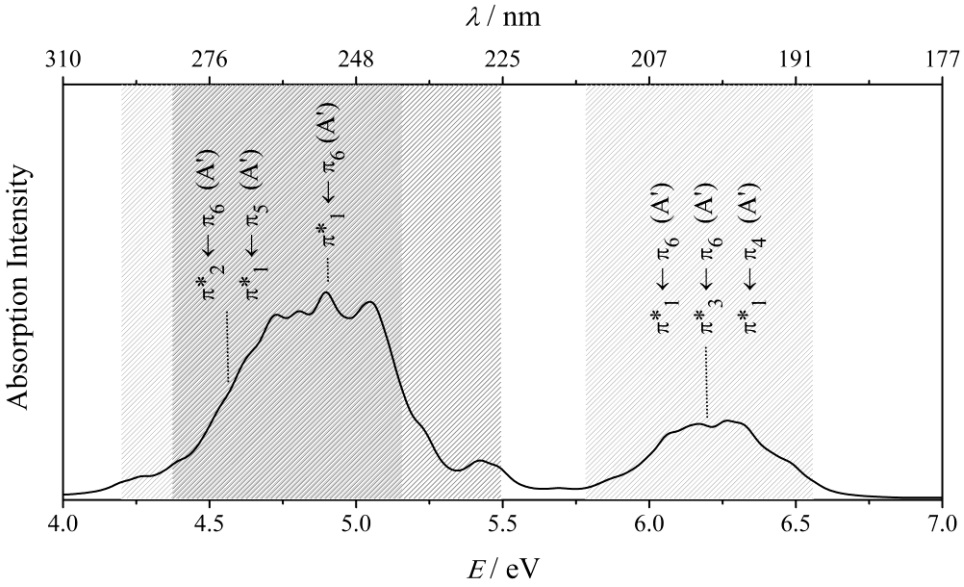

Figure 7.13. UV absorption spectra of *E*-cinnamonitrile as computed at the ADC(2)/MP2 level. The lighter and darker shaded overlays correspond to the S_1 and S_3 excitation bands, and the bright S_2 excitation band, respectively, for the Wigner-distributed ensemble.

7.3.5 Discussion

The nuclear and electronic dynamics are summarised in Sections 7.3.5.1 and 7.3.5.2, respectively.

7.3.5.1 Nuclear Dynamics

In TSHD initiated from the S_3 state, $S_2 \leftarrow S_3$ IC and $S_1 \leftarrow S_2$ IC occur *via* $pl\text{MECI}_{E,2\leftarrow3}$ and $pl\text{MECI}_{E,1\leftarrow2}$, respectively, with IC events occurring, on average, 186.3 ± 60.0 and 227.2 ± 66.1 pm $Da^{-½}$ from the corresponding intersection. Similarly, in TSHD initiated from the S_2 state, $S_1 \leftarrow S_2$ IC is *via* $pl\text{MECI}_{E,1\leftarrow2}$, with IC events occurring, on average, 161.2 ± 50.4 pm $Da^{-½}$ from the intersection. TSHD clarifies that $pl\text{MECI}_{E,2\leftarrow3}$ and $pl\text{MECI}_{E,1\leftarrow2}$ are the only MECI that are important when considering indirect accessing of the S_1 state from above. This can be illustrated in a visually-intuitive manner *via* least-squares alignment and overlay of the geometries at which IC is recorded, as in Fig. 7.14. Geometries at which $S_1 \leftarrow S_2$ IC is recorded in TSHD initiated from the S_2 and S_3 states are overlaid in Fig. 7.14a and 7.14d, respectively; geometries at which $S_2 \leftarrow S_3$ IC is recorded in TSHD initiated from the S_3 state are overlaid in Fig. 7.14c. All are planar to good approximation.

Geometries at which $S_0 \leftarrow S_1$ IC is recorded in TSHD initiated from the S_2 and S_3 states are overlaid in Fig. 7.14b and 7.14e, respectively. All correspond to $tp\text{MECI}_{E,\alpha}$. On inspection

of Fig. 7.14b and 7.14e, the reader will note that $r_{2,3}$ and $r_{3,11}$ can be found either above or below the plane of the benzyl subunit, indicating that twisting about $r_{3,4}$ can proceed in either a clockwise or anticlockwise manner to give the two possible stereoisomers of *tp*MECI$_{E,\alpha}$ and, indeed, that it does so with equal probability when the starting geometries and velocities are seeded randomly from the Wigner distribution.

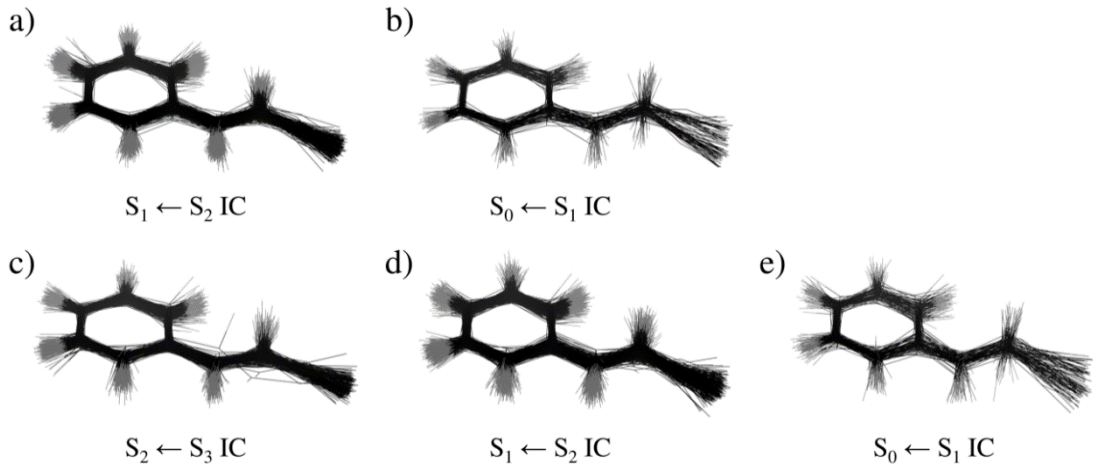

Figure 7.14. Overlay of geometries at which a) $S_1 \leftarrow S_2$ IC and b) $S_0 \leftarrow S_1$ IC is recorded in TSHD initiated from the S_2 state, and at which c) $S_2 \leftarrow S_3$ IC, d) $S_1 \leftarrow S_2$ IC, and e) $S_0 \leftarrow S_1$ IC is recorded in TSHD initiated from the S_3 state.

While the process of $S_0 \leftarrow S_1$ IC for the ensemble is on the order of hundreds of femtoseconds (Section 7.3.5.2) because each individual trajectory accesses *tp*MECI$_{E,\alpha}$ stochastically, the geometric changes necessary for any given trajectory to access *tp*MECI$_{E,\alpha}$ are ultrafast and occur over a few tens of femtoseconds. The evolution of $\theta_{\text{Pyr.}}$, $\phi_{2,3,4,5}$, and $\phi_{11,3,4,5}$ as a function of time is given in Fig. 7.15 for TSHD initiated in the S_2 state and in Fig. 7.16 for TSHD initiated in the S_3 state.

Out-of-plane displacement of $r_{3,11}$ is required to access *tp*MECI$_{E,\alpha}$ from *E*-S_1, and $\phi_{11,3,4,5}$ is, on average, 81.6 ± 14.0° (*cf.* 0.0° at equilibrium) at the point at which $S_0 \leftarrow S_1$ IC is recorded (Fig. 7.15c and 7.16c), but out-of-plane displacement of $r_{2,3}$ is not required to the same extent; $\phi_{2,3,4,5}$ is only, on average, 181.3 ± 21.4° (*cf.* 180.0° at equilibrium) at the point at which $S_0 \leftarrow S_1$ IC is recorded (Fig. 7.15b and 7.16b). The speed at which *tp*MECI$_{E,\alpha}$ can be accessed is therefore limited by the speed at which the hydrogen nuclei – not the heavier second-row nuclei – move; the necessary geometric changes are consequently able to occur on the ultrafast timescale. $\theta_{\text{Pyr.}}$ develops quickly with $\phi_{11,3,4,5}$; $\theta_{\text{Pyr.}}$ is, on average, 0.12 ± 0.04 at the point at which $S_0 \leftarrow S_1$ IC is recorded.

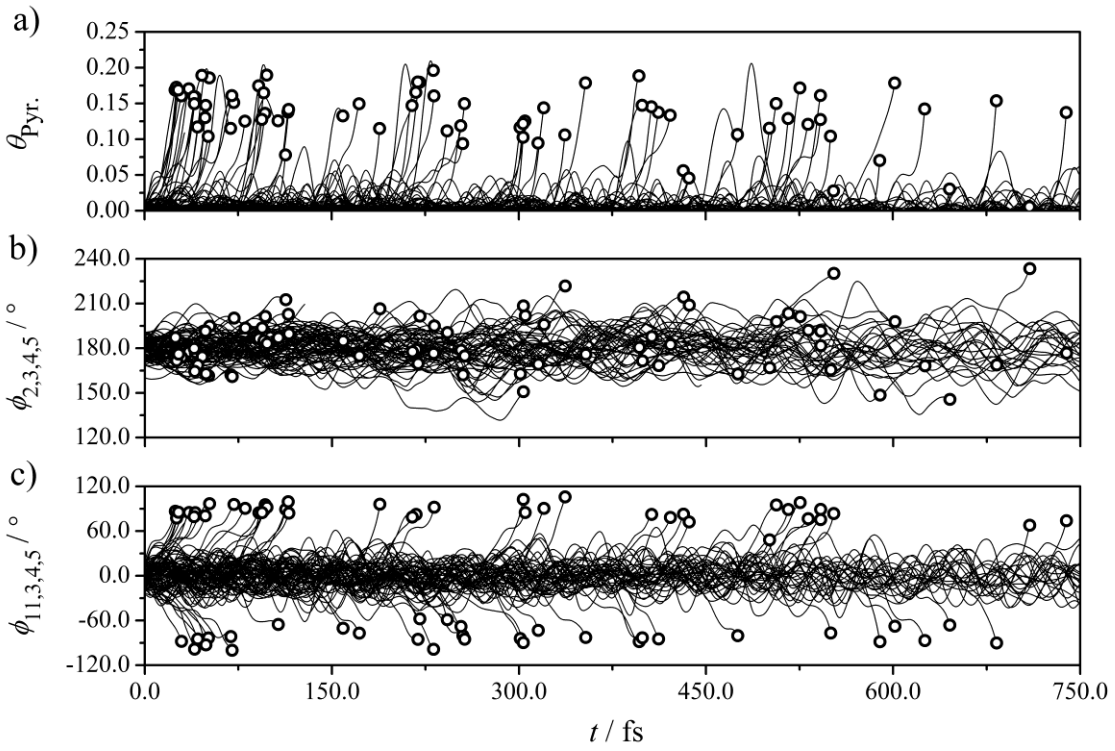

Figure 7.15. Evolution of a) $\theta_{Pyr.}$, b) $\phi_{2,3,4,5}$, and c) $\phi_{11,3,4,5}$ as a function of time, t, for TSHD initiated in the S_2 state. Circular markers indicate where $S_0 \leftarrow S_1$ IC was recorded.

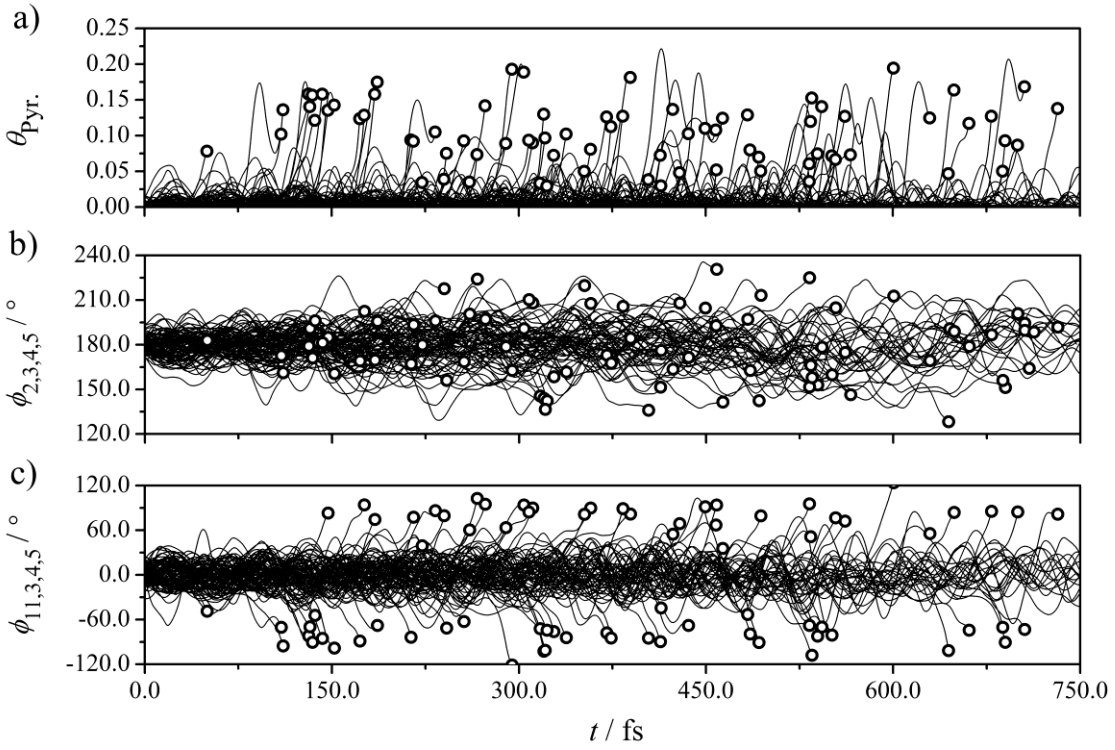

Figure 7.16. Evolution of a) $\theta_{Pyr.}$, b) $\phi_{2,3,4,5}$, and c) $\phi_{11,3,4,5}$ as a function of time, t, for TSHD initiated in the S_3 state. Circular markers indicate where $S_0 \leftarrow S_1$ IC was recorded.

Although some pyramidalisation is necessary to access *tp*MECI$_{E,\alpha}$, a small number of trajectories terminate with low $\theta_{\text{Pyr.}}$ (<0.05); these trajectories have a larger-than-average $\phi_{2,3,4,5}$, the evolution of which keeps pace with $\phi_{11,3,4,5}$ and supresses pyramidalisation.

7.3.5.2 Electronic Dynamics

The quality of TSHD can be assessed by inspection of the evolution of the D_1 diagnostic as a function of time for TSHD initiated in the S_2 (Fig. 7.17a) and S_3 (Fig. 7.17b) states. The D_1 diagnostic generally remains within the established applicability limit (<0.06; Section 7.3.3.2), but the ADC(2)/MP2 treatment is able to tolerate much larger D_1 diagnostic values (>0.15), attesting to the high stability numerical stability of this particular implementation. Indeed, as noted by Plasser *et al.*,[152] it is found that if the killswitch (Section 7.3.4) is disabled, trajectories can be recorded beyond *tp*MECI$_{E,\alpha}$ with negative $S_1 \leftarrow S_0$ transition energies, *i.e.* with the S_1 state being lower in energy than the reference state, and that the ADC(2)/MP2 treatment remains numerically stable in such cases.

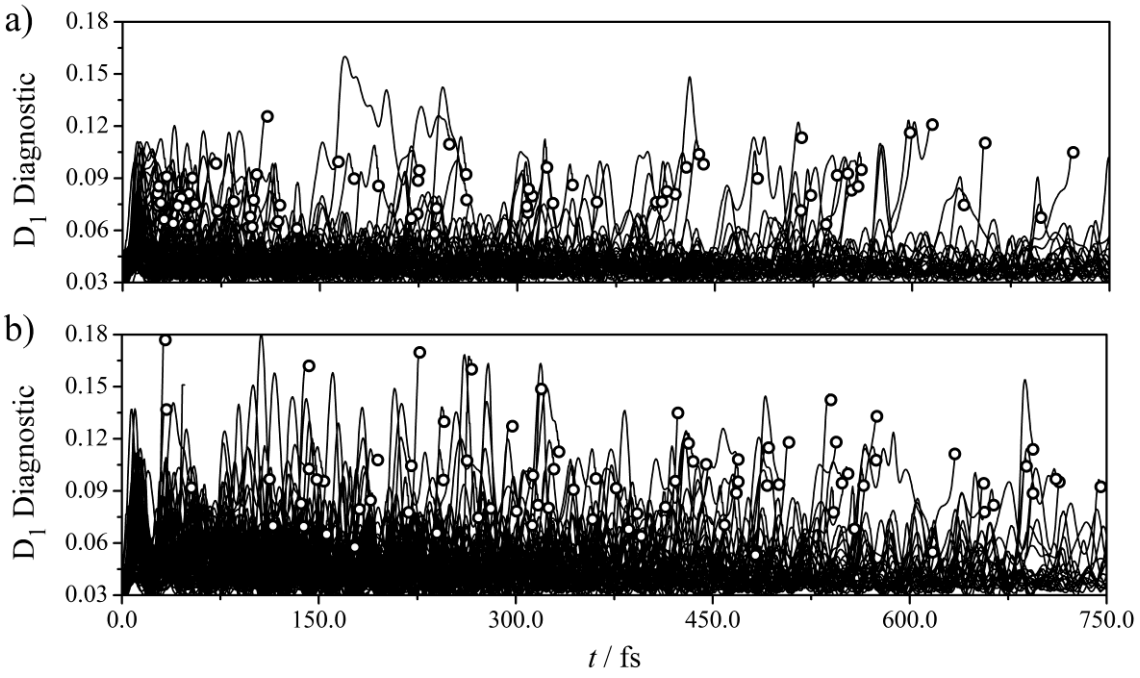

Figure 7.17. Evolution of the D_1 diagnostic as a function of time, *t*, for TSHD initiated in the a) S_2 and b) S_3 states. Circular markers indicate where $S_0 \leftarrow S_1$ IC was recorded.

The average D_1 diagnostic at the point at which the killswitch is triggered and trajectories terminated (Section 7.3.4) is 0.09 ± 0.02; predictably, the S_0 state is no longer able to be described well with a single reference when separated from the S_1 state by <0.1 eV.

The populations of the S_1 and S_2 states as a function of time for TSHD initiated in the S_2 state are plotted in Fig. 7.18; the populations of the S_1, S_2 and S_3 states as a function of time for TSHD initiated in the S_3 state are plotted in Fig. 7.19. The fitting of (bi)exponential functions to these data have allowed the lifetimes, τ, of the S_1, S_2, and S_3 states to be determined; these lifetimes are tabulated in Table 7.12.

Table 7.12. Lifetimes, τ,[a] of the S_1 ($\tau_{0\leftarrow1}$), S_2 ($\tau_{1\leftarrow2}$), and S_3 ($\tau_{2\leftarrow3}$) states at the ADC(2)/MP2 level, as determined from TSHD initiated in the S_2 and S_3 states.

Lifetime	TSHD (S_2)	TSHD (S_3)
$\tau_{0\leftarrow1}$	510(9)	402(15)
$\tau_{1\leftarrow2}$	5(1)	6(3)
$\tau_{2\leftarrow3}$	–	180(13)

[a] All lifetimes are tabulated in fs.

$S_1 \leftarrow S_2$ IC is ultrafast in TSHD initiated from the S_2 [$\tau_{1\leftarrow2}$ = 5(1) fs; Table 7.12] and S_3 [$\tau_{1\leftarrow2}$ = 6(3) fs; Table 7.12] states. In the latter case, a consequence of this is that population does not collect in the S_2 state (Fig. 7.19); deactivation *via* $S_1 \leftarrow S_2$ IC is an order of magnitude faster than population *via* $S_2 \leftarrow S_3$ IC [$\tau_{2\leftarrow3}$ = 180(13) fs; Table 7.12]. This is consistent with $S_1 \leftarrow S_2$ IC *via* *pl*$MECI_{E,1\leftarrow2}$, which is encountered along a natural relaxation coordinate, and $S_2 \leftarrow S_3$ IC *via* *pl*$MECI_{E,2\leftarrow3}$, which is not (Section 7.3.3.3). $S_0 \leftarrow S_1$ IC is recorded on the sub-ps timescale in TSHD initiated from the S_2 [$\tau_{0\leftarrow1}$ = 510(9) fs; Table 7.12] and S_3 [$\tau_{0\leftarrow1}$ = 402(15) fs; Table 7.12] states, with deactivation being faster in the latter case where the trajectories are more energetic.

The lifetime of the S_1 state, $\tau_{0\leftarrow1}$, represents only a lower bound to the actual lifetime due to the implementation of the killswitch (Section 7.3.4); it is a measure of how quickly *tp*$MECI_{E,\alpha}$ is accessed and not a direct measurement of $S_0 \leftarrow S_1$ IC. Robb *et al.*[322] have measured spectroscopically $\tau_{0\leftarrow1}$ and $\tau_{1\leftarrow2}$ for styrene; while the latter ($\tau_{1\leftarrow2}$ = 13 fs)[322] is in good quantitative agreement with $\tau_{1\leftarrow2}$ as determined here [$\tau_{1\leftarrow2}$ = 5(1) fs; Table 7.12], the former (*ca.* 19 ps)[322] is over an order of magnitude slower. It is quite likely that this is a consequence either of the aforementioned approximation, or of over-suppression of the barrier between *E*-S_1 and *tp*$MECI_{E,\alpha}$ at the ADC(2)/MP2 level (Section 7.3.3.2), but there are other factors to consider. Robb *et al.*[322] used narrower excitation windows (*cf.* Fig. 7.13) and provided controlled quantities of excess energy; under their conditions, a longer $\tau_{0\leftarrow1}$ was measured for styrene following $S_1 \leftarrow S_2$ IC than for direct photoexcitation to the S_1 state (Section 7.3.5.3) – a result that is not reproduced here. TSHD of styrene should be trivial, however, and is therefore recommended (Section 7.5).

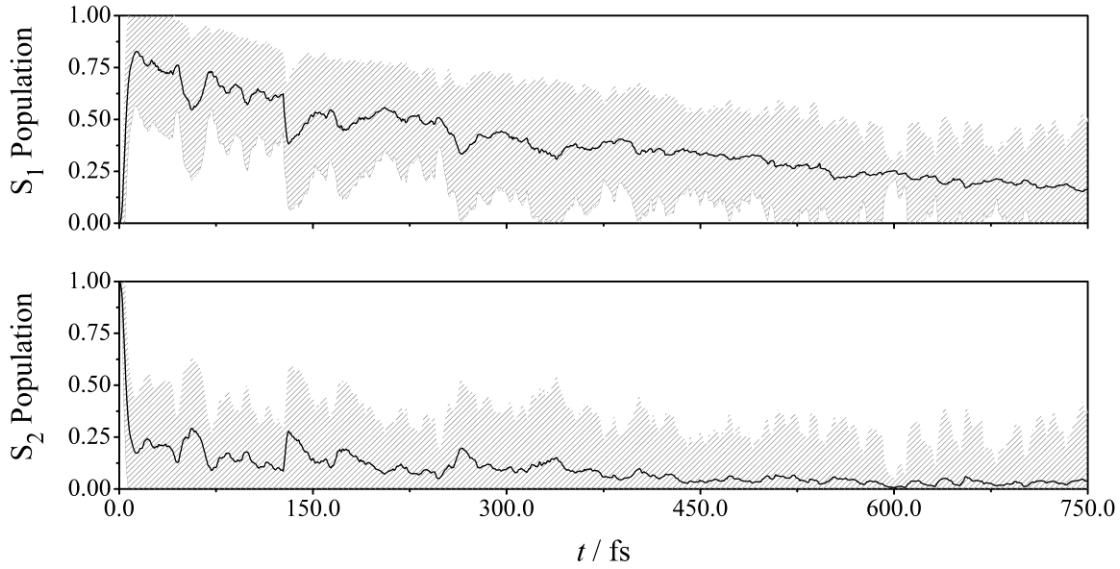

Figure 7.18. Populations of the S_1 and S_2 states as a function of time, *t*, for TSHD initiated in the S_2 state. An average and standard deviation (indicated by the shaded overlay) are plotted.

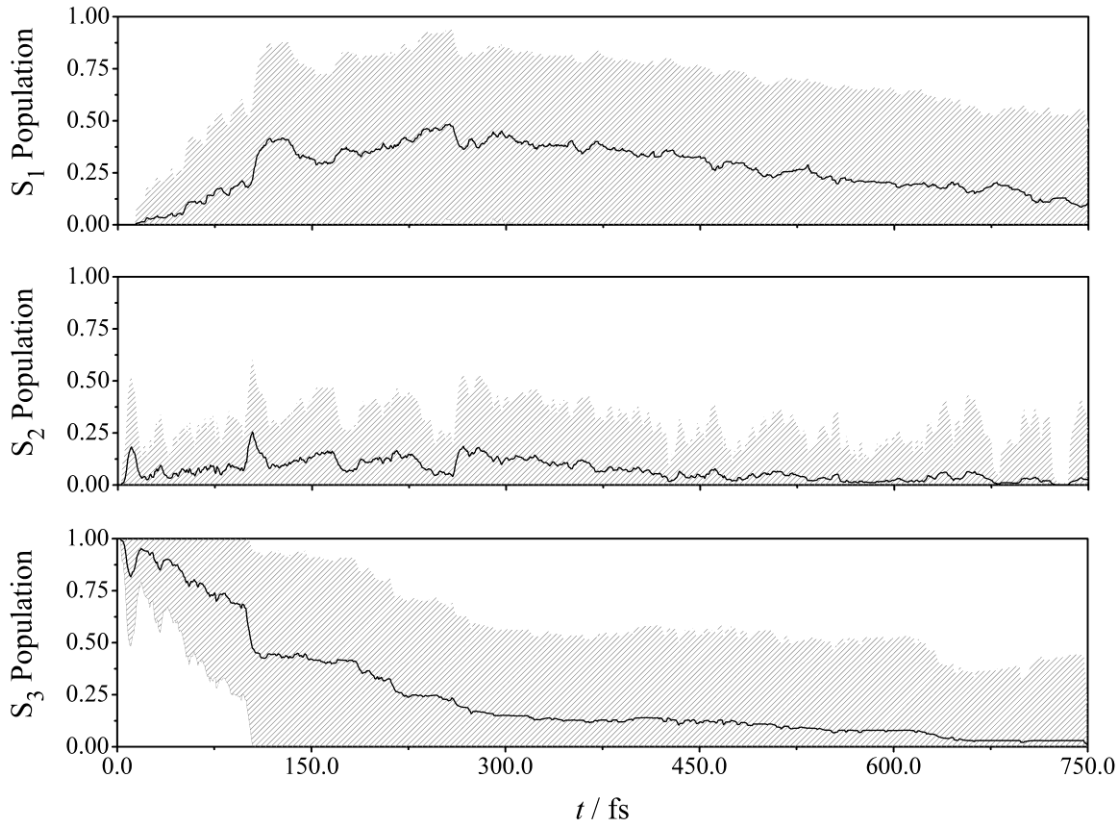

Figure 7.19. Populations of the S_1, S_2, and S_3 states as a function of time, *t*, for TSHD initiated in the S_3 state. An average and standard deviation (indicated by the shaded overlay) are plotted.

7.3.5.3 Velocity Vector Analysis

One might try to understand why $S_0 \leftarrow S_1$ IC is ultrafast when the S_1 state is populated indirectly some time after initial photoexcitation to the S_2 or S_3 state, but not when the S_1 state is populated directly; the answer is not so obvious. $\tau_{0\leftarrow1}$ does not appear to be governed entirely by excitation or kinetic energy; in TSHD initiated from the S_1 state, $\tau_{0\leftarrow1}$ is greater than in TSHD initiated from the S_2 state [$\tau_{0\leftarrow1}$ = 502(10) fs; Table 7.12], even though the difference in initial excitation and kinetic energy between the two Wigner ensembles is minimal. Furthermore, Robb *et al.*[322] have measured spectroscopically $\tau_{0\leftarrow1}$ for styrene with *ca.* 0.9 eV excess energy in the S_1 state (*ca.* 4 ps)[322] and *ca.* 0.3 eV excess energy in the S_2 state (*ca.* 19 ps);[322] in the former case, although less energy is provided, $\tau_{0\leftarrow1}$ is approximately five times faster than in the latter case. This result is particularly intriguing, but the reader should note that it is not reproduced here (Section 7.3.5.2).

The hypothesis of Robb *et al.*[322] – this being that "*...geometry changes as a result of ultrafast* [$S_1 \leftarrow S_2$ IC] *result in an S_1 population that is 'further' from an S_1/S_0 crossing...*"[322] – consequently does not explain the behaviour recorded here, and may not necessarily even explain the behaviour recorded for styrene. Only *tp*MECI$_{E,\alpha}$ is important to $S_0 \leftarrow S_1$ IC (Section 7.3.5.1) – this holds whether the S_1 state is populated directly or indirectly – and $S_1 \leftarrow S_2$ IC does not produce a population that is necessarily any further from, or closer to, *tp*MECI$_{E,\alpha}$ than is produced *via* direct photoexcitation to the S_1 state. In TSHD initiated from the S_2 and S_3 states, the trajectory swarm accesses the S_1 potential energy surface only 126.3 ± 21.1 and 211.1 ± 78.2 pm $Da^{-½}$, respectively, from the Franck-Condon point, and 716.5 ± 40.2 and 690.9 ± 65.3 pm $Da^{-½}$, respectively, from *tp*MECI$_{E,\alpha}$ – values that are comparable to those of the corresponding Wigner distributions. $\tau_{1\leftarrow2}$ is too short for significant geometric change to take place.

Statistical analysis has been applied to test for correlation between the time *tp*MECI$_{E,\alpha}$ was accessed by each individual trajectory and each of the following (initial) parameters: the excitation energy, kinetic energy, values of all 51 internal coordinates, and the sum projection, κ, of the velocity vectors of all nuclei towards *tp*MECI$_{E,\alpha}$. κ is defined in Eq. 7.2.

$$\kappa = \sum_{i}^{N} \frac{(\boldsymbol{v}_i)\cdot(\boldsymbol{g}_i)}{|\boldsymbol{g}_i|} \qquad \textbf{Eq. 7.2}$$

Summation takes place over all N nuclei in Eq. 7.2, each being associated with a velocity vector, $\boldsymbol{v}_i$, and geometric vector, $\boldsymbol{g}_i$, pointing in the direction of *tp*MECI$_{E,\alpha}$. All trajectories

that accessed *tp*MECI$_{E,\alpha}$ and were recorded *via* TSHD initiated in the S_1 state were included in the statistical analysis. No statistically significant correlation was found in any of these cases except in the latter; a correlation coefficient of −0.43, indicating a moderate negative correlation at the 95% confidence level (p = 0.004), was found between the time *tp*MECI$_{E,\alpha}$ was accessed and κ. The correlation is presented in Fig. 7.20.

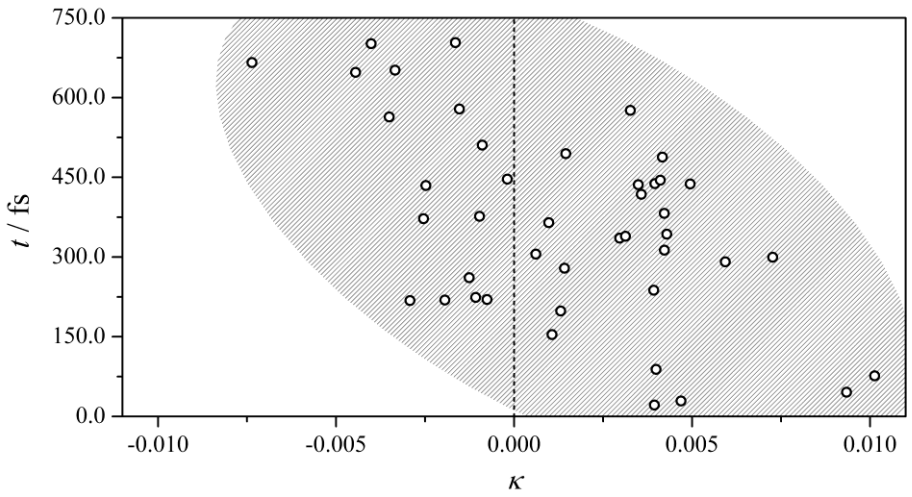

Figure 7.20. Correlation (r = −0.43, p = 0.004) between the time, t, *tp*MECI$_{E,\alpha}$ was accessed and κ in TSHD initiated in the S_1 state. The shaded overlay corresponds to the 95% confidence region.

The funneling effect of *pl*MECI$_{E,1\leftarrow2}$ is subsequently revealed when κ is calculated for trajectories taken from TSHD initiated in the S_2 state. $S_1 \leftarrow S_2$ IC *via pl*MECI$_{E,1\leftarrow2}$ aligns the velocity vectors towards *tp*MECI$_{E,\alpha}$. κ is calculated to be $6.3\times10^{-4} \pm 3.7\times10^{-3}$ at t = 0.0 fs (*i.e.* at the point of initialisation, where the velocity vectors are randomly seeded from the Wigner distribution) and $2.5\times10^{-3} \pm 3.7\times10^{-3}$ at the point that $S_1 \leftarrow S_2$ IC *via pl*MECI$_{E,1\leftarrow2}$ is recorded. Statistical significance testing reveals that the difference in κ between the two points is significant at the 99% confidence level [t(1) = 0.004]. The same result is obtained when κ is calculated for trajectories taken from TSHD initiated in the S_3 state; here, κ is calculated to be $1.8\times10^{-5} \pm 3.1\times10^{-3}$ at t = 0.0 fs and $3.6\times10^{-3} \pm 4.4\times10^{-3}$ at the point that $S_1 \leftarrow S_2$ IC *via pl*MECI$_{E,1\leftarrow2}$ is recorded. Statistical significance testing reveals that this result, too, is significant at the 95% confidence level [t(1) = 0.041].

$S_1 \leftarrow S_2$ IC *via pl*MECI$_{E,1\leftarrow2}$ can drive the trajectory swarm towards *tp*MECI$_{E,\alpha}$, accelerating $S_0 \leftarrow S_1$ IC when the S_1 state is accessed indirectly some time after initial photoexcitation to a higher-lying electronically-excited state.

7.4 Simulations of Time-Resolved Gas Electron Diffraction

The $Z \leftarrow E$ photoisomerisation of *E*-cinnamonitrile is, in principle, recordable *via* TRGED (Section 7.1). In this section, a TDMIC and TDRDC are simulated from TSHD initiated in the S_2 state (Section 7.3.4); the S_2 state is the brightest of the low-lying electronically-excited states considered in this Chapter (Section 7.3.1) and, consequently, the most likely state to be targeted in upcoming TRGED experiments.

To complete trajectories that were terminated earlier than 750 fs at *tp*$MECI_{E,\alpha}$ by invocation of the killswitch (Section 7.3.4), the subsequent dynamics were simulated crudely *via* LIIC. No preference for the *E* (*i.e.* frustrated $Z \leftarrow E$ photoisomerisation) or *Z* isomer (*i.e.* successful $Z \leftarrow E$ photoisomerisation) was assumed; geometries were generated *via* LIIC between the points at which trajectories were terminated (corresponding to *tp*$MECI_{E,\alpha}$; Section 7.3.5.1) and either *E*-S_0 or *Z*-S_0, with the choice being made randomly on a trajectory-by-trajectory basis. 50 intermediate geometries were generated *via* LIIC between *tp*$MECI_{E,\alpha}$ and *E*-S_0, corresponding to dynamics over 25 fs; this is consistent with the time taken to effect the necessary geometrical changes (Section 7.3.5.1). 200 intermediate geometries were generated *via* LIIC between *tp*$MECI_{E,\alpha}$ and *Z*-S_0, corresponding to dynamics over 100 fs. This timescale was chosen to approximate the time taken to effect the necessary geometrical changes in a small (five-trajectory) TSHD batch recorded at the MR-CIS(6,6) level. These TSHD allowed the trajectory swarm to be followed through *tp*$MECI_{E,\alpha}$ and onto the S_0-state potential energy surface.

To simulate the pre-time-zero signal, 100 additional S_0-state trajectories were computed as detailed for the S_1-, S_2-, and S_3-state trajectories in Section 7.3.4, but with each geometry propagated through time for 250 fs at the MP2 level. To reduce the computational cost, surface-hopping was switched off.

Simulations of the TDMIC and TDRDC, with a 120 fs IRF applied, are reproduced in Figs. 7.21 and 7.22, respectively. Simulations of the TDMIC and TDRDC pre-application of the IRF are reproduced in Figs. B3 and B4, respectively.

The signature of the $Z \leftarrow E$ photoisomerisation dynamics is subtle but, remarkably, remains discernible even after application of the IRF. The IRF – a 120 fs (FWHM) Gaussian kernel – was chosen to be comparable to that of the TRGED instrument at the SLAC National Accelerator Laboratory (as in earlier Chapters; Sections 5.4 and 6.4) but temporal resolution this high may not necessarily be required (Section 7.3.5.2).

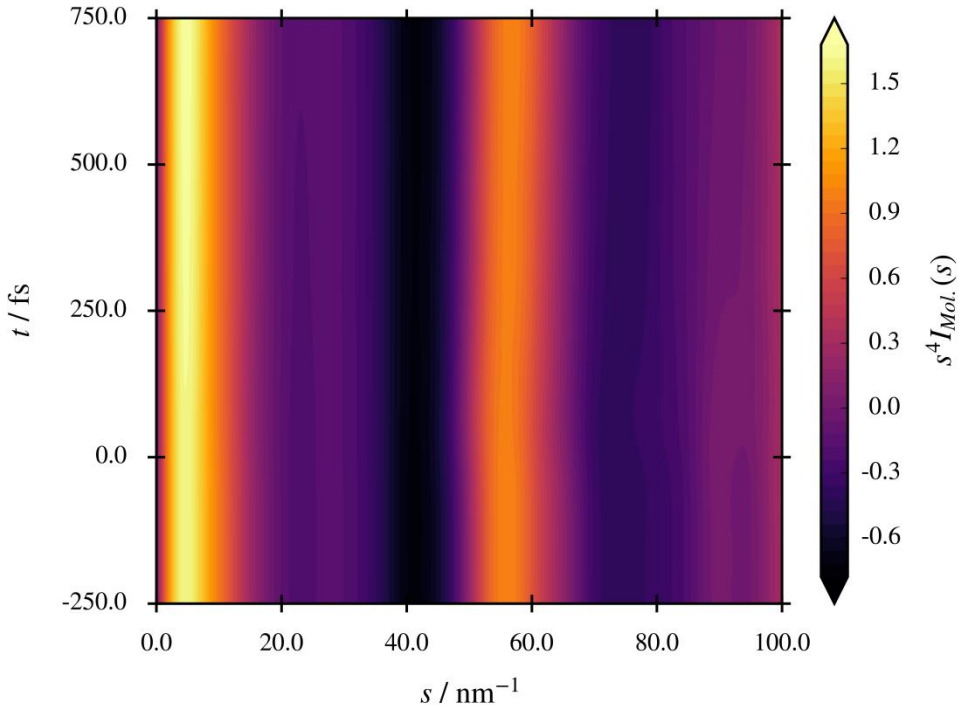

Figure 7.21. Theoretical TDMIC matrix for *E*-cinnamonitrile; convoluted with a 120 fs (FWHM) Gaussian kernel.

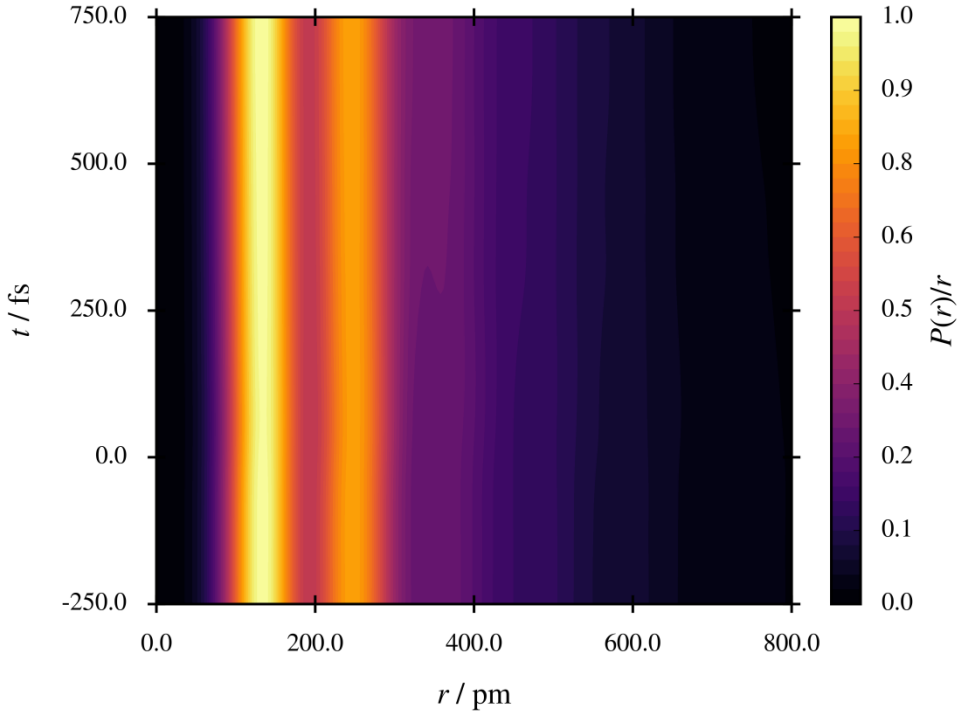

Figure 7.22. Theoretical TDRDC matrix for *E*-cinnamonitrile; transformed from a theoretical TDMIC matrix post-convolution with a 120 fs (FWHM) Gaussian kernel.

The effect of photoexcitation to the S_2 state on the internuclear distances between heavy nuclei (this being trivially predictable *via* valence bond theory) manifests in the TDMIC immediately at time zero; it is seen in the feature at *ca.* 70 – 80 nm^{-1}. Following $S_1 \leftarrow S_2$ IC and fast IVR, the feature at *ca.* 70 – 80 nm^{-1} recovers its pre-time-zero appearance *ca.* 250 fs post-photoexcitation. The features at *ca.* 20 – 25 and 90 – 95 nm^{-1} in the TDMIC respond to the loss of the longest internuclear distances following $Z \leftarrow E$ photoisomerisation and the appearance of new, shorter (non-bonded) carbon-nitrogen internuclear distances.

The appearance of these internuclear distances is apparent on transformation of TDMIC into the TDRDC; the growth of the feature at *ca.* 350 – 400 pm is consistent with the appearance of the shortest non-bonded carbon-nitrogen internuclear distances that are found in *Z*- (but not in *E*-) S_0 ($r_{1,6}$ = 357.2 pm, $r_{1,5}$ = 402.9 pm; MP2). The other non-bonded carbon-nitrogen internuclear distances in *Z*-S_0 ($r_{1,7}$ = 475.0 pm, $r_{1,8}$ = 599.7 pm, $r_{1,9}$ = 628.3 pm, $r_{1,10}$ = 544.6 pm; MP2) are not too different to those in *E*-S_0 ($r_{1,5}$ = 497.3 pm, $r_{1,6}$ = 567.8 pm, $r_{1,10}$ = 595.7 pm; MP2) and are also only weakly scattering; their appearance is consequently difficult to discern in the TDRDC by visual inspection alone.

7.5 Conclusions

TSHD simulations, recorded at the ADC(2)/MP2/cc-(p)VDZ level, have given insight into the $Z \leftarrow E$ photoisomerisation and IC dynamics of *E*-cinnamonitrile where initial photoexcitation is to one of the lower-lying electronically-excited states other than the S_1 state. $S_2 \leftarrow S_3$ IC and $S_1 \leftarrow S_2$ IC are ultrafast (sub-200-fs and sub-10-fs, respectively), and are followed by $S_0 \leftarrow S_1$ IC that occurs *via* $tp\text{MECI}_{E,\alpha}$ in all cases. In this Chapter, the suggestion that $S_1 \leftarrow S_2$ IC can speed up subsequent $S_0 \leftarrow S_1$ IC *via* a weak funnelling effect has been made on the basis of velocity vector analysis. The performance of the ADC(2)/MP2 treatment for this class of problem is impressive.

Complementary *ab initio* calculations at the SA4-CASSCF(12,12)/cc-(p)VDZ, MS-CASPT2(12,12)/cc-(p)VDZ, MR-CISD(6,6)/ cc-(p)VDZ, and ADC(2)/MP2/cc-(p)VDZ levels have given the first highly-detailed insight into the S_1, S_2, and S_3 potential energy surface geography for *E*- and *Z*-cinnamonitrile.

The potential for improvement in future work is nonetheless great. In order to obtain an improved description of the S_3 state, alternatives to the ADC(2)/MP2 treatment that are better able to account for double excitations should be considered, *e.g.* ADC(2)-*x*/MP2[324,325] or ADC(3)/MP2.[324,326] These treatments (particularly the latter) are likely to

provide the best possible balance of computational cost and high accuracy in the static frame of reference; they have the potential to improve on the accuracy with respect to experiment that can be obtained *via* MS-CASPT2 and MR-CISD for this class of problem. Evidently, however, a cost-effective multireference alternative should be sought for use with TSHD so that the $Z \leftarrow E$ photoisomerisation dynamics can be followed directly through *tp*MECI$_{E,\alpha}$. MR-CIS is an attractive alternative; a small (five-trajectory) TSHD batch has already been recorded at the MR-CIS(6,6) level and has given promising results, but this treatment is limited by the heavily-truncated 6-electron, 6-orbital reference space and requirement that one works in the very-small-basis limit. The MR-CIS treatment may be more suitable for styrene; TSHD coupled with an MR-CIS(8,8) treatment could be used to better understand the $Z \leftarrow E$ photoisomerisation dynamics recorded by Robb *et al.*[322] and test their hypothesis. The contemporary α-CASSCF treatment of Martínez *et al.*[327] is an even more attractive alternative; scaling of the state-averaged energies and splitting of the electronically-excited states separately, as in the α-CASSCF treatment, can be used to obtain results commensurate with those that can be computed at the MS-CASPT2 level at a fraction (*ca.* 1/100th)[327] of the computational cost. Critically, the correct ordering of electronically-excited states can be recovered.[327]

The high quality of the GED data, range, and ease of acquisition make *E*-cinnamonitrile a suitable candidate for future TRGED experiments; a TDMIC and TDRDC have been simulated to this end. TRGED experiments are being planned with João Pedro Nunes[106] and are likely to involve gas-phase molecular alignment techniques in order to extract the maximum amount of information from the TRGED data. This represents a potential future direction for the table-top TRGED instrument housed at the University of York[71,73,74] – the photoisomerisation of *E*-cinnamonitrile could be the first experiment of this kind for the Wann Electron Diffraction Group.

8 The Present and the Future

The future of "*photographing in the dark*" (Chapter 1) is bright. An emerging TRGED programme at Daresbury Laboratory (Daresbury, UK) promises to bring the technique closer to home and put the UK in a strong position to leapfrog international developments in the TRGED. If the Wann Electron Diffraction Group continues to press the advantages that they have developed over the course of this project, and in recent years,[73,74] group members will be in a strong position to lead by example the modernisation of GED and influence the direction of the next generation of TRGED experiments.

This concluding Chapter outlines the author's recommendations for consolidating and leveraging this advantage. It comprises suggestions for future development of the University of York gas electron diffractometer (Section 8.1) and the *py*naMICs code (Section 8.2), and a discussion of chemical samples of future interest (Sections 8.3 and 8.4) and a promising new frontier in time-resolved electron diffraction (Section 8.5).

8.1 University of York Gas Electron Diffractometer

Recommission of the University of York gas electron diffractometer[43] (Chapter 4) is one of the key highlights of this thesis. The University of York has joined a group of less than half a dozen institutions worldwide housing GED laboratories, and has been able to launch a new GED programme that has seen samples submitted from locations worldwide. During the course of this project, the author has logged over 200 hours of electron beam uptime on projects that are not reported in this thesis. In addition to the samples for which GED data have been reported here, data have also been acquired – and, in most cases, structural solutions have been derived – for the molecules in Fig. 8.1.

GED data have been acquired for 3,5-bis(trifluoromethyl)pyridine (Fig. 8.1a) and *n*-butyl phenyl ether (Fig. 8.1c) with Tomas Lock Feixas (Ph.D. student; University of York), for piperazine-(bis)borane (Fig. 8.1d), azetidine- (Fig. 8.1e), pyrrolidine- (Fig. 8.1f), piperidine- (Fig. 8.1g), and morpholine-borane (Fig. 8.1h) as part of a long-term collaboration with Ali J'ao and Dr. Sarah Masters (University of Canterbury, New Zealand), and for ferrocene (Fig. 8.1i), and dibromo- (Fig. 8.1j), tetrabromo- (Fig. 8.1k), and hexabromoferrocene (Fig. 8.1l) as part of two independent collaborations with Dr. Jason Lynam (University of York) and Dr. Ian Butler (Bangor University, UK), respectively.

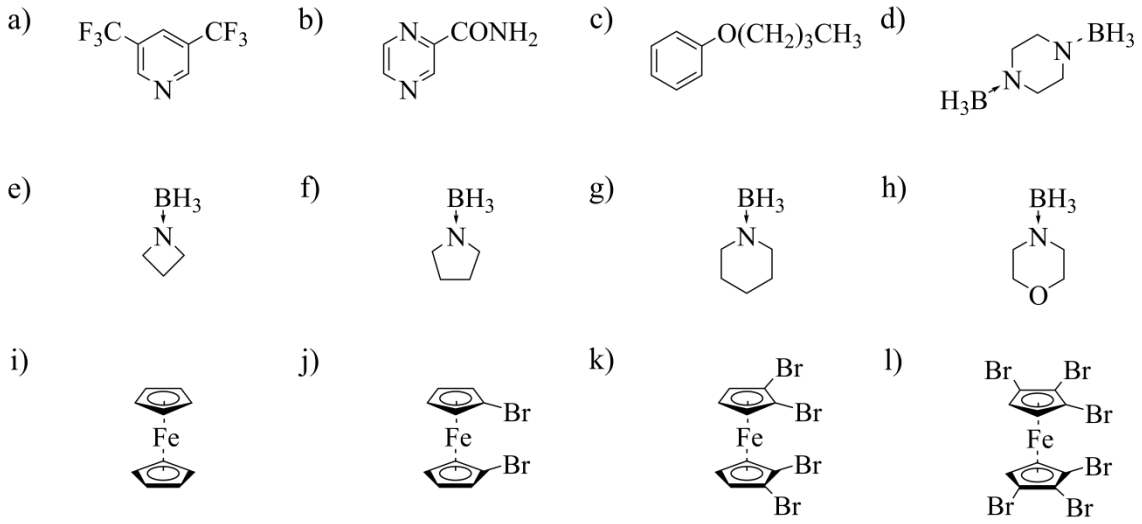

Figure 8.1. Molecules characterised *via* GED over the course of this project: a) 3,5-bis(trifluoromethyl)pyridine, b) pyrazinamide, c) *n*-butyl phenyl ether, d) piperazine-(bis)borane, e) azetidine-borane, f) pyrrolidine-borane, g) piperidine-borane, h) morpholine-borane, i) ferrocene, j) dibromoferrocene, k) tetrabromoferrocene, and l) hexabromoferrocene.

These GED data are designated for inclusion in eight publications, with four of the eight manuscripts in the advanced stages of preparation.

For the Wann Electron Diffraction Group to maintain their advantage in GED, upgrading the University of York gas electron diffractometer[43] is necessary to a) improve the workflow between receipt of a chemical sample and a structural solution (Section 8.1.1), and b) extend the range of samples accessible to study (Section 8.1.2).

8.1.1 Electron Beam Diagnostics

Beyond the anecdotal, little is understood about the profile of the electron beam produced by the University of York gas electron diffractometer[43] (Section 4.1.2), or how it is affected by the electron optics (Section 4.1.3). Optimisation of the electron beam is necessary in advance of data acquisition, but there is no way to assess reproducibly and quantitatively the quality of the electron beam. The operator must make a qualitative visual assessment of the extent to which the electron beam is optimised, based primarily on the brightness and spatial profile of the beam when projected onto the retractable scintillator screen (Fig. 4.1). It need not be explained to the reader why this is unsatisfactory. Operator bias and level of expertise both affect the assessment, and how long it takes to make; furthermore, it is difficult to estimate an appropriate exposure time for each image plate

without quantitative information – to do this, the operator must rely on intuition or iterative data acquisition.

A versatile electron beam diagnostic tool (Fig. 8.2b) has been designed to replace the existing scintillator screen (Fig. 8.2a). The tool fixes onto the retractable rod, **A**, replacing the existing scintillator screen, **B**, with a Faraday/electron beam cup, **C**, for performing electron beam current measurements. The signal is transmitted *via* wire, **D**, to an ammeter. A large-surface-area gadolinium oxysulfide scintillator screen (MCI Optonix DRZ), **E**, is mounted on the retractable rod; this scintillator screen can be used to visualise the electron beam, but also to record previews of GED patterns.

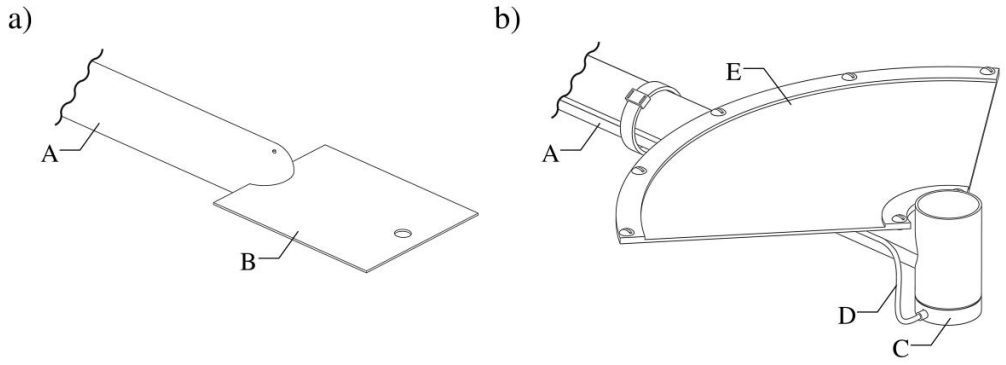

Figure 8.2. Illustrations of a) the existing scintillator screen, and b) the proposed electron beam diagnostic tool for the University of York gas electron diffractometer. The retractable rod (**A**), zinc sulfide scintillator screen (**B**), Faraday/electron beam cup (**C**) and transmission wire (**D**), and gadolinium oxysulfide scintillator screen (**E**) are indicated. Components **A** – **E** are referred to in Section 8.1.1.

The operator will no longer need to load a magazine of image plates, attain high vacuum, carry out a GED experiment, and subsequently scan the image plates (a process which may take an entire day) only to find that no GED data have been recorded, or that what has been recorded is not of useable quality (Section 2.4.3).

A new flange (Fig. 8.3) has also been designed to replace the lowest viewport (Fig. 4.1), providing the necessary feedthroughs and ports for the electron beam diagnostic tool to be used as described. A 7″ aluminium flange, **A**, accommodates an angled, CF40 lead glass viewport, **B**. A camera positioned on the out-of-vacuum side of the viewport will be able to image the scintillator screen of the electron beam diagnostic tool and acquire "*previews*" of diffraction patterns. With a perspective correction, these data might be extractable with XSTRACT,[74] allowing the operator to confirm the molecular structure/composition of the

sample before full data acquisition *via* exposure of the image plates. Three CF25 ports, **C**, **D**, and **E**, are available on the flange; two (**C** and **D**) are illustrated as blank CF25 flanges that might find future use, *e.g.* as thermocouple feedthroughs, while one (**E**) is a dedicated electrical feedthrough – with out-of-vaccum (**F**) and in-vacuum (**G**) connections – for the Faraday/electron beam cup on the electron beam diagnostic tool.

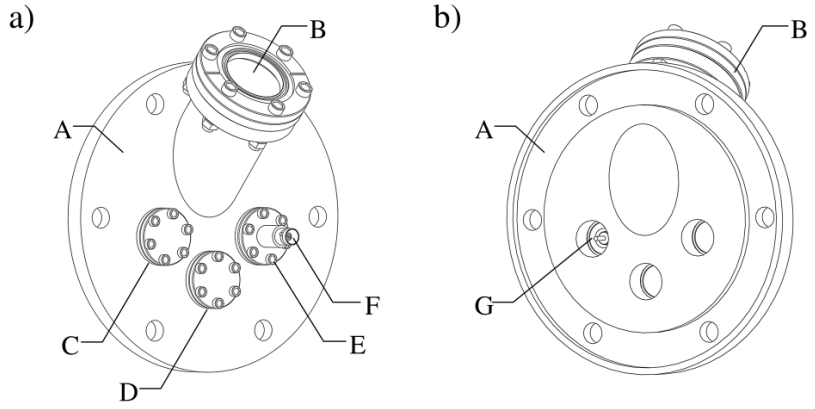

Figure 8.3. Illustration of the proposed flange for the University of York gas electron diffractometer. The flange (**A**), CF40 lead glass viewport (**B**), CF25 empty/blank flange ports (**C**, **D**), and CF25 electrical feedthrough (**E**) – with out-of-vaccum (**F**) and in-vacuum (**G**) connections – are indicated. Components **A** – **E** are referred to in Section 8.1.1.

8.1.2 Air-Heated Effusive Nozzle Upgrade

The air-heated effusive nozzle assembly (Section 4.1.4) installed in the University of York gas electron diffractometer[43] uses a metering valve (Swagelok SS-2MA-MH) rated up to temperatures of *ca.* 480 K.[328] This has been sufficient for all the samples for which GED data are reported in this thesis, but not for all the samples that the author has made attempts to acquire GED data for over the course of this project.

Replacement of the metering valve with a robust, industrial-grade valve (Swagelok SS-31RS4-G) is currently taking place. This valve is packed with graphite, extending its rating up to temperatures of *ca.* 730 K.[329] Installation promises to widen the range of low-volatility samples that are accessible to study *via* GED with the University of York gas electron diffractometer,[43] but a new aluminium insulating jacket needs to be machined first in order to integrate the valve into the sample delivery line. The existing aluminium insulating jacket cannot accommodate the valve, and is not effective at limiting sample condensation.

8.2 *py*naMICs

The *py*naMICs code delivers open-source, high-speed, and parallel simulation of TRGED data from TSHD *via* the NEA (Chapter 5). *py*naMICs outperforms its proprietary predecessor, TD-SIMMIC,[74] delivers high performance in benchmarking tests on desktop PCs and in the HPC environment, and displays good scaling behaviour when processing TSHD ranging from the routine to the highly ambitious. *py*naMICs is an important product of this project. The simulation of proof-of-principle TRGED data has proved instrumental in securing beam time at the SLAC National Accelerator Laboratory and in making the best use of the allocated time.[74] Further improvements to *py*naMICs are suggested (Sections 8.2.1 – 8.2.4) while the code is pending future release (Section 8.2.5).

8.2.1 Scattering Phases

The description of electron scattering can be improved over that given in Eq. 2.10 and 2.11 (and implemented in *py*naMICs; Section 5.1.1) by compensation for the phase shift that an electron experiences when scattered by two nuclei with nuclear charges $Z_i \neq Z_j$. Where $Z_i >> Z_j$, the phase shift can be significant. Of two electrons that have no initial phase difference, the electron accelerated to the greatest extent in the nuclear field effected by Z_i will experience a greater wavelength contraction than the other electron. The initial phases are not recovered even after the electrons have left the nuclear field and decelerated. The effect can lead to destructive interference, causing the diffraction pattern to disappear and reappears periodically with s. The necessary correction to Eq. 2.6 (and, by extension, to Eq. 2.10 and 2.11) is given in Eq. 8.1, where $\eta(s)$ are scattering phases.

$$I(s) = \frac{K^2}{R^2} I_0(s) \cdot \sum_i^N \sum_j^N |F_i(s)||F_j(s)| \cdot \underbrace{\cos[\eta_i(s) - \eta_j(s)]}_{\text{Phase Shift Correction}} \cdot \int_0^\infty P_{ij}(r) \frac{\sin(sr_{ij})}{sr_{ij}} dr \qquad \textbf{Eq. 8.1}$$

This effect should ideally be compensated for in *py*naMICs. The effect is likely to be encountered if the Wann Electron Diffraction Group continues to reconnect with its roots in heavy-element/inorganic structural chemistry (Section 4.3.1) and blend increasingly this background into their TRGED proposals.

8.2.2 Porting

The end-of-life (EOL) date for Python 2.7 is 1st January 2020. Consequently, *py*naMICs should be ported from Python 2 to Python 3 before release (Section 8.2.5) to guarantee

future compatibility. It might prove advantageous to develop a C/C++ version of *py*naMICs in parallel, capable of delivering faster execution, and having greater potential for parallelisation *via* MPI/GPU acceleration (Section 8.2.3).

8.2.3 GPU Acceleration

The current version of *py*naMICs is suitable for use with up to 64 CPU cores (Section 5.1). A C/C++ version of *py*naMICs (Section 8.2.2) with GPU acceleration *via* the Nvidia CUDA platform,[330] for example, has the potential to allow users to access up to several thousand CUDA cores, even on their desktop PC, and unlock performance considerably better than that showcased here (Sections 5.1.3 – 5.1.5).[330] As each individual parallel process is computationally inexpensive (Sections 5.1.4 and 5.1.5) and *py*naMICs can be trivially adapted to take advantage of additional processing power where the number of available cores exceeds the number of TSHD trajectories (Section 5.1.3), GPU acceleration has great potential in this area.

Future work in this direction might form part of an Nvidia GPU Grant Program application, allowing the author to secure an Nvidia Titan V GPU (5120 CUDA cores)[331] for proof-of-principle benchmarking. There are primary applications for the Nvidia Titan V GPU in data extraction and processing beyond GED/TRGED.

8.2.4 Graphical User Interface

The current version of *py*naMICs has a command-line interface (Section 5.1), but there are plans to develop a graphical user interface (GUI) before release (Section 8.2.5). The GUI will allow users to modify on-the-fly simulation parameters, *e.g.* the FWHM of the IRF (Section 5.1), and interactively obtain information on the nuclei and internuclear distances responsible for particular features in the TDMICs and TDRDCs.

8.2.5 Release

*py*naMICs will have an open-source release on conclusion of this project. The author is interested in pursuing options for an impactful release that targets directly the user base; integration of the code for *py*naMICs into an existing TSHD package, *e.g.* NEWTON-X,[267,268] or SHARC,[228–230] would be the ideal pathway to impact.

Integration of the *py*naMICs code into NEWTON-X[267,268] is a personal target for the author following the conclusion of this project; the development team has demonstrated a

commitment to incorporating tools for simulating experiment around their TSHD wrapper, and adding the code for *py*naMICs would expand the toolkit.

8.3 Future Studies on Photofission of Disulfide Bonds

Collectively, the synthesis (Section 6.2.1), gas-phase and solid-state characterisation (Sections 6.2.1 – 6.2.5), *ab initio* calculations (Sections 6.3.1 and 6.3.2), TSHD[254] (Sections 6.3.3 and 6.3.4), and TRGED of 1,2-dithiane stands out as the primary product of this project; they represent the sum result of three years of collaboration between theory and experiment in the Wann Electron Diffraction Group, and are testament to the success of the "*Roadmap to a Molecular Movie*"[74] strategy (Chapter 1).

Appreciating the richness of disulfide photochemistry, one might question the generality of the "Molecular Clackers" mechanism[254] (Section 6.3.4.1) and, furthermore, if it is possible to engineer the nuclear and electronic structure of a cyclic disulfide so as to change it. A number of other cyclic disulfides that the author has either already studied during the course of this project or recommends for future study are presented in Fig. 8.4.

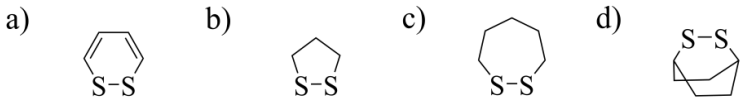

Figure 8.4. Cyclic disulfides recommended for future study in the Wann Electron Diffraction Group: a) 1,2-dithiin, b) 1,2-dithiolane, c) 1,2-dithiepane, and d) 2,3-dithiabicyclo[2.2.2]octane.

In 1,2-dithiin (Fig. 8.4a), the photoabsorption properties are changed considerably,[332] and TSHD reveals that the "Molecular Clackers" mechanism[254] is turned off. Photofission of the disulfide bond in 1,2-dithiin does not produce thiyl radicals; it results only in electronic reorganisation and, ultimately, yields a distribution of butenedithial isomers.

1,2-dithiolane (Fig. 8.4b), 1,2-dithiane, and 1,2-dithiepane (Fig. 8.4c) form a potential study on the effect of nuclear structure on the "Molecular Clackers" mechanism;[254] Cao and Chen[333] have studied these three molecules *via* TSHD in contemporary work. The synthesis, characterisation *via* GED, and TRGED of these three molecules is an obvious next step for the Wann Electron Diffraction Group.

In 2,3-dithiabicyclo[2.2.2]octane (Fig. 8.4d), the structural rigidity provided by the fused aliphatic rings enforces strict non-ergodic dynamics. The trajectory swarm does not appear

to dephase as strongly with time in this cyclic disulfide (*cf.* 1,2-dithiane; Chapter 6), making 2,3-dithiabicyclo[2.2.2]octane a strong candidate for future experimental and theoretical studies in the Wann Electron Diffraction Group.

8.4 Future Studies on Photoisomerisation

Comprehensive *ab initio* calculations (Sections 7.3.1 – 7.3.3) and TSHD (Sections 7.3.4 and 7.3.5) have revealed some details of the photoisomerisation of *E*-cinnamonitrile,[303] but the TRGED signature is subtle (Section 7.4). The Wann Electron Diffraction Group have previously considered tagging photoisomerisable molecules with silyl "*anchors*" to boost the signal;[73] this idea appears increasingly to be a promising way forward.

In contemporary work by Kawashima, Yamamura, and Kano,[334] new azobenzene derivatives [*E*-2-trifluorosilyl-4,4′-dimethylazobenzene, Fig. 8.5b; *E*-2,2′-di(trifluorosilyl)-4,4′-dimethylazobenzene, Fig. 8.5c] – termed "*photoisomerisable fluorophores*"[334] – are reported for the first time, and it has been demonstrated experimentally that, by intramolecular Si···N coordination with trifluorosilyl substituents, the isomerisation behaviour and fluorescent properties can be tuned, *i.e.* the competition between radiative and non-radiative deactivation can be affected.[334]

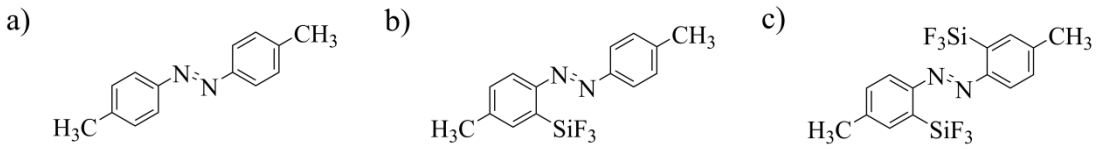

Figure 8.5. Azobenzenes recommended for future study in the Wann Electron Diffraction Group: a) *E*-4,4′-dimethylazobenzene, b) *E*-2-trifluorosilyl-4,4′-dimethylazobenzene, and c) *E*-2,2′-di(trifluorosilyl)-4,4′-dimethylazobenzene.

It is recommended that the Wann Electron Diffraction Group take particular interest in the azobenzenes of Kawashima, Yamamura, and Kano.[334] Their structural dynamics are suitable for study *via* TRGED and their fluorescent properties are suitable for study *via* fluorescence spectroscopy. A deep understanding of the behaviour (*cf.* 1,2-dithiane; Chapter 6) could be obtained by close collaboration of the two current Ph.D. students in the Wann Electron Diffraction Group – Tomas Lock Feixas, who is leading the next stages of the TRGED program, and Michi Burrow, who is leading the development of a gas-phase fluorescence spectroscopy experiment.

8.5 Time-Resolved Solution-Phase Electron Diffraction

As the spatiotemporal resolution of TRGED increases, so does the ambition with which the next generation of TRGED experiments are pursued. Among the emergent time-resolved diffraction techniques, the author recommends that the reader pay close attention to developments in (time-resolved) solution-phase electron diffraction in the near future.

Rankin writes, of solution-phase electron diffraction, that "*…studying structures of liquids is a slow and thankless task, so* [the reader] *needs to start when* [they] *are young to give* [themselves] *time to get somewhere*!"[92] He notes that "*…it is not difficult to collect diffraction data …it can be done relatively easily using electrons, X-rays, or neutrons…* [but] *the hard part is to know what to do with the data once they have been obtained, and how to interpret the results.*"[92] A number of researchers involved in the TRGED programme at the SLAC National Accelerator Laboratory – all still in the early stages of their careers – are taking on this exact challenge. Preliminary experiments in solution-phase electron diffraction are underway, allegedly with promising results.[335]

In order for time-resolved diffraction to become part of the "*chemist's toolbox*", the utility, applicability, and transparency of the technique have to become comparable to the existing tools: time-averaged diffraction, spectroscopy, spectrometry, and computational chemistry. If the promise of time-resolved diffraction is in dispensing with inference in chemical reactions (that generally occur in solution) and determining directly the structures of rare intermediates (that one can often only trap/stabilise *via* solvation and isolate in solution), then time-resolved solution-phase electron diffraction should, indeed, be considered the "*final frontier*".

Simulating data for time-resolved solution-phase electron diffraction is going to demand TSHD on considerably larger systems than those showcased in this project. Mixed quantum-mechanical/molecular-mechanical (QM/MM) TSHD is the obvious strategy; the author expects that the earliest TSHD in support of time-resolved solution-phase electron diffraction experiments will be of simple molecules treated quantum-mechanically with solvent shells treated *via* molecular mechanics. In the longer term, the author expects GPU acceleration and machine learning to effect a paradigm shift in this area, as many more configurations than can be realistically computed will need to be sampled to compensate for disorder and dynamics in the solution phase. Highly-efficient data analysis and screening protocols will also need to be developed in parallel to handle the quantity of data that will be produced in such studies. This is likely to be on the order of tens/hundreds of terabytes.

8.6 Structure and Dynamics by Experiment and Theory

To close this Chapter, the author borrows again the words of Rankin – one of the most prominent proponents of unifying experiment and theory in the GED community. In defence of structural studies on small molecules, Rankin writes "*…it is often assumed that almost all possible small molecules have already been made, but this is not the case* [as] *chemists continue to find ingenious ways of making new fundamental compounds.*"[92] In addition, Rankin encourages the structural chemist "*…to understand and use a wide range of techniques, both experimental and computational, if they are going to solve the structural problems that will continue to challenge* [the GED community]".[92] This ethos is at the heart of this thesis. To move directly from contemporary TRGED studies on di/triatomics and well-understood dynamics to TRGED studies of the most complex kind is a Herculean task for experimentalists and theoreticians alike. The structural dynamicist needs first to use concerted experiments *in vitro* and *in silico* to understand small-molecule structure and dynamics, bridging the gap between the ambitions and capabilities of the TRGED community. But are there other reasons to study small-molecule structure and dynamics?

It is not the case that all small molecules that can be synthesised have been synthesised. In collaboration with researchers at Carleton University (Ottawa, Canada) and the University of Canterbury (Christchurch, New Zealand), a number of small molecules have been synthesised for the first time and characterised *via* GED as part of the new programme established at the University of York (Chapter 4). It is not the case that there is nothing left to learn. Even "well-understood" small-molecule dynamics are not nearly as well-understood as one would think (Chapter 5), and it is clear that one still has to be cautious when interpreting experimental evidence without the guidance that a thorough theoretical study provides (Chapter 6). It is not the case that theoretical tools exist to treat any small molecule that one could think of. It is not unusual to encounter small molecules that challenge even the highest-level emergent electronic structure approaches (Chapter 7) – in fact, in theoretical photochemistry, one might consider it the rule.

The author leaves the reader with the following truism: no matter how simple a molecule one might imagine, one obtains more information from the concerted application of experiment and theory than from either in isolation. It is no longer sufficient for a structural dynamicist to be proficient in one area and "good enough" in the other; they must aim at mastering experiment and theory if they are to prepare themselves and their research group for the future.

Appendix A: Supplementary Information – Experiment

Table A1. Summary of experimental parameters relating to GED data collection for 4-(dimethylamino)benzonitrile.

Dataset Type	Short	Long
Nozzle-to-Image-Plate Distance / mm	234.5	487.0
Electron Wavelength / pm	5.85	5.85
$T_{\text{nozzle, av}}$ / K	423	423
$T_{\text{sample, av}}$ / K	433	433
Exposure Time / s	240	120

Table A2. Optimised Cartesian coordinates in Ångström (Å) and energy, E_{B2PLYP}, in atomic units (a.u.) of 4-(dimethylamino)benzonitrile as calculated at the B2PLYP/cc-pVDZ level.

$E_{\text{B2PLYP}} = -457.49382294$			
N	−0.115775	2.308332	0.000000
C	0.063596	3.030640	1.248011
C	0.063596	3.030640	−1.248011
C	−0.061688	0.928598	0.000000
C	−0.036473	0.191214	1.213770
C	−0.036473	0.191214	−1.213770
C	−0.012743	−1.199600	1.209464
C	−0.012743	−1.199600	−1.209464
C	−0.002772	−1.919747	0.000000
C	0.024551	−3.354589	0.000000
N	0.046567	−4.528099	0.000000
H	−0.034337	4.105314	1.053166
H	1.052536	2.848430	1.709522
H	−0.710270	2.753423	1.980805
H	−0.034337	4.105314	−1.053166
H	1.052536	2.848430	−1.709522
H	−0.710270	2.753423	−1.980805
H	−0.035781	0.706066	2.172574
H	−0.035781	0.706066	−2.172574
H	0.003523	−1.740358	2.157102
H	0.003523	−1.740358	−2.157102

Table A3. Optimised Cartesian coordinates in Ångström (Å) and energy, E_{B2PLYP}, in atomic units (a.u.) of 4-(dimethylamino)benzonitrile as calculated at the B2PLYP/cc-pVTZ level.

E_{B2PLYP} = −457.62082376			
N	−0.137672	2.290736	0.000000
C	0.008146	3.017301	1.246533
C	0.008146	3.017301	−1.246533
C	−0.067917	0.919636	0.000000
C	−0.033718	0.186829	1.206824
C	−0.033718	0.186829	−1.206824
C	0.008146	−1.194388	1.202192
C	0.008146	−1.194388	−1.202192
C	0.027023	−1.909649	0.000000
C	0.072547	−3.334235	0.000000
N	0.109291	−4.495156	0.000000
H	−0.104260	4.078588	1.050225
H	0.984523	2.854692	1.713933
H	−0.763045	2.728797	1.960704
H	−0.104260	4.078588	−1.050225
H	0.984523	2.854692	−1.713933
H	−0.763045	2.728797	−1.960704
H	−0.039364	0.697678	2.155360
H	−0.039364	0.697678	−2.155360
H	0.031078	−1.729991	2.139961
H	0.031078	−1.729991	−2.139961

Table A4. Optimised Cartesian coordinates in Ångström (Å) and energy, E_{B2PLYP}, in atomic units (a.u.) of 4-(dimethylamino)benzonitrile as calculated at the B2PLYP/cc-pVQZ level.

E_{B2PLYP} = −457.65223952			
N	−0.138190	2.289382	0.000000
C	0.008118	3.015178	1.245974
C	0.008118	3.015178	−1.245974
C	−0.068553	0.918983	0.000000
C	−0.034291	0.186864	1.206346
C	−0.034291	0.186864	−1.206346
C	0.008118	−1.193640	1.201885
C	0.008118	−1.193640	−1.201885
C	0.027184	−1.907907	0.000000
C	0.073391	−3.332502	0.000000
N	0.110619	−4.491889	0.000000
H	−0.100412	4.076126	1.049905
H	0.982893	2.848934	1.713578
H	−0.764366	2.729275	1.958615
H	−0.100412	4.076126	−1.049905
H	0.982893	2.848934	−1.713578
H	−0.764366	2.729275	−1.958615
H	−0.040501	0.697461	2.154466
H	−0.040501	0.697461	−2.154466
H	0.031149	−1.729151	2.139031
H	0.031149	−1.729151	−2.139031

Table A5. Optimised Cartesian coordinates in Ångström (Å) and energy, E_{B3LYP}, in atomic units (a.u.) of 4-(dimethylamino)benzonitrile as calculated at the B3LYP/cc-pVDZ level.

E_{B3LYP} = −458.48688213			
N	−0.000973	2.302823	0.000000
C	0.000059	3.033259	1.255254
C	0.000059	3.033259	−1.255254
C	−0.000483	0.925656	0.000000
C	−0.000232	0.187734	1.213548
C	−0.000232	0.187734	−1.213548
C	0.000059	−1.200202	1.208274
C	0.000059	−1.200202	−1.208274
C	0.000190	−1.922040	0.000000
C	0.000507	−3.354007	0.000000
N	0.000762	−4.519705	0.000000
H	−0.000768	4.109951	1.045460
H	0.893594	2.807293	1.865549
H	−0.892003	2.806374	1.867297
H	−0.000768	4.109951	−1.045460
H	0.893594	2.807293	−1.865549
H	−0.892003	2.806374	−1.867297
H	−0.000266	0.703231	2.172292
H	−0.000266	0.703231	−2.172292
H	0.000224	−1.741332	2.156051
H	0.000224	−1.741332	−2.156051

Table A6. Optimised Cartesian coordinates in Ångström (Å) and energy, E_{B3LYP}, in atomic units (a.u.) of 4-(dimethylamino)benzonitrile as calculated at the B3LYP/cc-pVTZ level.

E_{B3LYP} = −458.62590352			
N	−0.000156	2.289629	0.000000
C	0.000202	3.021725	1.252896
C	0.000202	3.021725	−1.252896
C	−0.000083	0.918743	0.000000
C	−0.000053	0.183818	1.206941
C	−0.000053	0.183818	−1.206941
C	−0.000053	−1.195846	1.201611
C	−0.000053	−1.195846	−1.201611
C	−0.000064	−1.913667	0.000000
C	−0.000059	−3.337463	0.000000
N	−0.000056	−4.491582	0.000000
H	−0.000085	4.087149	1.042896
H	0.885592	2.797870	1.855471
H	−0.884668	2.797548	1.856094
H	−0.000085	4.087149	−1.042896
H	0.885592	2.797870	−1.855471
H	−0.884668	2.797548	−1.856094
H	−0.000018	0.695164	2.156250
H	−0.000018	0.695164	−2.156250
H	−0.000035	−1.731916	2.140435
H	−0.000035	−1.731916	−2.140435

Table A7. Optimised Cartesian coordinates in Ångström (Å) and energy, E_{B3LYP}, in atomic units (a.u.) of 4-(dimethylamino)benzonitrile as calculated at the B3LYP/cc-pVQZ level.

E_{B3LYP} = −458.65984118			
N	−0.009073	2.289156	0.000000
C	0.000556	3.020869	1.252617
C	0.000556	3.020869	−1.252617
C	−0.004463	0.918606	0.000000
C	−0.002136	0.183946	1.206841
C	−0.002136	0.183946	−1.206841
C	0.000556	−1.195605	1.201703
C	0.000556	−1.195605	−1.201703
C	0.001731	−1.912804	0.000000
C	0.004685	−3.337155	0.000000
N	0.007044	−4.490279	0.000000
H	−0.008288	4.085703	1.043285
H	0.892621	2.801867	1.846087
H	−0.876697	2.791584	1.863388
H	−0.008288	4.085703	−1.043285
H	0.892621	2.801867	−1.846087
H	−0.876697	2.791584	−1.863388
H	−0.002353	0.695009	2.155677
H	−0.002353	0.695009	−2.155677
H	0.002100	−1.731432	2.139950
H	0.002100	−1.731432	−2.139950

Table A8. Optimised Cartesian coordinates in Ångström (Å) and energy, E_{B3P86}, in atomic units (a.u.) of 4-(dimethylamino)benzonitrile as calculated at the B3P86/cc-pVDZ level.

E_{B3P86} = −459.89413123			
N	−0.000426	2.294080	0.000000
C	0.000023	3.018618	1.249351
C	0.000023	3.018618	−1.249351
C	−0.000219	0.923796	0.000000
C	−0.000113	0.189532	1.210676
C	−0.000113	0.189532	−1.210676
C	0.000023	−1.194730	1.205701
C	0.000023	−1.194730	−1.205701
C	0.000087	−1.913527	0.000000
C	0.000236	−3.340487	0.000000
N	0.000358	−4.505671	0.000000
H	−0.000208	4.094610	1.040245
H	0.892792	2.792802	1.858953
H	−0.892217	2.792601	1.859628
H	−0.000208	4.094610	−1.040245
H	0.892792	2.792802	−1.858953
H	−0.892217	2.792601	−1.859628
H	−0.000136	0.707193	2.168320
H	−0.000136	0.707193	−2.168320
H	0.000093	−1.736505	2.152484
H	0.000093	−1.736505	−2.152484

Table A9. Optimised Cartesian coordinates in Ångström (Å) and energy, E_{B3P86}, in atomic units (a.u.) of 4-(dimethylamino)benzonitrile as calculated at the B3P86/cc-pVTZ level.

E_{B3P86} = −460.01998502			
N	0.000035	2.281224	0.000000
C	−0.000052	3.005851	1.246929
C	−0.000052	3.005851	−1.246929
C	0.000023	0.917134	0.000000
C	0.000015	0.186501	1.204603
C	0.000015	0.186501	−1.204603
C	0.000015	−1.189849	1.199504
C	0.000015	−1.189849	−1.199504
C	0.000015	−1.904479	0.000000
C	0.000013	−3.323973	0.000000
N	0.000012	−4.477906	0.000000
H	−0.000006	4.072169	1.039153
H	0.885309	2.780725	1.849653
H	−0.885509	2.780768	1.849532
H	−0.000006	4.072169	−1.039153
H	0.885309	2.780725	−1.849653
H	−0.885509	2.780768	−1.849532
H	0.000013	0.701309	2.153230
H	0.000013	0.701309	−2.153230
H	0.000011	−1.727658	2.137880
H	0.000011	−1.727658	−2.137880

Table A10. Optimised Cartesian coordinates in Ångström (Å) and energy, E_{B3P86}, in atomic units (a.u.) of 4-(dimethylamino)benzonitrile as calculated at the B3P86/cc-pVQZ level.

E_{B3P86} = −460.05296290			
N	0.000008	2.280817	0.000000
C	−0.000011	3.005030	1.246656
C	−0.000011	3.005030	−1.246656
C	0.000005	0.916949	0.000000
C	0.000003	0.186575	1.204485
C	0.000003	0.186575	−1.204485
C	0.000003	−1.189619	1.199545
C	0.000003	−1.189619	−1.199545
C	0.000003	−1.903681	0.000000
C	0.000003	−3.323675	0.000000
N	0.000003	−4.476564	0.000000
H	0.000000	4.070907	1.039558
H	0.884996	2.779816	1.848796
H	−0.885040	2.779826	1.848768
H	0.000000	4.070907	−1.039558
H	0.884996	2.779816	−1.848796
H	−0.885040	2.779826	−1.848768
H	0.000002	0.701152	2.152758
H	0.000002	0.701152	−2.152758
H	0.000002	−1.727282	2.137442
H	0.000002	−1.727282	−2.137442

Table A11. Optimised Cartesian coordinates in Ångström (Å) and energy, E_{B3PW91}, in atomic units (a.u.) of 4-(dimethylamino)benzonitrile as calculated at the B3PW91/cc-pVDZ level.

E_{B3PW91} = −458.31395228			
N	−0.000419	2.297206	0.000000
C	0.000023	3.024038	1.250394
C	0.000023	3.024038	−1.250394
C	−0.000210	0.924944	0.000000
C	−0.000108	0.188707	1.211232
C	−0.000108	0.188707	−1.211232
C	0.000023	−1.196804	1.206353
C	0.000023	−1.196804	−1.206353
C	0.000084	−1.916944	0.000000
C	0.000229	−3.345488	0.000000
N	0.000347	−4.511343	0.000000
H	−0.000250	4.100360	1.040581
H	0.893475	2.799658	1.860438
H	−0.892870	2.799392	1.861133
H	−0.000250	4.100360	−1.040581
H	0.893475	2.799658	−1.860438
H	−0.892870	2.799392	−1.861133
H	−0.000129	0.704792	2.170211
H	−0.000129	0.704792	−2.170211
H	0.000090	−1.737907	2.154132
H	0.000090	−1.737907	−2.154132

Table A12. Optimised Cartesian coordinates in Ångström (Å) and energy, E_{B3PW91}, in atomic units (a.u.) of 4-(dimethylamino)benzonitrile as calculated at the B3PW91/cc-pVTZ level.

E_{B3PW91} = −458.43769795			
N	0.000017	2.284543	0.000000
C	−0.000033	3.011294	1.248167
C	−0.000033	3.011294	−1.248167
C	0.000013	0.918390	0.000000
C	0.000009	0.185905	1.205380
C	0.000009	0.185905	−1.205380
C	0.000010	−1.191891	1.200379
C	0.000010	−1.191891	−1.200379
C	0.000010	−1.907888	0.000000
C	0.000010	−3.329357	0.000000
N	0.000010	−4.484099	0.000000
H	−0.000009	4.078330	1.039837
H	0.886199	2.787238	1.851509
H	−0.886317	2.787258	1.851444
H	−0.000009	4.078330	−1.039837
H	0.886199	2.787238	−1.851509
H	−0.886317	2.787258	−1.851444
H	0.000010	0.699595	2.155464
H	0.000010	0.699595	−2.155464
H	0.000009	−1.729259	2.140024
H	0.000009	−1.729259	−2.140024

Table A13. Optimised Cartesian coordinates in Ångström (Å) and energy, E_{B3PW91}, in atomic units (a.u.) of 4-(dimethylamino)benzonitrile as calculated at the B3PW91/cc-pVQZ level.

E_{B3PW91} = −458.47074658			
N	0.000005	2.284113	0.000000
C	−0.000007	3.010456	1.247872
C	−0.000007	3.010456	−1.247872
C	0.000003	0.918223	0.000000
C	0.000002	0.185978	1.205275
C	0.000002	0.185978	−1.205275
C	0.000002	−1.191665	1.200421
C	0.000002	−1.191665	−1.200421
C	0.000002	−1.907100	0.000000
C	0.000002	−3.329011	0.000000
N	0.000002	−4.482716	0.000000
H	0.000000	4.077058	1.040262
H	0.885876	2.786328	1.850639
H	−0.885906	2.786336	1.850620
H	0.000000	4.077058	−1.040262
H	0.885876	2.786328	−1.850639
H	−0.885906	2.786336	−1.850620
H	0.000001	0.699337	2.155050
H	0.000001	0.699337	−2.155050
H	0.000001	−1.728900	2.139580
H	0.000001	−1.728900	−2.139580

Table A14. Optimised Cartesian coordinates in Ångström (Å) and energy, $E_{PBEH1PBE}$, in atomic units (a.u.) of 4-(dimethylamino)benzonitrile as calculated at the PBEH1PBE/cc-pVDZ level.

$E_{PBEH1PBE}$ = −457.99628499			
N	0.000017	2.292877	0.000000
C	−0.000029	3.016236	1.247988
C	−0.000029	3.016236	−1.247988
C	0.000010	0.923733	0.000000
C	0.000008	0.189891	1.210018
C	0.000008	0.189891	−1.210018
C	0.000008	−1.193883	1.204900
C	0.000008	−1.193883	−1.204900
C	0.000010	−1.911869	0.000000
C	0.000010	−3.339412	0.000000
N	0.000010	−4.503082	0.000000
H	−0.000013	4.092440	1.039318
H	0.892539	2.790327	1.858151
H	−0.892643	2.790337	1.858092
H	−0.000013	4.092440	−1.039318
H	0.892539	2.790327	−1.858151
H	−0.892643	2.790337	−1.858092
H	0.000004	0.707720	2.167759
H	0.000004	0.707720	−2.167759
H	0.000007	−1.735923	2.151670
H	0.000007	−1.735923	−2.151670

Table A15. Optimised Cartesian coordinates in Ångström (Å) and energy, E_{PBEH1PBE}, in atomic units (a.u.) of 4-(dimethylamino)benzonitrile as calculated at the PBEH1PBE/cc-pVTZ level.

E_{PBEH1PBE} = −458.11730434			
N	−0.000003	2.280952	0.000000
C	0.000005	3.004158	1.246001
C	0.000005	3.004158	−1.246001
C	−0.000002	0.917725	0.000000
C	−0.000002	0.187264	1.204618
C	−0.000002	0.187264	−1.204618
C	−0.000002	−1.189257	1.199285
C	−0.000002	−1.189257	−1.199285
C	−0.000001	−1.903349	0.000000
C	−0.000001	−3.324269	0.000000
N	−0.000001	−4.477228	0.000000
H	0.000000	4.071513	1.039459
H	0.885881	2.778752	1.849386
H	−0.885861	2.778748	1.849398
H	0.000000	4.071513	−1.039459
H	0.885881	2.778752	−1.849386
H	−0.885861	2.778748	−1.849398
H	−0.000001	0.702326	2.153987
H	−0.000001	0.702326	−2.153987
H	−0.000001	−1.727678	2.138242
H	−0.000001	−1.727678	−2.138242

Table A16. Optimised Cartesian coordinates in Ångström (Å) and energy, E_{PBEH1PBE}, in atomic units (a.u.) of 4-(dimethylamino)benzonitrile as calculated at the PBEH1PBE/cc-pVQZ level.

E_{PBEH1PBE} = −458.14980527			
N	−0.000001	2.280530	0.000000
C	0.000002	3.003318	1.245698
C	0.000002	3.003318	−1.245698
C	−0.000001	0.917602	0.000000
C	0.000000	0.187364	1.204543
C	0.000000	0.187364	−1.204543
C	0.000000	−1.189037	1.199356
C	0.000000	−1.189037	−1.199356
C	−0.000001	−1.902559	0.000000
C	0.000000	−3.323934	0.000000
N	0.000000	−4.475921	0.000000
H	0.000000	4.070299	1.039830
H	0.885592	2.777797	1.848546
H	−0.885586	2.777796	1.848551
H	0.000000	4.070299	−1.039830
H	0.885592	2.777797	−1.848546
H	−0.885586	2.777796	−1.848551
H	0.000000	0.702146	2.153664
H	0.000000	0.702146	−2.153664
H	0.000000	−1.727367	2.137890
H	0.000000	−1.727367	−2.137890

Table A17. Optimised Cartesian coordinates in Ångström (Å) and energy, E_{HSEH1PBE}, in atomic units (a.u.) of 4-(dimethylamino)benzonitrile as calculated at the HSEH1PBE/cc-pVDZ level.

E_{HSEH1PBE} = −457.98667718			
N	0.000087	2.293141	0.000000
C	−0.000123	3.016656	1.248082
C	−0.000123	3.016656	−1.248082
C	0.000051	0.923914	0.000000
C	0.000033	0.189823	1.210235
C	0.000033	0.189823	−1.210235
C	0.000033	−1.194017	1.205152
C	0.000033	−1.194017	−1.205152
C	0.000039	−1.912458	0.000000
C	0.000035	−3.339529	0.000000
N	0.000034	−4.503542	0.000000
H	0.000000	4.092904	1.039386
H	0.892348	2.790591	1.858485
H	−0.892850	2.790711	1.858168
H	0.000000	4.092904	−1.039386
H	0.892348	2.790591	−1.858485
H	−0.892850	2.790711	−1.858168
H	0.000017	0.707699	2.168005
H	0.000017	0.707699	−2.168005
H	0.000023	−1.736050	2.151965
H	0.000023	−1.736050	−2.151965

Table A18. Optimised Cartesian coordinates in Ångström (Å) and energy, E_{HSEH1PBE}, in atomic units (a.u.) of 4-(dimethylamino)benzonitrile as calculated at the HSEH1PBE/cc-pVTZ level.

E_{HSEH1PBE} = −458.10803179			
N	−0.000027	2.281190	0.000000
C	0.000040	3.004626	1.246069
C	0.000040	3.004626	−1.246069
C	−0.000017	0.917886	0.000000
C	−0.000012	0.187145	1.204791
C	−0.000012	0.187145	−1.204791
C	−0.000012	−1.189418	1.199503
C	−0.000012	−1.189418	−1.199503
C	−0.000012	−1.903973	0.000000
C	−0.000011	−3.324355	0.000000
N	−0.000010	−4.477631	0.000000
H	0.000007	4.071950	1.039428
H	0.885931	2.779211	1.849480
H	−0.885777	2.779182	1.849574
H	0.000007	4.071950	−1.039428
H	0.885931	2.779211	−1.849480
H	−0.885777	2.779182	−1.849574
H	−0.000010	0.702179	2.154173
H	−0.000010	0.702179	−2.154173
H	−0.000009	−1.727767	2.138476
H	−0.000009	−1.727767	−2.138476

Table A19. Optimised Cartesian coordinates in Ångström (Å) and energy, E_{HSEH1PBE}, in atomic units (a.u.) of 4-(dimethylamino)benzonitrile as calculated at the HSEH1PBE/cc-pVQZ level.

E_{HSEH1PBE} = −458.14052111			
N	−0.000009	2.280766	0.000000
C	0.000012	3.003780	1.245768
C	0.000012	3.003780	−1.245768
C	−0.000005	0.917764	0.000000
C	−0.000003	0.187249	1.204715
C	−0.000003	0.187249	−1.204715
C	−0.000003	−1.189197	1.199575
C	−0.000003	−1.189197	−1.199575
C	−0.000004	−1.903181	0.000000
C	−0.000004	−3.324016	0.000000
N	−0.000003	−4.476323	0.000000
H	0.000001	4.070730	1.039798
H	0.885598	2.778242	1.848666
H	−0.885548	2.778230	1.848698
H	0.000001	4.070730	−1.039798
H	0.885598	2.778242	−1.848666
H	−0.885548	2.778230	−1.848698
H	−0.000002	0.702005	2.153848
H	−0.000002	0.702005	−2.153848
H	−0.000002	−1.727452	2.138128
H	−0.000002	−1.727452	−2.138128

Table A20. Summary of experimental parameters relating to GED data reduction and refinement for 4-(dimethylamino)benzonitrile.

Dataset Type	Short	Long
Δs / nm^{-1}	2.0	1.0
s_{min} / nm^{-1}	84.0	44.0
sw_1 / nm^{-1}	104.0	62.0
sw_2 / nm^{-1}	256.0	108.0
s_{max} / nm^{-1}	270.0	126.0
Correlation Parameter	0.4808	0.4988
Scale Factor (k)	0.0128(3)	0.0040(1)

Table A21. Least-squares correlation matrix[a] (×100).

	p_4	p_7	u_3	u_7	u_{27}	u_{95}	u_{109}	u_{134}	u_{145}	k_1
p_4	100							−57		
p_7		100							−71	
u_3			100					65		90
u_7				100			57			
u_{27}					100	61				
u_{95}						100				
u_{109}							100			
u_{134}								100		60
u_{145}									100	
k_1										100

[a] Only values ≥ 50% are tabulated. k_1 is a scale factor.

Table A22. Refined (r_{h1}) and theoretical[a] (r_e) parameter values[b] and SARACEN restraints applied in the least-squares refinement procedure.

	r_{h1}	r_e	Restraint
p_1	141.77(4)	140.77	–
p_2	2.31(10)	2.37	2.37(10)
p_3	1.33(3)	1.33	1.33(3)
p_4	3.08(21)	2.70	2.70(23)
p_5	6.81(14)	6.90	6.90(14)
p_6	2.44(32)	2.38	2.38(3)
p_7	113.81(33)	115.98	–
p_8	109.14(42)	108.91	108.91(48)
p_9	107.77(42)	107.82	107.82(44)
p_{10}	117.40(8)	117.44	117.44(7)
p_{11}	118.52(7)	118.54	118.54(7)
p_{12}	110.80(8)	110.80	110.80(8)
p_{13}	119.96(5)	119.96	119.96(5)
p_{14}	119.27(32)	118.56	–
p_{15}	–	8.49	–
p_{16}	–	−178.60	–

[a] Calculations at the B2PLYP/CBS level. [b] Interatomic distances (r) are tabulated in picometers (pm) and angles (a) and dihedrals (ϕ) are tabulated in degrees.

Table A23. Internuclear distances (r_a / pm), refined (u_{GED}) and theoretical (u_{h1}) amplitudes of vibration and restraints and distance corrections (k_{h1}) for 4-(dimethylamino)benzonitrile.[a]

Amp	Atomic Pair	r_a	u_{GED}	Restraint	k_{h1}	u_{h1}
u_{132}	$C_{5'}$–$H_{13'}$	107.5(4)	8.0 (Tied to u_{145})	–	0.4	7.5
u_{118}	C_5–H_{13}	107.5(4)	8.0 (Tied to u_{145})	–	0.4	7.5
u_{87}	C_4–H_{12}	107.5(4)	8.0 (Tied to u_{145})	–	0.4	7.5
u_{103}	$C_{4'}$–$H_{12'}$	107.5(4)	8.0 (Tied to u_{145})	–	0.4	7.5
u_{30}	C_2–H_9	108.4(4)	8.2 (Tied to u_{145})	–	0.3	7.6
u_{51}	$C_{2'}$–$H_{9'}$	108.4(4)	8.2 (Tied to u_{145})	–	0.3	7.6
u_{31}	C_2–H_{10}	109.2(4)	8.3 (Tied to u_{145})	–	0.2	7.8
u_{52}	$C_{2'}$–$H_{10'}$	109.2(4)	8.3 (Tied to u_{145})	–	0.2	7.8
u_{53}	$C_{2'}$–$H_{11'}$	109.3(4)	8.2 (Tied to u_{145})	–	0.8	7.7
u_{32}	C_2–H_{11}	109.3(4)	8.2 (Tied to u_{145})	–	0.8	7.7
u_{145}	C_7–N_8	113.8(3)	3.7(1)	–	0.1	3.5
u_3	N_1–C_3	137.2(2)	5.6(1)	–	−1.1	4.6
u_{76}	C_4–C_5	138.8(1)	5.4 (Tied to u_3)	–	0.0	4.5
u_{92}	$C_{4'}$–$C_{5'}$	138.8(1)	5.4 (Tied to u_3)	–	0.0	4.5
u_{107}	C_5–C_6	140.6(1)	5.6 (Tied to u_3)	–	0.2	4.6
u_{120}	$C_{5'}$–C_6	140.7(1)	5.6 (Tied to u_3)	–	0.2	4.6
u_{58}	C_3–C_4	142.0(1)	5.7 (Tied to u_3)	–	0.2	4.7
u_{59}	C_3–$C_{4'}$	142.0(1)	5.7 (Tied to u_3)	–	0.2	4.7
u_{133}	C_6–C_7	143.6(2)	5.6 (Tied to u_3)	–	0.1	4.6
u_2	N_1–$C_{2'}$	145.7(2)	5.6 (Tied to u_3)	–	−0.2	4.6

u_{1}	N_{1}−C_{2}	145.7(2)	5.6 (Tied to u_{3})	–	−0.2	4.6
u_{175}	H_{10}...H_{11}	174.8(7)	12.4 (Tied to u_{196})	–	−0.3	12.4
u_{196}	$H_{10'}$...$H_{11'}$	174.8(7)	12.4(13)	12.4(12)	−0.3	12.4
u_{166}	H_{9}...H_{10}	175.3(7)	12.6 (Tied to u_{196})	–	−0.7	12.6
u_{190}	$H_{9'}$...$H_{10'}$	175.3(7)	12.6 (Tied to u_{196})	–	−0.7	12.6
u_{191}	$H_{9'}$...$H_{11'}$	177.1(7)	12.4 (Tied to u_{196})	–	0.7	12.3
u_{167}	H_{9}...H_{11}	177.1(7)	12.4 (Tied to u_{196})	–	0.7	12.3
u_{11}	N_{1}...H_{9}	207.6(4)	12.3(5)	10.2(10)	−0.2	10.2
u_{14}	N_{1}...$H_{9'}$	207.6(4)	12.3 (Tied to u_{11})	–	−0.2	10.2
u_{15}	N_{1}...$H_{10'}$	211.4(4)	12.4 (Tied to u_{11})	–	−1.4	10.3
u_{12}	N_{1}...H_{10}	211.4(4)	12.4 (Tied to u_{11})	–	−1.4	10.3
u_{13}	N_{1}...H_{11}	211.5(4)	12.6 (Tied to u_{11})	–	0.7	10.5
u_{16}	N_{1}...$H_{11'}$	211.5(4)	12.6 (Tied to u_{11})	–	0.7	10.5
u_{116}	C_{5}...H_{12}	211.6(4)	11.8 (Tied to u_{11})	–	−0.4	9.8
u_{130}	$C_{5'}$...$H_{12'}$	211.6(4)	11.8 (Tied to u_{11})	–	−0.4	9.8
u_{105}	$C_{4'}$...$H_{13'}$	213.0(4)	11.9 (Tied to u_{11})	–	−0.1	9.9
u_{89}	C_{4}...H_{13}	213.0(4)	11.9 (Tied to u_{11})	–	−0.1	9.9
u_{143}	C_{6}...H_{13}	214.0(4)	11.9 (Tied to u_{11})	–	−0.5	9.9
u_{144}	C_{6}...$H_{13'}$	214.0(4)	11.9 (Tied to u_{11})	–	−0.5	9.9
u_{72}	C_{3}...$H_{12'}$	216.6(4)	11.9 (Tied to u_{11})	–	−0.1	9.9
u_{71}	C_{3}...H_{12}	216.6(4)	11.9 (Tied to u_{11})	–	−0.1	9.9
u_{168}	H_{9}...$H_{9'}$	224.0(21)	26.7 (Fixed)	–	13.0	26.7
u_{202}	$H_{11'}$...$H_{12'}$	226.9(11)	36.8 (Fixed)	–	18.8	36.8
u_{186}	H_{11}...H_{12}	227(11)	36.8 (Fixed)	–	18.8	36.8
u_{179}	H_{10}...H_{12}	230.4(9)	41.6 (Fixed)	–	−6.9	41.6
u_{198}	$H_{10'}$...$H_{12'}$	230.4(9)	41.7 (Fixed)	–	−6.9	41.7
u_{106}	C_{5}...$C_{5'}$	241.6(2)	5.4 (Tied to u_{4})	–	0.0	5.7
u_{206}	H_{12}...H_{13}	242.6(5)	16.1 (Fixed)	–	0.2	16.1
u_{209}	$H_{12'}$...$H_{13'}$	242.6(5)	16.1 (Fixed)	–	0.2	16.1
u_{75}	C_{4}...$C_{4'}$	242.7(2)	5.6 (Tied to u_{4})	–	0.2	5.9
u_{78}	C_{4}...C_{6}	243.1(2)	5.4 (Tied to u_{4})	–	−0.1	5.7
u_{93}	$C_{4'}$...C_{6}	243.1(2)	5.4 (Tied to u_{4})	–	−0.1	5.7
u_{4}	N_{1}...C_{4}	243.2(1)	5.8(2)	–	−1.2	6.1
u_{5}	N_{1}...$C_{4'}$	243.2(1)	5.8 (Tied to u_{4})	–	−1.2	6.1
u_{61}	C_{3}...$C_{5'}$	244.0(2)	8.6 (Tied to u_{134})	–	−0.4	5.7
u_{60}	C_{3}...C_{5}	244.0(2)	8.6 (Tied to u_{134})	–	−0.4	5.7
u_{121}	$C_{5'}$...C_{7}	246.3(2)	10.6 (Tied to u_{134})	–	−0.5	7.0
u_{40}	$C_{2'}$...C_{3}	246.5(4)	10.4 (Tied to u_{134})	–	1.3	6.8
u_{22}	C_{2}...C_{3}	246.5(4)	10.4 (Tied to u_{134})	–	1.3	6.8
u_{108}	C_{5}...C_{7}	246.7(2)	10.6 (Tied to u_{134})	–	−0.1	7.0
u_{36}	C_{2}...H_{12}	251.4(8)	27.1 (Tied to u_{134})	–	4.1	17.8
u_{55}	$C_{2'}$...$H_{12'}$	251.4(8)	27.1 (Tied to u_{134})	–	4.1	17.8
u_{21}	C_{2}...$C_{2'}$	254.2(9)	12.9 (Tied to u_{134})	–	2.8	8.4
u_{134}	C_{6}...N_{8}	256.3(3)	7.7(3)	–	−1.0	5.1
u_{33}	C_{2}...$H_{9'}$	257.4(14)	27.6 (Tied to u_{134})	–	3.8	18.1

u_{48}	$C_{2'}...H_{9}$	257.4(14)	27.4 (Tied to u_{134})	–	3.8	18.0
u_{155}	$C_{7}...H_{13'}$	266.0(3)	22.4 (Tied to u_{134})	–	−1.0	14.7
u_{154}	$C_{7}...H_{13}$	266.6(3)	22.4 (Tied to u_{134})	–	−0.3	14.7
u_{70}	$C_{3}...H_{11'}$	267.1(6)	31.8 (Tied to u_{134})	–	−5.3	20.8
u_{67}	$C_{3}...H_{11}$	267.1(6)	31.8 (Tied to u_{134})	–	−5.3	20.8
u_{18}	$N_{1}...H_{12'}$	267.6(2)	20.3 (Tied to u_{134})	–	−0.6	13.3
u_{17}	$N_{1}...H_{12}$	267.6(2)	20.3 (Tied to u_{134})	–	−0.6	13.3
u_{83}	$C_{4}...H_{11}$	270.0(9)	44.7 (Tied to u_{134})	–	3.0	29.3
u_{101}	$C_{4'}...H_{11'}$	270.0(9)	44.7 (Tied to u_{134})	–	3.0	29.3
u_{77}	$C_{4}...C_{5'}$	278.8(2)	8.8(2)	–	−0.1	6.5
u_{91}	$C_{4'}...C_{5}$	278.9(2)	8.8 (Tied to u_{77})	–	−0.1	6.5
u_{62}	$C_{3}...C_{6}$	283.8(2)	8.5 (Tied to u_{77})	–	−0.6	6.3
u_{23}	$C_{2}...C_{4}$	286.0(7)	13.9 (Tied to u_{77})	–	2.3	10.4
u_{42}	$C_{2'}...C_{4'}$	286.0(7)	13.9 (Tied to u_{77})	–	2.3	10.4
u_{69}	$C_{3}...H_{10'}$	287.8(6)	30.5 (Tied to u_{77})	–	11.0	22.7
u_{66}	$C_{3}...H_{10}$	287.8(6)	30.5 (Tied to u_{77})	–	11.0	22.7
u_{82}	$C_{4}...H_{10}$	292.5(9)	33.2 (Tied to u_{100})	–	5.6	33.2
u_{100}	$C_{4'}...H_{10'}$	292.5(9)	33.2(3)	33.2(3)	5.6	33.2
u_{35}	$C_{2}...H_{11'}$	316.1(9)	24.2 (Tied to u_{109})	–	−16.7	18.0
u_{50}	$C_{2'}...H_{11}$	316.1(9)	24.2 (Tied to u_{109})	–	−16.7	18.0
u_{183}	$H_{11}...H_{9'}$	325.2(15)	28.1 (Fixed)	–	−13.8	28.1
u_{170}	$H_{9}...H_{11'}$	325.2(15)	28.1 (Fixed)	–	−13.8	28.1
u_{65}	$C_{3}...H_{9}$	331.7(5)	14.1 (Tied to u_{109})	–	−2.5	10.5
u_{68}	$C_{3}...H_{9'}$	331.7(5)	14.1 (Tied to u_{109})	–	−2.5	10.5
u_{49}	$C_{2'}...H_{10}$	331.8(9)	40.4 (Tied to u_{109})	–	22.3	30.0
u_{34}	$C_{2}...H_{10'}$	331.8(9)	40.4 (Tied to u_{109})	–	22.3	30.0
u_{176}	$H_{10}...H_{9'}$	336.6(14)	37.5 (Fixed)	–	16.5	37.5
u_{169}	$H_{9}...H_{10'}$	336.6(14)	37.4 (Fixed)	–	16.5	37.4
u_{119}	$C_{5}...H_{13'}$	337.9(4)	12.8 (Tied to u_{109})	–	−1.1	9.5
u_{131}	$C_{5'}...H_{13}$	337.9(4)	12.8 (Tied to u_{109})	–	−1.1	9.5
u_{141}	$C_{6}...H_{12}$	338.1(4)	12.8 (Tied to u_{109})	–	−1.0	9.5
u_{142}	$C_{6}...H_{12'}$	338.2(4)	12.8 (Tied to u_{109})	–	−0.9	9.5
u_{88}	$C_{4}...H_{12'}$	340.1(4)	12.9 (Tied to u_{109})	–	−0.7	9.6
u_{102}	$C_{4'}...H_{12}$	340.1(4)	12.9 (Tied to u_{109})	–	−0.7	9.6
u_{74}	$C_{3}...H_{13'}$	340.3(4)	12.9 (Tied to u_{109})	–	−1.0	9.6
u_{73}	$C_{3}...H_{13}$	340.3(4)	12.9 (Tied to u_{109})	–	−1.0	9.6
u_{165}	$N_{8}...H_{13'}$	345.1(3)	27.6 (Tied to u_{109})	–	−2.2	20.5
u_{164}	$N_{8}...H_{13}$	346.2(3)	27.6 (Tied to u_{109})	–	−1.1	20.5
u_{185}	$H_{11}...H_{11'}$	347.3(9)	41.8 (Fixed)	–	−45.1	41.8
u_{122}	$C_{5'}...N_{8}$	348.4(3)	13.9 (Tied to u_{109})	–	−2.0	10.3
u_{109}	$C_{5}...N_{8}$	349.0(3)	13.9(7)	–	−1.4	10.3
u_{193}	$H_{9'}...H_{12'}$	356.4(9)	20.2 (Fixed)	–	0.6	20.2
u_{171}	$H_{9}...H_{12}$	356.4(9)	20.1 (Fixed)	–	0.6	20.1
u_{7}	$N_{1}...C_{5'}$	369.2(2)	9.8(2)	–	−2.1	6.4
u_{6}	$N_{1}...C_{5}$	369.2(2)	9.8 (Tied to u_{7})	–	−2.1	6.4

u_{94}	$C_{4'}...C_7$	373.4(2)	10.3 (Tied to u_7)	–	−1.1	6.8
u_{79}	$C_4...C_7$	373.7(2)	10.3 (Tied to u_7)	–	−0.8	6.8
u_{41}	$C_{2'}...C_4$	377.4(3)	11.9 (Tied to u_7)	–	0.8	7.9
u_{24}	$C_2...C_{4'}$	377.4(3)	11.9 (Tied to u_7)	–	0.8	7.8
u_{129}	$C_{5'}...H_{12}$	385.2(4)	14.6 (Tied to u_7)	–	−1.2	9.6
u_{117}	$C_5...H_{12'}$	385.2(4)	14.6 (Tied to u_7)	–	−1.2	9.6
u_{90}	$C_4...H_{13'}$	385.2(4)	14.6 (Tied to u_7)	–	−1.2	9.6
u_{104}	$C_{4'}...H_{13}$	385.3(4)	14.6 (Tied to u_7)	–	−1.1	9.6
u_{99}	$C_{4'}...H_{9'}$	387.8(7)	19.6 (Tied to u_7)	–	−2.3	12.9
u_{81}	$C_4...H_9$	387.8(7)	19.6 (Tied to u_7)	–	−2.3	12.9
u_{177}	$H_{10}...H_{10'}$	391.3(9)	61.3 (Fixed)	–	57.2	61.3
u_{98}	$C_{4'}...H_{11}$	398.2(5)	34.1 (Tied to u_7)	–	−13.1	22.4
u_{86}	$C_4...H_{11'}$	398.2(5)	34.1 (Tied to u_7)	–	−13.1	22.4
u_{112}	$C_5...H_{11}$	400.2(9)	46.6 (Tied to u_7)	–	−1.9	30.6
u_{128}	$C_{5'}...H_{11'}$	400.2(9)	46.6 (Tied to u_7)	–	−1.9	30.6
u_{184}	$H_{11}...H_{10'}$	410.6(10)	21.6 (Fixed)	–	2.0	21.6
u_{178}	$H_{10}...H_{11'}$	410.6(10)	21.6 (Fixed)	–	2.0	21.6
u_{54}	$C_{2'}...H_{12}$	413.4(3)	19.8 (Tied to u_8)	–	0.0	14.4
u_{37}	$C_2...H_{12'}$	413.4(3)	19.8 (Tied to u_8)	–	0.1	14.3
u_8	$N_1...C_6$	420.5(2)	9.3(3)	–	−2.4	6.8
u_{25}	$C_2...C_5$	424.2(7)	14.8 (Tied to u_8)	–	1.5	10.7
u_{44}	$C_{2'}...C_{5'}$	424.2(7)	14.7 (Tied to u_8)	–	1.5	10.7
u_{85}	$C_4...H_{10'}$	425.6(5)	36.9 (Tied to u_8)	–	18.7	26.8
u_{97}	$C_{4'}...H_{10}$	425.6(5)	36.9 (Tied to u_8)	–	18.7	26.8
u_{210}	$H_{13}...H_{13'}$	426.0(7)	12.9 (Fixed)	–	−2.4	12.9
u_{63}	$C_3...C_7$	426.6(3)	9.5 (Tied to u_8)	–	−1.6	6.9
u_{111}	$C_5...H_{10}$	428.5(9)	30.9 (Tied to u_{19})	–	10.4	36.3
u_{127}	$C_{5'}...H_{10'}$	428.5(9)	30.9 (Tied to u_{19})	–	10.4	36.2
u_{205}	$H_{12}...H_{12'}$	430.2(8)	12.9 (Fixed)	–	−1.7	12.9
u_{201}	$H_{11'}...H_{12}$	448.8(4)	23.7 (Fixed)	–	−16.5	23.7
u_{187}	$H_{11}...H_{12'}$	448.8(4)	23.7 (Fixed)	–	−16.5	23.7
u_{84}	$C_4...H_{9'}$	448.9(4)	10.7 (Tied to u_{19})	–	−3.6	12.5
u_{96}	$C_{4'}...H_9$	448.9(4)	10.7 (Tied to u_{19})	–	−3.5	12.6
u_{188}	$H_{11}...H_{13}$	453.1(10)	34.2 (Fixed)	–	2.6	34.2
u_{204}	$H_{11'}...H_{13'}$	453.2(10)	34.2 (Fixed)	–	2.6	34.2
u_{19}	$N_1...H_{13}$	455.3(4)	9.2(8)	10.8(11)	−2.6	10.8
u_{20}	$N_1...H_{13'}$	455.3(4)	9.2 (Tied to u_{19})	–	−2.5	10.8
u_{153}	$C_7...H_{12'}$	457.4(4)	9.6 (Tied to u_{19})	–	−2.0	11.3
u_{152}	$C_7...H_{12}$	457.8(4)	9.6 (Tied to u_{19})	–	−1.6	11.3
u_{192}	$H_{9'}...H_{12}$	465.1(5)	19.3 (Fixed)	–	−3.2	19.3
u_{172}	$H_9...H_{12'}$	465.1(5)	19.3 (Fixed)	–	−3.2	19.3
u_{181}	$H_{10}...H_{13}$	474.0(10)	40.6 (Fixed)	–	6.9	40.6
u_{200}	$H_{10'}...H_{13'}$	474.1(10)	40.6 (Fixed)	–	6.9	40.6
u_{197}	$H_{10'}...H_{12}$	474.2(4)	29.1 (Fixed)	–	19.1	29.1
u_{180}	$H_{10}...H_{12'}$	474.2(4)	29.1 (Fixed)	–	19.1	29.1

u_{95}	$C_{4'}...N_8$	480.6(3)	11.1(5)	–	−3.0	9.0
u_{80}	$C_4...N_8$	481.0(3)	11.1 (Tied to u_{95})	–	−2.6	9.0
u_{38}	$C_2...H_{13}$	485.5(8)	19.4 (Tied to u_{95})	–	1.6	15.8
u_{57}	$C_{2'}...H_{13'}$	485.5(8)	19.4 (Tied to u_{95})	–	1.6	15.7
u_{26}	$C_2...C_{5'}$	490.2(4)	10.3 (Tied to u_{95})	–	0.5	8.4
u_{43}	$C_{2'}...C_5$	490.2(4)	10.4 (Tied to u_{95})	–	0.5	8.4
u_{207}	$H_{12}...H_{13'}$	491.9(8)	11.9 (Fixed)	–	−2.5	11.9
u_{208}	$H_{12'}...H_{13}$	491.9(8)	11.9 (Fixed)	–	−2.5	11.9
u_{125}	$C_{5'}...H_{11}$	495.7(6)	32.7 (Tied to u_{95})	–	−14.0	26.5
u_{115}	$C_5...H_{11'}$	495.7(6)	32.7 (Tied to u_{95})	–	−14.0	26.5
u_{137}	$C_6...H_{11}$	499.3(8)	36.3 (Tied to u_{95})	–	−9.4	29.4
u_{140}	$C_6...H_{11'}$	499.3(8)	36.3 (Tied to u_{95})	–	−9.4	29.4
u_{27}	$C_2...C_6$	511.3(6)	10.1(7)	–	0.8	9.7
u_{45}	$C_{2'}...C_6$	511.3(6)	10.1 (Tied to u_{27})	–	0.8	9.7
u_{126}	$C_{5'}...H_{9'}$	525.5(7)	13.9 (Tied to u_{27})	–	−4.1	13.3
u_{110}	$C_5...H_9$	525.5(7)	13.9 (Tied to u_{27})	–	−4.1	13.3
u_{124}	$C_{5'}...H_{10}$	527.7(6)	35.1 (Tied to u_{64})	–	20.1	31.3
u_{114}	$C_5...H_{10'}$	527.7(6)	35.1 (Tied to u_{64})	–	20.2	31.3
u_{136}	$C_6...H_{10}$	530.2(8)	39.1 (Tied to u_{64})	–	16.9	34.9
u_{139}	$C_6...H_{10'}$	530.3(8)	39.1 (Tied to u_{64})	–	16.9	34.9
u_{64}	$C_3...N_8$	538.4(3)	8.2(6)	7.3(7)	−3.6	7.3
u_9	$N_1...C_7$	563.1(3)	8.1(5)	7.3(7)	−3.6	7.3
u_{123}	$C_{5'}...H_9$	571.4(4)	13.7 (Tied to u_9)	–	−5.1	12.4
u_{113}	$C_5...H_{9'}$	571.4(4)	13.7 (Tied to u_9)	–	−5.1	12.4
u_{56}	$C_{2'}...H_{13}$	584.8(5)	13.0 (Tied to u_9)	–	−0.6	11.8
u_{39}	$C_2...H_{13'}$	584.8(5)	13.0 (Tied to u_9)	–	−0.6	11.7
u_{173}	$H_9...H_{13}$	588.5(8)	18.2 (Fixed)	–	−4.0	18.2
u_{195}	$H_{9'}...H_{13'}$	588.5(8)	18.2 (Fixed)	–	−4.0	18.2
u_{189}	$H_{11}...H_{13'}$	593.8(7)	27.9 (Fixed)	–	−17.7	27.9
u_{203}	$H_{11'}...H_{13}$	593.8(7)	27.9 (Fixed)	–	−17.7	27.9
u_{135}	$C_6...H_9$	605.5(5)	14.3(13)	12.5(13)	−5.3	12.5
u_{138}	$C_6...H_{9'}$	605.5(5)	14.3 (Tied to u_{135})	–	−5.3	12.5
u_{182}	$H_{10}...H_{13'}$	627.6(7)	33.2 (Fixed)	–	21.6	33.2
u_{199}	$H_{10'}...H_{13}$	627.6(7)	33.2 (Fixed)	–	21.6	33.2
u_{151}	$C_7...H_{11'}$	632.2(9)	35.3 (Tied to u_{135})	–	−11.1	31.0
u_{148}	$C_7...H_{11}$	632.5(9)	35.3 (Tied to u_{135})	–	−10.9	31.0
u_{46}	$C_{2'}...C_7$	650.2(6)	12.5(7)	10.6(11)	−0.5	10.6
u_{28}	$C_2...C_7$	650.4(6)	12.5 (Tied to u_{46})	–	−0.3	10.6
u_{174}	$H_9...H_{13'}$	659.5(5)	15.9 (Fixed)	–	−6.1	15.9
u_{194}	$H_{9'}...H_{13}$	659.5(5)	15.9 (Fixed)	–	−6.1	15.9
u_{150}	$C_7...H_{10'}$	663.9(9)	46.6 (Tied to u_{10})	–	16.8	37.5
u_{147}	$C_7...H_{10}$	664.1(9)	46.6 (Tied to u_{10})	–	17.0	37.5
u_{10}	$N_1...N_8$	674.6(3)	9.7(6)	7.8(8)	−6.0	7.8
u_{161}	$N_8...H_{11'}$	738.3(10)	37.9 (Tied to u_{47})	–	−13.7	32.3
u_{158}	$N_8...H_{11}$	738.7(10)	37.9 (Tied to u_{47})	–	−13.3	32.3

u_{149}	$C_7...H_{9'}$	745.5(6)	15.7 (Tied to u_{47})	–	−7.1	13.4
u_{146}	$C_7...H_9$	745.6(6)	15.7 (Tied to u_{47})	–	−7.0	13.4
u_{47}	$C_{2'}...N_8$	759.6(7)	13.9(7)	11.8(12)	−3.0	11.8
u_{29}	$C_2...N_8$	759.9(7)	13.9 (Tied to u_{47})	–	−2.7	11.8
u_{160}	$N_8...H_{10'}$	771.2(10)	46.3 (Tied to u_{47})	–	14.8	39.5
u_{157}	$N_8...H_{10}$	771.5(10)	46.4 (Tied to u_{47})	–	15.2	39.6
u_{159}	$N_8...H_{9'}$	855.5(6)	14.1(14)	14.3(14)	−10.0	14.3
u_{156}	$N_8...H_9$	855.7(6)	14.1 (Tied to u_{159})	–	−9.8	14.3

[a] All values are tabulated in picometers (pm).

Table A24. Refined Cartesian coordinates in Ångström (Å) for the experimentally-determined structure of 4-(dimethylamino)benzonitrile obtained *via* GED.

	x	*y*	*z*
N	1.3856	0.0000	0.0000
C	2.1015	−1.2609	−0.1883
C	2.1015	1.2609	−0.1883
C	0.0000	0.0000	0.0000
C	−0.7369	−1.2121	0.0000
C	−0.7369	1.2121	0.0000
C	−2.1257	−1.2078	0.0000
C	−2.1257	1.2078	0.0000
C	−2.8440	0.0000	0.0000
C	−4.2829	0.0000	0.0000
N	−5.4209	0.0000	0.0000
H	3.1672	−1.0714	−0.1348
H	1.8836	−1.7237	−1.1545
H	1.8317	−1.9825	0.5807
H	3.1672	1.0714	−0.1348
H	1.8836	1.7237	−1.1545
H	1.8317	1.9825	0.5807
H	−0.2269	−2.1602	0.0000
H	−0.2269	2.1602	0.0000
H	−2.6600	−2.1424	0.0000
H	−2.6600	2.1424	0.0000

Table A25. Summary of experimental parameters relating to GED data collection for $Sn(TFA)_2$ and $Sn_2O(TFA)_2$.

Dataset Type	Short	Long
Nozzle-to-Image-Plate Distance / mm	234.5	477.0
Electron Wavelength / pm	5.85	5.85
$T_{\text{nozzle, av}}$ / K	473	473
$T_{\text{sample, av}}$ / K	363	363
Exposure Time / s	240	120

Table A26. Summary of experimental parameters relating to GED data collection for $Sn(TFA)_4$.

Dataset Type	Short	Long
Nozzle-to-Image-Plate Distance / mm	233.5	486.0
Electron Wavelength / pm	5.85	5.85
$T_{nozzle,\ av}$ / K	403	403
$T_{sample,\ av}$ / K	398	398
Exposure Time / s	240	120

Table A27. Optimised Cartesian coordinates in Ångström (Å) and energy, E_{M06}, in atomic units (a.u.) of $Sn(TFA)_2$ as calculated at the M06/*def*2-SVP level.

E_{M06} = −1265.69317741			
Sn	0.000000	0.000000	1.707022
O	−1.048348	1.833640	0.550225
C	0.000000	1.933400	−0.103957
O	0.994199	1.171554	0.069931
C	0.162487	3.028972	−1.168130
F	0.483841	2.481460	−2.329279
F	−0.944249	3.728492	−1.315563
F	1.140013	3.847870	−0.800076
O	1.048348	−1.833640	0.550225
C	0.000000	−1.933400	−0.103957
O	−0.994199	−1.171554	0.069931
C	−0.162487	−3.028972	−1.168130
F	−0.483841	−2.481460	−2.329279
F	0.944249	−3.728492	−1.315563
F	−1.140013	−3.847870	−0.800076

Table A28. Optimised Cartesian coordinates in Ångström (Å) and energy, E_{M06}, in atomic units (a.u.) of $Sn(TFA)_2$ as calculated at the M06/*def*2-TZVP level.

E_{M06} = −1266.92692674			
Sn	0.000000	0.000000	1.661333
O	−1.060324	1.813728	0.520094
C	0.000000	1.932403	−0.104085
O	0.994300	1.173759	0.070970
C	0.179608	3.063751	−1.136388
F	0.596088	2.566562	−2.288579
F	−0.944081	3.718808	−1.335749
F	1.094638	3.915121	−0.688893
O	1.060324	−1.813728	0.520094
C	0.000000	−1.932403	−0.104085
O	−0.994300	−1.173759	0.070970
C	−0.179608	−3.063751	−1.136388
F	−0.596088	−2.566562	−2.288579
F	0.944081	−3.718808	−1.335749
F	−1.094638	−3.915121	−0.688893

Table A29. Optimised Cartesian coordinates in Ångström (Å) and energy, E_{M06}, in atomic units (a.u.) of $Sn(TFA)_2$ as calculated at the M06/*def*2-QZVP level.

E_{M06} = −1266.98481147			
Sn	0.000000	0.000000	1.658676
O	−1.060599	1.812114	0.519136
C	0.000000	1.934108	−0.101899
O	0.993944	1.176451	0.073356
C	0.180116	3.066113	−1.134313
F	0.566287	2.563310	−2.294479
F	−0.935321	3.740119	−1.311906
F	1.117516	3.900630	−0.703567
O	1.060599	−1.812114	0.519136
C	0.000000	−1.934108	−0.101899
O	−0.993944	−1.176451	0.073356
C	−0.180116	−3.066113	−1.134313
F	−0.566287	−2.563310	−2.294479
F	0.935321	−3.740119	−1.311906
F	−1.117516	−3.900630	−0.703567

Table A30. Optimised Cartesian coordinates in Ångström (Å) and energy, E_{M11}, in atomic units (a.u.) of $Sn(TFA)_2$ as calculated at the M11/*def*2-SVP level.

E_{M11} = −1265.50275815			
Sn	0.000000	0.000000	1.730656
O	−1.039459	1.797096	0.574018
C	0.000000	1.881504	−0.093230
O	0.986139	1.110571	0.103145
C	0.157241	2.948860	−1.193475
F	0.454398	2.360371	−2.350230
F	−0.956721	3.652911	−1.336402
F	1.153452	3.774124	−0.864866
O	1.039459	−1.797096	0.574018
C	0.000000	−1.881504	−0.093230
O	−0.986139	−1.110571	0.103145
C	−0.157241	−2.948860	−1.193475
F	−0.454398	−2.360371	−2.350230
F	0.956721	−3.652911	−1.336402
F	−1.153452	−3.774124	−0.864866

Table A31. Optimised Cartesian coordinates in Ångström (Å) and energy, E_{M11}, in atomic units (a.u.) of $Sn(TFA)_2$ as calculated at the M11/*def*2-TZVP level.

E_{M11} = −1266.86015422			
Sn	0.000000	0.000000	1.691177
O	−1.050585	1.790073	0.550767
C	0.000000	1.887197	−0.092651
O	0.987683	1.118323	0.100031
C	0.172007	2.986154	−1.164197
F	0.577216	2.444564	−2.315643
F	−0.966841	3.639770	−1.369372
F	1.102798	3.859259	−0.753286
O	1.050585	−1.790073	0.550767
C	0.000000	−1.887197	−0.092651
O	−0.987683	−1.118323	0.100031
C	−0.172007	−2.986154	−1.164197
F	−0.577216	−2.444564	−2.315643
F	0.966841	−3.639770	−1.369372
F	−1.102798	−3.859259	−0.753286

Table A32. Optimised Cartesian coordinates in Ångström (Å) and energy, E_{M11}, in atomic units (a.u.) of $Sn(TFA)_2$ as calculated at the M11/*def*2-QZVP level.

E_{M11} = −1266.95488084			
Sn	0.000000	0.000000	1.682033
O	−1.051903	1.785698	0.548154
C	0.000000	1.890962	−0.091531
O	0.989295	1.124835	0.099004
C	0.169495	2.996352	−1.157457
F	0.555814	2.457914	−2.316783
F	−0.965383	3.660999	−1.345375
F	1.112537	3.858338	−0.752750
O	1.051903	−1.785698	0.548154
C	0.000000	−1.890962	−0.091531
O	−0.989295	−1.124835	0.099004
C	−0.169495	−2.996352	−1.157457
F	−0.555814	−2.457914	−2.316783
F	0.965383	−3.660999	−1.345375
F	−1.112537	−3.858338	−0.752750

Table A33. Optimised Cartesian coordinates in Ångström (Å) and energy, $E_{SOGGA11\text{-}X}$, in atomic units (a.u.) of $Sn(TFA)_2$ as calculated at the SOGGA11-X/*def*2-SVP level.

$E_{SOGGA11\text{-}X}$ = −1265.63534406			
Sn	0.000000	0.000000	1.685318
O	−1.051982	1.830643	0.536282
C	0.989796	1.178947	0.073337
O	0.000000	1.945485	−0.106251
C	0.162344	3.063504	−1.152672
F	0.529757	2.546991	−2.316789
F	−0.964340	3.731107	−1.318873
F	1.103417	3.911126	−0.748380
O	−0.989796	−1.178947	0.073337
C	1.051982	−1.830643	0.536282
O	0.000000	−1.945485	−0.106251
C	−0.162344	−3.063504	−1.152672
F	−0.529757	−2.546991	−2.316789
F	0.964340	−3.731107	−1.318873
F	−1.103417	−3.911126	−0.748380

Table A34. Optimised Cartesian coordinates in Ångström (Å) and energy, $E_{SOGGA11\text{-}X}$, in atomic units (a.u.) of $Sn(TFA)_2$ as calculated at the SOGGA11-X/*def*2-TZVP level.

$E_{SOGGA11\text{-}X}$ = −1266.92648297			
Sn	0.000000	0.000000	1.619275
O	−1.066852	1.801994	0.497060
C	0.992210	1.182456	0.063369
O	0.000000	1.947460	−0.112335
C	0.181549	3.118114	−1.105911
F	0.719858	2.687882	−2.239003
F	−0.972267	3.701356	−1.378021
F	0.997322	4.023518	−0.566955
O	−0.992210	−1.182456	0.063369
C	1.066852	−1.801994	0.497060
O	0.000000	−1.947460	−0.112335
C	−0.181549	−3.118114	−1.105911
F	−0.719858	−2.687882	−2.239003
F	0.972267	−3.701356	−1.378021
F	−0.997322	−4.023518	−0.566955

Table A35. Optimised Cartesian coordinates in Ångström (Å) and energy, $E_{\text{SOGGA11-X}}$, in atomic units (a.u.) of $Sn(TFA)_2$ as calculated at the SOGGA11-X/*def*2-QZVP level.

$E_{\text{SOGGA11-X}} = -1266.97630535$			
Sn	0.000000	0.000000	1.613998
O	−1.067231	1.799428	0.492956
C	0.992153	1.184646	0.061787
O	0.000000	1.948465	−0.113504
C	0.181888	3.123756	−1.101960
F	0.729995	2.701162	−2.232331
F	−0.972538	3.701480	−1.379468
F	0.988756	4.031128	−0.554325
O	−0.992153	−1.184646	0.061787
C	1.067231	−1.799428	0.492956
O	0.000000	−1.948465	−0.113504
C	−0.181888	−3.123756	−1.101960
F	−0.729995	−2.701162	−2.232331
F	0.972538	−3.701480	−1.379468
F	−0.988756	−4.031128	−0.554325

Table A36. Optimised Cartesian coordinates in Ångström (Å) and energy, $E_{\text{SOGGA11-X}}$, in atomic units (a.u.) of $Sn(TFA)_2$ as calculated at the SOGGA11-X/DZP-DKH level.

$E_{\text{SOGGA11-X}} = -7223.11576523$			
Sn	0.000000	0.000000	1.612842
O	−1.061598	1.837223	0.536052
C	0.000000	1.948392	−0.096176
O	0.979443	1.154423	0.076050
C	0.202365	3.090504	−1.109792
F	0.715135	2.624170	−2.244697
F	−0.939785	3.705880	−1.378547
F	1.055134	3.983672	−0.596984
O	1.061598	−1.837223	0.536052
C	0.000000	−1.948392	−0.096176
O	−0.979443	−1.154423	0.076050
C	−0.202365	−3.090504	−1.109792
F	−0.715135	−2.624170	−2.244697
F	0.939785	−3.705880	−1.378547
F	−1.055134	−3.983672	−0.596984

Table A37. Optimised Cartesian coordinates in Ångström (Å) and energy, $E_{SOGGA11\text{-}X}$, in atomic units (a.u.) of $Sn(TFA)_2$ as calculated at the SOGGA11-X/TZP-DKH level.

$E_{SOGGA11\text{-}X} = -7223.43971935$			
Sn	0.000000	0.000000	1.598760
O	−1.059238	1.815292	0.523365
C	0.000000	1.934374	−0.098943
O	0.977729	1.144936	0.069327
C	0.201989	3.092065	−1.099263
F	0.717390	2.642015	−2.234462
F	−0.939290	3.701919	−1.361764
F	1.045340	3.978358	−0.572807
O	1.059238	−1.815292	0.523365
C	0.000000	−1.934374	−0.098943
O	−0.977729	−1.144936	0.069327
C	−0.201989	−3.092065	−1.099263
F	−0.717390	−2.642015	−2.234462
F	0.939290	−3.701919	−1.361764
F	−1.045340	−3.978358	−0.572807

Table A38. Optimised Cartesian coordinates in Ångström (Å) and energy, E_{M06}, in atomic units (a.u.) of $Sn_2O(TFA)_2$ as calculated at the M06/*def*2-SVP level.

$E_{M06} = -1555.31109592$			
O	0.000000	0.000000	2.107330
Sn	1.456001	−1.055809	1.241794
Sn	−1.456001	1.055809	1.241794
O	0.000000	2.020142	−0.204815
C	1.072172	1.576845	−0.666501
O	1.643239	0.494192	−0.438086
C	1.784249	2.546835	−1.634150
F	2.269259	3.566818	−0.931037
F	2.782205	1.966446	−2.273252
F	0.929497	3.023039	−2.525925
O	0.000000	−2.020142	−0.204815
C	−1.072172	−1.576845	−0.666501
O	−1.643239	−0.494192	−0.438086
C	−1.784249	−2.546835	−1.634150
F	−2.269259	−3.566818	−0.931037
F	−2.782210	−1.966450	−2.273250
F	−0.929500	−3.023040	−2.525930

Table A39. Optimised Cartesian coordinates in Ångström (Å) and energy, E_{M06}, in atomic units (a.u.) of $Sn_2O(TFA)_2$ as calculated at the M06/*def*2-TZVP level.

E_{M06} = −1556.63610678			
O	0.000000	0.000000	2.065568
Sn	1.441379	1.038898	1.198573
Sn	−1.441379	−1.038898	1.198573
O	−1.708748	0.523912	−0.422447
C	−1.111917	1.588745	−0.663040
O	0.000000	1.981071	−0.273501
C	−1.908537	2.567575	−1.566448
F	−2.928100	3.057621	−0.866170
F	−1.168410	3.574546	−1.984139
F	−2.395079	1.935068	−2.621513
O	1.708748	−0.523912	−0.422447
C	1.111917	−1.588745	−0.663040
O	0.000000	−1.981071	−0.273501
C	1.908537	−2.567575	−1.566448
F	2.928100	−3.057621	−0.866170
F	1.168410	−3.574550	−1.984140
F	2.395079	−1.935070	−2.621510

Table A40. Optimised Cartesian coordinates in Ångström (Å) and energy, E_{M06}, in atomic units (a.u.) of $Sn_2O(TFA)_2$ as calculated at the M06/*def*2-QZVP level.

E_{M06} = −1556.70107571			
O	0.000000	0.000000	2.065354
Sn	1.441753	1.036272	1.204636
Sn	−1.441753	−1.036272	1.204636
O	−1.698962	0.521161	−0.419304
C	−1.106865	1.589086	−0.654413
O	0.000000	1.985759	−0.257964
C	−1.900154	2.556539	−1.573822
F	−2.998326	2.953226	−0.939082
F	−1.199097	3.622870	−1.899097
F	−2.263750	1.935220	−2.684671
O	1.698962	−0.521161	−0.419304
C	1.106865	−1.589086	−0.654413
O	0.000000	−1.985759	−0.257964
C	1.900154	−2.556539	−1.573822
F	2.998326	−2.953226	−0.939082
F	1.199097	−3.622870	−1.899100
F	2.263750	−1.935220	−2.684670

Table A41. Optimised Cartesian coordinates in Ångström (Å) and energy, E_{M11}, in atomic units (a.u.) of $Sn_2O(TFA)_2$ as calculated at the M11/*def*2-SVP level.

E_{M11} = −1554.89836428			
O	0.000000	0.000000	2.082411
Sn	1.442885	−1.083404	1.281121
Sn	−1.442885	1.083404	1.281121
O	0.000000	1.989831	−0.147188
C	1.048656	1.513593	−0.630176
O	1.602473	0.426799	−0.379092
C	1.721781	2.416895	−1.693911
F	1.963469	3.620683	−1.169738
F	2.866022	1.898073	−2.121743
F	0.899276	2.566247	−2.734181
O	0.000000	−1.989831	−0.147188
C	−1.048656	−1.513593	−0.630176
O	−1.602473	−0.426799	−0.379092
C	−1.721781	−2.416895	−1.693911
F	−1.963469	−3.620683	−1.169738
F	−2.866020	−1.898070	−2.121740
F	−0.899280	−2.566250	−2.734180

Table A42. Optimised Cartesian coordinates in Ångström (Å) and energy, E_{M11}, in atomic units (a.u.) of $Sn_2O(TFA)_2$ as calculated at the M11/*def*2-TZVP level.

E_{M11} = −1556.36439404			
O	0.000000	0.000000	2.051543
Sn	1.435490	−1.070803	1.242349
Sn	−1.435490	1.070803	1.242349
O	0.000000	1.988985	−0.176252
C	1.064815	1.533526	−0.636439
O	1.619600	0.446283	−0.404534
C	1.780518	2.486329	−1.635133
F	2.124945	3.617054	−1.000790
F	2.878928	1.934089	−2.144382
F	0.952982	2.802236	−2.637927
O	0.000000	−1.988985	−0.176252
C	−1.064815	−1.533526	−0.636439
O	−1.619600	−0.446283	−0.404534
C	−1.780518	−2.486329	−1.635133
F	−2.124945	−3.617054	−1.000790
F	−2.878930	−1.934090	−2.144380
F	−0.952980	−2.802240	−2.637930

Table A43. Optimised Cartesian coordinates in Ångström (Å) and energy, E_{M11}, in atomic units (a.u.) of $Sn_2O(TFA)_2$ as calculated at the M11/*def*2-QZVP level.

E_{M11} = −1556.46771071			
O	0.000000	0.000000	2.047599
Sn	1.431937	−1.065305	1.233184
Sn	−1.431937	1.065305	1.233184
O	0.000000	1.985434	−0.183310
C	1.071132	1.538144	−0.635319
O	1.629238	0.452915	−0.403951
C	1.791777	2.500086	−1.622376
F	2.127229	3.627455	−0.977846
F	2.895774	1.955538	−2.126659
F	0.971299	2.819675	−2.629423
O	0.000000	−1.985434	−0.183310
C	−1.071132	−1.538144	−0.635319
O	−1.629238	−0.452915	−0.403951
C	−1.791777	−2.500086	−1.622376
F	−2.127229	−3.627455	−0.977846
F	−2.895770	−1.955540	−2.126660
F	−0.971300	−2.819680	−2.629420

Table A44. Optimised Cartesian coordinates in Ångström (Å) and energy, $E_{SOGGA11\text{-}X}$, in atomic units (a.u.) of $Sn_2O(TFA)_2$ as calculated at the SOGGA11-X/*def*2-SVP level.

$E_{SOGGA11\text{-}X}$ = −1555.22139679			
O	0.000000	0.000000	2.041502
Sn	1.449558	−1.070045	1.203839
Sn	−1.449558	1.070045	1.203839
O	0.000000	1.900274	−0.331632
C	1.153369	1.564599	−0.664230
O	1.803687	0.550473	−0.341757
C	1.905490	2.563047	−1.576095
F	2.650025	3.362606	−0.811325
F	2.705446	1.930255	−2.420635
F	1.066750	3.313707	−2.271252
O	0.000000	−1.900274	−0.331632
C	−1.153369	−1.564599	−0.664230
O	−1.803687	−0.550473	−0.341757
C	−1.905490	−2.563047	−1.576095
F	−2.650025	−3.362606	−0.811325
F	−2.705450	−1.930260	−2.420640
F	−1.066750	−3.313710	−2.271250

Table A45. Optimised Cartesian coordinates in Ångström (Å) and energy, $E_{SOGGA11\text{-}X}$, in atomic units (a.u.) of $Sn_2O(TFA)_2$ as calculated at the SOGGA11-X/*def*2-TZVP level.

$E_{SOGGA11\text{-}X}$ = −1556.61033066			
O	0.000000	0.000000	2.008527
Sn	1.429650	−1.052697	1.166550
Sn	−1.429650	1.052697	1.166550
O	0.000000	1.916035	−0.335373
C	1.152721	1.577421	−0.662338
O	1.785071	0.543167	−0.376837
C	1.933300	2.612284	−1.521664
F	2.636442	3.399635	−0.702699
F	2.777175	2.016022	−2.350913
F	1.115821	3.375218	−2.230823
O	0.000000	−1.916035	−0.335373
C	−1.152721	−1.577421	−0.662338
O	−1.785071	−0.543167	−0.376837
C	−1.933300	−2.612284	−1.521664
F	−2.636442	−3.399635	−0.702699
F	−2.777180	−2.016020	−2.350910
F	−1.115820	−3.375220	−2.230820

Table A46. Optimised Cartesian coordinates in Ångström (Å) and energy, $E_{SOGGA11\text{-}X}$, in atomic units (a.u.) of $Sn_2O(TFA)_2$ as calculated at the SOGGA11-X/*def*2-QZVP level.

$E_{SOGGA11\text{-}X}$ = −1556.66621870			
O	0.000000	0.000000	2.001673
Sn	1.428519	−1.052149	1.163798
Sn	−1.428519	1.052149	1.163798
O	0.000000	1.911985	−0.338232
C	1.154119	1.577071	−0.661498
O	1.787354	0.544621	−0.374294
C	1.935074	2.614485	−1.517644
F	2.633073	3.403139	−0.696435
F	2.782978	2.021157	−2.343737
F	1.118453	3.375155	−2.228887
O	0.000000	−1.911985	−0.338232
C	−1.154119	−1.577071	−0.661498
O	−1.787354	−0.544621	−0.374294
C	−1.935074	−2.614485	−1.517644
F	−2.633073	−3.403139	−0.696435
F	−2.782980	−2.021160	−2.343740
F	−1.118450	−3.375160	−2.228890

Table A47. Optimised Cartesian coordinates in Ångström (Å) and energy, $E_{SOGGA11\text{-}X}$, in atomic units (a.u.) of $Sn_2O(TFA)_2$ as calculated at the SOGGA11-X/DZP-DKH level.

$E_{SOGGA11\text{-}X}$ = −13468.42020240			
O	0.000000	0.000000	1.973834
Sn	−1.772424	0.093961	1.197833
Sn	1.772424	−0.093961	1.197833
O	−1.052677	1.552379	−0.316350
C	0.098920	1.917634	−0.643647
O	1.204998	1.440108	−0.308959
C	0.149879	3.159339	−1.569328
F	0.000000	4.261413	−0.821332
F	1.307780	3.249456	−2.212301
F	−0.830704	3.130947	−2.467109
O	1.052677	−1.552379	−0.316350
C	−0.098920	−1.917634	−0.643647
O	−1.204998	−1.440108	−0.308959
C	−0.149879	−3.159339	−1.569328
F	0.000000	−4.261413	−0.821332
F	−1.307780	−3.249456	−2.212301
F	0.830704	−3.130947	−2.467109

Table A48. Optimised Cartesian coordinates in Ångström (Å) and energy, $E_{SOGGA11\text{-}X}$, in atomic units (a.u.) of $Sn_2O(TFA)_2$ as calculated at the SOGGA11-X/TZP-DKH level.

$E_{SOGGA11\text{-}X}$ = −13468.92089320			
O	0.000000	0.000000	1.963780
Sn	−1.742033	0.194316	1.172353
Sn	1.742033	−0.194316	1.172353
O	−0.950360	1.616093	−0.343302
C	0.216810	1.936161	−0.636750
O	1.291301	1.401412	−0.312804
C	0.326057	3.203517	−1.529186
F	0.000000	4.275514	−0.805751
F	1.551374	3.374063	−1.995945
F	−0.509566	3.124521	−2.557005
O	0.950360	−1.616093	−0.343302
C	−0.216810	−1.936161	−0.636750
O	−1.291301	−1.401412	−0.312804
C	−0.326057	−3.203517	−1.529186
F	0.000000	−4.275514	−0.805751
F	−1.551374	−3.374063	−1.995945
F	0.509566	−3.124521	−2.557005

Table A49. Optimised Cartesian coordinates in Ångström (Å) and energy, E_{M06}, in atomic units (a.u.) of $Sn(TFA)_4$ as calculated at the M06/*def*2-SVP level.

E_{M06} = −2316.91349099			
Sn	0.000000	0.000000	0.000000
O	0.000000	2.168435	0.317988
C	0.000000	2.394408	−0.926142
O	0.000000	1.456604	−1.739939
C	0.000000	3.859818	−1.381088
F	0.000000	3.951314	−2.691732
F	1.076801	4.457730	−0.900932
F	−1.076801	4.457730	−0.900932
O	0.000000	−2.168435	0.317988
C	0.000000	−2.394408	−0.926142
O	0.000000	−1.456604	−1.739939
C	0.000000	−3.859818	−1.381088
F	0.000000	−3.951314	−2.691732
F	1.076801	−4.457730	−0.900932
F	−1.076801	−4.457730	−0.900932
O	2.168435	0.000000	−0.317988
C	2.394408	0.000000	0.926142
O	1.456604	0.000000	1.739939
C	3.859818	0.000000	1.381088
F	3.951314	0.000000	2.691732
F	4.457730	−1.076801	0.900932
F	4.457730	1.076801	0.900932
O	−2.168435	0.000000	−0.317988
C	−2.394408	0.000000	0.926142
O	−1.456604	0.000000	1.739939
C	−3.859818	0.000000	1.381088
F	−3.951314	0.000000	2.691732
F	−4.457730	−1.076801	0.900932
F	−4.457730	1.076801	0.900932

Table A50. Optimised Cartesian coordinates in Ångström (Å) and energy, E_{M06}, in atomic units (a.u.) of $Sn(TFA)_4$ as calculated at the M06/*def*2-TZVP level.

E_{M06} = −2319.37909092			
Sn	0.000000	0.000000	0.000000
O	0.000000	2.135398	0.324253
C	0.000000	2.365574	−0.917616
O	0.000000	1.436904	−1.736140
C	0.000000	3.837518	−1.366232
F	0.000000	3.935414	−2.675278
F	1.075501	4.437258	−0.885907
F	−1.075501	4.437258	−0.885907
O	0.000000	−2.135398	0.324253
C	0.000000	−2.365574	−0.917616
O	0.000000	−1.436904	−1.736140
C	0.000000	−3.837518	−1.366232
F	0.000000	−3.935414	−2.675278
F	1.075501	−4.437258	−0.885907
F	−1.075501	−4.437258	−0.885907
O	2.135398	0.000000	−0.324253
C	2.365574	0.000000	0.917616
O	1.436904	0.000000	1.736140
C	3.837518	0.000000	1.366232
F	3.935414	0.000000	2.675278
F	4.437258	−1.075501	0.885907
F	4.437258	1.075501	0.885907
O	−2.135398	0.000000	−0.324253
C	−2.365574	0.000000	0.917616
O	−1.436904	0.000000	1.736140
C	−3.837518	0.000000	1.366232
F	−3.935414	0.000000	2.675278
F	−4.437258	−1.075501	0.885907
F	−4.437258	1.075501	0.885907

Table A51. Optimised Cartesian coordinates in Ångström (Å) and energy, E_{M06}, in atomic units (a.u.) of $Sn(TFA)_4$ as calculated at the M06/*def*2-QZVP level.

E_{M06} = −2319.49251729			
Sn	0.000000	0.000000	0.000000
O	0.000000	2.133713	0.324164
C	0.000000	2.364684	−0.916574
O	0.000000	1.437195	−1.734956
C	0.000000	3.837399	−1.364268
F	0.000000	3.936537	−2.672712
F	1.075175	4.436618	−0.883462
F	−1.075175	4.436618	−0.883462
O	0.000000	−2.133713	0.324164
C	0.000000	−2.364684	−0.916574
O	0.000000	−1.437195	−1.734956
C	0.000000	−3.837399	−1.364268
F	0.000000	−3.936537	−2.672712
F	1.075175	−4.436618	−0.883462
F	−1.075175	−4.436618	−0.883462
O	2.133713	0.000000	−0.324164
C	2.364684	0.000000	0.916574
O	1.437195	0.000000	1.734956
C	3.837399	0.000000	1.364268
F	3.936537	0.000000	2.672712
F	4.436618	−1.075175	0.883462
F	4.436618	1.075175	0.883462
O	−2.133713	0.000000	−0.324164
C	−2.364684	0.000000	0.916574
O	−1.437195	0.000000	1.734956
C	−3.837399	0.000000	1.364268
F	−3.936537	0.000000	2.672712
F	−4.436618	−1.075175	0.883462
F	−4.436618	1.075175	0.883462

Table A52. Optimised Cartesian coordinates in Ångström (Å) and energy, E_{M11}, in atomic units (a.u.) of $Sn(TFA)_4$ as calculated at the M11/*def*2-SVP level.

E_{M11} = −2316.77650596			
Sn	0.000000	0.000000	0.000000
O	0.000000	2.132375	0.319500
C	0.000000	2.380689	−0.924499
O	0.000000	1.446277	−1.738112
C	0.000000	3.854386	−1.369494
F	0.000000	3.944764	−2.688753
F	1.083464	4.454812	−0.884641
F	−1.083464	4.454812	−0.884641
O	0.000000	−2.132375	0.319500
C	0.000000	−2.380689	−0.924499
O	0.000000	−1.446277	−1.738112
C	0.000000	−3.854386	−1.369494
F	0.000000	−3.944764	−2.688753
F	1.083464	−4.454812	−0.884641
F	−1.083464	−4.454812	−0.884641
O	2.132375	0.000000	−0.319500
C	2.380689	0.000000	0.924499
O	1.446277	0.000000	1.738112
C	3.854386	0.000000	1.369494
F	3.944764	0.000000	2.688753
F	4.454812	−1.083464	0.884641
F	4.454812	1.083464	0.884641
O	−2.132375	0.000000	−0.319500
C	−2.380689	0.000000	0.924499
O	−1.446277	0.000000	1.738112
C	−3.854386	0.000000	1.369494
F	−3.944764	0.000000	2.688753
F	−4.454812	−1.083464	0.884641
F	−4.454812	1.083464	0.884641

Table A53. Optimised Cartesian coordinates in Ångström (Å) and energy, E_{M11}, in atomic units (a.u.) of $Sn(TFA)_4$ as calculated at the M11/*def*2-TZVP level.

E_{M11} = −2319.47858823			
Sn	0.000000	0.000000	0.000000
O	0.000000	2.108306	0.323714
C	0.000000	2.357560	−0.920132
O	0.000000	1.432383	−1.740580
C	0.000000	3.835325	−1.358709
F	0.000000	3.935929	−2.680973
F	1.086216	4.439761	−0.871154
F	−1.086216	4.439761	−0.871154
O	0.000000	−2.108306	0.323714
C	0.000000	−2.357560	−0.920132
O	0.000000	−1.432383	−1.740580
C	0.000000	−3.835325	−1.358709
F	0.000000	−3.935929	−2.680973
F	1.086216	−4.439761	−0.871154
F	−1.086216	−4.439761	−0.871154
O	2.108306	0.000000	−0.323714
C	2.357560	0.000000	0.920132
O	1.432383	0.000000	1.740580
C	3.835325	0.000000	1.358709
F	3.935929	0.000000	2.680973
F	4.439761	−1.086216	0.871154
F	4.439761	1.086216	0.871154
O	−2.108306	0.000000	−0.323714
C	−2.357560	0.000000	0.920132
O	−1.432383	0.000000	1.740580
C	−3.835325	0.000000	1.358709
F	−3.935929	0.000000	2.680973
F	−4.439761	−1.086216	0.871154
F	−4.439761	1.086216	0.871154

Table A54. Optimised Cartesian coordinates in Ångström (Å) and energy, E_{M11}, in atomic units (a.u.) of $Sn(TFA)_4$ as calculated at the M11/*def*2-QZVP level.

E_{M11} = −2319.66659259			
Sn	0.000000	0.000000	0.000000
O	0.000000	2.109252	0.326053
C	0.000000	2.357633	−0.916728
O	0.000000	1.432524	−1.737270
C	0.000000	3.835078	−1.357267
F	0.000000	3.934629	−2.679227
F	1.086074	4.440013	−0.870573
F	−1.086074	4.440013	−0.870573
O	0.000000	−2.109252	0.326053
C	0.000000	−2.357633	−0.916728
O	0.000000	−1.432524	−1.737270
C	0.000000	−3.835078	−1.357267
F	0.000000	−3.934629	−2.679227
F	1.086074	−4.440013	−0.870573
F	−1.086074	−4.440013	−0.870573
O	2.109252	0.000000	−0.326053
C	2.357633	0.000000	0.916728
O	1.432524	0.000000	1.737270
C	3.835078	0.000000	1.357267
F	3.934629	0.000000	2.679227
F	4.440013	−1.086074	0.870573
F	4.440013	1.086074	0.870573
O	−2.109252	0.000000	−0.326053
C	−2.357633	0.000000	0.916728
O	−1.432524	0.000000	1.737270
C	−3.835078	0.000000	1.357267
F	−3.934629	0.000000	2.679227
F	−4.440013	−1.086074	0.870573
F	−4.440013	1.086074	0.870573

Table A55. Optimised Cartesian coordinates in Ångström (Å) and energy, $E_{SOGGA11\text{-}X}$, in atomic units (a.u.) of $Sn(TFA)_4$ as calculated at the SOGGA11-X/*def*2-SVP level.

$E_{SOGGA11\text{-}X}$ = −2316.82492269			
Sn	0.000000	0.000000	0.000000
O	0.000000	2.156941	0.313825
C	0.000000	2.391863	−0.928596
O	0.000000	1.453111	−1.738483
C	0.000000	3.858116	−1.393900
F	0.000000	3.935733	−2.708341
F	1.078452	4.465536	−0.922910
F	−1.078452	4.465536	−0.922910
O	0.000000	−2.156941	0.313825
C	0.000000	−2.391863	−0.928596
O	0.000000	−1.453111	−1.738483
C	0.000000	−3.858116	−1.393900
F	0.000000	−3.935733	−2.708341
F	1.078452	−4.465536	−0.922910
F	−1.078452	−4.465536	−0.922910
O	2.156941	0.000000	−0.313825
C	2.391863	0.000000	0.928596
O	1.453111	0.000000	1.738483
C	3.858116	0.000000	1.393900
F	3.935733	0.000000	2.708341
F	4.465536	−1.078452	0.922910
F	4.465536	1.078452	0.922910
O	−2.156941	0.000000	−0.313825
C	−2.391863	0.000000	0.928596
O	−1.453111	0.000000	1.738483
C	−3.858116	0.000000	1.393900
F	−3.935733	0.000000	2.708341
F	−4.465536	−1.078452	0.922910
F	−4.465536	1.078452	0.922910

Table A56. Optimised Cartesian coordinates in Ångström (Å) and energy, $E_{\text{SOGGA11-X}}$, in atomic units (a.u.) of $Sn(TFA)_4$ as calculated at the SOGGA11-X/*def*2-TZVP level.

$E_{\text{SOGGA11-X}} = -2319.40649637$			
Sn	0.000000	0.000000	0.000000
O	0.000000	2.121597	0.323822
C	0.000000	2.361864	−0.918005
O	0.000000	1.429048	−1.733017
C	0.000000	3.835584	−1.375491
F	0.000000	3.924326	−2.690782
F	1.079189	4.444543	−0.901714
F	−1.079189	4.444543	−0.901714
O	0.000000	−2.121597	0.323822
C	0.000000	−2.361864	−0.918005
O	0.000000	−1.429048	−1.733017
C	0.000000	−3.835584	−1.375491
F	0.000000	−3.924326	−2.690782
F	1.079189	−4.444543	−0.901714
F	−1.079189	−4.444543	−0.901714
O	2.121597	0.000000	−0.323822
C	2.361864	0.000000	0.918005
O	1.429048	0.000000	1.733017
C	3.835584	0.000000	1.375491
F	3.924326	0.000000	2.690782
F	4.444543	−1.079189	0.901714
F	4.444543	1.079189	0.901714
O	−2.121597	0.000000	−0.323822
C	−2.361864	0.000000	0.918005
O	−1.429048	0.000000	1.733017
C	−3.835584	0.000000	1.375491
F	−3.924326	0.000000	2.690782
F	−4.444543	−1.079189	0.901714
F	−4.444543	1.079189	0.901714

Table A57. Optimised Cartesian coordinates in Ångström (Å) and energy, $E_{SOGGA11\text{-}X}$, in atomic units (a.u.) of $Sn(TFA)_4$ as calculated at the SOGGA11-X/*def*2-QZVP level.

$E_{SOGGA11\text{-}X} = -2319.50412150$			
Sn	0.000000	0.000000	0.000000
O	0.000000	2.120466	0.323860
C	0.000000	2.360683	−0.917081
O	0.000000	1.428527	−1.731776
C	0.000000	3.834530	−1.375045
F	0.000000	3.922812	−2.689624
F	1.078579	4.443525	−0.901708
F	−1.078579	4.443525	−0.901708
O	0.000000	−2.120466	0.323860
C	0.000000	−2.360683	−0.917081
O	0.000000	−1.428527	−1.731776
C	0.000000	−3.834530	−1.375045
F	0.000000	−3.922812	−2.689624
F	1.078579	−4.443525	−0.901708
F	−1.078579	−4.443525	−0.901708
O	2.120466	0.000000	−0.323860
C	2.360683	0.000000	0.917081
O	1.428527	0.000000	1.731776
C	3.834530	0.000000	1.375045
F	3.922812	0.000000	2.689624
F	4.443525	−1.078579	0.901708
F	4.443525	1.078579	0.901708
O	−2.120466	0.000000	−0.323860
C	−2.360683	0.000000	0.917081
O	−1.428527	0.000000	1.731776
C	−3.834530	0.000000	1.375045
F	−3.922812	0.000000	2.689624
F	−4.443525	−1.078579	0.901708
F	−4.443525	1.078579	0.901708

Table A58. Optimised Cartesian coordinates in Ångström (Å) and energy, $E_{\text{SOGGA11-X}}$, in atomic units (a.u.) of $Sn(TFA)_4$ as calculated at the SOGGA11-X/double-ζ-DKH level.

$E_{\text{SOGGA11-X}} = -8276.16859272$			
Sn	0.000000	0.000000	−0.000181
O	0.000000	2.090607	0.320971
C	0.000000	2.379824	−0.923008
O	0.000000	1.486813	−1.777088
C	0.000000	3.874727	−1.298575
F	0.000000	4.031960	−2.610086
F	1.081891	4.458163	−0.790785
F	−1.081891	4.458163	−0.790785
O	0.000000	−2.090607	0.320971
C	0.000000	−2.379824	−0.923008
O	0.000000	−1.486813	−1.777088
C	0.000000	−3.874727	−1.298575
F	0.000000	−4.031960	−2.610086
F	1.081891	−4.458163	−0.790785
F	−1.081891	−4.458163	−0.790785
O	2.090650	0.000000	−0.321054
C	2.379700	0.000000	0.922964
O	1.486575	0.000000	1.776924
C	3.874553	0.000000	1.298731
F	4.031611	0.000000	2.610264
F	4.458057	−1.081891	0.791020
F	4.458057	1.081891	0.791020
O	−2.090650	0.000000	−0.321054
C	−2.379700	0.000000	0.922964
O	−1.486575	0.000000	1.776924
C	−3.874553	0.000000	1.298731
F	−4.031611	0.000000	2.610264
F	−4.458057	−1.081891	0.791020
F	−4.458057	1.081891	0.791020

Table A59. Optimised Cartesian coordinates in Ångström (Å) and energy, $E_{\text{SOGGA11-X}}$, in atomic units (a.u.) of $Sn(TFA)_4$ as calculated at the SOGGA11-X/triple-ζ-DKH level.

$E_{\text{SOGGA11-X}} = -8276.66432784$			
Sn	0.000000	0.000000	−0.000143
O	0.000000	−2.100417	0.391147
C	0.000000	−2.366001	−0.844484
O	0.000000	−1.457545	−1.684898
C	0.000000	−3.849556	−1.266962
F	0.000000	−3.968444	−2.579257
F	−1.079058	−4.446069	−0.779346
F	1.079058	−4.446069	−0.779346
O	0.000000	2.100417	0.391147
C	0.000000	2.366001	−0.844484
O	0.000000	1.457545	−1.684898
C	0.000000	3.849556	−1.266962
F	0.000000	3.968444	−2.579257
F	−1.079058	4.446069	−0.779346
F	1.079058	4.446069	−0.779346
O	−2.100459	0.000000	−0.391210
C	−2.365911	0.000000	0.844450
O	−1.457366	0.000000	1.684767
C	−3.849421	0.000000	1.267085
F	−3.968170	0.000000	2.579393
F	−4.445986	1.079058	0.779533
F	−4.445986	−1.079058	0.779533
O	2.100459	0.000000	−0.391210
C	2.365911	0.000000	0.844450
O	1.457366	0.000000	1.684767
C	3.849421	0.000000	1.267085
F	3.968170	0.000000	2.579393
F	4.445986	1.079058	0.779533
F	4.445986	−1.079058	0.779533

Table A60. Summary of experimental parameters relating to GED data reduction and refinement for $Sn(TFA)_2$ and $Sn_2O(TFA)_2$.

Dataset Type	Short	Long
Δs / nm^{-1}	2.0	1.0
s_{min} / nm^{-1}	88.0	50.0
sw_1 / nm^{-1}	104.0	68.0
sw_2 / nm^{-1}	222.0	101.0
s_{max} / nm^{-1}	240.0	114.0
Correlation Parameter	0.4934	0.4957
Scale Factor (k)	0.0049(1)	0.0022(1)

Table A61. Summary of experimental parameters relating to GED data reduction and refinement for $Sn(TFA)_4$.

Dataset Type	Short	Long
Δs / nm^{-1}	2.0	1.0
s_{min} / nm^{-1}	90.0	54.0
sw_1 / nm^{-1}	104.0	68.0
sw_2 / nm^{-1}	240.0	101.0
s_{max} / nm^{-1}	262.0	114.0
Correlation Parameter	0.4936	0.4975
Scale Factor (k)	0.0023(1)	0.0010(1)

Table A62. Least-squares correlation matrix[a] (×100) for the refinement of $Sn(TFA)_2$ and $Sn_2O(TFA)_2$.

	p_1	p_3	p_4	p_7	p_{10}	p_{11}	p_{19}	u_1	u_2	u_3	u_{13}	u_{42}	k_1
p_1	100				−60		−74		−51				
p_3		100					66						
p_4			100					−53		−78			
p_7				100		−60						61	
p_{10}					100								50
p_{11}						100							
p_{19}							100		55				
u_1								100		69			
u_2									100		94		
u_3										100			
u_{13}											100		
u_{42}												100	65
k_1													100

[a] Only values ≥ 50% are tabulated. k_1 is a scale factor.

Table A63. Least-squares correlation matrix[a] (×100) for the refinement of $Sn(TFA)_4$.

	p_1	p_3	p_5	p_7	p_{10}	u_1	u_{35}	u_{42}	u_{53}	k_1
p_1	100		81			55				
p_3		100							54	
p_5			100							
p_7				100	78					
p_{10}					100					51
u_1						100				57
u_{35}							100	63		
u_{42}								100		
u_{53}									100	55
k_1										100

[a] Only values ≥ 50% are tabulated. k_1 is a scale factor.

Table A64. Refined (r_{h1}) and theoretical[a] (r_e) parameter values[b] and SARACEN restraints applied in the least-squares refinement of $Sn(TFA)_2$ and $Sn_2O(TFA)_2$.

	r_{h1}	r_e	Restraint
p_1	215.8(7)	217.6	–
p_2	−13.8(10)	−13.0	−13.0(7)
p_3	33.6(11)	30.1	30.1(18)
p_4	22.1(21)	21.5	21.5(18)
p_5	260.0(7)	257.4	–
p_6	317.2(7)	318.5	–
p_7	125.8(2)	124.8	–
p_8	−0.5(1)	−0.6	−0.6(1)
p_9	3.4(4)	3.4	3.4.(4)
p_{10}	153.1(6)	154.9	–
p_{11}	133.7(1)	132.7	–
p_{12}	110.7(1)	110.4	110.4(1)
p_{13}	120.8(3)	120.8	120.8(3)
p_{14}	97.5(3)	97.5	97.5(3)
p_{15}	−133.4[d]	−133.4	–
p_{16}	−12.4[d]	−12.4	–
p_{17}	107.3[d]	107.3	–
p_{18}	−69.8[d]	−69.8	–
p_{19}	137.4(17)	131.4	131.4(17)
p_{20}	70.7[d]	70.7	–
p_{21}	−169.5[d]	−169.5	–
p_{22}	−48.3[d]	−48.3	–
p_{23}	94.2(1)	94.2	–

[a] Calculations at the SOGGA11-X/TZP-DKH level. [b] Interatomic distances (r) are tabulated in picometers (pm) and angles (a) are tabulated in degrees.

Table A65. Refined (r_{h1}) and theoretical[a] (r_e) parameter values[b] and SARACEN restraints applied in the least-squares refinement of $Sn(TFA)_4$.

	r_{h1}	r_e	Restraint
p_1	218.6(3)	218.2	–
p_2	8.8(6)	9.1	9.1(5)
p_3	125.5(2)	125.1	–
p_4	2.7(4)	2.6	2.6(3)
p_5	247.4(6)	251.2	–
p_6	153.1(3)	154.3	154.3(3)
p_7	133.0(2)	132.3	–
p_8	0.8(8)	0.8	0.8(6)
p_9	117.8(4)	118.0	118.0(3)
p_{10}	111.0(2)	110.0	–
p_{11}	1.7(3)	1.7	1.7(3)
p_{12}	158.7(3)	158.9	158.9(4)

[a] Calculations at the SOGGA11-X/TZP-DKH level. [b] Interatomic distances (r) are tabulated in picometers (pm) and angles (a) are tabulated in degrees.

Table A66. Internuclear distances (r_a / pm), refined (u_{GED}) and theoretical (u_{h1}) amplitudes of vibration and restraints and distance corrections (k_{h1}) for $Sn(TFA)_2$ and $Sn_2O(TFA)_2$.[a]

Amp.	Atomic Pair	r_a	u_{GED}	Restraint	k_{h1}	u_{h1}
u_8	O_2–C_3	124.4(3)	2.9 (Tied to u_{42})	–	4.2	0.1
u_{93}	C_{12}–O_{13}	125.5(3)	2.8 (Tied to u_{42})	–	4.0	0.1
u_{80}	O_{11}–C_{12}	125.5(3)	2.8 (Tied to u_{42})	–	4.0	0.1
u_{21}	C_3–O_4	127.8(3)	2.8 (Tied to u_{42})	–	4.0	0.1
u_{42}	C_5...F_7	132.8(1)	3.8(1)	5.6(6)	5.6	0.1
u_{41}	C_5...F_6	133.4(1)	2.8 (Tied to u_{42})	–	4.1	0.1
u_{114}	C_{14}...F_{16}	133.6(1)	3.2 (Tied to u_{42})	–	4.7	0.1
u_{115}	C_{14}...F_{17}	133.8(1)	3.3 (Tied to u_{42})	–	4.7	0.1
u_{43}	C_5...F_8	134.0(1)	3.5 (Tied to u_{42})	–	5.1	0.1
u_{113}	C_{14}...F_{15}	134.8(1)	3.3 (Tied to u_{42})	–	4.8	0.1
u_{22}	C_3–C_5	152.6(6)	6.6(1)	5.1(5)	5.1	0.1
u_{94}	C_{12}–C_{14}	153.2(6)	6.6 (Tied to u_{22})	–	5.1	0.1
u_{57}	O_9–Sn_{10}	187.8(11)	5.5(1)	5.3(5)	5.3	0.1
u_9	O_2...O_4	210.6(11)	3.4 (Tied to u_3)	–	4.9	0.1
u_3	Sn_1–O_4	212.9(14)	9.5(6)	13.7(14)	13.7	0.4
u_{120}	F_{15}...F_{16}	215.6(3)	4.5 (Tied to u_3)	–	6.6	0.1
u_{48}	F_6...F_7	216.0(3)	9.0 (Tied to u_3)	–	13.0	0.3
u_{53}	F_7...F_8	216.2(3)	6.6 (Tied to u_3)	–	9.6	0.1
u_{49}	F_6...F_8	216.7(3)	5.6 (Tied to u_3)	–	8.1	0.1
u_{121}	F_{15}...F_{17}	217.2(3)	4.6 (Tied to u_3)	–	6.6	0.1
u_{125}	F_{16}...F_{17}	218.3(3)	4.4 (Tied to u_3)	–	6.4	0.1
u_{75}	Sn_{10}...$O_{13'}$	221.4(9)	6.5 (Tied to u_3)	–	9.4	0.2
u_{66}	Sn_{10}–O_{11}	221.4(9)	6.5 (Tied to u_3)	–	9.3	0.2

u_{81}	$O_{11}...O_{13}$	229.0(13)	3.8 (Tied to u_3)	–	5.5	0.1
u_{25}	$C_3–F_8$	233.8(6)	15.0 (Tied to u_1)	–	24.2	0.6
u_{97}	$C_{12}–F_{17}$	233.8(6)	4.9 (Tied to u_1)	–	7.9	0.1
u_{104}	$O_{13}...C_{14}$	234.8(10)	4.4 (Tied to u_1)	–	7.1	0.1
u_{82}	$O_{11}...C_{14}$	234.8(10)	4.4 (Tied to u_1)	–	7.1	0.1
u_1	$Sn_1–O_2$	235.1(14)	5.6(5)	9.1(9)	9.1	0.2
u_{23}	$C_3–F_6$	235.3(6)	15.3 (Tied to u_1)	–	24.6	0.5
u_{24}	$C_3–F_7$	236.0(6)	12.6 (Tied to u_1)	–	20.4	0.3
u_{96}	$C_{12}–F_{16}$	238.1(6)	4.7 (Tied to u_1)	–	7.5	0.1
u_{95}	$C_{12}–F_{15}$	238.9(6)	5.4 (Tied to u_1)	–	8.8	0.2
u_{10}	$O_2...C_5$	241.5(7)	4.8 (Tied to u_1)	–	7.7	0.1
u_{32}	$O_4...C_5$	250.2(14)	4.6 (Tied to u_1)	–	7.5	0.1
u_{106}	$O_{13}...F_{16}$	255.3(13)	18.9 (Tied to u_2)	–	18.8	0.7
u_{85}	$O_{11}...F_{17}$	266.4(12)	21.1 (Tied to u_2)	–	21.0	0.8
u_2	$Sn_1...C_3$	267.1(7)	7.0(3)	–	7.0	0.1
u_{34}	$O_4...F_7$	274.5(20)	50.3 (Tied to u_2)	–	50.1	5.4
u_{11}	$O_2...F_6$	275.0(8)	52.5 (Tied to u_2)	–	52.3	4.9
u_{60}	$O_9...O_{13}$	287.7(28)	13.8 (Tied to u_{13})	–	15.1	0.4
u_{58}	$O_9...O_{11}$	287.7(28)	13.7 (Tied to u_{13})	–	15.0	0.4
u_{83}	$O_{11}...F_{15}$	289.0(11)	30.5 (Tied to u_{13})	–	33.4	1.9
u_{13}	$O_2...F_8$	289.1(7)	66.7(23)	–	72.9	8.5
u_{16}	$O_2...O_{4'}$	302.6(16)	22.8 (Tied to u_{13})	–	24.9	1.0
u_{88}	$O_{11}...O_{13'}$	312.1(15)	16.8 (Tied to u_{74})	–	22.4	0.8
u_{59}	$O_9...C_{12}$	314.9(23)	11.4 (Tied to u_{74})	–	15.3	0.4
u_{74}	$Sn_{10}...C_{12'}$	317.2(7)	8.4(7)	11.2(11)	11.2	0.2
u_{67}	$Sn_{10}...C_{12}$	317.2(7)	8.1 (Tied to u_{74})	–	10.8	0.2
u_{105}	$O_{13}...F_{15}$	321.2(9)	25.9 (Tied to u_{74})	–	34.6	1.9
u_{33}	$O_4...F_6$	323.7(11)	95.3 (Tied to u_{65})	–	53.6	4.0
u_{35}	$O_4...F_8$	327.9(12)	56.9 (Tied to u_{74})	–	76.0	8.4
u_{14}	$O_2...O_{2'}$	327.9(21)	45.2 (Tied to u_{65})	–	25.5	0.4
u_{107}	$O_{13}...F_{17}$	328.9(8)	32.9 (Tied to u_{65})	–	18.5	0.5
u_{15}	$O_2...C_{3'}$	343.0(16)	45.6 (Tied to u_{65})	–	25.7	1.0
u_{86}	$O_{11}...O_{11'}$	344.8(20)	105.1 (Tied to u_{65})	–	59.2	−13.8
u_{12}	$O_2...F_7$	345.8(6)	44.1 (Tied to u_{65})	–	24.8	0.9
u_{84}	$O_{11}...F_{16}$	347.1(7)	22.5 (Tied to u_{65})	–	12.7	0.3
u_{65}	$Sn_{10}...Sn_{10'}$	348.6(5)	12.4(3)	7.0(7)	7.0	−1.0
u_{108}	$O_{13}...O_{13'}$	352.3(19)	97.5 (Tied to u_{65})	–	54.9	−10.3
u_{73}	$Sn_{10}...O_{11'}$	357.0(10)	32.3 (Tied to u_{65})	–	18.2	0.5
u_{68}	$Sn_{10}...O_{13}$	357.2(10)	30.4 (Tied to u_{65})	–	17.1	0.4
u_{87}	$O_{11}...C_{12'}$	358.1(10)	72.0 (Tied to u_{65})	–	40.5	2.3
u_{99}	$C_{12}...O_{13'}$	360.0(10)	65.6 (Tied to u_{65})	–	36.9	1.9
u_{36}	$O_4...O_{4'}$	371.0(28)	37.6 (Tied to u_{65})	–	21.1	−3.5
u_{98}	$C_{12}...C_{12'}$	374.3(11)	45.6 (Tied to u_{65})	–	25.6	−8.0
u_{27}	$C_3...O_{4'}$	381.4(14)	39.6 (Tied to u_{65})	–	22.3	0.6
u_{26}	$C_3...C_{3'}$	395.2(13)	41.8 (Tied to u_{65})	–	23.5	−2.1

u_{4}	$Sn_{1}...C_{5}$	419.8(7)	8.1(7)	–	8.3	0.1
u_{69}	$Sn_{10}...C_{14}$	453.0(9)	12.3 (Tied to u_{78})	–	14.0	0.2
u_{76}	$Sn_{10}...C_{14'}$	453.0(9)	11.9 (Tied to u_{78})	–	13.5	0.2
u_{61}	$O_{9}...C_{14}$	466.8(21)	18.7 (Tied to u_{78})	–	21.2	0.5
u_{17}	$O_{2}...C_{5'}$	470.9(12)	32.3 (Tied to u_{78})	–	36.5	1.5
u_{78}	$Sn_{10}...F_{16'}$	471.0(9)	22.1(6)	–	24.9	0.6
u_{72}	$Sn_{10}...F_{17}$	478.9(9)	23.9 (Tied to u_{78})	–	27.0	0.8
u_{7}	$Sn_{1}...F_{8}$	481.2(6)	24.6 (Tied to u_{78})	–	27.8	0.5
u_{6}	$Sn_{1}...F_{7}$	481.3(12)	19.9 (Tied to u_{78})	–	22.5	0.4
u_{5}	$Sn_{1}...F_{6}$	485.2(6)	21.3 (Tied to u_{78})	–	24.0	0.4
u_{18}	$O_{2}...F_{6'}$	487.1(13)	88.9 (Tied to u_{78})	–	100.4	10.5
u_{112}	$O_{13}...F_{17'}$	489.2(10)	54.2 (Tied to u_{70})	–	56.3	3.1
u_{89}	$O_{11}...C_{14'}$	494.4(10)	45.3 (Tied to u_{70})	–	47.1	2.2
u_{109}	$O_{13}...C_{14'}$	494.7(10)	41.7 (Tied to u_{70})	–	43.4	1.9
u_{70}	$Sn_{10}...F_{15}$	499.4(9)	38.4(55)	–	39.9	1.6
u_{19}	$O_{2}...F_{7'}$	504.0(14)	75.5 (Tied to u_{70})	–	78.5	6.1
u_{100}	$C_{12}...C_{14'}$	509.4(11)	38.2 (Tied to u_{77})	–	37.6	1.4
u_{103}	$C_{12}...F_{17'}$	512.6(11)	60.6 (Tied to u_{77})	–	59.7	3.3
u_{91}	$O_{11}...F_{16'}$	516.2(10)	57.9 (Tied to u_{77})	–	57.0	3.1
u_{62}	$O_{9}...F_{15}$	518.8(17)	41.6 (Tied to u_{77})	–	40.9	1.6
u_{37}	$O_{4}...C_{5'}$	521.5(12)	29.8 (Tied to u_{77})	–	29.3	0.8
u_{29}	$C_{3}...F_{6'}$	521.6(16)	91.0 (Tied to u_{77})	–	89.6	7.3
u_{92}	$O_{11}...F_{17'}$	525.2(9)	68.0 (Tied to u_{77})	–	67.0	4.1
u_{28}	$C_{3}...C_{5'}$	526.0(13)	36.3 (Tied to u_{77})	–	35.7	1.2
u_{77}	$Sn_{10}...F_{15'}$	527.4(9)	40.2(21)	–	39.6	1.5
u_{38}	$O_{4}...F_{6'}$	532.5(14)	63.0 (Tied to u_{77})	–	62.0	3.1
u_{63}	$O_{9}...F_{16}$	532.9(21)	24.6 (Tied to u_{77})	–	24.3	0.5
u_{64}	$O_{9}...F_{17}$	534.0(24)	21.4 (Tied to u_{77})	–	21.1	0.4
u_{79}	$Sn_{10}...F_{17'}$	536.9(8)	20.2 (Tied to u_{77})	–	19.9	0.3
u_{128}	$F_{17}...F_{17'}$	540.4(13)	111.5 (Tied to u_{77})	–	109.8	−10.2
u_{102}	$C_{12}...F_{16'}$	549.6(11)	76.8 (Tied to u_{71})	–	57.6	2.9
u_{71}	$Sn_{10}...F_{16}$	554.0(8)	20.8(16)	15.6(16)	15.6	0.2
u_{111}	$O_{13}...F_{16'}$	562.4(10)	81.4 (Tied to u_{71})	–	61.0	3.3
u_{20}	$O_{2}...F_{8'}$	574.5(13)	60.9 (Tied to u_{71})	–	45.7	1.6
u_{30}	$C_{3}...F_{7'}$	575.3(14)	103.2 (Tied to u_{71})	–	77.4	5.2
u_{119}	$C_{14}...F_{17'}$	587.7(13)	83.2 (Tied to u_{127})	–	82.4	5.2
u_{116}	$C_{14}...C_{14'}$	588.1(13)	56.6 (Tied to u_{127})	–	56.1	−19.2
u_{110}	$O_{13}...F_{15'}$	589.0(10)	39.6 (Tied to u_{127})	–	39.2	1.3
u_{40}	$O_{4}...F_{8'}$	591.7(13)	81.8 (Tied to u_{127})	–	81.1	5.6
u_{127}	$F_{16}...F_{17'}$	593.7(14)	107.0(10)	–	106.1	8.7
u_{45}	$C_{5}...F_{6'}$	597.2(20)	121.8 (Tied to u_{127})	–	120.7	11.3
u_{39}	$O_{4}...F_{7'}$	600.0(14)	57.7 (Tied to u_{127})	–	57.2	2.6
u_{90}	$O_{11}...F_{15'}$	604.7(10)	42.7 (Tied to u_{127})	–	42.3	1.5
u_{101}	$C_{12}...F_{15'}$	619.9(11)	30.3 (Tied to u_{127})	–	30.1	0.7
u_{31}	$C_{3}...F_{8'}$	620.7(13)	72.5 (Tied to u_{127})	–	71.8	4.0

u_{44}	$C_5...C_{5'}$	622.1(16)	55.5 (Tied to u_{127})	–	55.0	−7.2
u_{50}	$F_6...F_{6'}$	634.6(26)	176.6 (Tied to u_{127})	–	175.0	23.3
u_{51}	$F_6...F_{7'}$	636.8(21)	164.0 (Tied to u_{127})	–	162.5	21.8
u_{118}	$C_{14}...F_{16'}$	641.9(13)	81.4 (Tied to u_{127})	–	80.7	4.9
u_{126}	$F_{16}...F_{16'}$	659.4(13)	106.0 (Tied to u_{127})	–	105.0	−23.3
u_{46}	$C_5...F_{7'}$	683.5(16)	108.8 (Tied to u_{127})	–	107.8	8.6
u_{54}	$F_7...F_{7'}$	697.0(16)	131.3 (Tied to u_{127})	–	130.1	−48.6
u_{52}	$F_6...F_{8'}$	711.0(19)	143.0 (Tied to u_{127})	–	141.7	13.0
u_{124}	$F_{15}...F_{17'}$	719.9(13)	75.7 (Tied to u_{127})	–	75.0	3.7
u_{117}	$C_{14}...F_{15'}$	731.0(13)	47.5 (Tied to u_{127})	–	47.1	1.4
u_{47}	$C_5...F_{8'}$	732.3(15)	97.4 (Tied to u_{127})	–	96.6	5.9
u_{56}	$F_8...F_{8'}$	736.2(14)	113.1 (Tied to u_{127})	–	112.1	−56.5
u_{123}	$F_{15}...F_{16'}$	758.3(13)	74.3 (Tied to u_{127})	–	73.6	3.5
u_{55}	$F_7...F_{8'}$	767.2(16)	159.2 (Tied to u_{127})	–	157.8	15.3
u_{122}	$F_{15}...F_{15'}$	806.7(14)	36.2 (Tied to u_{127})	–	35.9	−42.5

[a] All values are tabulated in picometers (pm).

Table A67. Internuclear distances (r_a / pm), refined (u_{GED}) and theoretical (u_{h1}) amplitudes of vibration and restraints and distance corrections (k_{h1}) for $Sn(TFA)_4$.[a]

Amp	Atomic Pair	r_a	u_{GED}	Restraint	k_{h1}	u_{h1}
u_{25}	$C_3–O_4$	124.3(3)	1.7 (Tied to u_{53})	–	0.1	4.1
u_7	$O_2–C_3$	126.9(3)	1.8 (Tied to u_{53})	–	0.1	4.2
u_{52}	$C_5–F_6$	132.5(2)	2.4 (Tied to u_{53})	–	0.1	5.7
u_{53}	$C_5–F_7$	133.3(2)	2.8(4)	6.6(7)	0.2	6.6
u_{26}	$C_3–C_5$	152.9(3)	5.9(6)	5.0(5)	0.1	5.0
u_1	$Sn_1–O_2$	214.1(4)	6.0(3)	8.6(9)	0.2	8.6
u_{61}	$F_6...F_7$	214.4(2)	5.7 (Tied to u_1)	–	0.2	8.2
u_{67}	$F_7...F_8$	216.2(2)	6.5 (Tied to u_1)	–	0.2	9.4
u_8	$O_2...O_4$	221.7(5)	3.3 (Tied to u_1)	–	0.1	4.8
u_3	$Sn_1–O_4$	222.9(4)	7.5 (Tied to u_1)	–	0.3	10.8
u_{28}	$C_3...F_7$	235.4(4)	8.7 (Tied to u_1)	–	0.3	12.6
u_{27}	$C_3...F_6$	237.1(4)	5.9 (Tied to u_1)	–	0.1	8.4
u_{40}	$O_4...C_5$	238.4(6)	4.6 (Tied to u_1)	–	0.1	6.6
u_9	$O_2...C_5$	240.1(6)	4.7 (Tied to u_1)	–	0.1	6.8
u_2	$Sn_1...C_3$	247.3(6)	4.1(2)	5.9(6)	0.1	5.9
u_{41}	$O_4...F_6$	262.0(9)	17.4 (Tied to u_2)	–	1.2	24.8
u_{20}	$O_2...O_{4''}$	272.1(6)	12.6 (Tied to u_2)	–	0.5	18.0
u_{11}	$O_2...F_7$	284.8(7)	24.4 (Tied to u_2)	–	2.2	34.8
u_{19}	$O_2...C_{3''}$	316.1(7)	19.9 (Tied to u_{42})	–	0.7	20.9
u_{18}	$O_2...O_{2''}$	319.8(6)	21.6 (Tied to u_{42})	–	0.8	22.8
u_{42}	$O_4...F_7$	326.6(5)	37.6(17)	–	2.4	39.7
u_{43}	$O_4...O_{4'}$	336.7(11)	19.3 (Tied to u_{35})	–	−0.1	16.6
u_{10}	$O_2...F_6$	351.6(5)	13.8 (Tied to u_{35})	–	0.2	11.9
u_{35}	$C_3...O_{4''}$	351.7(7)	20.1(13)	17.4(17)	0.4	17.4

u_{34}	$C_3...C_{3''}$	354.9(9)	21.8 (Tied to u_{35})	–	0.5	18.8
u_{47}	$O_4...O_{4''}$	375.7(6)	20.7 (Tied to u_{35})	–	0.4	17.9
u_4	$Sn_1...C_5$	400.1(6)	10.2(5)	7.0(7)	0.1	7.0
u_{12}	$O_2...O_{2'}$	401.4(10)	17.0 (Tied to u_4)	–	0.1	11.6
u_{30}	$C_3...O_{4'}$	423.3(10)	19.5 (Tied to u_6)	–	0.3	15.1
u_{14}	$O_2...O_{4'}$	429.5(7)	19.6 (Tied to u_6)	–	0.3	15.1
u_{21}	$O_2...C_{5''}$	440.3(7)	39.1 (Tied to u_6)	–	1.0	30.1
u_{71}	$F_7...F_{8''}$	450.7(12)	149.2 (Tied to u_6)	–	13.0	114.9
u_{24}	$O_2...F_{8''}$	451.3(7)	88.1 (Tied to u_6)	–	5.0	67.9
u_{13}	$O_2...C_{3'}$	459.6(10)	14.2 (Tied to u_6)	–	0.1	11.0
u_6	$Sn_1...F_7$	461.7(7)	24.3(7)	18.7(19)	0.4	18.7
u_{39}	$C_3...F_{8''}$	465.0(9)	72.9 (Tied to u_6)	–	3.1	56.1
u_5	$Sn_1...F_6$	468.7(8)	17.9 (Tied to u_6)	–	0.2	13.8
u_{36}	$C_3...C_{5''}$	475.1(8)	37.1 (Tied to u_6)	–	0.8	28.6
u_{51}	$O_4...F_{8''}$	477.0(10)	49.4 (Tied to u_6)	–	1.4	38.1
u_{48}	$O_4...C_{5''}$	478.2(7)	28.6 (Tied to u_6)	–	0.5	22.0
u_{22}	$O_2...F_{6''}$	481.6(10)	58.9 (Tied to u_6)	–	2.0	45.4
u_{29}	$C_3...C_{3'}$	485.4(12)	14.5 (Tied to u_6)	–	−0.3	11.2
u_{60}	$C_5...F_{8''}$	530.5(10)	86.8 (Tied to u_{66})	–	5.2	77.6
u_{37}	$C_3...F_{6''}$	544.5(9)	47.6 (Tied to u_{66})	–	1.5	42.6
u_{23}	$O_2...F_{7''}$	547.3(7)	39.8 (Tied to u_{66})	–	1.2	35.6
u_{50}	$O_4...F_{7''}$	548.6(9)	50.7 (Tied to u_{66})	–	1.8	45.3
u_{44}	$O_4...C_{5'}$	568.4(11)	18.9 (Tied to u_{66})	–	0.3	16.9
u_{38}	$C_3...F_{7''}$	570.4(8)	54.3 (Tied to u_{66})	–	2.0	48.5
u_{49}	$O_4...F_{6''}$	570.7(6)	32.9 (Tied to u_{66})	–	0.7	29.4
u_{57}	$C_5...C_{5''}$	571.6(8)	49.9 (Tied to u_{66})	–	1.6	44.6
u_{66}	$F_6...F_{8''}$	578.9(11)	98.3(73)	87.8(88)	6.0	87.8
u_{45}	$O_4...F_{6'}$	595.7(15)	36.0 (Tied to u_{66})	–	0.9	32.2
u_{15}	$O_2...C_{5'}$	612.0(9)	13.4 (Tied to u_{66})	–	0.1	12.0
u_{58}	$C_5...F_{6''}$	633.5(8)	68.9 (Tied to u_{70})	–	2.8	61.7
u_{31}	$C_3...C_{5'}$	637.8(12)	14.8 (Tied to u_{70})	–	0.1	13.2
u_{46}	$O_4...F_{7'}$	639.1(10)	53.3 (Tied to u_{70})	–	1.9	47.7
u_{70}	$F_7...F_{7''}$	640.8(10)	121.3(104)	108.5(109)	8.7	108.5
u_{17}	$O_2...F_{7'}$	664.4(11)	30.6 (Tied to u_{70})	–	0.5	27.3
u_{59}	$C_5...F_{7''}$	673.5(8)	80.4 (Tied to u_{70})	–	3.7	72.0
u_{16}	$O_2...F_{6'}$	682.3(10)	23.3 (Tied to u_{70})	–	0.3	20.9
u_{32}	$C_3...F_{6'}$	684.9(14)	30.5 (Tied to u_{70})	–	0.5	27.3
u_{33}	$C_3...F_{7'}$	700.2(11)	43.9 (Tied to u_{70})	–	1.1	39.3
u_{64}	$F_6...F_{6''}$	713.8(9)	80.9 (Tied to u_{70})	–	3.4	72.4
u_{65}	$F_6...F_{7''}$	720.0(9)	103.0 (Tied to u_{70})	–	5.6	92.2
u_{72}	$F_7...F_{6''}$	782.0(10)	93.9 (Tied to u_{63})	–	3.9	80.1
u_{54}	$C_5...C_{5'}$	788.3(12)	18.8 (Tied to u_{63})	–	−0.3	16.0
u_{55}	$C_5...F_{6'}$	829.3(17)	38.0 (Tied to u_{63})	–	0.6	32.4
u_{62}	$F_6...F_{6'}$	848.6(25)	56.8 (Tied to u_{63})	–	0.7	48.4
u_{56}	$C_5...F_{7'}$	850.5(11)	55.0 (Tied to u_{63})	–	1.3	46.8

u_{68}	$F_7...F_{7'}$	893.8(14)	87.3 (Tied to u_{63})	–	3.1	74.4
u_{63}	$F_6...F_{7'}$	897.3(14)	73.7(2)	–	2.3	62.8
u_{69}	$F_7...F_{8'}$	922.6(13)	57.2 (Tied to u_{63})	–	1.3	48.8

[a] All values are tabulated in picometers (pm).

Table A68. Refined Cartesian coordinates in Ångström (Å) for the experimentally-determined structure of $Sn(TFA)_2$ obtained *via* GED.

	x	*y*	*z*
Sn	0.0000	0.0000	−1.6390
O	1.0391	−1.2922	0.0070
C	0.0287	−2.0100	0.1254
O	−0.9177	−1.6545	−0.6586
C	0.0049	−3.1802	1.1323
F	0.4790	−2.7953	2.3184
F	−1.2259	−3.6519	1.3021
F	0.7773	−4.1750	0.6732
O	−1.0391	1.2922	0.0070
C	−0.0287	2.0100	0.1254
O	0.9177	1.6545	−0.6586
C	−0.0049	3.1802	1.1323
F	−0.4790	2.7953	2.3184
F	1.2259	3.6519	1.3021
F	−0.7773	4.1750	0.6732

Table A69. Refined Cartesian coordinates in Ångström (Å) for the experimentally-determined structure of $Sn_2O(TFA)_2$ obtained *via* GED.

	x	*y*	*z*
O	0.0000	0.0000	−1.9128
Sn	−0.0043	1.7509	−1.2314
Sn	0.0043	−1.7509	−1.2314
O	−1.5611	1.1394	0.2156
C	−1.9409	−0.0048	0.5709
O	−1.5555	−1.1471	0.2156
C	−3.0769	−0.0076	1.6258
F	−4.2489	0.4035	1.0991
F	−3.2855	−1.2265	2.1318
F	−2.7513	0.8360	2.6126
O	1.5611	−1.1394	0.2156
C	1.9409	0.0048	0.5709
O	1.5555	1.1471	0.2156
C	3.0769	0.0076	1.6258
F	4.2489	−0.4035	1.0991
F	3.2855	1.2265	2.1318
F	2.7513	−0.8360	2.6126

Table A70. Refined Cartesian coordinates in Ångström (Å) for the experimentally-determined structure of $Sn(TFA)_4$ obtained *via* GED.

	x	*y*	*z*
Sn	0.0000	0.0000	0.0000
O	2.0088	0.7434	0.0000
C	2.4318	−0.4525	0.0000
O	1.6930	−1.4509	0.0000
C	3.9468	−0.6736	0.0000
F	4.2630	−1.9596	0.0000
F	4.4972	−0.1230	1.0814
F	4.4972	−0.1230	−1.0814
O	−2.0088	0.7434	0.0000
C	−2.4318	−0.4525	0.0000
O	−1.6930	−1.4509	0.0000
C	−3.9468	−0.6736	0.0000
F	−4.2630	−1.9596	0.0000
F	−4.4972	−0.1230	1.0814
F	−4.4972	−0.1230	−1.0814
O	0.0000	−0.7434	2.0088
C	0.0000	0.4525	2.4318
O	0.0000	1.4509	1.6930
C	0.0000	0.6736	3.9468
F	0.0000	1.9596	4.2630
F	−1.0814	0.1230	4.4972
F	1.0814	0.1230	4.4972
O	0.0000	−0.7434	−2.0088
C	0.0000	0.4525	−2.4318
O	0.0000	1.4509	−1.6930
C	0.0000	0.6736	−3.9468
F	0.0000	1.9596	−4.2630
F	−1.0814	0.1230	−4.4972
F	1.0814	0.1230	−4.4972

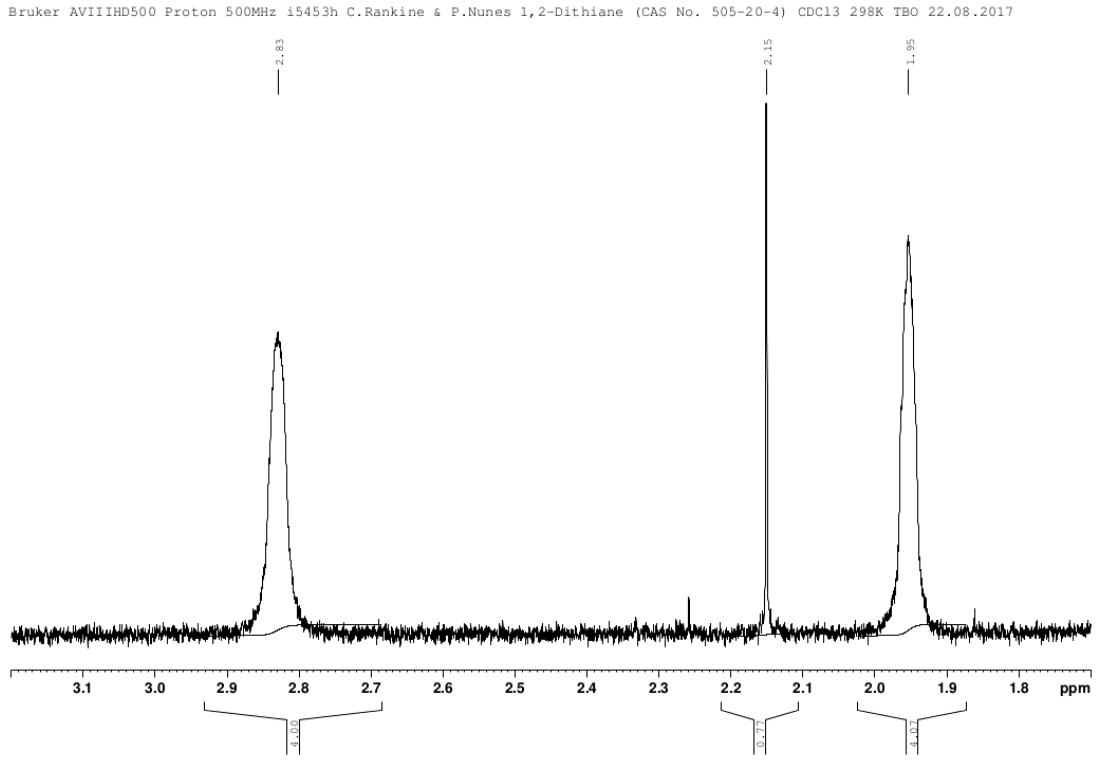

Figure A1. ^{1}H NMR (500 MHz, 298 K) of 1,2-dithiane in the region 1.7 – 3.2 ppm.

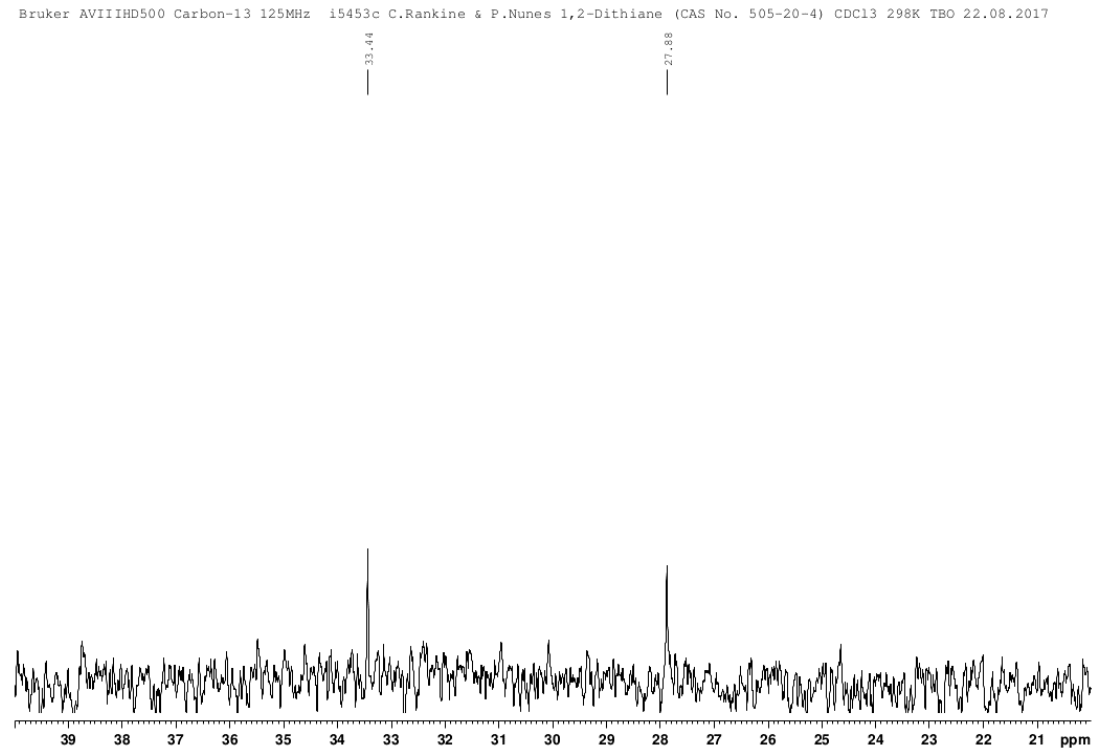

Figure A2. ^{13}C NMR (125 MHz, 298 K) of 1,2-dithiane in the region 20.0 – 40.0 ppm.

Table A71. Summary of experimental parameters relating to XRD data collection and refinement for 1,2-dithiane.

T / K	110.05(10)
Crystal Dimensions / mm	0.275 × 0.113 × 0.049
Wavelength / pm	1.54184 (Cu Kα)
2θ Range for Data Acquisition / °	17.39 – 134.11
hkl Index Range	$-6.0 \leq h \leq 6.0$; $-9.0 \leq k \leq 9.0$; $-7.0 \leq l \leq 8.0$
Number of Reflections Acquired	2503
Number of Independent Reflections	483
Number of Parameters	28
Goodness−of−Fit on F^2	1.098
Final R Indexes ($I \geq 2\sigma$)	$R_1 = 0.0270$; $wR_2 = 0.0697$
Final R Indexes (All Data)	$R_1 = 0.0296$; $wR_2 = 0.0728$
Flack Parameter	−0.03(4)

Table A72. Refined Cartesian coordinates in Ångström (Å) for the experimentally-determined structure of 1,2-dithiane obtained *via* XRD.

	x	*y*	*z*
S	0.9771	−0.3149	1.1115
S	−0.9771	0.3149	1.1115
C	1.5059	0.4212	−0.4653
C	−1.5059	−0.4212	−0.4653
C	0.7509	−0.1499	−1.6434
C	−0.7509	0.1499	−1.6434
H	1.3664	1.3805	−0.4316
H	−1.3664	−1.3805	−0.4316
H	2.4549	0.2630	−0.5883
H	−2.4549	−0.2630	−0.5883
H	0.8746	−1.1117	−1.6535
H	−0.8746	1.1117	−1.6535
H	1.1374	0.2039	−2.4593
H	−1.1374	−0.2039	−2.4593

Table A73. Summary of experimental parameters relating to GED data collection for 1,2-dithiane.

Dataset Type	Short	Long
Nozzle-to-Image-Plate Distance / mm	244.0	489.0
Electron Wavelength / pm	5.85	5.85
$T_{\text{nozzle, av}}$ / K	298	298
$T_{\text{sample, av}}$ / K	293	293
Exposure Time / s	240	120

Table A74. Optimised Cartesian coordinates in Ångström (Å) and energy, E_{B2PLYP}, in atomic units (a.u.) of 1,2-dithiane as calculated at the B2PLYP/cc-pVDZ level.

E_{B2PLYP} = −952.89776837			
S	−1.004923	0.301441	−1.126880
S	1.004923	−0.301441	−1.126880
C	−1.004923	1.215965	0.467261
C	1.004923	−1.215965	0.467261
C	−0.702296	0.312088	1.665727
C	0.702296	−0.312088	1.665727
H	−2.018179	1.642507	0.548362
H	2.018179	−1.642507	0.548362
H	−0.284979	2.046258	0.391423
H	0.284979	−2.046258	0.391423
H	−1.461736	−0.487840	1.705933
H	1.461736	0.487840	1.705933
H	−0.818713	0.910366	2.586431
H	0.818713	−0.910366	2.586431

Table A75. Optimised Cartesian coordinates in Ångström (Å) and energy, E_{B2PLYP}, in atomic units (a.u.) of 1,2-dithiane as calculated at the B2PLYP/cc-pVTZ level.

E_{B2PLYP} = −952.97899352			
S	−0.987920	0.312876	−1.120628
S	0.987920	−0.312876	−1.120628
C	−0.987920	1.223044	0.464048
C	0.987920	−1.223044	0.464048
C	−0.697546	0.317247	1.657812
C	0.697546	−0.317247	1.657812
H	−1.987328	1.652864	0.542328
H	1.987328	−1.652864	0.542328
H	−0.267188	2.037226	0.391761
H	0.267188	−2.037226	0.391761
H	−1.455578	−0.468363	1.694139
H	1.455578	0.468363	1.694139
H	−0.808580	0.907863	2.570666
H	0.808580	−0.907863	2.570666

Table A76. Optimised Cartesian coordinates in Ångström (Å) and energy, E_{B2PLYP}, in atomic units (a.u.) of 1,2-dithiane as calculated at the B2PLYP/cc-pVQZ level.

E_{B2PLYP} = −952.99892150			
S	−0.980271	0.319306	−1.118279
S	0.980271	−0.319306	−1.118279
C	−0.980271	1.227312	0.461719
C	0.980271	−1.227312	0.461719
C	−0.695566	0.320645	1.655551
C	0.695566	−0.320645	1.655551
H	−1.977337	1.660397	0.538389
H	1.977337	−1.660397	0.538389
H	−0.257272	2.038551	0.391924
H	0.257272	−2.038551	0.391924
H	−1.456911	−0.460247	1.691246
H	1.456911	0.460247	1.691246
H	−0.804037	0.911293	2.567283
H	0.804037	−0.911293	2.567283

Table A77. Optimised Cartesian coordinates in Ångström (Å) and energy, E_{B3LYP}, in atomic units (a.u.) of 1,2-dithiane as calculated at the B3LYP/cc-pVDZ level.

E_{B3LYP} = −953.67319910			
S	−1.004875	0.317179	−1.132493
S	1.004875	−0.317179	−1.132493
C	−1.004875	1.224653	0.473891
C	1.004875	−1.224653	0.473891
C	−0.701856	0.315401	1.669648
C	0.701856	−0.315401	1.669648
H	−2.020111	1.648330	0.553189
H	2.020111	−1.648330	0.553189
H	−0.288046	2.058669	0.400899
H	0.288046	−2.058669	0.400899
H	−1.465689	−0.481492	1.712236
H	1.465689	0.481492	1.712236
H	−0.815644	0.912967	2.592325
H	0.815644	−0.912967	2.592325

Table A78. Optimised Cartesian coordinates in Ångström (Å) and energy, E_{B3LYP}, in atomic units (a.u.) of 1,2-dithiane as calculated at the B3LYP/cc-pVTZ level.

E_{B3LYP} = −953.76099340			
S	−0.989141	0.327723	−1.126981
S	0.989141	−0.327723	−1.126981
C	−0.989141	1.231100	0.470211
C	0.989141	−1.231100	0.470211
C	−0.697142	0.321561	1.663193
C	0.697142	−0.321561	1.663193
H	−1.990485	1.658526	0.548491
H	1.990485	−1.658526	0.548491
H	−0.272036	2.049743	0.401085
H	0.272036	−2.049743	0.401085
H	−1.460111	−0.460622	1.704115
H	1.460111	0.460622	1.704115
H	−0.804373	0.912923	2.577584
H	0.804373	−0.912923	2.577584

Table A79. Optimised Cartesian coordinates in Ångström (Å) and energy, E_{B3LYP}, in atomic units (a.u.) of 1,2-dithiane as calculated at the B3LYP/cc-pVQZ level.

E_{B3LYP} = −953.78223355			
S	−0.982485	0.333049	−1.124960
S	0.982485	−0.333049	−1.124960
C	−0.982485	1.235110	0.467590
C	0.982485	−1.235110	0.467590
C	−0.695337	0.325190	1.661643
C	0.695337	−0.325190	1.661643
H	−1.981764	1.665301	0.544899
H	1.981764	−1.665301	0.544899
H	−0.263706	2.051483	0.401200
H	0.263706	−2.051483	0.401200
H	−1.461745	−0.452169	1.703296
H	1.461745	0.452169	1.703296
H	−0.799158	0.917439	2.574570
H	0.799158	−0.917439	2.574570

Table A80. Optimised Cartesian coordinates in Ångström (Å) and energy, E_{B3P86}, in atomic units (a.u.) of 1,2-dithiane as calculated at the B3P86/cc-pVDZ level.

E_{B3P86} = −954.87164334			
S	−0.996384	0.308656	−1.122273
S	0.996384	−0.308656	−1.122273
C	−0.996384	1.216734	0.465761
C	0.996384	−1.216734	0.465761
C	−0.697826	0.314632	1.658287
C	0.697826	−0.314632	1.658287
H	−2.008791	1.645568	0.543429
H	2.008791	−1.645568	0.543429
H	−0.277525	2.048074	0.389161
H	0.277525	−2.048074	0.389161
H	−1.462078	−0.480830	1.699602
H	1.462078	0.480830	1.699602
H	−0.813238	0.911296	2.579880
H	0.813238	−0.911296	2.579880

Table A81. Optimised Cartesian coordinates in Ångström (Å) and energy, E_{B3P86}, in atomic units (a.u.) of 1,2-dithiane as calculated at the B3P86/cc-pVTZ level.

E_{B3P86} = −954.95322714			
S	−0.980764	0.317912	−1.116368
S	0.980764	−0.317912	−1.116368
C	−0.980764	1.222924	0.461839
C	0.980764	−1.222924	0.461839
C	−0.693556	0.319685	1.651218
C	0.693556	−0.319685	1.651218
H	−1.980348	1.655820	0.538698
H	1.980348	−1.655820	0.538698
H	−0.260045	2.039152	0.389712
H	0.260045	−2.039152	0.389712
H	−1.456686	−0.463065	1.689313
H	1.456686	0.463065	1.689313
H	−0.803450	0.910097	2.565826
H	0.803450	−0.910097	2.565826

Table A82. Optimised Cartesian coordinates in Ångström (Å) and energy, E_{B3P86}, in atomic units (a.u.) of 1,2-dithiane as calculated at the B3P86/cc-pVQZ level.

E_{B3P86} = −954.97387963			
S	−0.974728	0.322764	−1.114490
S	0.974728	−0.322764	−1.114490
C	−0.974728	1.226605	0.459545
C	0.974728	−1.226605	0.459545
C	−0.692090	0.322611	1.649679
C	0.692090	−0.322611	1.649679
H	−1.972397	1.662239	0.535571
H	1.972397	−1.662239	0.535571
H	−0.252250	2.040638	0.390064
H	0.252250	−2.040638	0.390064
H	−1.457991	−0.456209	1.687545
H	1.457991	0.456209	1.687545
H	−0.799644	0.913243	2.563318
H	0.799644	−0.913243	2.563318

Table A83. Optimised Cartesian coordinates in Ångström (Å) and energy, E_{B3PW91}, in atomic units (a.u.) of 1,2-dithiane as calculated at the B3PW91/cc-pVDZ level.

E_{B3PW91} = −953.52398534			
S	−0.996697	0.310552	−1.123862
S	0.996697	−0.310552	−1.123862
C	−0.996697	1.219692	0.466201
C	0.996697	−1.219692	0.466201
C	−0.698081	0.316685	1.660755
C	0.698081	−0.316685	1.660755
H	−2.010013	1.647989	0.543629
H	2.010013	−1.647989	0.543629
H	−0.278526	2.052318	0.389657
H	0.278526	−2.052318	0.389657
H	−1.464722	−0.476974	1.704671
H	1.464722	0.476974	1.704671
H	−0.811030	0.915315	2.582093
H	0.811030	−0.915315	2.582093

Table A84. Optimised Cartesian coordinates in Ångström (Å) and energy, E_{B3PW91}, in atomic units (a.u.) of 1,2-dithiane as calculated at the B3PW91/cc-pVTZ level.

E_{B3PW91} = −953.60434707			
S	−0.981256	0.319552	−1.118044
S	0.981256	−0.319552	−1.118044
C	−0.981256	1.226057	0.462268
C	0.981256	−1.226057	0.462268
C	−0.693887	0.321852	1.653887
C	0.693887	−0.321852	1.653887
H	−1.981990	1.658598	0.538932
H	1.981990	−1.658598	0.538932
H	−0.260940	2.043562	0.389821
H	0.260940	−2.043562	0.389821
H	−1.459557	−0.459280	1.694412
H	1.459557	0.459280	1.694412
H	−0.801300	0.914277	2.568600
H	0.801300	−0.914277	2.568600

Table A85. Optimised Cartesian coordinates in Ångström (Å) and energy, E_{B3PW91}, in atomic units (a.u.) of 1,2-dithiane as calculated at the B3PW91/cc-pVQZ level.

E_{B3PW91} = −953.62500712			
S	−0.975468	0.324067	−1.116158
S	0.975468	−0.324067	−1.116158
C	−0.975468	1.229524	0.460023
C	0.975468	−1.229524	0.460023
C	−0.692490	0.324563	1.652302
C	0.692490	−0.324563	1.652302
H	−1.974349	1.664718	0.535897
H	1.974349	−1.664718	0.535897
H	−0.253412	2.044873	0.390115
H	0.253412	−2.044873	0.390115
H	−1.460707	−0.452887	1.692453
H	1.460707	0.452887	1.692453
H	−0.797784	0.917091	2.566119
H	0.797784	−0.917091	2.566119

Table A86. Optimised Cartesian coordinates in Ångström (Å) and energy, E_{PBEH1PBE}, in atomic units (a.u.) of 1,2-dithiane as calculated at the PBEH1PBE/cc-pVDZ level.

E_{PBEH1PBE} = −953.23257828			
S	−0.993723	0.306690	−1.119874
S	0.993723	−0.306690	−1.119874
C	−0.993723	1.215205	0.463195
C	0.993723	−1.215205	0.463195
C	−0.697051	0.314812	1.656294
C	0.697051	−0.314812	1.656294
H	−2.005215	1.646342	0.540682
H	2.005215	−1.646342	0.540682
H	−0.272963	2.045061	0.385947
H	0.272963	−2.045061	0.385947
H	−1.461772	−0.480351	1.696975
H	1.461772	0.480351	1.696975
H	−0.812604	0.911949	2.577439
H	0.812604	−0.911949	2.577439

Table A87. Optimised Cartesian coordinates in Ångström (Å) and energy, E_{PBEH1PBE}, in atomic units (a.u.) of 1,2-dithiane as calculated at the PBEH1PBE/cc-pVTZ level.

E_{PBEH1PBE} = −953.31147421			
S	−0.978465	0.316005	−1.114361
S	0.978465	−0.316005	−1.114361
C	−0.978465	1.222004	0.459445
C	0.978465	−1.222004	0.459445
C	−0.693034	0.319957	1.649743
C	0.693034	−0.319957	1.649743
H	−1.977932	1.657136	0.536081
H	1.977932	−1.657136	0.536081
H	−0.255632	2.037356	0.386770
H	0.255632	−2.037356	0.386770
H	−1.457122	−0.462881	1.687274
H	1.457122	0.462881	1.687274
H	−0.803047	0.911280	2.564526
H	0.803047	−0.911280	2.564526

Table A88. Optimised Cartesian coordinates in Ångström (Å) and energy, E_{PBEH1PBE}, in atomic units (a.u.) of 1,2-dithiane as calculated at the PBEH1PBE/cc-pVQZ level.

E_{PBEH1PBE} = −953.33201772			
S	−0.972781	0.320723	−1.112592
S	0.972781	−0.320723	−1.112592
C	−0.972781	1.225423	0.457321
C	0.972781	−1.225423	0.457321
C	−0.691610	0.322704	1.648232
C	0.691610	−0.322704	1.648232
H	−1.970547	1.663115	0.533129
H	1.970547	−1.663115	0.533129
H	−0.248288	2.038848	0.387192
H	0.248288	−2.038848	0.387192
H	−1.458413	−0.456452	1.685700
H	1.458413	0.456452	1.685700
H	−0.799399	0.914338	2.562135
H	0.799399	−0.914338	2.562135

Table A89. Optimised Cartesian coordinates in Ångström (Å) and energy, E_{HSEH1PBE}, in atomic units (a.u.) of 1,2-dithiane as calculated at the HSEH1PBE/cc-pVDZ level.

E_{HSEH1PBE} = −953.22472151			
S	−0.994177	0.307314	−1.120372
S	0.994177	−0.307314	−1.120372
C	−0.994177	1.215590	0.463790
C	0.994177	−1.215590	0.463790
C	−0.697171	0.314795	1.656657
C	0.697171	−0.314795	1.656657
H	−2.006004	1.646265	0.541229
H	2.006004	−1.646265	0.541229
H	−0.273637	2.045778	0.386679
H	0.273637	−2.045778	0.386679
H	−1.461890	−0.480507	1.697325
H	1.461890	0.480507	1.697325
H	−0.812711	0.911839	2.578034
H	0.812711	−0.911839	2.578034

Table A90. Optimised Cartesian coordinates in Ångström (Å) and energy, E_{HSEH1PBE}, in atomic units (a.u.) of 1,2-dithiane as calculated at the HSEH1PBE/cc-pVTZ level.

E_{HSEH1PBE} = −953.30372946			
S	−0.978817	0.316818	−1.114876
S	0.978817	−0.316818	−1.114876
C	−0.978817	1.222445	0.460054
C	0.978817	−1.222445	0.460054
C	−0.693117	0.320010	1.650124
C	0.693117	−0.320010	1.650124
H	−1.978523	1.657182	0.536623
H	1.978523	−1.657182	0.536623
H	−0.256223	2.038074	0.387541
H	0.256223	−2.038074	0.387541
H	−1.457249	−0.462835	1.687713
H	1.457249	0.462835	1.687713
H	−0.803060	0.911235	2.565063
H	0.803060	−0.911235	2.565063

Table A91. Optimised Cartesian coordinates in Ångström (Å) and energy, E_{HSEH1PBE}, in atomic units (a.u.) of 1,2-dithiane as calculated at the HSEH1PBE/cc-pVQZ level.

E_{HSEH1PBE} = −953.32425298			
S	−0.973059	0.321603	−1.113094
S	0.973059	−0.321603	−1.113094
C	−0.973059	1.225913	0.457905
C	0.973059	−1.225913	0.457905
C	−0.691665	0.322815	1.648607
C	0.691665	−0.322815	1.648607
H	−1.971056	1.663228	0.533634
H	1.971056	−1.663228	0.533634
H	−0.248803	2.039614	0.387967
H	0.248803	−2.039614	0.387967
H	−1.458574	−0.456280	1.686184
H	1.458574	0.456280	1.686184
H	−0.799316	0.914390	2.562647
H	0.799316	−0.914390	2.562647

Table A92. Summary of experimental parameters relating to GED data reduction and refinement for 1,2-dithiane.

Dataset Type	Short	Long
Δs / nm^{-1}	2.0	1.0
s_{min} / nm^{-1}	84.0	48.0
sw_1 / nm^{-1}	104.0	64.0
sw_2 / nm^{-1}	204.0	111.0
s_{max} / nm^{-1}	238.0	120.0
Correlation Parameter	0.4853	0.4953
Scale Factor (k)	0.203(4)	0.144(4)

Table A93. Least-squares correlation matrix[a] (×100)

	p_1	p_3	p_5	p_8	p_{11}	p_{12}	u_1	u_4	u_7	u_8	u_{15}	u_{22}	k_1	k_2
p_1	100	−59	−59				71		58					50
p_3		100	58	−57		50	−50							
p_5			100			93								
p_8				100	−50			50		62				
p_{11}					100									
p_{12}						100								
u_1							100		88					60
u_4								100		90		78		
u_7									100		52		58	60
u_8										100		58		
u_{15}											100		55	
u_{22}												100		
k_1													100	
k_2														100

[a] Only values ≥ 50% are tabulated. k_1 and k_2 are scale factors.

Table A94. Refined (r_{h1}) and theoretical[a] (r_e) parameter values[b] and SARACEN restraints[c] applied in the least-squares refinement procedure.

	r_{h1}	r_e	Restraint
p_1	205.7(2)	206.9	–
p_2	183.0(2)	182.6	–
p_3	152.1(5)	152.8	–
p_4	109.4(2)	109.1	109.1(6)
p_5	99.4(2)	99.1	–
p_6	104.9(2)	104.8	104.8(2)
p_7	108.4(1)	108.4	108.4(7)
p_8	111.9(3)	112.7	–
p_9	108.2(1)	108.2	108.2(8)
p_{10}	108.8(1)	108.8	108.8(4)
p_{11}	28.4(2)	28.2	28.2(3)
p_{12}	62.3(5)	61.8	61.8(5)

[a] Calculations at the B3LYP/CBS level. [b] Interatomic distances (r) are tabulated in picometers (pm) and angles (a) and dihedrals (ϕ) are tabulated in degrees.

Table A95. Internuclear distances (r_a / pm), refined (u_{GED}) and theoretical (u_{h1}) amplitudes of vibration and restraints and distance corrections (k_{h1}) for 1,2-dithiane.[a]

Amp	Atomic Pair	r_a	u_{GED}	Restraint	k_{h1}	u_{h1}
u_{15}	C_2–H_5	109.5(2)	6.6(3)	7.7(8)	0.4	7.7
u_{14}	C_2–H_4	109.5(2)	6.6 (Tied to u_{15})	–	0.4	7.7
u_{42}	C_3–H_7	109.5(2)	6.6 (Tied to u_{15})	–	0.4	7.7
u_{41}	C_3–H_6	109.5(2)	6.6 (Tied to u_{15})	–	0.4	7.7
u_{16}	C_2–C_3	152.1(5)	3.1 (Tied to u_{43})	–	0.2	5.2
u_{43}	C_3–$C_{3'}$	155.4(9)	3.1(4)	5.2(5)	0.2	5.2
u_{46}	H_6...H_7	175.9(4)	7.5 (Tied to u_{43})	–	0.1	12.4
u_{25}	H_4...H_5	177.1(4)	12.4 (Fixed)	–	0.0	12.4
u_1	S_1–C_2	182.9(2)	4.9(4)	–	0.1	5.4
u_7	S_1–$S_{1'}$	205.7(2)	5.0(3)	–	0.1	5.1
u_{18}	C_2...H_7	212.7(5)	10.6 (Tied to u_7)	–	−0.1	10.8
u_{17}	C_2...H_6	213.4(4)	10.5 (Tied to u_7)	–	−0.1	10.7
u_{34}	H_5...C_3	215.7(6)	10.6 (Tied to u_7)	–	−0.1	10.7
u_{45}	C_3...$H_{7'}$	216.4(10)	10.6 (Tied to u_7)	–	0.0	10.7
u_{44}	C_3...$H_{6'}$	217.0(18)	10.5 (Tied to u_7)	–	−0.1	10.7
u_{26}	H_4...C_3	217.4(8)	10.5 (Tied to u_7)	–	−0.1	10.6
u_2	S_1...H_4	235.3(4)	11.6(10)	11.1(11)	−0.2	11.1
u_3	S_1...H_5	240.3(3)	12.0 (Tied to u_2)	–	−0.2	11.5
u_{49}	H_7...$H_{7'}$	244.3(17)	16.4 (Fixed)	–	0.3	16.4
u_{28}	H_4...H_7	245.9(9)	17.2 (Fixed)	–	0.0	17.2
u_{27}	H_4...H_6	248.1(10)	12.5 (Fixed)	–	−1.2	12.5
u_{48}	H_6...$H_{7'}$	249.4(15)	17.3 (Fixed)	–	0.2	17.3
u_{36}	H_5...H_7	249.7(7)	16.4 (Fixed)	–	0.2	16.4
u_{22}	C_2...$C_{3'}$	258.0(7)	6.6(7)	7.1(7)	−0.2	7.1
u_{39}	H_5...$H_{6'}$	259.2(9)	17.4 (Fixed)	–	−1.4	17.4
u_4	S_1...C_3	277.8(4)	6.8(5)	–	−0.2	6.9
u_{38}	H_5...$C_{3'}$	280.3(11)	10.1 (Tied to u_4)	–	−1.0	10.3
u_{23}	C_2...$H_{6'}$	281.4(5)	15.4 (Tied to u_4)	–	−0.4	15.8
u_5	S_1...H_6	292.3(5)	16.7 (Tied to u_8)	–	−0.3	16.2
u_8	S_1...$C_{2'}$	296.3(4)	8.4(4)	–	−0.2	8.1
u_{35}	H_5...H_6	304.7(6)	17.3 (Fixed)	–	0.0	17.3
u_{10}	S_1...$H_{5'}$	304.8(5)	11.0 (Tied to u_8)	–	−1.2	10.7
u_{47}	H_6...$H_{6'}$	305.8(22)	12.6 (Fixed)	–	−1.1	12.6
u_{19}	C_2...$C_{2'}$	315.2(9)	11.1 (Tied to u_{11})	–	−0.3	8.0
u_{11}	S_1...$C_{3'}$	329.6(4)	10.7(3)	7.7(8)	−0.4	7.7
u_{21}	C_2...$H_{5'}$	346.7(10)	15.7 (Tied to u_{11})	–	−1.4	11.2
u_{24}	C_2...$H_{7'}$	348.8(9)	14.5 (Tied to u_{11})	–	−0.9	10.4
u_{31}	H_4...$C_{3'}$	352.1(7)	22.1 (Tied to u_{11})	–	−0.3	15.9
u_{12}	S_1...$H_{6'}$	367.7(6)	22.7(13)	15.9(16)	−1.0	15.9
u_6	S_1...H_7	371.9(4)	14.5 (Tied to u_{12})	–	−1.1	10.2
u_{40}	H_5...$H_{7'}$	376.8(13)	14.1 (Fixed)	–	−1.6	14.1

u_{32}	$H_4...H_{6'}$	381.2(7)	24.1 (Fixed)	–	0.6	24.1
u_9	$S_1...H_{4'}$	392.9(4)	16.7(17)	18.5(19)	−0.1	18.5
u_{37}	$H_5...H_{5'}$	405.9(11)	13.1 (Fixed)	–	−2.7	13.1
u_{20}	$C_2...H_{4'}$	414.6(9)	22.5 (Tied to u_{13})	–	−0.6	16.9
u_{13}	$S_1...H_{7'}$	426.8(5)	15.3(7)	11.5(12)	−1.3	11.5
u_{30}	$H_4...H_{5'}$	430.6(10)	21.3 (Fixed)	–	−1.5	21.3
u_{33}	$H_4...H_{7'}$	431.3(11)	17.4 (Fixed)	–	−1.3	17.4
u_{29}	$H_4...H_{4'}$	518.1(10)	19.0 (Fixed)	–	−1.6	19.0

[a] All values are tabulated in picometers (pm).

Table A96. Refined Cartesian coordinates in Ångström (Å) for the experimentally-determined structure of 1,2-dithiane obtained *via* GED.

	x	*y*	*z*
S	0.0000	1.0283	0.0000
S	0.0000	−1.0283	0.0000
C	−1.5882	1.3265	0.8580
C	−1.5882	−1.3265	−0.8580
C	−2.7690	0.7727	0.0762
C	−2.7690	−0.7727	−0.0762
H	−1.6459	2.4134	0.9725
H	−1.6459	−2.4134	−0.9725
H	−1.5362	0.8694	1.8511
H	−1.5362	−0.8694	−1.8511
H	−2.7816	1.2343	−0.9161
H	−2.7816	−1.2343	0.9161
H	−3.6886	1.0765	0.5860
H	−3.6886	−1.0765	−0.5860

Table A97. Summary of experimental parameters relating to GED data collection for *E*-cinnamonitrile.

Dataset Type	Short	Long
Nozzle-to-Image-Plate distance / mm	235.5	487.0
Electron wavelength / pm	5.85	5.85
$T_{\text{nozzle, av}}$ / K	448	448
$T_{\text{sample, av}}$ / K	443	443
Exposure Time / s	240	120

Table A98. Optimised Cartesian coordinates in Ångström (Å) and energy, E_{B2PLYP}, in atomic units (a.u.) of *E*-cinnamonitrile as calculated at the B2PLYP/cc-pVDZ level.

E_{B2PLYP} = −401.05250382			
N	−2.275864	−3.989467	0.000000
C	−1.496098	−3.111971	0.000000
C	−0.529930	−2.056672	0.000000
C	−0.895282	−0.752515	0.000000
C	0.000000	0.409238	0.000000
C	1.407057	0.300229	0.000000
C	2.207601	1.442588	0.000000
C	1.623409	2.718031	0.000000
C	0.229942	2.841605	0.000000
C	−0.572703	1.696972	0.000000
H	0.517212	−2.365935	0.000000
H	−1.965818	−0.525479	0.000000
H	1.881657	−0.682602	0.000000
H	3.294525	1.340341	0.000000
H	2.254196	3.609053	0.000000
H	−0.233725	3.829893	0.000000
H	−1.660974	1.795965	0.000000

Table A99. Optimised Cartesian coordinates in Ångström (Å) and energy, E_{B2PLYP}, in atomic units (a.u.) of *E*-cinnamonitrile as calculated at the B2PLYP/cc-pVTZ level.

E_{B2PLYP} = −401.16009201			
N	−2.251660	−3.966920	0.000000
C	−1.485665	−3.093669	0.000000
C	−0.527909	−2.043687	0.000000
C	−0.890522	−0.749328	0.000000
C	0.000000	0.406766	0.000000
C	1.398317	0.299921	0.000000
C	2.192524	1.435641	0.000000
C	1.610268	2.702469	0.000000
C	0.225677	2.824245	0.000000
C	−0.570476	1.685776	0.000000
H	0.508554	−2.349031	0.000000
H	−1.950108	−0.524174	0.000000
H	1.869502	−0.672312	0.000000
H	3.268435	1.336291	0.000000
H	2.233640	3.584890	0.000000
H	−0.233846	3.802010	0.000000
H	−1.647840	1.781964	0.000000

Table A100. Optimised Cartesian coordinates in Ångström (Å) and energy, E_{B2PLYP}, in atomic units (a.u.) of *E*-cinnamonitrile as calculated at the B2PLYP/cc-pVQZ level.

E_{B2PLYP} = −401.18686877			
N	−2.248543	−3.964527	0.000000
C	−1.483101	−3.092938	0.000000
C	−0.525471	−2.043169	0.000000
C	−0.889389	−0.750046	0.000000
C	0.000000	0.406350	0.000000
C	1.397577	0.300574	0.000000
C	2.190356	1.436362	0.000000
C	1.607383	2.701998	0.000000
C	0.223554	2.822650	0.000000
C	−0.571315	1.684144	0.000000
H	0.510335	−2.348753	0.000000
H	−1.948618	−0.525941	0.000000
H	1.869646	−0.670633	0.000000
H	3.265792	1.337993	0.000000
H	2.229743	3.584434	0.000000
H	−0.236460	3.799561	0.000000
H	−1.648203	1.779467	0.000000

Table A101. Optimised Cartesian coordinates in Ångström (Å) and energy, E_{B3LYP}, in atomic units (a.u.) of *E*-cinnamonitrile as calculated at the B3LYP/cc-pVDZ level.

E_{B3LYP} = −401.91954828			
N	−2.262690	−3.988684	0.000000
C	−1.493437	−3.112556	0.000000
C	−0.532523	−2.057568	0.000000
C	−0.891835	−0.753883	0.000000
C	0.000000	0.407875	0.000000
C	1.406773	0.304080	0.000000
C	2.203395	1.446068	0.000000
C	1.617137	2.718567	0.000000
C	0.225332	2.838861	0.000000
C	−0.573569	1.694599	0.000000
H	0.514512	−2.370348	0.000000
H	−1.961939	−0.524200	0.000000
H	1.884223	−0.677518	0.000000
H	3.290983	1.346367	0.000000
H	2.246217	3.611311	0.000000
H	−0.240642	3.826535	0.000000
H	−1.662155	1.792375	0.000000

Table A102. Optimised Cartesian coordinates in Ångström (Å) and energy, E_{B3LYP}, in atomic units (a.u.) of *E*-cinnamonitrile as calculated at the B3LYP/cc-pVTZ level.

E_{B3LYP} = −402.03715019			
N	−2.232271	−3.974540	0.000000
C	−1.477950	−3.100888	0.000000
C	−0.526391	−2.048247	0.000000
C	−0.885040	−0.754050	0.000000
C	0.000000	0.405517	0.000000
C	1.399373	0.308144	0.000000
C	2.186788	1.446683	0.000000
C	1.598489	2.709690	0.000000
C	0.214304	2.824059	0.000000
C	−0.575316	1.682869	0.000000
H	0.510972	−2.356155	0.000000
H	−1.945264	−0.527858	0.000000
H	1.877052	−0.661837	0.000000
H	3.264361	1.352925	0.000000
H	2.217940	3.596264	0.000000
H	−0.250808	3.800465	0.000000
H	−1.653900	1.775312	0.000000

Table A103. Optimised Cartesian coordinates in Ångström (Å) and energy, E_{B3LYP}, in atomic units (a.u.) of *E*-cinnamonitrile as calculated at the B3LYP/cc-pVQZ level.

E_{B3LYP} = −402.06599261			
N	−2.230759	−3.973257	0.000000
C	−1.476520	−3.100993	0.000000
C	−0.524551	−2.048224	0.000000
C	−0.884493	−0.754733	0.000000
C	0.000000	0.405314	0.000000
C	1.399105	0.308487	0.000000
C	2.185801	1.447313	0.000000
C	1.596899	2.709843	0.000000
C	0.212896	2.823540	0.000000
C	−0.576069	1.682047	0.000000
H	0.512080	−2.356324	0.000000
H	−1.944270	−0.529382	0.000000
H	1.877218	−0.660612	0.000000
H	3.262833	1.354204	0.000000
H	2.215578	3.596230	0.000000
H	−0.252425	3.799183	0.000000
H	−1.654103	1.773936	0.000000

Table A104. Optimised Cartesian coordinates in Ångström (Å) and energy, E_{B3P86}, in atomic units (a.u.) of *E*-cinnamonitrile as calculated at the B3P86/cc-pVDZ level.

E_{B3P86} = −403.13732378			
N	−2.277062	−3.964149	0.000000
C	−1.503760	−3.092231	0.000000
C	−0.540788	−2.046054	0.000000
C	−0.896089	−0.743894	0.000000
C	0.000000	0.407393	0.000000
C	1.401683	0.292336	0.000000
C	2.204837	1.425318	0.000000
C	1.629156	2.698738	0.000000
C	0.241826	2.829563	0.000000
C	−0.563427	1.694148	0.000000
H	0.504850	−2.362470	0.000000
H	−1.964985	−0.510283	0.000000
H	1.870594	−0.693103	0.000000
H	3.291058	1.317794	0.000000
H	2.264540	3.586285	0.000000
H	−0.216284	3.820223	0.000000
H	−1.650977	1.798698	0.000000

Table A105. Optimised Cartesian coordinates in Ångström (Å) and energy, E_{B3P86}, in atomic units (a.u.) of *E*-cinnamonitrile as calculated at the B3P86/cc-pVTZ level.

E_{B3P86} = −403.24348364			
N	−2.248591	−3.949389	0.000000
C	−1.488700	−3.080822	0.000000
C	−0.534574	−2.036527	0.000000
C	−0.889816	−0.743713	0.000000
C	0.000000	0.405117	0.000000
C	1.394442	0.295609	0.000000
C	2.188964	1.425156	0.000000
C	1.611495	2.689586	0.000000
C	0.231449	2.815102	0.000000
C	−0.565056	1.682781	0.000000
H	0.502752	−2.347078	0.000000
H	−1.949797	−0.513223	0.000000
H	1.863171	−0.679578	0.000000
H	3.266171	1.323183	0.000000
H	2.238142	3.571596	0.000000
H	−0.225831	3.795614	0.000000
H	−1.643700	1.781477	0.000000

Table A106. Optimised Cartesian coordinates in Ångström (Å) and energy, E_{B3P86}, in atomic units (a.u.) of *E*-cinnamonitrile as calculated at the B3P86/cc-pVQZ level.

E_{B3P86} = −403.27147730			
N	−2.247222	−3.948021	0.000000
C	−1.487496	−3.080837	0.000000
C	−0.532946	−2.036496	0.000000
C	−0.889279	−0.744391	0.000000
C	0.000000	0.404915	0.000000
C	1.394190	0.295929	0.000000
C	2.188028	1.425683	0.000000
C	1.610050	2.689634	0.000000
C	0.230226	2.814556	0.000000
C	−0.565671	1.682030	0.000000
H	0.503753	−2.347314	0.000000
H	−1.948938	−0.514736	0.000000
H	1.863389	−0.678515	0.000000
H	3.264823	1.324306	0.000000
H	2.236049	3.571532	0.000000
H	−0.227250	3.794460	0.000000
H	−1.643887	1.780276	0.000000

Table A107. Optimised Cartesian coordinates in Ångström (Å) and energy, E_{B3PW91}, in atomic units (a.u.) of *E*-cinnamonitrile as calculated at the B3PW91/cc-pVDZ level.

E_{B3PW91} = −401.76189712			
N	−2.260864	−3.980372	0.000000
C	−1.490974	−3.104549	0.000000
C	−0.530805	−2.053617	0.000000
C	−0.890538	−0.751400	0.000000
C	0.000000	0.406931	0.000000
C	1.403977	0.302332	0.000000
C	2.199831	1.442035	0.000000
C	1.615030	2.712512	0.000000
C	0.225616	2.833472	0.000000
C	−0.572337	1.691449	0.000000
H	0.515820	−2.368134	0.000000
H	−1.960892	−0.522651	0.000000
H	1.881287	−0.679480	0.000000
H	3.287367	1.341897	0.000000
H	2.244527	3.604981	0.000000
H	−0.239879	3.821353	0.000000
H	−1.660974	1.789648	0.000000

Table A108. Optimised Cartesian coordinates in Ångström (Å) and energy, E_{B3PW91}, in atomic units (a.u.) of *E*-cinnamonitrile as calculated at the B3PW91/cc-pVTZ level.

E_{B3PW91} = −401.86628140			
N	−2.232483	−3.966189	0.000000
C	−1.475859	−3.093695	0.000000
C	−0.524323	−2.044285	0.000000
C	−0.884386	−0.751294	0.000000
C	0.000000	0.404770	0.000000
C	1.396856	0.305670	0.000000
C	2.184122	1.442122	0.000000
C	1.597386	2.703749	0.000000
C	0.215051	2.819358	0.000000
C	−0.574181	1.680247	0.000000
H	0.514344	−2.352868	0.000000
H	−1.946149	−0.525655	0.000000
H	1.873945	−0.666263	0.000000
H	3.262979	1.347468	0.000000
H	2.218324	3.590979	0.000000
H	−0.249810	3.797383	0.000000
H	−1.654258	1.772429	0.000000

Table A109. Optimised Cartesian coordinates in Ångström (Å) and energy, E_{B3PW91}, in atomic units (a.u.) of *E*-cinnamonitrile as calculated at the B3PW91/cc-pVQZ level.

E_{B3PW91} = −401.89432208			
N	−2.231460	−3.964569	0.000000
C	−1.474930	−3.093504	0.000000
C	−0.522883	−2.044177	0.000000
C	−0.883918	−0.751849	0.000000
C	0.000000	0.404575	0.000000
C	1.396594	0.305807	0.000000
C	2.183316	1.442370	0.000000
C	1.596219	2.703598	0.000000
C	0.214116	2.818789	0.000000
C	−0.574653	1.679563	0.000000
H	0.515107	−2.353159	0.000000
H	−1.945349	−0.527002	0.000000
H	1.874036	−0.665424	0.000000
H	3.261744	1.348183	0.000000
H	2.216617	3.590632	0.000000
H	−0.250815	3.796257	0.000000
H	−1.654282	1.771459	0.000000

Table A110. Optimised Cartesian coordinates in Ångström (Å) and energy, E_{PBEH1PBE}, in atomic units (a.u.) of *E*-cinnamonitrile as calculated at the PBEH1PBE/cc-pVDZ level.

E_{PBEH1PBE} = −401.48327552			
N	−2.272187	−3.963785	0.000000
C	−1.499522	−3.093424	0.000000
C	−0.536713	−2.046047	0.000000
C	−0.894371	−0.746021	0.000000
C	0.000000	0.407399	0.000000
C	1.400892	0.294273	0.000000
C	2.202055	1.428005	0.000000
C	1.624581	2.699859	0.000000
C	0.237764	2.828555	0.000000
C	−0.565290	1.692173	0.000000
H	0.509319	−2.361107	0.000000
H	−1.963828	−0.514465	0.000000
H	1.871401	−0.690559	0.000000
H	3.288525	1.322205	0.000000
H	2.258617	3.588491	0.000000
H	−0.221933	3.818565	0.000000
H	−1.653166	1.794722	0.000000

Table A111. Optimised Cartesian coordinates in Ångström (Å) and energy, E_{PBEH1PBE}, in atomic units (a.u.) of *E*-cinnamonitrile as calculated at the PBEH1PBE/cc-pVTZ level.

E_{PBEH1PBE} = −401.58508735			
N	−2.243757	−3.951490	0.000000
C	−1.484166	−3.083996	0.000000
C	−0.529621	−2.037724	0.000000
C	−0.888073	−0.746575	0.000000
C	0.000000	0.405289	0.000000
C	1.394308	0.298197	0.000000
C	2.186681	1.429414	0.000000
C	1.606606	2.692657	0.000000
C	0.226360	2.815426	0.000000
C	−0.567827	1.681218	0.000000
H	0.508629	−2.347253	0.000000
H	−1.949350	−0.518529	0.000000
H	1.865395	−0.676709	0.000000
H	3.264874	1.329531	0.000000
H	2.231922	3.576597	0.000000
H	−0.233296	3.795694	0.000000
H	−1.647482	1.777661	0.000000

Table A112. Optimised Cartesian coordinates in Ångström (Å) and energy, E_{PBEH1PBE}, in atomic units (a.u.) of *E*-cinnamonitrile as calculated at the PBEH1PBE/cc-pVQZ level.

E_{PBEH1PBE} = −401.61261967			
N	−2.243008	−3.949789	0.000000
C	−1.483466	−3.083695	0.000000
C	−0.528323	−2.037581	0.000000
C	−0.887703	−0.747032	0.000000
C	0.000000	0.405099	0.000000
C	1.394051	0.298203	0.000000
C	2.186007	1.429482	0.000000
C	1.605671	2.692409	0.000000
C	0.225646	2.814889	0.000000
C	−0.568197	1.680600	0.000000
H	0.509307	−2.347594	0.000000
H	−1.948709	−0.519668	0.000000
H	1.865445	−0.676109	0.000000
H	3.263834	1.329957	0.000000
H	2.230570	3.576153	0.000000
H	−0.234034	3.794700	0.000000
H	−1.647472	1.776838	0.000000

Table A113. Optimised Cartesian coordinates in Ångström (Å) and energy, E_{HSEH1PBE}, in atomic units (a.u.) of *E*-cinnamonitrile as calculated at the HSEH1PBE/cc-pVDZ level.

E_{HSEH1PBE} = −401.47518639			
N	−2.274413	−3.963200	0.000000
C	−1.501529	−3.092537	0.000000
C	−0.538598	−2.046028	0.000000
C	−0.894902	−0.744945	0.000000
C	0.000000	0.407182	0.000000
C	1.401309	0.293283	0.000000
C	2.203209	1.426553	0.000000
C	1.626546	2.699139	0.000000
C	0.239561	2.828769	0.000000
C	−0.564365	1.692890	0.000000
H	0.507354	−2.361738	0.000000
H	−1.964220	−0.512456	0.000000
H	1.871144	−0.691924	0.000000
H	3.289655	1.320045	0.000000
H	2.261242	3.587340	0.000000
H	−0.219455	3.819140	0.000000
H	−1.652211	1.796167	0.000000

Table A114. Optimised Cartesian coordinates in Ångström (Å) and energy, E_{HSEH1PBE}, in atomic units (a.u.) of *E*-cinnamonitrile as calculated at the HSEH1PBE/cc-pVTZ level.

E_{HSEH1PBE} = −401.57728644			
N	−2.246293	−3.950629	0.000000
C	−1.486484	−3.082884	0.000000
C	−0.531812	−2.037592	0.000000
C	−0.888719	−0.745353	0.000000
C	0.000000	0.405062	0.000000
C	1.394696	0.297036	0.000000
C	2.187960	1.427652	0.000000
C	1.608889	2.691688	0.000000
C	0.228513	2.815579	0.000000
C	−0.566693	1.682011	0.000000
H	0.506284	−2.347860	0.000000
H	−1.949777	−0.516247	0.000000
H	1.864989	−0.678249	0.000000
H	3.266059	1.326911	0.000000
H	2.234956	3.575065	0.000000
H	−0.230306	3.796221	0.000000
H	−1.646249	1.779370	0.000000

Table A115. Optimised Cartesian coordinates in Ångström (Å) and energy, E_{HSEH1PBE}, in atomic units (a.u.) of *E*-cinnamonitrile as calculated at the HSEH1PBE/cc-pVQZ level.

E_{HSEH1PBE} = −401.60480892			
N	−2.245503	−3.948941	0.000000
C	−1.485729	−3.082607	0.000000
C	−0.530466	−2.037468	0.000000
C	−0.888330	−0.745833	0.000000
C	0.000000	0.404865	0.000000
C	1.394441	0.297065	0.000000
C	2.187265	1.427763	0.000000
C	1.607904	2.691471	0.000000
C	0.227745	2.815042	0.000000
C	−0.567093	1.681375	0.000000
H	0.507015	−2.348201	0.000000
H	−1.949122	−0.517428	0.000000
H	1.865062	−0.677614	0.000000
H	3.264999	1.327403	0.000000
H	2.233533	3.574666	0.000000
H	−0.231120	3.795217	0.000000
H	−1.646270	1.778506	0.000000

Table A116. Summary of experimental parameters relating to GED data reduction and refinement for *E*-cinnamonitrile.

Dataset Type	Short	Long
Δs / nm^{-1}	2.0	1.0
s_{min} / nm^{-1}	100.0	54.0
sw_1 / nm^{-1}	120.0	74.0
sw_2 / nm^{-1}	220.0	112.0
s_{max} / nm^{-1}	256.0	130.0
Correlation parameter	0.4936	0.4971
Scale factor (k)	0.0155(4)	0.0111(2)

Table A117. Least-squares correlation matrix[a] (×100).

	p_1	p_{13}	p_{14}	u_8	u_9	u_{48}	u_{75}	k_1
p_1	100			−55				
p_{13}		100	−81				57	
p_{14}			100				−63	
u_8				100				
u_9					100	66		83
u_{48}						100		65
u_{75}							100	
k_1								100

[a] Only values ≥ 50% are tabulated. k_1 is a scale factor.

Table A118. Refined (r_{h1}) and theoretical[a] (r_e) parameter values[b] and SARACEN restraints[c] applied in the least-squares refinement procedure.

	r_{h1}	r_e	Restraint
p_1	115.3(5)	115.3	–
p_2	139.9(1)	139.7	–
p_3	1.5(1)	1.4	1.4(1)
p_4	9.7(4)	9.6	9.6(3)
p_5	4.0(2)	4.0	4.0(2)
p_6	1.0(1)	1.0	1.0(1)
p_7	1.1(1)	1.1	1.1(1)
p_8	−0.4(1)	−0.3	−0.4(1)
p_9	0.2(1)	0.2	0.2(1)
p_{10}	0.4(1)	0.4	0.5(1)
p_{11}	108.1(4)	108.1	108.2(5)
p_{12}	122.5(5)	122.3	–
p_{13}	127.3(8)	127.1	–
p_{14}	124.2(8)	123.4	–
p_{15}	1.5(1)	1.5	1.5(1)
p_{16}	1.4(1)	1.5	1.5(1)
p_{17}	0.7(1)	0.7	0.7(1)
p_{18}	0.4(1)	0.4	0.4(1)
p_{19}	−0.4(1)	−0.4	−0.4(1)
p_{20}	115.6(2)	115.6	115.6(2)
p_{21}	117.5(2)	117.6	117.2(2)

[a] Calculations at the B3LYP/CBS level. [b] Interatomic distances (r) are tabulated in picometers (pm) and angles (a) and dihedrals (ϕ) are tabulated in degrees.

Table A119. Internuclear distances (r_a / pm), refined (u_{GED}) and theoretical (u_{h1}) amplitudes of vibration and restraints and distance corrections (k_{h1}) for *E*-cinnamonitrile.[a]

Amp	Atomic Pair	r_a	u_{GED}	Restraint	k_{h1}	u_{h1}
u_1	C_6–H_{13}	109.6(4)	6.4 (Tied to u_8)	–	1.6	7.5
u_2	C_7–H_{14}	109.6(4)	6.4 (Tied to u_8)	–	1.6	7.5
u_3	C_8–H_{15}	109.6(4)	6.4 (Tied to u_8)	–	1.6	7.5
u_4	C_9–H_{16}	109.6(4)	6.4 (Tied to u_8)	–	1.6	7.5
u_5	C_3–H_{11}	109.7(4)	6.5 (Tied to u_8)	–	1.6	7.6
u_6	C_{10}–H_{17}	109.7(4)	6.5 (Tied to u_8)	–	1.6	7.6
u_7	C_4–H_{12}	109.9(4)	6.5 (Tied to u_8)	–	1.7	7.6
u_8	N_1–C_2	115.7(5)	2.9(2)	3.4(3)	0.4	3.4
u_9	C_3–C_4	135.1(3)	4.6(2)	–	0.7	4.2
u_{10}	C_6–C_7	139.4(1)	4.9 (Tied to u_9)	–	0.9	4.5
u_{11}	C_9–C_{10}	139.5(1)	4.9 (Tied to u_9)	–	0.7	4.6
u_{12}	C_8–C_9	139.8(1)	4.9 (Tied to u_9)	–	0.8	4.6
u_{13}	C_7–C_8	140.0(1)	5.0 (Tied to u_9)	–	0.6	4.6
u_{14}	C_5–C_{10}	140.7(3)	5.0 (Tied to u_9)	–	0.7	4.6
u_{15}	C_5–C_6	141.0(1)	5.0 (Tied to u_9)	–	0.6	4.6
u_{16}	C_2–C_3	143.0(2)	5.0 (Tied to u_9)	–	0.8	4.6

u_{17}	C_4–C_5	147.2(2)	5.3 (Tied to u_9)	–	1.1	4.9
u_{18}	C_3...H_{12}	209.8(5)	13.0(6)	9.9(10)	1.8	9.9
u_{19}	C_2...H_{11}	214.0(4)	13.6 (Tied to u_{18})	–	1.5	10.4
u_{20}	C_4...H_{11}	213.1(7)	13.1 (Tied to u_{18})	–	0.7	9.9
u_{21}	C_7...H_{13}	215.7(3)	12.9 (Tied to u_{18})	–	2.0	9.8
u_{22}	C_6...H_{14}	215.4(3)	13.1 (Tied to u_{18})	–	1.6	9.9
u_{23}	C_{10}...H_{16}	215.7(3)	13.0 (Tied to u_{18})	–	1.3	9.9
u_{24}	C_9...H_{17}	215.2(3)	13.1 (Tied to u_{18})	–	1.4	9.9
u_{25}	C_8...H_{16}	215.8(3)	13.1 (Tied to u_{18})	–	1.4	9.9
u_{26}	C_5...H_{17}	216.4(4)	13.0 (Tied to u_{18})	–	1.5	9.9
u_{27}	C_9...H_{15}	216.0(3)	13.0 (Tied to u_{18})	–	1.4	9.9
u_{28}	C_8...H_{14}	215.9(3)	13.0 (Tied to u_{18})	–	1.3	9.9
u_{29}	C_7...H_{15}	216.2(3)	13.1 (Tied to u_{18})	–	1.2	10.0
u_{30}	C_5...H_{12}	218.2(10)	13.7 (Tied to u_{18})	–	2.5	10.4
u_{31}	C_5...H_{13}	216.1(3)	13.2 (Tied to u_{18})	–	0.8	10.0
u_{32}	H_{11}...H_{13}	235.1(19)	34.4 (Fixed)	–	14.5	34.4
u_{33}	H_{12}...H_{17}	241.2(15)	22.6 (Fixed)	–	11.3	22.6
u_{34}	C_8...C_{10}	241.6(2)	6.6 (Tied to u_{48})	–	1.1	5.7
u_{35}	C_7...C_9	241.7(2)	6.6 (Tied to u_{48})	–	1.0	5.7
u_{36}	C_6...C_{10}	241.8(3)	6.7 (Tied to u_{48})	–	1.1	5.8
u_{37}	C_6...C_8	241.9(1)	6.6 (Tied to u_{48})	–	0.9	5.7
u_{38}	C_2...C_4	243.6(6)	8.1 (Tied to u_{48})	–	1.1	7.0
u_{39}	C_5...C_7	243.3(2)	6.6 (Tied to u_{48})	–	1.0	5.7
u_{40}	C_5...C_9	243.5(2)	6.6 (Tied to u_{48})	–	0.7	5.7
u_{41}	H_{13}...H_{14}	247.9(4)	16.2 (Fixed)	–	2.3	16.2
u_{42}	C_4...C_{10}	246.7(9)	7.8 (Tied to u_{48})	–	2.0	6.7
u_{43}	H_{16}...H_{17}	247.3(4)	16.2 (Fixed)	–	1.2	16.2
u_{44}	H_{14}...H_{15}	248.5(4)	16.2 (Fixed)	–	1.2	16.2
u_{45}	H_{15}...H_{16}	248.4(4)	16.2 (Fixed)	–	1.1	16.2
u_{46}	C_3...C_5	251.2(8)	7.6 (Tied to u_{48})	–	−0.2	6.5
u_{47}	C_4...C_6	253.5(10)	7.7 (Tied to u_{48})	–	0.3	6.7
u_{48}	N_1...C_3	257.6(6)	5.9(2)	5.1(5)	0.2	5.1
u_{49}	C_{10}...H_{12}	265.6(10)	17.7 (Tied to u_{48})	–	7.3	15.3
u_{50}	C_2...H_{12}	264.1(11)	18.0 (Tied to u_{48})	–	2.2	15.5
u_{51}	C_4...H_{17}	265.9(15)	16.4 (Tied to u_{48})	–	2.8	14.2
u_{52}	C_4...H_{13}	276.3(15)	16.4 (Tied to u_{54})	–	−1.0	14.0
u_{53}	C_3...H_{13}	283.3(14)	23.8 (Tied to u_{54})	–	3.5	20.3
u_{54}	C_7...C_{10}	278.6(2)	7.6(3)	6.5(7)	1.3	6.5
u_{55}	C_6...C_9	279.1(2)	7.7 (Tied to u_{54})	–	0.9	6.6
u_{56}	C_6...H_{11}	285.7(18)	25.8 (Tied to u_{54})	–	2.3	22.0
u_{57}	C_5...C_8	281.3(2)	7.6 (Tied to u_{54})	–	0.7	6.5
u_{58}	C_5...H_{11}	278.8(19)	17.4 (Tied to u_{54})	–	−2.3	14.8
u_{59}	C_3...C_6	307.5(9)	11.2(1)	–	0.9	11.6
u_{60}	H_{11}...H_{12}	307.9(8)	11.9 (Fixed)	–	1.9	11.9
u_{61}	N_1...H_{11}	319.6(6)	13.5 (Tied to u_{59})	–	0.3	14.0

u_{62}	$C_8...H_{13}$	340.4(4)	10.0 (Tied to u_{74})	–	1.8	9.5
u_{63}	$C_8...H_{17}$	339.9(4)	10.1 (Tied to u_{74})	–	1.7	9.6
u_{64}	$C_{10}...H_{15}$	340.1(4)	10.0 (Tied to u_{74})	–	1.6	9.5
u_{65}	$C_9...H_{14}$	340.1(4)	10.0 (Tied to u_{74})	–	1.6	9.5
u_{66}	$C_6...H_{17}$	340.6(4)	10.0 (Tied to u_{74})	–	1.8	9.6
u_{67}	$C_7...H_{16}$	340.2(4)	10.1 (Tied to u_{74})	–	1.5	9.6
u_{68}	$C_6...H_{15}$	340.4(4)	10.1 (Tied to u_{74})	–	1.5	9.6
u_{69}	$C_{10}...H_{13}$	340.1(4)	10.1 (Tied to u_{74})	–	1.3	9.6
u_{70}	$C_5...H_{14}$	341.6(4)	10.1 (Tied to u_{74})	–	1.6	9.6
u_{71}	$C_5...H_{16}$	341.8(4)	10.0 (Tied to u_{74})	–	1.4	9.5
u_{72}	$C_6...H_{12}$	344.6(13)	11.2 (Tied to u_{74})	–	−0.8	10.6
u_{73}	$N_1...H_{12}$	346.0(14)	24.6 (Tied to u_{74})	–	1.3	23.4
u_{74}	$N_1...C_4$	348.8(8)	11.8(6)	–	0.2	11.2
u_{75}	$C_3...C_{10}$	370.4(11)	9.4(5)	7.6(8)	−2.2	7.6
u_{76}	$C_4...C_9$	375.5(6)	8.4 (Tied to u_{75})	–	1.7	6.8
u_{77}	$C_4...C_7$	379.7(7)	8.4 (Tied to u_{75})	–	0.8	6.8
u_{78}	$C_2...C_5$	381.7(5)	8.9 (Tied to u_{75})	–	0.5	7.1
u_{79}	$H_{12}...H_{13}$	378.2(16)	20.4 (Tied to u_{75})	–	−4.8	16.4
u_{80}	$C_{10}...H_{14}$	387.3(4)	11.9 (Tied to u_{75})	–	1.9	9.6
u_{81}	$C_7...H_{17}$	387.3(4)	11.9 (Tied to u_{75})	–	1.9	9.6
u_{82}	$C_9...H_{13}$	387.7(4)	12.0 (Tied to u_{75})	–	1.5	9.7
u_{83}	$C_6...H_{16}$	387.7(4)	12.0 (Tied to u_{75})	–	1.5	9.7
u_{84}	$C_5...H_{15}$	389.9(4)	11.9 (Tied to u_{75})	–	1.4	9.6
u_{85}	$C_9...H_{12}$	403.5(10)	18.8 (Tied to u_{75})	–	6.5	15.1
u_{86}	$C_3...H_{17}$	395.2(15)	19.2 (Tied to u_{75})	–	−2.2	15.4
u_{87}	$C_2...H_{13}$	416.3(15)	22.7 (Tied to u_{90})	–	−1.3	20.6
u_{88}	$C_7...H_{11}$	416.9(18)	24.4 (Tied to u_{90})	–	−1.8	22.1
u_{89}	$C_{10}...H_{11}$	410.6(19)	16.9 (Tied to u_{90})	–	−7.5	15.3
u_{90}	$C_4...C_8$	427.6(3)	7.8(10)	–	1.1	7.1
u_{91}	$H_{13}...H_{15}$	430.0(6)	13.1 (Fixed)	–	2.4	13.1
u_{92}	$H_{15}...H_{17}$	429.4(6)	13.0 (Fixed)	–	2.0	13.0
u_{93}	$H_{14}...H_{16}$	429.8(7)	13.0 (Fixed)	–	1.9	13.0
u_{94}	$H_{13}...H_{17}$	430.2(7)	13.0 (Fixed)	–	1.6	13.0
u_{95}	$C_3...C_7$	444.1(9)	12.8 (Tied to u_{90})	–	−0.6	11.6
u_{96}	$C_2...C_6$	447.6(9)	12.6 (Tied to u_{90})	–	−0.9	11.4
u_{97}	$C_7...H_{12}$	458.9(11)	12.7 (Tied to u_{90})	–	0.9	11.5
u_{98}	$C_4...H_{16}$	461.4(10)	12.4 (Tied to u_{90})	–	2.4	11.2
u_{99}	$H_{11}...H_{14}$	467.4(19)	27.5 (Fixed)	–	1.5	27.5
u_{100}	$H_{12}...H_{16}$	471.2(13)	19.3 (Fixed)	–	8.5	19.3
u_{101}	$C_4...H_{14}$	467.6(10)	12.3 (Tied to u_{90})	–	1.0	11.2
u_{102}	$H_{11}...H_{17}$	457.2(21)	19.4 (Fixed)	–	−8.4	19.4
u_{103}	$C_8...H_{12}$	482.8(10)	17.6 (Tied to u_{106})	–	3.7	13.5
u_{104}	$C_2...C_{10}$	486.4(8)	13.1 (Tied to u_{106})	–	0.3	10.0
u_{105}	$C_2...H_{17}$	487.8(14)	25.1 (Tied to u_{106})	–	1.4	19.2
u_{106}	$N_1...C_5$	490.8(7)	13.3(5)	10.2(10)	−0.7	10.2

u_{107}	$C_3...C_9$	489.9(8)	10.4 (Tied to u_{106})	–	−3.1	7.9
u_{108}	$H_{14}...H_{17}$	495.8(7)	12.0 (Fixed)	–	2.4	12.0
u_{109}	$H_{13}...H_{16}$	496.1(7)	12.0 (Fixed)	–	1.9	12.0
u_{110}	$C_3...H_{14}$	512.8(12)	16.6 (Tied to u_{113})	–	0.6	17.0
u_{111}	$C_8...H_{11}$	513.3(18)	19.2 (Tied to u_{113})	–	−7.1	19.6
u_{112}	$C_9...H_{11}$	510.5(18)	16.8 (Tied to u_{113})	–	−9.3	17.2
u_{113}	$C_3...C_8$	519.9(7)	9.5(1)	–	−2.5	9.7
u_{114}	$N_1...H_{13}$	526.1(15)	21.4 (Tied to u_{113})	–	−4.9	21.9
u_{115}	$C_4...H_{15}$	536.0(5)	9.8 (Tied to u_{113})	–	1.5	10.1
u_{116}	$H_{12}...H_{14}$	554.1(13)	14 .0(Fixed)	–	−0.1	14.0
u_{117}	$N_1...C_6$	560.5(10)	10.9(10)	–	−3.4	11.8
u_{118}	$N_1...H_{17}$	576.4(17)	24.7 (Tied to u_{117})	–	1.9	26.8
u_{119}	$C_2...C_7$	584.6(8)	10.5 (Tied to u_{117})	–	−1.8	11.4
u_{120}	$C_3...H_{16}$	581.9(11)	10.8 (Tied to u_{117})	–	−3.4	11.7
u_{121}	$H_{12}...H_{15}$	589.0(11)	15.6 (Fixed)	–	4.2	15.6
u_{122}	$N_1...C_{10}$	587.4(11)	15.2 (Tied to u_{117})	–	0.0	16.5
u_{123}	$C_2...C_9$	615.0(6)	10.5(8)	9.2(9)	−1.1	9.2
u_{124}	$H_{11}...H_{15}$	614.3(19)	22 (Fixed)	–	−7.4	22.0
u_{125}	$H_{11}...H_{16}$	610.1(20)	19.1 (Fixed)	–	−10.8	19.1
u_{126}	$C_3...H_{15}$	626.4(8)	14.2 (Tied to u_{123})	–	−2.5	12.5
u_{127}	$C_2...H_{14}$	651.8(12)	21.4 (Tied to u_{128})	–	−2.0	17.6
u_{128}	$C_2...C_8$	656.7(5)	11.3(8)	9.3(9)	−2.1	9.3
u_{129}	$N_1...C_7$	697.3(9)	13.4(11)	11.7(12)	−4.3	11.7
u_{130}	$C_2...H_{16}$	699.5(9)	14.0 (Fixed)	–	−0.8	14.0
u_{131}	$N_1...C_9$	719.4(9)	17.0 (Tied to u_{129})	–	−1.8	14.8
u_{132}	$C_2...H_{15}$	763.8(7)	15.6 (Tied to u_{134})	–	−2.4	12.1
u_{133}	$N_1...H_{14}$	763.6(12)	23.7 (Tied to u_{134})	–	−5.3	18.3
u_{134}	$N_1...C_8$	767.1(7)	14.2(9)	11.0(11)	−3.7	11.0
u_{135}	$N_1...H_{16}$	798.9(12)	26.7 (Tied to u_{134})	–	−1.1	20.7

[a] All values are tabulated in picometers (pm).

Table A120. Refined Cartesian coordinates in Ångström (Å) for the experimentally-determined structure of *E*-cinnamonitrile obtained *via* GED.

	x	*y*	*z*
N	6.9959	1.7500	0.0000
C	5.8553	1.9180	0.0000
C	4.4491	2.1251	0.0000
C	3.5700	1.1083	0.0000
C	2.1118	1.1989	0.0000
C	1.3962	2.4064	0.0000
C	0.0111	2.4068	0.0000
C	−0.6935	1.2040	0.0000
C	0.0000	0.0000	0.0000
C	1.3886	0.0000	0.0000
H	4.1295	3.1572	0.0000
H	3.9687	0.1019	0.0000
H	1.9308	3.3443	0.0000
H	−0.5258	3.3440	0.0000
H	−1.7734	1.2080	0.0000
H	−0.5405	−0.9350	0.0000
H	1.9204	−0.9411	0.0000

Appendix B: Supplementary Information – Theory

Table B1. Optimised Cartesian coordinates in Ångström (Å) and energy, E_{SCF}, in atomic units (a.u.) of *ap*-DITFE as calculated at the SA(5/4)-CASSCF(12,8) level using the basis sets and corresponding core potentials of Stoll and Preuss *et al.*[225,226]

E_{SCF} = −129.310907			
C	0.596263	−0.469826	0.000000
C	−0.596263	0.469825	0.000000
F	1.321578	−0.267009	1.062447
F	1.321574	−0.267011	−1.062449
F	−1.321578	0.267009	1.062447
F	−1.321574	0.267012	−1.062449
I	−0.060021	−2.655310	0.000000
I	0.060021	2.655310	0.000000

Table B2. Optimised Cartesian coordinates in Ångström (Å) and energy, E_{SCF}, in atomic units (a.u.) of *ap*-DITFE as calculated at the MS-CASPT2(12,8) level using the basis sets and corresponding core potentials of Stoll and Preuss *et al.*[225,226]

E_{SCF} = −130.260110			
C	0.584139	−0.490165	0.000000
C	−0.584143	0.490163	0.000000
F	1.332809	−0.264348	1.085132
F	1.332838	−0.264298	−1.085093
F	−1.332811	0.264349	1.085131
F	−1.332839	0.264299	−1.085093
I	−0.057133	−2.597490	−0.000043
I	0.057141	2.597491	−0.000043

Table B3. Optimised Cartesian coordinates in Ångström (Å) and energy, E_{SCF}, in atomic units (a.u.) of *sc*-DITFE as calculated at the SA(5/4)-CASSCF(12,8) level using the basis sets and corresponding core potentials of Stoll and Preuss *et al.*[225,226]

E_{SCF} = −129.305905			
C	0.648882	0.401828	1.049025
C	−0.648882	−0.401828	1.049025
F	1.278125	0.125076	2.160292
F	0.375876	1.675707	1.030751
F	−1.278125	−0.125076	2.160292
F	−0.375876	−1.675707	1.030752
I	2.050657	−0.084646	−0.670111
I	−2.050657	0.084646	−0.670111

Table B4. Optimised Cartesian coordinates in Ångström (Å) and energy, E_{SCF}, in atomic units (a.u.) of *sc*-DITFE as calculated at the MS-CASPT2(12,8) level using the basis sets and corresponding core potentials of Stoll and Preuss *et al.*[225,226]

E_{SCF} = −130.255904			
C	0.659729	0.390607	1.014940
C	−0.659729	−0.390607	1.014940
F	1.272117	0.102325	2.171501
F	0.374895	1.697788	1.016287
F	−1.272117	−0.102325	2.171501
F	−0.374895	−1.697788	1.016287
I	2.038307	−0.069018	−0.632771
I	−2.038307	0.069018	−0.632771

Table B5. Optimised Cartesian coordinates in Ångström (Å) and energy, E_{SCF}, in atomic units (a.u.) of *ap*-ITFE$^{\bullet}$ as calculated at the SA5-CASSCF(7,5) level using the basis sets and corresponding core potentials of Stoll and Preuss *et al.*[225,226]

E_{SCF} = −118.078434			
C	−1.037081	−0.355281	0.000000
C	−1.618267	1.009788	0.000000
F	−1.412454	−1.005942	1.065089
F	−1.412454	−1.005942	−1.065089
F	−1.389625	1.697649	−1.068402
F	−1.389625	1.697649	1.068402
I	1.294668	−0.304756	0.000000

Table B6. Optimised Cartesian coordinates in Ångström (Å) and energy, E_{SCF}, in atomic units (a.u.) of *sc*-ITFE$^{\bullet}$ as calculated at the SA5-CASSCF(7,5) level using the basis sets and corresponding core potentials of Stoll and Preuss *et al.*[225,226]

E_{SCF} = −118.074147			
C	−0.750410	0.550671	0.110723
C	−1.679457	−0.522587	−0.374714
F	−0.917599	1.623141	−0.612515
F	−0.998803	0.844088	1.361720
F	−2.907167	−0.114373	−0.460652
F	−1.598740	−1.623724	0.301866
I	1.423080	−0.131695	−0.070204

Table B7. Optimised Cartesian coordinates in Ångström (Å) and energy, E_{SCF}, in atomic units (a.u.) of λ^2-ITFE$^{\bullet}$ as calculated at the SA5-CASSCF(7,5) level using the basis sets and corresponding core potentials of Stoll and Preuss *et al.*[225,226]

E_{SCF} = −118.024099			
C	0.978780	0.732948	0.000000
C	0.939679	−0.771652	0.000000
F	1.487465	1.253974	1.069249
F	1.487465	1.253975	−1.069249
F	1.424357	−1.314421	1.070111
F	1.424355	−1.314421	−1.070111
I	−1.816588	0.050337	−0.000000

Table B8. Optimised Cartesian coordinates in Ångström (Å) and energy, E_{SCF}, in atomic units (a.u.) of the S_0 minimum-energy geometry of 1,2-dithiane as calculated at the SA3-CASSCF(10,8)/*def*2-SV(P) level.

E_{SCF} = −950.850873			
S	−1.020730	−0.327803	−1.139221
S	1.020730	0.327803	−1.139221
C	1.523476	−0.441732	0.484826
C	0.755303	0.134113	1.672489
C	−0.755303	−0.134113	1.672489
C	−1.523476	0.441732	0.484826
H	2.590012	−0.225451	0.576650
H	1.398697	−1.521610	0.400133
H	0.935665	1.212113	1.719364
H	1.177742	−0.293489	2.587549
H	−1.177742	0.293489	2.587549
H	−0.935665	−1.212113	1.719364
H	−1.398697	1.521610	0.400133
H	−2.590012	0.225451	0.576650

Table B9. Optimised Cartesian coordinates in Ångström (Å) and energy, E_{SCF}, in atomic units (a.u.) of the S_0 minimum-energy geometry of 1,2-dithiane as calculated at the MS-CASPT2(10,8)/*def*2-SV(P) level.

E_{SCF} = −951.573251			
S	−0.988402	−0.338562	−1.114543
S	0.988402	0.338562	−1.114543
C	1.505738	−0.429528	0.453186
C	−1.505738	0.429528	0.453186
C	0.754957	0.132758	1.659953
C	−0.754957	−0.132758	1.659953
H	2.588144	−0.219891	0.543392
H	−2.588144	0.219891	0.543392
H	1.375214	−1.523667	0.370983
H	−1.375214	1.523667	0.370983
H	0.936225	1.223021	1.708497
H	−0.936225	−1.223021	1.708497
H	1.188949	−0.306622	2.578751
H	−1.188949	0.306622	2.578751

Table B10. Optimised Cartesian coordinates in Ångström (Å) and energy, E_{SCF}, in atomic units (a.u.) of the S_0 minimum-energy geometry of 1,2-dithiane as calculated at the MR-CISD(6,4)/*def*2-SV(P) level.

E_{SCF} = −951.490784			
S	−1.005767	−0.322675	−1.117130
S	1.005767	0.322675	−1.117130
C	1.508122	−0.431614	0.456308
C	0.753209	0.133896	1.655049
C	−0.753209	−0.133896	1.655049
C	−1.508122	0.431614	0.456308
H	2.582123	−0.220594	0.550168
H	1.384736	−1.519200	0.381649
H	0.933011	1.217619	1.704028
H	1.183120	−0.299963	2.570139
H	−1.183120	0.299963	2.570139
H	−0.933011	−1.217619	1.704028
H	−1.384736	1.519200	0.381649
H	−2.582123	0.220594	0.550168

Table B11. Optimised Cartesian coordinates in Ångström (Å) and energy, E_{SCF}, in atomic units (a.u.) of the S_1 Van der Waals minimum-energy geometry of 1,2-dithiane as calculated at the SA3-CASSCF(10,8)/*def*2-SV(P) level.

E_{SCF} = −950.7780158			
S	−0.341082	−1.067627	−1.754736
S	0.353678	−1.081880	1.732236
C	−0.728757	0.414711	1.485618
C	0.009237	1.572190	0.792332
C	0.003407	1.605148	−0.740846
C	0.687473	0.455673	−1.485573
H	−1.049708	0.729225	2.478069
H	−1.606503	0.108338	0.916313
H	1.038967	1.620006	1.160069
H	−0.465775	2.498412	1.128108
H	0.512273	2.529668	−1.032883
H	−1.024594	1.697729	−1.101395
H	1.615366	0.145525	−1.001350
H	0.950279	0.776871	−2.496123

Table B12. Optimised Cartesian coordinates in Ångström (Å) and energy, E_{SCF}, in atomic units (a.u.) of the S_1 Van der Waals minimum-energy geometry of 1,2-dithiane as calculated at the MS-CASPT2(10,8)/*def*2-SV(P) level.

E_{SCF} = −951.478514			
S	1.610849	0.326539	−1.086670
S	−1.610849	−0.326539	−1.086670
C	−1.452116	0.712987	0.398778
C	1.452116	−0.712987	0.398778
C	−0.766129	0.014324	1.579465
C	0.766129	−0.014324	1.579465
H	−2.478541	0.998249	0.692009
H	2.478541	−0.998249	0.692009
H	−0.918689	1.640729	0.127204
H	0.918689	−1.640729	0.127204
H	−1.156391	−1.017888	1.660509
H	1.156391	1.017888	1.660509
H	−1.081465	0.535059	2.503965
H	1.081465	−0.535059	2.503965

Table B13. Optimised Cartesian coordinates in Ångström (Å) and energy, E_{SCF}, in atomic units (a.u.) of the S_1 Van der Waals minimum-energy geometry of 1,2-dithiane as calculated at the MR-CISD(6,4)/*def*2-SV(P) level.

E_{SCF} = −951.4060718			
S	−0.348072	−1.038637	−1.687862
S	0.362983	−1.070574	1.644226
C	−0.719102	0.370721	1.467464
C	0.000855	1.556530	0.805113
C	0.012046	1.601657	−0.722531
C	0.672563	0.435143	−1.456858
H	−1.050390	0.666473	2.469741
H	−1.601643	0.086410	0.880835
H	1.030930	1.616233	1.187446
H	−0.497463	2.473029	1.151839
H	0.543881	2.521742	−1.009036
H	−1.016354	1.712925	−1.094289
H	1.611897	0.134055	−0.972761
H	0.942400	0.752206	−2.474735

Table B14. Optimised Cartesian coordinates in Ångström (Å) and energy, E_{SCF}, in atomic units (a.u.) of the $MECI_{Sølling}$ geometry of 1,2-dithiane as calculated at the SA3-CASSCF(10,8)/*def*2-SV(P) level.

E_{SCF} = −950.775745			
S	−0.281781	−1.160181	−1.776601
S	0.352455	−0.916063	1.993495
C	−0.804821	0.397914	1.385872
C	0.044600	1.497342	0.689355
C	−0.035801	1.562682	−0.840597
C	0.645997	0.441283	−1.625142
H	−1.272993	0.821485	2.273334
H	−1.562873	0.006266	0.713393
H	1.093183	1.427326	0.998029
H	−0.292863	2.461688	1.072631
H	0.447786	2.498910	−1.138979
H	−1.078632	1.642329	−1.157798
H	1.637913	0.212832	−1.226517
H	0.797845	0.753748	−2.661329

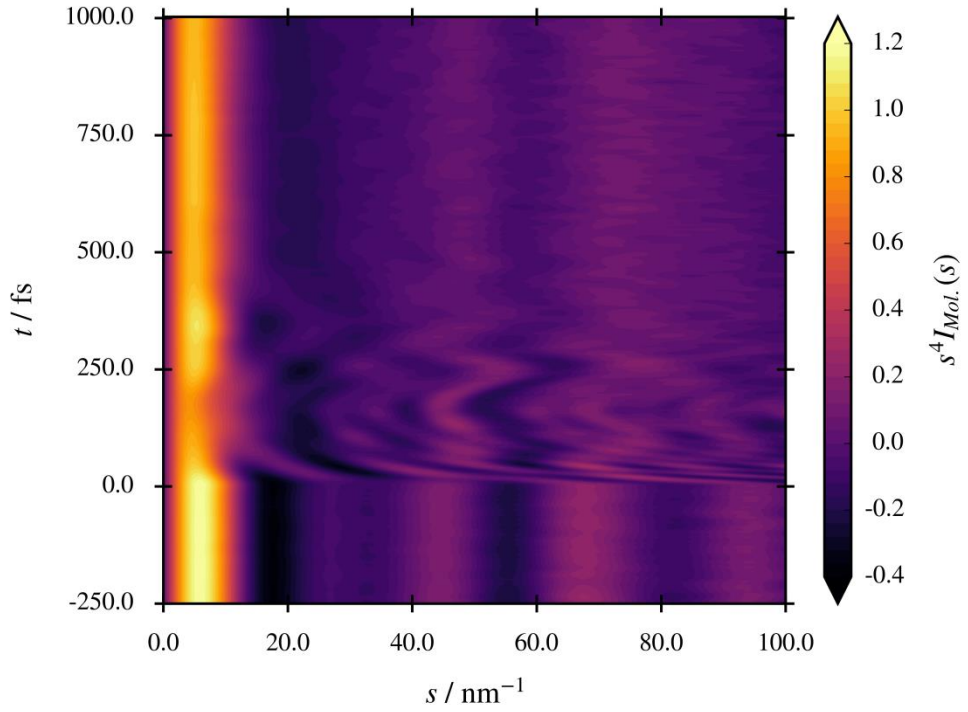

Figure B1. Theoretical TD-MIC matrix for 1,2-dithiane.

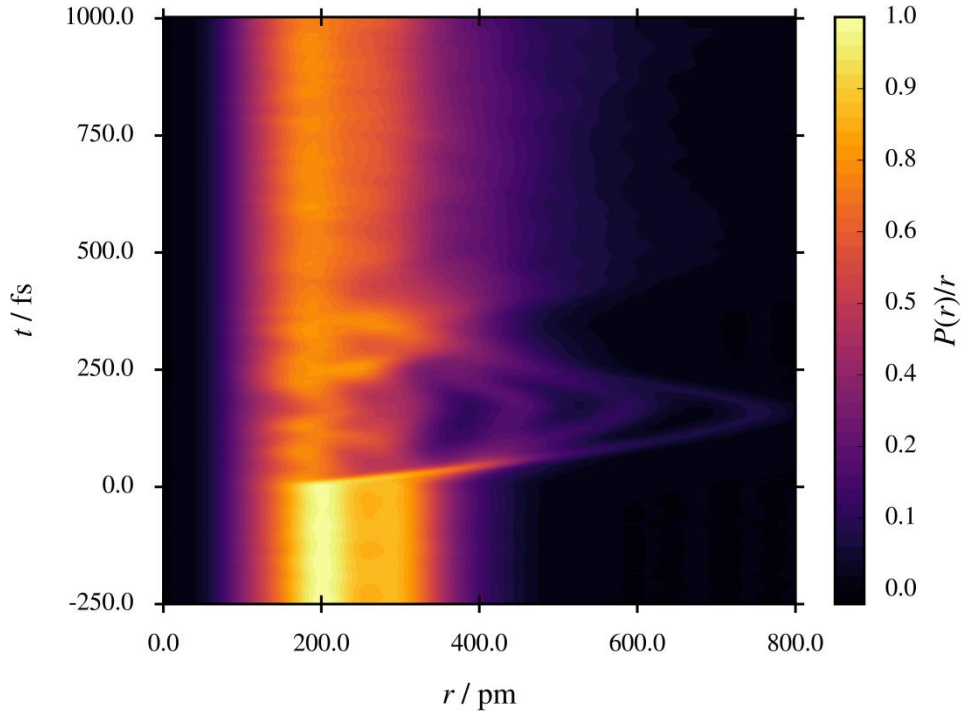

Figure B2. Theoretical TD-RDC matrix for 1,2-dithiane; transformed from the theoretical TD-MIC matrix (Fig. B1).

Table B15. Optimised Cartesian coordinates in Ångström (Å) and energy, E_{SCF}, in atomic units (a.u.) of the S_0 minimum-energy geometry of *E*-cinnamonitrile as calculated at the SA4-CASSCF(12,12)/cc-(p)VDZ level.

E_{SCF} = −399.505079			
N	4.594687	0.175987	0.000000
C	3.468490	−0.107872	0.000000
C	2.077100	−0.486027	0.000000
C	1.088978	0.435911	0.000000
C	−0.360461	0.183116	0.000000
C	−0.919560	−1.110656	0.000000
C	−2.301689	−1.288105	0.000000
C	−3.159446	−0.179701	0.000000
C	−2.618852	1.108390	0.000000
C	−1.232746	1.285586	0.000000
H	1.883619	−1.549803	0.000000
H	1.380821	1.480178	0.000000
H	−0.280664	−1.983576	0.000000
H	−2.712078	−2.290383	0.000000
H	−4.232895	−0.321914	0.000000
H	−3.271147	1.972841	0.000000
H	−0.823477	2.288779	0.000000

Table B16. Optimised Cartesian coordinates in Ångström (Å) and energy, E_{SCF}, in atomic units (a.u.) of the S_0 minimum-energy geometry of *E*-cinnamonitrile as calculated at the MS-CASPT2(12,12)/cc-(p)VDZ level.

E_{SCF} = −400.592405			
N	4.609883	0.170952	0.000000
C	3.468129	−0.120233	0.000000
C	2.078905	−0.493637	0.000000
C	1.093066	0.446513	0.000000
C	−0.358351	0.189883	0.000000
C	−0.911732	−1.112209	0.000000
C	−2.300501	−1.295361	0.000000
C	−3.163512	−0.183122	0.000000
C	−2.627874	1.114208	0.000000
C	−1.235289	1.297011	0.000000
H	1.869173	−1.569396	0.000000
H	1.393519	1.503776	0.000000
H	−0.258411	−1.992518	0.000000
H	−2.714016	−2.311294	0.000000
H	−4.250523	−0.331242	0.000000
H	−3.292728	1.986514	0.000000
H	−0.819037	2.312905	0.000000

Table B17. Optimised Cartesian coordinates in Ångström (Å) and energy, E_{SCF}, in atomic units (a.u.) of the S_0 minimum-energy geometry of *E*-cinnamonitrile as calculated at the MR-CISD(6,6)/cc-(p)VDZ level.

E_{SCF} = −400.043578			
N	4.570241	0.174401	0.000000
C	3.459356	−0.110097	0.000000
C	2.069221	−0.491928	0.000000
C	1.085205	0.437063	0.000000
C	−0.361085	0.183745	0.000000
C	−0.914909	−1.107842	0.000000
C	−2.294446	−1.286175	0.000000
C	−3.148126	−0.179557	0.000000
C	−2.612648	1.105521	0.000000
C	−1.231736	1.287500	0.000000
H	1.876508	−1.556433	0.000000
H	1.376541	1.482857	0.000000
H	−0.269950	−1.976852	0.000000
H	−2.705990	−2.286121	0.000000
H	−4.223035	−0.319526	0.000000
H	−3.271184	1.967295	0.000000
H	−0.823274	2.288909	0.000000

Table B18. Optimised Cartesian coordinates in Ångström (Å) and energy, E_{SCF}, in atomic units (a.u.) of the S_0 minimum-energy geometry of *Z*-cinnamonitrile as calculated at the SA4-CASSCF(12,12)/cc-(p)VDZ level.

E_{SCF} = −399.502258			
N	2.065333	−3.112352	0.000000
C	2.049156	−1.951023	0.000000
C	2.098662	−0.510769	0.000000
C	1.050278	0.345126	0.000000
C	−0.404737	0.121144	0.000000
C	−1.023078	−1.145919	0.000000
C	−2.413585	−1.255890	0.000000
C	−3.220808	−0.111971	0.000000
C	−2.621819	1.150639	0.000000
C	−1.230400	1.262294	0.000000
H	3.100389	−0.101564	0.000000
H	1.333074	1.391757	0.000000
H	−0.432846	−2.049264	0.000000
H	−2.867662	−2.239054	0.000000
H	−4.299717	−0.205450	0.000000
H	−3.232782	2.044896	0.000000
H	−0.777749	2.246721	0.000000

Table B19. Optimised Cartesian coordinates in Ångström (Å) and energy, E_{SCF}, in atomic units (a.u.) of the S_0 minimum-energy geometry of *Z*-cinnamonitrile as calculated at the MS-CASPT2(12,12)/cc-(p)VDZ level.

E_{SCF} = −400.591660			
N	1.972320	−3.125639	0.000000
C	2.007634	−1.947248	0.000000
C	2.104546	−0.512854	0.000000
C	1.060979	0.366192	0.000000
C	−0.395002	0.132083	0.000000
C	−1.001305	−1.147685	0.000000
C	−2.398570	−1.268248	0.000000
C	−3.215597	−0.124074	0.000000
C	−2.627913	1.151410	0.000000
C	−1.230456	1.274371	0.000000
H	3.128326	−0.119257	0.000000
H	1.347850	1.427208	0.000000
H	−0.391280	−2.055501	0.000000
H	−2.851514	−2.267198	0.000000
H	−4.307878	−0.227892	0.000000
H	−3.256145	2.050563	0.000000
H	−0.774317	2.273099	0.000000

Table B20. Optimised Cartesian coordinates in Ångström (Å) and energy, E_{SCF}, in atomic units (a.u.) of the S_0 minimum-energy geometry of *Z*-cinnamonitrile as calculated at the MR-CISD(6,6)/cc-(p)VDZ level.

E_{SCF} = −400.042029			
N	2.042510	−3.070332	0.000000
C	2.047783	−1.922705	0.000000
C	2.112900	−0.484266	0.000000
C	1.059832	0.369540	0.000000
C	−0.389324	0.129157	0.000000
C	−0.989056	−1.143145	0.000000
C	−2.376279	−1.266198	0.000000
C	−3.190623	−0.132841	0.000000
C	−2.610117	1.133042	0.000000
C	−1.224559	1.262655	0.000000
H	3.117019	−0.081880	0.000000
H	1.330111	1.420287	0.000000
H	−0.383444	−2.037703	0.000000
H	−2.822430	−2.251350	0.000000
H	−4.269973	−0.236009	0.000000
H	−3.236170	2.018704	0.000000
H	−0.781631	2.249267	0.000000

Table B21. Optimised Cartesian coordinates in Ångström (Å) and energy, E_{SCF}, in atomic units (a.u.) of the S_1 minimum-energy geometry of *E*-cinnamonitrile as calculated at the SA4-CASSCF(12,12)/cc-(p)VDZ level.

E_{SCF} = −399.344801			
N	4.605708	0.154394	0.000000
C	3.478137	−0.130871	0.000000
C	2.093002	−0.501835	0.000000
C	1.089803	0.443365	0.000000
C	−0.307509	0.197110	0.000000
C	−0.891832	−1.128838	0.000000
C	−2.321688	−1.307038	0.000000
C	−3.198375	−0.187713	0.000000
C	−2.653384	1.123406	0.000000
C	−1.232055	1.322240	0.000000
H	1.891043	−1.563230	0.000000
H	1.395907	1.483606	0.000000
H	−0.261018	−2.004676	0.000000
H	−2.723127	−2.311275	0.000000
H	−4.269354	−0.335206	0.000000
H	−3.305908	1.985837	0.000000
H	−0.834891	2.328134	0.000000

Table B22. Optimised Cartesian coordinates in Ångström (Å) and energy, E_{SCF}, in atomic units (a.u.) of the S_1 minimum-energy geometry of *E*-cinnamonitrile as calculated at the MS-CASPT2(12,12)/cc-(p)VDZ level.

E_{SCF} = −400.431401			
N	4.616875	0.154506	0.000000
C	3.473161	−0.144372	0.000000
C	2.093705	−0.510458	0.000000
C	1.088578	0.455835	0.000000
C	−0.305779	0.199489	0.000000
C	−0.883484	−1.127090	0.000000
C	−2.315056	−1.305076	0.000000
C	−3.200812	−0.189000	0.000000
C	−2.658501	1.125392	0.000000
C	−1.236040	1.322645	0.000000
H	1.873756	−1.583335	0.000000
H	1.402805	1.509112	0.000000
H	−0.241544	−2.013362	0.000000
H	−2.719582	−2.324032	0.000000
H	−4.285045	−0.344470	0.000000
H	−3.318632	2.000137	0.000000
H	−0.829936	2.341479	0.000000

Table B23. Optimised Cartesian coordinates in Ångström (Å) and energy, E_{SCF}, in atomic units (a.u.) of the S_1 minimum-energy geometry of *E*-cinnamonitrile as calculated at the MR-CISD(6,6)/cc-(p)VDZ level.

E_{SCF} = −399.852776			
N	1.980394	−3.100185	0.000000
C	2.028040	−1.952773	0.000000
C	2.116300	−0.524116	0.000000
C	1.052337	0.376556	0.000000
C	−0.313664	0.155247	0.000000
C	−0.949704	−1.130593	0.000000
C	−2.381876	−1.271337	0.000000
C	−3.246450	−0.145119	0.000000
C	−2.639870	1.132669	0.000000
C	−1.216518	1.279306	0.000000
H	3.124726	−0.135797	0.000000
H	1.351173	1.420049	0.000000
H	−0.355470	−2.031085	0.000000
H	−2.794013	−2.270013	0.000000
H	−4.320886	−0.259540	0.000000
H	−3.252469	2.026282	0.000000
H	−0.801982	2.276318	0.000000

Table B24. Optimised Cartesian coordinates in Ångström (Å) and energy, E_{SCF}, in atomic units (a.u.) of the S_1 minimum-energy geometry of *Z*-cinnamonitrile as calculated at the SA4-CASSCF(12,12)/cc-(p)VDZ level.

E_{SCF} = −399.342048			
N	2.069743	−3.122397	0.000000
C	2.063194	−1.959143	0.000000
C	2.118050	−0.526940	0.000000
C	1.054705	0.353302	0.000000
C	−0.348426	0.135324	0.000000
C	−0.997138	−1.161694	0.000000
C	−2.433609	−1.270701	0.000000
C	−3.262435	−0.115887	0.000000
C	−2.655489	1.166295	0.000000
C	−1.226117	1.297189	0.000000
H	3.119489	−0.118136	0.000000
H	1.351975	1.396073	0.000000
H	−0.415258	−2.068185	0.000000
H	−2.876744	−2.257249	0.000000
H	−4.338903	−0.214540	0.000000
H	−3.264258	2.060341	0.000000
H	−0.787071	2.285667	0.000000

Table B25. Optimised Cartesian coordinates in Ångström (Å) and energy, E_{SCF}, in atomic units (a.u.) of the S_1 minimum-energy geometry of *Z*-cinnamonitrile as calculated at the MS-CASPT2(12,12)/cc-(p)VDZ level.

E_{SCF} = −400.430654			
N	1.970824	−3.139080	0.000000
C	2.021379	−1.957252	0.000000
C	2.124344	−0.534281	0.000000
C	1.064025	0.375862	0.000000
C	−0.336397	0.153517	0.000000
C	−0.977061	−1.149421	0.000000
C	−2.415331	−1.273538	0.000000
C	−3.261646	−0.131071	0.000000
C	−2.658679	1.156986	0.000000
C	−1.228298	1.302332	0.000000
H	3.147847	−0.141296	0.000000
H	1.370429	1.431720	0.000000
H	−0.376734	−2.062849	0.000000
H	−2.847761	−2.280995	0.000000
H	−4.351098	−0.240422	0.000000
H	−3.280892	2.059781	0.000000
H	−0.793270	2.309338	0.000000

Table B26. Optimised Cartesian coordinates in Ångström (Å) and energy, E_{SCF}, in atomic units (a.u.) of the S_1 minimum-energy geometry of *Z*-cinnamonitrile as calculated at the MR-CISD(6,6)/cc-(p)VDZ level.

E_{SCF} = −399.852456			
N	1.980394	−3.100185	0.000000
C	2.028040	−1.952773	0.000000
C	2.116300	−0.524116	0.000000
C	1.052337	0.376556	0.000000
C	−0.313664	0.155247	0.000000
C	−0.949704	−1.130593	0.000000
C	−2.381876	−1.271337	0.000000
C	−3.246450	−0.145119	0.000000
C	−2.639870	1.132669	0.000000
C	−1.216518	1.279306	0.000000
H	3.124726	−0.135797	0.000000
H	1.351173	1.420049	0.000000
H	−0.355470	−2.031085	0.000000
H	−2.794013	−2.270013	0.000000
H	−4.320886	−0.259540	0.000000
H	−3.252469	2.026282	0.000000
H	−0.801982	2.276318	0.000000

Table B27. Optimised Cartesian coordinates in Ångström (Å) and energy, E_{SCF}, in atomic units (a.u.) of *tp*MECI$_{E,\alpha}$ as calculated at the SA4-CASSCF(12,12)/cc-(p)VDZ level.

E_{SCF} = −399.303529			
N	−0.414206	−0.448672	−4.600377
C	−0.290989	−0.466816	−3.444814
C	−0.306879	−0.611109	−2.044802
C	0.605086	−0.284388	−1.055665
C	0.272317	−0.112501	0.349130
C	−1.069527	−0.027843	0.776318
C	−1.357765	0.148432	2.126489
C	−0.321316	0.221821	3.068470
C	1.012524	0.127966	2.655949
C	1.307717	−0.040133	1.303488
H	0.388024	−1.550738	−1.824292
H	1.684966	−0.261214	−1.257944
H	−1.856227	−0.105784	0.041148
H	−2.388414	0.223754	2.449259
H	−0.553562	0.347505	4.118707
H	1.813291	0.182697	3.382425
H	2.340330	−0.115078	0.983542

Table B28. Optimised Cartesian coordinates in Ångström (Å) and energy, E_{SCF}, in atomic units (a.u.) of *tp*MECI$_{E,\beta}$ as calculated at the SA4-CASSCF(12,12)/cc-(p)VDZ level.

E_{SCF} = −399.280008			
N	−3.464233	−0.054159	0.331917
C	−2.434791	−0.512445	0.059459
C	−1.094952	−0.816013	−0.387577
C	−0.044681	0.039766	−0.040991
C	1.414859	−0.058798	−0.032789
C	2.094706	−1.293121	−0.111353
C	3.490629	−1.331534	−0.103614
C	4.231753	−0.145907	−0.038111
C	3.565756	1.083747	0.041001
C	2.172608	1.126874	0.058475
H	−1.019904	−1.651112	−1.090473
H	−0.351358	0.140641	−1.224111
H	1.533502	−2.217829	−0.164991
H	3.999975	−2.286136	−0.156325
H	5.314187	−0.179709	−0.040014
H	4.131576	2.005086	0.106339
H	1.654699	2.072819	0.145510

Table B29. Optimised Cartesian coordinates in Ångström (Å) and energy, E_{SCF}, in atomic units (a.u.) of *tp*MECI$_{Z,\alpha}$ as calculated at the SA4-CASSCF(12,12)/cc-(p)VDZ level.

E_{SCF} = −399.295209			
N	−2.800457	−1.214672	−2.744967
C	−1.720789	−1.194903	−2.298744
C	−0.378698	−0.988467	−1.988291
C	0.474716	−0.830015	−0.899498
C	0.191553	−0.369324	0.466861
C	−1.105769	−0.399059	1.017833
C	−1.313922	0.005434	2.336113
C	−0.240327	0.451371	3.118018
C	1.050602	0.483842	2.579332
C	1.265987	0.067810	1.265966
H	−0.267627	0.170133	−1.707209
H	1.538503	−0.955360	−1.101910
H	−1.938644	−0.749802	0.423632
H	−2.310566	−0.033337	2.757064
H	−0.408581	0.766655	4.140159
H	1.882660	0.833486	3.177455
H	2.266158	0.092357	0.850137

Table B30. Optimised Cartesian coordinates in Ångström (Å) and energy, E_{SCF}, in atomic units (a.u.) of *tp*MECI$_{Z,\beta}$ as calculated at the SA4-CASSCF(12,12)/cc-(p)VDZ level.

E_{SCF} = −399.278301			
N	−1.155393	−2.366612	−2.348381
C	−1.134207	−1.514865	−1.575459
C	−1.121452	−0.486661	−0.548590
C	−0.013435	0.249514	−0.136197
C	1.435206	0.074629	−0.099040
C	2.025355	−1.206935	−0.157507
C	3.412566	−1.346559	−0.084678
C	4.234209	−0.218417	0.016006
C	3.656803	1.057357	0.066380
C	2.271667	1.203932	0.027294
H	−2.108265	−0.269919	−0.143146
H	−0.322515	0.485797	−1.285722
H	1.402609	−2.087361	−0.245310
H	3.850715	−2.336727	−0.116629
H	5.310255	−0.331332	0.061379
H	4.286212	1.934452	0.155429
H	1.824031	2.186718	0.097419

Table B31. Optimised Cartesian coordinates in Ångström (Å) and energy, E_{SCF}, in atomic units (a.u.) of *pf*MECI$_E$ **E$_5$** as calculated at the SA4-CASSCF(12,12)/cc-(p)VDZ level.

E_{SCF} = −399.322475			
N	6.561428	2.520946	−3.012019
C	5.710045	2.004382	−2.433343
C	4.667267	1.356122	−1.711104
C	3.503200	2.024622	−1.316161
C	2.453051	1.415013	−0.653900
C	2.348270	0.191355	0.121559
C	1.169243	−0.670454	−0.022594
C	−0.060260	−0.027881	−0.178836
C	0.005452	1.358978	−0.021597
C	1.343419	1.943339	0.119330
H	4.810234	0.305419	−1.498156
H	3.399386	3.072547	−1.574686
H	3.149222	−0.095308	0.796324
H	1.272225	−1.746205	0.041708
H	−0.984547	−0.558616	−0.361767
H	−0.871524	1.989951	0.047871
H	1.497359	2.787119	0.785222

Table B32. Optimised Cartesian coordinates in Ångström (Å) and energy, E_{SCF}, in atomic units (a.u.) of *pf*MECI$_E$ **E$_7$** as calculated at the SA4-CASSCF(12,12)/cc-(p)VDZ level.

E_{SCF} = −399.316114			
N	6.249775	4.574443	−0.522509
C	5.212863	4.109023	−0.347978
C	3.913939	3.545125	−0.129531
C	3.718123	2.189759	−0.026488
C	2.461733	1.542631	0.170473
C	1.173662	2.262395	0.211268
C	0.133878	1.850835	1.133173
C	−0.001074	0.681421	0.269008
C	1.046808	−0.334462	0.220203
C	2.346521	0.126171	0.271272
H	3.101243	4.253192	−0.046349
H	4.588378	1.547315	−0.098949
H	1.037725	3.143741	−0.407510
H	−0.720661	2.497422	1.298387
H	−0.914305	0.537550	−0.300682
H	0.791122	−1.380018	0.105242
H	3.210930	−0.522734	0.319232

Table B33. Optimised Cartesian coordinates in Ångström (Å) and energy, E_{SCF}, in atomic units (a.u.) of *pf*MECI$_E$ **E$_8$** as calculated at the SA4-CASSCF(12,12)/cc-(p)VDZ level.

E_{SCF} = −399.307026			
N	7.242718	2.961912	−0.204690
C	6.270233	2.350640	−0.191540
C	5.063082	1.567851	−0.179050
C	3.849532	2.121832	0.049719
C	2.576302	1.398603	0.103922
C	2.422397	0.005831	0.214471
C	1.047698	−0.497341	0.157145
C	0.093380	0.047102	−0.793593
C	0.149714	1.216554	0.077769
C	1.339450	2.061335	0.133803
H	5.188700	0.510960	−0.373568
H	3.796773	3.193373	0.206286
H	3.238655	−0.671873	0.424727
H	0.774133	−1.345844	0.777510
H	−0.855360	−0.457326	−0.940672
H	−0.733120	1.511605	0.637123
H	1.247902	3.132447	0.260629

Table B34. Optimised Cartesian coordinates in Ångström (Å) and energy, E_{SCF}, in atomic units (a.u.) of *pf*MECI$_E$ **E$_9$** as calculated at the SA4-CASSCF(12,12)/cc-(p)VDZ level.

E_{SCF} = −399.314269			
N	6.403624	4.426275	−0.277371
C	5.330660	4.023880	−0.180571
C	3.989020	3.538246	−0.060870
C	3.703165	2.192931	−0.046317
C	2.405530	1.615181	0.075653
C	1.165499	2.315479	0.084387
C	0.064240	1.490467	−0.020081
C	0.309263	0.057706	0.085443
C	1.303521	−0.466632	1.024831
C	2.268282	0.141103	0.140736
H	3.220678	4.294056	0.022212
H	4.538743	1.506823	−0.126905
H	1.091808	3.393570	0.097119
H	−0.933612	1.861147	−0.217582
H	−0.291051	−0.634411	−0.496771
H	1.349204	−1.533708	1.212093
H	2.976545	−0.470304	−0.411875

Table B35. Optimised Cartesian coordinates in Ångström (Å) and energy, E_{SCF}, in atomic units (a.u.) of *pf*MECI$_{E,TS}$ **E$_5$** as calculated at the SA4-CASSCF(12,12)/cc-(p)VDZ level.

E_{SCF} = −399.321965			
N	6.994314	2.736333	−1.748162
C	6.051505	2.171319	−1.363623
C	4.905101	1.466942	−0.884753
C	3.677576	2.100515	−0.667556
C	2.535863	1.454011	−0.232816
C	2.331869	0.148132	0.375317
C	1.186347	−0.668755	−0.028056
C	0.003463	−0.006432	−0.371239
C	0.016840	1.369638	−0.118826
C	1.283765	1.974682	0.291402
H	5.023232	0.405047	−0.717184
H	3.606253	3.162447	−0.876005
H	2.996720	−0.203560	1.158138
H	1.265023	−1.748680	−0.007976
H	−0.868448	−0.523679	−0.747442
H	−0.876398	1.979834	−0.168490
H	1.285754	2.783504	1.015169

Table B36. Optimised Cartesian coordinates in Ångström (Å) and energy, E_{SCF}, in atomic units (a.u.) of *pf*MECI$_{E,TS}$ **E$_8$** as calculated at the SA4-CASSCF(12,12)/cc-(p)VDZ level.

E_{SCF} = −399.307716			
N	7.136457	3.014114	−0.150991
C	6.191757	2.377843	−0.144702
C	5.009486	1.557007	−0.139266
C	3.797016	2.082826	0.044907
C	2.524409	1.362139	0.082974
C	2.436179	−0.065511	0.159664
C	1.121046	−0.712251	0.114246
C	0.018496	0.018269	−0.509446
C	0.081695	1.388357	0.036197
C	1.342692	2.051732	0.125087
H	5.173397	0.500893	−0.304709
H	3.724928	3.157088	0.175912
H	3.316093	−0.676616	0.305003
H	0.953821	−1.594361	0.723745
H	−0.945305	−0.462599	−0.616962
H	−0.799009	1.863463	0.453722
H	1.348014	3.130140	0.240794

Table B37. Optimised Cartesian coordinates in Ångström (Å) and energy, E_{SCF}, in atomic units (a.u.) of the S_0 minimum-energy geometry of *E*-cinnamonitrile as calculated at the MP2/cc-(p)VDZ level.

E_{SCF} = −399.321630			
N	5.053022	0.200578	0.000000
C	3.902012	−0.096657	0.000000
C	2.514368	−0.469816	0.000000
C	1.527723	0.467530	0.000000
C	0.079814	0.209975	0.000000
C	−0.475454	−1.091698	0.000000
C	−1.865173	−1.271711	0.000000
C	−2.728640	−0.160102	0.000000
C	−2.189129	1.136900	0.000000
C	−0.797693	1.319000	0.000000
H	2.300412	−1.546137	0.000000
H	1.831013	1.525687	0.000000
H	0.176707	−1.974316	0.000000
H	−2.279488	−2.288478	0.000000
H	−3.816629	−0.306808	0.000000
H	−2.853498	2.010957	0.000000
H	−0.379367	2.335095	0.000000

Table B38. Optimised Cartesian coordinates in Ångström (Å) and energy, E_{SCF}, in atomic units (a.u.) of the S_0 minimum-energy geometry of *Z*-cinnamonitrile as calculated at the MP2/cc-(p)VDZ level.

E_{SCF} = −399.318856			
N	1.571929	−3.561128	0.000000
C	0.471870	−3.108249	0.000000
C	−0.874536	−2.609666	0.000000
C	−1.248574	−1.298519	0.000000
C	−0.440043	−0.070101	0.000000
C	0.976305	−0.039125	0.000000
C	1.655405	1.187827	0.000000
C	0.946714	2.402900	0.000000
C	−0.458171	2.384589	0.000000
C	−1.141780	1.160377	0.000000
H	−1.656612	−3.380251	0.000000
H	−2.336147	−1.128574	0.000000
H	1.557079	−0.967134	0.000000
H	2.753425	1.192579	0.000000
H	1.487666	3.358330	0.000000
H	−1.023945	3.325649	0.000000
H	−2.240585	1.150496	0.000000

Table B39. Optimised Cartesian coordinates in Ångström (Å) and energy, E_{SCF}, in atomic units (a.u.) of the S_1 minimum-energy geometry of *E*-cinnamonitrile as calculated at the ADC(2)/cc-(p)VDZ level.

E_{SCF} = −399.305140			
N	5.073477	0.175977	0.000000
C	3.918058	−0.119857	0.000000
C	2.536653	−0.477714	0.000000
C	1.538096	0.486550	0.000000
C	0.136070	0.223109	0.000000
C	−0.445379	−1.096112	0.000000
C	−1.879491	−1.271849	0.000000
C	−2.778395	−0.166188	0.000000
C	−2.225980	1.143001	0.000000
C	−0.803849	1.335817	0.000000
H	2.306829	−1.551391	0.000000
H	1.848447	1.543257	0.000000
H	0.194065	−1.986479	0.000000
H	−2.276796	−2.295880	0.000000
H	−3.862616	−0.325008	0.000000
H	−2.879355	2.024919	0.000000
H	−0.399835	2.357848	0.000000

Table B40. Optimised Cartesian coordinates in Ångström (Å) and energy, E_{SCF}, in atomic units (a.u.) of the S_1 minimum-energy geometry of *Z*-cinnamonitrile as calculated at the ADC(2)/cc-(p)VDZ level.

E_{SCF} = −399.300946			
N	1.609866	−3.492280	0.000000
C	0.478367	−3.106033	0.000000
C	−0.869622	−2.647557	0.000000
C	−1.278742	−1.314906	0.000000
C	−0.493334	−0.123039	0.000000
C	0.951905	−0.064497	0.000000
C	1.657158	1.196855	0.000000
C	0.982406	2.448391	0.000000
C	−0.435214	2.413068	0.000000
C	−1.155286	1.166337	0.000000
H	−1.641773	−3.428443	0.000000
H	−2.369403	−1.158602	0.000000
H	1.542992	−0.986764	0.000000
H	2.755175	1.164147	0.000000
H	1.533359	3.394969	0.000000
H	−1.013786	3.346596	0.000000
H	−2.254068	1.191758	0.000000

Table B41. Optimised Cartesian coordinates in Ångström (Å) and energy, $E_{F(ij)}$, in atomic units (a.u.) of *tp*MECI$_{E,\alpha}$ as calculated at the ADC(2)/cc-(p)VDZ level.

$E_{F(ij)}$ = −400.487032			
N	−0.490229	0.615025	−4.038745
C	−0.336974	−0.152049	−3.130655
C	−0.185111	−1.021109	−2.035129
C	0.774720	−0.636471	−0.978334
C	0.398227	−0.302754	0.347542
C	−0.984014	−0.276804	0.714049
C	−1.349635	0.068705	2.014472
C	−0.357689	0.390299	2.967780
C	1.009940	0.368305	2.619753
C	1.392269	0.025284	1.321771
H	−0.312260	−2.103361	−2.208167
H	1.866144	−0.607220	−1.197141
H	−1.719486	−0.526324	−0.064519
H	−2.409258	0.094648	2.300062
H	−0.653881	0.662795	3.990334
H	1.769602	0.622376	3.370327
H	2.453001	0.006559	1.033630

Table B42. Optimised Cartesian coordinates in Ångström (Å) and energy, $E_{F(ij)}$, in atomic units (a.u.) of *pl*MECI$_{E,1\leftarrow 2}$ as calculated at the ADC(2)/cc-(p)VDZ level.

$E_{F(ij)}$ = −400.351427			
N	5.046043	0.117557	0.000000
C	3.882285	−0.174991	0.000000
C	2.509293	−0.504478	0.000000
C	1.518080	0.510553	0.000000
C	0.123667	0.281066	0.000000
C	−0.440743	−1.067289	0.000000
C	−1.837941	−1.280895	0.000000
C	−2.737623	−0.188440	0.000000
C	−2.209386	1.139336	0.000000
C	−0.820323	1.377565	0.000000
H	2.247149	−1.570442	0.000000
H	1.864985	1.555549	0.000000
H	0.232846	−1.932800	0.000000
H	−2.220379	−2.309949	0.000000
H	−3.822218	−0.353673	0.000000
H	−2.898567	1.994416	0.000000
H	−0.437169	2.406914	0.000000

Table B43. Optimised Cartesian coordinates in Ångström (Å) and energy, $E_{\mathrm{F}(ij)}$, in atomic units (a.u.) of *pl*MECI$_{E,2\leftarrow3}$ as calculated at the ADC(2)/cc-(p)VDZ level.

$E_{\mathrm{F}(ij)}$ = −400.432854			
N	4.662116	0.198877	0.000000
C	3.514158	−0.106344	0.000000
C	2.127729	−0.494233	0.000000
C	1.138075	0.425393	0.000000
C	−0.335853	0.161809	0.000000
C	−0.887855	−1.101593	0.000000
C	−2.414969	−1.290414	0.000000
C	−3.267113	−0.175593	0.000000
C	−2.795404	1.105058	0.000000
C	−1.144861	1.312949	0.000000
H	1.926647	−1.572957	0.000000
H	1.428259	1.486170	0.000000
H	−0.272139	−2.008784	0.000000
H	−2.802571	−2.317507	0.000000
H	−4.354699	−0.345513	0.000000
H	−3.415403	2.009512	0.000000
H	−0.748345	2.334753	0.000000

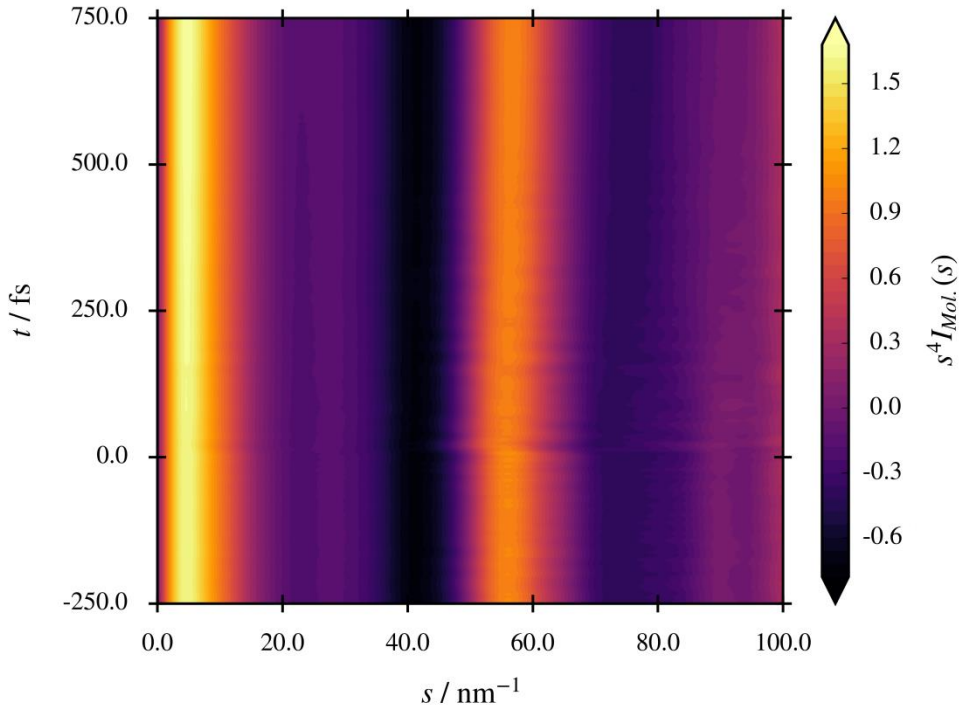

Figure B3. Theoretical TD-MIC matrix for *E*-cinnamonitrile.

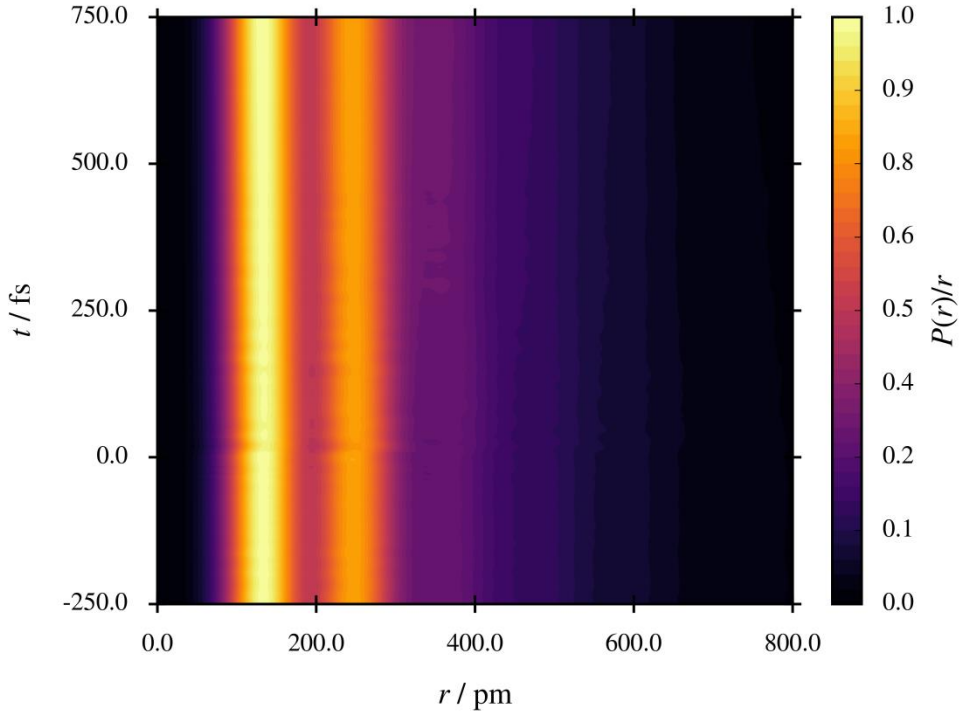

Figure B4. Theoretical TD-RDC matrix for *E*-cinnamonitrile; transformed from the theoretical TD-MIC matrix (Fig. B3).

List of Abbreviations

Abbreviations used in this thesis, and their definitions, are tabulated in this section. Abbreviations for institutions/geographical locations [*e.g.* DESY, TTX, SECUF (Chapter 1); UK, US, *etc.*] and software packages, where the name of the software package is an abbreviation [*e.g.* TDSIMMIC, ELSEPA (Chapter 4), *etc.*], are omitted.

Abbreviation	Definition
ADC(2)	Algebraic Diagrammatic Construction to the Second Order
CASPT2	Complete Active Space Perturbation Theory to the Second Order
CASSCF	Complete Active Space Self-Consistent Field
CBS	Complete Basis Set (Limit)
CI	Configuration Interaction
CIS	Configuration Interaction, Single Excitations
CISD	Configuration Interaction, Single and Double Excitations
CPU	Central Processing Unit
CVD	Chemical Vapour Deposition
DFT	Density Functional Theory
DITFE	Diiodotetrafluoroethane
DMABN	Dimethylaminobenzonitrile
DYNAMITE	Dynamic Interaction of Theory and Experiment
ED	Electron Diffraction
EOM	Equations of Motion
FCI	Full Configuration Interaction
FSSH	Fewest-Switches Surface-Hopping (Algorithm)
FTO	Fluorine-Doped Tin Oxide
FWHM	Full-Width Half-Maximum
GED	Gas Electron Diffraction
GPU	Graphical Processing Unit
GTO	Gaussian-Type Orbital
GUI	Graphical User Interface
HPC	High-Performance Computing
IC	Internal Conversion
IRF	Instrument Response Function
ITFE	Iodotetrafluoroethane
IVR	Intramolecular Vibrational (Energy) Redistribution
LIIC	Linear Interpolation in Internal Coordinates
MD	Molecular Dynamics
MECI	Minimum-Energy Conical Intersection
MIC	Molecular Intensity Curve
MOCED	Molecular-Orbital-Constrained Electron Diffraction
MP2	Møller-Plesset Perturbation Theory to the Second Order
MR	Multireference

Abbreviation	Definition
MRCI	Multireference Configuration Interaction
MRCIS	Multireference Configuration Interaction, Single Excitations
MRCISD	Multireference Configuration Interaction, Single and Double Excitations
MS	Multistate
MWD	Mass-Weighted Distance
NAMQC	Non-Adiabatic Mixed Quantum Classical (Dynamics)
NEA	Nuclear Ensemble Approach
NMR	Nuclear Magnetic Resonance
PANH	Polyaromatic Nitrogen Heterocycles
QM/MM	(Mixed) Quantum-Mechanical/Molecular-Mechanical (Approach)
RAM	Random-Access Memory
RDC	Radial Distribution Curve
RMS	Root-Mean-Square
RPSB	Retinal Protonated Schiff Base
SARACEN	Structural Analysis Restrained by Ab Initio Calculations for Electron Diffraction
TDDFT	Time-Dependent Density Functional Theory
TDMIC	Time-Dependent Molecular Intensity Curve (Matrix)
TDRDC	Time-Dependent Radial Distribution Curve (Matrix)
TFA	Trifluoroacetate (Functional Group)
TRED	Time-Resolved Electron Diffraction
TRGED	Time-Resolved Gas Electron Diffraction
TRGXRD	Time-Resolved Gas X-ray Diffraction
TRMS	Time-Resolved Mass Spectrometry
TRXRD	Time-Resolved X-ray Diffraction
TSHD	Trajectory Surface-Hopping Dynamics
UV	Ultraviolet
VHT	Very High Temperature
XFEL	X-ray Free Electron Laser
XRD	X-ray Diffraction

List of References

1. A. H. Zewail, *J. Phys. Chem. A*, 2000, **104**, 5660–5694.
2. M. Hada, K. Pichugin, and G. Sciaini, *Eur. Phys. J. Spec. Top.*, 2013, **222**, 1093–1123.
3. Nike Golf Juice Ball - Slow-Motion Watermelon Explosion. URL: youtube.com/watch?v=fogo9NQ1g6A, accessed 03/05/2019.
4. G. Sciaini and R. J. D. Miller, *Rep. Prog. Phys.*, 2011, **74**, 096101.
5. J. R. Dwyer, C. T. Hebeisen, R. Ernstorfer, M. Harb, V. B. Deyirmenjian, R. E. Jordan, and R. J. D. Miller, *Philos. Trans. R. Soc.*, 2006, **364**, 741–778.
6. M. Centurion, *J. Phys. B At. Mol. Opt. Phys.*, 2016, **49**, 062002.
7. M. Stefanou, K. Saita, D. V. Shalashilin, and A. Kirrander, *Chem. Phys. Lett.*, 2017, **683**, 300–305.
8. J. C. H. Spence, *Struct. Dyn.*, 2017, **4**, 044027.
9. O. Isnard, *C. R. Phys.*, 2007, **8**, 789–805.
10. A. A. Ischenko, V. V. Golubkov, V. P. Spiridonov, A. V. Zgurskii, A. S. Akhmanov, M. G. Vabischevich, and V. N. Bagratashvili, *Appl. Phys. B - Photophys. Laser Chem.*, 1983, **32**, 161–163.
11. J. D. Ewbank, J. Y. Luo, J. T. English, R. Liu, W. L. Faust, and L. Schäfer, *J. Phys. Chem.*, 1993, **97**, 8745–8751.
12. A. H. Zewail, J. C. Williamson, J. Cao, H. Ihee, and H. Frey, *Nature*, 1997, **386**, 159–162.
13. H. Ihee, V. A. Lobastov, U. M. Gomez, B. M. Goodson, R. Srinivasan, C. Y. Ruan, and A. H. Zewail, *Science*, 2001, **291**, 458–462.
14. P. Reckenthaeler, M. Centurion, W. Fuß, S. A. Trushin, F. Krausz, and E. E. Fill, *Phys. Rev. Lett.*, 2009, **102**, 213001.
15. C. J. Hensley, J. Yang, and M. Centurion, *Phys. Rev. Lett.*, 2012, **109**, 133202.
16. J. Yang, X. Zhu, T. J. A. Wolf, Z. Li, J. P. F. Nunes, R. Coffee, J. P. Cryan, M. Gühr, K. Hegazy, T. F. Heinz, K. Jobe, R. Li, X. Shen, T. Veccione, S. Weathersby, K. J. Wilkin, C. Yoneda, Q. Zheng, T. J. Martínez, M. Centurion, and X. J. Wang,

Science, 2018, **361**, 64–67.

17. K. Wilkin, R. Parrish, J. Yang, T. J. A. Wolf, J. P. F. Nunes, M. Guehr, R. Li, X. Shen, Q. Zheng, X. J. Wang, T. J. Martínez, and M. Centurion, 2019, arXiv:1904.01515.

18. T. J. A. Wolf, D. M. Sanchez, J. Yang, R. M. Parrish, J. P. F. Nunes, M. Centurion, R. Coffee, J. P. Cryan, M. Gühr, K. Hegazy, A. Kirrander, R. K. Li, J. Ruddock, X. Shen, T. Vecchione, S. P. Weathersby, P. M. Weber, K. Wilkin, H. Yong, Q. Zheng, X. J. Wang, M. P. Minitti, and T. J. Martínez, *Nature Chem.*, 2019, **11**, 504–509.

19. L. de Broglie, *C. R. Acad. Sci.*, 1923, **177**, 507–510.

20. C. Davisson and L. H. Germer, *Nature*, 1927, **119**, 558–560.

21. C. Davisson and L. H. Germer, *Phys. Rev.*, 1927, **30**, 705–740.

22. W. H. Bragg and W. L. Bragg, *Proc. R. Soc.*, 1913, **88**, 428–438.

23. H. Mark and R. Wierl, *Naturwiss.*, 1930, **18**, 205.

24. H. Mark and R. Wierl, *Naturwiss.*, 1930, **18**, 778–786.

25. P. Debye, L. Bewilogua, and F. Ehrhardt, *Phys. Zeits.*, 1929, **30**, 84.

26. D. Mansel, W. K. Heisenberg, and E. Rutherford, *Biogr. Mem. Fellows R. Soc.*, 1970, **16**, 175–232.

27. P. Debye, *Phys. Zeits.*, 1939, **40**, 507–508.

28. P. Debye, *Phys. Zeits.*, 1939, **40**, 66.

29. L. Pauling and L. O. Brockway, *J. Am. Chem. Soc.*, 1935, **57**, 2684–2692.

30. J. Karle and I. L. Karle, *J. Chem. Phys.*, 1947, **15**, 764–765.

31. I. L. Karle, D. Hoober, and J. Karle, *J. Chem. Phys.*, 1947, **15**, 765–765.

32. H. J. Yearian and W. M. Barss, *J. Appl. Phys.*, 1948, **19**, 700–704.

33. L. S. Bartell, L. O. Brockway, and R. H. Schwendeman, *J. Chem. Phys.*, 1955, **23**, 1854–1859.

34. P. A. Shaffer, V. Schomaker, and L. Pauling, *J. Chem. Phys.*, 1946, **14**, 659–664.

35. L. O. Brockway and L. S. Bartell, *Rev. Sci. Instrum.*, 1954, **25**, 569–575.

36. W. Zeil, J. Haase, and L. Wegmann, *Z. Instrum.*, 1966, **74**, 84–88.

37. R. J. F. Berger, M. Hoffmann, S. A. Hayes, and N. W. Mitzel, *Z. Naturforsch. B*, 2009, **64**, 1259–1268.

38. C. G. Reuter, Y. V. Vishnevskiy, S. Blomeyer, and N. W. Mitzel, *Z. Naturforsch. B*, 2016, **71**, 1–13.

39. G. V. Girichev, A. N. Utkin, and Y. F. Revichev, *Prib. i Tekhnika Eksp.*, 1984, **2**, 187–190.

40. G. V. Girichev, S. A. Shlykov, and Y. F. Revichev, *Prib. i Tekhnika Eksp.*, 1986, **4**, 167–169.

41. O. Bastiansen, O. Hassel, and E. Risberg, *Acta Chem. Scand.*, 1955, **9**, 232–238.

42. M. Fink and R. A. Bonham, *Rev. Sci. Instrum.*, 1970, **41**, 389–396.

43. C. D. Rankine, J. P. F. Nunes, T. W. B. Lock Feixas, S. Young, and D. A. Wann, *J. Phys. Chem. A*, 2018, **122**, 5656–5665.

44. K. Hedberg, *Struct. Chem.*, 2005, **16**, 93–109.

45. I. Karle and J. Karle, *Struct. Chem.*, 2005, **16**, 5–16.

46. A. P. Rood and J. Milledge, *J. Chem. Soc. Faraday Trans.*, 1984, **80**, 1145–1153.

47. G. Mourou and S. Williamson, *Appl. Phys. Lett.*, 1982, **41**, 44–45.

48. S. Williamson, G. Mourou, and J. C. M. Li, *Phys. Rev. Lett.*, 1984, **52**, 2364–2367.

49. J. D. Ewbank, L. Schäfer, D. W. Paul, O. J. Benston, and J. C. Lennox, *Rev. Sci. Instrum.*, 1984, **55**, 1598–1603.

50. J. D. Ewbank, L. Schäfer, D. W. Paul, D. L. Monts, and W. L. Faust, *Rev. Sci. Instrum.*, 1986, **57**, 967–972.

51. J. D. Ewbank, W. L. Faust, J. Y. Luo, J. T. English, D. L. Monts, D. W. Paul, Q. Dou, and L. Schäfer, *Rev. Sci. Instrum.*, 1992, **63**, 3352–3358.

52. L. R. Khundkar and A. H. Zewail, *J. Chem. Phys.*, 1990, **92**, 231–242.

53. J. Cao, H. Ihee, and A. H. Zewail, *Chem. Phys. Lett.*, 1998, **290**, 1–8.

54. J. Cao, H. Ihee, and A. H. Zewail, *Proc. Natl. Acad. Sci.*, 1999, **96**, 338–342.

55. H. Ihee, J. Kua, W. A. Goddard, and A. H. Zewail, *J. Phys. Chem. A*, 2002, **105**, 3623–3632.

56. H. Ihee, A. H. Zewail, and W. A. Goddard, *J. Phys. Chem. A*, 2002, **103**, 6638–6649.

57. H. Ihee, B. M. Goodson, R. Srinivasan, V. A. Lobastov, and A. H. Zewail, *J. Phys. Chem. A*, 2002, **106**, 4087–4103.

58. J. S. Feenstra, S. T. Park, and A. H. Zewail, *J. Chem. Phys.*, 2005, **123**, 221104.

59. C. Y. Ruan, V. A. Lobastov, R. Srinivasan, B. M. Goodson, H. Ihee, and A. H. Zewail, *Proc. Natl. Acad. Sci.*, 2001, **98**, 7117–7122.

60. D. Zhong, S. Ahmad, and A. H. Zewail, *J. Am. Chem. Soc.*, 1997, **119**, 5978–5979.

61. B. J. Siwick, J. R. Dwyer, R. E. Jordan, and R. J. D. Miller, *J. Appl. Phys.*, 2002, **92**, 1643–1648.

62. B. J. Siwick, J. R. Dwyer, R. E. Jordan, and R. J. D. Miller, *J. Appl. Phys.*, 2003, **94**, 807–808.

63. R. P. Chatelain, V. R. Morrison, C. Godbout, and B. J. Siwick, *Appl. Phys. Lett.*, 2012, **101**, 081901.

64. B. J. Siwick, J. R. Dwyer, R. E. Jordan, and R. J. D. Miller, *Science*, 2003, **302**, 1382–1385.

65. R. P. Chatelain, V. R. Morrison, B. L. M. Klarenaar, and B. J. Siwick, *Phys. Rev. Lett.*, 2014, **113**, 235502.

66. V. R. Morrison, R. P. Chatelain, K. L. Tiwari, A. Hendaoui, A. Bruhacs, M. Chaker, and B. J. Siwick, *Science*, 2014, **346**, 445–448.

67. M. R. Otto, L. P. R. de Cotret, D. A. Valverde-Chavez, K. L. Tiwari, N. Émond, M. Chaker, D. G. Cooke, and B. J. Siwick, *Proc. Natl. Acad. Sci.*, 2019, **116**, 450–455.

68. M. Gao, Y. Jiang, G. H. Kassier, and R. J. D. Miller, *Appl. Phys. Lett.*, 2013, **103**, 033503.

69. G. Sciaini, M. Harb, S. G. Kruglik, T. Payer, C. T. Hebeisen, F. J. Meyer zu Heringdorf, M. Yamaguchi, M. H. von Hoegen, R. Ernstorfer, and R. J. D. Miller, *Nature Lett.*, 2009, **458**, 56–60.

70. O. Zandi, K. J. Wilkin, Y. Xiong, and M. Centurion, *Struct. Dyn.*, 2017, **4**, 044022.

71. M. S. Robinson, P. D. Lane, and D. A. Wann, *Rev. Sci. Instrum.*, 2015, **86**, 013109.

72. M. S. Robinson, P. D. Lane, and D. A. Wann, *J. Phys. B At. Mol. Opt. Phys.*, 2016,

49, 034003.

73. M. S. Robinson, Ph.D. Thesis, University of York, 2015.

74. J. P. F. Nunes, Ph.D. Thesis, University of York, 2017.

75. F. M. Rudakov, J. B. Hastings, D. H. Dowell, J. F. Schmerge, and P. M. Weber, *Appl. Phys. Lett.*, 2006, **89**, 184109.

76. R. Li, C. Tang, Y. Du, W. Huang, Q. Du, J. Shi, L. Yan, and X. Wang, *Rev. Sci. Instrum.*, 2009, **80**, 083303.

77. R. Li, W. Huang, Y. Du, L. Yan, Q. Du, J. Shi, J. Hua, H. Chen, T. Du, H. Xu, and C. Tang, *Rev. Sci. Instrum.*, 2010, **81**, 036110.

78. P. Musumeci, J. T. Moody, C. M. Scoby, M. S. Gutierrez, H. A. Bender, and N. S. Wilcox, *Rev. Sci. Instrum.*, 2010, **81**, 013306.

79. P. Musumeci, J. T. Moody, C. M. Scoby, M. S. Gutierrez, and M. Westfall, *Appl. Phys. Lett.*, 2010, **97**, 063502.

80. P. Musumeci, J. T. Moody, C. M. Scoby, M. S. Gutierrez, M. Westfall, and R. K. Li, *J. Appl. Phys.*, 2010, **108**, 114513.

81. R. K. Li, P. Musumeci, H. A. Bender, N. S. Wilcox, and M. Wu, *J. Appl. Phys.*, 2011, **110**, 074512.

82. S. P. Weathersby, G. Brown, M. Centurion, T. F. Chase, R. Coffee, J. Corbett, J. P. Eichner, J. C. Frisch, A. R. Fry, M. Gühr, N. Hartmann, C. Hast, R. Hettel, R. K. Jobe, E. N. Jongewaard, J. R. Lewandowski, R. K. Li, A. M. Lindenberg, I. Makasyuk, J. E. May, D. McCormick, M. N. Nguyen, A. H. Reid, X. Shen, K. Sokolowski-Tinten, T. Vecchione, S. L. Vetter, J. Wu, J. Yang, H. A. Dürr, and X. J. Wang, *Rev. Sci. Instrum.*, 2015, **86**, 073702.

83. L. K. Rudge, S. Mathisen, P. Aden, R. J. Cash, J. A. Clarke, D. M. P. Holland, J. W. McKenzie, M. D. Roper, T. C. Q. Noakes, J. Jones, A. Kalinin, B. L. Militsyn, B. D. Muratori, D. Scott, F. Jackson, P. Williams, Y. Saveliev, D. Angal-Kalinin, and M. Surman, *Proc. 6th Int. Part. Accel. Conf.*, 2015.

84. J. Yang, M. Guehr, T. Vecchione, M. S. Robinson, R. Li, N. Hartmann, X. Shen, R. Coffee, J. Corbett, A. Fry, K. Gaffney, T. Gorkhover, C. Hast, K. Jobe, I. Makasyuk, A. Reid, J. Robinson, S. Vetter, F. Wang, S. Weathersby, C. Yoneda, M. Centurion, and X. J. Wang, *Nature Commun.*, 2016, **7**, 11232.

85. J. Yang, M. Guehr, X. Shen, R. Li, T. Vecchione, R. Coffee, J. Corbett, A. Fry, N. Hartmann, C. Hast, K. Hegazy, K. Jobe, I. Makasyuk, J. Robinson, M. S. Robinson, S. Vetter, S. Weathersby, C. Yoneda, X. J. Wang, and M. Centurion, *Phys. Rev. Lett.*, 2016, **117**, 153002.

86. M. P. Minitti, J. M. Budarz, A. Kirrander, J. S. Robinson, D. Ratner, T. J. Lane, D. Zhu, J. M. Glownia, M. Kozina, H. T. Lemke, M. Sikorski, Y. Feng, S. Nelson, K. Saita, B. Stankus, T. Northey, J. B. Hastings, and P. M. Weber, *Phys. Rev. Lett.*, 2015, **114**, 255501.

87. J. Yang, V. Makhija, V. Kumarappan, and M. Centurion, *Struct. Dyn.*, 2014, **1**, 044101.

88. J. Yang and M. Centurion, *Struct. Chem.*, 2015, **26**, 1513–1520.

89. J. Yang, J. Beck, C. J. Uiterwaal, and M. Centurion, *Nature Commun.*, 2015, **6**, 8172.

90. I. Hargittai and M. Hargittai, *Stereochemical Applications of Gas-Phase Electron Diffraction*, VCH Publishers Inc., New York, United States of America, 1988.

91. R. A. Bonham and M. Fink, *High-Energy Electron Scattering*, Van Nostrand Reinhold Co., New York, United States of America, 1974.

92. D. W. H. Rankin, N. W. Mitzel, and C. A. Morrison, in *Structural Methods in Inorganic Chemistry*, Wiley, Chichester, UK, 2013.

93. B. K. Vainshtein, *Structure Analysis by Electron Diffraction*, Pergamon Press Ltd., Oxford, UK, 1964.

94. S. L. Hinchley, H. E. Robertson, K. B. Borisenko, A. R. Turner, B. F. Johnston, D. W. H. Rankin, M. Ahmadian, J. N. Jones, and A. H. Cowley, *Dalton Trans.*, 2004, 2469–2476.

95. B. Andersen, H. M. Seip, T. G. Strand, and R. Stolevnik, *Acta Chem. Scand.*, 1969, **23**, 3224–3234.

96. Y. V. Vishnevskiy, UNEX, 2019, URL: unexproj.org.

97. D. A. Wann, Ph.D. Thesis, University of Edinburgh, 2005.

98. V. J. Klimkowski, J. D. Ewbank, C. Van Alsenoy, J. N. Scarsdale, and L. Schäfer, *J. Am. Chem. Soc.*, 1982, **104**, 1476–1480.

99. A. J. Blake, P. T. Brain, H. McNab, J. Miller, C. A. Morrison, S. Parsons, D. W. H. Rankin, H. E. Robertson, and B. A. Smart, *J. Phys. Chem.*, 1996, **100**, 12280–12287.

100. N. W. Mitzel, B. A. Smart, A. J. Blake, H. E. Robertson, and D. W. H. Rankin, *J. Phys. Chem.*, 1996, **100**, 9339–9347.

101. N. W. Mitzel and D. W. H. Rankin, *Dalton Trans.*, 2003, 3650–3662.

102. S. L. Hinchley, M. F. Haddow, and D. W. H. Rankin, *Dalton Trans.*, 2004, 384–391.

103. K. H. Steigerwald, *Optik*, 1949, **5**, 469–478.

104. S. L. Masters, G. V. Girichev, and S. A. Shylkov, *Dalton Trans.*, 2013, **42**, 3581–3586.

105. S. J. Atkinson, R. Noble-Eddy, and S. L. Masters, *J. Phys. Chem. A*, 2016, **120**, 2041–2048.

106. J. P. F. Nunes, Personal Communication, 2017.

107. S. Young, Ph.D. Thesis, University of York, 2015.

108. V. A. Sipachev, *J. Mol. Struct. THEOCHEM*, 1985, **121**, 143–151.

109. V. A. Sipachev, *J. Mol. Struct.*, 2001, **567**, 67–72.

110. Y. V. Vishnevskiy and Y. A. Zhabanov, *J. Phys. Conf. Ser.*, 2015, **633**, 012076.

111. D. A. Wann, R. J. Less, F. Rataboul, P. D. McCaffrey, A. M. Reilly, H. E. Robertson, P. D. Lickiss, and D. W. H. Rankin, *Organometallics*, 2008, **27**, 4183–4187.

112. D. A. Wann, A. M. Reilly, F. Rataboul, P. D. Lickiss, and D. W. H. Rankin, *Z. Naturforsch. B*, 2009, **6**, 1269–1275.

113. D. A. Wann, C. N. Dickson, P. D. Lickiss, H. E. Robertson, and D. W. H. Rankin, *Inorg. Chem.*, 2011, **12**, 2988–2994.

114. C. D. Rankine, S. J. Atkinson, M. R. Waterland, S. L. Masters, and D. A. Wann, *Struct. Chem.*, 2018, **29**, 803–813.

115. D. A. Wann, A. V. Zakharov, A. M. Reilly, P. D. McCaffrey, and D. W. H. Rankin, *J. Phys. Chem. A*, 2009, **113**, 9511–9520.

116. H. Lischka, D. Nachtigallová, A. J. A. Aquino, P. G. Szalay, F. Plasser, F. B. C. Machado, and M. Barbatti, *Chem. Rev.*, 2018, **118**, 7293–7361.

117. R. Crespo-Otero and M. Barbatti, *Chem. Rev.*, 2018, **118**, 7026–7068.

118. G. A. Worth and L. S. Cederbaum, *Annu. Rev. Phys. Chem.*, 2004, **55**, 127–158.

119. B. G. Levine and T. J. Martínez, *Annu. Rev. Phys. Chem.*, 2007, **58**, 613–634.

120. M. Barbatti, *WIREs Comput. Mol. Sci.*, 2011, **1**, 620–633.

121. D. R. Yarkony, *J. Phys. Chem. A*, 2001, **105**, 6277–6293.

122. J. von Neuman and E. Wigner, *Phys. Zeits.*, 1929, **30**, 467–470.

123. E. Teller, *J. Phys. Chem.*, 1937, **41**, 109–116.

124. J. P. Malhado and J. T. Hynes, *J. Chem. Phys.*, 2016, **145**, 194104.

125. A. Szabo and N. S. Ostlund, *Modern Quantum Chemistry: Introduction to Advanced Electronic Structure Theory*, Dover Publications, New York, United States of America, 1996.

126. B. O. Roos and P. R. Taylor, *Chem. Phys.*, 1980, **48**, 157–173.

127. V. Veryazov, P. Å. Malmqvist, and B. O. Roos, *Int. J. Quantum Chem.*, 2011, **111**, 3329–3338.

128. K. Andersson, P. Å. Malmqvist, B. O. Roos, A. J. Sadlej, and K. Wolinski, *J. Phys. Chem.*, 1990, **94**, 5483–5488.

129. K. Andersson, P. Å. Malmqvist, and B. O. Roos, *J. Chem. Phys.*, 1992, **96**, 1218–1226.

130. J. Finley, P. Å. Malmqvist, B. O. Roos, and L. Serrano-Andrés, *Chem. Phys. Lett.*, 1998, **288**, 299–306.

131. P. Pulay, *Int. J. Quantum Chem.*, 2011, **111**, 3273–3279.

132. M. Schüler, T. Kovar, H. Lischka, R. Shepard, and R. J. Harrison, *Theor. Chim. Acta*, 1993, **84**, 489–509.

133. H. Dachsel, H. Lischka, R. Shepard, J. Nieplocha, and R. J. Harrison, *J. Comput. Chem.*, 1997, **18**, 430–448.

134. H. Dachsel, J. Nieplocha, and R. Harrison, in *SC '98: 1998 ACM/IEEE Conference on Supercomputing*, 1998.

135. K. D. Vogiatzis, D. Ma, J. Olsen, L. Gagliardi, and W. A. De Jong, *J. Chem. Phys.*, 2017, **147**, 184111.

136. M. Barbatti and K. Sen, *Int. J. Quantum Chem.*, 2016, **116**, 762–771.

137. C. Zhu, S. Nangia, A. W. Jasper, and D. G. Truhlar, *J. Chem. Phys.*, 2004, **121**, 7658–7670.

138. C. Zhu, A. W. Jasper, and D. G. Truhlar, *J. Chem. Phys.*, 2004, **120**, 5543–5557.

139. C. Zhu, A. W. Jasper, and D. G. Truhlar, *J. Chem. Theory Comput.*, 2005, **1**, 527–540.

140. J. C. Tully, *J. Chem. Phys.*, 1990, **93**, 1061–1071.

141. S. Hammes-Schiffer and J. C. Tully, *J. Chem. Phys.*, 1994, **101**, 4657–4667.

142. M. Barbatti, What's the Biggest System We Can Do Dynamics? URL: barbatti.org/2017/03/13/whats-the-biggest-system-we-can-do-dynamics/, accessed 20/10/2019.

143. A. V. Titov, I. S. Ufimtsev, N. Luehr, and T. J. Martínez, *J. Chem. Theory Comput.*, 2013, **9**, 213–221.

144. E. G. Hohenstein, M. E. F. Bouduban, C. Song, N. Luehr, I. S. Ufimtsev, and T. J. Martínez, *J. Chem. Phys.*, 2015, **143**, 014111.

145. E. G. Hohenstein, N. Luehr, I. S. Ufimtsev, and T. J. Martínez, *J. Chem. Phys.*, 2015, **142**, 224103.

146. J. W. Snyder, B. F. E. Curchod, and T. J. Martínez, *J. Phys. Chem. Lett.*, 2016, **7**, 2444–2449.

147. C. Song, L.-P. Wang, and T. J. Martínez, *J. Chem. Theory Comput.*, 2016, **12**, 92–106.

148. R. M. Parrish, K. C. Thompson, and T. J. Martínez, *J. Chem. Theory Comput.*, 2018, **14**, 1737–1753.

149. ARCHER kAU Calculator. URL: archer.ac.uk/access/au-calculator/, accessed 27/04/2019.

150. E. Tapavicza, G. D. Bellchambers, J. C. Vincent, and F. Furche, *Phys. Chem. Chem. Phys.*, 2013, **15**, 18336–18348.

151. I. Tavernelli, *Acc. Chem. Res.*, 2015, **48**, 792–800.

152. F. Plasser, R. Crespo-Otero, M. Pederzoli, J. Pittner, H. Lischka, and M. Barbatti, *J.*

Chem. Theory Comput., 2014, **10**, 1395–1405.

153. J. W. Park and T. Shiozaki, *J. Chem. Theory Comput.*, 2017, **13**, 3676–3683.

154. L. Stojanović, S. Bai, J. Nagesh, A. F. Izmaylov, R. Crespo-Otero, H. Lischka, and M. Barbatti, *Molecules*, 2016, **21**, 1603–1617.

155. J. J. Szymczak, M. Barbatti, and H. Lischka, *Int. J. Quantum Chem.*, 2011, **111**, 3307–3315.

156. E. M. Page, D. A. Rice, K. Hagen, L. Hedberg, and K. Hedberg, *Inorg. Chem.*, 1982, **21**, 3280–3283.

157. E. M. Page, D. A. Rice, K. Hagen, L. Hedberg, and K. Hedberg, *Inorg. Chem.*, 1987, **26**, 467–468.

158. E. M. Page, D. A. Rice, K. Hagen, L. Hedberg, and K. Hedberg, *Inorg. Chem.*, 1991, **30**, 4758–4761.

159. K. Aarset, E. M. Page, and D. A. Rice, *J. Phys. Chem. A*, 1999, **103**, 5574–5580.

160. E. Johnsen, A. J. Downs, T. M. Greene, P. F. Souter, K. Aarset, E. M. Page, D. A. Rice, A. N. Richardson, P. T. Brain, D. W. H. Rankin, and C. R. Pulham, *Inorg. Chem.*, 2000, **39**, 719–727.

161. A. J. Downs, T. M. Greene, E. Johnsen, P. T. Brain, C. A. Morrison, S. Parsons, C. R. Pulham, D. W. H. Rankin, K. Aarset, I. M. Mills, E. M. Page, and D. A. Rice, *Inorg. Chem.*, 2001, **40**, 3484–3497.

162. K. Aarset and E. M. Page, *J. Phys. Chem. A*, 2004, **108**, 5474–5478.

163. K. Aarset, E. M. Page, and D. A. Rice, *J. Phys. Chem. A*, 2005, **109**, 4961–4965.

164. K. Aarset, E. M. Page, and D. A. Rice, *J. Phys. Chem. A*, 2006, **110**, 9014–9019.

165. K. Aarset, E. M. Page, and D. A. Rice, *J. Phys. Chem. A*, 2010, **114**, 7187–7190.

166. G. Bačić, C. D. Rankine, J. P. Masuda, D. A. Wann, and S. T. Barry, 2018, chemrXiv.7586459.

167. N. Tesla, *The Inventions, Researches and Writings of Nikola Tesla*, Van Nostrand Reinhold Co., New York, United States of America, 1894.

168. E. Lippert, W. Lüder, F. Moll, W. Nägele, H. Boos, H. Prigge, and I. Seibold-Blankenstein, *Angew. Chemie*, 1961, **73**, 695–706.

169. A. L. Sobolewski and W. Domcke, *Chem. Phys. Lett.*, 1996, **259**, 119–127.

170. A. L. Sobolewski, W. Sudholt, and W. Domcke, *J. Phys. Chem. A*, 1998, **102**, 2716–2722.

171. I. Georgieva, A. J. A. Aquino, F. Plasser, N. Trendafilova, A. Köhn, and H. Lischka, *J. Phys. Chem. A*, 2015, **119**, 6232–6243.

172. M. A. Kochman, A. Tajti, C. A. Morrison, and R. J. D. Miller, *J. Chem. Theory Comput.*, 2015, **11**, 1118–1128.

173. A. B. J. Parusel, G. Köhler, and M. Nooijen, *J. Phys. Chem. A*, 1999, **103**, 4056–4064.

174. L. Du and Z. Lan, *J. Chem. Theory Comput.*, 2015, **11**, 1360–1374.

175. B. F. E. Curchod, A. Sisto, and T. J. Martínez, *J. Phys. Chem. A*, 2017, **121**, 265–276.

176. O. Kajimoto, H. Yokoyama, Y. Ooshima, and Y. Endo, *Chem. Phys. Lett.*, 1991, **179**, 455–459.

177. R. G. Bird, J. L. Neill, V. J. Alstadt, J. W. Young, B. H. Pate, and D. W. Pratt, *J. Phys. Chem. A*, 2011, **115**, 9392–9398.

178. A. Heine, R. Herbst-Irmer, D. Stalke, W. Kühnle, and K. A. Zachariasse, *Acta Crystallogr. B - Struct. Sci.*, 1994, **50**, 363–373.

179. N. W. Mitzel, D. H. Brown, S. Parsons, P. T. Brain, C. R. Pulham, and D. W. H. Rankin, *Angew. Chemie - Int. Ed.*, 1998, **37**, 1670–1672.

180. N. W. Mitzel, C. Lustig, R. J. F. Berger, and N. Runeberg, *Angew. Chemie - Int. Ed.*, 2002, **41**, 2519–2522.

181. N. W. Mitzel, K. Vojinovic, T. Foerster, H. E. Robertson, K. B. Borisenko, and D. W. H. Rankin, *Chem. Eur. J.*, 2005, **11**, 5114–5125.

182. M. Hagemann, R. J. F. Berger, S. A. Hayes, H.-G. Stammler, and N. W. Mitzel, *Chem. Eur. J.*, 2008, **14**, 11027–11038.

183. M. Hagemann, A. Mix, R. J. F. Berger, T. Pape, and N. W. Mitzel, *Inorg. Chem.*, 2008, **47**, 10554–10564.

184. M. J. Frisch, G. W. Trucks, H. B. Schlegel, G. E. Scuseria, M. A. Robb, J. R. Cheeseman, G. Scalmani, V. Barone, G. A. Petersson, H. Nakatsuji, X. Li, M.

Caricato, A. Marenich, J. Bloino, B. G. Janesko, R. Gomperts, B. Mennucci, H. P. Hratchian, J. V. Ortiz, A. F. Izmaylov, J. L. Sonnenberg, D. Williams-Young, F. Ding, F. Lipparini, F. Egidi, J. Goings, B. Peng, A. Petrone, T. Henderson, D. Ranasinghe, V. G. Zakrzewski, J. Gao, N. Rega, G. Zheng, W. Liang, M. Hada, M. Ehara, K. Toyota, R. Fukada, J. Hasegawa, M. Ishida, T. Nakajimi, Y. Honda, O. Kitao, H. Nakai, T. Vreven, K. Throssell, J. A. Montgomery, J. E. Peralta, F. Ogliaro, M. J. Bearpark, J. Heyd, E. Brothers, K. N. Kudin, V. N. Staroverov, T. Keith, R. Kobayashi, J. Normand, K. Raghavachari, A. Rendell, J. C. Burant, S. S. Iyengar, J. Tomasi, M. Cossi, J. M. Millam, M. Klene, C. Adamo, R. Cammi, J. W. Ochterski, R. L. Martin, K. Morokuma, O. Farkas, J. B. Foresman, and D. J. Fox, GAUSSIAN09, Rev. D01, 2016, URL: gaussian.com.

185. S. Grimme, *J. Chem. Phys.*, 2006, **124**, 034108.

186. T. H. Dunning Jr., *J. Chem. Phys.*, 1989, **90**, 1007–1023.

187. A. D. Becke, *J. Chem. Phys.*, 1993, **98**, 5648–5652.

188. C. Lee, W. Yang, and R. G. Parr, *Phys. Rev. B - Condens. Matter Mater. Phys.*, 1988, **37**, 785–789.

189. J. P. Perdew, *Phys. Rev. B - Condens. Matter Mater. Phys.*, 1986, **33**, 8822–8824.

190. J. P. Perdew, J. A. Chevary, K. A. Jackson, M. R. Pederson, D. J. Singh, and C. Fiolhais, *Phys. Rev. B - Condens. Matter Mater. Phys.*, 1992, **46**, 6671–6687.

191. M. Ernzerhof and J. P. Perdew, *J. Chem. Phys.*, 1998, **109**, 3313–3320.

192. J. Heyd and G. E. Scuseria, *J. Chem. Phys.*, 2004, **121**, 1187–1192.

193. J. Heyd and G. E. Scuseria, *J. Chem. Phys.*, 2004, **120**, 7274–7280.

194. J. Heyd, J. E. Peralta, G. E. Scuseria, and R. L. Martin, *J. Chem. Phys.*, 2005, **123**, 174101.

195. J. Heyd, G. E. Scuseria, and M. Ernzerhof, *J. Chem. Phys.*, 2006, **124**, 219906.

196. A. W. Ross, M. Fink, and R. Hilderbrandt, *International Tables for Crystallography*, Kluwer Academic Publishers, Dordrecht, Netherlands, 1992, vol. C.

197. A. Andersson, N. Johansson, P. Bröms, N. Yu, D. Lupo, and W. R. Salaneck, *Adv. Mater.*, 1998, **10**, 859–863.

198. S. M. George, *Chem. Rev.*, 2010, **110**, 111–131.

199. V. S. Stafeeva, A. S. Mitiaev, A. M. Abakumov, A. A. Tsirlin, A. M. Makarevich, and E. V. Antipov, *Polyhedron*, 2007, **26**, 5365–5369.

200. T. Nakajima and K. Hirao, *Chem. Rev.*, 2012, **112**, 385–402.

201. R. Peverati and D. G. Truhlar, *J. Chem. Phys.*, 2011, **135**, 191102.

202. F. E. Jorge, A. Canal Neto, G. G. Camiletti, and S. F. Machado, *J. Chem. Phys.*, 2009, **130**, 064108.

203. C. L. Barros, P. J. P. de Oliveira, F. E. Jorge, A. Canal Neto, and M. Campos, *Mol. Phys.*, 2010, **108**, 1965–1972.

204. C. T. Campos and F. E. Jorge, *Mol. Phys.*, 2013, **111**, 165–171.

205. Y. Zhao and D. G. Truhlar, *Theor. Chem. Acc.*, 2008, **120**, 215–241.

206. R. Peverati and D. G. Truhlar, *J. Phys. Chem. Lett.*, 2011, **2**, 2810–2817.

207. F. Weigend and R. Ahlrichs, *Phys. Chem. Chem. Phys.*, 2005, **7**, 3297–3305.

208. B. A. Smart, L. E. Griffiths, C. R. Pulham, H. E. Robertson, N. W. Mitzel, and D. W. H. Rankin, *Dalton Trans.*, 1997, 1565–1569.

209. N. W. Alcock and V. L. Tracy, *Acta Crystallogr. B - Struct. Sci.*, 1979, **35**, 80–83.

210. M. Schürmann and F. Huber, *Acta Crystallogr. C - Struct. Chem.*, 1994, **50**, 1710–1713.

211. J. P. Bergsma, P. H. Berens, K. R. Wilson, D. R. Fredkin, and E. J. Heller, *J. Phys. Chem.*, 1984, **88**, 612–619.

212. M. Ruckenbauer, S. Mai, P. Marquetand, and L. González, *J. Chem. Phys.*, 2016, **144**, 074303.

213. W. Arbelo-González, R. Crespo-Otero, and M. Barbatti, *J. Chem. Theory Comput.*, 2016, **12**, 5037–5049.

214. H. R. Hudock and T. J. Martínez, *ChemPhysChem*, 2008, **9**, 2486–2490.

215. R. Crespo-Otero, M. Barbatti, H. Yu, N. L. Evans, and S. Ullrich, *ChemPhysChem*, 2011, **12**, 3365–3375.

216. R. Mitrić, U. Werner, and V. Bonačić-Koutecky, *J. Chem. Phys.*, 2008, **129**, 164118.

217. R. Mitrić, J. Petersen, M. Wohlgemuth, U. Werner, V. Bonačić-Koutecky, L. Wöste, and J. Jortner, *J. Phys. Chem. A*, 2011, **115**, 3755–3765.

218. A. Humeniuk, M. Wohlgemuth, T. Suzuki, and R. Mitrić, *J. Chem. Phys.*, 2013, **139**, 134104.

219. D. Polli, P. Altoè, O. Weingart, K. M. Spillane, C. Manzoni, D. Brida, G. Tomasello, G. Orlandi, P. Kukura, R. A. Mathies, M. Garavelli, and G. Cerullo, *Nature*, 2010, **467**, 440–443.

220. F. Salvat, A. Jablonski, and C. J. Powell, *Comput. Phys. Commun.*, 2005, **165**, 157–190.

221. J. H. Lee, T. K. Kim, J. Kim, Q. Kong, M. Cammarata, M. Lorenc, M. Wulff, and H. Ihee, *J. Am. Chem. Soc.*, 2008, **130**, 5834–5835.

222. J. Kim, S. Jun, J. Kim, and H. Ihee, *J. Phys. Chem. A*, 2009, **113**, 11059–11066.

223. H. Thomassen, S. Samdal, and K. Hedberg, *J. Am. Chem. Soc.*, 1992, **114**, 2810–2815.

224. F. Aquilante, J. Autschbach, R. K. Carlson, L. F. Chibotaru, M. G. Delcey, L. De Vico, I. Fdez. Galván, N. Ferré, L. M. Frutos, L. Gagliardi, M. Garavelli, A. Giussani, C. E. Hoyer, G. Li Manni, H. Lischka, D. Ma, P. Å. Malmqvist, T. Müller, A. Nenov, M. Olivucci, T. B. Pedersen, D. Peng, F. Plasser, B. Pritchard, M. Reiher, I. Rivalta, I. Schapiro, J. Segarra-Martí, M. Stenrup, D. G. Truhlar, L. Ungur, A. Valentini, S. Vancoillie, V. Veryazov, V. P. Vysotskiy, O. Weingart, F. Zapata, and R. Lindh, *J. Comput. Chem.*, 2016, **37**, 506–541.

225. G. Igel-Mann, H. Stoll, and H. Preuss, *Mol. Phys.*, 1988, **65**, 1321–1328.

226. A. Bergner, M. Dolg, W. Küchle, H. Stoll, and H. Preuss, *Mol. Phys.*, 1993, **80**, 1431–1441.

227. B. O. Roos, R. Lindh, P. Å. Malmqvist, V. Veryazov, and P. O. Widmark, *J. Phys. Chem. A*, 2004, **108**, 2851–2858.

228. S. Mai, M. Richter, M. Heindl, F. S. J. Menger, A. Atkins, M. Ruckenbauer, F. Plasser, M. Oppel, P. Marquetand, and L. González, SHARC, v1.0, 2018, URL: sharc-md.org.

229. S. Mai, P. Marquetand, and L. González, *WIREs Comput. Mol. Sci.*, 2018, **8**, e1370.

230. M. Richter, P. Marquetand, J. González-Vázquez, I. Sola, and L. González, *J. Chem. Theory Comput.*, 2011, **7**, 1253–1258.

231. W. C. Swope, H. C. Andersen, P. H. Berens, and K. R. Wilson, *J. Chem. Phys.*, 1982, **76**, 637–649.

232. B. F. E. Curchod, A. Sisto, and T. J. Martínez, *J. Phys. Chem. A*, 2017, **121**, 265–276.

233. P. O. Dral, M. Barbatti, and W. Thiel, *J. Phys. Chem. Lett.*, 2018, **9**, 5660–5663.

234. J. M. Thornton, *J. Mol. Biol.*, 1981, **151**, 261–287.

235. C. J. Reed, H. Lewis, E. Trejo, V. Winston, and C. Evilia, *Archaea*, 2013, **2013**, 373275.

236. G. Cacciapuoti, M. Porcelli, C. Bertoldo, M. De Rosa, and V. Zappia, *J. Biol. Chem.*, 1994, **269**, 24762–24769.

237. G. Cacciapuoti, F. Fuccio, L. Petraccone, P. Del Vecchio, and M. Porcelli, *Biochim. Biophys. Acta*, 2012, **1824**, 1136–1143.

238. C. Vieille and G. J. Zeikus, *Microbiol. Mol. Biol. Rev.*, 2001, **65**, 1–43.

239. D. R. Boutz, D. Cascio, J. Whitelegge, L. J. Perry, and T. O. Yeates, *J. Mol. Biol.*, 2007, **368**, 1332–1344.

240. W. Qiu, L. Wang, W. Lu, A. Boechler, D. A. R. Sanders, and D. Zhong, *Proc. Natl. Acad. Sci.*, 2007, **104**, 5366–5371.

241. W. Qiu, T. Li, L. Zhang, Y. Yang, Y.-T. Kao, L. Wang, and D. Zhong, *Chem. Phys.*, 2008, **350**, 154–164.

242. A. B. Stephansen, M. A. B. Larsen, L. B. Klein, and T. I. Sølling, *Chem. Phys.*, 2014, **442**, 77–80.

243. T. R. Ioerger, C. Du, and D. S. Linthicum, *Mol. Immunol.*, 1999, **36**, 373–386.

244. C. E. Crespo-Hernández, B. Cohen, P. M. Hare, and B. Kohler, *Chem. Rev.*, 2004, **104**, 1977–2019.

245. K. Kleinermanns, D. Nachtigallová, and M. S. de Vries, *Int. Rev. Phys. Chem.*, 2013, **32**, 308–342.

246. K. J. Zahnle and J. C. G. Walker, *Rev. Geophys.*, 1982, **20**, 280–292.

247. C. S. Cockell and G. Horneck, *Photochem. Photobiol.*, 2001, **73**, 447–451.

248. P. M. Rao, J. A. Copeck, and A. R. Knight, *Can. J. Chem.*, 1967, **45**, 1369–1374.

249. K. Sayamol and A. R. Knight, *Can. J. Chem.*, 1968, **46**, 999–1003.

250. A. B. Callear and D. R. Dickson, *Trans. Faraday Soc.*, 1970, **66**, 1987–1995.

251. S. Nourbakhsh, C. L. Liao, and C. Y. Ng, *J. Chem. Phys.*, 1990, **22**, 6587–6593.

252. C. W. Bookwalter, D. L. Zoller, P. L. Ross, and M. V. Johnston, *J. Am. Soc. Mass Spectrom.*, 1995, **6**, 872–876.

253. C. Luo, W. N. Du, X. M. Duan, J. Y. Liu, and Z. S. Li, *Chem. Phys. Lett.*, 2009, **469**, 242–246.

254. C. D. Rankine, J. P. F. Nunes, M. S. Robinson, P. D. Lane, and D. A. Wann, *Phys. Chem. Chem. Phys.*, 2016, **18**, 27170–27174.

255. A. B. Stephansen, R. Y. Brogaard, T. S. Kuhlman, L. B. Klein, J. B. Christensen, and T. I. Sølling, *J. Am. Chem. Soc.*, 2012, **134**, 20279–20281.

256. T. S. Kuhlman, Ph.D. Thesis, Technical University of Denmark, 2013.

257. T. I. Sølling, T. S. Kuhlman, A. B. Stephansen, L. B. Klein, and K. B. Møller, *ChemPhysChem*, 2014, **15**, 249–259.

258. J. M. Matxain, J. M. Asua, and F. Ruipérez, *Phys. Chem. Chem. Phys.*, 2016, **18**, 1758–1770.

259. M. O. Andreae and H. Raemdonck, *Science*, 1983, **221**, 744–747.

260. A. B. Stephansen, R. Y. Brogaard, T. S. Kuhlman, L. B. Klein, J. B. Christensen, and T. I. Sølling, *J. Am. Chem. Soc.*, 2012, **134**, 20279–20281.

261. R. Singh and G. M. Whitesides, *J. Am. Chem. Soc.*, 1990, **112**, 6304–6309.

262. O. G. Lowe, *J. Org. Chem.*, 1975, 2096–2098.

263. H. Lischka, R. Shepard, I. Shavitt, R. M. Pitzer, M. Dallos, T. Müller, P. G. Szalay, F. B. Brown, R. Ahlrichs, H. J. Böhm, A. Chang, D. C. Comeau, R. Gdanitz, H. Dachsel, C. Ehrhardt, M. Ernzerhof, P. Höchtl, S. Irle, G. Kedziora, T. Kovar, V. Parasuk, M. J. M. Pepper, P. Scharf, H. Schiffer, M. Schindler, M. Schüler, M. Seth, E. A. Stahlberg, J. G. Zhao, S. Yabushita, Z. Zhang, M. Barbatti, S. Matsika, M. Schuurman, D. R. Yarkony, S. R. Brozell, E. V. Beck, J. P. Blaudeau, M. Ruckenbauer, B. Sellner, F. Plasser, and J. J. Szymczak, COLUMBUS, v7.0, 2015, URL: univie.ac.at/columbus.

264. H. Lischka, R. Shepard, R. M. Pitzer, I. Shavitt, M. Dallos, T. Müller, P. G. Szalay,

M. Seth, G. S. Kedziora, S. Yabushita, and Z. Zhang, *Phys. Chem. Chem. Phys.*, 2001, **3**, 664–673.

265. H. Lischka, T. Müller, P. G. Szalay, I. Shavitt, R. M. Pitzer, and R. Shepard, *WIREs Comput. Mol. Sci.*, 2011, **1**, 191–199.

266. L. Meissner, *Chem. Phys. Lett.*, 1988, **146**, 204–210.

267. M. Barbatti, G. Granucci, M. Ruckenbauer, F. Plasser, R. Crespo-Otero, J. Pittner, M. Persico, and H. Lischka, NEWTON-X, v2.0, 2016, URL: newtonx.org.

268. M. Barbatti, M. Ruckenbauer, F. Plasser, J. Pittner, G. Granucci, M. Persico, and H. Lischka, *WIREs Comput. Mol. Sci.*, 2014, **4**, 26–33.

269. R. Shepard, *Int. J. Quantum Chem.*, 1987, **31**, 33–44.

270. R. Shepard, H. Lischka, P. G. Szalay, T. Kovar, and M. Ernzerhof, *J. Chem. Phys.*, 1992, **96**, 2085–2098.

271. H. Lischka, M. Dallos, and R. Shepard, *Mol. Phys.*, 2002, **100**, 1647–1658.

272. H. Lischka, M. Dallos, P. G. Szalay, D. R. Yarkony, and R. Shepard, *J. Chem. Phys.*, 2004, **120**, 7322–7329.

273. M. Dallos, H. Lischka, R. Shepard, D. R. Yarkony, and P. G. Szalay, *J. Chem. Phys.*, 2004, **120**, 7330–7339.

274. M. Barbatti, A. J. A. Aquino, and H. Lischka, *Phys. Chem. Chem. Phys.*, 2010, **12**, 4959–4967.

275. R. J. F. Berger, Personal Communication, 2017.

276. P. S. Engel, V. B. Gudimetla, J. S. Gancheff, and P. A. Denis, *J. Phys. Chem. A*, 2012, **116**, 8345–8351.

277. M. A. B. Larsen, A. B. Skov, C. M. Clausen, J. Ruddock, B. Stankus, P. M. Weber, and T. I. Sølling, *ChemPhysChem*, 2018, **19**, 2829–2834.

278. N. Hoffmann, *Chem. Rev.*, 2008, **108**, 1052–1103.

279. S. Samanta, T. M. McCormick, S. K. Schmidt, D. S. Seferos, and G. A. Woolley, *Chem. Commun.*, 2013, **49**, 10314–10316.

280. M. Dong, A. Babalhavaeji, S. Samanta, A. A. Beharry, and G. A. Woolley, *Acc. Chem. Res.*, 2015, **48**, 2662–2670.

281. W. J. Glover, T. Mori, M. S. Schuurman, A. E. Boguslavskiy, O. Schalk, A. Stolow, and T. J. Martínez, *J. Chem. Phys.*, 2018, **148**, 164303.

282. J. Quenneville and T. J. Martínez, *J. Phys. Chem. A*, 2003, **107**, 829–837.

283. C. Angeli, *J. Comput. Chem.*, 2008, **30**, 1319–1333.

284. H. Tao, T. K. Allison, T. W. Wright, A. M. Stooke, C. Khurmi, J. Van Tilborg, Y. Liu, R. W. Falcone, A. Belkacem, and T. J. Martínez, *J. Chem. Phys.*, 2011, **134**, 244306.

285. T. Mori, W. J. Glover, M. S. Schuurman, and T. J. Martínez, *J. Phys. Chem. A*, 2012, **116**, 2808–2818.

286. B. Sellner, M. Barbatti, T. Müller, W. Domcke, and H. Lischka, *Mol. Phys.*, 2013, **111**, 2439–2450.

287. V. Molina, M. Merchán, and B. O. Roos, *J. Phys. Chem. A*, 1997, **101**, 3478–3487.

288. L. Gagliardi, G. Orlandi, V. Molina, P. Å. Malmqvist, and B. Roos, *J. Phys. Chem. A*, 2002, **106**, 7355–7361.

289. M. Pederzoli, J. Pittner, M. Barbatti, and H. Lischka, *J. Phys. Chem. A*, 2011, **115**, 11136–11143.

290. A. Muždalo, P. Saalfrank, J. Vreede, and M. Santer, *J. Chem. Theory Comput.*, 2018, **14**, 2042–2051.

291. R. W. Schoenlein, L. A. Peteanu, R. A. Mathies, and C. V. Shank, *Science*, 1991, **254**, 412–415.

292. J. J. Szymczak, M. Barbatti, and H. Lischka, *J. Phys. Chem. A*, 2009, **113**, 11907–11918.

293. M. Ruckenbauer, M. Barbatti, T. Müller, and H. Lischka, *J. Phys. Chem. A*, 2013, **117**, 2790–2799.

294. J. W. Park and T. Shiozaki, *Mol. Phys.*, 2018, **116**, 2583–2590.

295. J. F. Kasting, *Science*, 1993, **259**, 920–926.

296. F. Raulin, C. Brassé, O. Poch, and P. Coll, *Chem. Soc. Rev.*, 2012, **41**, 5380–5393.

297. M. L. Cable, S. M. Hörst, R. Hodyss, P. M. Beauchamp, M. A. Smith, and P. A. Willis, *Chem. Rev.*, 2012, **112**, 1882–1909.

298. F. Raulin and T. Owen, *Space Sci. Rev.*, 2002, **104**, 377–394.

299. A. Coustenis, A. Salama, B. Schulz, S. Ott, E. Lellouch, T. Encrenaz, D. Gautier, and H. Feuchtgruber, *Icarus*, 2003, **161**, 383–403.

300. A. Coustenis, R. K. Achterberg, B. J. Conrath, D. E. Jennings, A. Marten, D. Gautier, C. A. Nixon, F. M. Flasar, N. A. Teanby, B. Bézard, R. E. Samuelson, R. C. Carlson, E. Lellouch, G. L. Bjoraker, P. N. Romani, F. W. Taylor, P. G. J. Irwin, T. Fouchet, A. Hubert, G. S. Orton, V. G. Kunde, S. Vinatier, J. Mondellini, M. M. Abbas, and R. Courtin, *Icarus*, 2007, **189**, 35–62.

301. A. Coustenis, D. E. Jennings, C. A. Nixon, R. K. Achterberg, P. Lavvas, S. Vinatier, N. A. Teanby, G. L. Bjoraker, R. C. Carlson, L. Piani, G. Bampasidis, F. M. Flasar, and P. N. Romani, *Icarus*, 2010, **207**, 461–476.

302. J. C. Loison, E. Hébrard, M. Dobrijevic, K. M. Hickson, F. Caralp, V. Hue, G. Gronoff, O. Venot, and Y. Bénilan, *Icarus*, 2015, **247**, 218–247.

303. D. N. Mehta-Hurt, J. A. Korn, P. Navotnaya, A. P. Parobek, R. M. Clayton, and T. S. Zwier, *J. Chem. Phys.*, 2015, **143**, 074304.

304. V. A. Krasnopolsky, *Icarus*, 2009, **201**, 226–256.

305. D. S. N. Parker, R. I. Kaiser, O. Kostko, T. P. Troy, M. Ahmed, A. M. Mebel, and A. G. G. M. Tielens, *Astrophys. J.*, 2015, **803**, 53–63.

306. J. C. Cochran, K. Hagen, G. Paulen, Q. Shen, S. Tom, M. Traetteberg, and C. Wells, *J. Mol. Struct.*, 1997, **413**, 313–326.

307. N. Yasuda, H. Uekusa, and Y. Ohashi, *Acta Crystallogr. E - Struct. Rep. Online*, 2001, **57**, 1189–1190.

308. R. Ahlrichs, M. Bär, M. Häser, H. Horn, C. Kölmel, *Chem. Phys. Lett.*, 1989, **162**, 165–169.

309. C. Hättig and F. Weigend, *J. Chem. Phys.*, 2000, **113**, 5154–5161.

310. C. Hättig and A. Köhn, *J. Chem. Phys.*, 2002, **117**, 6939–6951.

311. C. Hättig, *J. Chem. Phys.*, 2003, **118**, 7751–7761.

312. A. Köhn and C. Hättig, *J. Chem. Phys.*, 2003, **119**, 5021–5036.

313. B. G. Levine, J. D. Coe, and T. J. Martínez, *J. Phys. Chem. B*, 2008, **112**, 405–413.

314. R. Szabla, R. W. Góra, and J. Šponer, *Phys. Chem. Chem. Phys.*, 2016, **18**, 20208–20218.

315. R. Szabla, Personal Communication, 2018.

316. M. J. Bearpark, M. Olivucci, S. Wilsey, F. Bernardi, M. A. Robb, and G. Ciamician, *J. Am. Chem. Soc.*, 1995, **117**, 6944–6953.

317. V. Molina, M. Merchán, B. O. Roos, and P. Malmqvist, *Phys. Chem. Chem. Phys.*, 2000, **2**, 2211–2217.

318. Y. Amatatsu, *Chem. Phys. Lett.*, 2001, **344**, 200–206.

319. Y. Amatatsu, *J. Comput. Chem.*, 2002, **23**, 928–937.

320. Y. Amatatsu, *J. Comput. Chem.*, 2002, **23**, 950–956.

321. D. Cremer and J. A. Pople, *J. Am. Chem. Soc.*, 1975, **97**, 1354–1358.

322. A. D. G. Nunn, R. S. Minns, R. Spesyvtsev, M. J. Bearpark, M. A. Robb, and H. H. Fielding, *Phys. Chem. Chem. Phys.*, 2010, **12**, 15751–15759.

323. M. Sala, O. M. Kirkby, S. Guérin, and H. H. Fielding, *Phys. Chem. Chem. Phys.*, 2014, **16**, 3122–33.

324. A. Dreuw and M. Wormit, *WIREs Comput. Mol. Sci.*, 2015, **5**, 82–95.

325. J. H. Starcke, M. Wormit, J. Schirmer, and A. Dreuw, *Chem. Phys.*, 2006, **329**, 39–49.

326. P. H. P. Harbach, M. Wormit, and A. Dreuw, *J. Chem. Phys.*, 2014, **141**, 064113.

327. J. W. Snyder, R. M. Parrish, and T. J. Martínez, *J. Phys. Chem. Lett.*, 2017, **8**, 2432–2437.

328. Swagelok SS-2MA-MH. URL: swagelok.com/en/catalog/Product/Detail?part=SS-2MA-MH, accessed 29/08/2018.

329. Swagelok SS-31RS4-G. URL: swagelok.com/en/catalog/Product/Detail?part=SS-31RS4-G, accessed 29/08/2018.

330. Nvidia CUDA Zone. URL: developer.nvidia.com/cuda-zone, accessed 15/03/2019.

331. Nvidia Titan V. URL: nvidia.com/en-gb/titan/titan-v/, accessed 15/03/2019.

332. M. Mann, M. Petiau, and J. Fabian, *J. Mol. Model.*, 2000, **6**, 177–185.

333. J. Cao and D. C. Chen, *Phys. Chem. Chem. Phys.*, 2019, **21**, 4176–4183.

334. N. Kano, M. Yamamura, and T. Kawashima, *Dalton Trans.*, 2015, **44**, 16256–16265.

335. J. P. F. Nunes, Personal Communication, 2019.